Deformation, Dynamics, and Interactions of Soft Particles in Fluid Flow

Dmitry A. Fedosov
Institute of Complex Systems
Forschungszentrum Jülich

Habilitationsschrift
vorgelegt der Mathematisch-Naturwissenschaftlichen Fakultät
der Universität zu Köln
Köln, Oktober 2015

Contents

List of enclosed publications

1. **Microvascular blood flow resistance: role of red blood cell migration and dispersion**
   D. Katanov, G. Gompper, and D. A. Fedosov
   Microvascular Research, **99**:57-66, 2015.
2. **Dense brushes of stiff polymers or filaments in fluid flow**
   F. Römer and D. A. Fedosov
   Europhysics Letters, **109**:68001, 2015.
3. **Smoothed dissipative particle dynamics with angular momentum conservation**
   K. Müller, D. A. Fedosov, and G. Gompper
   Journal of Computational Physics, **281**:301-315, 2015.
4. [*] **Dynamical and rheological properties of soft colloid suspensions**
   R. G. Winkler, D. A. Fedosov, and G. Gompper
   Current Opinion in Colloid & Interface Science, **19**:594-610, 2014.
5. **Margination of micro- and nano-particles in blood flow and its effect on drug delivery**
   K. Müller, D. A. Fedosov, and G. Gompper
   Scientific Reports, **4**:4871, 2014.
6. **Deformation and dynamics of red blood cells in flow through cylindrical microchannels**
   D. A. Fedosov, M. Peltomäki, and G. Gompper
   Soft Matter, **10**:4258-4267, 2014.
7. **White blood cell margination in microcirculation**
   D. A. Fedosov and G. Gompper
   Soft Matter, **10**:2961-2970, 2014.
8. [*] **Computational biorheology of human blood flow in health and disease**
   D. A. Fedosov, M. Dao, G. E. Karniadakis, and S. Suresh
   Annals of Biomedical Engineering, **42**:368-387, 2014.
9. [*] **Multiscale modeling of blood flow: from single cells to blood rheology**
   D. A. Fedosov, H. Noguchi, and G. Gompper
   Biomechanics and Modeling in Mechanobiology, **13**:239-258, 2014.
10. **Conformational and dynamical properties of ultra-soft colloids in semi-dilute solutions under shear flow**
    S. P. Singh, D. A. Fedosov, A. Chatterji, R. G. Winkler, and G. Gompper
    Journal of Physics: Condensed Matter, **24**:464103, 2012.
11. **Semi-dilute solutions of ultra-soft colloids under shear flow**
    D. A. Fedosov, S. P. Singh, A. Chatterji, R. G. Winkler, and G. Gompper
    Soft matter, **8**:4109-4120, 2012.
12. **Margination of white blood cells in microcapillary flow**
    D. A. Fedosov, J. Fornleitner, and G. Gompper
    Physical Review Letters, **108**:028104, 2012.
13. **Predicting human blood viscosity in silico**
    D. A. Fedosov, W. Pan, B. Caswell, G. Gompper, and G. E. Karniadakis
    Proceedings of the National Academy of Sciences USA, **108**:11772-11777, 2011.

---

[*] Review articles

1 Introduction

Fluids, which correspond to suspensions of various solid and deformable particles, have long become part of our daily life. Examples include different foods, biofluids, cosmetics and hygiene products, and liquids used in a variety of technological devices and processes. Such liquids are very attractive because their properties (e.g., fluidity, lubrication, biofunctionality) are very versatile and can be tuned and controlled over a very wide range of material characteristics. In addition, the properties of such suspensions are often very sensitive to the surrounding conditions such as temperature, pressure, and external confinement. This motivates considerable research efforts directed to understand and control the structure and rheology of various particle suspensions.

One of the first theoretical investigations of the rheological properties of colloidal suspensions [1] has been performed by Albert Einstein more than a hundred years ago. In that classical paper [1], the dependence of the viscosity η of a hard-sphere suspension on the volume fraction ϕ has been predicted as

$$\eta = \eta_s \left[1 + 2.5\phi + \mathcal{O}(\phi^2)\right] , \tag{1}$$

where η_s is the solvent viscosity. This result describes the suspension viscosity to leading order in ϕ or equivalently in the regime $\phi \lesssim 0.1$. Furthermore, this approximation appears to be useful not only in case of rigid particles, but also for flexible particles such as linear- and star-polymers [2, 3, 4, 5] in the regime of small deformations or when the polymers remain in a near-spherical coiled configuration. In this case, an effective particle size through the so-called "hydrodynamic radius" can be defined in order to determine the volume fraction [4, 5].

The example above demonstrates that there exist some similarities between suspensions of rigid colloids and of deformable particles. However, it is clear that particle deformability introduces another important characteristic, making the behavior of such particles and the rheological properties of their suspensions to be much richer than their hard counterparts [6]. This creates additional challenges for the elucidation of their behavior in various suspensions; however, it also provides new opportunities and directions for the application of such materials, since their properties can be tuned over a wide range.

Soft-colloid suspensions with different rheological properties are utilized more and more in a wide range of applications. Perhaps, the most prominent example is polymer suspensions, which are part of many technological processes in rubber, plastic, textile, and automobile industries. There exist suspensions of linear and branched polymers, melts, and other complex compositions. This class of materials has been receiving considerable attention experimentally [7, 8, 9] and theoretically [10, 11, 12, 5] with a number of interesting developments in recent years. Suspensions of linear polymers have been investigated in great detail [10, 11, 5]. For instance, the macroscopic rheological properties of a suspension have been shown to directly correlate with the orientation and elongation of single polymer chains [13, 14, 15]. Currently, polymers with a more complex architecture such as star polymers, dendrimers, and hyperbranched polymers receive significant attention [3, 5]. In particular, their dynamics and deformation in flow is of interest in order to associate their behavior with the rheological properties of a suspension.

Another class of soft objects includes suspensions of vesicles, capsules, and cells. Vesicles and capsules are very interesting for a number of technological applications such as, for instance, carriers for drug delivery. On the other hand, such systems often serve as good model systems for suspensions of cells with the advantage that their properties can be rather well controlled, which can be challenging for biological cells. Vesicles and capsules consist of a membrane, which encloses a certain volume of fluid or fluid mixture. Hence, the properties of a membrane (e.g., elasticity, bending, viscosity) and the enclosed fluid are very important for determining the dynamics and deformation of vesicles and capsules. Suspensions of cells are mainly part of the biophysical and biomedical fields with a number of useful applications. One of the examples of such suspensions is blood, which consists primarily of deformable red blood cells (RBCs). The deformability of RBCs enables them to pass through the tiny vessels of the microvascular network, which might be impaired in several diseases such as malaria and sickle-cell anemia due to the stiffening of RBCs [16, 17]. Apart from RBCs, there also exist many other cells subjected to fluid flow with the examples of white blood cells (WBCs), platelets, and circulating tumor cells. In addition to the membrane properties, these cells also possess an inner cytoskeleton, making such cells viscoelastic. Different cells have distinct shapes, types of membrane and/or cytoskeletal elasticity, and therefore yield different rheological properties.

From the rheological point of view it is interesting to understand the relation between the macroscopic properties of a suspension and its micro-structure and the behavior of single soft particles. The suspension's micro-structure is governed by the dynamics and deformation of suspended particles in flow and their interactions. For example, changes in the viscosity of a suspension in response to shear flow (e.g., shear-thinning) can be associated with a change in the conformation or orientation of soft particles. Another large area, where the behavior of soft particles in flow is of great interest, is in the biomedical field and related to the sorting and detection of various particles within a suspension. The applications include the analysis of biosamples, detection of rare components, and their purification. The ability to sort and detect certain components based on their mechanical properties has a strong potential, because the mechanics of many cells is strongly correlated with their physical properties in the healthy or diseased state [16, 18].

The short overview of soft-particle suspensions above suggests a number of questions about the importance of shape and deformability of soft particles for their behavior in fluid flow and for the rheological response of their suspensions. Such questions can be for instance:

- Under what conditions does a simple theoretical description for hard spheres to describe soft-particle suspensions remain appropriate?
- Is such a description useful for high concentrations and when does it break down?
- Which similarities exist between different soft-colloid classes and when does the physical origin of their softness become important?
- How can the dependence of viscosity on the elastic moduli of the soft colloids, their viscous properties, and inter-colloid interactions be described?
- What is the role of shape, and how does the interplay between shape and deformability determine the rheological properties of a suspension?
- Can we devise an accurate enough description of certain systems in order to create a knowledge-based design for the applications of interest?

- How will mixtures of various soft colloids behave?
- ...

In order to establish a relation between the behavior of soft colloids in flow and their macroscopic rheological properties, an understanding of their non-equilibrium properties on the level of single particles is required. This task is often very difficult to achieve in experiments, and therefore, computer simulations provide a promising tool for insight into the dynamics of soft particles within artificial and biological fluids. The behavior of soft materials is not always governed by their atomic or molecular structure, and can emerge from physical arrangements at the mesoscopic level. Therefore, simulations of soft materials often require a multiscale resolution of physical phenomena which occur at the mesoscale. Moreover, a detailed atomistic representation becomes intractable due to the computational cost, since the investigation of many soft matter systems requires modeling on the scale of micrometers with the time scale of several seconds or even minutes. On the other hand, continuum methods may not capture important physical structures at the mesoscale due to the continuum assumption, and therefore, are often not suitable for the description of such systems. This has motivated the development of novel mesoscale simulation approaches in the recent years, which can capture relevant physics at the mesoscale and provide a detailed understanding of the behavior and interactions of soft particles in flow.

In this thesis, we review several mesoscopic approaches, which will be primarily applied to polymer solutions and blood flow. We will show how these methods can be applied to devise new scaling concepts for star-polymer solutions and to understand certain processes in microvascular blood flow. In particular, we will focus on the several specific problems including:

- **Rheology of star-polymer solutions**

  Star polymers can be thought of as soft colloids whose softness can be tuned by the number of arms attached to a common center. Thus, a star polymer with two arms corresponds to a linear polymer, while as the number of arms increases we approach a rigid colloidal particle. Star-polymer rheological properties are investigated for different functionalities, concentrations, and shear rates of flow. The rheological properties, characterized by the shear viscosity and the normal-stress coefficients, exhibit a universal behavior as function of a concentration-dependent Weissenberg number for various concentrations at a given arm length. In dilute solution, the zero-shear viscosity follows the Einstein relation (Eq. (1)) with an effective radius given by the hydrodynamic radius of a star polymer.

  Related publications: P10, P11, and P4.

- **Dense brushes of stiff polymers in fluid flow**

  Dense filamentous brush-like structures are common for many biological interfacial systems (e.g., glycocalyx layer in blood vessels) regulating the surface softness. We have developed a theoretical model which captures flow-induced deformation of a dense brush of stiff polymers and is validated by detailed mesoscopic simulations. Different contributions to brush deformation including hydrodynamic friction due to flow and steric excluded-volume interactions between grafted filaments are identified.

Related publications: P2.

- **Motion of single RBCs in tube flow**

  The motion of RBCs in the microvasculature is important for blood flow resistance and the cell partitioning within a microcirculation. We use mesoscale simulations to predict the phase diagram of shapes and dynamics of RBCs in cylindrical microchannels. The effect of different RBC states on the flow resistance, and the influence of RBC properties on the shape diagram are identified and discussed.

  Related publications: P6 and P9.

- **Development of blood flow in idealized vessels**

  Blood flow resistance in microcirculation has a strong impact on tissue perfusion. The flow resistance in a microvasculature is determined by the flow behavior of blood through the complex network of vessels. We investigate the development of blood flow and its resistance starting from a dispersed configuration of RBCs. We find the development of a cell-free layer, which forms near the vessel wall, to be nearly universal when scaled with a characteristic shear rate of the flow. The universality allows an estimation of the length of a vessel required for full flow development. We also develop a simple theoretical model which is able to describe the converged cell-free-layer thickness through the balance between a lift force on RBCs due to cell-wall hydrodynamic interactions and shear-induced effective pressure due to cell-cell interactions in flow.

  Related publications: P1, P8, and P9.

- **Blood rheology**

  The viscosity of blood serves as an indicator in the understanding and treatment of disease. We simulate blood rheology and analyze its non-Newtonian behavior relating it to the suspension's microstructure, deformation and dynamics of single RBCs. We also provide the first quantitative estimates of the magnitude of adhesive forces between RBCs. The models can easily be adapted to tune the properties of a much wider class of complex fluids including capsule and vesicle suspensions.

  Related publications: P13, P8, P9, and P4.

- **Margination of WBCs and micro- and nano-carriers in blood flow**

  Proper functioning of WBCs and drug carriers is not possible without their ability to adhere to vessel walls. In order to facilitate the adhesion, WBCs or micro- and nano-particles have to migrate toward the vessel walls in blood flow through a process called margination. We employ mesoscopic hydrodynamics simulations to better understand the margination process and to elucidate its dependence on various properties including hematocrit, flow rate, particle size and deformability. This study provides a comprehensive picture of particle margination in blood flow.

  Related publications: P5, P7, and P12.

Even though we discuss a limited number of different examples of soft particles under flow, such models are general enough and can be used to model not only the suspensions we illustrate, but also suspensions of polymers with much more complex structures, capsules, vesicles, and their various mixtures. Such mesoscopic models establish an indispensable tool for the investigation of various soft-particle suspensions leading to new insights into their behavior and rheology. These are often the first steps towards an understanding of the dynamics of single suspended components in relation to the macroscopic properties of such a suspension, leading to the theoretical basis for these types of soft systems.

This thesis is cumulative and organized as follows. Next, the basics of blood flow and polymer solutions are reviewed. In Sec. 2, we review the methodology, including several mesoscopic simulation techniques and models for RBCs and polymers. Section 3 presents shortly the results for the specific topics outlined above. In Sec. 4, we briefly summarize the results for soft particles in fluid flow and outline a number of future directions and ongoing projects. After that a number of published papers related to the presented results are included. Finally, we include a comprehensive list of references which can be useful for a scientist working in similar and related research fields.

1.1 Polymer architecture, dynamics, and rheology

Polymers are molecules consisting of a large number of repeating units or monomers. When the units are connected into a single sequence, the polymer is called linear. The number of subunits can range from several monomers to millions of repeating units. There exist a number of synthetic polymers such as polystyrene and polyethylene as well as biopolymers such as DNA and various proteins. Polymer suspensions and melts play an important role in different technologies, and are used, for instance, in various liquid products, plastics, and rubbers. Different polymer materials possess distinct properties in their tensile strength, melting point, mixing behavior, and chemical and optical characteristics. Therefore, there exist numerous examples of polymeric materials whose rheological properties are extremely versatile.

From the physical point of view, there is often no need to know the chemical details of single monomers, because the emerging material properties on large enough length scales are governed solely by the length of polymers and the size of their monomers. This is the main assumption in polymer physics, where various polymer models have been developed [19, 20, 12]. These include various scaling concepts for polymer structural and dynamical properties (e.g., Rouse and Zimm models) [19, 20, 12]. A simple polymer model in statistical physics is a random walk or a self-avoiding random walk, while in simulations a linear-polymer model is represented by a bead-spring chain. There are efforts to develop more sophisticated theoretical models; however, their advantage over the classical models is not very significant so far.

The new developments in chemistry allow to create much more sophisticated polymer structures. As an example, star polymers correspond to polymer structures, where a number of linear chains are connected to a common center. Thus, by changing the arm length (or the length of attached linear polymers) and the functionality (i.e., the number of attached polymers), star-polymer properties can be varied between linear polymers (for the functionality 2) to nearly hard-sphere colloids (large functionality, short arms) and ultra-soft colloids (intermediate functionality, long arms) [21, 22, 23]. Other examples include branched, ring, and dendrimer-like polymers [3]. Such polymers can be constructed from similar linear chains as well as from a number of distinct chains leading to very complex compositions. Theoretical models for polymers with complex structures have yet to be developed, and currently such systems are mainly investigated experimentally and in simulations.

Polymer suspensions are generally divided into several classes including dilute and semi-dilute solutions and melts. Dilute solutions correspond to the suspensions where inter-polymer interactions are not very significant. This condition is usually defined by an overlap concentration corresponding to a critical polymer concentration at which polymers start to overlap. Thus, a polymer solution is considered to be dilute below the overlap concentration, while above this concentration the polymer solution is in a semi-dilute regime. In contrast to polymer solutions, polymer melts have little or no suspending fluid and are almost entirely formed by polymer molecules.

Rheological properties of polymer suspensions and melts have been studied in a large number of investigations including experiments [7, 9, 8], theory [10, 11, 12], and simulations [12, 24, 25]. The rheology of polymer systems can be considered for a number of different flow conditions such as steady and oscillatory shear flows and extensional flow. For example, in a steady shear setup, the viscosity of a suspension as a function of applied shear rate is measured, while in the oscillatory shear flow, viscoelastic properties of polymer suspensions characterized by the complex modulus are obtained. Polymer suspensions under steady-shear flow often show a shear-thinning behavior such that their viscosity decreases as the shear rate of flow is increased. At low shear rates, such suspensions also yield a constant viscosity plateau, which is called the Newtonian plateau. The change in suspension's viscosity can be correlated with the changes in polymer confirmation and dynamics in flow. Thus, the polymers stretch along the shear-flow direction, get compressed along the orthogonal directions, and exhibit a preferred orientation with respect to the flow [26, 15, 27]. In addition, the polymers in shear flow exhibit tumbling dynamics characterized by their periodic stretching and collapse [26, 15, 27]. These changes in polymer confirmation and dynamics lead to a reduction of internal friction in polymeric systems and to the shear-thinning behavior.

1.2 Blood cells and blood flow

The cardiovascular system is a closed circuit which can be divided into three major sections: the heart, large vessels, and the microcirculation. The main function of the heart and large vessels is to maintain continuous blood flow within the vessel network, while blood flow in the microcirculation plays a profound role in various physiological processes [28, 29, 30, 31] and pathologies [32, 33, 34] in the organism. Main functions of blood are the transport of oxygen and nutrients to cells of the body, removal of waste products such as carbon dioxide and urea, and circulation of molecules and cells which mediate the organism's defense and immune response and play a fundamental role in the tissue repair process. The microcirculation (or microvascular network) [28, 30, 31] is comprised of the smallest vessels (e.g., arterioles, capillaries, venules) with diameters up to about 100 μm. Typically, the microcirculation geometry resembles a tree-like structure following the route of blood passing through arterioles, capillaries, and venules. Blood flow in microcirculation is extremely complex and diverse with dramatic changes in flow rates and patterns. This complexity is attributed to non-trivial vessel geometries and blood rheological properties [28, 29, 35, 36] which depend on blood-cell mechanical characteristics, aggregation interactions, local hematocrit (RBC volume fraction), and flow conditions.

Abnormal blood flow is often correlated with a broad range of disorders and diseases which include hypertension, anemia, atherosclerosis, malaria, and thrombosis [16, 17]. Understanding the rheological properties and dynamics of blood cells and blood flow is crucial for many biomedical and bioengineering applications. Examples include the development of blood substitutes, the design of blood flow assisting devices, and drug delivery. In addition, understanding the vital blood related processes in health and disease may aid in the development of new effective treatments.

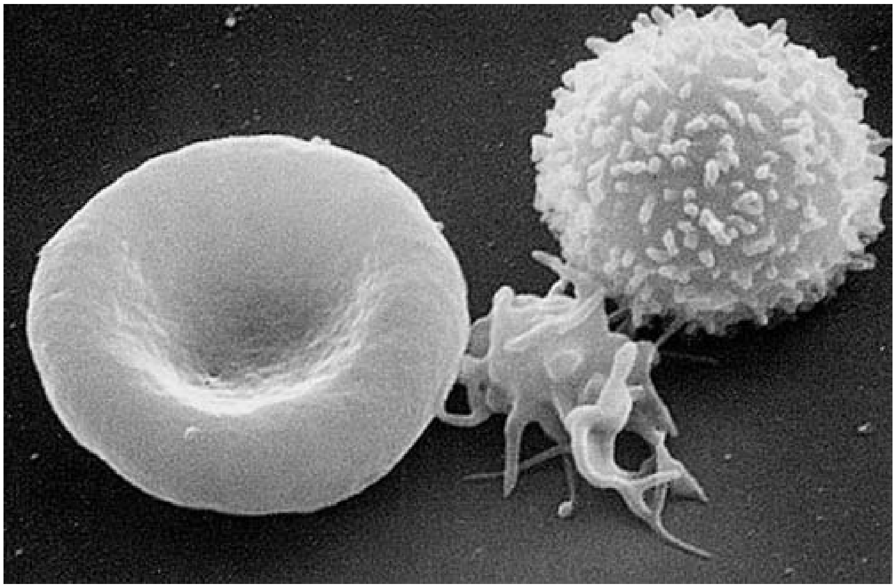

Figure 1: A scanning electron micrograph of blood cells. From left to right: human erythrocyte, thrombocyte (platelet), leukocyte. Source: Electron Microscopy Facility at The National Cancer Institute at Frederick (NCI-Frederick).

Blood consists of erythrocytes or RBCs, leukocytes or WBCs, thrombocytes or platelets, and plasma containing various proteins, molecules, and ions. Figure 1 shows a scanning electron micrograph of blood cells. RBCs constitute approximately 45% of the total blood volume, WBCs around 0.7%, and the rest is taken up by blood plasma and its substances. One microliter of blood contains about 5 million RBCs, roughly 5 thousand WBCs, and approximately a quarter million platelets.

Human RBCs have a relatively simple structure in comparison to other eukaryotic cells [37]. RBCs resemble biconcave disks with an average diameter of approximately 8 μm and contain a viscous cytosol enclosed by a membrane. At the stage of the RBC formation, the nucleus and other organelles that are generally present in other eukaryotic cells are ejected, leaving behind a relatively homogeneous cytoplasm and no inner cytoskeleton. RBC cytoplasm is a hemoglobin-rich solution, which is able to bind oxygen. Therefore, the main RBC function is oxygen supply and delivery to body tissues. The RBC membrane consists of a lipid bilayer with an attached network of the spectrin proteins linked by short filaments of actin. The lipid bilayer is considered to be a nearly viscous and area preserving membrane [37], while the RBC's elasticity is attributed to the attached spectrin network, as is the integrity of the entire RBC when subjected to severe deformations in the capillaries as small as 3 μm. The cytosol viscosity is about 5-6 times larger than that of blood plasma under physiological conditions. Mechanical and rheological characteristics of RBCs and their dynamics are governed by: membrane elastic and viscous properties, bending resistance, and the viscosities of the external/internal fluids.

In comparison to RBCs, WBCs have one or multiple nuclei, are stiffer than RBCs and have a spherical shape. WBCs are an important part of the body's immune system. They protect the body against invading bacteria, parasites, and viruses by killing these microorganisms through phagocytosis ingestion and other antigen-specific cytotoxic mechanisms. There exist different types of leukocytes (e.g., neutrophils, eosinophils, basophils, monocytes, and lymphocytes), each of which is designed to fight a specific type of infection.

Freely circulating WBCs are able to adhere to the vascular endothelium, which is a crucial step in the immune response [38]. Rolling along the vessel wall allows WBCs to efficiently monitor for potential molecular signals, since the rolling velocity at the vessel wall is much smaller than that of the blood flow. In fact, microfluidic experiments [39] showed that WBCs adhere only above a critical threshold of shear. Firm adhesion of leukocytes is generally recognized as the final step of WBC adhesive dynamics within a vessel with further cross-endothelium migration into the surrounding tissue.

2 Methodology

Simulations of complex fluids, consisting of a solvent and various suspended particles such as colloids and cells, are a difficult problem. Strictly speaking, the involved length- and time-scales range between the atomistic scale of the solvent and the mesoscopic scale of the suspended particles, which typically start from several nanometers and finish with micrometers. In addition, many physical properties such as the softness of particles, the hydrodynamic interactions between them and with walls, and thermal fluctuations need to be included.

Simulations at the molecular level are very limited in terms of the length- and time-scales. These limits currently correspond to the submicrometer length and times on the order of several microseconds. In order to overcome such strong restrictions, several mesoscale hydrodynamics simulation approaches have been developed recently, including the lattice Boltzmann method (LBM) [40], dissipative particle dynamics (DPD) [41, 42], smoothed dissipative particle dynamics (SDPD) [43, 44], and multi-particle collision dynamics (MPC) [45, 46, 47]. These methods are being actively developed and to date they are already considered as rather well-established techniques for the numerical investigation of the dynamics of complex fluids.

Even though here we mainly focus on modeling of polymer solutions and blood flow, simulations of complex fluids generally require the two main components: fluid flow and suspended particles. Modeling fluid flow of a Newtonian solvent can be performed using, for example, continuum approaches, where the incompressible Navier-Stokes equation [48]

$$\frac{\partial \mathbf{u}}{\partial t} + (\mathbf{u} \cdot \nabla)\mathbf{u} = -\frac{1}{\rho}\nabla p + \nu \nabla^2 \mathbf{u}, \qquad \nabla \cdot \mathbf{u} = 0, \tag{2}$$

can be used. Here, $\mathbf{u}$ is the fluid velocity, ρ is the density, p is the pressure, and ν is the kinematic viscosity. The advantages of continuum techniques are the speed and robustness of such methods and rather well-established numerical schemes and codes. However, in these methods it is often non-trivial to incorporate some features present at the micro- and meso-scale, for instance thermal fluctuations. Another class of efficient simulation methods to model fluid flow corresponds to mesoscopic particle-based methods such as DPD and SDPD, which will be mainly used in this thesis. In comparison to the continuum approaches, particle-based techniques are generally more expensive computationally; however, desired micro- and mesoscopic features can be included here rather straightforwardly. Therefore, particle-based methods are very popular in modeling complex fluids at the micro- and meso-scale.

In the next several sections, we review employed mesoscopic particle-based methods, polymer and membrane models. However, we still need to discuss the coupling between fluid flow and particle deformation. Often such coupling can be performed using frictional forces on both the fluid and suspended particles in order to match their local velocities [49]. Thus, fluid stresses can be transferred to the suspended particles and induce their deformation, while in return the particles exert resisting-to-deformation forces onto the fluid.

2.1 Mesoscopic simulation techniques

Mesoscopic simulation approaches are being developed in order to be able to access much longer length and times scales than those achieved when modeling at the molecular level is employed. Common to these approaches is a simplified, coarse-grained description of the fluid and suspended structures in order to achieve high computational efficiency, while keeping the essential physical features on the length scales of interest. Specifically, hydrodynamic interactions between suspended particles are captured through a mesoscopic representation of a solvent.

2.1.1 Dissipative particle dynamics (DPD)

DPD [41, 42] is a mesoscopic simulation technique, where a system consists of a collection of N fluid particles with mass m_i, position $\mathbf{r}_i$, and velocity $\mathbf{v}_i$, and each individual particle represents a cluster of atoms or molecules. The dynamics of DPD particles is governed by Newton's second law of motion,

$$\begin{aligned} d\mathbf{r}_i &= \mathbf{v}_i dt, \\ d\mathbf{v}_i &= \frac{1}{m_i}\sum_{i\neq j}\mathbf{F}_{ij}dt = \frac{1}{m_i}\sum_{i\neq j}(\mathbf{F}^C_{ij} + \mathbf{F}^D_{ij} + \mathbf{F}^R_{ij})dt, \end{aligned} \tag{3}$$

where $\mathbf{F}_{ij}$ is the total force acting between the two particles i and j within a selected cutoff radius r_c. The total force is a sum of three pairwise forces: conservative ($\mathbf{F}^C_{ij}$), dissipative ($\mathbf{F}^D_{ij}$), and random ($\mathbf{F}^R_{ij}$) forces given by

$$\begin{aligned} \mathbf{F}^C_{ij} &= a_{ij}(1 - r_{ij}/r_c)\mathbf{e}_{ij}, \\ \mathbf{F}^D_{ij} &= -\gamma_{ij}\omega^D(r_{ij})(\mathbf{v}_{ij}\cdot\mathbf{e}_{ij})\mathbf{e}_{ij}, \\ \mathbf{F}^R_{ij} &= \sigma_{ij}\omega^R(r_{ij})\xi_{ij}dt^{-1/2}\mathbf{e}_{ij}, \end{aligned} \tag{4}$$

where $\mathbf{v}_{ij} = \mathbf{v}_i - \mathbf{v}_j$, $\mathbf{r}_{ij} = \mathbf{r}_i - \mathbf{r}_j$, $r_{ij} = |\mathbf{r}_{ij}|$ and $\mathbf{e}_{ij} = \mathbf{r}_{ij}/|\mathbf{r}_{ij}|$. The coefficients a_{ij}, γ_{ij}, and σ_{ij} characterize the strength of the conservative, dissipative, and random forces, respectively. Both $\omega^D(r_{ij})$ and $\omega^R(r_{ij})$ are distance-dependent weight functions. ξ_{ij} is a random number generated from a Gaussian distribution with zero mean and unit variance.

The dissipative and random forces act together as a thermostat to maintain an equilibrium temperature T and generate the correct equilibrium Gibbs-Boltzmann distribution. Therefore, they must satisfy the fluctuation-dissipation theorem [42] given by the conditions $\omega^D(r_{ij}) = [\omega^R(r_{ij})]^2$ and $\sigma^2 = 2\gamma k_B T$. In the original DPD method [41, 42], the weight function has been chosen as $\omega^R(r_{ij}) = (1 - r_{ij}/r_c)^k$ with $k = 1$, while different choices for this exponent have been made in other studies [50, 51] in order to increase the viscosity of the DPD fluid. The equations of motion (3) are integrated using the velocity-Verlet algorithm [52].

2.1.2 Smoothed dissipative particle dynamics (SDPD)

The SDPD method, originally proposed by Español and Revenga [43], is a mesoscopic particle-based hydrodynamic technique which has been derived from the smoothed particle hydrodynamics (SPH) [53, 54] and DPD [41, 42] methods. The SPH method is obtained by a Lagrangian discretization of the Navier-Stokes equation [53, 54]. In SDPD, the particle density ρ_i is defined as

$$\rho_i = \sum_j m_j W_{ij}, \tag{5}$$

where the weighting function W_{ij} is assumed to be, for instance, the Lucy function $W(r) = \frac{105}{16\pi r_c^3}\left(1+3\frac{r}{r_c}\right)\left(1-\frac{r}{r_c}\right)^3$ [53]; however, other choices for this function also exist. Hence, the density at the position of particle i can be computed using its neighboring particles located within a sphere with a radius r_c.

The discretization of the Navier-Stokes equation [43] leads to the two deterministic forces: conservative (C) and dissipative (D), while a proper fluctuation-dissipation balance, as in DPD, results into a random (R) force. The full set of inter-particle forces is given by

$$\begin{aligned}
\mathbf{F}_{ij}^C &= \left(\frac{p_i}{\rho_i^2}+\frac{p_j}{\rho_j^2}\right) F_{ij}\mathbf{r}_{ij},\\
\mathbf{F}_{ij}^D &= -\gamma_{ij}\left(\mathbf{v}_{ij}+\mathbf{e}_{ij}\mathbf{e}_{ij}\cdot\mathbf{v}_{ij}\right),\\
\mathbf{F}_{ij}^R &= \sigma_{ij}\left(d\overline{\mathbf{W}}_{ij}+\frac{1}{3}tr[d\mathbf{W}_{ij}]\mathbb{1}\right)\cdot\mathbf{e}_{ij},
\end{aligned} \tag{6}$$

where p_i and p_j are particle pressures assumed to follow a selected equation of state. Note that $W(r)$ is chosen such that $\nabla W(r) = -\mathbf{r}F(r)$ with $F(r) = \frac{315}{4\pi r_c^5}\left(1-\frac{r}{r_c}\right)^2$. The coefficients γ_{ij} and σ_{ij} define the strength of dissipative and random forces and are equal to $\gamma_{ij} = \frac{5\eta}{3}\frac{F_{ij}}{\rho_i\rho_j}$ and $\sigma_{ij} = 2\sqrt{k_BT\gamma_{ij}}$, respectively. The notation $tr[d\mathbf{W}_{ij}]$ corresponds to the trace of a random matrix of independent Wiener increments $d\mathbf{W}_{ij}$, and $d\overline{\mathbf{W}}_{ij}$ is the traceless symmetric part. The time evolution of velocities and positions of particles is determined by Newton's second law (Eq. (3)) as in DPD.

Generally, the set of forces in SDPD is similar to that in DPD; however, the SDPD method has a direct connection to the Navier-Stokes equation. The advantage of the SDPD approach over DPD is that the dynamic viscosity of a fluid and its equation of state can be a direct input, while in DPD such properties are not known *a priori* and need to be determined from simulations. Thus, the fluid compressibility and viscosity in SDPD can be well controlled.

2.1.3 Smoothed dissipative particle dynamics with angular momentum conservation

Even though the SDPD method has several advantages over DPD, the original SDPD method [43] does not conserve the angular momentum. This can be traced back to the existence of a lateral friction in SDPD, i.e. two particles slow down when they move past each other, and thereby loose angular momentum. Recent numerical simulations using the MPC method [55] have illustrated that angular momentum conservation is essential in some problems including the Taylor-Couette flow with two immiscible fluids and vesicle tank-treading in shear flow. We have extended the original SDPD method [44] (enclosed publication P3) in order to fix the violation of angular momentum conservation. The extension of the original SDPD formulation [43] is performed through the introduction of a spin variable for every particle $\boldsymbol{\omega}_i$. In addition, each particle is also characterized by a moment of inertia I_i analogously to the already defined particle mass. In order to obtain discretized equations for the SDPD formulation with spin, we consider the NS equation with spin [56] given by

$$\rho \frac{d\mathbf{u}}{dt} = -\nabla p + (\eta + \eta_r)\nabla^2 \mathbf{u} + \left(\frac{\eta}{3} + \xi - \eta_r\right) \nabla\nabla \cdot \mathbf{u} + 2\eta_r \nabla \times \boldsymbol{\omega}, \tag{7}$$

where η is the dynamic shear viscosity, ξ is the bulk viscosity, η_r is the rotational viscosity, and $\boldsymbol{\omega}$ is the spin angular velocity.

The discretization of the NS equation with spin and the fluctuation-dissipation relation lead to a set of forces: conservative (C), dissipative (D), rotational (R), and a fluctuation force [44] given by

$$\begin{aligned}
\mathbf{F}_{ij}^{C} &= \left(\frac{p_i}{\rho_i^2} + \frac{p_j}{\rho_j^2}\right) F_{ij} \mathbf{r}_{ij}, \\
\mathbf{F}_{ij}^{D} &= -\left(\gamma_{ij}^{a} \left(\mathbf{v}_{ij} + \frac{\mathbf{e}_{ij}\left(\mathbf{e}_{ij} \cdot \mathbf{v}_{ij}\right)}{3}\right)\right) - \frac{2\gamma_{ij}^{b}}{3} \mathbf{e}_{ij}\left(\mathbf{e}_{ij} \cdot \mathbf{v}_{ij}\right), \qquad (8) \\
\mathbf{F}_{ij}^{R} &= -\gamma_{ij}^{a} \frac{\mathbf{r}_{ij}}{2} \times \left(\boldsymbol{\omega}_i + \boldsymbol{\omega}_j\right), \\
\tilde{\mathbf{F}}_{ij} &= \left(\sigma_{ij}^{a} d\overline{\boldsymbol{W}}_{ij} + \sigma_{ij}^{b} \frac{1}{3} tr[d\boldsymbol{W}_{ij}] \mathbb{1}\right) \cdot \frac{\mathbf{e}_{ij}}{dt},
\end{aligned}$$

(9)

where

$$\gamma_{ij}^{a} = \left(\frac{20\eta}{3} - 4\xi\right) \frac{F_{ij}}{\rho_i \rho_j}, \quad \gamma_{ij}^{b} = \left(17\xi - \frac{40\eta}{3}\right) \frac{F_{ij}}{\rho_i \rho_j}, \tag{10}$$

and $\sigma_{ij}^{a,b} = 2\sqrt{k_B T \gamma_{ij}^{a,b}}$. It is important to note that these equations are only valid for $2\eta/3 \leq \xi \leq 5\eta/3$, such that the friction coefficients $(\gamma_{ij}^{a} + 2\gamma_{ij}^{b})/3$ and γ_{ij}^{a} are positive.

The conservative force controls locally the pressure field in the system. The dissipative force provides translational friction leading to the reduction of the velocity difference between two particles. Finally, the rotational force is also dissipative, but acts on particles' angular velocities such that a spin of one particle leads to a change in translational and angular velocity of another particle. In this way, the translational angular momentum, which is lost in a "collision", is stored as particle spin, and can be restored as translational angular momentum later on. Another simplification which can be made is the reduction to a single dissipative parameters γ_{ij} such that $\xi = 20\eta/21$ [44] and

$$\gamma_{ij}^{a} = \gamma_{ij}^{b} = \gamma_{ij} = \frac{20\eta}{7} \frac{F_{ij}}{\rho_i \rho_j}, \qquad \sigma_{ij}^{a} = \sigma_{ij}^{b} = \sigma_{ij} = 2\sqrt{k_B T \gamma_{ij}}. \tag{11}$$

The time evolution of the position and the translational and angular velocity of a particle i follows Newton's second law as

$$\dot{\mathbf{r}}_i = \mathbf{v}_i, \quad \dot{\mathbf{v}}_i = \sum_j \frac{1}{m_j} \mathbf{F}_{ij}, \quad \dot{\boldsymbol{\omega}}_i = \sum_j \frac{1}{I_j} \mathbf{N}_{ij}, \tag{12}$$

where $\mathbf{N}_{ij}$ is the torque exerted by particle j on particle i and is given by $\mathbf{N}_{ij} = \frac{1}{2}\mathbf{r}_{ij} \times \mathbf{F}_{ij}$. This leads to local and global angular momentum conservation. Equation (12) is integrated using the velocity-Verlet algorithm [52].

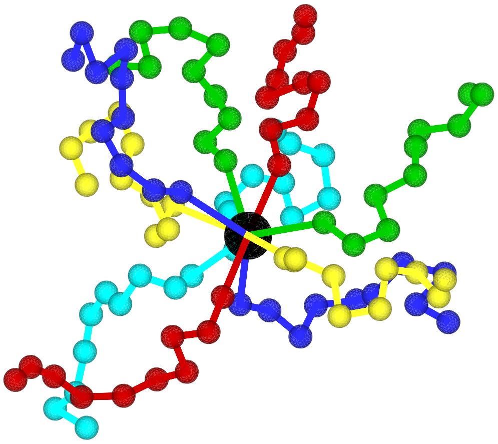

Figure 2: A star polymer represented by a bead-spring model. A number of arms (polymer chains) $f = 10$ drawn with different colors are connected to a common central bead (black sphere). The length of each arm is $N_m = 10$. Reproduced with permission from Ref. [4].

2.2 Polymer models

On the mesoscopic level, a linear polymer is represented by the bead-spring chain model, where a number of beads (or particles) are connected by harmonic springs with the potential

$$U_s = \frac{k_s}{2}(l - l_0)^2, \tag{13}$$

where k_s is the spring constant, l is the instantaneous bond length, and l_0 is the equilibrium bond length. Often k_s is chosen large enough such that even under strong fluid stresses the change in the bond length remains less than a few percent.

Excluded-volume interactions between polymer monomers are implemented through the repulsive (truncated and shifted) Lennard-Jones (LJ) potential [52]

$$U_{LJ}(r) = 4\epsilon \left[\left(\frac{\sigma}{r}\right)^{12} - \left(\frac{\sigma}{r}\right)^{6} + \frac{1}{4} \right] \Theta(2^{1/6} - r), \tag{14}$$

where $\Theta(r)$ is the Heaviside step function ($\Theta(r) = 0$ for $r < 0$ and $\Theta(r) = 1$ for $r \geq 0$).

Star polymers are modeled by connecting a number of linear chains to a common center with harmonic springs, which is illustrated in Fig. 2. Since many polymer arms are attached to the central particle, the equilibrium bond length of each center-arm connection and LJ diameter of the central bead are taken to be larger than those for a normal monomer.

2.3 RBC membrane model

The RBC membrane is modeled by a triangulated mesh [58, 59, 60, 49, 61, 62, 63], see Fig. 3. A total of N_v particles constitute the mesh vertices and $N_s = 3(N_v - 2)$ springs follow the edges of the mesh, reproducing the stretching elasticity of the membrane (U_{sp}). A total

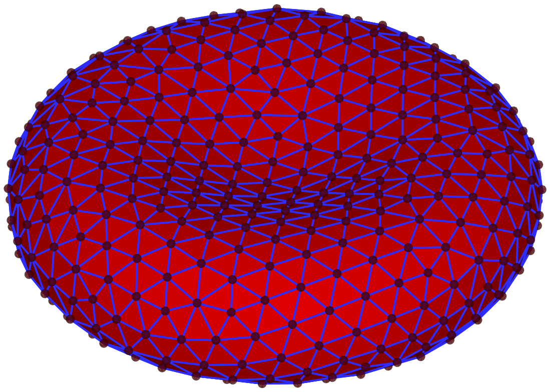

Figure 3: Mesoscopic representation of a RBC membrane by a triangular network of bonds. Reproduced with permission from Ref. [57].

of $N_t = 2N_v - 4$ triangles make up the entire membrane surface and incident triangles have an associated potential energy (U_{bend}) related to the angle between them, associated with membrane bending rigidity. Furthermore, local and global area constraints (U_{area}) are enforced along with a global volume constraint (U_{vol}). Formally, the total energy of a RBC is then

$$U_{tot} = U_{sp} + U_{bend} + U_{area} + U_{vol}. \tag{15}$$

The total contribution of springs is given by

$$U_{sp} = \sum_{j \in 1 \ldots N_s} \left[\frac{k_B T l_m \left(3x_j^2 - 2x_j^3\right)}{4\zeta \left(1 - x_j\right)} + \frac{k_p}{l_j} \right], \tag{16}$$

where l_j is the length of spring j, l_m is the maximum permitted spring extension, $x_j = l_j/l_m$ is the fractional extension towards maximum length, ζ is the persistence length, and k_p is the spring constant. The equilibrium length of each spring l_{0_j} is set in accordance with an initial triangulated mesh of a stress-free biconcave RBC shape [62, 63].

The membrane curvature elasticity can be described by the bending energy

$$U_{bend} = \sum_{j \in 1 \ldots N_s} k_b \left[1 - \cos\left(\theta_j - \theta_0\right)\right], \tag{17}$$

where k_b is the bending coefficient, θ_j is the instantaneous angle between the two triangles incident on edge j, and θ_0 is the spontaneous angle.

Finally, the area and volume constraints are accounted for by two potentials

$$\begin{aligned} U_{area} &= k_a \frac{\left(A - A_r\right)^2}{2A_r} + \sum_{j \in 1 \ldots N_t} k_d \frac{\left(A_j - A_j^0\right)^2}{2A_j^0}, \\ U_{vol} &= k_v \frac{\left(V - V_r\right)^2}{2V_r}, \end{aligned} \tag{18}$$

where k_a, k_d, and k_v are the global area, local area, and volume constraint coefficients, respectively. A is the instantaneous surface area of the membrane, A_j is the instantaneous area of the j-th triangle in the network, and V is the instantaneous RBC volume. The desired total surface area A_r, individual triangle area A_j^0, and interior volume V_r are set in accordance with the initial triangulation [62, 63].

We relate the RBC model's variables to physical macroscopic properties of the RBC membrane by linear analysis for a regular hexagonal network [62, 63]. The membrane shear modulus is related to the spring variables by

$$\mu_0 = \frac{\sqrt{3}k_BT}{4\zeta l_m x_0}\left(\frac{x_0}{2\left(1-x_0\right)^3} - \frac{1}{4\left(1-x_0\right)^2} + \frac{1}{4}\right) + \frac{3\sqrt{3}k_p}{4l_0^3}, \tag{19}$$

with $x_0 = l_0/l_m$. The area-compression K and Young's Y moduli are found as $K = 2\mu_0 + k_a + k_d$ and $Y = \frac{4K\mu_0}{K+\mu_0}$. The Helfrich model is employed to describe the bending coefficient k_b in terms of macroscopic bending rigidity κ [64], yielding $k_b = 2\kappa/\sqrt{3}$.

To prevent mixing between intra- and extra-cellular fluids, bounce-back reflections for the solvent particles are introduced at a RBC membrane. Furthermore, the RBC is coupled to fluid flow via viscous friction between the N_v mesh vertices and local fluid particles. The dissipative and random force components of the DPD method are used to achieve these interactions [63]. No-slip boundary conditions at membrane vertices are enforced by careful selection of the friction parameter γ in the dissipative force $\mathbf{F}^D$. A fluid sheared over the effective surface of a membrane vertex exerts a friction force on the membrane given as $\mathbf{F}_v = \int_{V_h} ng(r)\mathbf{F}^D dV$, where n is the fluid number density, $g(r)$ is the radial distribution function of fluid particles about the membrane vertices, and V_h is the hemisphere volume of fluid situated above the vertex. Equating this integral to the total force required by a continuum hydrodynamical description leads to an expression for the calculation of γ [63].

3 Results

3.1 Rheology of star-polymer solutions

Star polymers are constructed from f linear polymer arms, which are connected with one of their ends to a common center. Each polymer arm can contain N_m monomers. By changing the arm length $L = N_m l$ and the functionality f, star polymers can mimic linear polymers (for $f = 2$), hard-sphere colloids (large f, short arms), and ultra-soft colloids (intermediate f, long arms) [21, 22, 23]. Many of the existing studies have focused on the equilibrium properties of star polymers [21, 65, 66, 67, 68]. Due to the architecture of star polymers, the monomer density in the core region is relatively high in comparison with that in the corona. The inhomogeneous density distribution within a star polymer yields an ultra-soft interaction between two stars for sufficiently long chains [21, 22, 68]. The dynamical and rheological properties of star-polymer solutions are much less studied. Polymer self-diffusion has been investigated in experiments [69, 23] showing that it decreases according to a power law with increasing polymer concentration c. Note that star-polymer diffusion is faster in solution than that of hard-sphere colloids due to the deformability and ultra-soft interactions of star polymers. The softness of star polymers is also responsible for the slower increase of the zero-shear viscosity with concentration in comparison to hard particles [69, 23].

Previous theoretical and simulation investigations have focused on the behavior of single star polymers in shear flow [70, 71] and on the frictional interactions between two stars [72]. The rheology of concentrated solutions has been studied using a simplified soft-particle model [73, 74], which should mimic a star-polymer through a coarse-grained description; however, this model ignores the deformability of star-polymers in flow. We

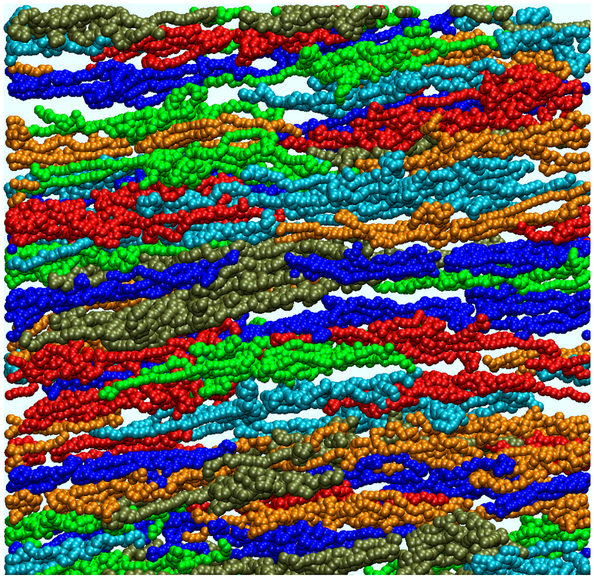

Figure 4: Simulation snapshot of a star-polymer solution with functionality $f = 10$, arm length $N_m = 30$, and concentration $c/c^* = 0.75$ (c^* is the overlap concentration). High shear rate with concentration-dependent Weissenberg number $Wi_c = 153$ is shown. The multiple colors serve to make different star polymers easily distinguishable. Reproduced with permission from Ref. [4].

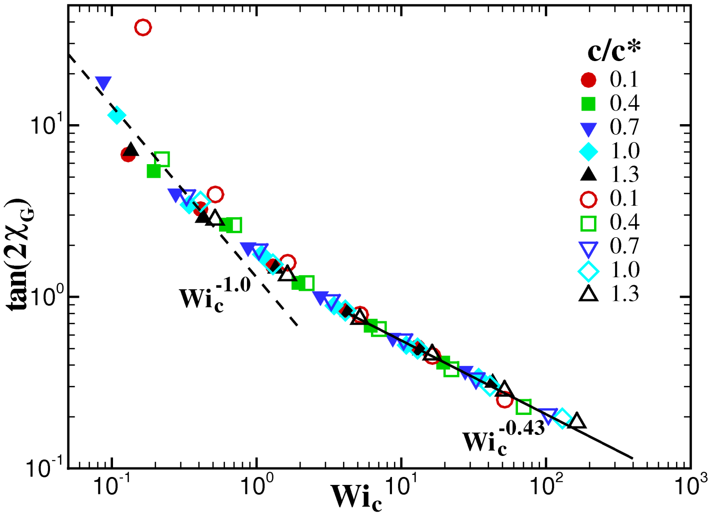

Figure 5: Orientation of star polymers characterized by $\tan(2\chi_G)$, see Eq. (20), as a function of Wi_c. DPD simulation results for various star-polymer concentrations, as indicated, and $N_m = 10$ (filled symbols) and $N_m = 20$ (open symbols). The dashed black line indicates a scaling behavior $\tan(2\chi_G) \sim {Wi_c}^{-1}$ and the solid black line corresponds to $\tan(2\chi_G) \sim {Wi_c}^{-0.43}$. Reproduced with permission from Ref. [4].

have investigated the flow behavior of semidilute solutions of star polymers including their configurational and dynamical properties and rheology [4, 75]. The generated shear flow is characterized by the Weissenberg number $Wi = \dot{\gamma}\tau_z$, where $\tau_z = \eta_s N_m^2 l^3/k_B T$ is the Zimm relaxation time of a polymer arm in dilute solution. However, it is clear that the relaxation time of a star polymer has to be different at various concentrations, and therefore a concentration-dependent Weissenberg number Wi_c is employed [4, 75].

Star polymers in flow experience strong deformation as illustrated in Fig. 4. In addition, they align in flow, which can be characterized by the angle χ_G computed as the angle between the eigenvector of the gyration tensor G with the largest eigenvalue and the flow direction given by [4]

$$\tan(2\chi_G) = \frac{2G_{xy}}{G_{xx} - G_{yy}}. \tag{20}$$

The alignment angle of star polymers as a function of Wi_c for different concentrations is shown in Fig. 5. Shifting different curves for various concentrations onto a single master curve in Fig. 5 supplies the scaling factors for Wi_c, which represent the ratios of concentration-dependent relaxation times. At low shear rates, the angle χ_G is close to the equilibrium value $\pi/4$ and it follows the expected scaling behavior [76, 14] $\tan(2\chi_G) \sim {Wi_c}^{-1}$. At high Wi_c, star polymers deform considerably, and the angle χ_G decreases due to alignment of the stars along the flow direction and follows the scaling law of $\tan(2\chi_G) \sim {Wi_c}^{-0.43}$. The star-polymer deformation characteristics (G_{xx} and G_{yy}) also show a universal behavior when plotted against Wi_c [4].

Rheological properties of the star-polymer solutions are characterized through measured viscosities and the first and second normal-stress coefficients, which display plateaus at low shear rates for many polymeric fluids. Figure 6 shows viscosities of the star-polymer solutions for various arm lengths and concentrations. The curves are normalized by the

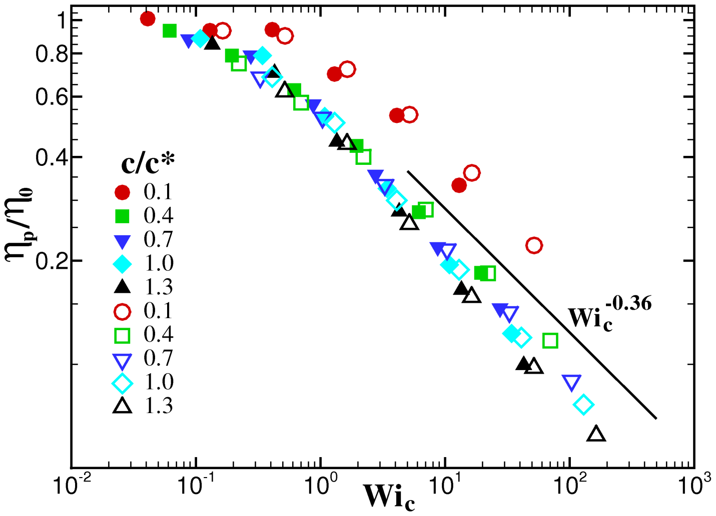

Figure 6: Shear-rate-dependent viscosity of simulated star-polymer solutions for various arm lengths and concentrations as a function of Wi_c. DPD simulation results for various star-polymer concentrations, as indicated, and $N_m = 10$ (filled symbols) and $N_m = 20$ (open symbols). Only polymer contributions to the viscosity are shown. The viscosity curves are scaled with the corresponding values of the zero-shear viscosity η_0 for different concentrations. The solid line indicates the power-law dependence $\eta_p \sim Wi_c^{-0.36}$. Reproduced with permission from Ref. [4].

corresponding zero-shear viscosity η_0 in order to find a scaling behavior. At $Wi_c > 1$, the viscosities exhibit a power-law decay with increasing shear rate. The power-law exponent seems to depend on the star-polymer concentration such that at low concentrations it is equal to approximately -0.3, while at high star concentrations $c/c^* \simeq 1.3$ it is about -0.4. Thus, the viscosity curves do not show a universal behavior [4]. Such a dependence has not yet been identified by any theory and appears to be independent of the arm length. The first and second normal-stress coefficients also show some non-universality in their scaling for different concentrations [4]. It has not yet been clarified what causes these differences for various concentrations, which do not exist for linear-polymer solutions [2]. The dynamics of star polymers under flow is different from that of linear polymers, which exhibit tumbling motion [27], whereas star polymers show a tank-treading-like rotation [70] for functionalities $f > 5$. The rotational frequency of this motion appears to depend considerably on the star-polymer concentration, which has been attributed to the screening of hydrodynamic interactions at high concentrations [75]. In addition, the tank-treading dynamics of star polymers in shear flow shows a striking resemblance to the tank-treading behavior of lipid vesicles [4], which can be described by the Keller and Skalak model [77]. This indicates that there is a similarity between the dynamics of star polymers and vesicles within a solution.

3.2 Dense brushes of stiff polymers in fluid flow

Polymer brushes have been investigated in many studies [78, 79, 80], because they are an important part of various technological and biological interfacial systems. Major research efforts have focused on brushes with flexible polymers (i.e., with negligible bending stiffness on the polymer length), while brushes with stiff filaments (i.e., with non-negligible bending resistance at the scale of contour length) have received limited attention. Such brushes are present in many biophysical systems, for example, lubricating aggrecan brushes in joints [81] and the endothelial glycocalyx layer in blood vessels [82, 83]. In addition, recent technological applications of cantilevered micro- and nano-rod arrays [84] or high-density brushes [85] have been suggested in the context of functionalized surfaces [86].

There exist a few simulation [88, 89, 90] and theoretical [90, 91, 92] studies, where the equilibrium and mechanical properties of stiff-polymer brushes have been investigated. For example, simulations of polymer-brush compression [93, 94] have shown that for the initial deformation such brushes can be much softer mechanically than those made out of flexible polymers. The main reason is that the grafted polymers in flexible-polymer brushes are already in a collapsed (coiled) state, making the brush rather dense and not very susceptible to deformation. In contrast, the flexural rigidity of polymers in stiff-polymer brushes significantly limits polymer collapse, and therefore such a brush is not so dense and the initial deformation of the brush corresponds to the bending of semiflexible grafted polymers. Non-equilibrium properties of a stiff-polymer brush have been studied in simulations [95] with the focus on the response of a glycocalyx layer in blood vessels to fluid flow. The flow-induced deformation of grafted semiflexible polymers has been considered in a mean-field approach [96], where the steric interactions between polymers were not taken into account, limiting the model's applicability to the deformation of brushes with low grafting densities. We have extended this theoretical model [87] to predict flow-induced deformation of a dense brush of stiff polymers or filaments. In addition, we have also performed a systematic study of the deformation of a semiflexible-polymer brush in flow using mesoscopic simulations (see Fig. 7) for a wide range of grafting densities, polymer-bending rigidities, and shear rates.

Our mean-field approach [87] for brush deformation in shear flow assumes identical bending of all grafted polymers. Thus, a single semiflexible polymer, subjected to a hydrodynamic

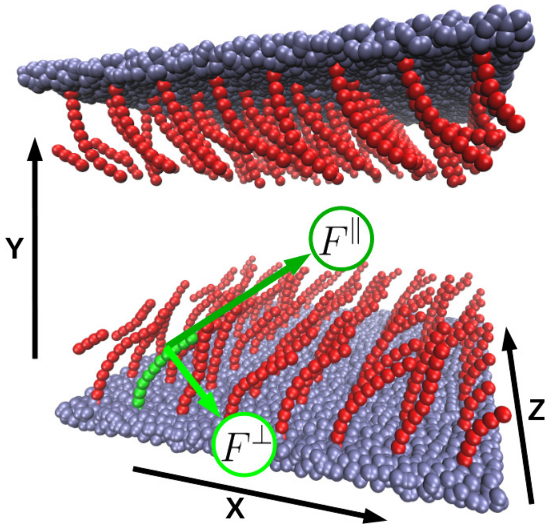

Figure 7: Simulation snapshot of a polymer brush under flow with shear flow in x direction. Semiflexible polymers are grafted on both walls. Reproduced with permission from Ref. [87].

drag force due to fluid flow and steric interactions due to its neighbors in the grafted lattice, is considered. We consider the torque balance for a circular rod [97] such that external forces ($\mathbf{F}(s) = (F_x(s);\ F_y(s))$) are counteracted by the rods's elastic resistance, as

$$EI \frac{d\mathbf{r}(s)}{ds} \times \frac{d^3\mathbf{r}(s)}{ds^3} = \mathbf{F}(s) \times \frac{d\mathbf{r}(s)}{ds}, \tag{21}$$

where EI is the polymer bending rigidity and $\mathbf{r}(s)$ is the position on a polymer at curve-linear coordinate s along the polymer. This equation can be further reduced to the formulation in terms of the local angle $\theta(s)$ [87] as

$$EI \frac{d^2\theta(s)}{ds^2} = F_y(s) \sin\theta(s) - F_x(s) \cos\theta(s), \tag{22}$$

with the boundary conditions of $\theta(s)|_{s=0} = \theta_0$ at the grafted surface and $d\theta/ds|_{s=L} = \theta_0$ at the free end.

The force $\mathbf{F}(s)$ on the filament has two contributions: 1) drag force ($\mathbf{F}^{\mathrm{d}}(s)$) due to fluid flow and 2) a force due to excluded-volume interactions ($\mathbf{F}^{\mathrm{v}}(s)$). These forces at a position s can be computed as an integral over local force densities at the filament [87]. The drag force is approximated by using the velocity profile within the brush and friction coefficients from the slender body theory [98]. The local velocity $u_x(s)$ within the brush is described by the Brinkman equation [99] for flow in porous media as [87]

$$\frac{d^2u_x(s)}{ds^2} = \zeta(s)u_x(s)\frac{\sigma}{d^2}\cos\theta(s) - \frac{du_x(s)}{ds}\frac{d\theta(s)}{ds}\tan\theta(s), \tag{23}$$

where $\zeta(s)$ is the position-dependent friction coefficient, σ is the grafting density, and d is the polymer thickness. This equation is the same as that used in the theory for semiflexible-polymer brushes with low grafting densities [96]. Boundary conditions for Eq. (23) are $u_x(s)|_{s=0} = 0$ and $du_x(s)/ds|_{s=L} = \dot{\gamma}|_{s=L}\cos\theta(L)$, where L is the polymer length. To describe the steric interactions between the filaments, we introduce a discrete polymer representation similar to that in simulations [87]. Thus, a polymer consists of N beads with the diameter d. The excluded-volume interactions between beads are approximated by a repulsive potential and the steric interactions are computed as a discrete sum of these forces, representing the integral over the local force density.

Figure 8 presents the relative brush height as a function of the shear rate at the top of the brush, normalized by the bending rigidity of the polymers. The predictions from the theoretical model and simulations agree well. Here, we also show the universality of brush deformation in terms of polymer bending rigidity characterized by l_p/L (l_p is the persistence length), if polymers are stiff enough with $l_p/L \gtrsim 10$. Clearly, this universal behavior is expected to break down when EI/L becomes small and comparable to k_BT, i.e. when the grafted polymers become rather flexible. In this case entropic effects have to be considered in addition.

The theoretical model predicts quantitatively the flow-induced deformation of a stiff-polymer brush and its effect on fluid flow. It quantifies the relative contributions of fluid friction, polymer bending resistance, and steric excluded-volume interactions between polymers. As an example, in Ref. [87] we have computed the effect of a brush on the flow resistance, which can be used for the estimation of the influence of the glycocalyx layer on blood flow in microvessels.

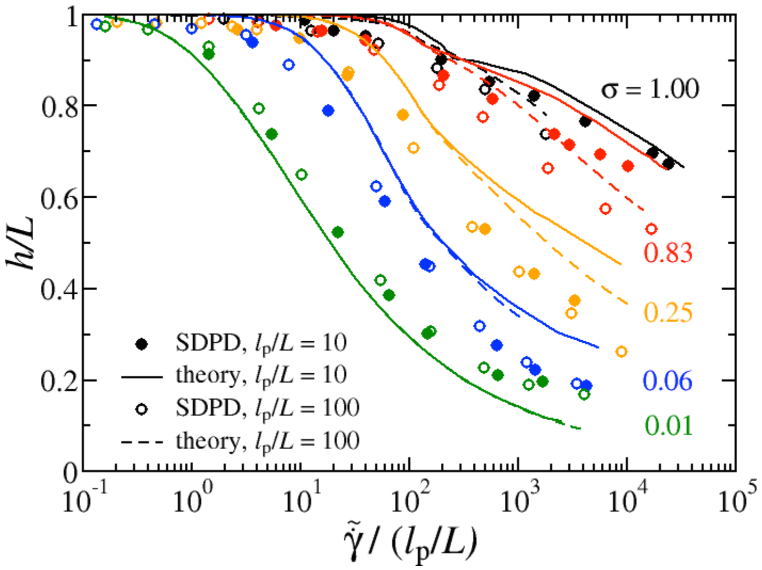

Figure 8: Relative brush height as a function of the shear rate at the top of a brush normalized by polymer elasticity from simulations and the theoretical model for different scaled grafting densities $\sigma = (d/a_{lat})^2$ (a_{lat} is a constant of the square lattice), as indicated. Two bending rigidities of $l_p/L = 10$ and 100 are considered. Reproduced with permission from Ref. [87].

3.3 Motion of single RBCs in tube flow

The motion of single RBCs in a cylindrical tube flow mimics their traveling through small vessels in the microvasculature. Since RBCs are very flexible, they are subject to strong deformation in the microcirculation, which depends on local flow and/or geometrical constraints. RBC deformation has been found to be important in the reduction of blood flow resistance [60, 63, 100, 101, 57] and for the release of ATP and oxygen delivery [102, 103]. The knowledge about the behavior of RBCs in micro-flows will also help in the development of lab-on-a-chip applications [104, 105] for the analysis of blood samples and the detection of diseased cells.

Before we discuss the behavior of RBCs in tube flow, we shortly touch upon the dynamics of RBCs in shear flow to point out some similarities. RBC dynamics in shear flow has been investigated experimentally [106, 107, 108], theoretically [109, 107, 110], and in simulations [61, 63, 111, 112, 113]. Experimental investigations [106, 107, 108] have shown that RBCs tumble at low shear rates and tank-tread at high shear rates. The tank-treading motion of a RBC can be imagined as the periodic motion of the RBC membrane, while the inclination angle of the cell remains nearly fixed. The tank-treading membrane motion is possible for RBCs, because they have no inner cytoskeleton; similarly this motion also occurs for capsules and vesicles. The existence of the transition from tumbling to tank-treading is due to a minimum energy state of the RBC membrane such that an energy barrier has to be exceeded in order for a RBC to tank-tread [106]. Note that the experiments [106, 107, 108] have been performed at the viscosity contrast (the ratio between the cytosol and suspending-fluid viscosity) close to unity or even lower, while under physiological conditions the viscosity contrast is equal to about 5-6. Tank-treading of vesicles appears to be suppressed at high enough viscosity contrasts ($\sim 5-7$) [114, 115], and therefore it is plausible to expect that the tank-treading of RBCs might not be relevant under

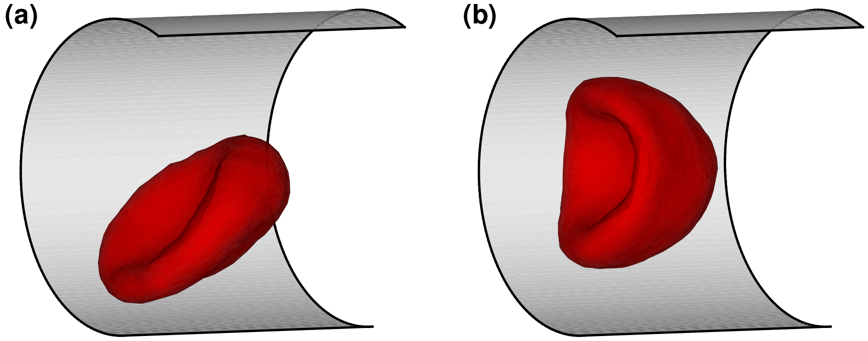

Figure 9: Simulation snapshots of a RBC in tube flow (from left to right). (a) an off-center slipper cell shape and (b) a parachute shape. Reproduced with permission from Ref. [116].

physiological conditions.

RBCs in Poiseuille flow also show rich behavior, characterized by various shapes including parachutes and slippers [117, 60, 118, 61, 119, 120, 100, 121, 101, 116], as illustrated in Fig. 9. Parachutes are characterized by a symmetric shape similar to a semi-spherical cap and they flow in the center of a tube without significant membrane motion. In contrast, slippers are non-symmetric RBC shapes, where the membrane is subjected to a tank-treading motion. Thus, slippers are mainly differentiated from parachutes by an asymmetric shape and the membrane motion. Experimental studies [120, 118] have illustrated the two types of slippers, a non-centered slipper [120] and centered slipper [118], where the latter may closely resemble a parachute shape. Slipper shapes have been also found in simulations using 2D [100, 101] and 3D models [116].

Recent 2D simulations [100, 101] have yielded a phase diagram of various shapes including parachute, slipper, and a snaking dynamics, as a function of RBC confinement and flow strength. The snaking dynamics is characterized by a wiggling motion of a discocyte shape near the tube center. We have employed 3D simulations [116] to generate a similar diagram of RBC shapes in tube flow, which is only qualitatively similar to the diagram in 2D. Figure 10 shows the RBC shape diagram in 3D for different flow rates and confinements. The flow rate is characterized by a non-dimensional shear rate $\dot{\gamma}^*$, which is a product of the average shear rate (or pseudo-shear rate) and the characteristic relaxation time of a RBC [116]. The confinement χ is the ratio of an effective RBC diameter and the tube diameter. At strong confinements and high flow rates, parachutes are mainly found, while low confinements lead predominantly to off-center slippers. When the flow rate is small enough, off-center tumbling RBCs are found, which can be explained by the existence of the tumbling-to-tank-treading transition mentioned above for RBCs in shear flow. In contrast to the 3D model results, this region is absent in 2D simulations [100, 101], since this transition cannot be captured by a 2D model. Another prominent difference between the phase diagrams in Fig. 10 and in 2D simulations [100, 101] is the existence of the "confined slipper" in 2D at high confinements which is absent in 3D. Slippers at high confinements in 3D are hindered due to the cylindrical shape of a tube, which makes a confined slipper configuration energetically unfavorable, since it would have to conform the wall curvature.

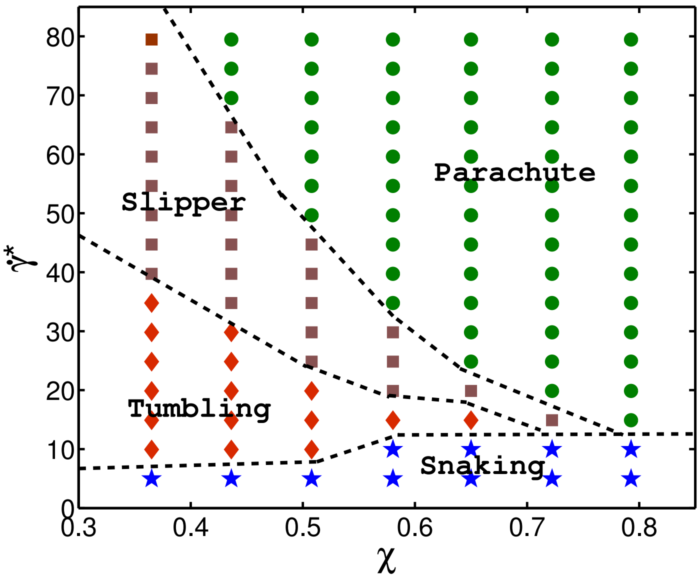

Figure 10: A phase diagram of RBC shapes in tube flow for the average membrane properties of a healthy RBC. Different dynamic states, depending on the flow strength characterized by a non-dimensional flow rate $\dot{\gamma}^*$ and the confinement χ, are depicted by symbols: parachute (green circles), slipper (brown squares), tumbling (red diamonds) and snaking (blue stars) discocyte. The phase-boundary lines are drawn approximately to guide the eye. Reproduced with permission from Ref. [116].

The results in Fig. 10 have been obtained for the viscosity contrast of unity. Therefore, they may not fully reflect the behavior of RBCs in microcirculation and the investigation of RBC dynamics in tube flow for a physiological viscosity contrast remains one of our on-going projects. The study in Ref. [116] has also focused on the investigation of the effect of membrane elasticity on RBC dynamics in microcapillary flow. Changes in RBC membrane properties lead to a shift of boundaries between different RBC shapes and dynamics illustrated in Fig. 10. Consequently, it should be possible to detect such changes based on the observation of RBCs in flow and simulations can provide the basis for a quantitative interpretation of these observations. The ability to interpret changes in RBC behavior can be helpful in the analysis of blood in various blood-related diseases and disorders.

3.4 Development of blood flow in idealized vessels

Blood flow in idealized vessels (or tubes) has been investigated in a number of experiments [122, 123, 124, 125] and simulations [126, 127, 128, 119, 129, 130]. In tube flow, RBCs migrate away from the wall toward the tube center resulting a near-wall layer free of RBCs [131, 132], as illustrated in Fig. 11. The migration of RBCs away from the wall is mediated by cell-wall hydrodynamic interactions in flow, which is referred to as a lift force [133, 134, 135] and arises due to the non-spherical discocyte shape and high deformability of RBCs. The layer of fluid void of RBCs near the wall is called RBC free layer (RBC-FL) or cell free layer (CFL).

The viscosity in the RBC-FL is much smaller than that in the tube center populated with RBCs. Therefore, if the thickness of RBC-FL is considerable in comparison with the tube diameter, the effect of the RBC-FL on blood-flow resistance can be significant. This is the reason for the effective blood viscosity appearing to be smaller in microvessels in comparison to much larger vessels in the microvasculature. The effect of the decrease in the apparent blood viscosity with decreasing tube diameter is called Fahraeus-Lindqvist effect [122, 125] and is strongly correlated with the thickness of the RBC-FL.

Blood flow in the microcirculation is quite complex and the distribution of RBCs in a vessel cross-section can be significantly disturbed at vessel bifurcations and junctions, leading to a reduced RBC-FL and an increased flow resistance [136]. After a distortion of RBC-FL at a vessel junction has occurred, RBCs will migrate toward the center of the following vessel segment, leading to a dynamic recovery of the RBC-FL thickness. Thus, the flow resistance in the microvasculature depends on the degree of RBC dispersion at vessel bifurcations and the corresponding recovery length of the RBC-FL in relation to the characteristic length of straight vessel segments in microcirculation.

In order to investigate the importance of this effect, we have studied the convergence of blood flow in idealized vessels starting from a dispersed configuration of RBCs [137]. Hence, the thickness of the RBC-FL is followed in time, after the flow has been turned on. Figure 12(a) presents the development of the RBC-FL thickness $\delta(t)$ for different pressure gradients for the case of tube hematocrit $H_t = 0.45$. Here, the time is scaled by the pseudo-shear rate $\bar{\dot{\gamma}}$ of the fully-developed flow. We observe a rapid increase of the RBC-FL thickness up to about $t\bar{\dot{\gamma}} \approx 25$, followed by a plateau thickness δ_f when the RBC-FL has converged. The same curves normalized by δ_f are shown in Fig. 12(b), where we see that they practically fall on top of each other. This indicates that the shear rate $\bar{\dot{\gamma}}$ is the only relevant time scale for the convergence of the RBC-FL and the flow profile. A similar conclusion has been also drawn for other hematocrits with $H_t \leq 0.45$ [137]. Therefore, the convergence of the RBC-FL to δ_f appears to be nearly independent of hematocrit and is reached within $t\bar{\dot{\gamma}} \lesssim 25$. In addition, this conclusion is valid for different vessel diameters D in the range 10 µm $< D <$ 100 µm [137], corresponding to the vessel sizes where the RBC-FL thickness can play a significant role for blood-flow resistance in the microvasculature.

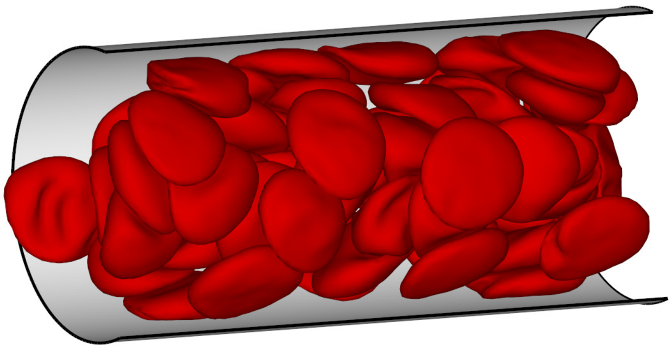

Figure 11: A simulation snapshot of blood flow (RBCs only) in a tube with a diameter $D = 20\ \mu m$ and at tube hematocrit $H_t = 0.45$. The thin layer between the RBC core and the tube walls is the cell-free layer. Reproduced with permission from Ref. [17].

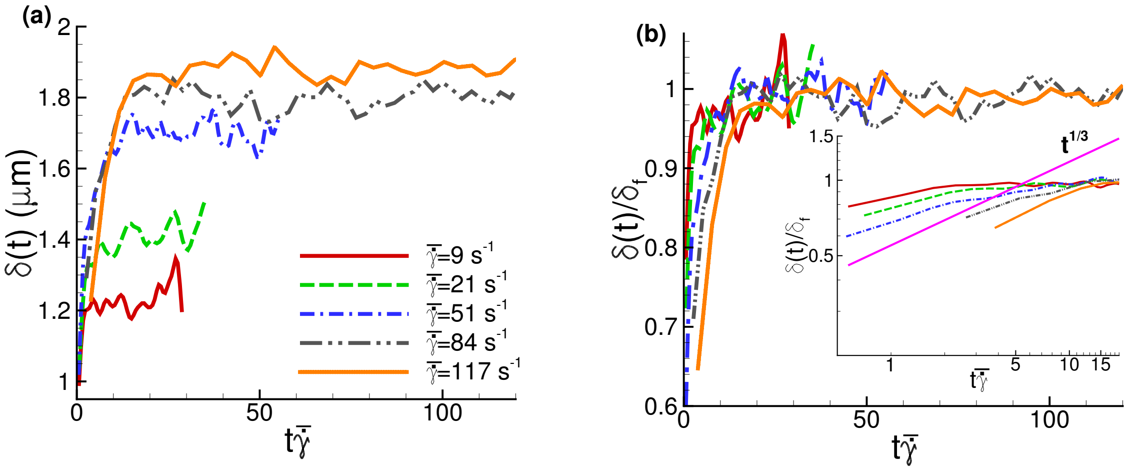

Figure 12: Development of the RBC-FL thickness for the case of $H_t = 0.45$ and $D = 20$ µm. The time is scaled by the pseudo-shear rate $\bar{\dot{\gamma}}$. (a) The RBC-FL thickness development for various pseudo-shear rates. (b) The same set of data as in plot (a) with all curves normalized by the plateau value of the RBC-FL thickness δ_f. The inset in (b) is a log-log plot illustrating a power-law behavior of the RBC-FL curves at small $t\bar{\dot{\gamma}}$. Reproduced with permission from Ref. [137].

The RBC-FL development results allow us to estimate the length and time required for the RBC-FL convergence. The flow convergence time is equal to about $t_c \lesssim 25/\bar{\dot{\gamma}} = 25D/\bar{v}$. Consequently, the convergence length is found as $l_c \lesssim \bar{v}t_c = 25D$ [137]. As an example, for $D = 20$ µm the convergence length is equal to approximately $l_c \lesssim 0.5$ mm, independently of the flow rate and H_t. Thus, the effect of the RBC core distortion past vessel bifurcations on the blood-flow resistance can practically be neglected if $L \gg 25D$; however, it may considerably affect the flow resistance if L is smaller than or comparable to $25D$. Characteristic lengths of microvessels between bifurcations [28] are on the order of $0.5-1$ mm. Hence, the contribution to flow resistance due to the RBC dispersion effect at vessel junctions is expected to be rather small for vessels with diameters $D \lesssim 20$ µm, while in vessels with larger diameters (20 µm $\lesssim D \lesssim$ 100 µm) this contribution cannot be ignored.

We have also developed a simple physical model to describe the mechanisms which govern the final RBC-FL thickness. The thickness δ_f is defined by the balance of the lift force on RBCs driving them away from the wall [133, 134, 135] and RBC-RBC interactions or collisions in flow dispersing them. Hence, to describe δ_f theoretically, the lift force on RBCs, which compresses the cell core of the flow, should be balanced by an effective pressure due to RBC collisions in flow. An effective pressure Π in a sheared colloidal suspension has been defined through an effective temperature in Ref. [138] as

$$\Pi = n(k_B T + c_s \eta_{eff} \dot{\gamma} V_r) Z, \tag{24}$$

where $n = H_t/V_r$ is the RBC number density, c_s is a constant, η_{eff} is an effective suspension viscosity, $\dot{\gamma}$ is the shear rate, and Z is the compressibility. The first term in Eq. (24) corresponds to the thermal contribution of pressure, while the second term describes the shear-induced component due to particle interactions or collisions in flow [139, 140, 141]. The pressure inside the flow core has to be balanced by the surface pressure Π_s from a hydrodynamic lift force (F_l) on RBCs [142, 143, 135, 141] and by an entropic repulsion of

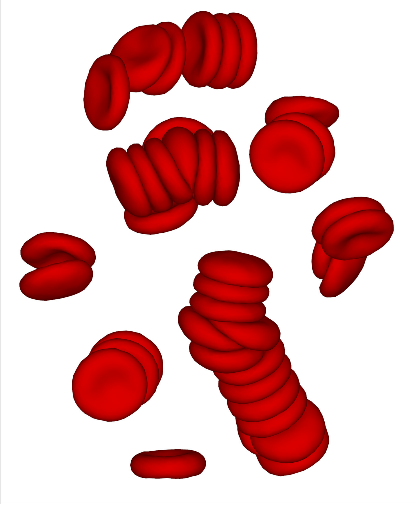

Figure 13: Aggregated RBCs resembling stacked-disk structures in equilibrium at $H_t = 0.1$. Reproduced with permission from Ref. [57].

RBCs (F_e) from the wall. Such surface pressure can be approximated as [137]

$$\Pi_s = \frac{F_e + F_l}{D_r^2} = \frac{k_B T}{h D_r^2} + \frac{c_l \eta_o \dot{\gamma} D_r^2}{h^2}, \tag{25}$$

where h is the distance from the RBC center-of-mass to the wall, D_r is the RBC diameter, and c_l is a constant. The balance between these two pressures ($\Pi_s = \Pi$) has been shown to capture semi-quantitatively the final RBC-FL thickness for different shear rates [137]. These results are also relevant for the flow of a suspension of other deformable particles such as vesicles, capsules, and cells. Their migration mechanisms are expected to be similar; however, quantitatively the predictions will change, because the lift force and shear-induced interactions depend on the properties and dynamics of specific particles.

3.5 Blood rheology

The mechanics and behavior of RBCs in flow govern rheological properties of blood due to their high volume fraction. In addition, a number of experiments [144, 145, 146] indicated that RBCs can form aggregate structures called “rouleaux”, which resemble stacks of disks (see Fig. 13). The aggregation property of RBCs is correlated with plasma proteins (e.g., fibrinogen) [145, 146] such that an increase in their concentration results in stronger RBC-RBC interactions. The origin of inter-RBC aggregation forces is believed to be either depletion interactions between RBCs [147] due to the presence of a number of suspended molecules and proteins in the plasma or macromolecular bridging due to potential interactions of plasma molecules with the RBC membrane [148]. Both hypotheses are plausible and the exact origin of RBC aggregation interactions has not yet been identified. Rouleaux structures formed under normal physiological conditions are rather delicate and can already break at relatively small shear rates. At high shear rates, the aggregation interactions become unimportant, leading to a full dispersion of RBCs [149]. This process is reversible and rouleaux can form again if the shear rate becomes small enough.

The viscosity of blood has been measured in several rheological experiments [144, 150, 151]. Here, we need to clearly differentiate between whole blood, where RBC aggregation is

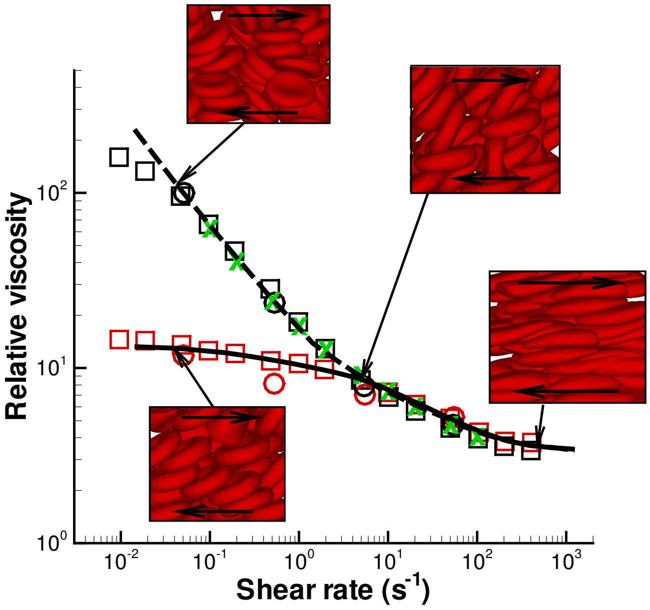

Figure 14: Blood relative viscosity (suspension viscosity normalized by plasma viscosity) as a function of shear rate at $H_t = 0.45$. Simulation results [152] are shown as black full and dashed lines. Experimental data are for: **Whole blood**: green crosses - Merrill et al. [144]; black circles - Chien et al. [150], black squares - Skalak et al. [151]. **Non-aggregating RBC suspension**: red circles - Chien et al. [150]; red squares - Skalak et al. [151]. Reproduced with permission from Ref. [57].

present, and the non-aggregating RBC suspension, which is obtained by removing the blood plasma and re-suspending RBCs into a neutral protein-free solution. In simulations, these two cases are distinguished through the aggregation interactions which can be turned on or off. Figure 14 shows blood viscosity obtained from a RBC suspension in simple shear flow [152] in comparison to the experimental measurements [144, 150, 151]. The simulation predictions agree well with the experimental data, capturing the effect of RBC aggregation on viscosity at low shear rates. The viscosity of whole blood at low shear rates can be several times larger than that of a non-aggregating RBC suspension. Other simulation investigations [153, 154, 155] have attempted to capture the aggregation effect; however, the viscosity predictions from these studies did not reproduce the steep increase in viscosity at low shear rates.

As no experimental measurements of RBC aggregation forces exist, the strength of RBC aggregation in simulations has been calibrated based on the viscosity value for a single low shear rate [152]. After the correct model predictions for whole blood viscosity were obtained, the model has been used to estimate the maximum force required to break up two aggregated RBCs. The break-up force for two aggregated RBCs in the normal direction was found to be in the range 3.0 pN to 7 pN. Thus, the aggregation forces are quite small, which makes them consistent with the experimental observations that rouleaux structures are rather delicate and can break up at relatively low shear rates.

Due to the formation of aggregation structures, whole blood is believed to have a yield stress, which is a threshold shear stress required for flow to begin [144, 156, 157]. The existence of yield stress is difficult to confirm directly in both experiments and simulations, and it is usually found by an extrapolation of available viscosity data to zero shear rate. For blood, it has been performed based on available rheological data [144, 156, 157] yielding a value between 0.0015 and 0.005 Pa at $H_t = 0.45$. Our simulation model supports the existence of yield stress for whole blood with a magnitude of about 0.0017 Pa. However, the simulation model predicts no measurable yield stress for a non-aggregating RBC suspension.

The shear-dependent viscosity and yield stress in blood should be correlated with RBC deformability, dynamics, and inter-cell interactions. Such detailed information is not available experimentally, but can be obtained in simulations. In Ref. [152], the local microstructure of blood has been examined and no significant structures were found for the non-aggregating RBC suspension over a wide range of shear rates. In contrast, for whole blood several pronounced peaks in the radial distribution function have been found at low shear rates, indicating the existence of small rouleaux consisting of several RBCs. This supports that the steep increase in blood viscosity at low shear rates and yield stress for whole blood are due to the RBC aggregation interactions such that larger rouleaux structures have to be broken apart before blood is able to flow. The structural data in Ref. [152] also indicates that the shear-thinning behavior of a non-aggregating RBC suspension is not related to any microstructural changes.

To identify the reason for the shear-thinning behavior of a non-aggregating RBC suspension, we took a closer look at the dynamics of single RBCs. In Sec. 3.3, we have briefly discussed that the dynamics of a single RBC in shear flow can be described by the tumbling motion at low shear rates and tank-treading motion at high shear rates. Similar RBC behavior is also found for sheared RBCs within a suspension [152]. Since the viscosity measurements are performed at $H_t = 0.45$, cell crowding hinders free RBC tumbling, leading to a larger resistance to flow. As RBCs start tank-treading at high enough shear rates, a reduction of shear stresses due to lower tumbling constraints occurs, resulting in a lower viscosity of the suspension. Thus, the stretching of RBCs along the flow direction and switching of their dynamics from tumbling to tank-treading are likely to be the main reasons for the shear-thinning behavior of a non-aggregating RBC suspension [152].

This computational model for RBC suspensions is general enough to be employed in investigations of other cell, vesicle, and capsule suspensions. It should be possible to tune the rheological behavior of a suspension by changing the solvent viscosity, material properties of suspended cells, and inter-cell aggregation interactions. In Fig. 15, several examples of the tunable properties of RBC-like suspensions are presented. Results for stiffer cells with 10 times higher Young's modulus than that for healthy RBCs (red curves) show a considerable increase in viscosity. It is not entirely surprising, as it is known that hardened RBCs lead to an increase in their suspension viscosity [158, 159]. An increase in the RBC rigidity is also highly relevant in many hematologic disorders and diseases such as malaria, sickle-cell anemia, and spherocytosis. Another example in Fig. 15 illustrates the expected decrease, relative to whole blood, in the suspension viscosity for a two-fold reduction in the aggregation strength. Thus, a significant change in the suspension viscosity can be induced by the deformability of suspended particles and their interactions.

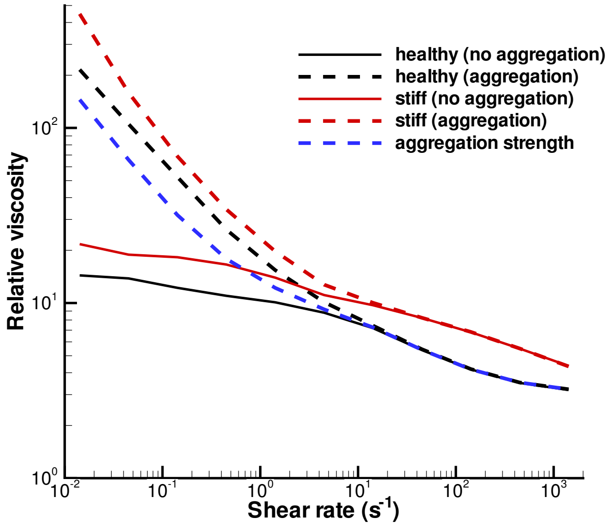

Figure 15: Tunable properties of cell suspensions. Black lines are viscosities of healthy blood with and without aggregation. The blue line illustrates a decrease in RBC aggregation strength by a factor of two. Red lines represent the viscosities of hardened RBC suspensions with a 10 times larger Young's modulus than that for healthy RBCs.

3.6 Margination of WBCs, and micro- and nano-carriers in blood flow

White blood cells (WBCs) are part of our organism's defense system and are mainly located in the blood stream and in the lymphatic system. In case of a problem (e.g., inflammation), WBCs are able to adhere to the vascular endothelium [160, 161] and transmigrate into the surrounding tissue [38]. Prior to vessel wall adhesion, WBCs migrate toward the vessel walls in blood flow [162, 163, 164] through a process called *margination*. WBC margination is a consequence of interactions of these cells with RBCs in blood flow. In fact, one of the important physical components of the margination process is the lift force [133, 134, 135] due to hydrodynamic interactions of cells with walls. The lift force on RBCs is expected to be larger than that on WBCs due to the non-spherical discocyte shape and high deformability of RBCs and the competition of these forces on RBCs and WBCs may lead to the segregation effect or the margination of WBCs.

WBC margination shows a non-trivial dependence on various blood flow properties including hematocrit, flow rate, vessel geometry, and RBC aggregation. For instance, *in vivo* experiments on WBC adhesion [164] have demonstrated a high WBC adhesion rate at low flow rates characteristic for venular blood flow and high $H_t > 0.45$. In contrast, *in vitro* experiments on WBC adhesion in glass tubes [165] suggested no sensitivity of WBC adhesion to H_t. Similarly, a 2D simulation study [166] has also suggested no significant effect of H_t on WBC margination. In contradiction to the apparent H_t independence of WBC margination are recent microfluidic experiments [167], which have shown that the most pronounced WBC margination occurs within an intermediate range of $H_t \simeq 0.2 - 0.3$, while at both lower and higher H_t values WBC margination is reduced. In our recent

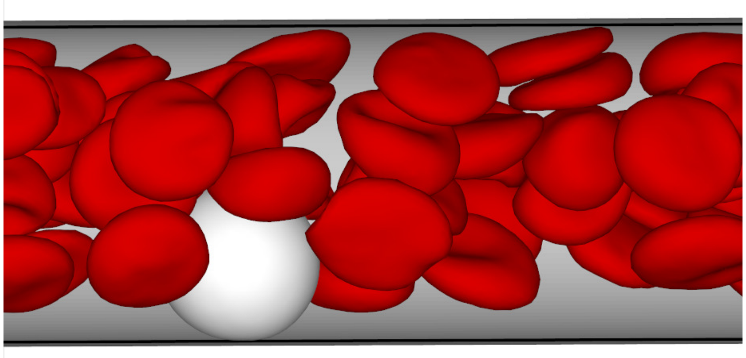

Figure 16: Simulation snapshot of RBCs (red) and a marginated WBC (white). The flow is from the left to the right. $H_t = 0.3$ and $\dot{\gamma}^* = 32$. Reproduced with permission from Ref. [169].

simulation work in both 2D [168] and 3D [169], we were able to reconcile the existing contradicting observations of WBC margination dependence on H_t, showing that a strong margination effect is achieved for an intermediate range of H_t values. The apparent inconsistency with experiments [165] and simulations [166], which indicated no dependence of WBC margination on H_t, has been explained by the fact that the H_t values used in these studies fall almost entirely into the region of a strong WBC margination predicted in Refs. [168, 169].

Figure 16 shows an example blood flow with a marginated WBC for $H_t = 0.3$ and $\dot{\gamma}^* = 32$. A non-dimensional shear rate $\dot{\gamma}^*$ is the product of the average shear rate (or pseudo-shear rate) and the characteristic relaxation time of a RBC [169]. During the course of simulations we measure the center-of-mass distribution of a WBC within the tube, which reflects the probability of a WBC to be at a certain position in the tube. From the WBC distribution we compute the margination probability defined as the probability of the WBC center-of-mass to be within a distance r_w away from the wall. Figure 17 presents the WBC margination diagram for $r_w < 5.5\ \mu m$. The WBC radius was set to 5 μm in all simulations and thus, the condition $r_w < 5.5\ \mu m$ is equivalent to a maximum distance of 0.5 μm between the WBC surface and the wall. The diagram shows that WBC margination is strongest within the range of $H_t = 0.2 - 0.4$. At low H_t, the concentration of RBCs is small leading to a weak WBC margination. At high H_t, WBC margination is also attenuated due to interactions of a WBC with RBCs in flow. In Refs. [168, 169], we have shown that for low enough H_t the region in front of a marginated WBC remains virtually free of RBCs, which could otherwise interfere with the WBC and lift it off the wall. However, at large enough H_t, due to RBC crowding a marginated WBC may often encounter RBCs in front, which help to effectively displace it away from the wall, leading to a low margination probability. Finally, WBC margination becomes weaker for higher flow rates, which is consistent with experimental observations that WBC margination and adhesion primarily occurs in venules and not in arterioles [164, 170, 167]. As an estimation, the flow rates in the venular part of the microcirculation correspond to the values of $\dot{\gamma}^* \lesssim 90$, while in the arteriolar part the flow rates are higher with $\dot{\gamma}^* \gtrsim 120$ [28, 171].

In Ref. [169], an estimation of the increase in flow resistance due to the presence of a marginated WBC has also been performed. Marginated WBCs increase the flow resistance

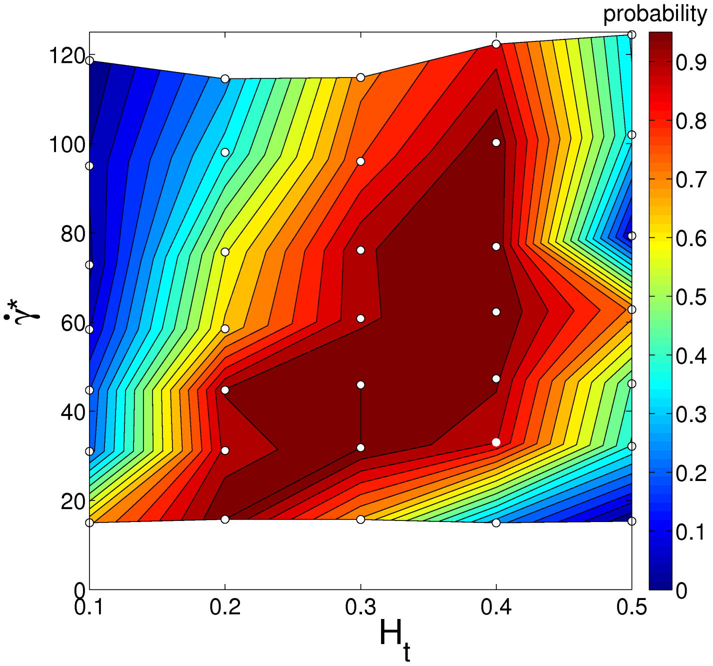

Figure 17: WBC margination-probability diagram calculated for $r_w < 5.5\ \mu m$, where r_w is the distance of the WBC center-of-mass from the wall. The small white circles in the diagram indicate performed simulations. No aggregation interactions between RBC were imposed here. Reproduced with permission from Ref. [169].

by up to about 30% for vessel diameters of 20 μm; this effect on the flow resistance is expected to subside for much larger tube diameters. The WBC margination results are also relevant for the margination of other cells in blood flow with a similar size and deformability properties. For instance, circulating tumor cells are similar in size and are rather stiff [172, 173], indicating that they will mainly marginate in the venular part of microcirculation, and therefore the tissue invasion by tumor cells should largely occur from venules. The WBC margination results are also relevant for microfluidic flow, where the separation of WBCs or circulating tumor cells from whole blood can be of interest.

Similarly to WBCs, margination of micro- and nano-carriers used for drug delivery applications [175, 176] can be expected in blood flow. Successful delivery of micro- and nano-carriers strongly depends on their binding to specific targeted sites, which will be affected by their margination properties. Here, in addition to the various blood flow conditions, we are mainly interested in the effect of particle characteristics such as size, shape, and deformability on their margination. The role of particle size and shape in the efficient delivery is a multi-faceted problem. For example, large enough particles with a diameter (D_p) greater than approximately 4 µm become trapped in the smallest capillaries of the body [177] and recent experiments suggest that large particles with $D_p \gtrsim 3$ µm are subject to an enhanced phagocytosis [178]. On the other hand, microfluidic experiments [179] indicate that spherical particles with the size of 2 µm adhere much more frequently than their sub-micron counterparts. Furthermore, nano-particles with a size below $20 - 30$ nm are rapidly excreted through the kidneys [180]. Adhesion of various particles has been studied experimentally [181, 182] and theoretically [183, 184], with the outcome that oblate ellipsoids are subject to stronger adhesion than spheres with the same volume. These studies

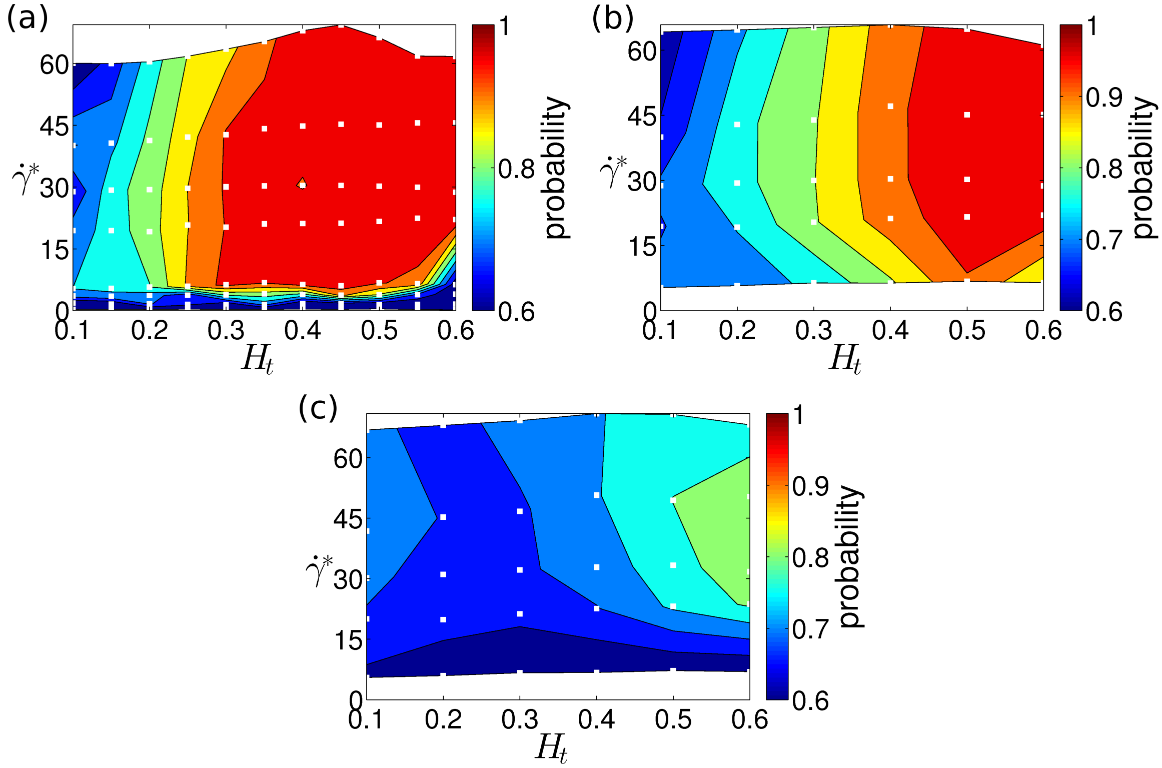

Figure 18: Dependence of margination on particle size. Probability diagrams of particle margination for various H_t and $\dot{\gamma}^*$ values and for circular 2D particles with the sizes (a) $D_p = 0.3D_r$ (1.83 µm), (b) $D_p = 0.15D_r$ (0.91 µm), (c) $D_p = 0.04D_r$ (0.25 µm). The white squares (□) indicate the values of H_t and $\dot{\gamma}^*$ for which simulations were performed. The margination probability is calculated based on the RBC-FL thickness. Reproduced with permission from Ref. [174].

show that particle size and shape are also very important parameters for the design of efficient drug-delivery carriers. To better understand the adhesion potential of micro- and nano-particles, we have investigated the margination of particles with different properties in blood flow [174, 185].

Figure 18 presents margination diagrams for circular particles of different sizes (simulations in 2D). The comparison of diagrams clearly indicates that the region of high margination probability becomes smaller with decreasing particle size. The reason for the reduction in margination probability is related to the ratio between particle size and the thickness of the RBC-FL [174, 185]. If the particle has a size similar to the RBC-FL thickness, its distribution shows a pronounced peak in the RBC-FL indicating that the particle spends a lot of time very close to the wall. As the size of a particle is decreased, its margination becomes worse, because its distribution in the RBC-FL does not have a strong peak and smaller particles can also fit better between RBCs in the cellular core of the flow. In fact, the distribution of particles smaller than roughly 250 nm is close to the distribution of the blood plasma, indicating that they can be incorporated well within inter-RBC gaps. This result shows that the margination properties of such small nano-particles can be directly inferred from local H_t distributions. Our numerical observations are also supported by recent *in vivo* experiments [186] which have shown that particles with a size of about 1 µm are located closer to the vessel wall than smaller nano-particles.

The simulation results in Refs. [174, 185] have also shown that particle margination is most pronounced in small vessels such as capillaries, indicating that their adhesion is most probable in the capillary part of the microvasculature. Particle deformability worsens their margination properties [185], which is similar to the case of WBCs [168]. Ellipsoidal particles possess slightly worse margination properties in comparison with the spherical particles; however, the adhesion of ellipsoids appears to be significantly better [181, 182]. As a conclusion, our simulations suggest that ellipsoidal particles of micron size are favorable for drug delivery in comparison with sub-micron spherical particles [174, 185].

4 Discussion and outlook

4.1 Summary and conclusions

The examples given above and the considerable amount of work in soft matter and biophysics demonstrate that the behavior and rheology of soft-particle suspensions have many generic features as well as many specific aspects which differentiate such systems. For instance, generic features are softness of interactions, the shear-thinning behavior of various suspensions, the tank-treading and tumbling motion of individual particles in a solution, the deformation and interactions in flow, etc. This indicates that the physical mechanisms, which govern the behavior of such systems, are often similar in spite of the apparent differences among various soft systems. One of the examples we showed is the tank-treading motion which occurs for star polymers, vesicles, and RBCs, even though structurally these objects are very different. Shear thinning of various suspensions of soft particles is, perhaps, even more generic and may occur due to structural changes within a suspension, the deformability and alignment of soft particles in flow, and the break-up of aggregates in the case of attractive inter-particle interactions.

Despite many similarities among various soft matter systems, their behavior still shows many differences and specificities both quantitatively and qualitatively. For example, capsules and RBCs possess shear elasticity in comparison to vesicles, which is responsible for the existence of tumbling-to-tank-treading transition at low viscosity contrasts between inner and outer fluids. Another example is the internal viscosity (or friction) which can be changed and controlled for vesicles, capsules, and cells, but such a possibility does not exist in polymer systems. Here, internal viscosity would be one of the parameters for tuning the rheological properties of a suspension. It is also important to note that distinct suspensions may show similar behavior in one regime, but a very different response in another. For example, star-polymer solutions at low shear rates display rheological properties similar to a suspension of rigid-sphere colloids, because the deformation of star-polymers in that regime is very small. With increasing shear rate, star polymers deform and their rheological properties become dissimilar to those of hard-sphere colloids.

A computational framework (e.g., presented methods or other simulation approaches) based on mesoscopic modeling is also rather generic and often can be applied to various soft-matter systems, including polymers, proteins, vesicles, capsules, and cells. This means that such methods should be able to capture many of the generic features of soft-particle suspensions at least qualitatively. However, what makes a simulation powerful is the ability to take a step further and to provide not only qualitative, but also quantitative predictions. At this step, the specificities of a particular system become very important and the corresponding model has to include all the relevant physical details in order to describe the specific features of a particular system. The development of quantitative and realistic models is practically impossible without proper experimental input, making interactions with experimentalists essential. There are already many examples of simulations validated by experiments and used for the quantification of more sophisticated experimental measurements. More importantly, many computational models already attempt to go beyond experimental predictions in order to generate and/or test new physical and biological hypotheses. Hence, such simulations can be employed to guide and optimize experimental tools and settings for a better understanding of involved physical mechanisms.

The number of the parameters relevant for soft-particle suspensions is very large, including molecular length, stiffness, monomer density within macromolecules, internal viscosity, membrane bending rigidity, membrane shear modulus, particle shape and size, and particle interactions. This poses difficulties in the systematic investigation of their behavior and rheological properties; however, it also offers entirely new possibilities for tuning their properties. Here, accurate modeling of such suspensions opens up great opportunities, since simulations are usually more robust and significantly cheaper than equivalent large sets of experiments. Moreover, the rapid development of the computational capacity of modern supercomputers allows to perform very large and sophisticated simulations, which can closely mimic, extend, or even replace various experimental systems. More work is required in the future to explore the full application potential of such systems and to gain a deeper insight into the relation between microscopic properties and the emergent macroscopic behavior.

4.2 Current research directions

Finally, we would also like to outline a few current research directions. Blood flow will remain an important research topic in the future, because the methods developed and the results obtained so far open the doors to address a broad range of biophysical and biomedical problems and questions. One of the current issues is the viscosity contrast between the cytosol and plasma and its effect on the dynamics of single RBCs and blood flow in microvessels. The examples of RBC dynamics and blood flow shown in this thesis are based on the assumption of the viscosity contrast of unity, while the physiological ratio is close to $5-6$. Our preliminary data indicate that the realistic viscosity contrast for a RBC suppresses its tank-treading motion leading to new types of dynamics with significant cell deformations. This effect considerably alters the behavior of single RBCs in microvessels. The viscosity contrast is also likely to change the lift force on flowing RBCs, which in turn alters the migration of RBCs away from the walls. Thus, in this project we depart further away from a more generic RBC model and move closer to a quantitative model for RBCs and blood flow.

Another research direction corresponds to simulations of blood flow in microcirculation. Here, an extension of the employed simulation techniques is required in order to model blood flow in complex vessel geometries and small microvascular networks. The main aim of this research is to better understand blood flow in microvasculature and devise empirical or theoretical models for the behavior of blood cells around bifurcations and vessel junctions, their partitioning and traversal through a microvascular network. Such models will help us understand the perfusion of the microvasculature, blood flow regulation, and the delivery of oxygen and drug carriers. Another important aspect of this research direction is blood flow in various blood-related diseases and disorders, where the structure and perfusion of microcirculation can change and the alteration of blood cell properties may occur.

We also pursue modeling of microfluidic flow. Our main interest in this project is the behavior of soft particles in microfluidics with application to particle sorting and detection of rare solutes. In such devices, a number of physical phenomena can be relevant, including migration in flow, deformability, particle interactions, adhesiveness, device geometry, etc. In relation to this project, we also investigate the behavior of various mixtures, for example, polymers and cells. This leads to new physical insights for such systems, but is also relevant and useful in many biophysical and biomedical applications.

We also investigate the swimming behavior of microswimmers. The motility and manipulation of microswimmers can lead to a number of potential applications ranging from cargo delivery to micromixing within microfluidic systems. In particular, we are interested in an artificial microswimmer represented by the Janus colloid whose one half is coated with gold. Under external laser irradiation, the gold cap is able to absorb heat leading to a local temperature gradient, which results in microswimmer propulsion due to thermophoresis. Recent experiments [187, 188] have shown that Janus particle propulsion can be significantly altered in binary mixtures near a critical point; however, this behavior remains poorly understood. Thus, we investigate the behavior of Janus colloids in critical mixtures using particle-based mesoscopic numerical simulations.

References

[1] A. Einstein. A new determination of molecular dimensions. *Ann. Physik*, 19:289–305, 1906.

[2] C.-C. Huang, R. G. Winkler, G. Sutmann, and G. Gompper. Semidilute polymer solutions at equilibrium and under shear flow. *Macromolecules*, 43:10107–10116, 2010.

[3] D. Vlassopoulos and M. Cloitre. Tunable rheology of dense soft deformable colloids. *Curr. Opin. Colloid Interface Sci.*, 19:561–574, 2014.

[4] D. A. Fedosov, S. P. Singh, A. Chatterji, R. G. Winkler, and G. Gompper. Semidilute solutions of ultra-soft colloids under shear flow. *Soft Matter*, 8:4109–4120, 2012.

[5] R. G. Winkler, D. A. Fedosov, and G. Gompper. Dynamical and rheological properties of soft colloid suspensions. *Curr. Opin. Colloid Interface Sci.*, 19:594–610, 2014.

[6] J. Vermant and H. H. Winter. Special issue devoted to novel trends in rheology. *Rheol. Acta*, 52:189190, 2013.

[7] R. B. Bird, R. C. Armstrong, and O. Hassager. *Dynamics of polymeric liquids, Fluid mechanics.* John Wiley & Sons, New York, second edition, 1987.

[8] J. Bent, L. R. Hutchings, R. W. Richards, T. Gough, R. Spares, P. D. Coates, I. Grillo, O. G. Harlen, D. J. Read, R. S. Graham, A. E. Likhtman, D. J. Groves, T. M. Nicholson, and T. C. B. McLeish. Neutron-mapping polymer flow: scattering, flow visualization, and molecular theory. *Science*, 301:1691–1695, 2003.

[9] D. T. N. Chen, Q. Wen, P. A. Janmey, J. C. Crocker, and A. G. Yodh. Rheology of soft materials. *Annu. Rev. Condens. Matter Phys.*, 1:301–322, 2010.

[10] R. B. Bird, C. F. Curtiss, R. C. Armstrong, and O. Hassager. *Dynamics of polymeric liquids, Kinetic theory.* John Wiley & Sons, New York, second edition, 1987.

[11] H. C. Öttinger. *Stochastic processes in polymeric fluids.* Springer, Berlin, 1996.

[12] M. Rubinstein and R. C. Colby. *Polymer physics.* Oxford University Press, Oxford, 2003.

[13] R. M. Jendrejack, J. J. de Pablo, and M. D. Graham. Stochastic simulations of DNA in flow: dynamics and the effects of hydrodynamic interactions. *J. Chem. Phys.*, 116:7752–7759, 2002.

[14] R. G. Winkler. Conformational and rheological properties of semiflexible polymers in shear flow. *J. Chem. Phys.*, 133:164905, 2010.

[15] C. M. Schroeder, R. E. Teixeira, E. S. G. Shaqfeh, and S. Chu. Dynamics of DNA in the flow-gradient plane of steady shear flow: observations and simulations. *Macromolecules*, 38:1967–1978, 2005.

[16] M. Diez-Silva, M. Dao, J. Han, C.-T. Lim, and S. Suresh. Shape and biomechanical characteristics of human red blood cells in health and disease. *MRS Bulletin*, 35:382–388, 2010.

[17] D. A. Fedosov, M. Dao, G. E. Karniadakis, and S. Suresh. Computational biorheology of human blood flow in health and disease. *Ann. Biomed. Eng.*, 42:368–387, 2014.

[18] D. Di Carlo. A mechanical biomarker of cell state in medicine. *J. Lab. Autom.*, 17:32–42, 2012.

[19] P. G. de Gennes. *Scaling concepts in polymer physics.* Cornell University Press, Ithaca, 1979.

[20] M. Doi and S. F. Edwards. *The theory of polymer dynamics.* Oxford University Press, New York, 1986.

[21] M. Daoud and J. P. Cotton. Star shaped polymers: a model for the conformation and its concentration dependence. *J. Phys. France*, 43:531–538, 1982.

[22] C. N. Likos, H. Löwen, M. Watzlawek, B. Abbas, O. Jucknischke, J. Allgaier, and D. Richter. Star polymers viewed as ultrasoft colloidal particles. *Phys. Rev. Lett.*, 80:4450–4453, 1998.

[23] D. Vlassopoulos and G. Fytas. From polymers to colloids: engineering the dynamic properties of hairy particles. *Adv. Polym. Sci.*, 236:1–54, 2010.

[24] M. Kröger. Simple models for complex nonequilibrium fluids. *Phys. Rep.*, 390:453–551, 2004.

[25] R. G. Winkler, S. P. Singh, C.-C. Huang, D. A. Fedosov, K. Mussawisade, A. Chatterji, M. Ripoll, and G. Gompper. Mesoscale hydrodynamics simulations of particle suspensions under shear flow: from hard to ultrasoft colloids. *Eur. Phys. J. Special Topics*, 222:2773–2786, 2013.

[26] D. E. Smith, H. P. Babcock, and S. Chu. Single-polymer dynamics in steady shear flow. *Science*, 283:1724–1727, 1999.

[27] C.-C. Huang, G. Sutmann, G. Gompper, and R. G. Winkler. Tumbling of polymers in semidilute solution under shear flow. *Europhys. Lett.*, 93:54004, 2011.

[28] A. S. Popel and P. C. Johnson. Microcirculation and hemorheology. *Annu. Rev. Fluid Mech.*, 37:43–69, 2005.

[29] H. H. Lipowsky. Microvascular rheology and hemodynamics. *Microcirculation*, 12:5–15, 2005.

[30] A. R. Pries and T. W. Secomb. Blood flow in microvascular networks. In R. F. Tuma, W. N. Duran, and K. Ley, editors, *Handbook of Physiology, The Cardiovascular System, Microcirculation*, pages 3–36. Academic Press, San Diego, 2008.

[31] T. W. Secomb and A. R. Pries. The microcirculation: physiology at the mesoscale. *J. Physiol.*, 589:1047–1052, 2011.

[32] R. K. Jain. Determinants of tumor blood flow: a review. *Cancer Res.*, 48:2641–2658, 1988.

[33] G. W. Schmid-Schönbein and D. Granger, editors. *Molecular basis for microcirculatory disorders.* Springer, New York, 2003.

[34] S. Adams, H. Brown, and G. Turner. Breaking down the blood-brain barrier: signaling a path to cerebral malaria? *Trends Parasitol.*, 18:360–366, 2002.

[35] A. R. Pries, T. W. Secomb, and P. Gaehtgens. Biophysical aspects of blood flow in the microvasculature. *Cardiovasc. Res.*, 32:654–667, 1996.

[36] A. R. Pries and T. W. Secomb. Rheology of the microcirculation. *Clin. Hemorheol. Microcirc.*, 29:143–148, 2003.

[37] Y. C. Fung. *Biomechanics: Mechanical properties of living tissues.* Springer-Verlag, New York, second edition, 1993.

[38] T. A. Springer. Traffic signals on endothelium for lymphocyte recirculation and leukocyte emigration. *Annu. Rev. Physiol.*, 57:827–872, 1995.

[39] E. B. Finger, K. D. Puri, R. Alon, M. B. Lawrence, U. H. von Andrian, and T. A. Springer. Adhesion through L-selectin requires a threshold hydrodynamic shear. *Nature*, 379:266–269, 1996.

[40] S. Succi. *The Lattice Boltzmann equation for fluid dynamics and beyond.* Oxford University Press, Oxford, 2001.

[41] P. J. Hoogerbrugge and J. M. V. A. Koelman. Simulating microscopic hydrodynamic

phenomena with dissipative particle dynamics. *Europhys. Lett.*, 19:155–160, 1992.

[42] P. Español and P. Warren. Statistical mechanics of dissipative particle dynamics. *Europhys. Lett.*, 30:191–196, 1995.

[43] P. Español and M. Revenga. Smoothed dissipative particle dynamics. *Phys. Rev. E*, 67:026705, 2003.

[44] K. Müller, D. A. Fedosov, and G. Gompper. Smoothed dissipative particle dynamics with angular momentum conservation. *J. Comp. Phys.*, 281:301–315, 2015.

[45] A. Malevanets and R. Kapral. Mesoscopic model for solvent dynamics. *J. Chem. Phys.*, 110:8605–8613, 1999.

[46] R. Kapral. Multiparticle collision dynamics: simulation of complex systems on mesoscales. *Adv. Chem. Phys.*, 140:89–146, 2008.

[47] G. Gompper, T. Ihle, D. M. Kroll, and R. G. Winkler. Multi-particle collision dynamics: a particle-based mesoscale simulation approach to the hydrodynamics of complex fluids. *Adv. Polym. Sci.*, 221:1–87, 2009.

[48] J. F. Wendt, editor. *Computational Fluid Dynamics.* Springer, Berlin, 3rd edition, 2009.

[49] M. M. Dupin, I. Halliday, C. M. Care, L. Alboul, and L. L. Munn. Modeling the flow of dense suspensions of deformable particles in three dimensions. *Phys. Rev. E*, 75:066707, 2007.

[50] X. Fan, N. Phan-Thien, S. Chen, X. Wu, and T. Y. Ng. Simulating flow of DNA suspension using dissipative particle dynamics. *Phys. Fluids*, 18:063102, 2006.

[51] D. A. Fedosov, G. E. Karniadakis, and B. Caswell. Dissipative particle dynamics simulation of depletion layer and polymer migration in micro- and nanochannels for dilute polymer solutions. *J. Chem. Phys.*, 128:144903, 2008.

[52] M. P. Allen and D. J. Tildesley. *Computer simulation of liquids.* Clarendon Press, New York, 1991.

[53] L. B. Lucy. A numerical approach to the testing the fission hypothesis. *Astronom. J.*, 82:1013–1024, 1977.

[54] J. J. Monaghan. Smoothed particle hydrodynamics. *Rep. Prog. Phys.*, 68:1703–1759, 2005.

[55] I. O. Götze, H. Noguchi, and G. Gompper. Relevance of angular momentum conservation in mesoscale hydrodynamics simulations. *Phys. Rev. E*, 76:046705, 2007.

[56] D. W. Condiff and J. S. Dahler. Fluid mechanical aspects of antisymmetric stress. *Phys. Fluids*, 7:842–854, 1964.

[57] D. A. Fedosov, H. Noguchi, and G. Gompper. Multiscale modeling of blood flow: from single cells to blood rheology. *Biomech. Model. Mechanobiol.*, 13:239–258, 2014.

[58] D. E. Discher, D. H. Boal, and S. K. Boey. Simulations of the erythrocyte cytoskeleton at large deformation. II. Micropipette aspiration. *Biophys. J.*, 75:1584–1597, 1998.

[59] J. Li, M. Dao, C. T. Lim, and S. Suresh. Spectrin-level modeling of the cytoskeleton and optical tweezers stretching of the erythrocyte. *Biophys. J.*, 88:3707–3719, 2005.

[60] H. Noguchi and G. Gompper. Shape transitions of fluid vesicles and red blood cells in capillary flows. *Proc. Natl. Acad. Sci. USA*, 102:14159–14164, 2005.

[61] I. V. Pivkin and G. E. Karniadakis. Accurate coarse-grained modeling of red blood cells. *Phys. Rev. Lett.*, 101:118105, 2008.

[62] D. A. Fedosov, B. Caswell, and G. E. Karniadakis. Systematic coarse-graining of spectrin-level red blood cell models. *Comput. Meth. Appl. Mech. Eng.*, 199:1937–1948, 2010.

[63] D. A. Fedosov, B. Caswell, and G. E. Karniadakis. A multiscale red blood cell model with accurate mechanics, rheology, and dynamics. *Biophys. J.*, 98:2215–2225, 2010.

[64] W. Helfrich. Elastic properties of lipid bilayers: theory and possible experiments. *Z. Naturforschung C*, 28:693–703, 1973.

[65] T. M. Birshtein and E. B. Zhulina. Conformations of star-branched macromolecules. *Polymer*, 25:1453–1461, 1984.

[66] T. M. Birshtein, E. B. Zhulina, and O. V. Borisov. Temperature-concentration diagram for a solution of star-branched macromolecules. *Polymer*, 27:1078–1086, 1986.

[67] G. S. Grest, K. Kremer, and T. A. Witten. Structure of many-arm star polymers: a molecular dynamics simulation. *Macromolecules*, 20:1376–1383, 1987.

[68] C. N. Likos. Effective interactions in soft condensed matter physics. *Phys. Rep.*, 348:267–439, 2001.

[69] D. Vlassopoulos, G. Fytas, T. Pakula, and J. Roovers. Multiarm star polymers dynamics. *J. Phys. Condens. Matter*, 13:R855–R876, 2001.

[70] M. Ripoll, R. G. Winkler, and G. Gompper. Star polymers in shear flow. *Phys. Rev. Lett.*, 96:188302, 2006.

[71] M. Ripoll, R. G. Winkler, and G. Gompper. Hydrodynamic screening of star polymers in shear flow. *Eur. Phys. J. E*, 23:349–354, 2007.

[72] S. P. Singh, R. G. Winkler, and G. Gompper. Non-equilibrium forces between dragged ultrasoft colloids. *Phys. Rev. Lett.*, 107:158301, 2011.

[73] J. T. Padding, E. van Ruymbeke, D. Vlassopoulos, and W. J. Briels. Computer simulation of the rheology of concentrated star polymer suspensions. *Rheol. Acta*, 49:473–484, 2010.

[74] W. J. Briels, D. Vlassopoulos, K. Kang, and J. K. G. Dhont. Constitutive equations for the flow behavior of entangled polymeric systems: application to star polymers. *J. Chem. Phys.*, 134:124901, 2011.

[75] S. P. Singh, D. A. Fedosov, A. Chatterji, R. G. Winkler, and G. Gompper. Conformational and dynamical properties of ultra-soft colloids in semi-dilute solutions under shear flow. *J. Phys.: Condens. Matter*, 24:464103, 2012.

[76] C. Aust, M. Kröger, and S. Hess. Structure and dynamics of dilute polymer solutions under shear flow via nonequilibrium molecular dynamics. *Macromolecules*, 32:5660–5672, 1999.

[77] S. R. Keller and R. Skalak. Motion of a tank-treading ellipsoidal particle in a shear flow. *J. Fluid Mech.*, 120:27–47, 1982.

[78] J. Klein. Shear, friction, and lubrication forces between polymer-bearing surfaces. *Annu. Rev. Mater. Sci.*, 26:581–612, 1996.

[79] N. Ayres. Polymer brushes: applications in biomaterials and nanotechnology. *Polym. Chem.*, 1:769–777, 2010.

[80] K. Binder, T. Kreer, and A. Milchev. Polymer brushes under flow and in other out-of-equilibrium conditions. *Soft Matter*, 7:7159–7172, 2011.

[81] L. Han, D. Dean, C. Ortiz, and A. J. Grodzinsky. Lateral nanomechanics of cartilage aggrecan macromolecules. *Biophys. J.*, 92:1384–1398, 2007.

[82] S. Weinbaum, X. Zhang, Y. Han, H. Vink, and S. C. Cowin. Mechanotransduction and flow across the endothelial glycocalyx. *Proc. Natl. Acad. Sci. USA*, 100:7988–7995, 2003.

[83] S. Weinbaum, J. M. Tarbell, and E. R. Damiano. The structure and function of the endothelial glycocalyx layer. *Annu. Rev. Biomed. Eng.*, 9:121–167, 2007.

[84] B. A. Evans, A. R. Shields, R. L. Carroll, S. Washburn, M. R. Falvo, and R. Superfine. Magnetically actuated nanorod arrays as biomimetic cilia. *Nano Lett.*, 7:1428–1434, 2007.

[85] Y. Higaki, R. Okazaki, and A. Takahara. Semirigid biobased polymer brush: poly(α-methylene-γ-butyrolactone) brushes. *ACS Macro Lett.*, 1:1124–1127, 2012.

[86] H. Merlitz, G.-L. He, C.-X. Wu, and J.-U. Sommer. Nanoscale brushes: how to build a smart surface coating. *Phys. Rev. Lett.*, 102:115702, 2009.

[87] F. Römer and D. A. Fedosov. Dense brushes of stiff polymers or filaments in fluid flow. *Europhys. Lett.*, 109:68001, 2015.

[88] C.-M. Chen and Y.-A. Fwu. Monte Carlo simulations of polymer brushes. *Phys. Rev. E*, 63:011506, 2000.

[89] A. Milchev and K. Binder. Semiflexible polymers grafted to a solid planar substrate: changing the structure from polymer brush to "polymer bristle". *J. Chem. Phys.*, 136:194901, 2012.

[90] M. A. Carignano and I. Szleifer. Statistical thermodynamic theory of grafted polymeric layers. *J. Chem. Phys.*, 98:5006–5018, 1993.

[91] D. V. Kuznetsov and Z. Y. Chen. Semiexible polymer brushes: a scaling theory. *J. Chem. Phys.*, 109:7017–7027, 1998.

[92] G. G. Kim and K. Char. Semiflexible polymer brushes: most probable configuration approach based on cotinuous chain model. *Bull. Korean Chem. Soc.*, 20:1026–1030, 1999.

[93] A. Milchev and K. Binder. Bending or buckling: compression-induced phase transition in a semi-flexible polymer brush. *Europhys. Lett.*, 102:58003, 2013.

[94] A. Milchev and K. Binder. Unconventional ordering behavior of semi-flexible polymers in dense brushes under compression. *Soft Matter*, 10:3783–3797, 2014.

[95] M. Deng, X. Li, H. Liang, B. Caswell, and G. E. Karniadakis. Simulation and modelling of slip flow over surfaces grafted with polymer brushes and glycocalyx fibres. *J. Fluid Mech.*, 711:192–211, 2012.

[96] Y. W. Kim, V. Lobaskin, C. Gutsche, F. Kremer, P. Pincus, and R. R. Netz. Nonlinear response of grafted semiflexible polymers in shear flow. *Macromolecules*, 42:3650–3655, 2009.

[97] L. D. Landau and E. M. Lifshitz. *Theory of Elasticity.* Pergamon Press, London, 1970.

[98] R. G. Cox. The motion of long slender bodies in a viscous fluid Part 1. General theory. *J. Fluid Mech.*, 44:791–810, 1970.

[99] H. C. Brinkman. A calculation of the viscous force exerted by a flowing fluid on a dense swarm of particles. *Appl. Sci. Res.*, 1:27–34, 1949.

[100] B. Kaoui, N. Tahiri, T. Biben, H. Ez-Zahraouy, A. Benyoussef, G. Biros, and C. Misbah. Complexity of vesicle microcirculation. *Phys. Rev. E*, 84:041906, 2011.

[101] N. Tahiri, T. Biben, H. Ez-Zahraouy, A. Benyoussef, and C. Misbah. On the problem of slipper shapes of red blood cells in the microvasculature. *Microvasc. Res.*, 85:40–45, 2013.

[102] R. S. Sprague, M. L. Ellsworth, A. H. Stephenson, M. E. Kleinhenz, and A. J. Lonigro. Deformation-induced ATP release from red blood cells requires CFTR activity. *Am. J. Physiol.*, 275:H1726–H1732, 1998.

[103] A. M. Forsyth, J. Wan, P. D. Owrutsky, M. Abkarian, and H. A. Stone. Multiscale approach to link red blood cell dynamics, shear viscosity, and ATP release. *Proc. Natl. Acad. Sci. USA*, 108:10986–10991, 2011.

[104] J. A. Davis, D. W. Inglis, K. J. Morton, D. A. Lawrence, L. R. Huang, S. Y. Chou, J. C. Sturm, and R. H. Austin. Deterministic hydrodynamics: taking blood apart. *Proc. Nat. Acad. Sci. USA*, 103:14779–14784, 2006.

[105] H. Craighead. Future lab-on-a-chip technologies for interrogating individual molecules. *Nature*, 442:387–393, 2006.

[106] T. M. Fischer. Shape memory of human red blood cells. *Biophys. J.*, 86:3304–3313, 2004.

[107] M. Abkarian, M. Faivre, and A. Viallat. Swinging of red blood cells under shear flow. *Phys. Rev. Lett.*, 98:188302, 2007.

[108] J. Dupire, M. Socol, and A. Viallat. Full dynamics of a red blood cell in shear flow. *Proc. Natl. Acad. Sci. USA*, 109:20808–20813, 2012.

[109] J. M. Skotheim and T. W. Secomb. Red blood cells and other nonspherical capsules in shear flow: oscillatory dynamics and the tank-treading-to-tumbling transition. *Phys. Rev. Lett.*, 98:078301, 2007.

[110] P. M. Vlahovska, Y.-N. Young, G. Danker, and C. Misbah. Dynamics of a non-spherical microcapsule with incompressible interface in shear flow. *J. Fluid Mech.*, 678:221–247, 2011.

[111] H. Noguchi. Dynamic modes of microcapsules in steady shear flow: effects of bending and shear elasticities. *Phys. Rev. E*, 81:056319, 2010.

[112] A. Z. K. Yazdani and P. Bagchi. Phase diagram and breathing dynamics of a single red blood cell and a biconcave capsule in dilute shear flow. *Phys. Rev. E*, 84:026314, 2011.

[113] Z. Peng, X. Li, I. V. Pivkin, M. Dao, G. E. Karniadakis, and S. Suresh. Lipid bilayer and cytoskeletal interactions in a red blood cell. *Proc. Natl. Acad. Sci. USA*, 110:13356–13361, 2013.

[114] H. Noguchi and G. Gompper. Dynamics of fluid vesicles in shear flow: effect of the membrane viscosity and thermal fluctuations. *Phys. Rev. E*, 72:011901, 2005.

[115] V. Vitkova, M.-A. Mader, B. Polack, C. Misbah, and T. Podgorski. Micro-macro link in rheology of erythrocyte and vesicle suspensions. *Biophys. J.*, 95:L33–L35, 2008.

[116] D. A. Fedosov, M. Peltomäki, and G. Gompper. Deformation and dynamics of red blood cells in flow through cylindrical microchannels. *Soft Matter*, 10:4258–4267, 2014.

[117] P. Gaehtgens, C. Dührssen, and K. H. Albrecht. Motion, deformation, and interaction of blood cells and plasma during flow through narrow capillary tubes. *Blood Cells*, 6:799–812, 1980.

[118] M. Abkarian, M. Faivre, R. Horton, K. Smistrup, C. A. Best-Popescu, and H. A. Stone. Cellular-scale hydrodynamics. *Biomed. Mater.*, 3:034011, 2008.

[119] J. L. McWhirter, H. Noguchi, and G. Gompper. Flow-induced clustering and alignment of vesicles and red blood cells in microcapillaries. *Proc. Natl. Acad. Sci. USA*, 106:6039–6043, 2009.

[120] G. Tomaiuolo, M. Simeone, V. Martinelli, B. Rotoli, and S. Guido. Red blood cell deformation in microconfined flow. *Soft Matter*, 5:3736–3740, 2009.

[121] D. A. Reasor Jr, J. R. Clausen, and C. K. Aidun. Coupling the lattice-Boltzmann and spectrin-link methods for the direct numerical simulation of cellular blood flow. *Int. J. Num. Meth. Fluids*, 68:767–781, 2012.

[122] R. Fåhraeus and T. Lindqvist. The viscosity of the blood in narrow capillary tubes. *Am. J. Phys.*, 96:562–568, 1931.

[123] W. Reinke, P. Gaehtgens, and P. C. Johnson. Blood viscosity in small tubes: effect of shear rate, aggregation, and sedimentation. *Am. J. Physiol.*, 253:H540–H547, 1987.

[124] G. Bugliarello and J. Sevilla. Velocity distribution and other characteristics of steady and pulsatile blood flow in fine glass tubes. *Biorheology*, 7:85–107, 1970.

[125] A. R. Pries, D. Neuhaus, and P. Gaehtgens. Blood viscosity in tube flow: dependence on diameter and hematocrit. *Am. J. Physiol.*, 263:H1770–H1778, 1992.

[126] D. A. Fedosov, B. Caswell, A. S. Popel, and G. E. Karniadakis. Blood flow and cell-free layer in microvessels. *Microcirculation*, 17:615–628, 2010.

[127] S. K. Doddi and P. Bagchi. Three-dimensional computational modeling of multiple deformable cells flowing in microvessels. *Phys. Rev. E*, 79:046318, 2009.

[128] M. M. Dupin, I. Halliday, C. M. Care, and L. L. Munn. Lattice Boltzmann modelling of blood cell dynamics. *Int. J. Comp. Fluid Dynamics*, 22:481–492, 2008.

[129] J. B. Freund and M. M. Orescanin. Cellular flow in a small blood vessel. *J. Fluid Mech.*, 671:466–490, 2011.

[130] H. Lei, D. A. Fedosov, B. Caswell, and G. E. Karniadakis. Blood flow in small tubes: quantifying the transition to the non-continuum regime. *J. Fluid Mech.*, 722:214–239, 2013.

[131] H. L. Goldsmith, G. R. Cokelet, and P. Gaehtgens. Robin Fahraeus: evolution of his concepts in cardiovascular physiology. *Am. J. Physiol.*, 257:H1005–H1015, 1989.

[132] G. R. Cokelet and H. L. Goldsmith. Decreased hydrodynamic resistance in the two-phase flow of blood through small vertical tubes at low flow rates. *Circ. Res.*, 68:1–17, 1991.

[133] I. Cantat and C. Misbah. Lift force and dynamical unbinding of adhering vesicles under shear flow. *Phys. Rev. Lett.*, 83:880–883, 1999.

[134] M. Abkarian, C. Lartigue, and A. Viallat. Tank treading and unbinding of deformable vesicles in shear flow: determination of the lift force. *Phys. Rev. Lett.*, 88:068103, 2002.

[135] S. Messlinger, B. Schmidt, H. Noguchi, and G. Gompper. Dynamical regimes and hydrodynamic lift of viscous vesicles under shear. *Phys. Rev. E*, 80:011901, 2009.

[136] P. K. Ong, S. Jain, and S. Kim. Spatio-temporal variations in cell-free layer formation near bifurcations of small arterioles. *Microvasc. Res.*, 83:118–125, 2012.

[137] D. Katanov, G. Gompper, and D. A. Fedosov. Microvascular blood flow resistance: role of red blood cell migration and dispersion. *Microvasc. Res.*, 99:57–66, 2015.

[138] H. M. Vollebregt, R. G. M. van der Sman, and R. M. Boom. Model for particle migration in bidisperse suspensions by use of effective temperature. *Faraday Discuss.*, 158:89–103, 2012.

[139] D. Leighton and A. Acrivos. Measurement of shear-induced self-diffusion in concentrated suspensions of spheres. *J. Fluid Mech.*, 177:109–131, 1987.

[140] M. Frank, D. Anderson, E. R. Weeks, and J. F. Morris. Particle migration in pressure-driven flow of a Brownian suspension. *J. Fluid Mech.*, 493:363–378, 2003.

[141] X. Grandchamp, G. Coupier, A. Srivastav, C. Minetti, and T. Podgorski. Lift and down-gradient shear-induced diffusion in red blood cell suspensions. *Phys. Rev. Lett.*, 110:108101, 2013.

[142] S. Sukumaran and U. Seifert. Influence of shear flow on vesicles near a wall: a numerical study. *Phys. Rev. E*, 64:011916, 2001.

[143] G. Coupier, B. Kaoui, T. Podgorski, and C. Misbah. Noninertial lateral migration of vesicles in bounded poiseuille flow. *Phys. Fluids*, 20:111702, 2008.

[144] E. W. Merrill, E. R. Gilliland, G. Cokelet, H. Shin, A. Britten, and R. E. Wells Jr. Rheology of human blood near and at zero flow. Effects of temperature and hematocrit level. *Biophys. J.*, 3:199–213, 1963.

[145] E. W. Merrill, E. R. Gilliland, T. S. Lee, and E. W. Salzman. Blood rheology: effect of fibrinogen deduced by addition. *Circ. Res.*, 18:437–446, 1966.

[146] S. Chien, S. Usami, R. J. Dellenback, and M. I. Gregersen. Shear-dependent interaction of plasma proteins with erythrocytes in blood rheology. *Am. J. Physiol.*, 219:143–153, 1970.

[147] B. Neu and H. J. Meiselman. Depletion-mediated red blood cell aggregation in polymer solutions. *Biophys. J.*, 83:2482–2490, 2002.

[148] S. Chien and K.-M. Jan. Ultrastructural basis of the mechanism of rouleaux formation. *Microvasc. Res.*, 5:155–166, 1973.

[149] Z. Qin, L.-G. Durand, L. Allard, and G. Cloutier. Effects of a sudden flow reduction on red blood cell rouleau formation and orientation using RF backscattered power. *Ultrasound Med. Biol.*, 24:503–511, 1998.

[150] S. Chien, S. Usami, H. M. Taylor, J. L. Lundberg, and M. I. Gregersen. Effects of hematocrit and plasma proteins on human blood rheology at low shear rates. *J. Appl. Physiol.*, 21:81–87, 1966.

[151] R. Skalak, S. R. Keller, and T. W. Secomb. Mechanics of blood flow. *J. Biomech. Eng.*, 103:102–115, 1981.

[152] D. A. Fedosov, W. Pan, B. Caswell, G. Gompper, and G. E. Karniadakis. Predicting human blood viscosity in silico. *Proc. Natl. Acad. Sci. USA*, 108:11772–11777, 2011.

[153] P. Bagchi, P. C. Johnson, and A. S. Popel. Computational fluid dynamic simulation of aggregation of deformable cells in a shear flow. *J. Biomech. Eng.*, 127:1070–1080, 2005.

[154] T. Wang, T.-W. Pan, Z. W. Xing, and R. Glowinski. Numerical simulation of rheology of red blood cell rouleaux in microchannels. *Phys. Rev. E*, 79:041916, 2009.

[155] Y. Liu and W. K. Liu. Rheology of red blood cell aggregation by computer simulation. *J. Comp. Phys.*, 220:139–154, 2006.

[156] G. Cokelet, E. W. Merrill, E. R. Gilliland, H. Shin, A. Britten, and R. E. Wells Jr. The rheology of human blood-measurement near and at zero shear rate. *Trans. Soc. Rheol.*, 7:303–317, 1963.

[157] A. L. Copley, C. R. Huang, and R. G. King. Rheogoniometric studies of whole human blood at shear rates from 1,000-0.0009 sec^{-1}. Part I. Experimental findings. *Biorheology*, 10:17–22, 1973.

[158] S. Chien, S. Usami, R. J. Dellenback, and M. I. Gregersen. Blood viscosity: influence of erythrocyte deformation. *Science*, 157:827–829, 1967.

[159] D. E. Brooks, J. W. Goodwin, and G. V. F. Seaman. Interactions among erythrocytes under shear. *J. Appl. Physiol.*, 28:172–177, 1970.

[160] K. Ley and T. F. Tedder. Leukocyte interactions with vascular endothelium. New insights into selectin-mediated attachment and rolling. *J. Immunol.*, 155:525–528, 1995.

[161] R. Alon, D. A. Hammer, and T. A. Springer. Lifetime of the P-selectin-carbohydrate bond and its response to tensile force in hydrodynamic flow. *Nature (London)*, 374:539–542, 1995.

[162] U. Bagge and R. Karlsson. Maintenance of white blood cell margination at the passage through small venular junctions. *Microvasc. Res.*, 20:92–95, 1980.

[163] H. L. Goldsmith and S. Spain. Margination of leukocytes in blood flow through

small tubes. *Microvasc. Res.*, 27:204–222, 1984.

[164] J. C. Firrell and H. H. Lipowsky. Leukocyte margination and deformation in mesenteric venules of rat. *Am. J. Physiol.*, 256:H1667–H1674, 1989.

[165] K. B. Abbitt and G. B. Nash. Rheological properties of the blood influencing selectin-mediated adhesion of flowing leukocytes. *Am. J. Physiol.*, 285:H229–H240, 2003.

[166] J. B. Freund. Leukocyte margination in a model microvessel. *Phys. Fluids*, 19:023301, 2007.

[167] A. Jain and L. L. Munn. Determinants of leukocyte margination in rectangular microchannels. *PLoS ONE*, 4:e7104, 2009.

[168] D. A. Fedosov, J. Fornleitner, and G. Gompper. Margination of white blood cells in microcapillary flow. *Phys. Rev. Lett.*, 108:028104, 2012.

[169] D. A. Fedosov and G. Gompper. White blood cell margination in microcirculation. *Soft Matter*, 10:2961–2970, 2014.

[170] M. J. Pearson and H. H. Lipowsky. Influence of erythrocyte aggregation on leukocyte margination in postcapillary venules of rat mesentery. *Am. J. Physiol.*, 279:H1460–H1471, 2000.

[171] A. R. Pries, T. W. Secomb, and P. Gaehtgens. Structure and hemodynamics of microvascular networks: heterogeneity and correlations. *Am. J. Physiol.*, 269:H1713–H1722, 1995.

[172] M. J. Rosenbluth, W. A. Lam, and D. A. Fletcher. Force microscopy of nonadherent cells: a comparison of leukemia cell deformability. *Biophys. J.*, 90:2994–3003, 2006.

[173] K. G. Phillips, P. Kuhn, and O. J. T. McCarty. Physical biology in cancer. 2. The physical biology of circulating tumor cells. *Am. J. Physiol.*, 306:C80–C88, 2014.

[174] K. Müller, D. A. Fedosov, and G. Gompper. Margination of micro- and nano-particles in blood flow and its effect on drug delivery. *Sci. Rep.*, 4:4871, 2014.

[175] M. Ferrari. Cancer nanotechnology: opportunities and challenges. *Nat. Rev. Cancer*, 5:161–171, 2005.

[176] R. K. Jain and T. Stylianopoulos. Delivering nanomedicine to solid tumors. *Nat. Rev. Clin. Oncol.*, 7:653–664, 2010.

[177] J. D. Slack, M. Kanke, G. H. Simmons, and P. P. DeLuca. Acute hemodynamic effects and blood pool kinetics of polystyrene microspheres following intravenous administration. *J. Pharm. Sci.*, 70:660–664, 1981.

[178] M. Herant, V. Heinrich, and M. Dembo. Mechanics of neutrophil phagocytosis: experiments and quantitative models. *J. Cell Sci.*, 119:1903–1913, 2006.

[179] K. Namdee, A. J. Thompson, P. Charoenphol, and O. Eniola-Adefeso. Margination propensity of vascular-targeted spheres from blood flow in a microfluidic model of human microvessels. *Langmuir*, 29:2530–2535, 2013.

[180] W. H. De Jong, W. I. Hagens, P. Krystek, M. C. Burger, A. J. A. M. Sips, and R. E. Geertsma. Particle size-dependent organ distribution of gold nanoparticles after intravenous administration. *Biomaterials*, 29:1912–1919, 2008.

[181] F. Gentile, C. Chiappini, D. Fine, R. C. Bhavane, M. S. Peluccio, M. M.-C. Cheng, X. Liu, M. Ferrari, and P. Decuzzi. The effect of shape on the margination dynamics of non-neutrally buoyant particles in two-dimensional shear flows. *J. Biomech.*, 41:2312–2318, 2008.

[182] A. J. Thompson, E. M. Mastria, and O. Eniola-Adefeso. The margination propensity of ellipsoidal micro/nanoparticles to the endothelium in human blood flow. *Biomaterials*, 34:5863–5871, 2013.

[183] P. Decuzzi and M. Ferrari. The adhesive strength of non-spherical particles mediated

by specific interactions. *Biomaterials*, 27:5307–5314, 2006.

[184] S. Dasgupta, T. Auth, and G. Gompper. Wrapping of ellipsoidal nano-particles by fluid membranes. *Soft Matter*, 9:5473–5482, 2013.

[185] K. Müller, D. A. Fedosov, and G. Gompper. Understanding particle margination in blood flow - a step toward optimized drug delivery systems. *Med. Eng. Phys.*, page in print, 2015.

[186] T.-R. Lee, M. Choi, A. M. Kopacz, S.-H. Yun, W. K. Liu, and P. Decuzzi. On the near-wall accumulation of injectable particles in the microcirculation: smaller is not better. *Sci. Rep.*, 3:2079, 2013.

[187] G. Volpe, I. Buttinoni, D. Vogt, H.-J. Kümmerer, and C. Bechinger. Microswimmers in patterned environments. *Soft Matter*, 7:8810–8815, 2011.

[188] I. Buttinoni, G. Volpe, F. Kümmel, G. Volpe, and C. Bechinger. Active Brownian motion tunable by light. *J. Phys.: Condens. Matter*, 24:284129, 2012.

Acknowledgments

Many people have contributed to this work and helped me in the last several years, and therefore, it is very difficult to acknowledge all contributions. First of all, I would like to thank my mentors, direct colleagues, and scientific collaborators for the discussions, contributions, and support. In particular, I would like to thank Gerhard Gompper and Roland G. Winkler at the Institute of Complex Systems, Forschungszentrum Jülich, who helped me to change the way of looking at various physical systems such that the main aim of any investigation is always to better understand underlying mechanisms. This helped me to find the right balance between theoretical, practical, and numerical views at the problem of interest.

I am also very thankful to my students (Kathrin Müller, Dinar Katanov, Johannes Mauer, Ewan Henry, Masoud Hoore, Fatemeh Alidadi) and Postdocs (Frank Römer, Zunmin Zhang, Davod Alizadehrad) who contributed a lot to the research results in this thesis. They have participated in discussions, brought new ideas and solutions, and did not give up in spite of many problems on the way. I would also like to thank current and former members of the Theoretical Soft Matter and Biophysics group at the Institute of Complex Systems, Forschungszentrum Jülich for scientific discussions, the lively atmosphere in the group, and help during these years.

Most of this work would also not be possible without a number of scientific collaborators. In particular, I would like to acknowledge Bruce Caswell and George E. Karniadakis from Brown University, USA; Timo Betz from the University of Münster, Germany; Hervé Turlier and Jean-Francois Joanny from the Institut Curie, France; Stefan Holm, Jason Beech, and Jonas Tegenfeldt from Lund University, Sweden. I am also very thankful to many colleagues in the research field all over the world, who participated in discussions and helped me at conferences, through personal visits, emails, and phone calls.

The presented results were generated using the Jülich Supercomputing Center. I would also like to acknowledge financial support from the Alexander von Humboldt Foundation enabling me to perform the research of my choice. I also acknowledge financial support from the German Science Foundation and the European Commission.

Finally, I would like to thank my family (Kathrin, Maria, and Ilia) for their support, help, and love.

Appendix. Enclosed publications

P1: Microvascular blood flow resistance: role of red blood cell migration and dispersion

D. Katanov, G. Gompper, and D. A. Fedosov

Microvascular Research, **99**:57-66, 2015.

Microvascular Research 99 (2015) 57–66

Contents lists available at ScienceDirect

Microvascular Research

journal homepage: www.elsevier.com/locate/ymvre

Microvascular blood flow resistance: Role of red blood cell migration and dispersion

Dinar Katanov, Gerhard Gompper, Dmitry A. Fedosov [*]

Theoretical Soft Matter and Biophysics, Institute of Complex Systems and Institute for Advanced Simulation, Forschungszentrum Jülich, 52425 Jülich, Germany

ARTICLE INFO

Article history:
Accepted 11 February 2015
Available online 25 February 2015

Keywords:
Cell-free layer
Microcirculation
Lift force
Shear-induced pressure
Mesoscopic simulation
Smoothed dissipative particle dynamics

ABSTRACT

Microvascular blood flow resistance has a strong impact on cardiovascular function and tissue perfusion. The flow resistance in microcirculation is governed by flow behavior of blood through a complex network of vessels, where the distribution of red blood cells across vessel cross-sections may be significantly distorted at vessel bifurcations and junctions. In this paper, the development of blood flow and its resistance starting from a dispersed configuration of red blood cells is investigated in simulations for different hematocrit levels, flow rates, vessel diameters, and aggregation interactions between red blood cells. Initially dispersed red blood cells migrate toward the vessel center leading to the formation of a cell-free layer near the wall and to a decrease of the flow resistance. The development of cell-free layer appears to be nearly universal when scaled with a characteristic shear rate of the flow. The universality allows an estimation of the length of a vessel required for full flow development, $l_c \lesssim 25D$, for vessel diameters in the range $10\ \mu\text{m} < D < 100\ \mu\text{m}$. Thus, the potential effect of red blood cell dispersion at vessel bifurcations and junctions on the flow resistance may be significant in vessels which are shorter or comparable to the length l_c. Aggregation interactions between red blood cells generally lead to a reduction of blood flow resistance. The simulations are performed using the same viscosity for both external and internal fluids and the RBC membrane viscosity is not considered; however, we discuss how the viscosity contrast may affect the results. Finally, we develop a simple theoretical model which is able to describe the converged cell-free-layer thickness at steady-state flow with respect to flow rate. The model is based on the balance between a lift force on red blood cells due to cell-wall hydrodynamic interactions and shear-induced effective pressure due to cell–cell interactions in flow. We expect that these results can also be used to better understand the flow behavior of other suspensions of deformable particles such as vesicles, capsules, and cells.

Introduction

Flow resistance of a full cardiovascular system is mainly attributed to the resistance of blood flow within microvasculature or microcirculation (Lipowsky et al., 1980; Popel and Johnson, 2005; Pries and Secomb, 2008; Secomb and Pries, 2011), which is comprised of the smallest vessels (e.g., arterioles, capillaries, venules) with diameters up to about 100 μm. In particular, the flow resistance in microvasculature is governed by the flow behavior of blood through a complex network of vessels, and therefore, the knowledge about bulk blood properties is far from sufficient to predict the behavior of blood and its flow resistance in microcirculation. For instance, experimental measurements (Lipowsky et al., 1980; Pries et al., 1994; Pries and Secomb, 2005) of blood flow resistance in vivo have shown that it may be several times larger than that in in vitro experiments on blood flow in glass tubes (Reinke et al., 1987; Pries et al., 1992). Several potential contributions to an increased blood flow resistance in vivo have been suggested. These include vessel irregularities, bifurcations, and junctions, which may affect the distribution of red blood cells (RBCs) in a vessel cross-section (Pries et al., 1994; Secomb and Hsu, 1997; Pries et al., 1989), the presence of endothelial surface layer (or glycocalyx) (Vink and Duling, 1996; Weinbaum et al., 2007) at the vessel walls (Pries and Secomb, 2005; Pries et al., 1997), and the length of vessel sections between bifurcations and junctions (Popel and Johnson, 2005; Pries et al., 1996).

The endothelial surface layer resembles a polymeric brush at a vessel wall with an estimated thickness of about 0.5 − 1.5 μm (Pries et al., 2000; Yen et al., 2012). Its effect on an increased flow resistance can be interpreted as an effective reduction of the vessel diameter due to the glycocalyx, and a large enough thickness of this layer (~2 μm) provides a plausible explanation for the discrepancy of experimentally measured blood flow resistances in vivo and in vitro (Pries and Secomb, 2005; Pries et al., 1997). However, contribution of the other effects has not been rigorously studied. As an example, RBCs in microvessels migrate away from the walls leading to a layer near a

---

[*] Corresponding author.
E-mail addresses: d.katanov@fz-juelich.de (D. Katanov), g.gompper@fz-juelich.de (G. Gompper), d.fedosov@fz-juelich.de (D.A. Fedosov).

http://dx.doi.org/10.1016/j.mvr.2015.02.006
0026-2862/

wall void of RBCs (Goldsmith et al., 1989; Cokelet and Goldsmith, 1991). This layer is called cell-free layer (CFL) or RBC-free layer, and its thickness is directly associated with the blood flow resistance (Popel and Johnson, 2005; Reinke et al., 1987; Fedosov et al., 2010a). In the microvasculature, blood flow and in particular the distribution of RBCs in a vessel cross-section can be significantly disturbed at bifurcations and junctions resulting in a reduced CFL thickness and an increased flow resistance (Ong et al., 2012). After the RBC distribution is distorted at a vessel bifurcation, in the following vessel segment RBCs will migrate toward the vessel center leading to a dynamic development and recovery of the CFL thickness. Thus, the flow resistance in microcirculation is affected by the degree of RBC dispersion at vessel junctions and the length of the CFL recovery after the distortion in comparison to a characteristic length of vessel segments between bifurcations in microvascular networks.

RBC migration and the development of CFL are governed by hydrodynamic interactions of RBCs with channel walls (Cantat and Misbah, 1999; Abkarian et al., 2002; Coupier et al., 2008) and cell–cell interactions or collisions in flow (Kumar and Graham, 2012; Grandchamp et al., 2013). The former RBC-wall interaction is usually referred to as a lift force (Cantat and Misbah, 1999; Abkarian et al., 2002; Coupier et al., 2008; Messlinger et al., 2009), while the latter one is called shear-induced diffusion or shear-induced normal stress (Grandchamp et al., 2013; Leighton and Acrivos, 1987). The lift force drives RBCs away from the vessel walls, while the cell–cell interactions lead to an effective dispersion of RBCs. The balance between these two contributions at steady flow results in a converged thickness of the RBC flow core and CFL. Clearly, the CFL development and its final thickness are functions of a number of parameters including hematocrit (volume fraction of RBCs), flow rate, vessel diameter, and aggregation interactions between RBCs. There exists a diffusion-based model (Carr, 1989; Carr and Xiao, 1995), which predicts a recovery length of CFL symmetry after it is distorted behind vessel bifurcations. However, the model has several adjustable parameters.

The main focus of this paper is a systematic investigation of CFL development in microvessels for a number of blood flow conditions using mesoscopic simulations (Fedosov et al., 2014a, 2014b). We use the smoothed dissipative particle dynamics method (Español and Revenga, 2003) to study the development of blood flow for various flow conditions starting from a fully-dispersed configuration of RBCs. Following the migration of RBCs away from the walls, the CFL thickness is dynamically monitored until it converges to a constant value of a fully-developed flow. The time evolution of CFL thickness appears to be nearly universal with respect to the flow rate for physiological hematocrit levels $H_t \leq 0.45$; this range of hematocrit levels is also directly relevant for healthy microcirculatory blood flow (Lipowsky et al., 1980; Pries et al., 1986). This allows us to define a length l_c for the development of CFL, which is nearly independent of the flow rate and shorter than or equal to $25D$, for vessel diameters in the range 10 μm < D < 100 μm. Thus, the effect of RBC dispersion at vessel bifurcations and junctions on the flow resistance may be significant in vessels which are shorter or comparable to the length l_c, while in longer vessel sections it can be practically neglected. Aggregation interactions between RBCs result in a reduction of blood flow resistance, since they aid to maintain a more compact RBC flow core.

Finally, we also develop a simple theoretical model which describes well the final CFL thickness when the flow has converged. The model considers the balance between a lift force on RBCs due to cell-wall hydrodynamic interactions and shear-induced effective pressure due to cell–cell interactions in flow. This model supports the idea that these are the two main mechanisms which govern the final CFL thickness. Similar ideas have also been applied to describe dispersion of RBCs after injection (Grandchamp et al., 2013). We hope that our results will help to better understand also the flow behavior of other suspensions of deformable particles such as vesicles, capsules, and cells, and will trigger new investigations in this area.

The paper is organized as follows. In the second section, we briefly introduce the simulation techniques employed for RBC and flow simulations and describe the simulation setup. The third section presents simulation results and the theoretical model, while in the fourth section implications of the results are discussed. We conclude in the fifth section with a brief summary.

Models & methods

We employ the smoothed dissipative particle dynamics (SDPD) method (Español and Revenga, 2003) to model fluid flow. SDPD is a mesoscopic simulation technique, where each SDPD particle corresponds to a small volume of fluid instead of individual atoms or molecules. The RBC membrane is represented by a triangulated network model (Discher et al., 1998; Noguchi and Gompper, 2005; Fedosov et al., 2010b; Fedosov et al., 2010c) and coupled to fluid flow using friction forces.

Smoothed dissipative particle dynamics

SDPD (Español and Revenga, 2003) is a mesoscopic hydrodynamics method based on two popular approaches: the smoothed particle hydrodynamics (Lucy, 1977; Monaghan, 1992) and the dissipative particle dynamics (Hoogerbrugge and Koelman, 1992; Español and Warren, 1995) methods. In SDPD, a simulation system consists of N point particles with mass m_i, position $\mathbf{r}_i$, and velocity $\mathbf{v}_i$. The Newton's second law of motion governs the evolution of particle positions and velocities over time as

$$d\mathbf{r}_i = \mathbf{v}_i dt, \quad d\mathbf{v}_i = \frac{1}{m_i}\left(\mathbf{F}_i^C + \mathbf{F}_i^D + \mathbf{F}_i^R\right)dt, \tag{1}$$

where $\mathbf{F}^C$, $\mathbf{F}^D$, and $\mathbf{F}^R$ are conservative, dissipative, and random forces due to inter-particle interactions, respectively. The equations of motion above are integrated using the velocity-Verlet algorithm (Allen and Tildesley, 1991). The three pairwise forces on particle i are defined as follows

$$\begin{aligned}
\mathbf{F}_i^C &= \sum_j \left(\frac{p_i}{\rho_i^2} + \frac{p_j}{\rho_j^2}\right) w_{ij}\mathbf{r}_{ij}, \\
\mathbf{F}_i^D &= -\sum_j \gamma_{ij}\left(\mathbf{v}_{ij} + \left(\mathbf{v}_{ij}\cdot\mathbf{e}_{ij}\right)\mathbf{e}_{ij}\right), \\
\mathbf{F}_i^R &= \sum_j \sigma_{ij}\left(d\overline{\mathbf{W}}_{ij}^S + \frac{1}{3} tr(\mathbb{1})\left[d\mathbf{W}_{ij}\right]\right)\cdot\mathbf{e}_{ij},
\end{aligned} \tag{2}$$

where $\mathbf{e}_{ij} = \mathbf{r}_{ij}/|\mathbf{r}_{ij}|$ and $\mathbf{v}_{ij} = \mathbf{v}_i - \mathbf{v}_j$. p_i and p_j are particle pressures assumed to follow the equation of state $p = p_0(\rho/\rho_0)^\alpha - b$, where p_0, ρ_0, α, and b are selected parameters. Density of particles is calculated locally and determined as $\rho_i = \sum_j W_L(r_{ij})$ with $W_L(r) = \frac{105}{16\pi r_c^3}\left(1 + 3\frac{r}{r_c}\right)\left(1 - \frac{r}{r_c}\right)^3$ being the Lucy function (Lucy, 1977), where r_c is the cutoff radius. Furthermore, $\nabla W_L(r) = -\mathbf{r}w(r)$ such that $w(r) = \frac{315}{4\pi r_c^5}\left(1 - \frac{r}{r_c}\right)^2$ and $w_{ij} = w(r_{ij})$. The coefficients γ_{ij} and σ_{ij} define the strength of dissipative and random forces and are defined as $\gamma_{ij} = \frac{5\eta_0}{3}\frac{w_{ij}}{\rho_i\rho_j}$ and $\sigma_{ij} = 2\sqrt{k_B T\gamma_{ij}}$, where η_0 is the desired dynamic viscosity of fluid and k_BT is the energy unit. The notation $tr[d\mathbf{W}_{ij}]$ corresponds to the trace of a random matrix of independent Wiener increments $d\mathbf{W}_{ij}$, and $d\overline{\mathbf{W}}_{ij}^S$ is the traceless symmetric part.

Table 1 presents the fluid simulation parameters in units of the fluid particle mass m, the cutoff radius r_c, and the thermal energy k_BT. Even though SDPD allows one to directly input desired fluid viscosity η_0, the measured dynamic viscosity η of SDPD fluid might be slightly

Table 1
SDPD fluid parameters used in simulations. Mass, length, and energy for SDPD fluid are measured in units of the fluid particle mass m, the cutoff radius r_c, and the thermal energy k_BT, respectively. p_0, ρ_0, b, and α are parameters for the pressure equation, n is the number density of fluid particles, and η_0 and η are the desired and measured dynamic viscosities of the SDPD fluid. In all simulations, we have set $m = 1$, $r_c = 1.5$, and $k_BT = 0.4$.

$\frac{p_0 r_c^3}{k_B T}$	$\rho_0 r_c^3$	α	$\frac{b r_c^3}{k_B T}$	$\frac{\eta_0 r_c^2}{\sqrt{m k_B T}}$	$n r_c^3$	$\frac{\eta r_c^2}{\sqrt{m k_B T}}$
675	10.125	7	675	266.8	10.125	284.6

different. The assumption that $\eta = \eta_0$ is reliable only if each SDPD particle has a large enough number of neighboring particles, which may require large enough r_c and/or density of fluid particles n. Consequently, we advise to always check validity of the approximation directly using a shear flow simulation. For instance, SDPD fluid with the parameters in Table 1 yields slightly larger fluid viscosity measured in a shear flow setup than η_0.

Red blood cell model

To simulate RBCs a triangulated spring-network model (Discher et al., 1998; Noguchi and Gompper, 2005; Fedosov et al., 2010b; Fedosov et al., 2010c) has been employed. Each RBC is constructed by a collection of N_v particles linked by $N_s = 3(N_v - 2)$ springs with the following potential

$$U_{sp} = \sum_{j \in 1 \dots N_s} \left[\frac{k_B T l_m \left(3x_j^2 - 2x_j^3\right)}{4p\left(1 - x_j\right)} + \frac{k_p}{l_j} \right], \tag{3}$$

where l_j is the length of the j-th spring, l_m is the maximum spring extension, $x_j = l_j/l_m$, p is the persistence length, and k_p is the spring constant. This spring definition allows us to define a nonzero equilibrium spring length l_0. The bending rigidity of a membrane is modeled as follows

$$U_{bend} = \sum_{j \in 1 \dots N_s} k_b \left[1 - cos\left(\theta_j - \theta_0\right)\right], \tag{4}$$

where k_b is the bending constant, θ_j is the instantaneous angle between two neighboring triangles having a shared edge j, and θ_0 is the angle representing the spontaneous curvature, which is set to zero in all simulations. Finally, to mimic area-incompressibility of the lipid bilayer and incompressibility of the inner cytosol, we use two constraints with the potentials given by

$$\begin{aligned} U_{area} &= k_a \frac{(A - A_r)^2}{2A_r} + \sum_j k_d \frac{\left(A_j - A_j^0\right)^2}{2A_j^0}, \\ U_{vol} &= k_v \frac{(V - V_r)^2}{2V_r}, \end{aligned} \tag{5}$$

where k_a, k_d, and k_v are the global area, local area, and volume constraint coefficients, respectively. A and V are the instantaneous RBC area and volume, while A_j is the instantaneous area of an individual triangle in a triangulated network. A_r, A_j^0, and V_r are the desired total RBC area, area of the j-th face (set according to the initial triangulation), and total RBC volume, respectively.

The RBC model parameters (e.g., p, k_p, k_b) can be related to macroscopic membrane properties (e.g., shear, Young's, and bending moduli) through a linear analysis for a regular hexagonal network (Fedosov et al., 2010b, 2010c). For instance, the membrane shear modulus is given by

$$\mu_0 = \frac{\sqrt{3} k_B T}{4 p l_m x_0} \left(\frac{x_0}{2(1 - x_0)^3} - \frac{1}{4(1 - x_0)^2} + \frac{1}{4} \right) + \frac{3\sqrt{3} k_p}{4 l_0^3}, \tag{6}$$

where $x_0 = l_0/l_m$. The corresponding area-compression K and Young's Y moduli can be found as $K = 2\mu_0 + k_a + k_d$ and $Y = 4K\mu_0/(K + \mu_0)$. The bending coefficient k_b in Eq. (4) can be expressed in terms of the macroscopic bending rigidity κ of the Helfrich model (Helfrich, 1973) as $k_b = 2\kappa/\sqrt{3}$. The coefficients k_a, k_d, and k_v can be selected large enough to approximate properly area-incompressibility of the lipid bilayer and incompressibility of the inner cytosol. Thus, the necessary model parameters are calculated directly from desired macroscopic RBC properties. In addition, we also employ a “stress-free” model of a RBC obtained by computational annealing such that equilibrium length l_0^i for each spring is set to the corresponding edge length within initial membrane triangulation (Fedosov et al., 2010b; Fedosov et al., 2010c). This also implies that $l_m^i = l_0^i \times x_0$ is set individually with $x_0 = 2.2$, see Refs. Fedosov et al. (2010b) and (2010c) for more details.

To describe RBC properties, we define an effective RBC diameter as $D_r = \sqrt{A_r/\pi}$. The average effective diameter for a healthy RBC is equal to $D_r = 6.5$ μm (Evans and Skalak, 1980). Table 2 outlines RBC parameters for simulations in units of D_r and k_BT, and the corresponding average values for a healthy RBC in physical units.

Coupling between RBCs and the fluid flow is done through viscous friction (Fedosov et al., 2010b) between cell vertices and the surrounding fluid particles. The coupling is implemented via dissipative particle dynamics interactions (Hoogerbrugge and Koelman, 1992; Español and Warren, 1995) using dissipative and random forces similar to F^D and F^R above. The strength γ of the dissipative force is adjusted to satisfy no-slip boundary conditions at a membrane. Using an approximation of linear shear flow near the membrane, the coefficient γ can be expressed in terms of fluid density n, interaction cutoff radius r_c', number density of membrane particles n_m, and fluid viscosity η (Fedosov et al., 2010b). This formulation results in satisfaction of the no-slip BCs for the linear shear flow over a flat membrane; however, it also serves as an excellent approximation for no-slip at the membrane surface. Note that conservative interactions between fluid and membrane particles are turned off, which implies that the radial distribution function is structureless, i.e. $g(r) = 1$.

RBC aggregation model

For blood, the attractive cell–cell interactions are crucial to represent aggregation of RBCs. These forces are approximated by the Morse potential $U(r) = D_e\left[e^{2\beta(r_0 - r)} - 2e^{\beta(r_0 - r)}\right]$, where r is the separation distance, r_0 is the zero force distance, D_e is the well depth of the potential, and β characterizes the interaction range. The Morse potential parameters were chosen as $\beta = 1.5$ μm^{-1}, $r_0 = 0.3$ μm, and $D_e = 0.3 k_BT$. For more details see Ref. Fedosov et al. (2011).

Table 2
RBC characteristics in units of the effective RBC diameter D_r and k_BT, and the corresponding average values for a healthy RBC in physical units. N_v is the number of membrane vertices, A_r is the RBC membrane area, V_r is the RBC volume, T is the temperature, Y_r is the membrane Young's modulus, κ_r is the membrane bending rigidity, and k_d, k_a, and k_v are the local area, global area, and volume constraint coefficients, respectively. In all simulations, we have chosen $A_r = 133.5$ and $k_BT = 0.4$, which implies that $D_r = 6.5$.

RBC parameters	Scaled units	Physical units
N_v	500	
A_r		133.5×10^{-12} m^2
D_r	$\sqrt{A_r/\pi}$	6.5×10^{-6} m
V_r	$0.34\ D_r^3$	93×10^{-18} m^3
T		310 K
Y_r	$1.82 \times 10^5 \frac{k_BT}{D_r^2}$	18.9×10^{-6} N/m
κ_r	$70\ k_BT$	3×10^{-19} J
k_d	$4.2 \times 10^4 \frac{k_BT}{D_r^2}$	4.3×10^{-6} N/m
k_a	$2.1 \times 10^6 \frac{k_BT}{D_r^2}$	2.1×10^{-4} N/m
k_v	$1.4 \times 10^7 \frac{k_BT}{D_r^3}$	220 N/m^2

Cell-free layer

Cell-free layer (CFL) is a fluid layer close to the channel wall void of RBCs. In Poiseuille flow, CFL forms due to a hydrodynamically-induced lift force on RBCs close to a wall (Cantat and Misbah, 1999; Abkarian et al., 2002; Messlinger et al., 2009) leading to their migration toward the tube center and leaving a near-wall fluid layer free of RBCs. Fluid viscosity in the CFL region is similar to that of plasma, whose viscosity is considerably lower than the effective viscosity in the tube center populated by RBCs. Thus, a CFL serves as an effective lubrication layer for the RBC core to flow and its thickness is directly associated with the resistance of blood flow. The thickness of the CFL is generally larger for lower hematocrit levels and larger vessel diameters (Maeda et al., 1996; Kim et al., 2007). The measurement of the CFL thickness δ in simulations is done by projecting RBC vertices of a simulation snapshot onto a plane and fitting a curve which describes the edge of RBC core in flow (Fedosov et al., 2010a). The average distance from the wall to the RBC edge is assumed to be the CFL thickness. To reduce errors in the CFL measurements a number of simulation snapshots at different times are considered.

Simulation setup

The simulation setup contains a single periodic cylindrical channel with a diameter $D = 15$ μm and 80 μm and the length of $L = 60$ μm. The channel is filled with fluid particles and suspended RBCs. The average plasma viscosity under healthy conditions is assumed to be $\eta = 0.0012$ Pa · s. For simplicity, the fluid viscosity inside a RBC is set to be the same as that of blood plasma. The flow is driven by a constant force f applied to each solvent particle, which is equivalent to a constant pressure gradient $\Delta P/L = fn$, where ΔP is the pressure drop and n is the number density of solvent particles. To characterize the flow we define an average (or pseudo) shear rate $\bar{\dot{\gamma}}$ as

$$\bar{\dot{\gamma}} = \bar{v}/D, \tag{7}$$

where $\bar{v} = Q/A$ is the average flow velocity with a volumetric flow rate Q through a cross-sectional area $A = \pi D^2/4$.

Before the start of flow, RBCs are distributed almost randomly in the tube as shown in Fig. 1(a). This distribution is achieved by running a simulation without a flow for some time, which allows RBCs to diffuse and reach their equilibrium distribution. After that the flow is started and the development of CFL is measured in time as RBCs migrate away from the wall. For comparison Fig. 1(b) illustrates the distribution of RBCs for $D = 40$ μm, $H_t = 0.3$, and $\bar{\dot{\gamma}} = 298$ s^{-1} after the blood flow has been fully developed. Clearly, RBCs have migrated toward the channel center yielding a CFL near the wall.

Results

Cell-free layer evolution

We first investigate the development of the CFL in blood flow. Already in the absence of flow, a non-zero CFL thickness is measured due to the entropic repulsion (e.g., due to hindered rotational motion) between RBCs and the tube wall. In addition, since we consider relatively small vessel diameters, a non-zero wall curvature prevents RBCs from fully conforming with its cylindrical shape, which also results in a non-zero CFL thickness. After the flow is started, RBCs migrate away from the wall, and the development of the CFL is monitored in time. Fig. 2(a) shows the evolution of the CFL thickness $\delta(t)$ for different driving forces (or pressure gradients) for the case of $H_t = 0.3$ and $D = 20$ μm. The time is normalized by the $\bar{\dot{\gamma}}$ value of the fully-developed flow. The CFL curves show a rapid increase of the CFL thickness up to about $t\bar{\dot{\gamma}} \approx 25$ followed by a plateau, which we will also refer to as a final CFL thickness δ_f. The values of δ_f are larger for higher flow rates; however, the growth is clearly limited by excluded-volume interactions between RBCs in the flow core and is expected to approach a constant value for large $\bar{\dot{\gamma}}$.

Fig. 2(b) presents the same CFL curves with their plateau values scaled by δ_f. The scaled CFL curves appear to be similar indicating that the shear rate $\bar{\dot{\gamma}}$ is the only relevant time scale here. Thus, the development of CFL for $H_t = 0.3$ is mainly governed by shear forces in flow. A similar conclusion can be drawn for low H_t supported by our simulation data for $H_t = 0.15$ (not shown here) and for higher H_t shown in Fig. 3. Some discrepancies between the curves in Figs. 2(b) and 3(b) for different shear rates indicate that there may exist a second relaxation time. The initial fast time scale is governed by $\bar{\dot{\gamma}}$ and corresponds to RBC migration away from the wall as it was discussed before. The second time scale is related to cell–cell interactions in flow such that RBCs in the core of the flow have to re-arrange and reach a denser flow-induced packing. This time scale is slower than that for RBC migration, and appears to be more noticeable for larger H_t values. This process is also illustrated in Fig. 4 by the development of hematocrit profile for $H_t = 0.45$. While the initial shift of the local hematocrit curve away from the wall is rather rapid, the further development of local RBC density in the bulk appears to be slower. However, the convergence of the CFL to δ_f is nearly independent of hematocrit ($H_t \leq 0.45$) and occurs within $t\bar{\dot{\gamma}} \lesssim 25$.

To verify that the conclusions made so far do not change significantly for vessel diameters in the range 10 μm < D < 100 μm, we performed a

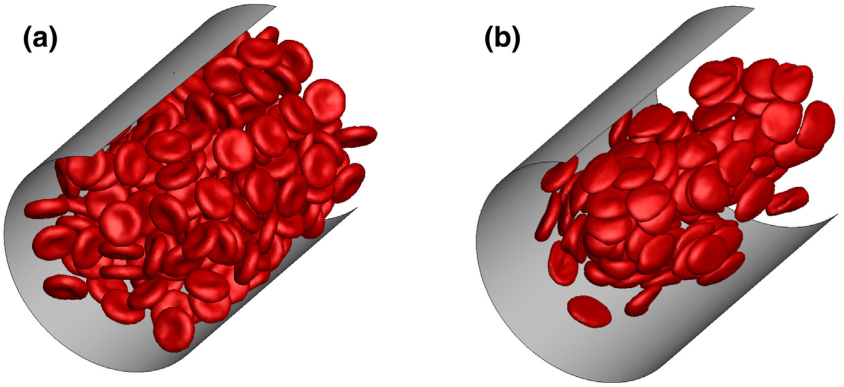

Fig. 1. Simulation snapshots for $D = 40$ μm and $H_t = 0.3$. (a) Before the flow is applied, RBCs are distributed nearly randomly in the tube. (b) After the flow has converged for $\bar{\dot{\gamma}} = 298$ s^{-1}. The CFL region can be clearly seen.

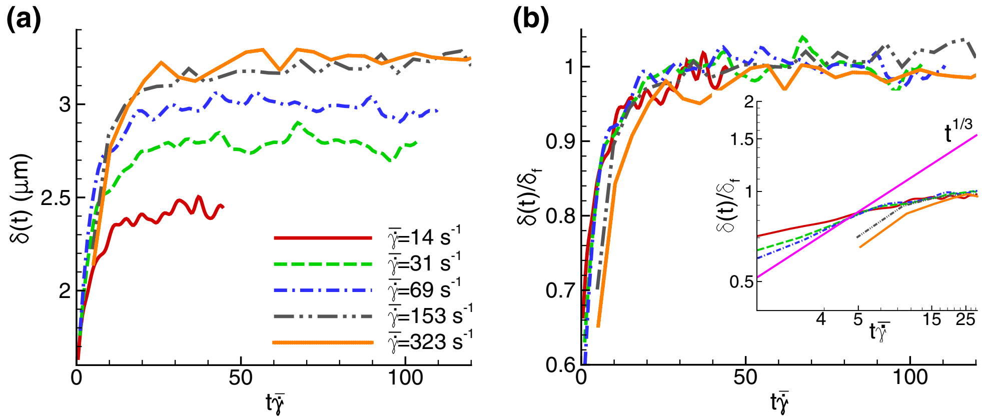

Fig. 2. Development of the CFL thickness in time after flow has been started for the case of $H_t = 0.3$ and $D = 20$ μm. The time is normalized by the pseudo-shear rate. (a) The CFL thickness evolution for different pseudo-shear rates. (b) The same set of data as in plot (a) with all curves normalized by the plateau value of the CFL thickness δ_f at large $\bar{\dot\gamma}$. The inset in (b) is a log–log plot illustrating a power-law behavior of the CFL curves at small $t\bar{\dot\gamma}$.

number of simulations for $D = 15, 40,$ and 80 μm. The CFL dynamics for $D = 40$ μm is shown in Fig. 5(a) for different H_t values. Furthermore, Fig. 5(b) presents a comparison of the CFL convergence for different vessel diameters and pseudo-shear rates. In all simulated cases the convergence of CFL thickness is reached by the time $t\bar{\dot\gamma}\lesssim 25$, in agreement with the simulation data for $D = 20$ μm in Figs. 2 and 3.

Effect of RBC aggregation

The presence of aggregation interactions between RBCs leads in general to a larger CFL thickness. Fig. 6 compares the development of CFL thickness for the cases with/without aggregation interactions. Initially, the CFL for the simulations with RBC aggregation seems to develop similarly to the cases without RBC aggregation present. However, attractive interactions between RBCs lead to a larger final CFL thickness δ_f in comparison with that without aggregation. The dynamics of CFL development appears to be not significantly affected by the presence of RBC aggregation such that δ_f plateau is roughly reached at $t\bar{\dot\gamma}\approx 25$, independent of RBC aggregation properties. Note that the strength of RBC aggregation used here corresponds to normal aggregation level in blood under healthy conditions (Fedosov et al., 2011), and stronger aggregation interactions between RBCs, which may be present in some blood diseases and disorders, may alter the conclusions. However, we expect that effective attraction between RBCs should shorten the time for CFL convergence rather than extend it and therefore, the estimated CFL development time should become even faster for stronger RBC aggregation. Finally, at high enough flow rates ($\bar{\dot\gamma}\gtrsim 50$ s^{-1} for the healthy aggregation level) RBC aggregation should not make a significant contribution to blood flow properties (Fedosov et al., 2011), see also Fig. 7(a).

Theoretical model for CFL

The importance of CFL thickness is its direct correlation with blood flow resistance. The larger the CFL, the lower the resistance to blood flow will be, which has been found in the Fahraeus–Lindqvist effect (Fåhraeus and Lindqvist, 1931). The final CFL thickness δ_f increases with flow rate and channel diameter as illustrated in Fig. 7. Also, RBC aggregation enhances the CFL at least at small enough flow rates. The final CFL thickness δ_f is a consequence of the lift force on RBCs driving them away from the wall (Cantat and Misbah, 1999; Abkarian et al., 2002; Messlinger et al., 2009) and cell–cell interactions or collisions in

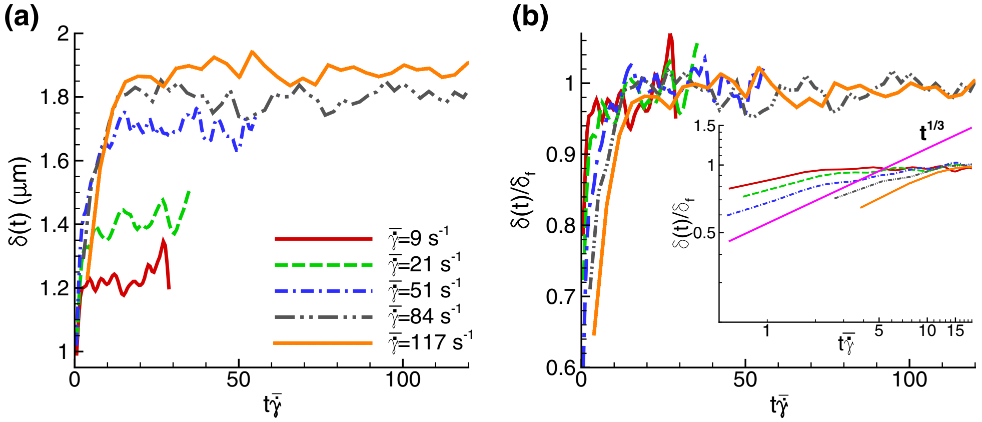

Fig. 3. Development of the CFL thickness in time after flow has been started for the case of $H_t = 0.45$ and $D = 20$ μm. The time is normalized by the pseudo-shear rate $\bar{\dot\gamma}$. (a) The CFL thickness evolution for different pseudo-shear rates. (b) The same set of data as in plot (a) with all curves normalized by the plateau value of the CFL thickness δ_f. The inset in (b) is a log–log plot illustrating a power-law behavior of the CFL curves at small $t\bar{\dot\gamma}$.

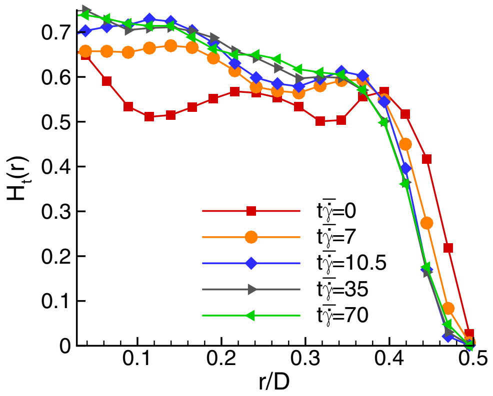

Fig. 4. Development of the hematocrit profile in time after flow has been started for the case of $H_t = 0.45$, $D = 20$ μm and $\bar{\dot{\gamma}} = 117\ \mathrm{s}^{-1}$. Different lines correspond to different times.

the bulk of flow dispersing the RBCs. Thus, to describe δ_f with respect to different shear rates theoretically, the lift force on RBCs, which compresses the cell core of the flow, should be balanced by an effective pressure due to collisions in flow. Following the idea based on an effective temperature in Ref. Vollebregt et al. (2012), a particle pressure Π in a sheared colloidal suspension can be described as

$$\Pi = n\left(k_B T + c_s \eta_{eff}\ \dot{\gamma}\ V_r\right) Z, \tag{8}$$

where $n = H_t/V_r$ is the RBC number density, c_s is a constant, η_{eff} is an effective suspension viscosity, $\dot{\gamma}$ is the shear rate, and Z is the compressibility. The first term in Eq. (8) corresponds to the thermal contribution of pressure, while the second term represents the shear-induced component due to particle interactions or collisions in flow (Grandchamp et al., 2013; Leighton and Acrivos, 1987; Frank et al., 2003). The compressibility Z for a suspension of spherical colloids has a number of different theoretical approximations, where that by

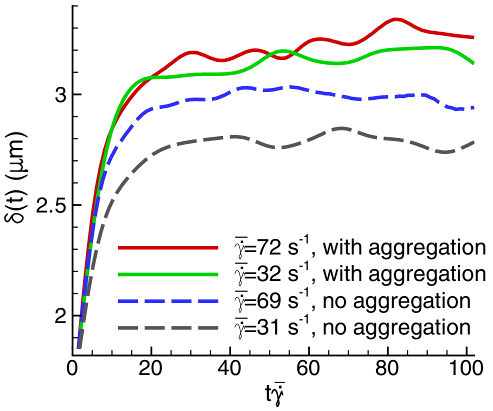

Fig. 6. Effect of RBC aggregation. CFL development over time for blood flow with/without RBC aggregation interactions. $D = 20$ μm and $H_t = 0.3$.

Carnahan & Starling (Carnahan and Starling, 1969) is perhaps the most successful one with

$$Z(\phi) = \frac{1+\phi+\phi^2-\phi^3}{(1-\phi)^\alpha}, \tag{9}$$

where ϕ is the particle volume fraction and $\alpha = 3$. For RBCs, the compressibility Z is likely to increase slower with ϕ than that for rigid spheres, so that α is likely to be smaller than 3. However, exact details are not so important here, since our goal is a semi-quantitative approximation of CFL.

The particle pressure inside the flow core is balanced by the surface pressure Π_s, which arises from a hydrodynamic lift force on RBCs and an entropic repulsion of RBCs from the wall due to hindered rotational motion. The entropic repulsion force can be approximated as $F_e = k_B T/h$ (e.g., for a rigid disk), where h is the distance from the cell's center-of-mass to the wall. This force is only important at distances smaller than the disk radius and at very low shear rates $\left(\bar{\dot{\gamma}} < 1\right)$; for instance, it provides a non-zero CFL thickness in absence of flow. Here, we omit any dependence of F_e on the shear rate (in general, F_e should

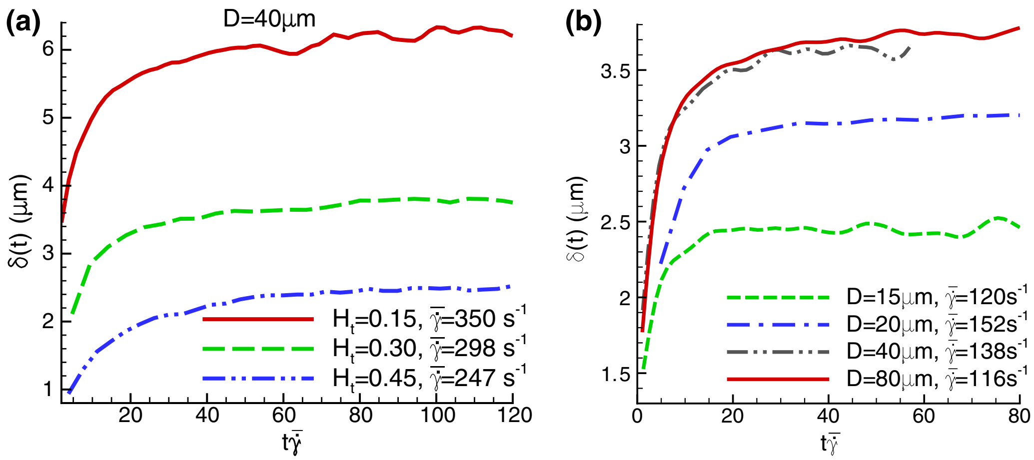

Fig. 5. Development of the CFL thickness in time after flow has been started. The time is normalized by the pseudo-shear rate $\bar{\dot{\gamma}}$. (a) Simulations for $D = 40$ μm and different H_t values. (b) CFL thickness development for different vessel diameters and pseudo-shear rates.

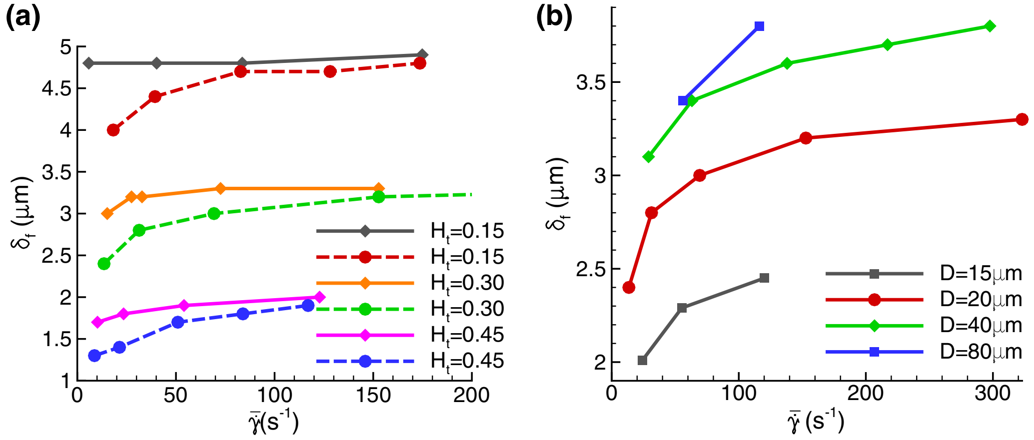

Fig. 7. CFL thickness for a converged flow for different flow rates and channel diameters. (a) Final CFL thickness δ_f for $D = 20$ μm. Solid lines correspond to simulations with aggregation interactions between RBCs, while the dashed lines are simulations without RBC aggregation. (b) Final CFL thickness δ_f for different vessel diameters D and $H_t = 0.3$.

reduce with increasing shear rate), since its contribution becomes negligible in comparison with the lift force already for $\bar{\dot\gamma} \geq 1$. Thus, the surface pressure can be approximated as

$$\Pi_s = \frac{F_e + F_l}{D_r^2} = \frac{k_B T}{h D_r^2} + \frac{c_l \eta_o \,\dot\gamma\, D_r^2}{h^2}, \qquad (10)$$

where F_l is the lift force (Coupier et al., 2008; Grandchamp et al., 2013; Messlinger et al., 2009; Sukumaran and Seifert, 2001) and c_l is a constant. In general, the lift force would depend on particle properties (e.g., rigidity, viscosity contrast between inner and outer fluids) and its dynamics (e.g., tank-treading or tumbling, inclination angle), so that Eq. (10) should be considered as an expression which captures general trends of a lift force on RBCs. The balance between these two pressures ($\Pi_s = \Pi$) allows us to describe semi-quantitatively the CFL thickness for different shear rates. As an approximation in both Eqs. (8) and (10), we assume that $\dot\gamma = \bar{\dot\gamma}$ of the tube flow, while η_{eff} in Eq. (8) is calculated according to the empirical relations for blood flow in tubes (Pries et al., 1992). Also, for the compressibility Z in Eq. (9) we assume that $\alpha = 2$, since a suspension of RBCs should be more compressible than that of hard spheres. Fig. 8 presents the simulation data for δ_f against fits of the theoretical model with $c_s = 10^{-4}$ and $c_l = 10^{-3}$. The symbols correspond to simulation data, while the solid lines with corresponding colors are fits by the theoretical model. In spite of the simplicity of the model, the theoretical fits describe the data quite well, especially for a fixed diameter $D = 20$ μm and different H_t values. The agreement for different diameters and $H_t = 0.3$ is less satisfactory.

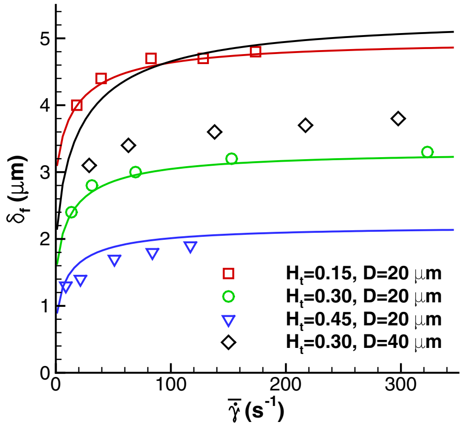

Fig. 8. Final CFL thickness for different flow rates, hematocrit levels, and channel diameters. The symbols correspond to simulation data, while the solid lines with corresponding colors are fits by the theoretical model with $c_s = 10^{-4}$ and $c_l = 10^{-3}$. (For interpretation of the references to color in this figure, the reader is referred to the web version of this article.)

Discussion

Our simulations show that the initial rapid RBC migration away from the wall is nearly independent of the various conditions, such as hematocrit and flow rate, when scaled with the characteristic shear rate. This indicates that initially the shear rate is the only relevant time scale for the RBC migration. An experimental investigation of vesicle migration away from a wall (Coupier et al., 2008) has shown that vesicle displacement Δy follows a power-law behavior $\Delta y \sim t^{\beta}$. A log–log plot of the CFL development curves shown as an inset in Figs. 2 and 3 indicates that the initial rapid CFL-thickness increase is close to a power-law behavior with an exponent equal to or smaller than 1/3. The value of 1/3 corresponds to the dependence of lift force on the distance h as $F_l \sim 1/h^2$ for the migration of single cells. However, the initial migration of RBCs appears to be slower than the power-law behavior with an exponent 1/3 due to cell–cell interactions. At later times, the RBC migration slows down even further and another time scale corresponding to the relaxation of RBC core becomes relevant. This can be seen better for the case of $H_t = 0.45$ in Fig. 3, where cell–cell interactions affect the CFL convergence. However, for all investigated hematocrit levels ($H_t \leq 0.45$) the rearrangement process of RBCs in the flow core only weakly affects the time for CFL convergence as shown in Figs. 2 and 3.

Another important conclusion, which can be drawn from the CFL development results, is that the length of blood-flow convergence to steady state is practically independent of the flow rate for vessel diameters in the range 10 μm < D < 100 μm. Thus, for physiological hematocrit levels, including those for normal microvascular blood flow (Lipowsky et al., 1980; Pries et al., 1986), the flow convergence time is equal to about $t_c \lesssim 25/\bar{\dot\gamma} = 25D/\bar{v}$. Then, the length required for the flow to converge is $l_c \lesssim \bar{v} t_c = 25D$; for instance, for $D = 20$ μm,

$l_c \lesssim 0.5$ mm, independently of the flow rate and H_t. In vessels with a diameter smaller than about 10 μm, the CFL thickness might be difficult to define properly, since the vessel diameter is comparable to or smaller than the RBC size; this makes the estimation for the length of blood flow convergence rather unpractical. In vessels with a diameter larger than 100 μm, the CFL thickness becomes small in comparison with D, and therefore its effect on blood flow resistance can be nearly neglected.

The estimation of the convergence length for blood flow has direct implications for quantifying this effect on the flow resistance in microcirculation. Microcirculatory blood flow is not always steady, since, for instance, the distribution of RBCs in a vessel cross-section can be significantly distorted at bifurcations leading to a diminished CFL and an increase in the flow resistance. Following the flow development after a dispersion of RBCs, we can estimate an effective increase in resistance. For this purpose, we divide a length L of the channel into a number of slices of thickness Δx. Then, the pressure drop $\Delta P(x_i)$ at every slice i is equal to

$$\Delta P(x_i) = \frac{128 Q \eta(x_i) \Delta x}{\pi D^4}, \tag{11}$$

where $\eta(x_i)$ is the effective viscosity at a slice i, which is a monotonically decreasing function of x as $x \to L$, since the CFL develops and its thickness increases. When, the CFL thickness comes to a plateau value, the local effective viscosity would also saturate. On the other hand, $\Delta P = (128 Q \eta_{eff} L)/(\pi D^4) = \sum_i \Delta P(x_i)$. Thus, the effective viscosity over the channel length L can be expressed as

$$\eta_{eff} = \frac{1}{L} \sum_i \eta(x_i) \Delta x \approx \frac{1}{L} \int_0^L \eta(x) dx = \overline{\eta}. \tag{12}$$

The effective resistance over the channel length L characterized by η_{eff} will mainly depend on L and the initial dispersion of RBCs which would affect $\eta(0)$. The performed simulations correspond to the worst-case scenario of RBC dispersion, since they are allowed initially to diffuse and fill up the full channel cross-section. Therefore, the maximum value of $\eta(0)$ can be estimated as the bulk viscosity of blood for a given tube H_t, which is normally several times larger than the plasma viscosity for physiological H_t values. However, the RBC core distortion past vessel bifurcations in blood flow is likely to be less than that assumed initially in simulations and hence, $\eta(0)$ is generally expected to be even smaller in microvasculature. With respect to the vessel length L, the effect of potential RBC dispersion can be practically neglected if $L \gg 25D$; however, it may noticeably increase the flow resistance if L is smaller than or comparable to $25D$, which is an approximate CFL convergence length. Characteristic lengths of microvascular vessels between bifurcations (Popel and Johnson, 2005) are on the order $0.5 - 1$ mm. Thus, the contribution to blood flow resistance due to the potential RBC dispersion at vessel bifurcations and junctions is expected to be rather small for vessels with diameters $D \lesssim 20$ μm, while in vessels with larger diameters (20 μm $\lesssim D \lesssim$ 100 μm) this contribution should be significant.

Aggregation interactions between RBCs lead to a reduction of blood flow resistance evidenced by the increased terminal CFL thicknesses in Fig. 7(a). The corresponding flow resistances characterized by the relative viscosity are shown in Fig. 9. The relative viscosity is defined as $\eta_{rel} = Q_{plasma}/Q_{RBC}$, where Q_{plasma} corresponds to the rate of flow of plasma without RBCs, while Q_{RBC} is the flow rate of blood for the same pressure gradient. Analogously, $\eta_{rel} = \eta_{app}/\eta$, where η_{app} is the apparent blood viscosity in tube flow. The curves in Fig. 9 demonstrate that aggregation interactions in blood lead to a decrease in flow resistance at least at the low flow rates, which is qualitatively consistent with the experimental results (Reinke et al., 1987). These low flow rates would be relevant in the venular part of microcirculatory blood flow. It is also likely that the aggregation interactions between RBCs would lead to a lower distortion of RBC flow core at bifurcations further contributing to the reduction of flow resistance.

The theoretical model for the δ_f thickness confirms that the main mechanisms for CFL formation are the lift force which drives RBCs away from the wall and the shear-induced pressure due to cell–cell interactions in flow which disperses RBCs. Thus, δ_f corresponds to a CFL thickness when these two driving forces balance each other. The value of c_s for RBC suspension is considerably smaller than that estimated for colloidal suspensions ($c_s = 1/9$) in Ref. Vollebregt et al. (2012). This might be due to an alignment of RBCs in flow such that the effective particle size for inter-cell collisions is much reduced. Another uncertainty comes from the assumption for the function Z whose value might be well overestimated. The value of c_l in this work also appears to be much smaller than that suggested for single vesicles ($c_l \approx 0.1 - 0.2$) in Refs. Messlinger et al. (2009) and Sukumaran and Seifert (2001). A reduction in lift force is likely to happen due to the alignment of RBCs in flow and their increased concentration. However, the ratio of the constants c_s and c_l, which determines the value of δ_f at large $\bar{\dot{\gamma}}$, is not very far from the above estimations (Messlinger et al., 2009; Vollebregt et al., 2012; Sukumaran and Seifert, 2001). Due to a number of simplifying assumptions, the discrepancies between the δ_f values and the fits in Fig. 8 are not entirely surprising and can be easily alleviated by changing the constants c_s and c_l, which are likely to be sensitive to different RBC dynamics and local concentration. Finally, following these arguments we can often anticipate the changes in CFL thickness and flow resistance. For example, for rigidified RBCs the lift force should be considerably reduced, and therefore, it should result in a smaller CFL thickness. Furthermore, more spherical suspended cells and/or particles than RBCs are also subject to a reduced lift force from the wall.

In our simulations, we employed same viscosity for the suspending fluid and RBC cytosol and neglected the RBC membrane viscosity. For a healthy RBC, the viscosity contrast λ, defined as the ratio of cytosol over blood plasma viscosity, is approximately $\lambda = 5$. Recent experiments (Vitkova et al., 2008) and simulations (Yazdani and Bagchi, 2011) indicate that the viscosity contrast strongly affects the tumbling-to-tank-treading transition, which is known to shift to higher shear rates with increase in the viscosity contrast. For high enough $\lambda \gtrsim 5$, the tank-treading motion of a single RBC might be suppressed. In addition, a non-zero membrane viscosity further intensifies this effect increasing the effective viscosity difference (Noguchi and Gompper, 2004). Thus, the tank-treading of a RBC membrane is strongly suppressed, but still partially possible due to effective confinement

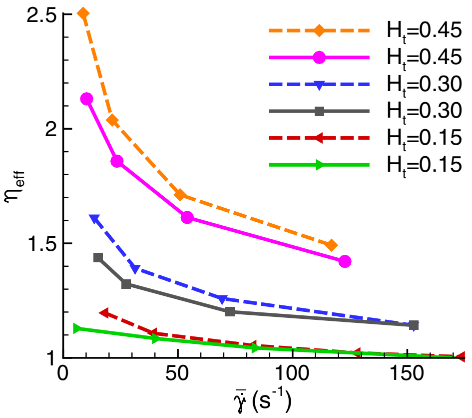

Fig. 9. Relative viscosity (the ratio of blood apparent viscosity to plasma viscosity) of blood flow for different H_t values, flow rates, and RBC aggregation. $D = 20$ μm. The data are shown by dashed lines for systems without aggregation interactions and by solid lines for the simulations where RBC aggregation interactions were present.

interactions between RBCs. The preference for tumbling dynamics of RBCs will likely lead to a reduction of the lift force on RBCs (Coupier et al., 2008; Messlinger et al., 2009) and an enhancement of cell dispersion in the RBC core. Such changes would result in a smaller CFL thickness of the developed flow and a larger flow resistance in comparison with the case of $\lambda = 1$ investigated here. Due to a smaller lift force, the migration of RBCs away from the wall will also likely become slower. However, it is difficult to predict the length required for the CFL convergence, since the final CFL thickness will also be affected by the viscosity contrast. Thus, this issue requires further investigation.

Finally, the simulation predictions for the CFL convergence and the required vessel length need experimental validation. An experimental setup would require measurements of the CFL thickness at a number of consecutive positions along a tube or a vessel. For instance, an experiment with sudden flow start-up might be an option. Alternatively, an experiment, where the changes in CFL right after a tube inflow are monitored, would be mimicked by the simulations. Several experiments on measurements of the CFL near bifurcations (Pries et al., 1989; Ong et al., 2012) already exist; however, a direct comparison with the presented simulation data is not feasible.

Summary

We have investigated the development of CFL in blood flow starting from a fully dispersed cell configuration. RBCs migrate away from the wall due to a lift force which arises from cell-wall hydrodynamic interactions. The convergence of CFL thickness toward a constant δ_f value at steady-state flow appears to be nearly universal if scaled with the average shear rate, and the corresponding power-law behavior has a similarity with that of a single vesicle migrating away from a wall. Aggregation interactions between RBCs lead to a larger CFL thickness in comparison to the flow where attractive interactions between cells are absent. The final CFL thickness δ_f is well described by a theoretical argument that at steady state a balance between lift forces on RBCs and shear-induced effective pressure due to cell–cell interactions in flow exists. The theoretical model describes quite well the δ_f dependence on shear rate in spite of many simplifying assumptions made.

Our results allow us to estimate the effect of a reduced CFL thickness on blood flow resistance which may occur, for instance, at vessel bifurcations where RBCs can get dispersed. The universality of CFL convergence with respect to flow rate results in the estimation for the vessel length l_c required for full CFL development to be less than or equal to $25D$ for vessel diameters in the range $10\ \mu\text{m} < D < 100\ \mu\text{m}$. Thus, in vessels with a length comparable to or shorter than $25D$ the effect of RBC dispersion on the flow resistance might be considerable, while in much longer vessels this effect may be neglected. Quantitatively, this effect can be taken into account by averaging the effective fluid viscosity $\eta(x)$ along the vessel length, which is directly associated with the CFL development. Finally, the presented results are not only relevant for blood flow, but also for a flow of suspension of deformable particles such as vesicles, capsules, and cells. Their migration mechanisms are expected to be similar, even though quantitatively the current predictions may be altered, since the lift force and shear-induced pressure depend on the properties and dynamics of specific particles. We hope that the presented results will trigger further investigations of such systems in order to better understand their flow properties.

Acknowledgments

Dinar Katanov acknowledges support by the International Helmholtz Research School of Biophysics and Soft Matter (IHRS BioSoft). Dmitry A. Fedosov acknowledges funding by the Alexander von Humboldt Foundation (Sofja Kovalevskaja Award). We also gratefully acknowledge a CPU time grant by the Jülich Supercomputing Center.

References

Abkarian, M., Lartigue, C., Viallat, A., 2002. Tank treading and unbinding of deformable vesicles in shear flow: determination of the lift force. Phys. Rev. Lett. 88, 068103.
Allen, M.P., Tildesley, D.J., 1991. Computer Simulation of Liquids. Clarendon Press, New York.
Cantat, I., Misbah, C., 1999. Lift force and dynamical unbinding of adhering vesicles under shear flow. Phys. Rev. Lett. 83, 880–883.
Carnahan, N.F., Starling, K.E., 1969. Equation of state for nonattracting rigid spheres. J. Chem. Phys. 51, 635–636.
Carr, R.T., 1989. Estimation of hematocrit profile symmetry recovery length downstream from a bifurcation. Biorheology 26, 907–920.
Carr, R.T., Xiao, J., 1995. Plasma skimming in vascular trees: numerical estimates of symmetry recovery lengths. Microcirculation 2, 345–353.
Cokelet, G.R., Goldsmith, H.L., 1991. Decreased hydrodynamic resistance in the two-phase flow of blood through small vertical tubes at low flow rates. Circ. Res. 68, 1–17.
Coupier, G., Kaoui, B., Podgorski, T., Misbah, C., 2008. Noninertial lateral migration of vesicles in bounded Poiseuille flow. Phys. Fluids 20, 111702.
Discher, D.E., Boal, D.H., Boey, S.K., 1998. Simulations of the erythrocyte cytoskeleton at large deformation. II. Micropipette aspiration. Biophys. J. 75, 1584–1597.
Español, P., Revenga, M., 2003. Smoothed dissipative particle dynamics. Phys. Rev. E 67, 026705.
Español, P., Warren, P., 1995. Statistical mechanics of dissipative particle dynamics. Europhys. Lett. 30, 191–196.
Evans, E.A., Skalak, R., 1980. Mechanics and Thermodynamics of Biomembranes. CRC Press, Inc., Boca Raton, Florida.
Fåhraeus, R., Lindqvist, T., 1931. The viscosity of the blood in narrow capillary tubes. Am. J. Phys. 96, 562–568.
Fedosov, D.A., Caswell, B., Popel, A.S., Karniadakis, G.E., 2010a. Blood flow and cell-free layer in microvessels. Microcirculation 17, 615–628.
Fedosov, D.A., Caswell, B., Karniadakis, G.E., 2010b. A multiscale red blood cell model with accurate mechanics, rheology, and dynamics. Biophys. J. 98, 2215–2225.
Fedosov, D.A., Caswell, B., Karniadakis, G.E., 2010c. Systematic coarse-graining of spectrin-level red blood cell models. Comput. Meth. Appl. Mech. Eng. 199, 1937–1948.
Fedosov, D.A., Pan, W., Caswell, B., Gompper, G., Karniadakis, G.E., 2011. Predicting human blood viscosity in silico. Proc. Natl. Acad. Sci. U. S. A. 108, 11772–11777.
Fedosov, D.A., Dao, M., Karniadakis, G.E., Suresh, S., 2014a. Computational biorheology of human blood flow in health and disease. Ann. Biomed. Eng. 42, 368–387.
Fedosov, D.A., Noguchi, H., Gompper, G., 2014b. Multiscale modeling of blood flow: from single cells to blood rheology. Biomech. Model. Mechanobiol. 13, 239–258.
Frank, M., Anderson, D., Weeks, E.R., Morris, J.F., 2003. Particle migration in pressure-driven flow of a Brownian suspension. J. Fluid Mech. 493, 363–378.
Goldsmith, H.L., Cokelet, G.R., Gaehtgens, P., 1989. Robin Fahraeus: evolution of his concepts in cardiovascular physiology. Am. J. Physiol. 257, H1005–H1015.
Grandchamp, X., Coupier, G., Srivastav, A., Minetti, C., Podgorski, T., 2013. Lift and down-gradient shear-induced diffusion in red blood cell suspensions. Phys. Rev. Lett. 110, 108101.
Helfrich, W., 1973. Elastic properties of lipid bilayers: theory and possible experiments. Z. Naturforsch. C 28, 693–703.
Hoogerbrugge, P.J., Koelman, J.M.V.A., 1992. Simulating microscopic hydrodynamic phenomena with dissipative particle dynamics. Europhys. Lett. 19, 155–160.
Kim, S., Kong, R.L., Popel, A.S., Intaglietta, M., Johnson, P.C., 2007. Temporal and spatial variations of cell-free layer width in arterioles. Am. J. Physiol. 293, H1526–H1535.
Kumar, A., Graham, M.D., 2012. Mechanism of margination in confined flows of blood and other multicomponent suspensions. Phys. Rev. Lett. 109, 108102.
Leighton, D., Acrivos, A., 1987. Measurement of shear-induced self-diffusion in concentrated suspensions of spheres. J. Fluid Mech. 177, 109–131.
Lipowsky, H.H., Usami, S., Chien, S., 1980. In vivo measurements of “apparent viscosity” and microvessel hematocrit in the mesentery of the cat. Microvasc. Res. 19, 297–319.
Lucy, L.B., 1977. A numerical approach to the testing the fission hypothesis. Astron. J. 82, 1013–1024.
Maeda, N., Suzuki, Y., Tanaka, J., Tateishi, N., 1996. Erythrocyte flow and elasticity of microvessels evaluated by marginal cell-free layer and flow resistance. Am. J. Physiol. 271, H2454–H2461.
Messlinger, S., Schmidt, B., Noguchi, H., Gompper, G., 2009. Dynamical regimes and hydrodynamic lift of viscous vesicles under shear. Phys. Rev. E 80, 011901.
Monaghan, J.J., 1992. Smoothed particle hydrodynamics. Annu. Rev. Astron. Astrophys. 30, 543–574.
Noguchi, H., Gompper, G., 2004. Fluid vesicles with viscous membranes in shear flow. Phys. Rev. Lett. 93, 258102.
Noguchi, H., Gompper, G., 2005. Shape transitions of fluid vesicles and red blood cells in capillary flows. Proc. Natl. Acad. Sci. U. S. A. 102, 14159–14164.
Ong, P.K., Jain, S., Kim, S., 2012. Spatio-temporal variations in cell-free layer formation near bifurcations of small arterioles. Microvasc. Res. 83, 118–125.
Popel, A.S., Johnson, P.C., 2005. Microcirculation and hemorheology. Annu. Rev. Fluid Mech. 37, 43–69.
Pries, A.R., Secomb, T.W., 2005. Microvascular blood viscosity in vivo and the endothelial surface layer. Am. J. Physiol. 289, H2657–H2664.
Pries, A.R., Secomb, T.W., 2008. Blood flow in microvascular networks. In: Tuma, R.F., Duran, W.N., Ley, K. (Eds.), Handbook of Physiology, The Cardiovascular System, Microcirculation. Academic Press, San Diego, pp. 3–36.
Pries, A.R., Ley, K., Gaehtgens, P., 1986. Generalization of the Fahraeus principle for microvessel networks. Am. J. Physiol. 251, H1324–H1332.
Pries, A.R., Ley, K., Claassen, M., Gaehtgens, P., 1989. Red cell distribution at microvascular bifurcations. Microvasc. Res. 38, 81–101.

Pries, A.R., Neuhaus, D., Gaehtgens, P., 1992. Blood viscosity in tube flow: dependence on diameter and hematocrit. Am. J. Physiol. 263, H1770–H1778.
Pries, A.R., Secomb, T.W., Gessner, T., Sperandio, M.B., Gross, J.F., Gaehtgens, P., 1994. Resistance to blood flow in microvessels in vivo. Circ. Res. 75, 904–915.
Pries, A.R., Secomb, T.W., Gaehtgens, P., 1996. Biophysical aspects of blood flow in the microvasculature. Cardiovasc. Res. 32, 654–667.
Pries, A.R., Secomb, T.W., Jacobs, H., Sperandio, M., Osterloh, K., Gaehtgens, P., 1997. Microvascular blood flow resistance: role of endothelial surface layer. Am. J. Physiol. 273, H2272–H2279.
Pries, A.R., Secomb, T.W., Gaehtgens, P., 2000. The endothelial surface layer. Pflugers Arch. 440, 653–666.
Reinke, W., Gaehtgens, P., Johnson, P.C., 1987. Blood viscosity in small tubes: effect of shear rate, aggregation, and sedimentation. Am. J. Physiol. 253, H540–H547.
Secomb, T.W., Hsu, R., 1997. Resistance to blood flow in nonuniform capillaries. Microcirculation 4, 421–427.
Secomb, T.W., Pries, A.R., 2011. The microcirculation: physiology at the mesoscale. J. Physiol. 589, 1047–1052.
Sukumaran, S., Seifert, U., 2001. Influence of shear flow on vesicles near a wall: a numerical study. Phys. Rev. E 64, 011916.
Vink, H., Duling, B.R., 1996. Identification of distinct luminal domains for macromolecules, erythrocytes, and leukocytes within mammalian capillaries. Circ. Res. 79, 581–589.
Vitkova, V., Mader, M.-A., Polack, B., Misbah, C., Podgorski, T., 2008. Micro–macro link in rheology of erythrocyte and vesicle suspensions. Biophys. J. 95, L33–L35.
Vollebregt, H.M., van der Sman, R.G.M., Boom, R.M., 2012. Model for particle migration in bidisperse suspensions by use of effective temperature. Faraday Discuss. 158, 89–103.
Weinbaum, S., Tarbell, J.M., Damiano, E.R., 2007. The structure and function of the endothelial glycocalyx layer. Annu. Rev. Biomed. Eng. 9, 121–167.
Yazdani, A.Z.K., Bagchi, P., 2011. Phase diagram and breathing dynamics of a single red blood cell and a biconcave capsule in dilute shear flow. Phys. Rev. E 84, 026314.
Yen, W.-Y., Cai, B., Zeng, M., Tarbell, J.M., Fu, B.M., 2012. Quantification of the endothelial surface glycocalyx on rat and mouse blood vessels. Microvasc. Res. 83, 337–346.

P2: Dense brushes of stiff polymers or filaments in fluid flow

F. Römer and D. A. Fedosov

Europhysics Letters, **109**:68001, 2015.

A LETTERS JOURNAL EXPLORING
THE FRONTIERS OF PHYSICS

March 2015

EPL, **109** (2015) 68001
doi: `10.1209/0295-5075/109/68001`

`www.epljournal.org`

Dense brushes of stiff polymers or filaments in fluid flow

F. RÖMER and D. A. FEDOSOV

Theoretical Soft Matter and Biophysics, Institute of Complex Systems and Institute for Advanced Simulation, Forschungszentrum Jülich - 52425 Jülich, Germany

received 18 November 2014; accepted in final form 2 March 2015

PACS `82.35.Gh` – Polymers on surfaces; adhesion
PACS `83.10.Bb` – Kinematics of deformation and flow
PACS `83.50.Ax` – Steady shear flows, viscometric flow

Abstract – Dense filamentous brush-like structures are present in many biological interfacial systems (*e.g.*, glycocalyx layer in blood vessels) to control their surface properties. Such structures can regulate the softness of a surface and modify fluid flow. In this letter, we propose a theoretical model which predicts quantitatively flow-induced deformation of a dense brush of stiff polymers or filaments, whose persistence length is larger or comparable to their contour length. The model is validated by detailed mesoscopic simulations and characterizes different contributions to brush deformation including hydrodynamic friction due to flow and steric excluded-volume interactions between grafted filaments. This theoretical model can be used to describe the effect of a stiff-polymer brush on fluid flow and to aid in the quantification of experiments.

Introduction. – Polymer brushes have been subject to enormous interest in the last several decades due to their importance in various technological and biological systems [1–3]. However, the main focus of most experimental, theoretical, and simulation studies has been on the behavior of brushes consisting of grafted flexible polymers (*i.e.*, with negligible flexural stiffness on the length of a polymer). Brushes with stiff chains, whose persistence length is larger or comparable to the contour length, have received limited attention to date, in spite of their frequent presence in many biophysical systems. Dense filamentous brush-like structures often serve as structural elements in the human body with the examples of lubricating aggrecan brushes in joints [4], endothelial glycocalyx layer in blood vessels [5,6], periciliary layer of lung airway [7], and hair cells in the inner ear mediating the sense of hearing and balance [8,9]. Better understanding of their non-equilibrium behavior, for instance their response to flow, will lead to insights into the functionality of the respective structures and the effects of pathological alterations. Technologically, brushes with stiff grafted elements, such as cantilevered micro- and nano-rod arrays [10] or high-density brushes [11], can be used in nanofluidic devices [12] or in the context of functionalized surfaces [13].

Equilibrium properties of stiff-polymer brushes have been investigated in a few simulation [14–16] and theoretical [16–18] studies predicting the brush height. *In silico* compression tests of dense semiflexible-polymer brushes [19,20] have shown that such brushes might be much softer mechanically than the brushes made out of flexible polymers making them useful in micro-flow applications. As an example, the response of a glycocalyx layer in blood vessels to fluid flow has been studied in simulations [21] predicting a flow-rate–dependent increase in the flow resistance. Recently, a mean-field approach [22] has been developed to describe the flow-induced deformation of grafted semiflexible polymers. In this theory, the steric interactions between polymers have been neglected limiting the model's applicability to the deformation of a single grafted polymer.

In this letter, we develop a theoretical model which is able to describe quantitatively the flow-induced deformation of a dense stiff-polymer brush and its effect on flow. The model is applicable to the brushes where individual grafted polymers or filaments possess a persistence length which is larger or comparable to their total contour length. To validate this model we perform corresponding mesoscopic simulations for a wide range of conditions including polymer elasticity, grafting density, and flow rate. The model allows us to identify the importance of different contributions to brush deformation such as hydrodynamic friction due to flow and steric excluded-volume interactions between polymers. This model can be employed for the quantification of experiments in biological settings and for the development of brush interfaces with specific surface properties. It can be also used to describe the

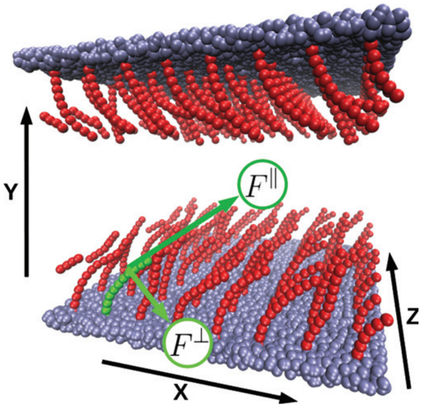

Fig. 1: (Colour on-line) Snapshot of a SDPD simulation system with shear flow in the x-direction. Stiff polymers are grafted on both walls. The fluid particles are not shown.

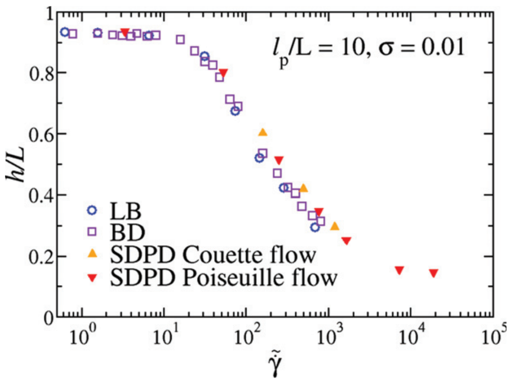

Fig. 2: (Colour on-line) Comparison of different simulation methods. Relative polymer brush height (h/L) as a function of non-dimensional shear rate $\tilde{\dot{\gamma}}$ from Brownian-dynamics and lattice-Boltzmann simulations [22] and the SDPD simulations of this work.

behavior of a stiff-polymer brush in flow, where explicit brush modeling is difficult or unfeasible.

Simulations. – To illustrate the system of interest, fig. 1 presents the simulation setup, where a slit-like geometry with a height D is employed. Both the top and bottom walls are covered by stiff polymers grafted on the square lattice with a constant a_{lat}. The polymers are built up from $N = 11$ bonded beads with a diameter $d = 1.0$ and the potential energy given by

$$U = \sum_{i=1}^{N-1} \left[\frac{k_s}{2d} \left[r_{i,i+1} - d \right]^2 + \frac{EI}{d} \left[1 - \cos\theta_i \right] \right], \tag{1}$$

where k_s is the spring constant, $r_{i,i+1}$ is the distance between the beads i and $i+1$, EI is the bending rigidity, θ_i is the angle between two consecutive springs, and $EI/k_s = d^2/16$. The polymers are stiffly anchored at the surface by fixing the bead $i = 1$ at the surface and the bead $i = 0$ inside the surface. To prevent overlap between beads, the purely repulsive, shifted, and truncated at $r_c = d$ Lennard-Jones (LJ) potential [23] is introduced with the parameters $\epsilon = k_BT$ and $2^{1/6}\sigma_{LJ} = d$, where k_BT is the thermal energy unit.

To model the fluid flow, we employ the smoothed dissipative particle dynamics (SDPD) method [24] using a density of $n_s = 3$ for both fluid and wall particles. Interactions of the fluid particles with the polymer beads are mediated by friction forces. Shear flow is generated by moving one of the walls with a constant velocity. The Poiseuille flow is driven by an external force f_q which acts on each fluid particle in the x-direction. This corresponds to a pressure drop ΔP along the slit length l_x such that $f_q n_s = \Delta P/l_x$.

To characterize the simulated systems we use several dimensionless parameters such as the bending rigidity of the grafted polymers,

$$\frac{l_p}{L} = \frac{EI}{k_BTL}, \tag{2}$$

grafting density $\sigma = (d/a_{\text{lat}})^2$, and non-dimensional shear rate,

$$\tilde{\dot{\gamma}} = \frac{\eta L^3}{k_BT}\dot{\gamma}. \tag{3}$$

Here, l_p/L is the ratio of polymer persistence and contour lengths, η is the fluid's viscosity, and $\dot{\gamma}$ is the shear rate on top of a brush. The effective brush height h is calculated using the first moment of the polymer-bead density profile similar to that in ref. [21],

$$h = 2\frac{\int y\rho(y)\mathrm{d}y}{\int \rho(y)\mathrm{d}y}. \tag{4}$$

To verify our simulation model, we compare in fig. 2 the SDPD results with previous simulations of grafted semiflexible polymers in shear flow using the Brownian-dynamics and lattice-Boltzmann methods [22]. The SDPD results of this work are in excellent agreement with the previous simulations of similar brush systems [22]. In addition, we have also tested whether the type of shear flow (*e.g.*, Couette or Poiseuille) over a brush may have a considerable effect. Figure 2 shows that brush deformation appears to be nearly independent of the flow applied and can be well characterized by $\tilde{\dot{\gamma}}$. To span a wide range of conditions, we have simulated systems with grafting densities σ in the range from 0.01 to 1 (which corresponds to SC close packing), polymer elasticities l_p/L between 10 and 100, and shear rates $\tilde{\dot{\gamma}}$ between 10^1 and 10^6. Note that the grafted polymers are relatively stiff with $l_p/L > 1$, and, therefore, entropic conformational changes such as polymer coiling can be practically neglected. The corresponding Reynolds numbers $Re = vLn_s/\eta$, with v being the velocity at the brush top, have been kept between 10^{-6} and 10^{-1} to ensure no inertial effects. Monitoring of bond lengths has shown that no significant extension ($\lesssim 1\%$) of polymers has been present, and thus, polymer stretching can be neglected.

Theory. – Our mean-field approach to describe the behavior of stiff polymer brushes in shear flow assumes identical deformation for all polymers. Thus, we consider a single polymer as an elastic cantilever which is subject to a hydrodynamic drag force due to fluid flow and steric interactions due to its neighboring polymers in the lattice. The polymer deformation is described by its internal curve-linear coordinate $s \in [0, L]$ and the angle $\theta(s)$ between the y-axis and a local tangent line at s. The correspondence of internal coordinates to the Cartesian coordinates is simply done as $x(s) = \int_0^s \sin\theta(s')\,\mathrm{d}s'$ and $y(s) = \int_0^s \cos\theta(s')\,\mathrm{d}s'$.

The torque balance for a circular rod [25], where external forces ($\mathbf{F}(s) = (F_x(s);\ F_y(s))$) are counteracted by the rods's elastic resistance, leads to

$$EI\frac{\mathrm{d}\mathbf{r}(s)}{\mathrm{d}s} \times \frac{\mathrm{d}^3\mathbf{r}(s)}{\mathrm{d}s^3} = \mathbf{F}(s) \times \frac{\mathrm{d}\mathbf{r}(s)}{\mathrm{d}s}, \qquad (5)$$

where $\mathbf{r}(s)$ is the position on a rod at s such that $\mathrm{d}\mathbf{r}(s)/\mathrm{d}s = (\sin\theta(s);\ \cos\theta(s))$. This equation formulated in terms of the local angle $\theta(s)$ reduces to

$$EI\frac{\mathrm{d}^2\theta(s)}{\mathrm{d}s^2} = F_y(s)\sin\theta(s) - F_x(s)\cos\theta(s), \qquad (6)$$

with the boundary conditions of $\theta(s)|_{s=0} = \theta_0$ at the grafted surface and $\mathrm{d}\theta/\mathrm{d}s|_{s=L} = 0$ at the free end. θ_0 characterizes the grafting angle between the polymer beam and the surface's normal and can generally be a constant or a function of stress applied to the beam. However, in the current study we investigate perpendicular grafting of stiff filaments to a surface with $\theta_0 = 0$.

The force $\mathbf{F}(s)$ consists of two contributions: i) drag force ($\mathbf{F}^{\mathrm{d}}(s)$) from fluid flow and ii) a force due to excluded-volume interactions ($\mathbf{F}^{\mathrm{v}}(s)$), and thus, $\mathbf{F}(s) = \mathbf{F}^{\mathrm{d}}(s) + \mathbf{F}^{\mathrm{v}}(s)$. Note that beam stretching is neglected. The force at a position s can be found as an integral over local force density ($\mathbf{f}(s) = \mathbf{f}^{\mathrm{d}}(s) + \mathbf{f}^{\mathrm{v}}(s)$) such that

$$\mathbf{F}(s) = \int_s^L \mathbf{f}(s')\mathrm{d}s'. \qquad (7)$$

The force density of the drag force exerted on a stiff polymer is given by

$$\begin{aligned} f_x^{\mathrm{d}}(s) &= f_\perp^{\mathrm{d}}(s)\cos\theta(s) + f_\parallel^{\mathrm{d}}(s)\sin\theta(s) = \\ &\quad \left(\zeta_\perp\cos^2\theta(s) + \zeta_\parallel\sin^2\theta(s)\right)\eta u_x(s) = \zeta(s)\eta u_x(s), \\ f_y^{\mathrm{d}}(s) &= f_\perp^{\mathrm{d}}(s)\sin\theta(s) - f_\parallel^{\mathrm{d}}(s)\cos\theta(s) = \\ &\quad \eta u_x(s)\sin\theta(s)\cos\theta(s)\left(\zeta_\perp - \zeta_\parallel\right), \end{aligned} \qquad (8)$$

where $f_\perp^{\mathrm{d}}(s)$ and $f_\parallel^{\mathrm{d}}(s)$ are the corresponding normal and parallel components of the force density with the convention that $f_\perp^{\mathrm{d}}(s)$ is directed with the x-axis and down to the wall (see fig. 1), while $f_\parallel^{\mathrm{d}}(s)$ has a tangential direction toward the increase of the s-coordinate. $\zeta_\perp$ and $\zeta_\parallel$ are the normal and tangential components of the friction coefficient per unit length, $\zeta(s) = \zeta_\parallel\sin^2\theta(s) + \zeta_\perp\cos^2\theta(s)$, and $u_x(s)$ is the local flow velocity and $u_y(s) = 0$. The friction coefficients are approximated using the slender body theory [26] for a thin cylinder similar to that in ref. [27],

$$\begin{aligned} \zeta^\perp &= \frac{8\pi}{\ln(L/d) - \frac{1}{2} + \ln(2)}, \\ \zeta^\parallel &= \frac{4\pi}{\ln(L/d) - \frac{3}{2} + \ln(2)}. \end{aligned} \qquad (9)$$

Note that these friction coefficients describe a drag on an isolated rod. If we neglect hydrodynamic interactions, the drag force on a polymer can be described using a single friction coefficient $\zeta = \zeta_\parallel = \zeta_\perp = 3\pi$ as in ref. [22]. In this case, the force density $f_y^{\mathrm{d}}(s)$ vanishes. The differences in model predictions using these two limiting cases for the friction coefficients will be discussed further in text.

The local velocity $u_x(s)$ depends on hydrodynamic penetration into the brush [28] and is described by the Brinkman equation [29] for flow in porous media as

$$\frac{\mathrm{d}^2u_x(y)}{\mathrm{d}y^2} = \zeta(y)\frac{\sigma}{d^2}\frac{u_x(y)}{\cos\theta(y)}. \qquad (10)$$

The same equation has been also used in the theory by Kim *et al.* [22]. Boundary conditions for eq. (10) are $u_x(y)|_{y=0} = 0$ and $\mathrm{d}u_x(y)/\mathrm{d}y|_{y_{max}} = \dot\gamma|_{s=L}$. Equation (10) in internal coordinates becomes

$$\frac{\mathrm{d}^2u_x(s)}{\mathrm{d}s^2} = \zeta(s)u_x(s)\frac{\sigma}{d^2}\cos\theta(s) - \frac{\mathrm{d}u_x(s)}{\mathrm{d}s}\frac{\mathrm{d}\theta(s)}{\mathrm{d}s}\tan\theta(s), \qquad (11)$$

with $u_x(s)|_{s=0} = 0$ and $\mathrm{d}u_x(s)/\mathrm{d}s|_{s=L} = \dot\gamma|_{s=L}\cos\theta(L)$ being boundary conditions.

To introduce the steric interactions between the filaments, we discretize the beam into $N = \lfloor L/d \rfloor$ spheres similar to the polymer representation in simulations, where the symbol $\lfloor * \rfloor$ denotes the integer floor function. Since identical deformation of all polymers is assumed, only steric interactions in the plane of beam deformation need to be considered. Therefore, the calculation of volume exclusion interactions includes only the two neighbors surrounding a beam in the flow direction. Finally, the force density $\mathbf{f}_n^{\mathrm{v}}$ on a sphere $n \in [0, \dots, N-1]$ in a discretized beam due to excluded-volume interactions is computed by a sum over all spheres j of neighboring polymers within the plane of beam deformation as

$$\mathbf{f}_n^{\mathrm{v}} = \sum_j \frac{\mathbf{g}_{nj}}{d}, \qquad (12)$$

where $\mathbf{g}_{nj}$ is the force between spheres n and j approximated by a simple repulsive force,

$$\mathbf{g}_{ij} = \left\{ \begin{array}{ll} r_{ij} \leqslant d: & \epsilon_g \dfrac{k_BT}{d}\left[(d/r_{ij})^\alpha - 1\right]\dfrac{\mathbf{r}_{ij}}{r_{ij}} \\ r_{ij} > d: & 0 \end{array} \right\}, \qquad (13)$$

where $r_{ij} = |\mathbf{r}_{ij}|$, and ϵ_g and α are parameters controlling the softness of inter-bead interactions. This force definition appears to be very robust, and the results are hardly affected by ϵ_g and α, if $\epsilon_g \gtrsim 50$ and $\alpha \geq 3$, since the interactions become hard enough. Thus, in order to have a larger time step for a numerical solver, we use $\epsilon_g = 50$ and $\alpha = 3$ in the theoretical model, while in simulations the employed LJ potential is harder. The volume exclusion force $\mathbf{F}^{\mathrm{v}}(s)$ is calculated through the integral in eq. (7), whose discrete representation is given by

$$\mathbf{F}^{\mathrm{v}}(s) = \mathbf{f}^{\mathrm{v}}_{\lfloor s/d \rfloor}\left(d\lceil s/d \rceil - s/d\right) + \sum_{n=\lceil s/d \rceil}^{N-1} \mathbf{f}^{\mathrm{v}}_n d, \qquad (14)$$

where the symbol $\lceil * \rceil$ denotes the integer ceiling function.

Direct numerical solving of eq. (6) appeared to be difficult for high grafting densities and shear rates, *i.e.* in the regime where excluded-volume interactions dominate. Therefore, we substituted eq. (6) with its time-dependent version given by

$$\frac{\partial\theta}{\partial t} = EI\frac{\partial^2\theta}{\partial s^2} - F_y(s)\sin\theta + F_x(s)\cos\theta, \qquad (15)$$

where θ becomes a function of s and time t. Finally, eqs. (15) and (11) are solved numerically for a given set of parameters (elasticity, grafting density, and shear rate on top of a brush) using the following iterative procedure. i) Initially, we guess a beam configuration and the polymer is discretized into 10^2 elements. Then, eq. (11) is solved using a boundary value problem (BVP) solver for ordinary differential equations [30] in order to obtain the velocity profile. ii) At this step, the calculation of the hydrodynamic drag force $\mathbf{F}^{\mathrm{d}}(s)$ and the volume-exclusion interaction force $\mathbf{F}^{\mathrm{v}}(s)$ is performed following eqs. (8) and (14), respectively. iii) As a next step, eq. (15) is integrated using the DuFort-Frankel scheme [31], and the resulting configuration is taken as an initial guess for a new cycle. This iteration is repeated until the convergence condition $\sum_i \|\theta_i(t) - \theta_i(t-\Delta t)\| \leq 10^{-7}$ is satisfied, where Δt is the time step.

Results and discussion. – Figure 3(a) presents our main result, the relative brush height as a function of the shear rate on top of the brush normalized by the bending rigidity of the polymers for the case of two friction coefficients from eq. (9). The predictions of our theoretical model are in good quantitative agreement with the corresponding SDPD simulations for two different bending rigidities of $l_p/L = 10$ and 100. Brush deformation for different elasticities of the grafted polymers shows a universal behavior with respect to the polymer bending rigidity, if polymers are stiff enough with $l_p/L \gtrsim 10$. Clearly, the theory is expected to fail when EI/L becomes smaller or comparable to k_BT (or if $l_p/L \lesssim 1$) or when the grafted polymers can be considered rather flexible. In this case entropic effects have to be necessarily included, which is out of the scope of this work.

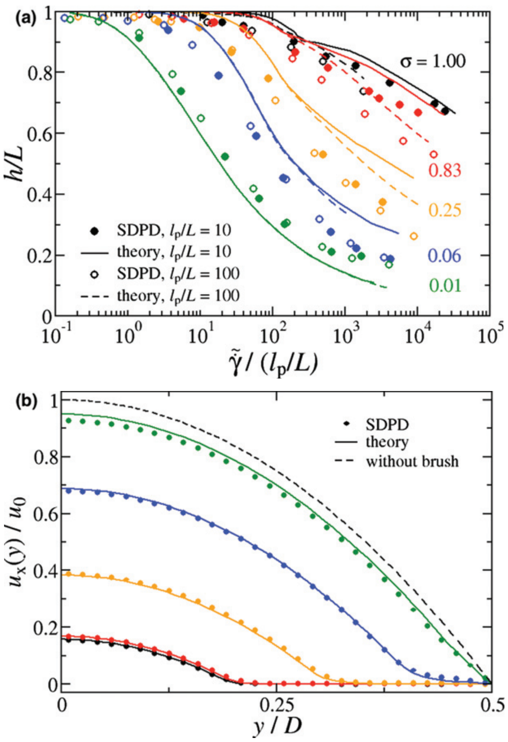

Fig. 3: (Colour on-line) (a) Relative brush height as a function of the shear rate on top of a brush normalized by polymer elasticity from SDPD simulations and the theoretical model for different grafting densities. Two bending rigidities of $l_p/L = 10$ and 100 are considered. (b) Normalized velocity profiles for pressure-driven flow in a micro-channel with walls functionalized with stiff polymers. The dots represent data from simulations and the solid lines refer to the theory for grafting densities (from top to bottom) $\sigma = 0.01$, 0.06, 0.25, 0.83 and 1.0. The dashed line shows the velocity profile for an unperturbed Poiseuille flow and the same pressure gradient.

Some deviations between theoretical predictions and simulations are observed at high grafting densities ($\sigma \gtrsim 0.5$) and flow rates due to a better packing of deformed stiff polymers. Remember that the theory assumes identical deformation for all fibers such that possible deformation in the flow vorticity direction (z-axis) is not considered. Thus, the theory overpredicts the effect of excluded-volume interactions, which can be seen in fig. 3(a) for $\sigma = 1.0$ where the theory estimates a larger brush height in comparison to that obtained in simulations. The curve for $\sigma = 1.0$ also nicely illustrates the onset of excluded-volume effects with respect to shear rate by a significant change in the slope of brush height occurring at approximately $EI\frac{\mathrm{d}^2\theta}{\mathrm{d}s^2} \sim F^{\mathrm{v}}_y \sin\theta - F^{\mathrm{v}}_x \cos\theta$. Thus, at large shear rates the brush height is mainly determined by the excluded-volume interactions.

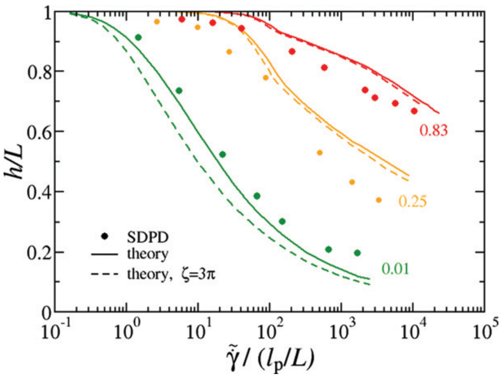

Fig. 4: (Colour on-line) Comparison of the relative brush height for different choices of the friction coefficients in the theoretical model. Solid lines correspond to the case of two friction coefficients from eq. (9), while the dashed lines represent model predictions for $\zeta = \zeta_{\parallel} = \zeta_{\perp} = 3\pi$. The data are shown for grafting densities $\sigma = 0.01$, 0.25, and 0.83 and $l_p/L = 10$.

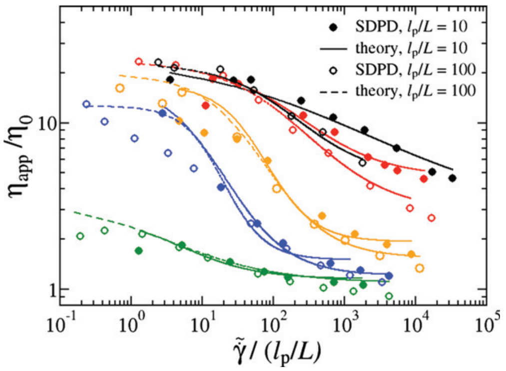

Fig. 5: (Colour on-line) Relative apparent viscosity as a function of the shear rate on top of the brush scaled by elasticity. The dots and circles represent data from simulations and the solid and dashed lines refer to the theory for grafting densities (from top to bottom) $\sigma = 1.0$, 0.83, 0.25, 0.06 and 0.01.

To further support the validity of the theoretical model, we present the correspondence of fluid velocities in fig. 3(b). An excellent agreement of theoretical and simulated velocity profiles indicates that the approximation using the Brinkman equation (eq. (11)) properly captures the frictional effect of the brush on fluid flow for a wide range of grafting densities. However, we need to mention that at the lowest grafting density studied ($\sigma = 0.01$), the Brinkman equation overestimates the influence of the brush on flow. Therefore, in this single case we simply assumed a constant shear rate $\frac{\mathrm{d}u}{\mathrm{d}y} = \dot{\gamma}|_{y=h}$ within the brush, which matches very well the simulated velocity profile, as shown in fig. 3(b).

The model predictions in fig. 3 correspond to the case of two friction coefficients from eq. (9), which were derived for a single isolated rod [26]. Thus, they are expected to provide a reasonable approximation for the friction on filaments at low grafting densities. As the grafting density is increased, hydrodynamic interactions are expected to get screened leading to the loss of hydrodynamic correlations between different segments of a polymer. In this case, a single friction coefficient $\zeta = \zeta_{\parallel} = \zeta_{\perp} = 3\pi$ can be assumed. Figure 4 presents the comparison of model predictions using the two different choices of friction coefficients for various grafting densities and $l_p/L = 10$. As expected, the friction coefficient of 3π leads to an overestimation of the applied drag for low grafting densities, and the other choice (eq. (9)) appears to be better. At high grafting densities, the difference in model predictions using different friction coefficients nearly vanishes, even though the choice of $\zeta = 3\pi$ has been expected to be the best. This indicates that at high grafting densities the brush height is mainly determined by the excluded-volume interactions and moderate changes in the applied friction play a secondary role.

The effect of stiff-polymer brush on the fluid flow can be characterized by an increase of the flow resistance due to the presence of a brush. Figure 5 shows that the relative apparent viscosity, the ratio of the apparent viscosity (obtained by fitting the Poiseuille law to the resulting flow rate) to the fluid viscosity, might strongly increase if a brush is hardly deformed, and becomes smaller as the brush gets bent by the flow. Qualitatively, this effect can be understood by a change in an effective channel diameter. The flow-induced brush deformation can be used for a flow control in microfluidics and is directly related to an increase in blood flow resistance in small vessels whose surface is covered by glycocalyx having a brush-like structure [5,6]. *In vivo* experiments on blood flow resistance [32] reveal a much higher resistance in small vessels ($D \lesssim 35\,\mu$m) in comparison to *in vitro* experiments in glass tubes [33]. This effect is mainly attributed to the glycocalyx layer at vessel walls [34], and the theoretical model of this work can provide its quantitative description.

Conclusion. – In conclusion, the presented theoretical model is able to predict quantitatively the flow-induced deformation of a brush of stiff polymers or filaments and its effect on fluid flow. The model quantifies the relative contributions of fluid friction, polymer bending resistance, and steric excluded-volume interactions between polymers. In comparison to the analytic mean-field approach by Kim *et al.* [22], the presented theoretical model significantly extends the range of model applicability to high grafting densities of stiff polymers and strong deformations under flow. In particular, the current model explicitly includes the effect of excluded-volume interactions between different polymers. We expect that this model will be used for the quantification of biological and technological experiments with stiff brush-like structures, and can be extended to include direct mechanical deformations due to external forces (*e.g.*, brush-cell interactions).

* * *

We would like to thank M. Deng and G. E. Karniadakis for useful discussions. We also gratefully acknowledge the computing time granted on the supercomputer JUROPA at Jülich Supercomputing Centre (JSC). DAF acknowledges funding by the Alexander von Humboldt Foundation.

REFERENCES

[1] Klein J., *Annu. Rev. Mater. Sci.*, **26** (1996) 581.
[2] Ayres N., *Polym. Chem.*, **1** (2010) 769.
[3] Binder K., Kreer T. and Milchev A., *Soft Matter*, **7** (2011) 7159.
[4] Han L., Dean D., Ortiz C. and Grodzinsky A. J., *Biophys. J.*, **92** (2007) 1384.
[5] Weinbaum S., Zhang X., Han Y., Vink H. and Cowin S. C., *Proc. Natl. Acad. Sci. U.S.A.*, **100** (2003) 7988.
[6] Weinbaum S., Tarbell J. M. and Damiano E. R., *Annu. Rev. Biomed. Eng.*, **9** (2007) 121.
[7] Button B., Cai L.-H., Ehre C., Kesimer M., Hill D. B., Sheehan J. K., Boucher R. C. and Rubinstein M., *Science*, **337** (2012) 937.
[8] Tolomeo J. A. and Holley M. C., *Biophys. J.*, **73** (1997) 2241.
[9] Hudspeth A. J. and Corey D. P., *Proc. Natl. Acad. Sci. U.S.A.*, **74** (1977) 2407.
[10] Evans B. A., Shields A. R., Carroll R. L., Washburn S., Falvo M. R. and Superfine R., *Nano Lett.*, **7** (2007) 1428.
[11] Higaki Y., Okazaki R. and Takahara A., *ACS Macro Lett.*, **1** (2012) 1124.
[12] Adiga S. P. and Brenner D. W., *J. Funct. Biomater.*, **3** (2012) 239.
[13] Merlitz H., He G.-L., Wu C.-X. and Sommer J.-U., *Phys. Rev. Lett.*, **102** (2009) 115702.
[14] Chen C.-M. and Fwu Y.-A., *Phys. Rev. E*, **63** (2000) 011506.
[15] Milchev A. and Binder K., *J. Chem. Phys.*, **136** (2012) 194901.
[16] Carignano M. A. and Szleifer I., *J. Chem. Phys.*, **98** (1993) 5006.
[17] Kuznetsov D. V. and Chen Z. Y., *J. Chem. Phys.*, **109** (1998) 7017.
[18] Kim G. G. and Char K., *Bull. Korean Chem. Soc.*, **20** (1999) 1026.
[19] Milchev A. and Binder K., *EPL*, **102** (2013) 58003.
[20] Milchev A. and Binder K., *Soft Matter*, **10** (2014) 3783.
[21] Deng M., Li X., Liang H., Caswell B. and Karniadakis G. E., *J. Fluid Mech.*, **711** (2012) 192.
[22] Kim Y. W., Lobaskin V., Gutsche C., Kremer F., Pincus P. and Netz R. R., *Macromolecules*, **42** (2009) 3650.
[23] Weeks J. D., Chandler D. and Andersen H. C., *J. Chem. Phys.*, **54** (1971) 5237.
[24] Español P. and Revenga M., *Phys. Rev. E*, **67** (2003) 026705.
[25] Landau L. D. and Lifshitz E. M., *Theory of Elasticity* (Pergamon Press, London) 1970.
[26] Cox R. G., *J. Fluid Mech.*, **44** (1970) 791.
[27] Wiggins C. H., Riveline D., Ott A. and Goldstein R. E., *Biophys. J.*, **74** (1998) 1043.
[28] Milner S. T., *Macromolecules*, **24** (1991) 3704.
[29] Brinkman H. C., *Appl. Sci. Res.*, **1** (1949) 27.
[30] Kierzenka J. and Shampine L. F., *ACM Trans. Math. Softw.*, **27** (2001) 299.
[31] Du Fort E. C. and Frankel S. P., *Math. Comput.*, **7** (1953) 135.
[32] Pries A. R., Secomb T. W., Gessner T., Sperandio M. B., Gross J. F. and Gaehtgens P., *Circ. Res.*, **75** (1994) 904.
[33] Pries A. R., Neuhaus D. and Gaehtgens P., *Am. J. Physiol.*, **263** (1992) H1770.
[34] Pries A. R. and Secomb T. W., *Am. J. Physiol.*, **289** (2005) H2657.

P3: Smoothed dissipative particle dynamics with angular momentum conservation

K. Müller, D. A. Fedosov, and G. Gompper

Journal of Computational Physics, **281**:301-315, 2015.

Journal of Computational Physics 281 (2015) 301–315

Contents lists available at ScienceDirect

Journal of Computational Physics

www.elsevier.com/locate/jcp

Smoothed dissipative particle dynamics with angular momentum conservation

Kathrin Müller, Dmitry A. Fedosov*, Gerhard Gompper

Theoretical Soft Matter and Biophysics, Institute of Complex Systems and Institute for Advanced Simulation, Forschungszentrum Jülich, 52425 Jülich, Germany

ARTICLE INFO

Article history:
Received 25 April 2014
Received in revised form 15 August 2014
Accepted 9 October 2014
Available online 16 October 2014

Keywords:
Mesoscopic simulation
Smoothed particle hydrodynamics
Tank-treading vesicle
Taylor–Couette flow
Shear flow
Keller–Skalak theory

ABSTRACT

Smoothed dissipative particle dynamics (SDPD) combines two popular mesoscopic techniques, the smoothed particle hydrodynamics and dissipative particle dynamics (DPD) methods, and can be considered as an improved dissipative particle dynamics approach. Despite several advantages of the SDPD method over the conventional DPD model, the original formulation of SDPD by Español and Revenga (2003) [9], lacks angular momentum conservation, leading to unphysical results for problems where the conservation of angular momentum is essential. To overcome this limitation, we extend the SDPD method by introducing a particle spin variable such that local and global angular momentum conservation is restored. The new SDPD formulation (SDPD+a) is directly derived from the Navier–Stokes equation for fluids with spin, while thermal fluctuations are incorporated similarly to the DPD method. We test the new SDPD method and demonstrate that it properly reproduces fluid transport coefficients. Also, SDPD with angular momentum conservation is validated using two problems: (i) the Taylor–Couette flow with two immiscible fluids and (ii) a tank-treading vesicle in shear flow with a viscosity contrast between inner and outer fluids. For both problems, the new SDPD method leads to simulation predictions in agreement with the corresponding analytical theories, while the original SDPD method fails to capture properly physical characteristics of the systems due to violation of angular momentum conservation. In conclusion, the extended SDPD method with angular momentum conservation provides a new approach to tackle fluid problems such as multiphase flows and vesicle/cell suspensions, where the conservation of angular momentum is essential.

1. Introduction

Mesoscopic hydrodynamic simulations, such as the lattice Boltzmann (LB) method [1], dissipative particle dynamics (DPD) [2–4], multi-particle collision dynamics (MPC) [5,6], smoothed particle hydrodynamics (SPH) [7,8] etc., are frequently used to investigate a wide range of problems including colloidal and polymer solutions, dynamics of microswimmers, tissue growth, and flow behavior of vesicles and cells. All these examples include mesoscopic length scales (e.g., the size of suspended particles) rendering the modeling on atomistic level impossible. A continuum approximation is also not appropriate

---

* Corresponding author.
E-mail addresses: k.mueller@fz-juelich.de (K. Müller), d.fedosov@fz-juelich.de (D.A. Fedosov), g.gompper@fz-juelich.de (G. Gompper).

http://dx.doi.org/10.1016/j.jcp.2014.10.017

for such problems due to the loss of necessary mesoscopic details. Thus, large scientific efforts have been invested to derive reliable and efficient mesoscopic simulation techniques, which are able to tackle a wide range of problems.

A recently established mesoscopic method, smoothed dissipative particle dynamics (SDPD) [9], combines advantages of two popular techniques namely SPH and DPD. The SDPD method for fluid flow is directly derived using a discretization of the Navier–Stokes equation similar to SPH, while the inclusion of thermal fluctuations in SDPD is similar to that in the DPD formalism. SDPD can also be considered as an improved DPD method. Advantages of the SDPD method over conventional DPD include the possibility of using an arbitrary equation of state, direct input of transport properties, and a well-defined physical scale of discretized elements or fluid particles. In addition, it has been shown that the SDPD method produces proper scaling of thermal fluctuations for different fluid particle sizes [10]. The SDPD method has been already applied to a number of problems including simulations of different particles [11] and polymers [12] in a suspension, single red blood cells in tube flow [13], margination of leukocytes [14], and margination of different particles [15] in blood flow.

Despite the advantages of SDPD over the DPD method, the original SDPD formulation [9] does not conserve angular momentum, both locally and globally. Recent numerical simulations using the MPC method [16] have shown that angular momentum conservation is essential in some problems including Taylor–Couette flow with two immiscible fluids and vesicle tank-treading in shear flow. A violation of angular momentum conservation may lead to an asymmetric stress tensor and spurious unphysical torques, resulting in erroneous simulation results. In both DPD and SDPD methods, the system consists of a number of point particles. The particle interactions are determined by the three pairwise forces: conservative, dissipative, and random. In DPD, all forces between a pair of particles are directed along the line connecting two particle centers, which automatically leads to angular momentum conservation. However, in SDPD, dissipative and random forces possess not only a part along the inter-particle axis as in DPD, but also a component perpendicular to the inter-particle axis. This perpendicular part of dissipative and random forces destroys local and global angular momentum conservation. There exist a version of the SDPD method with angular momentum conservation [17], where the perpendicular component of dissipative and random forces has been neglected resulting in a method formulation very similar to DPD. In this method the input viscosity has to be scaled by a theoretically defined coefficient which depends on space dimension. The method has been shown to properly capture the torque on a rotating particle under shear [11] and the dynamics of two rotating discs [18]. However, it is advantageous to keep a perpendicular component of the dissipative force, since it provides much more efficient control over fluid transport properties than the component along inter-particle axis alone [19].

To derive a consistent version of SDPD with angular momentum conservation, we introduce a spin variable, such that each SDPD particle possesses an angular velocity. This idea is similar to that of the fluid particle (FPM) model [20], where every particle possesses an angular velocity; however, FPM lacks a direct connection to the discretization of the Navier–Stokes equation. Also, a spin variable has been introduced in the single-particle DPD formulation [21], where a colloidal particle can be represented by a single DPD particle with spin. Consistent SDPD formulation with angular momentum conservation is obtained by a direct discretization of the Navier–Stokes equation for a fluid with spin [22]. The resulting formulation is similar to the original SDPD method [9] with the addition of a rotational friction force which governs particle-spin interactions similar to the FPM method. First simulation tests show that the newly derived method represents properly transport properties of a simple fluid performing similar to the original SDPD method. Then, the new SDPD method is validated using several problems where angular momentum conservation plays an essential role [16]. First, the Taylor–Couette flow with two immiscible fluids is simulated showing that the extended SDPD method results in predictions in agreement with the analytical solution derived from the Navier–Stokes equation. The original SDPD method applied to this problem fails to capture correctly the corresponding flow profiles. Another fluid flow problem considered for validation of the new SDPD method is a tank-treading vesicle in shear flow, which has been described theoretically by Keller and Skalak [23]. Vesicle tank-treading in shear flow corresponds to rotational motion of a membrane around the vesicle center-of-mass, while the vesicle preserves its stationary shape with a finite inclination angle. The new SDPD formulation results in predictions of vesicle inclination angles and tank-treading frequencies for several viscosity contrasts between inner and outer fluids in agreement with the Keller–Skalak theory [23], while the SDPD method without angular momentum conservation clearly fails to capture quantitatively correct dynamics.

The paper is organized as follows. In Section 2, the new SDPD approach with conservation of local and global angular momentum is derived. In Section 3, we provide simulation results for simple SDPD fluids including measurements of fluid transport properties and simulation results for the Taylor–Couette flow with two immiscible fluids. In Section 4, a tank-treading vesicle in shear flow is investigated. Finally, we conclude in Section 5 with a brief summary.

2. SDPD with angular momentum conservation

The SDPD method proposed by Español and Revenga [9] is a mesoscopic particle-based hydrodynamic approach which has been derived from the SPH [7,24] and DPD [2,3] simulation methods. More details on the DPD method are provided in Appendix A.

In the SPH method, a field variable $\tilde{g}(\mathbf{r})$ is replaced by the convolution integral of a field $g(\mathbf{r})$ and a kernel function $W(\mathbf{r}, h)$ as,

$$\tilde{g}(\mathbf{r}) \approx \int_V g(\mathbf{r}') W(\mathbf{r} - \mathbf{r}', h)\, dV', \tag{1}$$

where the kernel function has to be differentiable and depends on the distance $|\mathbf{r}-\mathbf{r}'|$ and the smoothing length h. In addition, the integral over $W(\mathbf{r}-\mathbf{r}',h)$ has to be normalized and the condition $\lim_{h\to 0} W(\mathbf{r}-\mathbf{r}',h)=\delta(\mathbf{r}-\mathbf{r}')$ needs to be satisfied. For $W(\mathbf{r},h)$ being the delta function, we would have $\tilde{g}(\mathbf{r})=g(\mathbf{r})$. The convolution integral is discretized using small fluid volumes (or particles) such that $\rho(\mathbf{r}')dV'\to m_j$ with m_j being the mass and $\rho(\mathbf{r}')\to\rho(\mathbf{r}_j)$ being the mass density of particle j at the position vector $\mathbf{r}_j$. The discretized convolution integral is then given by

$$\tilde{g}(\mathbf{r}_i)\approx\sum_{j=1}^{N}\frac{m_j}{\rho(\mathbf{r}_j)}g(\mathbf{r}_j)W\big(|\mathbf{r}_i-\mathbf{r}_j|,h\big), \tag{2}$$

where N is the number of particles (Lagrangian discretization points) within the volume V characterized by the smoothing radius h. Furthermore, derivatives of the field variable $g(\mathbf{r})$ follow similar approximation strategy which is described in Appendix B. Further in the text, we will also use the notations $\rho(\mathbf{r}_j)=\rho_j$, $g(\mathbf{r}_j)=g_j$, and $W(|\mathbf{r}_i-\mathbf{r}_j|,h)=W_{ij}$.

Using the SPH formalism, the continuity equation $d\rho/dt=-\rho\nabla\cdot\mathbf{v}$ becomes (see Eq. (B.10))

$$\frac{d\rho_i}{dt}=\sum_j m_j\mathbf{v}_{ij}\cdot\nabla_i W_{ij}, \tag{3}$$

where $\nabla_i W_{ij}$ can be analytically calculated. The particle density ρ_i is defined as

$$\rho_i=\sum_j m_j W_{ij}. \tag{4}$$

Hence, the density of particle i can be computed using its neighboring particles located within a sphere with a radius h. Similarly, different terms of the Navier–Stokes (NS) equation can be discretized to obtain the equations which govern particle dynamics, see Appendix B for more details.

To extend the original SDPD formulation [9], which lacks angular momentum conservation, we introduce a spin variable for every particle ω_i. In addition, each particle will also possess a moment of inertia I_i analogously to the already defined particle mass. We also define a function $F(\mathbf{r}_{ij})=F_{ij}\geq 0$ such that $\nabla_i W_{ij}=-\mathbf{r}_{ij}F_{ij}$. In order to obtain discretized equations for the SDPD formulation with spin, we consider the NS equation with spin [25],

$$\rho\frac{d\mathbf{v}}{dt}=-\nabla p+(\eta+\eta_r)\nabla^2\mathbf{v}+\left(\frac{\eta}{3}+\xi-\eta_r\right)\nabla\nabla\cdot\mathbf{v}+2\eta_r\nabla\times\omega, \tag{5}$$

where p is the pressure, η is the dynamic shear viscosity, ξ is the bulk viscosity, η_r is the rotational viscosity, and ω is the spin angular velocity. The introduced spin variable can be interpreted in two different ways. On the one hand, it is an approach used to recover angular momentum conservation in the SDPD formulation. On the other hand, the spin can be thought of as an effective angular velocity of a fluid volume represented by a particle. However, it should not be confused with a molecular spin. The discretization of the NS equation with spin provides a consistent model, where translational and rotational friction interactions are properly balanced unlike the FPM model which does not have a direct connection to the NS equation.

Using the rules in Eqs. (B.11)–(B.15) of Appendix B and the Newton's second law of motion $m_i d\mathbf{v}_i/dt=\mathbf{F}_i$, the discretization of the NS equation (5) yields the three forces: conservative (C), dissipative (D), and rotational (R) given by

$$\begin{aligned}
\mathbf{F}_{ij}^C &= \left(\frac{p_i}{\rho_i^2}+\frac{p_j}{\rho_j^2}\right)F_{ij}\mathbf{r}_{ij},\\
\mathbf{F}_{ij}^D &= -\left(\frac{5\eta}{3}+3\eta_r-\xi\right)\frac{F_{ij}}{\rho_i\rho_j}\mathbf{v}_{ij}-5\left(\frac{\eta}{3}+\xi-\eta_r\right)\frac{F_{ij}}{\rho_i\rho_j}\hat{\mathbf{e}}_{ij}(\hat{\mathbf{e}}_{ij}\cdot\mathbf{v}_{ij}),\\
\mathbf{F}_{ij}^R &= -2\eta_r\frac{F_{ij}}{\rho_i\rho_j}\mathbf{r}_{ij}\times(\boldsymbol{\omega}_i+\boldsymbol{\omega}_j),
\end{aligned} \tag{6}$$

where p_i is the particle pressure and $\hat{\mathbf{e}}_{ij}=\mathbf{r}_{ij}/|\mathbf{r}_{ij}|$. The conservative force controls locally the pressure field in the system. The dissipative force provides translational friction leading to the reduction of the velocity difference between two particles. Finally, the rotational force is also dissipative, but acts on particles' angular velocities such that a spin of one particle leads to a change in translational and angular velocity of another particle.

The defined set of deterministic forces in Eq. (6) can be referred to as an SPH discretization with angular momentum conservation. However, the SDPD method also incorporates consistently thermal fluctuations by appending a random force to the set of forces in Eq. (6). Here, the combination of dissipative, rotational, and random forces has to satisfy the fluctuation–dissipation balance. Similar to the FPM framework [20], we define a tensor $\mathcal{T}_{ij}=A(r_{ij})\mathbb{1}+B(r_{ij})\hat{\mathbf{e}}_{ij}\hat{\mathbf{e}}_{ij}$, where $A(r)$ and $B(r)$ are some functions of inter-particle distance and $\mathbb{1}$ is the unity matrix. The dissipative and rotational forces in Eq. (6) can be written in a tensorial form as

$$\mathbf{F}^D_{ij} = -\mathcal{T}_{ij}\cdot\mathbf{v}_{ij}, \qquad \mathbf{F}^R_{ij} = -\mathcal{T}_{ij}\cdot\left(\frac{\mathbf{r}_{ij}}{2}\times(\boldsymbol{\omega}_i + \boldsymbol{\omega}_j)\right), \tag{7}$$

which implies that $\eta_r = 5\eta/3 - \xi$,

$$A(r_{ij}) = 4\left(\frac{5\eta}{3} - \xi\right)\frac{F_{ij}}{\rho_i\rho_j}, \quad \text{and} \quad B(r_{ij}) = 10\left(\xi - \frac{2\eta}{3}\right)\frac{F_{ij}}{\rho_i\rho_j}. \tag{8}$$

Following the general framework of the FPM [20], the random force can be defined as

$$\tilde{\mathbf{F}}_{ij}dt = \sqrt{2k_BT}\left(\tilde{A}(r_{ij})d\overline{\mathcal{W}}^S_{ij} + \frac{\tilde{B}(r_{ij})}{3}\mathrm{tr}[d\mathcal{W}_{ij}]\mathbb{1} + \tilde{C}(r_{ij})d\mathcal{W}^A_{ij}\right)\cdot\hat{\mathbf{e}}_{ij}, \tag{9}$$

where $d\mathcal{W}_{ij}$ is a matrix of independent Wiener increments, $\mathrm{tr}[d\mathcal{W}_{ij}]$ is the trace of this matrix, $d\overline{\mathcal{W}}^S_{ij} = \frac{1}{2}(d\mathcal{W}_{ij} + d\mathcal{W}_{ij}) - \frac{1}{3}\mathrm{tr}[d\mathcal{W}_{ij}]$ is the traceless symmetric part, and $d\mathcal{W}^A_{ij} = \frac{1}{2}(d\mathcal{W}_{ij} - d\mathcal{W}_{ij})$ is the antisymmetric part. The functions $\tilde{A}(r)$, $\tilde{B}(r)$, and $\tilde{C}(r)$ are related to $A(r)$ and $B(r)$ of the tensor $\mathcal{T}_{ij}$ as $A(r) = \frac{1}{2}(\tilde{A}(r)^2 + \tilde{C}(r)^2)$ and $B(r) = \frac{1}{2}(\tilde{A}(r)^2 - \tilde{C}(r)^2) + \frac{1}{3}(\tilde{B}(r)^2 - \tilde{A}(r)^2)$ [20]. To further simplify the expression in Eq. (9), we select $\tilde{C}(r) = 0$ leading to

$$\tilde{A}(r_{ij}) = \left(2\left(\frac{20\eta}{3} - 4\xi\right)\frac{F_{ij}}{r_ir_j}\right)^{1/2} \quad \text{and} \quad \tilde{B}(r_{ij}) = \left(2\left(17\xi - \frac{40\eta}{3}\right)\frac{F_{ij}}{r_ir_j}\right)^{1/2}. \tag{10}$$

The full set of forces for the SDPD method with angular momentum conservation is finally given by

$$\begin{aligned}
\mathbf{F}^C_{ij} &= \left(\frac{p_i}{\rho_i^2} + \frac{p_j}{\rho_j^2}\right)F_{ij}\mathbf{r}_{ij},\\
\mathbf{F}^D_{ij} &= -\gamma^a_{ij}\left(\mathbf{v}_{ij} + \frac{\hat{\mathbf{e}}_{ij}(\hat{\mathbf{e}}_{ij}\cdot\mathbf{v}_{ij})}{3}\right) - \frac{2\gamma^b_{ij}}{3}\hat{\mathbf{e}}_{ij}(\hat{\mathbf{e}}_{ij}\cdot\mathbf{v}_{ij}),\\
\mathbf{F}^R_{ij} &= -\gamma^a_{ij}\frac{\mathbf{r}_{ij}}{2}\times(\boldsymbol{\omega}_i + \boldsymbol{\omega}_j),\\
\tilde{\mathbf{F}}_{ij} &= \left(\sigma^a_{ij}d\overline{\mathcal{W}}^S_{ij} + \sigma^b_{ij}\frac{1}{3}\mathrm{tr}[d\mathcal{W}_{ij}]\mathbb{1}\right)\cdot\frac{\hat{\mathbf{e}}_{ij}}{dt},
\end{aligned} \tag{11}$$

where

$$\gamma^a_{ij} = \left(\frac{20\eta}{3} - 4\xi\right)\frac{F_{ij}}{\rho_i\rho_j}, \qquad \gamma^b_{ij} = \left(17\xi - \frac{40\eta}{3}\right)\frac{F_{ij}}{\rho_i\rho_j}, \tag{12}$$

and $\sigma^{a,b}_{ij} = 2\sqrt{k_BT\gamma^{a,b}_{ij}}$. It is important to note that these equations are only valid for $2\eta/3 \le \xi \le 5\eta/3$, such that the friction coefficients $(\gamma^a_{ij} + 2\gamma^b_{ij})/3$ and γ^a_{ij} are positive. Another simplification which can be made is the reduction to a single dissipative parameters γ_{ij} such that $\xi = 20\eta/21$ and

$$\gamma^a_{ij} = \gamma^b_{ij} = \gamma_{ij} = \frac{20\eta}{7}\frac{F_{ij}}{\rho_i\rho_j}, \qquad \sigma^a_{ij} = \sigma^b_{ij} = \sigma_{ij} = 2\sqrt{k_BT\gamma_{ij}}. \tag{13}$$

Time evolution of the position and the translational and angular velocity of a particle i follows the Newton's second law as

$$\dot{\mathbf{r}}_i = \mathbf{v}_i, \qquad \dot{\mathbf{v}}_i = \sum_j \frac{1}{m_j}\mathbf{F}_{ij}, \qquad \dot{\boldsymbol{\omega}}_i = \sum_j \frac{1}{I_j}\mathbf{N}_{ij}, \tag{14}$$

where $\mathbf{N}_{ij}$ is the torque exerted by particle j on particle i and is given by $\mathbf{N}_{ij} = \frac{1}{2}\mathbf{r}_{ij}\times\mathbf{F}_{ij}$. This leads to local and global angular momentum conservation. Equation (14) is integrated using the velocity-Verlet algorithm [26]. Finally, in simulations we use the Lucy function

$$W(r) = \frac{105}{16\pi h^3}\left(1 + 3\frac{r}{h}\right)\left(1 - \frac{r}{h}\right)^3, \tag{15}$$

as a kernel function [7], which leads to $F(r) = \frac{315}{4\pi h^5}(1 - \frac{r}{h})^2$. The equation of state for the pressure is chosen to be

$$p = p_0\left(\frac{\rho}{\rho_0}\right)^\alpha + b, \tag{16}$$

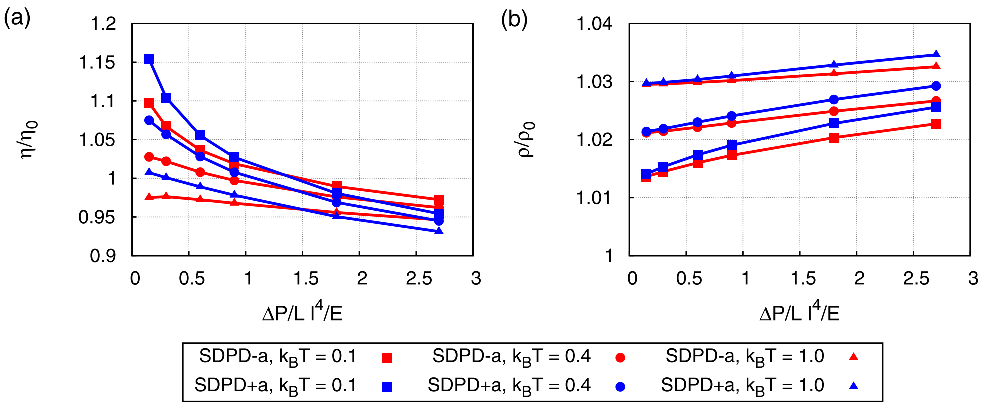

Fig. 1. Fluid properties of SDPD+a (blue) and SDPD-a (red) for different temperatures and pressure gradients $\Delta P/L$, for a channel of length L. (a) Measured viscosity η normalized by $\eta_0 = 50\sqrt{mE}/l^2$. (b) Particle density ρ normalized by $\rho_0 = 3m/l^3$. The considered energy levels are $k_BT \in \{0.1, 0.4, 1\}E$, while $h = 1.5l$. (For interpretation of the references to color in this figure legend, the reader is referred to the web version of this article.)

where ρ_0 is the reference density, and the parameters p_0, α, and b can be freely selected. This pressure equation yields the speed of sound $c^2 = p_0\alpha/\rho_0$, which can be easily controlled through the above parameters resulting in a good approximation of fluid incompressibility [24,27].

The derived SDPD method with angular momentum conservation will be referred to as **SDPD+a** further in text. The SDPD method without angular momentum conservation [9] will be called **SDPD-a**. For SDPD-a, the forces are very similar to those in Eq. (11); however, the rotational force contribution is excluded. The conservative force is kept the same, while the dissipative force assumes a coefficient $\gamma_{ij} = 5\eta F_{ij}/(3\rho_i\rho_j)$ [9] using the formulation with a single dissipative parameter as in Eq. (13), which leads to $\xi = 0$.

In both simulation methods, it is important to consider how the mass and for SDPD+a the moment of inertia of a fluid particle have to be assigned. For flows with low Reynolds numbers *Re* (i.e., in the Stokes regime), which is the main interest of the current study, the simulation results are independent of the choice of m and I. However, for high enough *Re*, particle mass should correspond to the mass of a fluid volume described by a single particle, since in SDPD particle volume can be defined. For SDPD+a, our proposition is to define similarly the moment of inertia as that of a sphere with the same volume as a simulated particle, which agrees with the suggestion in Ref. [20]. This would also lead to the moment of inertia to be a function of the particle density.

3. Simulations with a simple SDPD fluid

3.1. SDPD fluid properties

In comparison with the DPD method, an advantage of SDPD is that transport coefficients such as fluid viscosity can be directly specified, while in DPD they often need to be computed in a separate simulation for selected fluid parameters. Furthermore, in SDPD the volume of a fluid particle is clearly defined as $V = m/\rho$, which also determines a physical size of the particle [9]. To test the validity of SDPD discretization, we calculate fluid viscosity and particle density directly in simulations for several specified viscosities, temperatures, densities, and smoothing lengths. A reverse-Poiseuille flow setup [28], where the flow in two halves of a computational domain is driven in opposite directions applying the same force f per particle, is used to calculate fluid viscosity using an analytical solution of the Hagen–Poiseuille equation [29]. The particle density is computed on the fly by averaging ρ over all particles.

We introduce the basic units for the mass, m (e.g., fluid particle mass), length, l, and energy, E. In the simulations, this corresponds to setting $m = 1$, $l = 1$, and $E = 1$. For flows with low enough Reynolds number *Re*, results should be independent of the choice of m and I. We have tested our simulations for $\eta_0 = 25\sqrt{mE}/l^2$, $\rho_0 = 3m/l^3$, and the five-fold increase of particle mass and moment of inertia. As presented in Fig. 9, the results are hardly affected by the choice of I and m.

The size of a fully-periodic simulation domain has been set to $20l \times 40l \times 10l$, where the flow was driven along the y-axis. Model parameters for the pressure equation (16) have been set to $p_0 = 100E/l^3$, $b = -100E/l^3$, and $\alpha = 7$. For the SDPD+a fluid, the moment of inertia of every particle has been set to $I = 1ml^2$. To cover a broad range of the parameter values, we performed simulations for four different viscosities $\eta_0 \in \{25, 50, 100, 120\}\sqrt{mE}/l^2$, three energy levels $k_BT \in \{0.1, 0.4, 1\}E$, two densities $\rho_0 \in \{3, 5\}m/l^3$, and two smoothing lengths $h \in \{1.5, 3.0\}l$. For a physical fluid with ρ_0, η_0, and k_BT, it is then straightforward to determine m, l, and E. The corresponding Reynolds numbers, defined as $Re = \rho\bar{U}W/(2\eta)$, with W being the channel width, are ranging from 0.01 to 4.3. The total number of fluid particles N is equal to either 24 000 or 40 000 depending on the chosen density. The mean particle spacing $\Delta x = (1/n)^{1/3}$, with $n = \rho/m$ being the number density, is

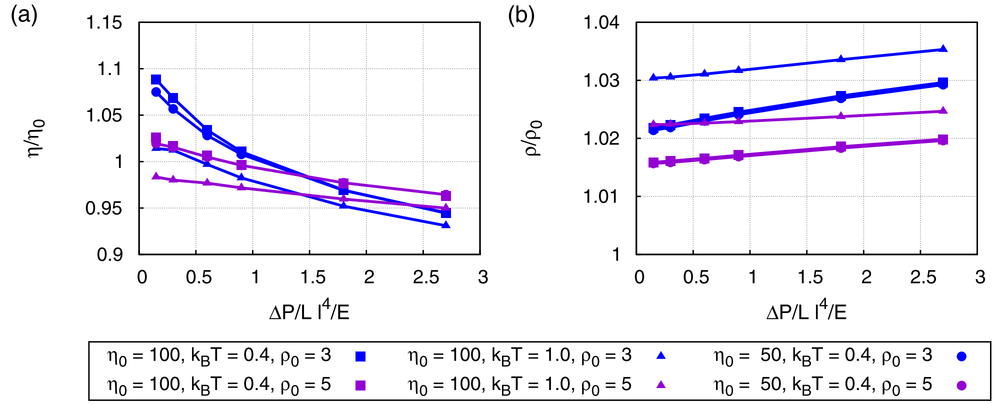

Fig. 2. Fluid properties of an SDPD+a fluid for different pressure gradients $\Delta P/L$, for a channel of length L and particle densities $\rho_0 = 3m/l^3$ (blue) and $\rho_0 = 5m/l^3$ (purple). (a) Measured viscosity η normalized by $\eta_0 \in \{50, 100\}\sqrt{mE}/l^2$. (b) Particle density ρ normalized by ρ_0. Different energy levels $k_B T \in \{0.4, 1\}E$ were considered, while $h = 1.5l$. (For interpretation of the references to color in this figure legend, the reader is referred to the web version of this article.)

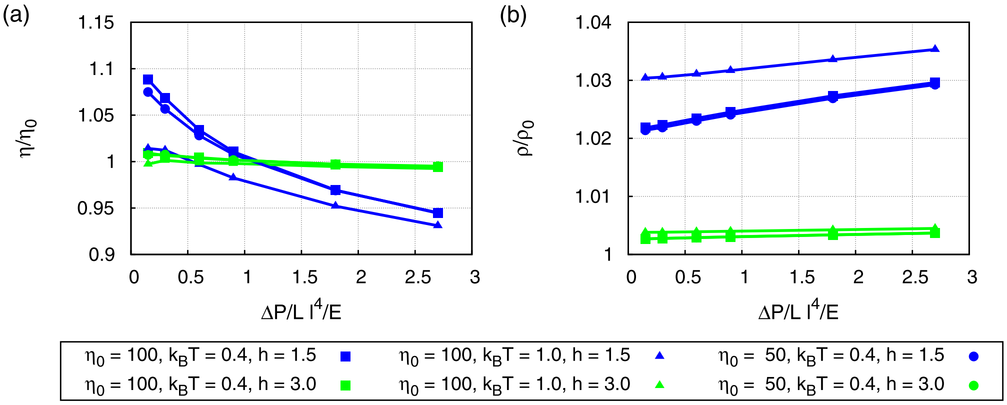

Fig. 3. Fluid properties of an SDPD+a fluid for different pressure gradients $\Delta P/L$, for a channel of length L and smoothing lengths $h = 1.5l$ (blue) and $h = 3.0l$ (green). (a) Measured viscosity η normalized by $\eta_0 \in \{50, 100\}\sqrt{mE}/l^2$. (b) Particle density ρ normalized by $\rho_0 = 3m/l^3$. Different energy levels $k_B T \in \{0.4, 1\}E$ were considered. (For interpretation of the references to color in this figure legend, the reader is referred to the web version of this article.)

either $\Delta x \approx 0.7$ or $\Delta x \approx 0.6$ leading to a ratio of smoothing length and mean particle spacing of $h/\Delta x \in \{2.2, 2.6, 4.3, 5.1\}$, and an average number of neighboring particles N_n of $N_\text{n} \in \{42, 70, 339, 565\}$, depending on the choice of h and ρ_0.

Fig. 1(a) displays the measured viscosity η normalized by the specified viscosity η_0 with respect to the applied pressure gradient $\Delta P/L = f\rho_0/m$, for a channel of length L, and for a case of $h = 1.5l$. For both SDPD+a and SDPD-a fluids, the measured viscosity is slightly higher than η_0 for small pressure gradients, but smaller than η_0 for high pressure gradients. This effect appears to be more pronounced for a lower temperature. The particle density measurements presented in Fig. 1(b) show a slight deviation from the specified value of $\rho_0 = 3m/l^3$. However, for both SDPD+a and SDPD-a fluids the particle density values are similar. In addition, our simulations show that the particle density does not depend on the specified viscosity, since it is governed by local fluid structure of particles within a radius h which is characterized by the radial distribution function.

Fig. 2 presents similar measurements of fluid viscosity and particle density for an SDPD+a fluid using different ρ_0 values. As the particle density is increased, the mean particle spacing is reduced and the fluid properties are better approximated resulting in a smaller variation of the measured properties from the specified values. A better result obtained for higher densities is due to a larger number of neighboring particles within the interaction radius h, which leads to a better approximation for discretized terms of the NS equation. These results agree well with convergence studies of SPH depending on the smoothing length and the mean particle spacing [30]. Similar trends are also observed for the SDPD-a fluid. Fig. 3 illustrates fluid viscosity and particle density of a SDPD+a fluid for different smoothing lengths h; an SDPD-a fluid yields similar results. With increasing h the measured values move closer to the specified ones and the temperature dependence practically vanishes. This effect is again due to a larger number of neighboring particles within h leading to smaller discretization errors for larger h values. However, computational cost may increase considerably for larger h, since it is proportional to h^3

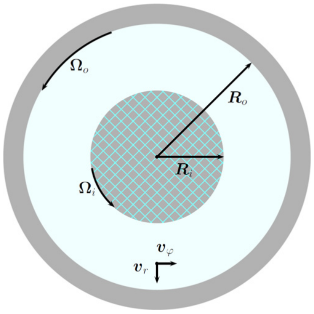

Fig. 4. A sketch of two cylinders with radii R_o and R_i where the subscripts 'o' and 'i' denote the outer and inner cylinders, respectively. Taylor–Couette flow can be generated by rotation of the outer cylinder with a rotational frequency Ω_o. In simulations with two immiscible fluids, the inner cylinder (shaded area) is replaced by another fluid which cannot mix with the fluid inside the gap between two cylindrical surfaces. (For interpretation of the references to color in this figure legend, the reader is referred to the web version of this article.)

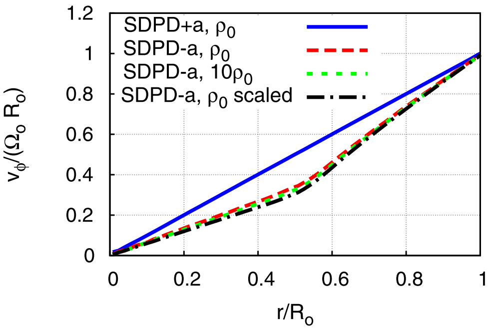

Fig. 5. Angular velocity v_ϕ profiles for the Taylor–Couette flow with two immiscible fluids using both SDPD+a and SDPD-a methods. Radial position r is normalized by the cylinder radius R_o, while angular velocity is scaled with the cylinder angular velocity $\Omega_o R_o$. The SDPD+a method leads to a correct linear profile, while the SDPD-a method fails to do so due to violation of angular momentum conservation. The SDPD-a results for different resolution with $\rho = 10\rho_0$ and for a twice larger system size (marked as "scaled") show hardly any dependence on fluid resolution.

or to the number of neighboring particles. Typically it is suggested to use about 50–60 neighboring particles in SDPD [31]; however, slightly smaller values are also possible in simulations if small variations of fluid properties are acceptable.

3.2. Taylor–Couette flow of two immiscible fluids

Taylor–Couette flow usually refers to a fluid flow in the gap between two rotating cylinders as shown in Fig. 4. However, we consider a setup, where the inner cylinder is replaced by another immiscible fluid such that no mixing between the two fluids at R_i can occur. A solution of the incompressible NS equation for this problem yields a linear angular velocity profile $v_\phi(r) = \Omega_0 r$ across both immiscible fluids, where r is the radial position. Note that this solution is independent of the viscosity values of the immiscible fluids. Here, it is also assumed that the system has infinite length in the cylinder-axis direction and the angular velocity $\Omega_o R_o$ is small enough to ensure that no Taylor–Couette instabilities occur.

Recent numerical simulations with a similar setup [16] have shown that the conservation of angular momentum is necessary to obtain correct velocity and torque profiles across immiscible fluids with different viscosities. To test our new implementation of the SDPD+a method, the Taylor–Couette flow with two immiscible fluids has been simulated. Both inner and outer fluids had the following parameters $p_0 = 100E/l^3$, $b = -100E/l^3$, $\alpha = 7$, $\rho_0 = 3m/l^3$, $h = 1.5l$, and $k_BT = 0.4E$, while the ratio of fluid viscosities was set to $\eta_i/\eta_o = 3$. The computational domain was assumed to be periodic in the cylinder-axis direction, while the cylinder wall was modeled by a layer of frozen particles with a thickness h whose structure (e.g., radial distribution function) was the same as that of the fluids. To prevent mixing of the fluids and particle penetration into the wall, specular reflection of particles has been imposed at cylindrical surfaces with $r = R_i$ and $r = R_o$. The wall particles were rotated with a constant angular frequency Ω_o in order to generate flow. The corresponding Reynolds number is $Re = \rho\Omega_o R_o R_i/\eta_o \approx 0.3$. Particle mass and inertia do not effect the simulation results, as shown in Fig. 10 for simulations with a two-fold increase/decrease of the mass and moment of inertia. Figure 5 shows angular velocity profiles for the Taylor–Couette flow using both SDPD+a and SDPD-a methods. The SDPD+a simulation properly captures a linear profile of angular velocity, while the SDPD-a method leads to distinct slopes within the regions of different viscosities. This example illustrates the importance of angular momentum conservation and provides a validation for the new SDPD approach.

A resolution study shows that these results are unaffected by an increase of fluid resolution in the SDPD-a method. Simulations with different densities $\rho \in \{2, 3, 5, 10\}\rho_0$ and a larger system size have led to the same angular velocities (up to a statistical averaging error) as presented in Fig. 5. A similar result is mentioned in Ref. [11], where the measured system

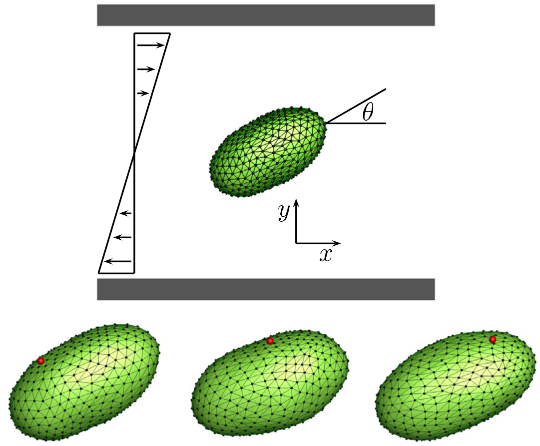

Fig. 6. Simulation snapshots of a tank-treading vesicle in shear flow for $\lambda = 2$. An xy-plane view, where the flow is in x direction. The red sphere is attached to a fixed position on a vesicle in order to illustrate the TT motion of the membrane; however, it is just a marker used for visualization and introduced at post-processing stage. Note that small shape fluctuations are clearly visible. (For interpretation of the references to color in this figure legend, the reader is referred to the web version of this article.)

properties were independent on the mean particle spacing of an SPH approach without angular momentum conservation. Thus, increase of resolution in SDPD-a does not seem to resolve the problem of angular momentum conservation. Currently, the origin of this observation is not clear and requires further investigation.

4. Tank-treading of a vesicle in shear flow

Flow dynamics of soft deformable objects such as liquid droplets, lipid vesicles, red blood cells, and elastic capsules has attracted a lot of scientific interest recently due to a wide range of possible applications. For instance, a number of experiments [32–34], theoretical approaches [23,35–37], and simulations [38,36,39–42] have shown that fluid vesicles exhibit a rich dynamical behavior in shear flow including tank-treading (TT) and tumbling (TB) motion. The tumbling motion corresponds to vesicle rotation around its center-of-mass nearly as a rigid body. A tank-treading vesicle in shear flow shows a stationary shape with a finite inclination angle $\theta > 0$ with respect to the flow direction, while the membrane is rotating around the center-of-mass of the vesicle, see Fig. 6. The occurrence of different vesicle motion is governed by the viscosity contrast $\lambda = \eta_i/\eta_o$ between fluids inside and outside the vesicle with viscosities η_i and η_o, respectively. A physical explanation for the TT-to-TB transition can be derived from the two components of shear flow: an elongational part which tends to stretch and align a vesicle along the $x = y$ axis with an inclination angle of $\theta = \pi/4$ and a rotational part of the flow which exerts a torque on the vesicle membrane. Increasing of viscosity contrast leads to higher shear stresses inside the vesicle opposing its TT motion, which results in an effective torque and decrease of the vesicle inclination angle. Thus, for high enough λ a transition from TT to TB motion occurs. Keller and Skalak (KS) [23] derived a theory which predicts the TT-to-TB transition. Moreover, the KS theory is able to predict the inclination angle θ in the vesicle TT regime.

The KS theory assumes a fixed ellipsoidal shape $(r_1/a_1)^2 + (r_2/a_2)^2 + (r_3/a_3)^2 = 1$, where r_i, $i \in \{1, 2, 3\}$ are the Cartesian coordinates and a_i are the semiaxes of the ellipsoid. The motion of a vesicle is derived by considering energy balance between the energy supplied by the fluid and the energy which dissipates on the membrane and inside the vesicle. This balance leads to a differential equation given by

$$\frac{d\theta}{dt} = \frac{1}{2}\dot{\gamma}\big(B\cos(2\theta) - 1\big), \tag{17}$$

where $\dot{\gamma}$ is the shear rate. If $B > 1$, the vesicle is in the TT regime, and hence, a steady inclination angle can be found as $\theta = 0.5\arccos(1/B)$, where B is a function of vesicle shape and viscosity contrast given by

$$B = f_0\left(f_1 + \frac{1}{f_1}\left(\frac{1}{1 + f_2(\lambda - 1)}\right)\right),$$

$$f_0 = \frac{2}{a_1/a_2 + a_2/a_1},$$

$$f_1 = 0.5(a_1/a_2 - a_2/a_1),$$

$$f_2 = 0.5g\big(\alpha_1^2 + \alpha_2^2\big),$$

Table 1
Vesicle parameters in units of energy $k_B T$ and effective vesicle radius R_0. k_d is the local area constraint coefficient, k_a is the global area constraint coefficient, k_v is the volume constraint coefficient, κ is the bending rigidity, and $\dot{\gamma}$ is the shear rate normalized by a characteristic vesicle relaxation time $\tau = \eta_o R_0^3/\kappa$ with η_o being the outer fluid viscosity.

$k_d/(k_B T/R_0^2)$	$k_a/(k_B T/R_0^2)$	$k_v/(k_B T/R_0^3)$	$\kappa/k_B T$	$\dot{\gamma}\tau$
1145	11 450	12 256	21.7	0.36

$$g = \int_0^\infty (\alpha_1^2 + s)^{-3/2} (\alpha_2^2 + s)^{-3/2} (\alpha_3^2 + s)^{-1/2} \, ds,$$

$$\alpha_i = \frac{a_i}{a_1 a_2 a_3}. \tag{18}$$

Note that the KS theory does not consider vesicle's membrane viscosity.

4.1. Vesicle model and simulation setup

The vesicle membrane is modeled by a collection of N_v particles on an ellipsoidal surface, which are connected by N_s edges forming a triangulated network of N_t triangles. An illustration of a vesicle structure is shown in Fig. 6. The network edges can be modeled by very soft springs to approximate the absence of a shear elasticity of a vesicle membrane and to preserve the network structure. However, the use of a spring potential appears not to be necessary, if a local area constraint for network triangles is employed maintaining the network structure. Thus, the membrane model omits any spring-like connections leading exactly to a vanishing shear elasticity of the membrane. The model incorporates local/global area and volume constraints which mimic incompressibility of the membrane and inner fluid, respectively, and are given by

$$V_{\text{area}} = \frac{k_a (A - A_0^{tot})^2}{2 A_0^{tot}} + \sum_{j \in 1 \ldots N_t} \frac{k_d (A_j - A_0^j)^2}{2 A_0^j}, \tag{19}$$

$$V_{\text{volume}} = \frac{k_v (V - V_0^{tot})^2}{2 V_0^{tot}}, \tag{20}$$

where k_a, k_d and k_v are the global area, local area, and volume constraint coefficients. The term A_j is the instantaneous area of triangle j, and A and V are the total vesicle area and volume, while A_0^j is the desired area of triangle j, and A_0^{tot} and V_0^{tot} are the desired total area and volume, respectively [43,44]. The local area constraint preserves a regular network without crossing of edges (without explicit spring connections), while the values of A_0^j are set to triangular areas of an initially triangulated vesicle surface. Membrane bending resistance is implemented using the potential energy

$$V_{\text{bending}} = \sum_{j \in 1 \ldots N_s} k_b \big(1 - \cos(\Theta_j)\big), \tag{21}$$

where k_b is the bending constant and Θ_j are the instantaneous angles between two adjacent triangles having a common edge j. The bending constant is related to Helfrich's macroscopic bending rigidity κ [45] as $\kappa = \sqrt{3} k_b/2$ [43,44]. This construction works well for fluid vesicles, which deviate in their shape not too much from a sphere, as here. For more anisotropic shapes or for large deformations, triangles can become very elongated and the discretization incorrect. In this case dynamic triangulation has to be employed [46,47].

The simulated ellipsoidal vesicle has a prolate shape with $a_1 > a_2 = a_3$ and an aspect ratio of $a_1/a_2 \approx 1.7$. The ellipsoid is characterized by a reduced volume $V^* = V/(4\pi R_0^3/3)$, where $R_0 = \sqrt{A_0^{tot}/(4\pi)}$ is the effective vesicle radius. In simulations we employ an ellipsoidal vesicle with $V^* \approx 0.93$, because an ellipsoid with this reduced volume has a nearly constant shape in shear flow [36]; nearly negligible vesicle deformation in flow justifies the comparison of simulation results with the KS theory, where a vesicle assumes a constant TT path. Vesicle simulation parameters are given in Table 1. The vesicle is placed in a box of size $L_x = 9.3R_0$ and $L_y = L_z = 5.6R_0$; the box size is large enough to neglect potential finite-size effects as it has been shown in Ref. [36]. Periodic boundary conditions are applied in x and z direction, while shear flow is generated in the x direction with the flow velocity $\mathbf{v} = \dot{\gamma}(y - L_y/2)\hat{\mathbf{e}}_x$ and $\dot{\gamma}$ being the shear rate. Recent numerical simulations [48,49] have shown that the inclination angle also depends on the Reynolds number $Re = \dot{\gamma}\rho_0 R_0^2/\eta_o$. Therefore, in all simulations we have selected $Re < 0.1$ to avoid inertial effects.

Two solid walls at $y = \pm L_y/2$ with no-slip boundary conditions are modeled with frozen wall particles. In addition, fluid particles are subject to bounce-back reflection at the walls to prevent particle penetration though the walls. The fluid parameters have been chosen as $p_0 = 100E/l^3$, $b = -100E/l^3$, $\alpha = 7$, $\rho_0 = 3m/l^3$, $h = 1.5l$, and $k_B T = 0.4E$.

Coupling between vesicle membrane motion and fluid flow is performed through friction interactions between vesicle vertices and the surrounding fluid particles using the DPD dissipative and random forces (see Appendix A); this friction coupling is identical to that used for red blood cells in flow in Refs. [43,44]. Note that for membrane-fluid coupling, DPD forces

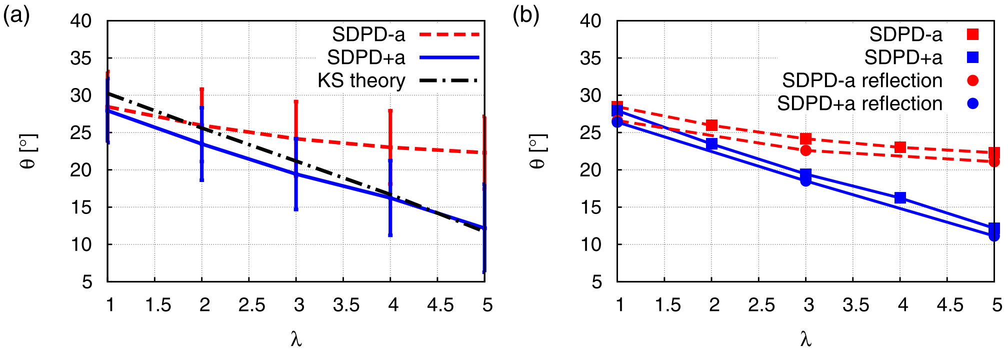

Fig. 7. (a) Comparison of inclination angles θ of a TT vesicle in shear flow obtained from SDPD+a (blue) and SDPD-a (red) simulations and from the KS theory (black) for different viscosity ratios λ. The 'exchange' method for fluid separation is employed. (b) Comparison of the 'exchange' and 'reflection' methods for the separation of inner and outer fluids at the membrane surface for different λ values. The 'reflection' method does not strictly conserve angular momentum at the membrane. (For interpretation of the references to color in this figure legend, the reader is referred to the web version of this article.)

are used (not SDPD) providing conservation of angular momentum automatically. To simulate two distinct fluids separated by a membrane, two different strategies are employed. The first method for fluid separation implements bounce-back reflections of fluid particles at the membrane surface; this method will be referred to as the 'reflection' method further in the text. Current implementation of fluid-particle reflections provides local conservation of momentum, while angular momentum is not strictly conserved at the membrane. Another method for fluid separation does not consider particle reflections, but employs tracking of fluid particles such that a type of the particle crossing the membrane can be altered; this method will be referred to as the 'exchange' method further below. Thus, the type of an outer-fluid particle is changed to the type of an inner-fluid particle if this particle crosses the membrane from outside to inside and vice versa. This method for fluid separation at the membrane leads to local conservation of angular momentum. Both particle types possess the same mass and moment of inertia and therefore, local mass and momentum are conserved. Furthermore, it has been monitored that the average density remains constant, while the fluctuations around the average are very small.

4.2. Simulation results

The inclination angle of a TT vesicle in shear flow is calculated by

$$\theta = \arctan(u_y/u_x), \tag{22}$$

where $\mathbf{u} = (u_x, u_y, u_z)$ is the eigenvector of the moments of inertia tensor with the smallest eigenvalue. Fig. 7(a) compares inclination angles obtained from simulations with SDPD+a and SDPD-a fluids and from the KS theory for different viscosity ratios λ. Here, the 'exchange' method for fluid separation at the membrane is used. The simulation results obtained with an SDPD+a fluid agree very well with the KS theory predictions, while the results using an SDPD-a fluid show a significant overestimation of the inclination angle at large λ. The results for $\lambda = 1$ from both SDPD+a and SDPD-a cases coincide indicating that angular momentum conservation does not affect simulation results if inner and outer fluids have the same viscosity. The deviations of the SDPD+a results from the KS theory predictions might be due to small shape fluctuations of the vesicle and/or numerical errors indicated by error bars in Fig. 7(a). Comparison of simulated inclination angles using the 'exchange' and 'reflection' methods for the separation of inner and outer fluids at the membrane is shown in Fig. 7(b). The 'reflection' method does not strictly conserve angular momentum at the membrane; however, the corresponding effect on θ seems to be rather small. Use of the 'reflection' method leads to a slight shift of vesicle inclination angles to smaller values.

Another property of a TT vesicle in shear flow which can be compared is the TT frequency found from the KS theory as

$$\omega = \frac{0.5}{f_1} \frac{\dot{\gamma} \cos(2\theta)}{1 + f_2(\lambda - 1)}. \tag{23}$$

Fig. 8 displays the average TT frequency $\langle\omega\rangle$ normalized by the shear rate $\dot{\gamma}$ and obtained from simulations with SDPD+a and SDPD-a fluids and from the KS theory for different viscosity ratios λ. The SDPD+a predictions for $\langle\omega\rangle$ are close to the theoretical predictions for all simulated viscosity ratios. Again, the small deviations of the SDPD+a results from the KS theory predictions might be due to vesicle shape fluctuations and/or numerical errors. However, simulations with an SDPD-a fluid clearly fail to provide correct predictions in comparison with the theoretical values. As expected, the values of TT frequency are underestimated for the SDPD-a case, which is associated with the overestimation of inclination angles in Fig. 7. In case of the SDPD-a fluid, the presence of two different viscosities leads to an asymmetric stress tensor [16] adding a stress contribution which suppresses TT frequency and results in an increased inclination angle. In case of $\lambda = 1$, the stress tensor is symmetric even for the SDPD-a fluid leading to correct predictions of vesicle dynamics in shear flow.

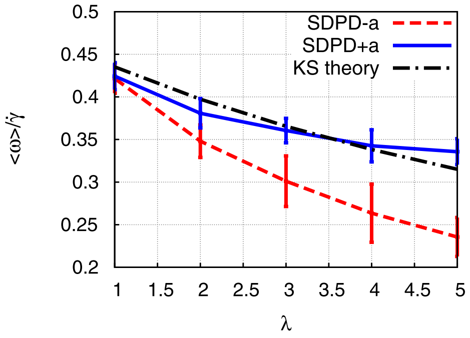

Fig. 8. Comparison of the average TT frequency $\langle\omega\rangle$ normalized by the shear rate $\dot{\gamma}$ and obtained from SDPD+a (blue) and SDPD-a (red) simulations and from the KS theory (black) for different viscosity ratios λ. The 'exchange' method for fluid separation is employed. (For interpretation of the references to color in this figure legend, the reader is referred to the web version of this article.)

5. Summary

We presented an extension of the original SDPD method [9], which satisfies local and global angular momentum conservation. In the new method (SDPD+a), each particle possesses an angular velocity, and its rotational contribution has been derived from the NS equation with spin following the SPH formalism. This leads to a spin variable similar to the FPM model [20]. Thermal fluctuations in SDPD+a have been also included similar to those in FPM [20] and in SDPD without angular momentum conservation (SDPD-a) [9]. Fluid properties measured directly in simulations support the correctness of the SDPD+a derivation and implementation, since measured values of fluid viscosity and particle density are very close to the specified ones. Furthermore, simulations of Taylor–Couette flow with two immiscible fluids show that SDPD+a leads to correct predictions of flow profiles in agreement with analytical results, while SDPD-a fails to capture properly flow characteristics due to violation of angular momentum conservation. Finally, simulations of vesicle dynamics in shear flow reveal that angular momentum conservation is essential to obtain correct results for the inclination angle and the rotational frequency of a tank-treading vesicle if there exists a viscosity contrast λ between inner and outer fluids. For $\lambda \neq 1$ the SDPD+a method predicts vesicle characteristics in agreement with the Keller–Skalak theory for a vesicle in shear flow, while SDPD-a overestimates the inclination angle and underestimates the TT frequency. In conclusion, the new SDPD method with angular momentum conservation is able to correctly model flows where angular momentum conservation is necessary.

Acknowledgements

This work has been supported by the DFG Research Unit FOR 1543 SHENC – Shear Flow Regulation in Hemostasis. Dmitry A. Fedosov acknowledges funding by the Alexander von Humboldt Foundation (Sofja Kovalevskaja Award). Kathrin Müller acknowledges support by the International Helmholtz Research School of Biophysics and Soft Matter (IHRS BioSoft). We also gratefully acknowledge a CPU time grant by the Jülich Supercomputing Center.

Appendix A. Dissipative particle dynamics

The DPD method [2,3] is a mesoscopic particle simulation technique, where each particle represents a *molecular cluster* rather than an individual atom, and can be thought of as a soft lump of fluid. The conservative force F^C in DPD controls fluid compressibility, while the pair of dissipative F^D and random forces F^R defines a local thermostat in order to keep a DPD system at an equilibrium temperature. The DPD forces are local and act only within a selected cutoff radius r_c. The conservative force is typically defined as

$$\mathbf{F}_{ij}^C = \hat{\mathbf{e}}_{ij} \begin{cases} a_{ij}(1 - r_{ij}/r_c), & \text{for } r_{ij} \le r_c, \\ 0, & \text{for } r_{ij} > r_c, \end{cases} \tag{A.1}$$

where a_{ij} is the repulsion coefficient between particles i and j, $\hat{\mathbf{e}}_{ij} = \mathbf{r}_{ij}/r_{ij}$, and $r_{ij} = |\mathbf{r}_i - \mathbf{r}_j|$. The dissipative force defined as

$$\mathbf{F}_{ij}^D = -\gamma\omega^D(r_{ij})(\mathbf{v}_{ij} \cdot \hat{\mathbf{e}}_{ij})\hat{\mathbf{e}}_{ij} \tag{A.2}$$

reduces the velocity difference $\mathbf{v}_{ij} = \mathbf{v}_i - \mathbf{v}_j$ between two particles, and hence, provides friction in a simulated system. Here, $\omega^D(r_{ij})$ is a weight function and γ is the dissipative force coefficient. The random force in DPD is given by

$$\mathbf{F}_i j^R = \sigma\omega^R(r_{ij})\xi_{ij} dt^{-1/2}\hat{\mathbf{e}}_{ij}, \tag{A.3}$$

$\omega^R(r_{ij})$ is the weight function, σ is the random force coefficient, and dt is the timestep. A random number ξ_{ij} has to be symmetric ($\xi_{ij} = \xi_{ji}$) with zero mean ($\langle\xi\rangle = 0$) and unit variance; different random numbers have been used in DPD including Gaussian and uniform distributions.

To satisfy the fluctuation–dissipation balance, the pair of dissipative and random forces has to fulfill the conditions [3]

$$\omega^D(r_{ij}) = \left(\omega^R(r_{ij})\right)^2, \qquad \sigma = \sqrt{2k_B T\gamma}. \tag{A.4}$$

In general, the weight functions can be arbitrarily chosen; however, a typical choice is

$$\omega^D(r_{ij}) = \begin{cases} (1 - r_{ij}/r_c)^k, & \text{for } r_{ij} \le r_c, \\ 0, & \text{for } r_{ij} > r_c, \end{cases} \tag{A.5}$$

where the exponent $k = 1$ was used in the original DPD method [4]. Other values of k (e.g. 0.25) have been also employed in order to increase the viscosity of a DPD fluid [50,51]. The equation of state of a DPD fluid [4] and the corresponding speed of sound c_s are given by

$$p = k_B T + \alpha a \rho^2, \tag{A.6}$$

$$c_s^2 = \frac{\partial p}{\partial \rho} = 2\alpha a \rho, \tag{A.7}$$

where a is the repulsive coefficient. Thus, in DPD the speed of sound can be controlled by changing the repulsive coefficient and/or fluid density. A significant increase of a may affect the timestep and lead to freezing artifacts [3], while an increase in particle density affects considerably the computational cost.

Appendix B. Calculation of derivatives

We summarize the calculation of derivatives of field variables similar to those in SPH [24]. Using Eq. (2), the first derivative of a field g can be approximated as

$$\frac{\partial \tilde{g}}{\partial x} \approx \sum_{j=1}^{N} \frac{m_j}{\rho_j} g \frac{\partial W_{ij}}{\partial x_i}, \tag{B.1}$$

where the notations are identical to those in the main text. A disadvantage of this approximation is that the derivative does not vanish for g being a constant function. Therefore, a better approximation is given by

$$\frac{\partial \tilde{g}}{\partial x} = \frac{1}{\phi}\left(\frac{\partial(\tilde{g}\phi)}{\partial x} - \tilde{g}\frac{\partial \phi}{\partial x}\right), \tag{B.2}$$

where ϕ must be a differentiable function. Following Eq. (B.1), we then obtain

$$\frac{\partial \tilde{g}}{\partial x} \approx \frac{1}{\phi_i} \sum_{j=1}^{N} \frac{m_j}{\rho_j} \phi_j (g_j - g_i) \frac{\partial W_{ij}}{\partial x_i}. \tag{B.3}$$

When $\phi = 1$, Eq. (B.3) reduces to

$$\frac{\partial \tilde{g}}{\partial x} \approx \sum_{j} \frac{m_j}{\rho_j} g_{ji} \frac{\partial W_{ij}}{\partial x_i}, \tag{B.4}$$

where $g_{ji} = g_j - g_i$. In Eq. (B.3), $\phi = \rho$ can be also selected, yielding an approximation for the first derivative as

$$\frac{\partial \tilde{g}}{\partial x} \approx \frac{1}{\rho_i} \sum_{j} m_j g_{ji} \frac{\partial W_{ij}}{\partial x_i}. \tag{B.5}$$

The choice for different discretizations ($\phi = 1$ or $\phi = \rho$) may depend on a problem of interest. For instance, when different interacting fluids with large density ratios are considered, it has been shown that the approximation in Eq. (B.3) with $\phi = 1$ is more accurate than that with $\phi = \rho$, because ρ in Eq. (B.4) is included directly inside the sum [52,24]. Furthermore, if only a single fluid is employed, an approximation $\phi_i \approx \rho_j$ can be used making the above choices for ϕ equivalent.

There exists another definition for the first derivative,

$$\frac{\partial \tilde{g}}{\partial x} = \phi\left(\frac{\partial}{\partial x}\left(\frac{\tilde{g}}{\phi}\right) + \frac{\tilde{g}}{\phi^2}\frac{\partial \phi}{\partial x}\right). \tag{B.6}$$

Following the SPH formalism [24] we obtain

$$\frac{\partial \tilde{g}}{\partial x} \approx \phi_i \sum_{j=1}^{N} \frac{m_j}{\rho_j}\left(\frac{g_j}{\phi_j} + \frac{g_i}{\phi_i^2}\phi_j\right)\frac{\partial W_{ij}}{\partial x_i}. \tag{B.7}$$

As a result, a choice of $\phi = 1$ here leads to

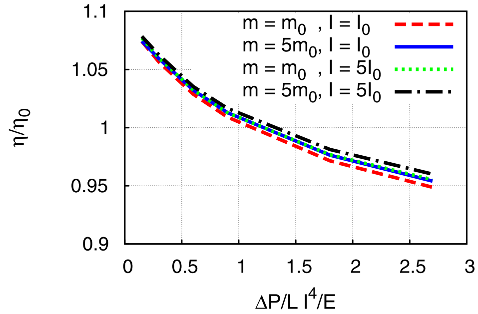

Fig. 9. Measured viscosity η, scaled by $\eta_0 = 25\sqrt{mE}/l^2$ depending on the pressure gradient $\Delta P/L$, with L being the channel length for different mass and moment of inertia values. The density is $\rho_0 = 3m/l^3$. Although both, mass and moment of inertia, are varied, the measured values of η are hardly affected.

$$\frac{\partial \tilde{g}}{\partial x} \approx \sum_{j=1}^{N} \frac{m_j}{\rho_j}(g_j + g_i)\frac{\partial W_{ij}}{\partial x_i}, \tag{B.8}$$

while for $\phi \approx \rho$ Eq. (B.7) becomes

$$\frac{\partial \tilde{g}}{\partial x} \approx \rho_i \sum_{j=1}^{N} m_j \left(\frac{g_j}{\rho_j^2} + \frac{g_i}{\rho_i^2}\right)\frac{\partial W_{ij}}{\partial x_i}. \tag{B.9}$$

A set of equations above defines different approximations of first derivatives, which can be used to derive discretizations of other differential operators in the NS equation. For instance, using Eq. (B.5) the gradient of $g(\mathbf{r})$ can be approximated as

$$\nabla \tilde{g} \approx -\frac{1}{\rho_i}\sum_j m_j g_{ij} \nabla_i W_{ij}, \tag{B.10}$$

where $g_{ij} = g_i - g_j$. Similarly, the divergence and the curl of a vector field $\tilde{\mathbf{G}}(\mathbf{r})$ are discretized as

$$\nabla_i \cdot \tilde{\mathbf{G}}_i \approx -\frac{1}{\rho_i}\sum_j m_j \mathbf{G}_{ij} \cdot \nabla_i W_{ij}, \tag{B.11}$$

$$\nabla_i \times \tilde{\mathbf{G}}_i \approx -\rho_i \sum_j \frac{m_j}{\rho_i \rho_j}(\mathbf{G}_j + \mathbf{G}_i) \times \nabla_i W_{ij}. \tag{B.12}$$

The second derivatives are then given by

$$\nabla_i(\nabla_i \cdot \tilde{\mathbf{G}}_i) \approx -\sum_j m_j \frac{F_{ij}}{\rho_i \rho_j}\left(5\hat{\mathbf{e}}_{ij}(\hat{\mathbf{e}}_{ij} \cdot \mathbf{G}_{ij}) - \mathbf{G}_{ij}\right) \tag{B.13}$$

and

$$\nabla_i^2 \tilde{g}_i \approx -2\sum_j m_j \frac{F_{ij}}{\rho_i \rho_j} g_{ij}, \tag{B.14}$$

where $\hat{\mathbf{e}}_{ij} = \mathbf{r}_{ij}/r_{ij}$ is the unity vector along the separation direction of particles i and j [9].

The curl of a vector field $\mathbf{G}$ can be approximated as

$$\nabla_i \times \tilde{\mathbf{G}}_i \approx \phi_i \sum_j \frac{m_j}{\rho_j} \nabla_i W(r_{ij}) \times \left(\frac{\mathbf{G}_j}{\phi_j} + \frac{\phi_j \mathbf{G}_i}{\phi_i^2}\right), \tag{B.15}$$

where a selection of $\phi = 1$ leads to

$$\nabla_i \times \tilde{\mathbf{G}}_i \approx \sum_j \frac{m_j}{\rho_j} \nabla_i W(r_{ij}) \times (\mathbf{G}_j + \mathbf{G}_i), \tag{B.16}$$

while $\phi = \rho$ results in

$$\nabla_i \times \tilde{\mathbf{G}}_i \approx \rho_i \sum_j m_j \nabla_i W(r_{ij}) \times \left(\frac{\mathbf{G}_j}{\rho_j^2} + \frac{\mathbf{G}_i}{\rho_i^2}\right). \tag{B.17}$$

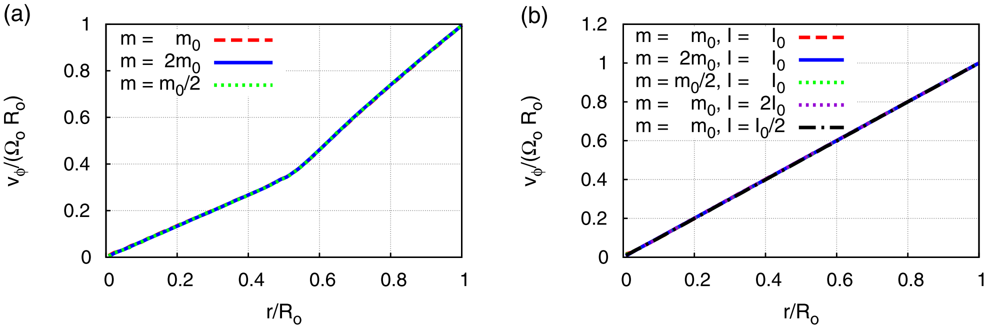

Fig. 10. Angular velocity v_ϕ profiles for the Taylor–Couette flow with two immiscible fluids using both (a) SDPD-a and (b) SDPD+a methods for different mass m and moment of inertia I. The radial position r is normalized by the cylinder radius R_o, while the angular velocity is scaled with the cylinder angular velocity $\Omega_o R_o$. For all masses and moments of inertia the same results are obtained.

Appendix C. Verification of mass and inertia independence of simulation results

A number of simulations were performed to verify that simulation results are independent of the choice for particle mass and moment of inertia for low enough *Re* numbers. Fig. 9 illustrates that the effect of both mass and moment of inertia on the measured viscosity can be neglected for the studied range of flow *Re* numbers, while Fig. 10 presents a similar test for the Taylor–Couette flow using both SDPD-a and SDPD+a methods.

References

[1] S. Succi, The Lattice Boltzmann Equation for Fluid Dynamics and Beyond, Oxford University Press, Oxford, 2001.
[2] P.J. Hoogerbrugge, J.M.V.A. Koelman, Simulating microscopic hydrodynamic phenomena with dissipative particle dynamics, Europhys. Lett. 19 (1992) 155–160.
[3] P. Español, P. Warren, Statistical mechanics of dissipative particle dynamics, Europhys. Lett. 30 (1995) 191–196.
[4] R.D. Groot, P.B. Warren, Dissipative particle dynamics: bridging the gap between atomistic and mesoscopic simulation, J. Chem. Phys. 107 (1997) 4423–4435.
[5] A. Malevanets, R. Kapral, Mesoscopic model for solvent dynamics, J. Chem. Phys. 110 (1999) 8605–8613.
[6] G. Gompper, T. Ihle, D.M. Kroll, R.G. Winkler, Multi-particle collision dynamics: a particle-based mesoscale simulation approach to the hydrodynamics of complex fluids, Adv. Polym. Sci. 221 (2009) 1–87.
[7] L.B. Lucy, A numerical approach to the testing the fission hypothesis, Astron. J. 82 (1977) 1013–1024.
[8] J.J. Monaghan, Smoothed particle hydrodynamics, Annu. Rev. Astron. Astrophys. 30 (1992) 543–574.
[9] P. Español, M. Revenga, Smoothed dissipative particle dynamics, Phys. Rev. E 67 (2003) 026705.
[10] A. Vázquez-Quesada, M. Ellero, P. Español, Consistent scaling of thermal fluctuations in smoothed dissipative particle dynamics, J. Chem. Phys. 130 (2009) 034901.
[11] X. Bian, S. Litvinov, R. Qian, M. Ellero, N.A. Adams, Multiscale modeling of particle in suspension with smoothed dissipative particle dynamics, Phys. Fluids 24 (2012) 012002.
[12] S. Litvinov, M. Ellero, X. Hu, N.A. Adams, Smoothed dissipative particle dynamics model for polymer molecules in suspension, Phys. Rev. E 77 (2008) 066703.
[13] D.A. Fedosov, M. Peltomäki, G. Gompper, Deformation and dynamics of red blood cells in flow through cylindrical microchannels, Soft Matter 10 (2014) 4258–4267.
[14] D.A. Fedosov, G. Gompper, White blood cell margination in microcirculation, Soft Matter 10 (2014) 2961–2970.
[15] K. Müller, D.A. Fedosov, G. Gompper, Margination of micro- and nano-particles in blood flow and its effect on drug delivery, Sci. Rep. 4 (2014) 4871.
[16] I.O. Götze, H. Noguchi, G. Gompper, Relevance of angular momentum conservation in mesoscale hydrodynamics simulations, Phys. Rev. E 76 (2007) 046705.
[17] X.Y. Hu, N.A. Adams, Angular-momentum conservative smoothed particle dynamics for incompressible viscous flows, Phys. Fluids 18 (2006) 101702.
[18] X. Bian, M. Ellero, A splitting integration scheme for the SPH simulation of concentrated particle suspensions, Comput. Phys. Commun. 185 (1) (2014) 53–62.
[19] C. Junghans, M. Praprotnik, K. Kremer, Transport properties controlled by a thermostat: an extended dissipative particle dynamics thermostat, Soft Matter 4 (2008) 156–161.
[20] P. Español, Fluid particle model, Phys. Rev. E 57 (1998) 2930–2948.
[21] W. Pan, I.V. Pivkin, G.E. Karniadakis, Single-particle hydrodynamics in DPD: a new formulation, Europhys. Lett. 84 (2008) 10012.
[22] S.R. de Groot, P. Mazur, Non-equilibrium Thermodynamics, North-Holland, Amsterdam, 1962.
[23] S.R. Keller, R. Skalak, Motion of a tank-treading ellipsoidal particle in a shear flow, J. Fluid Mech. 120 (1982) 27–47.
[24] J.J. Monaghan, Smoothed particle hydrodynamics, Rep. Prog. Phys. 68 (2005) 1703–1759.
[25] D.W. Condiff, J.S. Dahler, Fluid mechanical aspects of antisymmetric stress, Phys. Fluids 7 (1964) 842–854.
[26] M.P. Allen, D.J. Tildesley, Computer Simulation of Liquids, Clarendon Press, New York, 1991.
[27] G.K. Batchelor, An Introduction to Fluid Dynamics, Cambridge University Press, Cambridge, 2000.
[28] D.A. Fedosov, G.E. Karniadakis, B. Caswell, Steady shear rheometry of dissipative particle dynamics models of polymer fluids in reverse Poiseuille flow, J. Chem. Phys. 132 (2010) 144103.
[29] S.P. Sutera, R. Skalak, The history of Poiseuille's law, Annu. Rev. Fluid Mech. 25 (1993) 1–19.
[30] M. Ellero, N.A. Adams, SPH simulations of flow around a periodic array of cylinders confined in a channel, Int. J. Numer. Methods Eng. 86 (2011) 1027–1040.
[31] M. Serrano, Comparison between smoothed dissipative particle dynamics and Voronoi fluid particle model in a shear stationary flow, Physica A 362 (2006) 204–209.

[32] M. Abkarian, C. Lartigue, A. Viallat, Tank treading and unbinding of deformable vesicles in shear flow: determination of the lift force, Phys. Rev. Lett. 88 (2002) 068103.
[33] V. Kantsler, V. Steinberg, Transition to tumbling and two regimes of tumbling motion of a vesicle in shear flow, Phys. Rev. Lett. 96 (2006) 036001.
[34] M.-A. Mader, V. Vitkova, M. Abkarian, A. Viallat, T. Podgorski, Dynamics of viscous vesicles in shear flow, Eur. Phys. J. E 19 (2006) 389–397.
[35] R. Tran-Son-Tay, S.P. Sutera, P.R. Rao, Determination of red blood cell membrane viscosity from rheoscopic observations of tank-treading motion, Biophys. J. 46 (1984) 65–72.
[36] H. Noguchi, G. Gompper, Dynamics of fluid vesicles in shear flow: effect of the membrane viscosity and thermal fluctuations, Phys. Rev. E 72 (2005) 011901.
[37] C. Misbah, Vacillating breathing and tumbling of vesicles under shear flow, Phys. Rev. Lett. 96 (2006) 028104.
[38] H. Noguchi, G. Gompper, Fluid vesicles with viscous membranes in shear flow, Phys. Rev. Lett. 93 (2004) 258102.
[39] A. Yazdani, P. Bagchi, Three-dimensional numerical simulation of vesicle dynamics using a front-tracking method, Phys. Rev. E 85 (2012) 056308.
[40] H. Noguchi, G. Gompper, Swinging and tumbling of fluid vesicles in shear flow, Phys. Rev. Lett. 98 (2007) 128103.
[41] H. Zhao, E.S.G. Shaqfeh, The dynamics of a vesicle in simple shear flow, J. Fluid Mech. 674 (2011) 578–604.
[42] D.A. Fedosov, H. Noguchi, G. Gompper, Multiscale modeling of blood flow: from single cells to blood rheology, Biomech. Model. Mechanobiol. 13 (2014) 239–258.
[43] D.A. Fedosov, B. Caswell, G.E. Karniadakis, Systematic coarse-graining of spectrin-level red blood cell models, Comput. Methods Appl. Mech. Eng. 199 (2010) 1937–1948.
[44] D.A. Fedosov, B. Caswell, G.E. Karniadakis, A multiscale red blood cell model with accurate mechanics, rheology, and dynamics, Biophys. J. 98 (2010) 2215–2225.
[45] W. Helfrich, Elastic properties of lipid bilayers: theory and possible experiments, Z. Naturforsch. C 28 (1973) 693–703.
[46] G. Gompper, D.M. Kroll, Random surface discretizations and the renormalization of the bending rigidity, J. Phys. I France 6 (1996) 1305–1320.
[47] G. Gompper, D.M. Kroll, Triangulated-surface models of fluctuating membranes, in: D.R. Nelson, T. Piran, S. Weinberg (Eds.), Statistical Mechanics of Membranes and Surfaces, 2nd edition, World Scientific, Singapore, 2004, pp. 359–426.
[48] S. Messlinger, B. Schmidt, H. Noguchi, G. Gompper, Dynamical regimes and hydrodynamic lift of viscous vesicles under shear, Phys. Rev. E 80 (2009) 011901.
[49] A. Laadhari, P. Saramito, C. Misbah, Vesicle tumbling inhibited by inertia, Phys. Fluids 24 (2012) 031901.
[50] X. Fan, N. Phan-Thien, S. Chen, X. Wu, T.Y. Ng, Simulating flow of DNA suspension using dissipative particle dynamics, Phys. Fluids 18 (2006) 063102.
[51] D.A. Fedosov, I.V. Pivkin, G.E. Karniadakis, Velocity limit in DPD simulations of wall-bounded flows, J. Comp. Phys. 227 (2008) 2540–2559.
[52] A. Colagrossi, M. Landrini, Numerical simulation of interfacial flows by smoothed particle hydrodynamics, J. Comp. Phys. 191 (2003) 448–475.

P4: Dynamical and rheological properties of soft colloid suspensions

R. G. Winkler, D. A. Fedosov, and G. Gompper

Current Opinion in Colloid & Interface Science, **19**:594-610, 2014.

Current Opinion in Colloid & Interface Science 19 (2014) 594–610

Contents lists available at ScienceDirect

Current Opinion in Colloid & Interface Science

journal homepage: www.elsevier.com/locate/cocis

Dynamical and rheological properties of soft colloid suspensions

Roland G. Winkler, Dmitry A. Fedosov, Gerhard Gompper *

Theoretical Soft Matter and Biophysics, Institute of Complex Systems and Institute for Advanced Simulation, Forschungszentrum Jülich, D-52425 Jülich, Germany

ARTICLE INFO

Article history:
Received 12 September 2014
Received in revised form 23 September 2014
Accepted 24 September 2014
Available online 2 October 2014

Keywords:
Ultrasoft colloids
Vesicles
Blood cells
Elasticity
Dynamics
Tumbling
Tank-treading
Rheology
Viscosity
Shear thinning

ABSTRACT

Soft colloids comprise a wide class of materials, ranging from linear polymers over polymeric assemblies, such as star polymers and dendrimers, to vesicles, capsules, and even cells. Suspensions of such colloids exhibit remarkable responses to imposed flow fields. This is related to their ability to undergo conformational changes and elastic deformations, and the adaptation of their dynamical behavior. The rational design of soft particles for targeted applications or the unraveling of their biological function requires an understanding of the relation between their microscopic properties and their macroscopic response. Here, mesoscale computer simulations provide an invaluable tool to tackle the broad range of length and time scales. In this article, we discuss recent theoretical and simulation results on the rheological behavior of ultrasoft polymeric colloids, vesicles, capsules, and cells. The properties of both, individual particles and semi-dilute suspensions, are addressed.

1. Introduction

The theoretical understanding of the rheological properties of colloidal suspensions started in 1906, more than a hundred years ago, with the now classical paper [1] of Albert Einstein, in which he predicted the viscosity η of a suspension of hard spheres to depend on the volume fraction Φ to leading order as

$$\eta = \eta_s \left[1 + \frac{5}{2}\Phi + O\left(\Phi^2\right)\right], \tag{1}$$

where η_s is the solvent viscosity. This result has turned out to be extremely useful, in particular because it does apply not only to hard spheres in the regime of $\Phi \lesssim 0.1$, but also to much more flexible objects like coiled linear polymers, when an appropriate radius of the coil, the "hydrodynamic radius" R_H, is employed to determine the volume fraction.

This raises the question about the importance of shape and deformability of soft colloids for the rheological behavior of their suspensions. Is it sufficient to define an appropriate hydrodynamic radius and otherwise employ the theoretical description of hard spheres? What is the maximum volume fraction to which such a description might be accurate and useful? Do all soft colloids behave the same, or is the physical origin of their softness important? What is the dependence of viscosity on the elastic moduli of the soft colloids? What is the role of shape, and how do shape and deformability together determine the rheological properties of a suspension?

There is a large range of applications, in which the rheological behavior of soft-colloid suspensions plays an important role. From a technological point of view, polymer suspensions are probably the most dominant. However, even this long-studied class of materials has seen several interesting developments in recent years. For linear polymers, semi-dilute solutions have been studied in detail, and the relation of orientation and elongation of single chains to the macroscopic rheological properties has been elucidated. More importantly, polymers with a more complex architecture have been investigated, such as star polymers, dendrimers, and hyperbranched polymers.

Vesicles, capsules, and cells are another class of soft objects. Capsules are also interesting for technological applications. However, the main focus of such suspensions is in the biomedical field. The blood is a suspension of mainly red blood cells, with a volume fraction of nearly 50%. Red blood cells are of biconcave shape, and are highly deformable because they have to squeeze through the tiny vessels of microvascular network. Thus, the deformability of red blood cells, which may get reduced in diseases such as malaria or diabetes, and its effect on blood

---

* Corresponding author.
E-mail addresses: r.winkler@fz-juelich.de (R.G. Winkler), d.fedosov@fz-juelich.de (D.A. Fedosov), g.gompper@fz-juelich.de (G. Gompper).

http://dx.doi.org/10.1016/j.cocis.2014.09.005
1359-0294/© 2014 Elsevier Ltd. All rights reserved.

viscosity are very important for blood flow. Similarly, vesicles and capsules are used as model systems for cells, but also as drug-delivery vehicles. They may differ from cells by their shape and type of membrane elasticity, and thus show different rheological properties.

To establish a relation between the structure of soft colloids and their macroscopic rheological properties, the microscopic understanding of their non-equilibrium properties is desired. This is difficult to achieve experimentally. Here, computer simulations are the appropriate tool for microscopic insight into soft matter and biofluid dynamics. In particular, recently developed novel mesoscale simulation approaches provide a detailed microscopic understanding and structure–function relationships, and shed light on universal non-linear dependencies.

In general, soft colloids show much richer rheological properties than their hard counterparts [2]. This poses additional challenges for the understanding and prediction of their behavior in semidilute and dense suspensions. However, it also offers new opportunities in terms of applications, because the variation of particle properties implies the tunability of rheological behavior over a wide range.

2. Simulation techniques

During the last few decades, various mesoscale simulation approaches have been developed to bridge the length- and time-scale gap inherent in soft matter systems. Prominent examples are the lattice Boltzmann (LB) method [3–5], the dissipative particle dynamics (DPD) [6–8], and the multiparticle collision dynamics (MPC) approach [9–11], which is based on the direct simulation Monte Carlo (DSMC) approach [12]. Common to these approaches is a simplified, coarse-grained description of the solvent degrees of freedom in order to achieve high computational efficiency while keeping the essential features of the microscopic physics on the length scales of interest—specifically, hydrodynamics. Embedded objects, such as polymers or colloids are treated by conventional molecular dynamics simulations.

2.1. Dissipative particle dynamics

In dissipative particle dynamics (DPD), each particle represents a *molecular cluster* rather than an individual atom, and can be thought of as a soft lump of fluid. The DPD system consists of N point particles, which interact through three pairwise forces denoted as conservative, dissipative, and random forces. The conservative force controls fluid compressibility, while the dissipative force supplies fluid viscosity. The DPD system is kept at equilibrium temperature with a local thermostat, which is formed by the pair of dissipative and random forces. The time evolution of velocities and positions of particles is determined by the Newton's second law of motion.

2.2. Multiparticle collision dynamics

In the multiparticle collision dynamics approach, the fluid is represented by a large number of point particles, which move in continuous space with a continuous distribution of velocities. Dynamically, the particles undergo alternating streaming and collision steps. In the streaming step, they move ballistically with their respective velocities for a time interval, which is denoted as collision time. Interactions between the particles appear in the collision step. Thereby, the system is coarse-grained into a grid of cubic cells, which define the collision environment. Only particles within a cell interact with each other by a momentum-conserving stochastic process, which leads to build-up of fluid correlations. Various collision rules have been proposed [9,13,14], however, the originally proposed Stochastic Rotation Dynamics (SRD) implementation is still preferentially used [9]. Here, the relative fluid particle velocities within a collision cell are rotated around a randomly oriented axis by a defined angle. The algorithm exhibits unconditional stability [9] incorporates thermal fluctuations, and hydrodynamic interactions [15]. Since it is particle-based, the MPC method can easily be combined with other simulation approaches such as molecular dynamics simulations. Moreover, mechanical expressions can be exploited to calculate, e.g., the stress tensor [16], or to implement an appropriate temperature control [17].

2.3. Polymer model

Typically coarse-grained models are used in simulations, where polymers are represented as bead-spring or bead-rod chains [18–21]. Stiffness is introduced by harmonic next-nearest neighbor interactions. To build a star polymer, linear polymers are connected to a common central particle. Thereby, the respective bond length might be chosen larger than that of other bonds, in order to accommodate the required particles in the core region [22•,23]. Excluded volume interactions are modeled by a truncated and shifted purely-repulsive Lennard-Jones potential.

2.4. Membrane models

Depending on a suspended particle of interest, a membrane model may need to incorporate elastic and viscous properties of a membrane, its bending resistance, and the viscosity contrast between inner and outer fluids. One class of models can be referred to as continuum approaches, where membrane properties follow some constitutive relations. For example, in-plane membrane shear elasticity can be described by Hookean or neo-Hookean law, while out-of-plane deformations are controlled by curvature elasticity [24–26]. Another class of membrane models corresponds to the network model of a membrane, which is built by a set of points which form a two-dimensional triangulated network on a membrane surface [27–31•,32•]. These models typically incorporate bending and stretching resistance, and area and volume constraints. In addition, viscoelastic membrane properties can be mediated by springs with attached dashpots [31•]. These network models assume a fixed connectivity; however, there exist a network model for a fluidic membrane (e.g., used for modeling fluid vesicles) which employs a dynamically triangulated network [27,28,33]. The fluidic membrane combined with a fixed elastic network leads to a two-layer membrane model [28,33]. Recently, a model of two continuous layers has been developed [34•], which allows for sliding and detachment of the two corresponding layers.

In continuum methods, coupling between membrane deformation and fluid flow is often implemented through the immersed boundary method (IBM) [24,35] or front tracking method (FTM) [25], which advect vertices with the local fluid velocity and exert membrane forces onto the fluid flow. Alternatively, fluid–structure interactions can be implemented through viscous coupling. In particle-based methods, the no-slip boundary conditions at the membrane surface are implemented through viscous force coupling in DPD [31•] or collisions in MPC [28] between fluid particles and membrane vertices.

3. Polymeric particles

Studies of the rheological properties of polymer systems have a long history, driven by the importance of these materials in industrial applications. Correspondingly, there is a wide-range of literature on various aspects of polymer solutions and melts including experiments [36,37•,38], theory [18,20,39], and simulations [20,40–42]. Here, we will mainly address computer simulation studies of the polymer dynamics in dilute and semidilute suspensions. Thereby, we want to cover linear polymers and more complex structures such as star polymers and dendrimers. There are other colloidal polymeric structures, e.g., hyperbranched polymers [43•] or polymer networks as in microgels. However, far less simulation studies have been performed for such particles, most likely due to the significantly larger number of "monomers" necessary to model the branched structures. There is a wide-range of simulation studies on polymer melts [39,40,44,45] with emphasis on polymer entanglements. The latter aspect goes beyond the scope of this article.

A broad spectrum of simulation approaches has been applied to study the non-equilibrium properties of linear polymers in shear flow. The various techniques are specified, and the respective references are provided in Ref. [46•]. More recent studies employing MPC are presented in Refs. [22•,23,42,47•,48,49,50•,51•].

3.1. Linear polymers: structure and dynamics in shear flow

3.1.1. Structure and dynamics in shear flow

The properties of linear polymers under shear flow have intensively been studied during the last decade by various computer simulation approaches (cf. Ref. [46•]). The interest was particularly triggered by experimental studies on DNA molecules, which reveal large conformational changes and an intriguing dynamics [52–55]. Figs. 1 and 2 illustrate the monomer density distribution of a polymer and their deformation under flow as obtained from simulations. The polymers are stretched along the flow direction, compressed along the orthogonal directions, and exhibit a preferred orientation with respect to the flow. These properties depend on shear rate in a particular manner and are ultimately linked to the macroscopic rheological behavior of the polymers.

Typically, the extension—specifically in experiments [54,56]—the mean square end-to-end distances, or the radius of gyration tensor components along and transverse to the flow direction are considered. The respective longitudinal part increases with increasing shear rate and slowly approaches a maximum, which is smaller than that corresponding to a fully stretched chain [46•,52]. This is a consequence of the continuous end-over-end tumbling dynamics with a non-stationary deformation. The transverse parts decrease with increasing shear rate according to a power law. Similar to convective boundary layers, which occur in the Graetz–Levecque problem in thermal/mass transport where the boundary-layer thickness is governed by a balance of cross-stream diffusion and down-stream convection at high Péclet numbers [57], scaling arguments have been provided for the dependence of the polymer radius of gyration R_{gy} along the gradient direction on the shear rate $\dot{\gamma}$ by balancing monomer convection and diffusion [19,56,58]. Typically, the flow strength is characterized by the Weissenberg number $Wi = \dot{\gamma}\,\tau$, where τ is the longest relaxation time of a polymer. Equating the time for the transverse diffusive transport of a monomer R_{gy}^2/D, where D is the diffusion coefficient, with that of the streamwise active transport over the length scale R_{gx} of the deformed polymer $R_{gx}/(\dot{\gamma}\,R_{gy})$, leads to [19]

$$R_{gy} \sim \dot{\gamma}^{-1/3}. \tag{2}$$

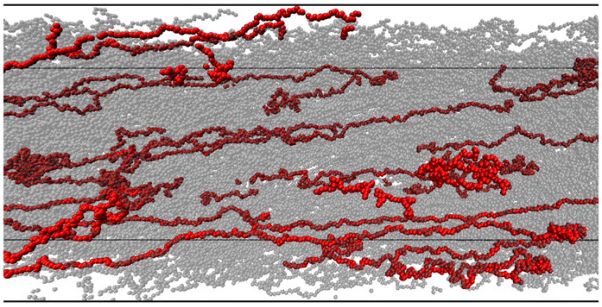

Fig. 2. Snapshot of a systems with 800 polymers of length $N_m = 250$ for the Weissenberg number $Wi_c = 184$. For illustration, some of the chains are highlighted in red.
From Ref. [48].

Thereby, it is assumed that the deformation along the flow direction is essentially independent of the shear rate. Theory [46•] and simulation results [47•,58] confirm the later assumption for large shear rates. An alternative expression is obtained under the assumption that a monomer drags along other monomers, i.e., its diffusion coefficient is reduced by cooperative effects. Setting $D \sim D_0/R_{gy}$, the above considerations yield

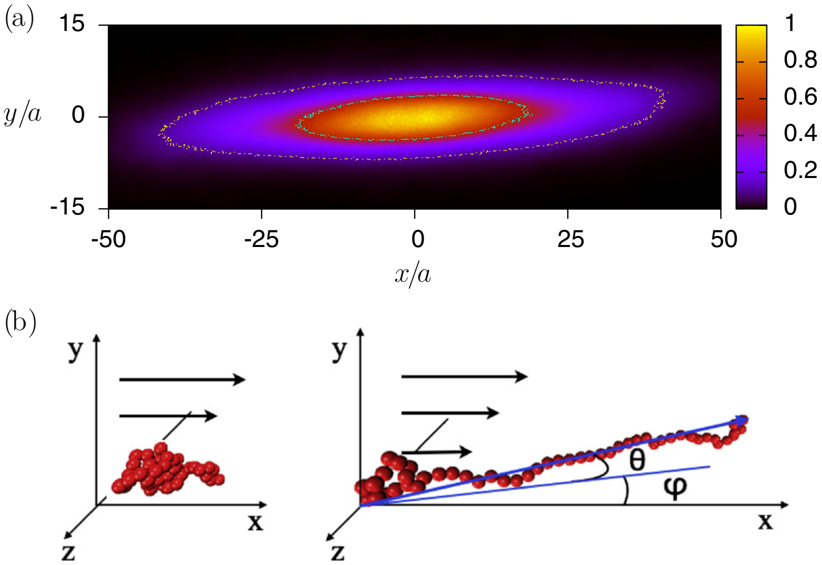

Fig. 1. (a) Monomer density distribution in the flow-gradient plane for $N_p = 3000$, $N_m = 250$, i.e., $c/c^* = 10.38$, and $Wi_c = 569$. The contour lines for the densities 0.1 (outer) and 0.5 (inner) are highlighted to emphasize the non-ellipticity of the shape. (b) Illustration of polymer stretching (right) and recoiling (left). θ is the angle between the end-to-end vector and its projection onto the flow-gradient plane and φ is the angle between this projection and the flow direction.
From Ref. [48].

$R_{gy} \sim \dot{\gamma}^{-1/4}$ [59•]. Both power-law dependencies have been observed in simulations [56,58,59•]. Thereby, the smaller exponent 1/4 is typically seen at smaller shear rates [56,58,59•] and the larger at high shear rates [19,58,59•].

An essential aspect for the non-equilibrium shear response is the finite length and inextensibility of a polymer, which is implicitly assumed in the above scaling arguments. Exploiting this fact, the dependence $R_{gy} \sim \dot{\gamma}^{-1/3}$ can be derived theoretically in a different way [46•]. For a long and flexible polymer, its mean square radius of gyration is related to the longest relaxation time τ via $R_{gy}^2 \sim \tau$. The inextensibility constraint links the various spatial components of the polymer [46•], which implies

$$\tau\left(1 + \dot{\gamma}^2\tau^2\right) = \text{const.} \tag{3}$$

The quadratic dependence on the shear rate naturally appears even in a lowest order perturbation theory for the polymer deformation along the flow direction, because R_g^2 is independent of the direction of shear. Hence, $\tau \sim \dot{\gamma}^{-2/3}$, or $R_{gy} \sim \dot{\gamma}^{-1/3}$. The full theoretical expression indicates a slow cross-over from an unperturbed polymer to the asymptotic behavior (2) at large shear rates. Thereby, an intermediate regime can be approximated by the relation $R_{gy} \sim \dot{\gamma}^{-1/4}$ over a small range of R_{gy} values. Here, very accurate experiments and simulations are required to separate the various scaling regimes or support the gradual change of R_{gy}.

The preferred alignment angle can be calculated by the components of the radius of gyration tensor, which yields in the asymptotic limit of large shear rates the dependence $\dot{\gamma}^{-1/3}$ [46•]. This is confirmed by simulations [47•].

First direct experimental observations of the tumbling dynamics of DNA molecules have been presented in Ref. [56]. Various attempts have been undertaken to characterize the tumbling motion by a characteristic tumbling time τ_T and to find the respective shear-rate dependence (cf. Ref. [48,50•]). Simulations and experiments provide a reasonable estimate of τ_T by direct counting of end-over-end tumbling events [54,56]. Alternatively, power spectral densities (PSD) have been determined for various correlation functions, which yield the sublinear dependence $\tau_T \sim \dot{\gamma}^{-2/3}$ [47•,54,58,60–62•]. This is consistent with the results obtained by counting tumbling events, as long as thermal motion is important [54,62•]. In the athermal limit, a linear dependence on the shear rate is observed [62•], in agreement with expectations for Jeffrey orbits [63]. Various other correlation functions have been considered, involving fluctuations of extensions along the shear and gradient directions [54,56,60,61] or those of the radius of gyration tensor components along these axes [48], which provide typically non-periodic functions [48,50•,54,56]. Here, the tight linkage of the polymer deformations along the respective spatial directions during a tumbling cycle is important.

Tumbling can also be characterized by the distribution of time intervals between successive tumbling events [55,64–66•]. Various criteria can be applied to distinguish tumbling events, e.g., the time interval between comparable polymer conformations [55] — characterized by the polymer extension — or that between successive crossings of the end-to-end vector of the shear-vorticity plane or the gradient-vorticity plane [65]. Since the distribution of tumbling events is typically non-Markovian, it can be rather complicated. However, the distributions should decay exponentially for sufficiently long time intervals, where the events are almost independent. From the exponential function, a decay time can then be extracted and identified as tumbling time. A priori, neither the equivalence of the various definitions is evident, nor it is clear that the same tumbling time or even the same dependence on shear rate, at least qualitatively, is obtained. However, recent theoretical calculations [46•,65] and simulations [48–50•] suggest that the decay time is closely related to the stationary-state end-to-end-vector relaxation time of a polymer and that the tumbling time exhibits the shear rate dependence $\tau_T \sim \dot{\gamma}^{-2/3}$. The latter follows directly from the above considerations, namely that $\tau_T = \tau$.

Computer simulation studies at extremely high Weissenberg numbers unravel another non-linear phenomenon, where the polymers shrink in size along the flow direction with increasing *Wi* [59•,67,68]. Thereby, the transverse components approach a constant value. In the presence of hydrodynamics, the effect is attributed to strong hydrodynamic drag forces, which lead to recirculating flows inside a polymer coil and thus to compaction due to entanglement effects [68]. The very large shear rates necessary for compactification are difficult to achieve in experiments, which is the reason why the phenomenon has not been observed so far.

So far, we have mainly addressed flexible polymers. Semiflexible polymers, where the persistence length is comparable with the contour length exhibit additional features. Here, a more or less gradual change of the behavior from that of a flexible to a rodlike polymer is expected with increasing stiffness. Indeed, rods also align with the flow and exhibit a tumbling motion. For the dynamical behavior, however, the presence or lacking of thermal noise plays a major role. Athermal rods in shear flow exhibit so-called Jeffrey orbits, with a rotation frequency which depends linearly on shear rate, i.e., the characteristic time is $\tau \sim \dot{\gamma}^{-1}$ [62•,63,69]. In the presence of noise, however, the same dependence as for flexible polymers is obtained [62•]. This has been predicted by theory [46•] and is observed in computer simulations [54] and experiments [70]. However, recent theoretical studies suggest the relation $\tau_T \sim \dot{\gamma}^{-3/4}$ for the tumbling time over a broad range of shear rates for semiflexible polymers [71]. According to the above scaling relation, this would also modify the shear thinning behavior. This aspect deserves further studies. So far, investigations of semidilute solutions of semiflexible polymers indicate a non-power-law decay of the viscosity in the shear thinning region [72•].

3.1.2. Rheological properties in shear flow

As mentioned before, the average anisotropic shape of a polymer determines its rheological behavior. This is illustrated by the following scaling consideration [19]. The tensile force F_x on the molecule along the flow direction is $F_x \sim \zeta\, \dot{\gamma}\, R_{gy}$, with ζ being the friction coefficient. By the virial theorem, the stress tensor is given by $\sigma_{xy} \sim F_x R_{gy}$, and hence the viscosity by

$$\eta = \sigma_{xy}/\,\dot{\gamma}\ \sim R_{gy}^2 \sim \dot{\gamma}^{-2/3} \tag{4}$$

in the asymptotic limit of large shear rates, with the radius of gyration of Eq. (2) [19]. This is consistent with more precise analytical calculations [46•] and agrees also with simulation results [19,58]. Thus, the strong deformation of the polymer leads to pronounced shear thinning, where the shear viscosity decreases by a power-law $\eta \sim \dot{\gamma}^{-\xi}$. Thereby, experiments and simulations [18–20,39,46•,47•,55,58,73,74] suggest exponents ranging from $0.4 < \xi < 0.85$ [18], i.e., a broad range of exponents. This is partially explained by the broad crossover between the zero-shear rate plateau and the limiting behavior for $\dot{\gamma} \to \infty$.

The first normal stress coefficient, defined as $\Psi_1 = (\sigma_{xx} - \sigma_{yy})/\dot{\gamma}^2$ [18,20], can be approximated by $\Psi_1 \sim \sigma_{xx}/\dot{\gamma}^2 \sim F_x R_{gx} \dot{\gamma}^2 \sim R_{gy} R_{gx}/\,\dot{\gamma}$ to derive a scaling relation. As for the derivation of Eq. (3), we set $R_{gy} \sim \tau^{1/2}$ and $R_{gx} \sim\ \dot{\gamma}\, \tau^{3/2}$, which leads to

$$\Psi_1 \sim \tau^2 \sim \dot{\gamma}^{-4/3} \tag{5}$$

in agreement with the more precise calculation in Refs. [18,20,46•]. In contrast to the viscosity, the dependence in Eq. (5) agrees very well with experiments for a broad range of polymer solutions [18,56,58] and a wide spectrum of simulations [19,47•,58,74]. This could be related to the fact that normal stresses are easier to determine than shear stresses.

The second normal stress coefficient $\Psi_2 = (\sigma_{yy} - \sigma_{zz})/\dot{\gamma}^2$ is determined by hydrodynamic and excluded-volume interactions [18,20, 47*], and hence depends significantly on concentration. For semidilute solutions, our simulations yield the decay $|\Psi_2| \sim Wi_c^{-4/3}$ of the magnitude of Ψ_2 (Ψ_2 is negative) with increasing shear rate, i.e., it decays with the same exponent as Ψ_1 [47*]. At low concentrations, we could not extract a clear power-law dependence, since the values of Ψ_2 decrease significantly with decreasing concentration.

We would like to emphasize once more the intimate connection between the structural, dynamical, and rheological properties of flexible polymers in shear flow. The above scaling considerations, and more precise analytical considerations [46*], show that all these quantities depend on the relaxation behavior of the polymer, which in turn is determined by the applied shear flow. Hence, here, we established a relation between the microscopic properties of the system and its macroscopic behavior.

At small shear rates, a polymer solution is in the Newtonian regime and the viscosity is independent of $\dot{\gamma}$. However, the zero-shear viscosity η_0 depends on the polymer concentration, which is often presented in the form [47*]

$$\eta_0 = \eta_s \left(1 + [\eta] + k_H([\eta]c)^2 + \ldots\right). \tag{6}$$

Here, $[\eta]$ is the intrinsic viscosity, c is the polymer concentration, and k_H is the Huggins coefficient [36,47*]. The term $k_H([\eta]c)^2$ depends on hydrodynamic interactions [47*]. For flexible polymers, k_H is in the range of 0.2–0.8 and depends on the solvent quality [47*]. Typically, the value $k_H = 0.3$ is found experimentally for flexible polymers in good solvents [47*]. Fig. 3 shows the dependence of the zero-shear viscosity on concentration for polymers of various lengths [47*]. The solid line indicates the power-law increase

$$\eta_0 = \eta_s (c/c^*)^{1/(3\nu-1)} \tag{7}$$

of η_0 as predicted by a blob model of the polymer [75]. The inset plot depicts the relative viscosity

$$\eta_R = \frac{\eta_0 - \eta_s}{\eta_s[\eta]c} = 1 + k_H[\eta]c + \ldots. \tag{8}$$

The comparison with the simulation data for various polymer lengths yields the coefficient $k_H = 0.35$ [47*], which is in close agreement with the experimental result.

Hard sphere suspensions obey the Einstein relation (1). As discussed in Ref. [47*], the same relation applies to dilute polymer solutions, when the hydrodynamic radius of a polymer is used to define the volume fraction.

As for dilute systems, a polymer in a semidilute suspension is aligned, deformed, and thus exhibits shear thinning. An example of the polymer contribution to the viscosity is displayed in Fig. 4 for polymers of various lengths N_m and various concentrations. A concentration independent universal behavior is obtained, when the respective quantities are represented as function of the concentration-dependent Weissenberg number $Wi_c = \dot{\gamma}\,\tau_c$, with the concentration-dependent longest relaxation time τ_c of a polymer. Thus, the same (asymptotic) scaling relations as for a dilute system apply for a semidilute system. A closer look, however, shows that partial screening of hydrodynamic interactions with increasing polymer concentration leads to different relaxation behaviors of the end-to-end vector components along the various spatial directions, where the relaxation times obey $\tau_x \leq \tau_y \leq \tau_z$ [50*].

3.2. Star polymers

Linking polymers at a common center by one of their ends leads to novel polymeric materials with tunable properties [76]. Two extreme limits of such particles are colloidal particles with short grafted polymers, e.g., polymeric latex spheres of varying grafting density [77,78], or a small connecting center with comparable long polymer arms—star polymers [76,79,80]. Here, we will focus on star polymers. By varying the arm number (functionality f) and arm length of a star polymer, its properties can be tuned continuously from those of flexible linear polymers to spherical colloidal particles with ultrasoft interactions. Thereby, the structural, dynamical, and rheological properties of star-polymer solutions strongly depend on the arm number, their length, and their concentration c [22*,23,42,51*,76,81–88*,89,90]. Experimentally, non-equilibrium properties have been considered for a wide range of functionalities and concentrations [76,77,91–93].

3.2.1. Structure and dynamics in shear flow

Similar to flexible polymers, shear flow deforms and aligns star polymers as displayed in Figs. 5 and 6 [22*,23,51*,89]. Individual arms are stretched along the flow direction with increasing shear rate. For a given functionality, we find a universal dependence of the deformation on the concentration-dependent Weissenberg number $Wi_c = \beta(c/c^*)\,\dot{\gamma}\,\tau_z$, where $\tau_z \sim N_m^2$ is the Zimm relaxation time and β is a concentration

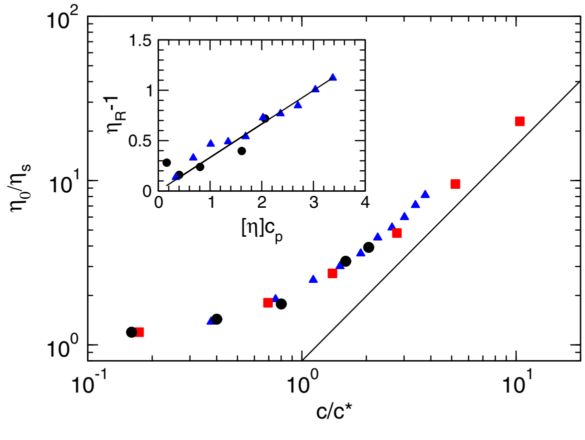

Fig. 3. Dependence of the zero-shear viscosity on the scaled concentration c/c^* for the polymer lengths $N_m = 40$ (▲), $N_m = 50$ (●), and $N_m = 250$ (■). The solid line indicates the power-law $(c/c^*)^{1/(3\nu-1)}$ with $\nu = 0.6$. In the inset, $\eta_R - 1$, Eq. (7), is shown as function of $[\eta]c$ for $N_m = 40$ (▲) and $N_m = 50$ (●); the slope of the solid line is 0.35, which corresponds to the Huggins constant of polymers in good solvent.
From Ref. [47*].

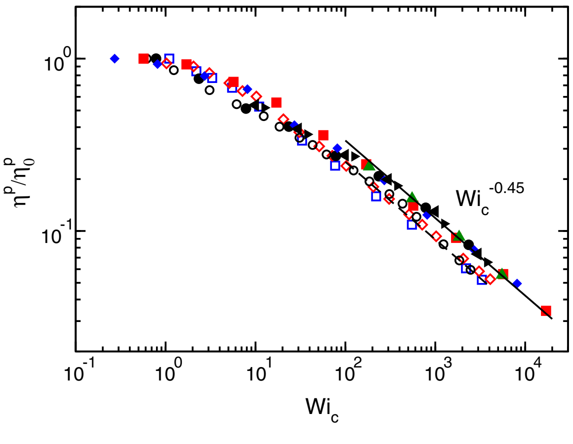

Fig. 4. Dependence of the normalized polymer contribution to shear viscosity on Wi_c. Open symbols correspond to systems of polymer length $N_m = 50$ for $c/c^* = 0.16$ (○), $c/c^* = 1.6$ (◊), and $c/c^* = 2.08$ (□). Filled symbols denote results for $N_m = 250$ with the concentration $c/c^* = 0.17$ (●), $c/c^* = 0.35$ (◀), $c/c^* = 1.38$ (▶), $c/c^* = 2.77$ (▲), $c/c^* = 5.19$ (♦), and $c/c^* = 10.38$ (■).
From Ref. [47*].

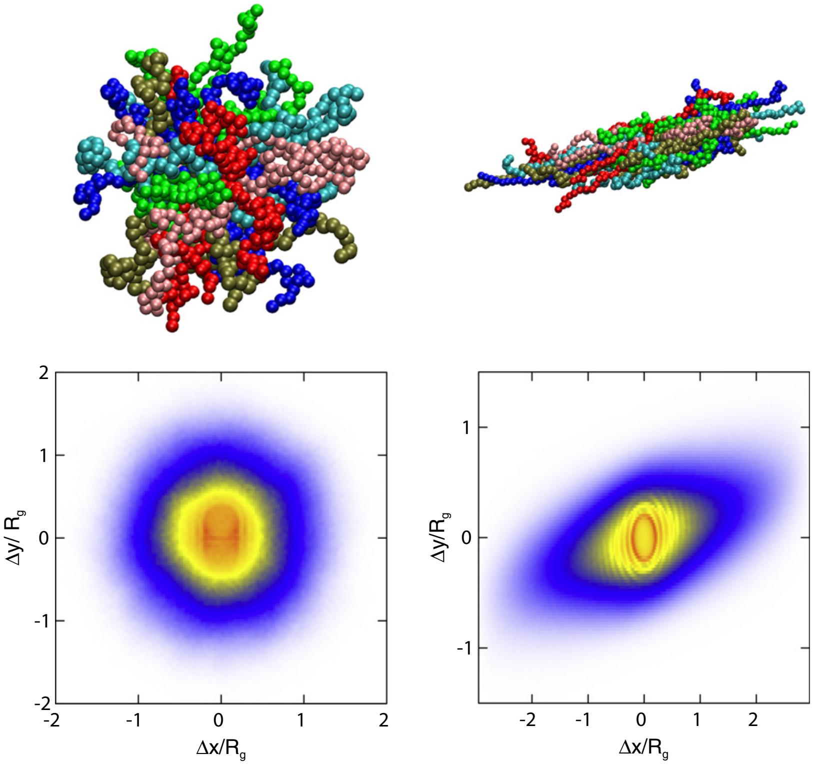

Fig. 5. Star polymer conformations (top) and monomer density distributions at equilibrium (left) and under shear flow (right).
From Ref. [51•].

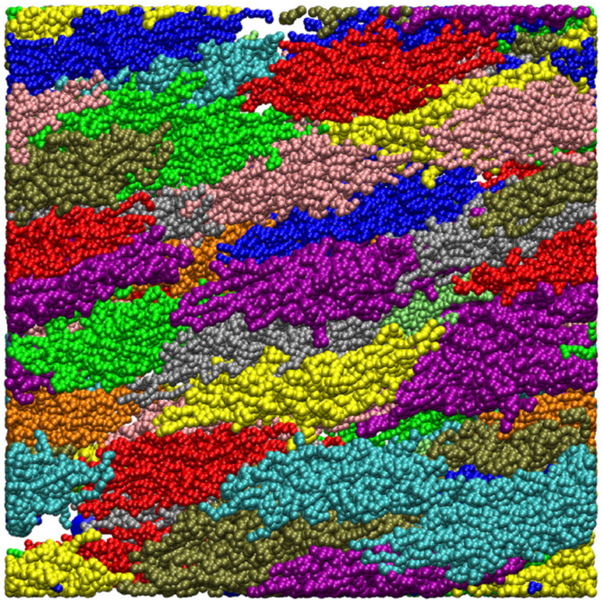

Fig. 6. Simulation snapshot of a solution of star polymers with $f = 50$, $c/c^* = 1.46$, and the Weissenberg number $Wi_c \approx 10^2$. Only star polymers with their centers in a slice of thickness of $3R_{g0}$ parallel to the flow-gradient plane are shown, where R_{g0} is the radius of gyration at equilibrium. Multiple colors are used to distinguish the various star polymers more easily.
From Ref. [23].

dependent factor [22•]. Along the gradient and vorticity directions, star polymers shrink for $Wi_c > 1$. Thereby, the compression along the vorticity direction is quite small compared to that in gradient direction [22•, 89]. As expected, the factor $\beta(c/c^*)$ increases strongly with increasing concentration in a nonlinear manner. Thereby, the values for the various functionalities and arm lengths follow a universal curve [22•,23].

We find a universal stretching behavior for stars of various functionalities in terms of a functionality-dependent Weissenberg number $\phi_f Wi_c$ in dilute solution, where the factor ϕ_f accounts for the functionality dependence [23]. At higher concentrations, however, a weaker stretching is observed at large $\phi_f Wi_c$. The radius of gyration tensor component along the gradient direction decays slower with increasing shear rate at higher concentrations. Thereby stars of different functionalities exhibit a universal behavior at a particular concentration [23]. Surprisingly, the scale factor ϕ_f decreases with increasing functionality as $\phi_f \sim f^{-2/3}$, i.e., the relaxation time of the shear response decreases with increasing functionality [23]. This is in contrast to the relaxation time of an individual polymer arm, which is predicted to follow the dependence $f^{(2-3\nu)/2}$, with $(2-3\nu)/2 \simeq 0.1$ for $\nu \approx 0.6$ [82]. A possible explanation for the discrepancy is that the simulation results of [23] are derived for moderate arm lengths and functionalities, while the scaling arguments apply to very long arms and large functionalities. It would certainly be interesting to investigate star-polymer relaxation times in equilibrium in more detail to clarify this problem.

At equilibrium, the arms of a star polymer exhibit conformational properties similar to those of an individual polymer under good solvent conditions. This is reflected in the scaling properties of the arm structure factor, which exhibits the dependence $q^{-1/\nu}$ with $\nu \approx 0.63$ on the scattering vector. Under shear flow, the arms are stretched, which is manifested by an increase of ν up to $\nu \approx 0.8$ for large shear rates [23]. This indicates that the arms are never fully stretched in the ensemble average.

The connectivity of the polymer arms drastically alters the non-equilibrium dynamical behavior of a star polymer. Similar to individual polymers, stars with a few arms only ($f \lesssim 4$) exhibit a tumbling motion, with a cyclic stretching and collapse of the whole star polymer. For large f, however, the stars rather exhibit a tank-treading-like motion [23,89,94], reminiscent to the dynamics of vesicles [95–97]. However, individual arms still undergo tumbling motion with a cyclic stretching and collapse of individual arms [51•]. The conformational changes are visible in Figs. 5 and 6. Along the vorticity direction, the center-to-end vector correlation function decays exponentially with time, with a shear-rate-dependent relaxation time. The latter scales as $\dot{\gamma}^{-2/3}$ for $Wi_c > 10$, as for linear polymers. Along the shear and gradient directions, the relaxation dynamics is tightly coupled and the respective center-to-end vector component correlation functions exhibit a damped oscillatory behavior [51•].

The rotation of the star polymer also affects the fluid flow field. Specifically, the flow lines in the interior of the star polymer are closed, i.e., the internal fluid is screened from the outer one [94]. The rotation dynamics can be quantified by an angular rotation frequency ω_z [23,89]. For shear rates $\phi_f Wi_c \ll 1$, the frequency assumes the expected value $|\omega_z| = \dot{\gamma}/2$. For large shear rates, the magnitude of the rotation frequency increases as $|\omega_z| \sim \dot{\gamma}^{\zeta}$ with increasing $\dot{\gamma}$. Thereby, the exponent ζ depends strongly on concentration. In dilute solution, we find $\zeta \approx 0$ almost independent of the functionality [23,89], whereas above the overlap concentration $\zeta \approx 0.35$. Simulations of dilute systems without hydrodynamic interactions yield $\zeta \approx 0.4$ [94]. Thus, the lack or presence of hydrodynamic interactions has a significant influence on the star's rotational dynamics. Qualitatively, an increase of the polymer concentration has the same effect on ω_z as suppression of hydrodynamic interactions. Hence, we interpret the increase of ζ as an indication of screening of hydrodynamic interactions in star polymer solutions at concentrations far above the overlap concentration.

The shear-rate dependence of the rotation frequencies extracted from the simulation data for various functionalities can be reproduced well by the Keller–Skalak (KS) model for vesicles [95] over a broad range of shear rates [23]. Thereby, we identify the axis of the effective ellipsoid with the square root of the respective major axis of the radius of gyration tensor [23].

The diffusive dynamics of the center-of-mass of a star polymer is significantly slowed down with increasing concentration at equilibrium. However, under shear flow, the dynamics is enhanced, and we find diffusion coefficients along the gradient and vorticity direction, which grow by an order of magnitude, when we increase the Weissenberg number from unity to 10^2 [51•]. A similar behavior has been reported for the diffusive dynamics of colloidal particles in glasses [98,99]. At higher concentration, close spatial proximity of the star polymers leads to caging. The respective star polymers rattle in their cage until a certain rearrangement of the neighborhood opens a route to escape. Above the“ escape time”, the star polymers exhibit Brownian motion. Shear promotes fast and considerable rearrangements of the star polymers, particularly since they are dragged along the flow direction by shear. Thus, the star polymers can escape easily from the local neighborhood, which is reflected in the shear enhanced dynamics.

3.2.2. Rheological properties in shear flow

The flow induced deformation and alignment of star polymers determines the rheological properties of the suspension. Fig. 7 illustrates the dependence of the stress tensor on the Weissenberg number and concentration. For $Wi_c > 1$, the shear stress strongly depends on the concentration. The sublinear increase of the shear stress implies shear thinning of the suspension. Simulations reveal a universal dependence of η on $\phi_f Wi_c (> 1)$ for low concentrations independent of functionality [51•]. Here, the viscosity can be described by the power-law $\eta \sim \dot{\gamma}^{-0.3}$ for $\phi_f Wi_c > 1$. For higher concentrations, again a universal curve is obtained for various functionalities, but with the steeper slope of $\eta \sim \dot{\gamma}^{-0.4}$ [51•]. Interestingly, simulations did not show a zero shear-rate plateau for concentrations significantly above the overlap concentration. This points toward the presence of yield stress in such systems.

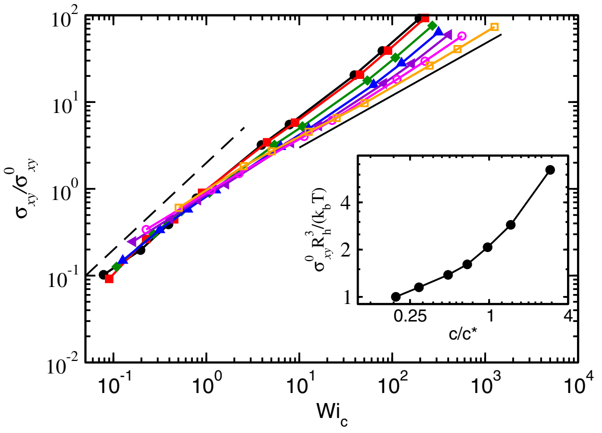

Fig. 7. Normalized shear stress σ_{xy} as a function of Wi_c for the concentrations $c/c^* = 0.2$, 0.29, 0.49, 0.68, 0.97, 1.46, 2.92 (top to bottom) and the functionality $f = 50$. The dashed and solid lines indicate the power-laws $\sigma_{xy} \sim Wi_c$ and $\sigma_{xy} \sim Wi_c^{0.6}$, respectively. The inset displays the dependence of the scale factor σ^0_{xy} on concentration, where R_H is the hydrodynamic radius.
From Ref. [51•].

Zero-shear viscosities η_0 for star polymers of various functionalities from experiments and simulations are displayed in Fig. 8 [76,77]. The zero-shear viscosity increases rapidly with concentration. The simulation data are well described by the relation $\eta_0/\eta_s = 2.5\phi + 6.2\phi^2$, which implies a faster increase than that for linear polymers, where $\eta_0/\eta_s = 2.5\phi + 6.25 k_H \phi^2$ with the Huggins coefficient $k_H \simeq 0.3$ [47•]. Furthermore, the zero-shear viscosity as a function of c/c^* depends only very weakly on the arm length. The figure shows a very consistent trend of an increase of the zero-shear viscosity with increasing functionality at constant concentration c/c^*, and demonstrates the crossover of star-polymer properties from ultra-soft to hard-sphere colloids with increasing f. Other simulations yield a near power-law increase of the star-polymer zero-shear rate viscosity in the range $0.1 < c/c^* < 4$ for functionalities in the range $10 \le f \le 50$ [51•].

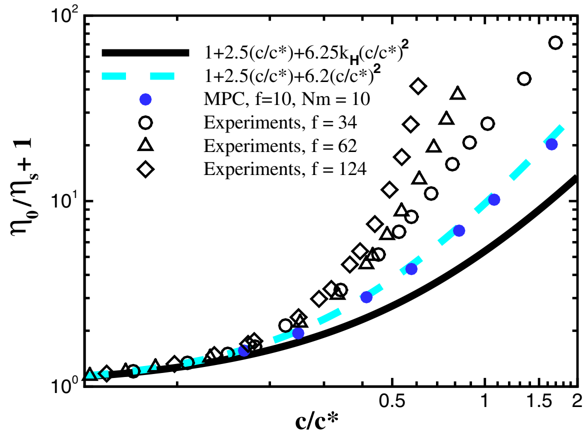

Fig. 8. Experimental and simulation results for the zero-shear viscosity of star polymer suspensions. Experimental results (open symbols) for functionalities $f \ge 34$ are extracted from Fig. 6 of Ref. [77]. They are compared with the simulation results for star polymers with $f = 10$ (closed symbols, dashed line) and that for linear polymers [47•] (solid line).
From Ref. [22•].

The viscosity of star-polymer solutions of very high functionality $f \simeq 390$ has also been measured experimentally at concentrations in the fluid and glassy phases [93]. In the semidilute regime, the shear stress shows a linear increase at low shear rates, followed by a less pronounced growth with an effective exponent of approximately 0.5; this effective exponent decreases with increasing concentration [93]. Both observations are consistent with our simulation results. The exponent of the power law of the shear stress for intermediate Weissenberg numbers is important, because a value larger than unity signals shear banding. Such a behavior has indeed been predicted for concentrated solutions [100]. On the basis of our simulations, no shear banding is predicted for stars with $f \leq 50$ in the investigated concentration range. We expect that considerably larger functionalities are necessary to observe shear banding.

The first normal stress coefficient and the magnitude of the second one decrease with increasing shear rate [42,51•]. Thereby, Ψ_1 exhibits the dependence $\Psi_1 \sim (\phi_f Wi_c)^{-1}$ on the shear rate and functionality ($f \gtrsim 10$). This exponent is different from that of flexible polymers. The reason for the observed difference is yet unexplained. We also find quite pronounced second normal stress coefficients. They decrease as $|\Psi_2| \sim (\phi_f Wi_c)^{-4/3}$ for $\phi_f Wi_c > 1$, i.e., show the same exponent as concentrated polymer solutions. Since excluded-volume interactions mainly determine Ψ_2, the large magnitudes of the second normal stress differences for dilute and concentrated systems point toward strong excluded-volume interactions, both intramolecular at low concentrations, as well as intermolecular at higher concentrations.

3.3. Dendrimers

Dendrimers form another class of ultrasoft colloids with tunable properties [101]. As for star polymers, their dynamical and rheological properties strongly depend on the structural unit, from which the hierarchical entity emerges. However, so far comparably little is known about their rheological properties.

3.3.1. Structure and dynamics in flow

Dendrimers are deformed and aligned by a shear flow [102•,103], with a weak compression along the gradient direction and an even weaker effect along the vorticity direction. The elongation in the flow direction depends on the dendrimer rigidity. The simulations of Ref. [102•] indicate a power-law increase in the range $0.1 < Wi < 50$, with a slope somewhat smaller than unity. This is in contrast to linear and star polymers, where the elongation increases initially quadratically [23,47•]. Therefore, a suitable relaxation time for the determination of the Weissenberg number seems to be

$$\tau = \frac{\eta l^3 (2G+1)^{3\nu}}{k_B T}, \tag{9}$$

where G is the number of generations, l is the bond length, and $\nu = 0.588$ is the Flory exponent [102•].

3.3.2. Rheological properties

Shear simulations of dendrimers reveal shear thinning at sufficiently high shear rates with an approximate power-law decay $\dot{\gamma}^{-\zeta}$ [43•,103, 104]. For the exponent, the values $\zeta = 1/3$ [104] and $\zeta = 0.55$–0.6 [103] have been reported. In Ref. [103], the exponent is found to be independent of topology by comparing linear polymers with dendrimers. The viscosity curves normalized by the zero-shear viscosity for dendrimers and linear polymers collapse as function of the reduced shear rate $[\eta]M\eta_s/(N_A k_B T)\,\dot{\gamma}$, where M is the molecular weight and N_A is the Avogadro constant.

The dendrimer zero-shear viscosity $[\eta_0]$ exhibits a molecular weight dependence, which is very different from that, e.g., of linear polymers [103,104]. For a dendrimer, $[\eta_0]$ increases initially at low molecular weight, passes through a maximum, and decreases for a large number of monomers. In contrast, for linear polymers, the viscosity increases in a power-law manner. Shear-thinning of dendrimers has been also found in simulations of elongational flow [43•].

The first and second normal stress coefficients also decay for large shear rates with a power-law $|\Psi_{1,2}| \sim \dot{\gamma}^{-4/3}$, similar to star polymers [103].

In general, very little quantitative studies of dendrimer rheology have been performed. This is certainly a consequence of the considerably larger computational cost of simulations due to the required large number of particles.

4. Vesicles, capsules, and cells

Droplets, vesicles, capsules and cells are all small bags of an internal fluid, which is separated from the embedding, outside fluid by a closed interface or membrane. The dynamics of such objects, in particular under flow, depends on the physical origin of their deformability, like the surface tension at constant volume for droplets, the membrane bending rigidity at fixed volume and surface-area for vesicles, and, in addition, the membrane shear elasticity for capsules and cells. Therefore, these systems have to be investigated independently to understand the relation between the elasticity of the particles and the rheological behavior of their suspensions.

Suspensions of vesicles, capsules, and cells receive more and more attention due to their importance in technological and biomedical applications. Examples include various cell organelles, drug delivery carriers, cosmetic and food industry applications, and tissue components.

4.1. Vesicles

A vesicle consists of a fluidic lipid bilayer membrane of fixed area A, which encloses a fluid volume V. Their shapes and deformations are controlled by the curvature elasticity of the membrane, which is governed by the bending rigidity κ.

In the dilute regime, the vesicle dynamics under shear flow shows three different types of motion: tank-treading (TT), tumbling (TB) and vacillating-breathing (VB) (also called trembling or swinging). In the tank-treading regime, the vesicle shape is stationary, characterized by a constant value of the inclination angle φ of the eigenvector of the radius-of-gyration tensor with the largest eigenvalue and the flow direction, but a rotational motion of a tracer particle attached to the lipid membrane. In the tumbling regime, the whole vesicle rotates, almost like a rigid object. In the vacillating–breathing regime, the shape deformation of the vesicle becomes important, which leads to an oscillation of the shape between a positive and a negative inclination angle. The stability of these types of vesicle dynamics depends on viscosity contrast $\lambda = \eta_{in}/\eta_{out}$, where η_{in} and η_{out} are the fluid viscosities of the inner and outer fluids, and shear rate $\dot{\gamma}$, with TT and TB occurring at low and high λ, respectively [95,105–115•].

For tank-treading quasi-spherical vesicles in three dimensions (3D), the viscosity of a dilute suspension has been predicted to be [116,117]

$$\eta/\eta_{out} = 1 + \frac{5}{2}\Phi\left[1 - \frac{\Delta}{40\pi}(23\lambda + 32)\right] \tag{10}$$

as a function of excess area $\Delta = 4\pi[(A/(4\pi))(4\pi/(3V))^{2/3} - 1]$ and viscosity contrast λ, where Φ is the vesicle volume fraction. Thus, the intrinsic viscosity $\eta_I = (\eta - \eta_{out})/(\eta_{out}\Phi)$ is predicted to be a decreasing function of Δ and λ. Furthermore, η_I is foreseen to exhibit a cusp-like minimum at the tank-treading to tumbling (or tank-treading to vacillating-breathing) transition, and then to increase again with increasing λ [116,117]. This latter behavior has been also found in the numerical calculations of a two-dimensional vesicle by the boundary-integral approach [118].

These theoretical predictions have been tested experimentally [119, 120]. While a decrease of η_I with increasing λ was found in Ref. [119], in good agreement with the theoretical prediction in Eq. (10), in contrast, an increase of η_I was observed in Ref. [120]. However, the available experimental results are not conclusive so far for the following reasons. First, vesicle sizes in suspensions are typically polydisperse. Second, viscosity measurements require a minimum volume fraction Φ of vesicles, typically 5% to 10%, and are therefore difficult to extrapolate to the dilute limit [120]. Indeed, recent experiments [121] demonstrate that vesicle interactions become relevant for the suspension's viscosity for Φ around 10%.

This has stimulated new simulation studies of vesicles in shear flow in narrow channels [122•–124]. Because of the high numerical cost of vesicle simulations in 3D, these simulations have been performed using 2D model systems. Here, the systems investigated in Ref. [122•] and Refs. [123,124] differ by their presence or absence of thermal fluctuations, which concerns both cross-streamline diffusion as well as membrane undulations.

We discuss first the simulation results for a system with thermal noise. The snapshots of vesicle conformations displayed in Fig. 9 show the typical collision process of two vesicles, which are slightly displaced in the vertical direction, and therefore move with different velocities in the flow direction. As the vesicles collide, their long axes rotate together to align first with the flow direction, possibly a bit further. Then, the vesicles separate again and the vesicle axis rotates back to its unperturbed inclination angle [122•]. This time-dependence obtained in the simulations is in good agreement with experimental results [120]. Similar results have also been obtained from simulations in 3D (without thermal noise) [125•]. The intrinsic viscosity of the same system is shown as a function of viscosity contrast and reduced shear rate $\dot{\gamma}^*$ in Fig. 10. Here, the reduced shear rate is defined as $\dot{\gamma}^* = \dot{\gamma} * \tau$, where $\tau = \eta_{out} R_0^3/\kappa$ is the characteristic vesicle relaxation time with average vesicle radius R_0. In the tank-treading regime, the viscosity is found to be an increasing function of λ, in agreement with the experiments of Ref. [120]. Simultaneously, the suspension shows a pronounced shear-thinning behavior, which makes it difficult in the simulation to reach the low-shear-rate plateau [122•].

The rheological behavior in the absence of thermal noise seems to be substantially different. In this case, the normalized effective viscosity of the suspension in a 2D narrow channel with $\Phi = 0.06$ is nearly indistinguishable from the viscosity at very high dilution, which decreases with increasing λ [123]. Only in the TB regime with $\lambda \gtrsim 20$, the viscosity of the suspension is significantly enhanced. This effect occurs, because in the steady state TT vesicles order in a single line with approximately the same distances between them. At higher concentrations, vesicles can arrange in two or three files [124]. Simulations of vesicle suspensions in unbounded shear flow in 3D (also without thermal noise) show a very similar dependence on the viscosity contrast for $\Phi = 0.1$ and $\Phi = 0.2$ [125•].

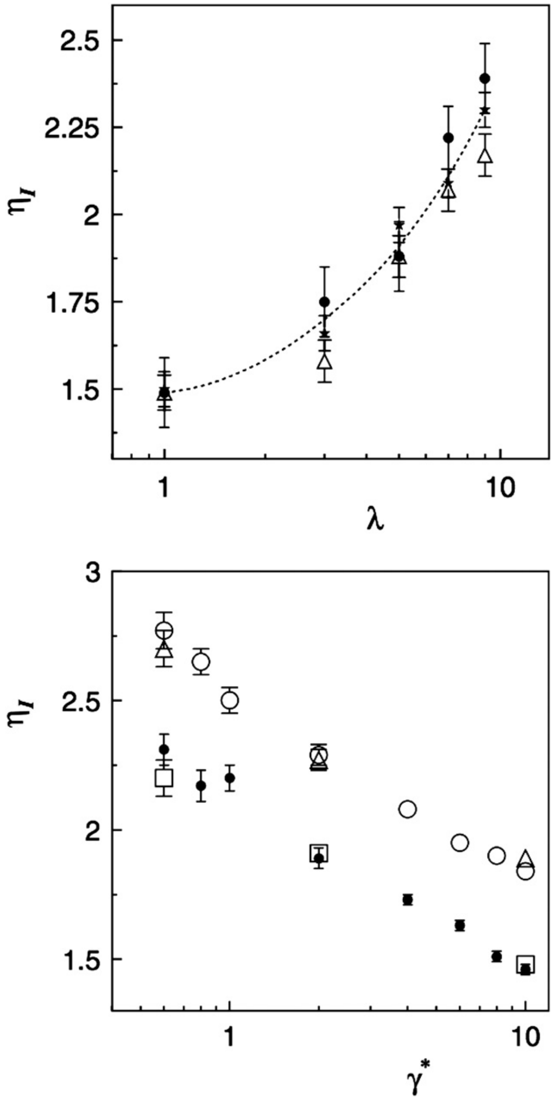

Fig. 10. Intrinsic viscosity $\eta_I = (\eta - \eta_{out})/(\eta_{out}\Phi)$ of a vesicle suspension as a function of (top) the viscosity contrast λ for reduced shear rate $\gamma^* = 2.0$, reduced area $A^* = 0.8$, and concentrations $\Phi = 0.05$ (●), 0.09 (△), and 0.14 (⋆) (the dashed line is the interpolation to the data, the tank-treading-to-tumbling transition is predicted to occur at $\lambda_c \simeq 3.7$ in the Keller–Skalak (KS) theory [95]); (bottom) the reduced shear rate γ^* for reduced area $A^* = 0.8$, concentration $\Phi = 0.28$, and viscosity contrasts $\lambda = 2.0$ (●, □) and 5.0 (○, △).
From Ref. [122•].

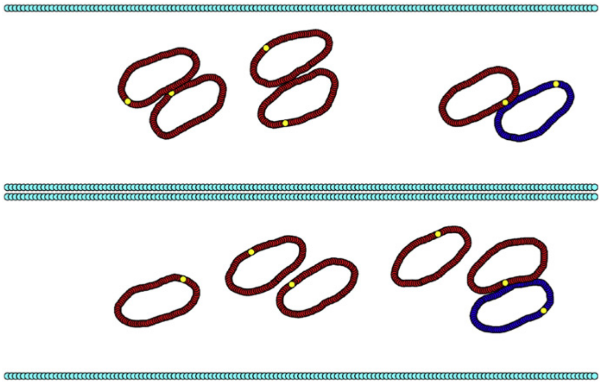

Fig. 9. Configurations at consecutive times with time lag $\dot{\gamma}\, t = 16$ of 2D vesicles with viscosity contrast $\lambda = 1.0$, reduced area $A^* = 0.8$ (the area in units of the area of a circle of equal perimeter length), reduced shear rate $\dot{\gamma}^* = 2.0$, and volume fraction $\Phi = 0.14$. One point of each vesicle membrane is colored yellow for visualization of its evolution during tank-treading, and one vesicle blue for visualization of the translational motion.
From Ref. [122•].

If these differences in the rheological behavior can indeed be traced back to the presence or absence of thermal fluctuations, then this raises the important questions (i) of the mechanism which affects the viscosity so strongly, and (ii) in which systems noise plays an important role, and in which not. It has been found in 2D [113] and 3D [110] systems that vesicles have highly convoluted shapes and show an irregular dynamics in and near the vacillating-breathing regime, in agreement with experimental observations [108], which indicates the importance of thermal noise. More detailed studies, both experimental [126•] and theoretical [127,128•], show that the flow indeed strongly amplifies the effect of thermal fluctuations. In the vacillating-breathing regime, a vesicle finds itself on the edge of a wrinkling instability, where thermally-excited spatial modes are amplified. Fluctuations should be important for low membrane bending rigidities (which increases membrane undulations) and low external fluid viscosity (which increases rotational and translational diffusion coefficients).

Vesicles in capillary flow have also been investigated extensively, in particular using 2D models. Since there is no shear elasticity in 2D (i.e., the membrane is a closed line), the vesicles are also often called red blood cells. We focus here on the rheological behavior in narrow channels. A suspension of discocyte-shaped vesicles is shown to be shear-thinning, in particular near capillary numbers of order unity [129,130], due to the flow-induced deformation from the discocyte to the parachute shape, and the focusing of the vesicles in the center of the channel. Surprisingly, the predictions for the behavior for small flow velocities differ between 2D and 3D: the eigenvector of the radius-of-gyration tensor with the smallest eigenvalue points in the flow direction in 2D, but is perpendicular to it in 3D. Further work is required to clarify these issues.

4.2. Capsules

Capsules are often referred to particles with an elastic membrane whose area may not be strictly conserved. Thus, capsule deformation in flow may also lead to area dilation. In contrast to vesicles, capsule membrane is elastic. Dynamics of a single capsule in flow has been investigated experimentally [131–133] and theoretically [134–136•], and in simulations [137–139], while the rheology of capsule suspension has been mainly studied in numerical simulations [26,140•,141,142,143•].

4.2.1. Dynamics of single capsules

Several authors have studied the flow-induced deformation of synthetic capsules, which consisted of liquid drops surrounded by thin polymeric membranes [131–133,144]. The experimental results have been fitted with the theory for small capsule deformations in flow [134] showing good agreement up to moderate capsule deformations. At large deformations a non-linear behavior is expected to have a contribution. More recent experiments on polyamide microcapsules in shear flow [132,133] have shown shape oscillations and membrane wrinkling. The results have been fitted by the theory [134], even though the theory assumes a steady capsule shape without oscillations. The instability of capsule shape and wrinkling in shear flow has been theoretically investigated in Ref. [135], where a critical shear rate for the instability and the wavelength of wrinkling have been predicted.

Dynamics of capsules in shear flow is also characterized by the two states: tumbling and tank-treading. The transition can be triggered by a viscosity contrast between the inner and outer fluids similar to that for vesicles, which has been first described by the Keller–Skalak theory [95]. The KS theory assumes a fixed path for a tank-treading capsule, and therefore, does not reflect shape oscillations. Improved theories [145,146] for red blood cells (or also capsules) have added an energy barrier for tank-treading due to membrane elasticity. For a spherical capsule this barrier becomes very small, while it increases as a capsule departs further from a spherical shape. Thus, tumbling-to-tank-treading transition may also depend on the elastic barrier for non-spherical capsules, for instance RBCs. Recent theories [136•,138] have also included membrane oscillations, which appear to be crucial for correct prediction of capsule dynamics. When cell shape deformation is also taken into account, two types of oscillation modes coexist: one induced by the shape deformation similar to fluid vesicles and the other induced by the tank-treading energy barrier [147]. For non-spherical capsules accompanied by a local energy minimum, coupling of these two modes generates a complicated phase behavior.

4.2.2. Rheology of capsule suspensions

The rheology of capsule suspension has been investigated in a number of simulations [26,140•,141,142,143•] with a common conclusion that capsule suspension exhibits shear thinning. Also, suspension's viscosity strongly depends on the volume fraction of capsules. Rheology of a dilute capsule suspension has been studied in Ref. [140•] showing a shear-thinning behavior. However, the dependence of suspension's viscosity on the viscosity ratio (λ) between inner and outer fluids surrounding capsule shows a non-trivial behavior. An initial increase of λ from unity leads to a decrease of the suspension's viscosity, while a further increase in λ may result in an increase of suspension's viscosity. This effect is related to the transition from a tank-treading behavior of capsules to tumbling at high enough values of λ.

The rheology of capsule suspensions at moderate concentrations has been investigated in Refs. [141–143•]. Apart from a shear-thinning behavior, microstructure of the suspension has been discussed including also single capsule properties such as orientation and deformation. The measurements of the normal stress differences [141,142] have shown an unexpected behavior, such that the first normal stress difference is negative at low shear rates and becomes positive as the shear rate is increased. The numerical results of Ref. [142] have also indicated that at high enough concentration of capsules a yield stress may appear even without any aggregation interactions between capsules. The study in Ref. [143•] have considered inertial effects on the suspension's rheology in Poiseuille flow. The apparent viscosity of capsule suspension may decrease with an increasing Reynolds number for relatively soft capsules. This effect is related to strong capsule deformations.

4.3. Blood cells and blood flow

Red blood cells (RBCs) combine the properties of both vesicles and capsules with the membrane comprising viscoelastic and area-preserving properties with a finite bending stiffness. Human RBCs have a biconcave shape with a diameter ranging between 6 μm and 8 μm and a thickness of about 2 μm. A RBC membrane is constructed from a lipid bilayer with an attached spectrin–protein cytoskeleton, which provides integrity for a RBC since it is subject to substantial deformations in microcirculatory blood flow. The inner fluid of a RBC is a hemoglobin solution, which can be considered nearly Newtonian and is about 5 times more viscous than the blood plasma.

Mimicking RBC structure, a complete RBC model needs to include elastic energy of the spectrin network, a curvature energy to describe bending resistance of the lipid bilayer, conservation of both the cell area and volume to represent the area incompressibility of the lipid bilayer and incompressibility of a cytosol, membrane viscosity, and the viscosity contrast between the cytosol and blood plasma. The RBC biconcave shape corresponds to the reduced volume $V^* = V_0/\left(\frac{4}{3}\pi R_0^3\right)$ with V_0 being the RBC volume and $R_0 = \sqrt{A_0/(4\pi)} = 3.25$ μm, where A_0 is the area of a RBC. The reduced volume of a healthy RBC is equal to about $V^* = 0.6$. More details on RBC and blood flow modeling can be found in recent reviews [148,149••,150••,151].

4.3.1. Shapes and dynamics of single RBCs in flow

The behavior of single RBCs in flow inevitably affects blood rheological properties. Deformation and dynamics of RBCs have been investigated experimentally in various flows including shear flow [146,152,153••] and tube or Poiseuille flow [154,155].

Similar to the dynamics described for vesicles and capsules, RBCs in shear flow exhibit tumbling and tank-treading motion [146,152,153••]. An experimental study [152] has shown that the existence of these two states is due a RBC minimum energy state such that a certain energy barrier has to be exceeded in order for a RBC to tank-tread. Similarly to vesicles and capsules, this transition can be also induced by the viscosity contrast between the cytosol and the suspending fluid, where the latter one is normally varied in experiments. Furthermore, a tank-treading

RBC is also subject to a swinging motion around the tank-treading inclination angle [146].

The first theoretical predictions of RBC dynamics [145,146] have been derived from the Keller–Skalak theory for vesicles [95] by adding an elastic energy barrier for the tank-treading motion. These theories have qualitatively captured the tumbling-to-tank-treading transition; however, at high enough viscosity contrast ($\lambda \gtrsim 3$–4) theoretical predictions led to a relatively wide region of an intermediate dynamics with a co-existence of both tumbling and tank-treading states. In contrast, experiments [146,153••] and numerical simulations [30,31•,34•,147,156] of RBC dynamics in shear flow have not provided any evidence for the existence of the intermittent region. Recent theories and simulations [136•,138] were able to resolve this issue and found that the prediction of the intermittent region in previous works has been due to the assumption of a fixed tank-treading path of RBCs. Thus, RBC deformation during tank-treading is important. There also exist breathing dynamics [156] around the tumbling-to-tank-treading transition, which is characterized by strong membrane deformation. Recent experiments [153••] and simulations [157] have shown the existence of another dynamical state called rolling, where a RBC just rolls in shear flow with the orientation along the vorticity direction. This transition has been attributed to anisotropic properties of a membrane leading to a rolling state, in which RBC deformations might be reduced. Finally, RBC simulations with a non-zero membrane viscosity [31•] have shown that this property might be essential to quantitatively capture RBC dynamics in shear flow.

RBCs in Poiseuille flow show rich behavior characterized by various shapes including parachutes and slippers [28,30,33,154,155,158–162•]. Parachutes correspond to a symmetric shape similar to a semi-spherical cap which flow in the center of a tube practically without any membrane motion. In contrast, slippers are asymmetric RBCs in tube flow whose membrane is in motion (e.g., tank-treading). There exist two types of slippers observed in experiments, a non-centered slipper [155] and a centered slipper [154], where the latter may closely resemble parachute shape. Slipper shapes have been also simulated using 2D [159•,161] and 3D models [162•].

2D simulations in slits [159•,161] have been used to predict a phase diagram of various shapes including parachutes, slippers, and a snaking dynamics, depending on RBC confinement and flow strength. The snaking dynamics is referred to an oscillating RBC dynamics near the tube center. Recent 3D simulations [162•] have also resulted in a diagram of RBC shapes in tube flow, which is only qualitatively similar to the diagram in 2D. Fig. 11 presents the RBC shape diagram in 3D for different flow rates and confinements. The parachute shape is mainly found at strong confinements and high flow rates, while off-center slippers are predominantly observed at low confinements. At low enough flow rates off-center tumbling RBCs are also found, which are due to the existence of the tumbling-to-tank-treading transition described above. This region is not present in 2D simulations [159•,161], since this transition cannot be captured by a 2D model. At small shear rates $\dot{\gamma}^*$, a snaking region is observed with a RBC performing a periodic oscillatory motion near the center line. However, in contrast to snaking in 2D [159•,161], the snaking motion in 3D is fully three dimensional and may have an orbital drift, which is similar to a RBC rolling motion in shear flow [153••,157]. Another prominent difference between the phase diagrams in Fig. 11 and in 2D simulations [159•,161] is the existence of the "confined slipper" in 2D at high confinements which is absent in 3D. Slippers at high confinements in 3D are suppressed due to the cylindrical shape of a tube, since a confined slipper would have to follow the wall curvature, which is energetically unfavorable.

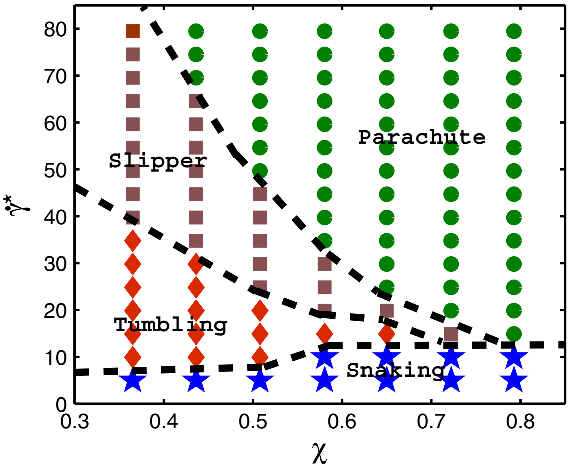

Fig. 11. A phase diagram of RBC shapes in tube flow for $Y_r = 18.9 \times 10^{-6}$ N/m, $\kappa_r = 3 \times 10^{-19}$ J, which correspond to average membrane properties of a healthy RBC. Various dynamic states, depending on the flow strength characterized by $\dot{\gamma}^*$ and the confinement χ, are depicted by symbols: parachute (green circles), slipper (brown squares), tumbling (red diamonds) and snaking (blue stars) discocyte. The phase-boundary lines are drawn approximately to guide the eye.
From Ref. [162•].

4.3.2. Blood rheology

Blood rheological characteristics are determined by the properties and dynamics of RBCs due to their high volume fraction or hematocrit. Blood rheology has been measured in a number of experiments [163–165]. Early experiments [163,166] have found that RBCs in whole blood (i.e., freshly drawn and stabilized against coagulation) are able to aggregate into structures called "rouleaux", which resemble stacks of coins. The aggregation between RBCs is mediated by the plasma proteins [166], which has been verified by an addition of fibrinogen to blood [166]. Rouleaux structures are very fragile and form at rest or at sufficiently slow flows. An increase of shear rate would lead to a break-up of the rouleaux structures resulting eventually in a fully dispersed RBC suspension. The aggregation process is reversible and rouleaux can re-form at low shear rates. Due to aggregation interactions between RBCs, whole blood shows a non-zero yield stress (a threshold stress for flow to begin) [163,167].

The viscosity of whole blood and of non-aggregating RBC suspension has been measured in experiments [163–165] and modeled in simulations [32•,168•]. Fig. 12 presents the comparison of the relative viscosity (the RBC suspension viscosity normalized by the viscosity of the suspending media) from simulations and experiments. Blood viscosity exhibits a shear-thinning behavior. A qualitatively similar behavior has been found for capsule suspensions [140•,141] and for a suspension of RBC-like particles [26,142,160]. Clearly, a tremendous increase of viscosity at low shear rates is due to the aggregation between RBCs. RBC aggregation has also been investigated for two-cell and multiple-cell aggregates [169,170] with a focus on their behavior in flow. The first attempts to estimate the dependence of viscosity on RBC aggregation [24] were not able to reproduce blood rheology due to a very small simulated system of up to ten aggregated RBCs.

Matching of the viscosity predictions in simulations [168•] with the experimental measurements [163–165] allows one to calibrate RBC aggregation interactions. Then, a step further is a direct calculation of aggregation forces between two RBCs, a property which has never been measured in experiments. Simulations [168•] predict that the force required for a break-up of two RBCs in the normal direction is in the range of 3.0 pN to 7 pN, while the tangential force needed for a sliding break-up is in the range of 1.5 pN to 3 pN. A fluid shear stress required for RBC disaggregation has been measured in shear flow experiments [171], and lies between 0.01 Pa and 0.1 Pa, while simulations result in a value of about 0.02 *Pa*.

Existence of a non-zero yield stress in whole blood is attributed to rouleaux structures [163,167]. A direct confirmation of yield stress is not possible in both experiments and simulations, and therefore,

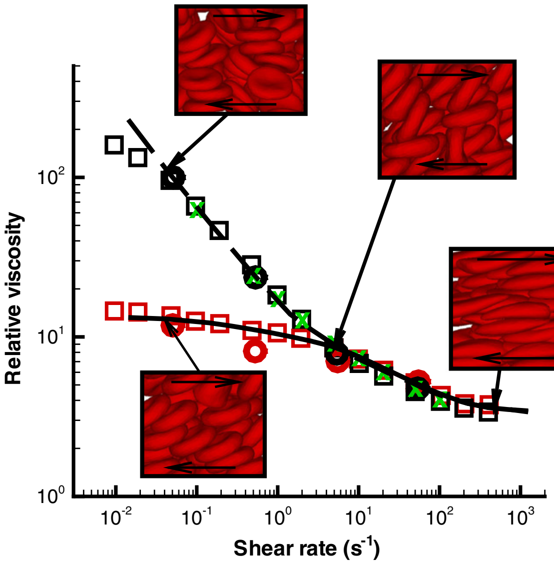

Fig. 12. Non-Newtonian relative viscosity (the cell suspension viscosity normalized by plasma viscosity) of whole blood as a function of shear rate at $H_t = 0.45$ and 37 °C: simulation results [168•] are shown as black full and dashed lines; experimental data are for: whole blood: green crosses — Merrill et al. [163]; black circles — Chien et al. [164], and black squares — Skalak et al. [165]. Non-aggregating RBC suspension: red circles — Chien et al. [164]; red squares — Skalak et al. [165].
From Ref. [149••].

available measurements are usually extrapolated to zero shear rate, which has been done, for example, for blood in Ref. [166]. The extrapolation for soft capsules and cells is often convenient to perform in the Casson coordinates $\left(\dot{\gamma}^{1/2}, \tau_{xy}^{1/2}\right)$, where $\dot{\gamma}$ is the shear rate and τ_{xy} is the shear stress [172]. Fig. 13 shows simulated data for $H_t = 0.45$ [168•] in Casson coordinates. Extrapolation to zero shear rate clearly results in a non-zero yield stress for whole blood, while for a non-aggregating RBC suspension yield stress vanishes. Simulations [168•] predict τ_y to be approximately 0.0017 Pa, while experimental measurements [163] lie between 0.0015 and 0.005 Pa. Yield stress in a RBC suspension may also exist at very high (non-physiological) hematocrit values [142].

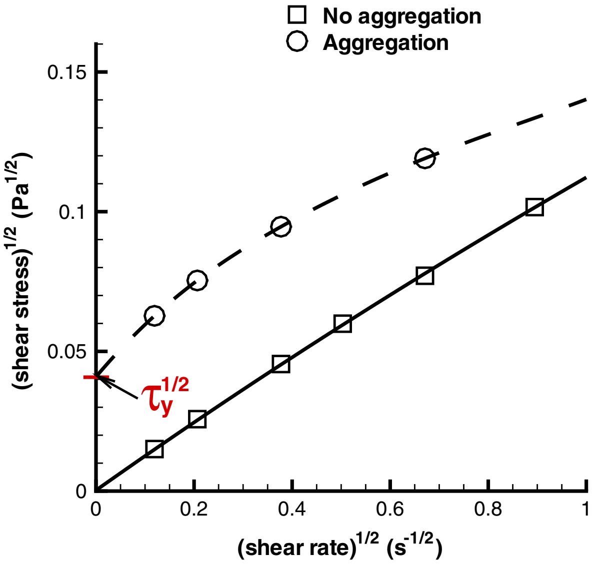

Fig. 13. RBC aggregation and yield stress. A Casson plot with a polynomial fit showing the extrapolated intercept τ_y for simulated suspensions with (dashed lines) and without (solid lines) aggregation at $H_t = 0.45$.
From Ref. [149••].

The non-Newtonian viscosity and yield stress in blood can be connected to RBC membrane properties, dynamics, and aggregation interactions. Measurements on a single cell level in a RBC suspension may be difficult or unfeasible in experiments, while simulations are ideal for that. The local microstructure of blood can be described by the radial distribution function (RDF) of RBC centers shown in Fig. 14(a) [168•]. No significant structures are found for the non-aggregating case, while structures of 2–4 cells can be detected in whole blood for low shear rates. However, any microstructure is completely lost at high shear rates, and therefore the shear-thinning of a non-aggregating RBC suspension is not related to microstructural changes. This also clearly indicates that the aggregation interactions between RBCs are responsible for the steep increase in blood viscosity at low shear rates and for yield stress, since larger rouleaux structures have to be destroyed for blood to flow.

Deformation and dynamics of single RBCs within the suspension is illustrated in Fig. 14(b) and (c) for different shear rates [168•]. Tumbling of RBCs at low shear rates is supported by the nearly constant RBC asphericity of about 0.154 (equilibrium value for a discocyte shape) and by the broad orientation-angle (θ) distribution in Fig. 14(c). Also, RBC tumbling is partially hindered in non-aggregating suspensions due to crowding in comparison with the theoretical prediction for tumbling of a single RBC. In contrast, RBC aggregation results in a nearly uniform orientation-angle distribution at low shear rates. At high shear rates, RBCs are subject to tank-treading dynamics supported by a narrow θ distribution in Fig. 14(c). A significant increase of the asphericity in Fig. 14(b) also indicates strong RBC elongation at high shear rates. In the range of shear rates, between 5 s^{-1} and 200 s^{-1}, RBCs strongly deform which is indicated by a smaller RBC asphericity than that in equilibrium (Fig. 14(b)). Thus, in this range RBCs attain on average a more spherical shape, which leads to shear thinning through a reduction of shear stresses due to lower tumbling constraints in comparison with the biconcave RBC shape. Moreover, the tumbling-to-tank-treading transition further decreases the shear stresses resulting in shear thinning.

4.3.3. Blood flow

Behavior of RBCs and blood rheological properties govern the flow of blood in microvessels. A well-known effect which describes a dependence of the apparent blood viscosity on vessel diameter is the Fahraeus–Lindqvist effect [173] which predicts a decrease in the effective blood resistance with decreasing tube diameter [174]. The apparent viscosity is found as

$$\eta_{app} = \frac{\pi \Delta P D^4}{128 Q L} = \frac{\Delta P D^2}{32 \overline{v} L}, \tag{11}$$

where D is the tube diameter, Q is the flow rate, and $\Delta P/L$ is the pressure gradient in a tube of length L. For convenience, we normalize the apparent viscosity by the plasma viscosity to obtain relative viscosity of blood as $\eta_{rel} = \eta_{app}/\eta_o$, where η_o is the plasma viscosity. Fig. 15 compares simulation results [175] against the empirical fit to experiments [174]. The Fahraeus–Lindqvist effect serves as one of the validation tests for blood flow models, and this test has been also performed in other scientific investigations [25,35,176•–178].

The Fahraeus–Lindqvist effect arises from the behavior of RBCs in blood flow. In Poiseuille flow, RBCs migrate to the tube center due to a hydrodynamic lift force [179]. The migration of RBCs yields a RBC free layer next to the wall, which effectively can reduce average blood flow resistance (or viscosity). Thus, the thickness of the RBC free layer is directly associated with the Fahraeus–Lindqvist effect. The RBC free

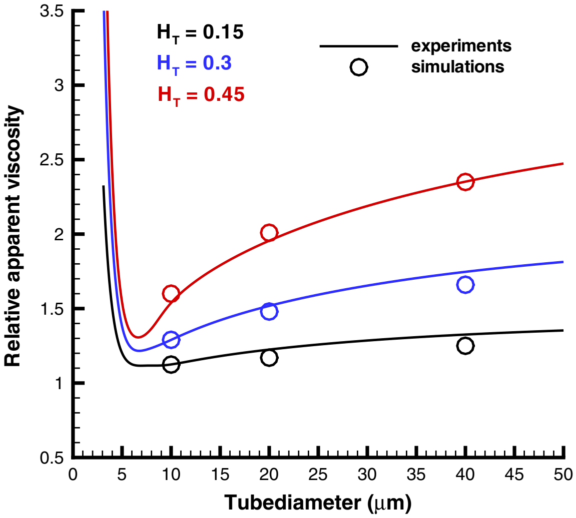

Fig. 15. Simulated relative apparent viscosity of blood [175] in comparison with experimental data [174] for different H_T values and tube diameters.
From Ref. [149••].

layer has been measured experimentally [180,181] and in simulations [35,175,176•–178].

The structure and dynamics of RBCs in blood flow have also been investigated in simulations [33,177,178]. In microcapillaries with a diameter comparable with the RBC size, RBCs may have a disordered configuration, form a train of parachutes, or get arranged into a zigzag structure [33,182,183], depending on their concentration and flow rate.

5. Discussion

The considerable amount of work on the dynamics and rheology of soft colloidal particles under flow has revealed both generic and very specific aspects of these systems. For example, two generic aspects are the tank-treading and tumbling motion of individual particles in solution, and the shear-thinning behavior of semi-dilute suspensions. Tank-treading occurs for star polymers, and for vesicles, soft capsules, and red blood cells with small viscosity contrast; tumbling motion is found for linear polymers, and for vesicles, stiff capsules, and red blood cells with large viscosity contrast. Shear thinning is related to the deformability and alignment of soft particles in flow, and the break-up of aggregates in the case of attractive interactions, and is therefore a property which is shared by all soft-particle suspensions.

However, many properties are quantitatively or qualitatively different, and are very specific for certain systems. For example, the control and variation of the viscosity of the internal fluid of vesicles, capsules and cells have no counterpart in polymeric systems. Therefore, the viscosity contrast can only be employed in the former case to tune rheological properties. A second example is the oscillatory dynamics at the

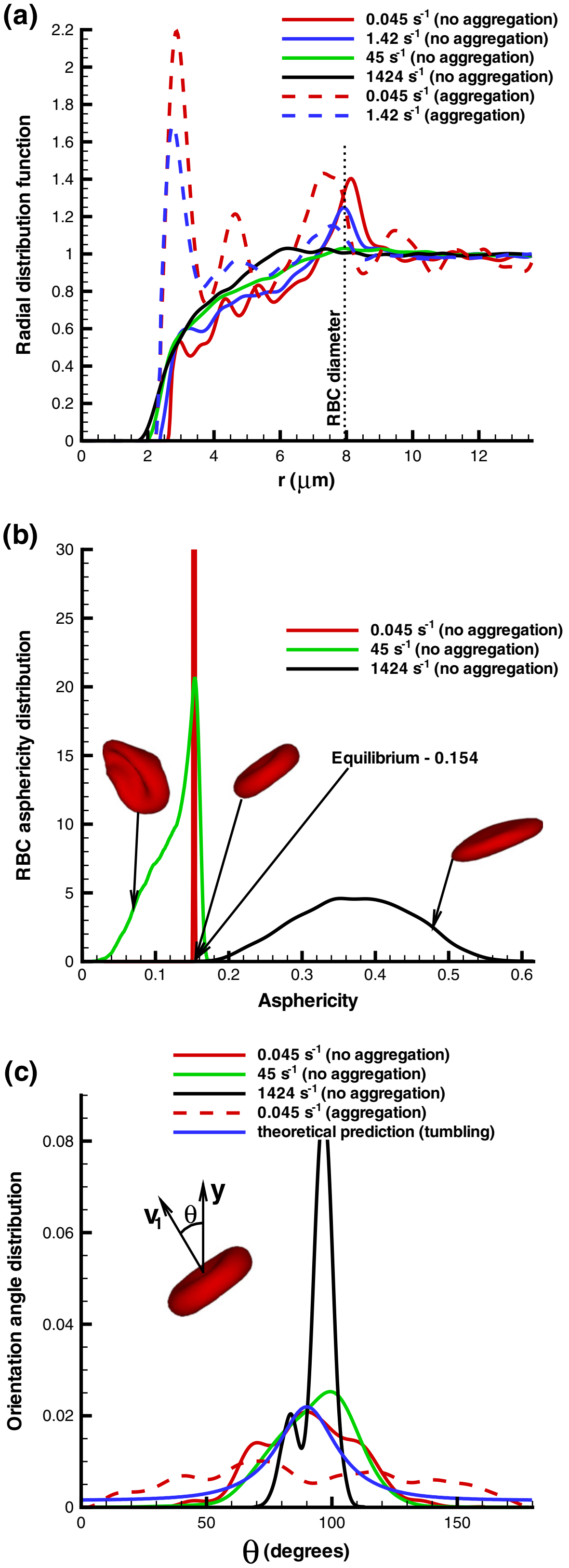

Fig. 14. Structural and dynamical properties of RBC suspension at $H_t = 0.45$ with sample snapshots of RBC conformations. (a) RBC suspension's structure characterized by the radial distribution function. (b) RBC asphericity distributions to describe cell deformations through the deviation from a spherical shape. The asphericity is defined as $[(\lambda_1-\lambda_2)^2+(\lambda_2-\lambda_3)^2+(\lambda_3-\lambda_1)^2]/(2R_g^4)$, where $\lambda_1 \le \lambda_2 \le \lambda_3$ are the eigenvalues of the gyration tensor and $R_g^2 = \lambda_1+\lambda_2+\lambda_3$. The asphericity for a RBC in equilibrium is equal to 0.154. (c) Orientational angle distributions for various shear rates. The RBC orientational angle is defined by the angle between the eigenvector V_1 of the gyration tensor and the flow-gradient direction (y). The theoretical prediction curve corresponds to the orientational angle distribution of a single tumbling RBC in shear flow calculated using the theory in Ref. [146].
From Ref. [168•].

boundary between tank-treading and tumbling, which is found for vesicles, capsules and red blood cells. In the former case, this is related to the dependence of the rotational force on the instantaneous elongation of the particle, while in the latter case it is due to the non-spherical, elastically anisotropic shape of the membrane. This strongly limits the use of vesicle models to describe the behavior of capsules and red blood cells!

However, the dependence of the dynamical and rheological properties of soft particle suspensions on several parameters like the polymer length, polymer stiffness, monomer density within macromolecules, internal viscosity, membrane bending rigidity, membrane shear modulus, particle shape, and particle interactions, offers entirely new possibilities for tuning flow properties. More work is needed in the future to explore the full application potential of these systems. This also requires deeper insights into the relation between microscopic properties and the emergent macroscopic behavior.

Acknowledgments

D.A.F. acknowledges funding by the Alexander von Humboldt Foundation (Sofja Kovalevskaja Award). G.G. and R.G.W. acknowledge financial support by the German Research Foundation (DFG) within SFB TR6 *Physics of Colloidal Dispersions in External Fields* as well as the EU through the FP7-Infrastructure Project ESMI (Grant No. 262348). We thank the Jülich Supercomputing Centre (JSC) at the Forschungszentrum Jülich for providing computer resources.

References•,••

[1] Einstein A. A new determination of molecular dimensions. Ann Phys 1906;19:289.

[2] Vermant J, Winter H. Special issue devoted to novel trends in rheology. Rheol Acta 2013;52:189. http://dx.doi.org/10.1007/s00397-013-0702-x.

[3] McNamara G, Zanetti G. Use of the Boltzmann equation to simulate lattice-gas automata. Phys Rev Lett 1988;61:2332.

[4] Shan X, Chen H. Lattice Boltzmann model for simulating flows with multiple phases and components. Phys Rev E 1993;47:1815. http://dx.doi.org/10.1103/PhysRevE.47.1815.

[5] He X, Luo LS. Theory of the lattice Boltzmann method: from the Boltzmann equation to the lattice Boltzmann equation. Phys Rev E 1997;56:6811. http://dx.doi.org/10.1103/PhysRevE.56.6811.

[6] Hoogerbrugge PJ, Koelman JMVA. Simulating microscopic hydrodynamics phenomena with dissipative particle dynamics. Europhys Lett 1992;19:155.

[7] Espanol P, Warren PB. Statistical-mechanics of dissipative particle dynamics. Europhys Lett 1995;30:191.

[8] Espanol P. Hydrodynamics from dissipative particle dynamics. Phys Rev E 1995;52:1734.

[9] Malevanets A, Kapral R. Mesoscopic model for solvent dynamics. J Chem Phys 1999;110:8605.

[10] Kapral R. Multiparticle collision dynamics: simulation of complex systems on mesoscales. Adv Chem Phys 2008;140:89.

[11] Gompper G, Ihle T, Kroll DM, Winkler RG. Multi-particle collision dynamics: a particle-based mesoscale simulation approach to the hydrodynamics of complex fluids. Adv Polym Sci 2009;221:1. http://dx.doi.org/10.1007/978-3-540-87706-6_1.

[12] Bird GA. Molecular gas dynamics and the direct simulation of gas flows. Oxford: Oxford University Press; 1994.

[13] Allahyarov E, Gompper G. Mesoscopic solvent simulations: multiparticle-collision dynamics of three-dimensional flows. Phys Rev E 2002;66:036702.

[14] Noguchi H, Kikuchi N, Gompper G. Particle-based mesoscale hydrodynamic techniques. EPL 2007;78:10005.

[15] Huang CC, Gompper G, Winkler RG. Hydrodynamic correlations in multiparticle collision dynamics fluids. Phys Rev E 2012;86:056711. http://dx.doi.org/10.1103/PhysRevE.86.056711.

[16] Winkler RG, Huang CC. Stress tensors of multiparticle collision dynamics fluids. J Chem Phys 2009;130:074907. http://dx.doi.org/10.1063/1.3077860.

[17] Huang CC, Chatterji A, Sutmann G, Gompper G, Winkler RG. Cell-level canonical sampling by velocity scaling for multiparticle collision dynamics simulations. J Comput Phys 2010;229:168. http://dx.doi.org/10.1016/j.jcp.2009.09.024.

[18] Bird RB, Curtiss CF, Armstrong RC, Hassager O. Dynamics of Polymer Liquids, vol. 2. New York: John Wiley & Sons; 1987.

[19] Jendrejack RM, de Pablo JJ, Graham MD. Stochastic simulations of DNA in flow: dynamics and the effects of hydrodynamic interactions. J Chem Phys 2002;116:7752.

[20] Öttinger HC. Stochastic processes in polymeric fluids. Berlin: Springer; 1996.

[21] Mussawisade K, Ripoll M, Winkler RG, Gompper G. Dynamics of polymers in a particle based mesoscopic solvent. J Chem Phys 2005;123:144905. http://dx.doi.org/10.1063/1.2041527.

[22•] Fedosov DA, Singh SP, Chatterji A, Winkler RG, Gompper G. Semidilute solutions of ultra-soft colloids under shear flow. Soft Matter 2012;8:4109. http://dx.doi.org/10.1039/c2sm07009j.
Simulation study of star polymers of low functionality in shear flow using mesoscale methods. Universal aspects in terms of concentration and shear rate are discussed for structural and rheological properties.

[23] Singh SP, Fedosov DA, Chatterji A, Winkler RG, Gompper G. Conformational and dynamical properties of ultra-soft colloids in semi-dilute solutions under shear flow. J Phys Condens Matter 2012;24:464103. http://dx.doi.org/10.1088/0953-8984/24/46/464103.

[24] Liu Y, Liu WK. Rheology of red blood cell aggregation by computer simulation. J Comp Physiol 2006;220:139–54.

[25] Doddi SK, Bagchi P. Three-dimensional computational modeling of multiple deformable cells flowing in microvessels. Phys Rev E 2009;79:046318.

[26] MacMeccan RM, Clausen JR, Neitzel GP, Aidun CK. Simulating deformable particle suspensions using a coupled lattice-Boltzmann and finite-element method. J Fluid Mech 2009;618:13–39.

[27] Gompper G, Kroll DM. Triangulated-surface models of fluctuating membranes. In: Nelson DR, Piran T, Weinberg S, editors. Statistical mechanics of membranes and surfaces. 2nd ed. Singapore: World Scientific; 2004. p. 359–426 (chap. 12).

[28] Noguchi H, Gompper G. Shape transitions of fluid vesicles and red blood cells in capillary flows. Proc Natl Acad Sci U S A 2005;102:14159–64.

[29] Dupin MM, Halliday I, Care CM, Alboul L, Munn LL. Modeling the flow of dense suspensions of deformable particles in three dimensions. Phys Rev E 2007;75:066707.

[30] Pivkin IV, Karniadakis GE. Accurate coarse-grained modeling of red blood cells. Phys Rev Lett 2008;101:118105.

[31•] Fedosov DA, Caswell B, Karniadakis GE. A multiscale red blood cell model with accurate mechanics, rheology, and dynamics. Biophys J 2010;98:2215–25.
A multiscale membrane model based on a network of springs, which incorporates viscoelastic properties, bending rigidity, and area and volume conservation. The model has been tested against a number of experiments on single red blood cells.

[32•] Reasor Jr DA, Clausen JR, Aidun CK. Rheological characterization of cellular blood in shear. J Fluid Mech 2013;726:497–516.
A three-dimensional numerical study of blood rheology. Shear rheology of blood has been investigated including shear-thinning, yield stress, and normal-stress differences.

[33] McWhirter JL, Noguchi H, Gompper G. Flow-induced clustering and alignment of vesicles and red blood cells in microcapillaries. Proc Natl Acad Sci U S A 2009;106:6039–43.

[34•] Peng Z, Li X, Pivkin IV, Dao M, Karniadakis GE, Suresh S. Lipid bilayer and cytoskeletal interactions in a red blood cell. Proc Natl Acad Sci USA 2013;110:13356–61.
A two layer membrane model representing separately a lipid bilayer and spectrin cytoskeleton of a red blood cell. The model allows for sliding and detachment of the two corresponding layers.

[35] Bagchi P. Mesoscale simulation of blood flow in small vessels. Biophys J 2007;92:1858–77.

[36] Bird RB, Armstrong RC, Hassager O. Dynamics of Polymer Liquids, vol. 1. New York: John Wiley & Sons; 1987.

[37•] Chen DT, Wen Q, Janmey PA, Crocker JC, Yodh AG. Rheology of soft materials. Annu Rev Condens Matter Phys 2010;1:301. http://dx.doi.org/10.1146/annurev-conmatphys-070909-104120.
Experimental approaches are reviewed, which are suitable for colloids, polymers, and cells. Special emphasis is on non-equilibrium aspects such as shear thinning.

[38] Bent J, Hutchings L, Richards R, Gough T, Spares R, Coates P, et al. Neutron-mapping polymer flow: scattering, flow visualization, and molecular theory. Science 2003;301:1691.

[39] Rubinstein M, Colby RC. Polymer physics. Oxford: Oxford University Press; 2003.

[40] Kröger M. Simple models for complex nonequilibrium fluids. Phys Rep 2004;390:453.

[41] Graham MD. Drag reduction in turbulent flow of polymer solutions. Rheol Rev 2004;2:143.

[42] Winkler RG, Singh SP, Huang CC, Fedosov DA, Mussawisade K, Chatterji A, et al. Mesoscale hydrodynamics simulations of particle suspensions under shear flow: from hard to ultrasoft colloids. Eur Phys J Spec Top 2013;222:2773. http://dx.doi.org/10.1140/epjst/e2013-02057-0.

[43•] Hajizadeh E, Todd BD, Daivis PJ. Nonequilibrium molecular dynamics simulation of dendrimers and hyperbranched polymer melts undergoing planar elongational flow. J Rheol 2014;58:281.
Numerical investigation of the universal rheological properties of hyperbranched polymers under elongational and shear flow, revealing a strong influence of branching on the shear thinning behavior.

[44] Liu L, Padding JT, den Otter WK, Briels WJ. Coarse-grained simulations of moderately entangled star polyethylene melts. J Chem Phys 2013;138:244912.

[45] Everaers R, Sukumaran SK, Grest GS, Svaneborg C, Sivasubramanian A, Kremer K. Rheology and microscopic topology of entangled polymeric liquids. Science 2004;303:823.

[46•] Winkler RG. Conformational and rheological properties of semiflexible polymers in shear flow. J Chem Phys 2010;133:164905. http://dx.doi.org/10.1063/1.3497642.
Theoretical investigation of semiflexible polymers in shear flow, linking the polymer dynamics with its rheological behavior.

[47•] Huang CC, Winkler RG, Sutmann G, Gompper G. Semidilute polymer solutions at equilibrium and under shear flow. Macromolecules 2010;43:10107. http://dx.doi.org/10.1021/ma101836x.
Simulation study of polymer suspensions by a mesoscale simulation approach, addressing the universal conformational and rheological properties in terms of shear rate and concentration.

• Of special interest.

•• Of outstanding interest.

[48] Huang CC, Sutmann G, Gompper G, Winkler RG. Tumbling of polymers in semidilute solution under shear flow. EPL 2011;93:54004. http://dx.doi.org/10.1209/0295-5075/93/54004.

[49] Huang CC, Gompper G, Winkler RG. Non-equilibrium properties of semidilute polymer solutions under shear flow. J Phys Conf Ser 2012;392:012003. http://dx.doi.org/10.1088/1742-6596/392/1/012003.

[50•] Huang CC, Gompper G, Winkler RG. Non-equilibrium relaxation and tumbling times of polymers in semidilute solution. J Phys: Condens Matter 2012;24:284131. http://dx.doi.org/10.1088/0953-8984/24/28/284131.
Simulation study of polymer suspensions by a mesoscale simulation approach. The non-equilibrium relaxation dynamics is analysed and linked to the tumbling behavior.

[51•] Singh SP, Chatterji A, Gompper G, Winkler RG. Dynamical and rheological properties of ultrasoft colloids under shear flow. Macromolecules 2013;46:8026. http://dx.doi.org/10.1021/ma401571k.
Mesoscale simulation study of star polymers of various functionalities in shear flow addressing universal aspects for structural, dynamical, and rheological properties.

[52] Smith DE, Babcock HP, Chu S. Single-polymer dynamics in steady shear flow. Science 1999;283:1724.

[53] LeDuc P, Haber C, Boa G, Wirtz D. Dynamics of individual flexible polymers in a shear flow. Nature 1999;399:564.

[54] Schroeder CM, Teixeira RE, Shaqfeh ESG, Chu S. Characteristic periodic motion of polymers in shear flow. Phys Rev Lett 2005;95:018301.

[55] Gerashchenko S, Steinberg V. Statistics of tumbling of a single polymer molecule in shear flow. Phys Rev Lett 2006;96:038304.

[56] Teixeira RE, Babcock HP, Shaqfeh ESG, Chu S. Shear thinning and tumbling dynamics of single polymers in the flow-gradient plane. Macromolecules 2005;38:581.

[57] Batchelor GK. An introduction to fluid mechanics. Cambridge: Cambridge University Press; 1990.

[58] Schroeder CM, Teixeira RE, Shaqfeh ESG, Chu S. Dynamics of DNA in the flow-gradient plane of steady shear flow: observations and simulations. Macromolecules 2005;38:1967.

[59•] Dalal SI, Albaugh A, Hoda N, Larson RG. Tumbling and deformation of isolated polymer chains in shearing flow. Macromolecules 2012;45:9493. http://dx.doi.org/10.1021/ma3014349.
Numerical analysis of the non-equilibrium conformational and dynamical properties of individual polymers up to extremely high shear rates by Brownian dynamics simulations.

[60] Delgado-Buscalioni R. Cyclic motion of a grafted polymer under shear flow. Phys Rev Lett 2006;96:088303.

[61] Zhang Y, Donev A, Weisgraber T, Alder BJ, Graham MG, de Pablo JJ. Tethered DNA dynamics in shear flow. J Chem Phys 2009;130:234902.

[62•] Kobayashi H, Yamamoto R. Tumbling motion of a single chain in shear flow: a crossover from Brownian to non-Brownian behavior. Phys Rev E 2010;81:041807.
Simulation study of the tumbling dynamics of polymers with emphasis on the influence of thermal fluctuations.

[63] Jefferey GB. The motion of ellipsoidal particles immersed in a viscous fluid. Proc R Soc London, Ser A 1922;102:161.

[64] Chertkov M, Kolokolov I, Lebedev A, Turitsyn K. Polymers statistics in a random flow with mean shear. J Fluid Mech 2005;531:251.

[65] Winkler RG. Semiflexible polymers in shear flow. Phys Rev Lett 2006;97:128301. http://dx.doi.org/10.1103/PhysRevLett.97.128301.

[66•] Usabiaga FB, Delgado-Buscalioni R. Characteristic times of polymer tumbling under shear flow. Macromol Theory Simul 2011;20:466.
Brownian dynamics simulation study of the tumbling dynamics of polymers.

[67] Petera D, Muthukumar M. Brownian dynamics simulation of beadrod chains under shear with hydrodynamic interaction. J Chem Phys 1999;111:7614.

[68] Sendner C, Netz RR. Single flexible and semiflexible polymers at high shear: non-monotonic and non-universal stretching response. Eur Phys J E 2009;30:75.

[69] Dhont JKG, Briels WJ. Rod-like Brownian particles in shear flow; chap. 3a. Weinheim: Wiley-VCH; 2007 147. http://dx.doi.org/10.1002/9783527617067.ch3b.

[70] Harasim M, Wunderlich B, Peleg O, Kröger M, Bausch AR. Direct observation of the dynamics of semiflexible polymers in shear flow. Phys Rev Lett 2013;110:108302. http://dx.doi.org/10.1103/PhysRevLett.110.108302.

[71] Lang PS, Obermayer B, Frey E. Dynamics of a semiflexible polymer or polymer ring in shear flow. Phys Rev E 2014;89:022606.

[72•] Huber B, Harasim M, Wunderlich B, Kröger M, Bausch AR. Microscopic origin of the non-Newtonian viscosity of semiflexible polymer solutions in the semidilute regime. ACS Macro Lett 2014;3:136.
Experimental study of the rheological properties of actin filaments in shear flow.

[73] Aust C, Kröger M, Hess S. Structure and dynamics of dilute polymer solutions under shear flow via nonequilibrium molecular dynamics. Macromolecules 1999;32:5660.

[74] Liu T. Flexible polymer chain dynamics and rheological properties in steady flows. J Chem Phys 1989;90:5826.

[75] Raspaud E, Lairez D, Adam M. On the number of blobs per entanglement in semidilute and good solvent solution: melt influence. Macromolecules 1995;28:927.

[76] Vlassopoulos D, Cloitre M. Tunable rheology of dense soft deformable colloids. Curr Opin Colloid Interface Sci 2014;19:561.

[77] Vlassopoulos D, Fytas G, Pakula T, Roovers J. Multiarm star polymers dynamics. J Phys Condens Matter 2001;13:R855.

[78] Castaing JC, Allain C, Auroy P, Auvray L, Pouchelon A. Nanosized hairy grains: a model system to understand the reinforcement. Europhys Lett 1996;36:153.

[79] Roovers J, Zhou LL, Toporowski PM, van der Zwan M, Iatrou H, Hadjichristidis N. Regular star polymers with 64 and 128 arms. Models for polymeric micelles. Macromolecules 1993;26:4324.

[80] Seghrouchni R, Petekidis G, Vlassopoulos D, Fytas G, Semenov AN, Roovers J, et al. Controlling the dynamics of soft spheres: from polymeric to colloidal behavior. Europhys Lett 1998;42:271.

[81] Grest GS, Kremer K, Witten TA. Structure of many-arm star polymers: a molecular dynamics simulation. Macromolecules 1987;20:1376.

[82] Grest GS, Kremer K, Milner ST, Witten TA. Relaxation of self-entangled many-arm star polymers. Macromolecules 1989;22:1904.

[83] Likos CN, Löwen H, Watzlawek M, Abbas B, Jucknischke O, Allgaier J, et al. Star polymers viewed as ultrasoft colloidal particles. Phys Rev Lett 1998;80:4450.

[84] Jusufi A, Watzlawek M, Löwen H. Effective interaction between star polymers. Macromolecules 1999;32:4470.

[85] Likos CN. Effective interactions in soft condensed matter physics. Phys Rep 2001;348:267.

[86] Fetters LJ, Kiss AD, Pearson DS, Quack GF, Vitus FJ. Rheological behavior of star-shaped polymers. Macromolecules 1993;26:647.

[87] Stellbrink J, Lonetti B, Rother G, Willner L, Richter D. Shear induced structures of soft colloids: Rheo-SANS experiments on kinetically frozen PEP-PEO diblock copolymer micelles. J Phys Condens Matter 2008;20:404206.

[88•] Vlassopoulos D, Fytas G. From polymers to colloids: engineering the dynamic properties of hairy particles. Adv Polym Sci 2010;236:1.
Review of the structural, dynamical, and rheological properties of star polymers.

[89] Ripoll M, Winkler RG, Gompper G. Star polymers in shear flow. Phys Rev Lett 2006;96:188302. http://dx.doi.org/10.1103/PhysRevLett.96.188302.

[90] Gupta S, Kundu SK, Stellbrink J, Willner L, Richter D. Advanced rheological characterization of soft colloidal model systems. J Phys Condens Matter 2012;24:464102.

[91] Pakula T, Vlassopoulos D, Fytas G, Roovers J. Structure and dynamics of melts of multiarm polymer stars. Macromolecules 1998;31:8931.

[92] Helgeson ME, Wagner NJ, Vlassopoulos D. Viscoelasticity and shear melting of colloidal star polymer glasses. J Rheol 2007;51:297.

[93] Erwin BM, Cloitre M, Gauthierd M, Vlassopoulos D. Dynamics and rheology of colloidal star polymers. Soft Matter 2010;6:2825.

[94] Ripoll M, Winkler RG, Gompper G. Hydrodynamic screening of star polymers in shear flow. Eur Phys J E 2007;23:349. http://dx.doi.org/10.1140/epje/i2006-10220-0.

[95] Keller SR, Skalak R. Motion of a tank-treading ellipsoidal particle in a shear flow. J Fluid Mech 1982;120:27.

[96] Kantsler V, Steinberg V. Orientation and dynamics of a vesicle in tank-treading motion in shear flow. Phys Rev Lett 2005;95:258101. http://dx.doi.org/10.1103/PhysRevLett.95.258101.

[97] Noguchi H, Gompper G. Swinging and tumbling of fluid vesicles in shear flow. Phys Rev Lett 2007;98:128103. http://dx.doi.org/10.1103/PhysRevLett.98.128103.

[98] Krüger M, Weysser F, Fuchs M. Tagged-particle motion in glassy systems under shear: comparison of mode coupling theory and Brownian dynamics simulations. Eur Phys J E 2011;34:88.

[99] Harrer CJ, Winter D, Horbach J, Fuchs M, Voigtmann T. Force-induced diffusion in microrheology. J Phys Condens Matter 2012;24:464105.

[100] Briels WJ, Vlassopoulos D, Kang K, Dhont JKG. Constitutive equations for the flow behavior of entangled polymeric systems: application to star polymers. J Chem Phys 2011;134:124901.

[101] Ballauff M, Likos CN. Dendrimers in solution: insight from theory and simulation. Angew Chem Int Ed 2004;43:2998. http://dx.doi.org/10.1002/anie.200300602.

[102•] Nikoubashman A, Likos CN. Branched polymers under shear. Macromolecules 2010;43:1610.
The universal conformational properties of model dendrimers are studied by mesoscale simulations.

[103] Bosko JT, Ravi Prakash J. Effect of molecular topology on the transport properties of dendrimers in dilute solution at Î˜ temperature: a Brownian dynamics study. J Chem Phys 2008;128:034902.

[104] Lyulin AV, Davies GR, Adolf DB. Brownian dynamics simulations of dendrimers under shear flow. Macromolecules 2000;33:3294.

[105] Noguchi H, Gompper G. Fluid vesicles with viscous membranes in shear flow. Phys Rev Lett 2004;93:258102. http://dx.doi.org/10.1103/PhysRevLett.93.258102.

[106] Noguchi H, Gompper G. Dynamics of fluid vesicles in shear flow: effect of membrane viscosity and thermal fluctuations. Phys Rev E 2005;72:011901. http://dx.doi.org/10.1103/PhysRevE.72.011901.

[107] Kantsler V, Steinberg V. Orientation and dynamics of a vesicle in tank-treading motion in shear flow. Phys Rev Lett 2005;95:258101.

[108] Kantsler V, Steinberg V. Transition to tumbling and two regimes of tumbling motion of a vesicle in shear flow. Phys Rev Lett 2006;96:036001.

[109] Misbah C. Vacillating breathing and tumbling of vesicles under shear flow. Phys Rev Lett 2006;96:028104.

[110] Noguchi H, Gompper G. Swinging and tumbling of fluid vesicles in shear flow. Phys Rev Lett 2007;98:128103. http://dx.doi.org/10.1103/PhysRevLett.98.128103.

[111] Lebedev VV, Turitsyn KS, Vergeles SS. Dynamics of nearly spherical vesicles in an external flow. Phys Rev Lett 2007;99:218101.

[112] Vlahovska PM, Gracia RS. Dynamics of a viscous vesicle in linear flows. Phys Rev E 2007;75:016313.

[113] Messlinger S, Schmidt B, Noguchi H, Gompper G. Dynamical regimes and hydrodynamic lift of viscous vesicles under shear. Phys Rev E 2009;80:011901. http://dx.doi.org/10.1103/PhysRevE.80.011901.

[114] Zhao H, Shaqfeh ESG. The dynamics of a vesicle in simple shear flow. J Fluid Mech 2011;674:578–604.

[115] Abreu D, Levant M, Steinberg V, Seifert U. Fluid vesicles in flow. Adv Colloid Interface Sci 2014;208:129–41.
A comprehensive review of the dynamics of fluid vesicles in shear and capillary flow, with emphasis on tumbling, tank-treading, trembling and wrinkling of single vesicles.

[116] Danker G, Misbah C. Rheology of a dilute suspension of vesicles. Phys Rev Lett 2007;98:088104.

[117] Danker G, Biben T, Podgorski T, Verdier C, Misbah C. Dynamics and rheology of a dilute suspension of vesicles: higher-order theory. Phys Rev E 2007;76:041905.

[118] Ghigliotti G, Biben T, Misbah C. Rheology of a dilute two-dimensional suspension of vesicles. J Fluid Mech 2010;653:489.

[119] Vitkova V, Mader MA, Polack B, Misbah C, Podgorski T. Micro-macro link in rheology of erythrocyte and vesicle suspensions. Biophys J 2008;95:L33–5.

[120] Kantsler V, Segre E, Steinberg V. Dynamics of interacting vesicles and rheology of vesicle suspension in shear flow. EPL 2008;82:58005.

[121] Levant M, Deschamps J, Afik E, Steinberg V. Characteristic spatial scale of vesicle pair interactions in a plane linear flow. Phys Rev E 2012;85:056306.

[122•] Lamura A, Gompper G. Dynamics and rheology of vesicle suspensions in wall-bounded shear flow. EPL 2013;102:28004. http://dx.doi.org/10.1209/0295-5075/102/28004.
Numerical study of two-dimensional vesicle suspension in shear flow, using meso-scale hydrodynamics simulations to investigate vesicle interactions in the presence of thermal noise.

[123] Thiébaud M, Misbah C. Rheology of a vesicle suspension with finite concentration: a numerical study. Phys Rev E 2013;88:062707.

[124] Thiébaud M, Shen Z, Harting J, Misbah C. Prediction of anomalous blood viscosity in confined shear flow. Phys Rev Lett 2014;112:238304.

[125•] Zhao H, Shaqfeh ESG. The dynamics of a non-dilute vesicle suspension in a simple shear flow. J Fluid Mech 2013;725:709–31.
Numerical study using the boundary-integral method in three dimensions of vesicle suspension in shear flow to investigate vesicle dynamics and interactions, as well as rheology, in the absence of thermal noise.

[126•] Levant M, Steinberg V. Amplification of thermal noise by vesicle dynamics. Phys Rev Lett 2012;109:268103.
Experimental study of the interplay of thermal membrane fluctuations, trembling dynamics, and flow-induced wrinkling.

[127] Abreu D, Seifert U. Effect of thermal noise on vesicles and capsules in shear flow. Phys Rev E 2012;86:010902(R).

[128•] Abreu D, Seifert U. Noisy nonlinear dynamics of vesicles in flow. Phys Rev Lett 2013;110:238103.
Theoretical study of quasi-spherical vesicles in shear flow close to the tumbling-to-tank-treading transition, which shows strong sensitivity to the thermal fluctuations.

[129] Lázaro GR, Hernández-Machadoa A, Pagonabarraga I. Rheology of red blood cells under flow in highly confined microchannels: I. effect of elasticity. Soft Matter 2014;10:7195–206.

[130] Lázaro GR, Hernández-Machadoa A, Pagonabarraga I. Rheology of red blood cells under flow in highly confined microchannels. II. effect of focusing and confinement. Soft Matter 2014;10:7207–17.

[131] Chang KS, Olbricht WL. Experimental studies of the deformation and breakup of a synthetic capsule in steady and unsteady simple shear flow. J Fluid Mech 1993;250:609–33.

[132] Walter A, Rehage H, Leonhard H. Shear-induced deformations of polyamide microcapsules. Colloid Polym Sci 2000;278:169–75.

[133] Walter A, Rehage H, Leonhard H. Shear induced deformation of microcapsules: shape oscillations and membrane folding. Colloids Surf A 2001;183–185:123–32.

[134] Barthés-Biesel D. Mechanics of encapsulated droplets. Progr Colloid Polym Sci 1998;111:58–64.

[135] Finken R, Seifert U. Wrinkling of microcapsules in shear flow. J Phys Condens Matter 2006;18:L185–91.

[136•] Vlahovska PM, Young YN, Danker G, Misbah C. Dynamics of a non-spherical microcapsule with incompressible interface in shear flow. J Fluid Mech 2011;678:221–47.
A theory for capsule dynamics in shear flow. The analysis takes into account the membrane fluidity, area-incompressibility, and bending resistance.

[137] Ramanujan S, Pozrikidis C. Deformation of liquid capsules enclosed by elastic membranes in simple shear flow: large deformations and the effect of fluid viscosities. J Fluid Mech 1998;361:117–43.

[138] Finken R, Kessler S, Seifert U. Micro-capsules in shear flow. J Phys Condens Matter 2011;23:184113.

[139] Lac E, Barthés-Biesel D. Deformation of a capsule in simple shear flow: effect of membrane prestress. Phys Fluids 2005;17:072105.

[140•] Bagchi P, Kalluri RM. Dynamic rheology of a dilute suspension of elastic capsules: effect of capsule tank-treading, swinging and tumbling. J Fluid Mech 2011;669:498–526.
A numerical study of rheology of a dilute suspension of capsules. Effects of viscosity ratio between internal and external fluids, shear rate, and surface-area dilatation on the rheology of capsule suspension have been considered.

[141] Clausen JR, Reasor Jr DA, Aidun CK. The rheology and microstructure of concentrated non-colloidal suspensions of deformable capsules. J Fluid Mech 2011;685:202–34.

[142] Gross M, Krüger T, Varnik F. Rheology of dense suspensions of elastic capsules: normal stresses, yield stress, jamming and confinement effects. Soft Matter 2014;10:4360–72.

[143•] Krüger T, Kaoui B, Harting J. Interplay of inertia and deformability on rheological properties of a suspension of capsules. J Fluid Mech 2014;751:725–45.
A three-dimensional numerical study of the rheology of capsule suspension, with emphasis on the effects of inertia and capsule deformability. Viscosity and suspension microstructure have been investigated.

[144] Chang KS, Olbricht WL. Experimental studies of the deformation of a synthetic capsule in extensional flow. J Fluid Mech 1993;250:581–608.

[145] Skotheim JM, Secomb TW. Red blood cells and other nonspherical capsules in shear flow: oscillatory dynamics and the tank-treading-to-tumbling transition. Phys Rev Lett 2007;98:078301.

[146] Abkarian M, Faivre M, Viallat A. Swinging of red blood cells under shear flow. Phys Rev Lett 2007;98:188302.

[147] Noguchi H. Dynamic modes of microcapsules in steady shear flow: effects of bending and shear elasticities. Phys Rev E 2010;81:056319.

[148] Li X, Vlahovska PM, Karniadakis GE. Continuum- and particle-based modeling of shapes and dynamics of red blood cells in health and disease. Soft Matter 2013;9:28–37.

[149•] Fedosov DA, Noguchi H, Gompper G. Multiscale modeling of blood flow: from single cells to blood rheology. Biomech Model Mechanobiol 2014;13:239–58.
A comprehensive review of modeling single cells and their suspensions in flow, with emphasis on the behavior of red blood cells in flow and on blood flow in health and disease.

[150•] Freund JB. Numerical simulation of flowing blood cells. Annu Rev Fluid Mech 2014;46:67–95.
A comprehensive review of modeling red blood cells and blood flow, with emphasis on different methods for modeling fluid flow, cell membrane deformation, and their coupling.

[151] Fedosov DA, Dao M, Karniadakis GE, Suresh S. Computational biorheology of human blood flow in health and disease. Ann Biomed Eng 2014;42:368–87.

[152] Fischer TM. Shape memory of human red blood cells. Biophys J 2004;86:3304–13.

[153••] Dupire J, Socol M, Viallat A. Full dynamics of a red blood cell in shear flow. Proc Natl Acad Sci U S A 2012;109:20808–13.
An experimental study of red blood cell dynamics in shear flow. The paper describes different dynamic states of a red blood cell including tumbling, tank-treading, and rolling and the transitions between them.

[154] Abkarian M, Faivre M, Horton R, Smistrup K, Best-Popescu CA, Stone HA. Cellular-scale hydrodynamics. Biomed Mater 2008;3:034011.

[155] Tomaiuolo G, Simeone M, Martinelli V, Rotoli B, Guido S. Red blood cell deformation in microconfined flow. Soft Matter 2009;5:3736–40.

[156] Yazdani AZK, Bagchi P. Phase diagram and breathing dynamics of a single red blood cell and a biconcave capsule in dilute shear flow. Phys Rev E 2011;84:026314.

[157] Cordasco D, Bagchi P. Orbital drift of capsules and red blood cells in shear flow. Phys Fluids 2013;25:091902.

[158] Gaehtgens P, Dührssen C, Albrecht KH. Motion, deformation, and interaction of blood cells and plasma during flow through narrow capillary tubes. Blood Cells 1980;6:799–812.

[159•] Kaoui B, Tahiri N, Biben T, Ez-Zahraouy H, Benyoussef A, Biros G, et al. Complexity of vesicle microcirculation. Phys Rev E 2011;84:041906.
A two-dimensional numerical study of a red blood cell in Poiseuille flow. The study considers a wide range of flow rates and cell confinements leading to a phase diagram of different shapes including parachutes and slippers.

[160] Reasor Jr DA, Clausen JR, Aidun CK. Coupling the lattice-Boltzmann and spectrin-link methods for the direct numerical simulation of cellular blood flow. Int J Numer Methods Fluids 2012;68:767–81.

[161] Tahiri N, Biben T, Ez-Zahraouy H, Benyoussef A, Misbah C. On the problem of slipper shapes of red blood cells in the microvasculature. Microvasc Res 2013;85:40–5.

[162•] Fedosov DA, Peltomäki M, Gompper G. Deformation and dynamics of red blood cells in flow through cylindrical microchannels. Soft Matter 2014;10:4258–67.
A three-dimensional numerical study of a red blood cell in Poiseuille flow. The study encompasses a wide range of flow rates, cell confinements and properties resulting in several phase diagrams of red blood cell shapes and its different dynamic states.

[163] Merrill EW, Gilliland ER, Cokelet G, Shin H, Britten A, Wells Jr RE. Rheology of human blood near and at zero flow. Effects of temperature and hematocrit level. Biophys J 1963;3:199–213.

[164] Chien S, Usami S, Taylor HM, Lundberg JL, Gregersen MI. Effects of hematocrit and plasma proteins on human blood rheology at low shear rates. J Appl Physiol 1966;21:81–7.

[165] Skalak R, Keller SR, Secomb TW. Mechanics of blood flow. J Biomech Eng 1981;103:102–15.

[166] Merrill EW, Gilliland ER, Lee TS, Salzman EW. Blood rheology: effect of fibrinogen deduced by addition. Circ Res 1966;18:437–46.

[167] Copley AL, Huang CR, King RG. Rheogoniometric studies of whole human blood at shear rates from 1,000–0.0009 sec^{-1}. Part I. Experimental findings. Biorheology 1973;10:17–22.

[168•] Fedosov DA, Pan W, Caswell B, Gompper G, Karniadakis GE. Predicting human blood viscosity in silico. Proc Natl Acad Sci U S A 2011;108:11772–7.
A three-dimensional numerical study of blood rheology. Non-Newtonian viscosity and yield stress of blood have been investigated with the correspondence to the microstructure of red blood cell suspension and dynamics of single cells.

[169] Bagchi P, Johnson PC, Popel AS. Computational fluid dynamic simulation of aggregation of deformable cells in a shear flow. J Biomech Eng 2005;127:1070–80.

[170] Wang T, Pan TW, Xing ZW, Glowinski R. Numerical simulation of rheology of red blood cell rouleaux in microchannels. Phys Rev E 2009;79:041916.

[171] Chien S, Sung LA, Kim S, Burke AM, Usami S. Determination of aggregation force in rouleaux by fluid mechanical technique. Microvasc Res 1977;13:327–33.

[172] Casson N. Rheology of disperse systems. New York: Pergamon Press; 1992.
[173] Fåhraeus R, Lindqvist T. The viscosity of the blood in narrow capillary tubes. Am J Physiol 1931;96:562–8.
[174] Pries AR, Neuhaus D, Gaehtgens P. Blood viscosity in tube flow: dependence on diameter and hematocrit. Am J Physiol 1992;263:H1770–8.
[175] Fedosov DA, Caswell B, Popel AS, Karniadakis GE. Blood flow and cell-free layer in microvessels. Microcirculation 2010;17:615–28.
[176] • Freund JB, Orescanin MM. Cellular flow in a small blood vessel. J Fluid Mech 2011; 671:466–90.
A three-dimensional numerical study of blood flow in microtubes. Apparent blood viscosity, the development of red-blood-cell-free layer, and cell deformation in tube flow have been studied.
[177] Alizadehrad D, Imai Y, Nakaaki K, Ishikawa T, Yamaguchi T. Quantification of red blood cell deformation at high-hematocrit blood flow in microvessels. J Biomech 2012;45:2684–9.
[178] Lei H, Fedosov DA, Caswell B, Karniadakis GE. Blood flow in small tubes: quantifying the transition to the non-continuum regime. J Fluid Mech 2013;722: 214–39.
[179] Abkarian M, Lartigue C, Viallat A. Tank treading and unbinding of deformable vesicles in shear flow: determination of the lift force. Phys Rev Lett 2002;88:068103.
[180] Maeda N, Suzuki Y, Tanaka J, Tateishi N. Erythrocyte flow and elasticity of microvessels evaluated by marginal cell-free layer and flow resistance. Am J Physiol 1996;271:H2454–61.
[181] Kim S, Kong RL, Popel AS, Intaglietta M, Johnson PC. Temporal and spatial variations of cell-free layer width in arterioles. Am J Physiol 2007;293: H1526–35.
[182] McWhirter JL, Noguchi H, Gompper G. Deformation and clustering of red blood cells in microcapillary flows. Soft Matter 2011;7:10967. http://dx.doi.org/10.1039/C1SM05794D.
[183] McWhirter JL, Noguchi H, Gompper G. Ordering and arrangement of deformed red blood cells in flows through microcapillaries. New J Phys 2012;14:085026. http://dx.doi.org/10.1088/1367-2630/14/8/085026.

P5: Margination of micro- and nano-particles in blood flow and its effect on drug delivery

K. Müller, D. A. Fedosov, and G. Gompper

Scientific Reports, **4**:4871, 2014.

SCIENTIFIC REPORTS

OPEN

SUBJECT AREAS:
FLUID DYNAMICS
BIOLOGICAL PHYSICS
COMPUTATIONAL BIOPHYSICS

Margination of micro- and nano-particles in blood flow and its effect on drug delivery

Kathrin Müller, Dmitry A. Fedosov & Gerhard Gompper

Theoretical Soft Matter and Biophysics, Institute of Complex Systems and Institute for Advanced Simulation, Forschungszentrum Jülich, 52425 Jülich, Germany.

Received
20 February 2014

Accepted
10 April 2014

Published
2 May 2014

Correspondence and requests for materials should be addressed to D.A.F. (d.fedosov@fz-juelich.de)

Drug delivery by micro- and nano-carriers enables controlled transport of pharmaceuticals to targeted sites. Even though carrier fabrication has made much progress recently, the delivery including controlled particle distribution and adhesion within the body remains a great challenge. The adhesion of carriers is strongly affected by their margination properties (migration toward walls) in the microvasculature. To investigate margination characteristics of carriers of different shapes and sizes and to elucidate the relevant physical mechanisms, we employ mesoscopic hydrodynamic simulations of blood flow. Particle margination is studied for a wide range of hematocrit values, vessel sizes, and flow rates, using two- and three-dimensional models. The simulations show that the margination properties of particles improve with increasing carrier size. Spherical particles yield slightly better margination than ellipsoidal carriers; however, ellipsoidal particles exhibit a slower rotational dynamics near a wall favoring their adhesion. In conclusion, micron-sized ellipsoidal particles are favorable for drug delivery in comparison with sub-micron spherical particles.

The use of targeted micro- and nano-carriers for the delivery of imaging agents and drugs provides a promising strategy for early detection and treatment of diseases, e.g., of cancer[1,2]. However, the design of particles carrying different contrast agents and drugs as well as their physical delivery are very challenging tasks. Micro- and nano-particle fabrication, which needs to address several issues such as bio-compatibility, durability, binding to specific targets, and the ability of controlled release, has been strongly advanced in recent years[3–7]. Nevertheless, the development of efficient strategies for the delivery of carriers, including their distribution in the organism following systemic administration[8] and their transport through biological barriers[8–10] (e.g., microvascular walls, interstitial space, and cell membranes), requires a much more detailed understanding of the relevant physical and biological mechanisms[2,8,11,12].

Successful delivery of micro- and nano- carriers strongly depends on their efficient binding to specific targeted sites. Consequently, the distribution of carriers within vessel cross-sections plays an important role, since binding of carriers is only possible in case of direct particle-wall interactions. The cross-sectional distribution of micro- and nano-particles depends on several relevant parameters, which concern blood flow properties (such as flow rate, red blood cell deformability, and hematocrit – the volume fraction of red blood cells), vessel size, and particle characteristics (such as size, shape, and deformability). The migration of various suspended particles or cells toward walls in blood flow, which is often referred to as *margination*, has been observed experimentally for white blood cells[13,14], platelets[15,16], and rigid micro-particles[17,18]. Particle margination is mediated by red blood cells (RBCs), which migrate to the vessel center[19] due to hydrodynamic interactions with the walls (called lift force)[20,21] leading to a RBC-free layer near the walls. More precisely, the occurrence of margination is a consequence of the competition between lift forces on RBCs and suspended particles, and their interactions in flow[22]. However, the dependence of margination efficiency on particle size and shape remains largely unexplored so far.

The role of particle size and shape in the efficient delivery is a multi-faceted problem. Large enough particles with a characteristic diameter (D_p) greater than about 4 µm may become trapped in the smallest capillaries of the body[23]. In addition, recent experiments suggest that large particles with $D_p \gtrsim 3$ µm are subject to an enhanced phagocytosis[24]. However, recent microfluidic experiments[25] have shown that spheres with the size of 2 µm show a significantly higher adhesion density than particles with a size of 200 nm and 500 nm. Other experiments[26] indicate that liposomes with $D_p < 70$ nm and $D_p > 300$ nm have shorter circulation times than those having an intermediate size of $D_p \approx 150$–200 nm. Furthermore, nano-particles with a size below 20–30 nm are rapidly excreted through the kidneys[27]. Experiments with discoidal particles[28] have shown that they accumulate in the organs better than their spherical counterparts; however, particle internalization by macrophages appears to be worse for elongated particles[29]. Adhesion of different particles has been studied experimentally[30,31] and theoretically[32,33], with the result that oblate ellipsoids are subject to stronger adhesion than spheres with the same volume. To better understand the adhesion potential of micro- and nano-particles, a quantitative description of particle margination under realistic blood flow conditions is required.

In this work, we investigate the role of particle size and shape on the margination efficiency, and therefore on their adhesion potential. Several sizes ranging from about hundred nanometers to a few micrometers and two different shapes (spherical and ellipsoidal) are considered. The margination of micro- and nano-particles is studied numerically for a wide range of hematocrit values, vessel sizes, and flow rates using a combination of two-dimensional (2D) and three-dimensional (3D) models. Our results indicate that large particles possess a larger probability of being marginated than small particles. As the particle size becomes very small (less than about 100–200 nm), the particle distribution within vessel cross-section can be described well by the plasma volume around flowing RBCs. Furthermore, spherical particles marginate better than ellipsoids, however the adhesion efficiency of ellipsoidal particles is expected to be superior in comparison to that of spheres due to their slower rotational dynamics near a wall. Finally, we discuss what size and shape of micro- and nano-carriers may be best suited for biomedical applications.

Results

Blood is modeled as a suspension of RBCs and micro- or nano-particles, while blood flow is studied in idealized microvessels using simulations in 2D and 3D, see Fig. 1 and Methods section for details. The 3D blood model has been shown to properly capture essential properties of blood flow in microchannels[34] as well as blood rheological characteristics[35,36]. To study micro- and nano-particle margination for a wide range of conditions, we also exploit a 2D blood flow model due to its numerical efficiency; however, we will show that the 2D model is able to qualitatively reproduce the required blood flow characteristics and the particle margination effect in comparison with the 3D model.

Blood flow characteristics. The simulated system corresponds to a cylindrical microvessel in 3D with the diameter W or to a channel in 2D with the width W. We focus here on channel width $W = 20$ µm, but the cases of $W = 10$ µm and $W = 40$ µm are also discussed. In flow direction, periodic boundary conditions are assumed and blood flow is driven by a constant force applied to all solvent particles, which is equivalent to a prescribed pressure drop. The hematocrit H_t is defined as the volume fraction of RBCs. To characterize the flow strength, we define a non-dimensional shear rate in both 2D and 3D as

$$\dot{\gamma}^* = \bar{\dot{\gamma}}\tau = \bar{\dot{\gamma}}\frac{\eta D_r^3}{\kappa_r}, \qquad (1)$$

where $\bar{\dot{\gamma}} = \bar{v}/W$ is the average shear rate (or pseudo shear rate) and $\bar{v}$ is the average flow velocity computed from the flow rate, while τ defines a characteristic RBC relaxation time. Here, η is the solvent's dynamic viscosity, $D_r = \sqrt{A_0/\pi}$ in 3D and $D_r = L_0/\pi$ in 2D are the corresponding RBC diameters, where A_0 is the RBC surface area in 3D and L_0 is the cell contour length in 2D, and κ_r is the RBC membrane bending rigidity. The RBCs are further characterized in 2D by the reduced area $A^* = 4A_0/\left(\pi D_r^2\right) = 0.46$, and in 3D by the reduced volume $V^* = 6V_0/\left(\pi D_r^3\right) = 0.64$, where A_0 is enclosed RBC area in 2D and V_0 is the enclosed RBC volume in 3D. Typical values for healthy RBCs are $D_r = 6.5$ µm in 3D, while $D_r = 6.1$ µm in 2D, $\eta = 1.2 \times 10^{-3}$ Pa s, and κ_r lies within the range of 50–70k_BT for the physiological temperature $T = 37$°C. Suspended micro- and nano-particles are characterized by the diameter for spheres and by the long axis for disks, denoted D_p in both cases.

Particle margination in 2D and 3D. Margination of micro- and nano-particles in blood flow depends on H_t, W, and $\dot{\gamma}^*$. Figures 2(a),(b) illustrate the distribution of carriers of size $D_p = 0.28D_r$ (1.83 µm) for two H_t values in 3D. For better visibility, the carrier positions from a few snapshots are superimposed in the plot. The carrier surfaces are colored according to their radial position in the channel, with yellow color indicating a position near the channel center, while blue color corresponds to a position near the wall. Clearly, the carriers are marginating better for the case of larger H_t.

Carrier positions in blood flow sampled over time lead to particle distributions, which reflect the probability of a particle to be at a certain distance from the wall. Figure 2(c) shows several center-of-mass distributions of circular particles in 2D with $D_p = 0.3D_r$ (1.83 µm) for several H_t values and $\dot{\gamma}^* \approx 29.3$. The RBC-free layer (RBCFL) thickness, which is computed from simulation snapshots through the analysis of the RBC core boundary[34] similar to experimental measurements[37] (see Supplementary Fig. S1), is depicted by small arrows. The distributions have been averaged over the halves of the channel due to symmetry. Figure 2 shows that the carriers migrate into the RBCFL and remain quasi-trapped there. With increasing H_t, the carriers marginate better, as indicated by the development of a strong peak in the distribution near the wall at $y/W = 0$, and the motion of the peak position towards the wall. This is due to a decrease in the RBCFL thickness leading to a smaller available space for the particles. This trend is in agreement with experimental observations[17] and simulations[38–40] of margination of blood platelets, which have a comparable size.

To quantify and compare particle margination for a wide range of flow and particle parameters, we define the margination probability as a fraction of particles whose center-of-mass is located within the near-wall layer of thickness δ. The choice of δ depends on the exact problem to be addressed, and several possibilities can be considered. To describe particle margination into the vicinity of a vessel wall, it is natural to select δ to be the RBCFL thickness. Typical values of RBCFL thickness and their dependence on H_t are displayed in Supplementary Fig. S2. Figures 3(a),(b) present margination probability diagrams of particles for a wide range of H_t and $\dot{\gamma}^*$ values corresponding to 3D and 2D simulations, respectively; the comparison shows that roughly $\dot{\gamma}^*_{3D} \approx 1.2\dot{\gamma}^*_{2D}$. Particle margination strongly depends on H_t as well as on shear rate. At low H_t values, particle margination is expected to be weak, while at high H_t the margination might be also attenuated due to particle-RBC interactions near a wall. The latter effect has been described for a marginating white blood

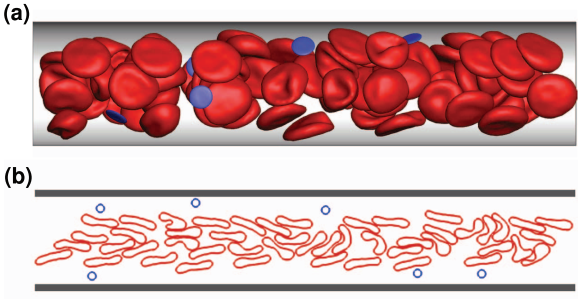

Figure 1 | Snapshots of cell and particle conformations in microchannels in 3D and 2D. RBCs are colored in red and suspended particles in blue. (a) 3D simulation snapshot of blood flow for $H_t = 0.3$ and $\dot{\gamma}^* \approx 39$. (b) 2D simulation snapshot of blood flow for $H_t = 0.3$ and $\dot{\gamma}^* \approx 29.3$.

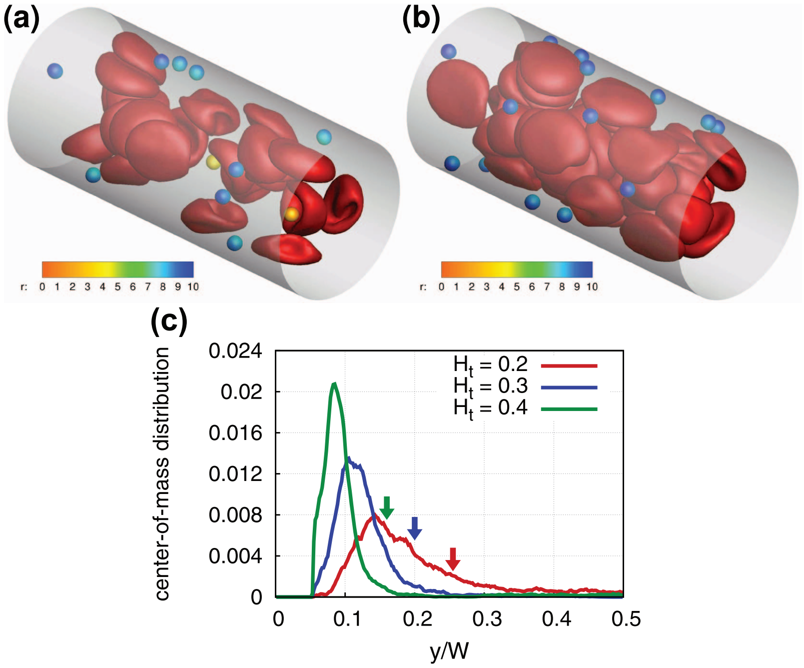

Figure 2 | **Particle distributions in blood flow.** Illustrations of 3D simulations of blood flow for the shear rate of $\dot{\gamma}^* \approx 59$ and different hematocrit values (a) $H_t = 0.2$ and (b) $H_t = 0.4$. RBCs are drawn in red, while spherical carriers with a size of $D_p = 0.28D_r$ (1.83 μm) are colored according to their radial position r. For better contrast, carrier positions from several time instances are superimposed in the plots. (c) Center-of-mass distributions of carriers for various H_t values at $\dot{\gamma}^* \approx 29.3$. 2D simulation results for circular particles with $D_p = 0.3D_r$ (1.83 μm). The wall is at $y/W = 0$. The arrows indicate the boundary of the RBCFL for the different hematocrits, marked by corresponding colors.

cell[41] and is expected to subside for particles substantially smaller than a RBC, i.e. of sub-micrometer size. A pronounced dependence of particle margination on shear rate is observed at low flow rates. In the limit of very small flow rates ($\dot{\gamma}^* \lesssim 1$), the RBC distribution should be nearly uniform, and therefore, the RBCFL and consequently particle margination should almost vanish. As the shear rate is increased, the RBCFL thickness grows rapidly[42], leading to a substantial increase in particle margination.

The simulated values of $\dot{\gamma}^*$ cover the range of flow rates characteristic for the venular part of microcirculation ($\bar{\dot{\gamma}} \lesssim 80\ \mathrm{s}^{-1}$ for $W \approx 20$ μm), where it is estimated that $\dot{\gamma}^* \lesssim 90$ in 3D ($\dot{\gamma}^* \lesssim 77$ in 2D), while in arteriolar part the flow rates are higher ($\bar{\dot{\gamma}} \gtrsim 110\ \mathrm{s}^{-1}$ for $W \approx 20$ μm) with $\dot{\gamma}^* \gtrsim 120$ in 3D[43,44]. The considered range of shear rates is also relevant for tumor microvasculature, since blood flow velocities in tumors are much reduced in comparison to those under normal conditions, due to high geometric resistance and vessel permeability[45,46]. Furthermore, the margination probability diagrams in Figs. 3(a),(b) show that the strongest particle margination occurs in the range of $H_t = 0.25$–0.6. This region has a considerable overlap with the characteristic hematocrits in the body's microvascular networks in the range $H_t = 0.2$–0.4. A strong particle margination at high H_t values seems to be an advantage for drug delivery to tumors, since blood within tumor microvasculature is often subject to hemoconcentration due to plasma leakage[47]. We also note that particle margination obtained from 3D simulations displays a higher margination probability at lower H_t values than that in the corresponding 2D system. This difference arises from the variation in RBCFL thicknesses in 2D and 3D systems. Thus, RBCFLs in 3D tubes are thinner than those in 2D channels for the same H_t values due to cylindrical curvature of the geometry, which affects close-packing of flowing RBCs. In order to relate simulations with similar RBCFL thicknesses, 3D margination data should be compared with 2D data at a larger hematocrit (by about 0.1–0.2), see Supplementary Fig. S2. In addition, the 3D data also shows a decrease of particle margination at

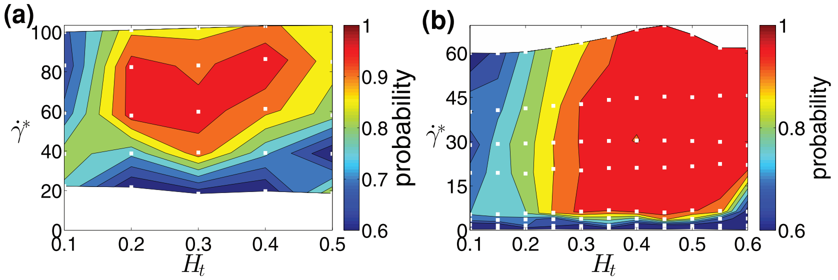

Figure 3 | **Particle margination in 3D and 2D.** Probability diagrams of particle margination with respect to $\dot{\gamma}^*$ and H_t in (a) 3D and (b) 2D, where the margination probability is defined as a probability of a particle center-of-mass to be within the RBCFL. The white squares (□) indicate the values of H_t and $\dot{\gamma}^*$ for which simulations have been performed.

high shear rates. Nevertheless, both 2D and 3D simulations show qualitatively similar trends for the dependence of carrier margination on H_t and $\dot{\gamma}^*$. Therefore, we conclude that 2D simulations are able to properly capture particle margination properties in blood flow. Further, we will often employ a 2D system due to its robustness and low computational cost in comparison with a 3D system.

Dependence of margination on particle size. The discussion above considered the margination of micron-size particles. There is also a strong interest in nano-carriers, with sizes starting from several nanometers. Figures 4(a),(b) show margination diagrams of particles with $D_p = 0.15D_r$ (0.91 μm) and $D_p = 0.04D_r$ (250 nm), respectively. The comparison of Figs. 4(a),(b) and Fig. 3(b) for $D_p = 0.3D_r$ (1.83 μm) reveals that the region of high margination probability becomes smaller with decreasing particle size. To illustrate the reason for the reduction in margination probability with decreasing particle size, we present in Fig. 4(c) the distributions of particles with different sizes for $H_t = 0.3$ and $\dot{\gamma}^* \approx 29.3$. For large enough particles, we observe a pronounced peak in the distribution next to the wall due to their interactions with RBCs, since their size is comparable with the RBCFL thickness. Even though small particles are also marginated, their distribution within the RBCFL is more uniform and their presence around the vessel center line is more probable than that for larger particles. Thus, the cumulative probability for a single particle to be within the RBCFL is lower for nano-carriers than that for micro-particles. Recent *in vivo* experiments[48] also support our numerical observations that particles with a size of about 1 μm are located closer to the vessel wall than smaller nano-particles. Noteworthy is that the distribution of the smallest particles with $D_p = 0.04D_r$ closely approaches the distribution computed as the excess fluid volume of flowing RBCs. This indicates that the distribution of particles smaller in size than roughly 250 nm can be well approximated by the distribution of the blood plasma, and therefore, their margination properties can be directly inferred from local H_t distributions.

To decide on a suitable particle size for efficient drug delivery, a number of different considerations have to be taken into account. A direct interpretation of probabilities in Figs. 3(b) and 4(a),(b) suggests that larger particle sizes are more favorable for drug delivery due to their better margination properties. To further support this proposition, we consider another definition for the margination probability based on $\delta = 0.5D_p + s$, which characterizes the fraction of carriers whose closest surface point is not further away from the wall than a distance s. We denote such a layer as "potential adhesion layer", since particle margination into a thin near-wall layer is a necessary precondition for adhesion. Even though the distance s is motivated by direct receptor-ligand interactions which occur within several nanometers, resolution restrictions in our mesoscale simulation approach do not allow the selection of smaller distances than approximately $s = 0.031D_r$ in 3D or $s = 0.033D_r$ in 2D, which corresponds to about 200 nm. Nevertheless, the distance of several hundred nanometers becomes relevant for particle-wall interactions in case of a carrier whose surface is decorated by tethered molecules[49]. Another definition for margination probability can also be based on a fixed layer thickness δ, thus it does not depend on H_t or on particle size. Margination diagrams for this definition are illustrated in Supplementary Fig. S3.

Figure 5(a) presents the margination probability into the potential adhesion layer (p_s) in 2D at $\dot{\gamma}^* \approx 29.3$. At very small H_t, the fraction of particles within the potential adhesion layer is small for all particle sizes; however, the smallest studied particles seem to be slightly more advantageous here. Remember that the interpretation of 2D margination data for a RBCFL thickness with respect to the same RBCFL thickness in 3D requires a shift in H_t values such that the range of $H_t = 0.15$–0.4 in 3D corresponds to approximately the range of $H_t = 0.3$–0.6 in 2D. For the range of $H_t = 0.3$–0.6, Fig. 5 clearly shows that

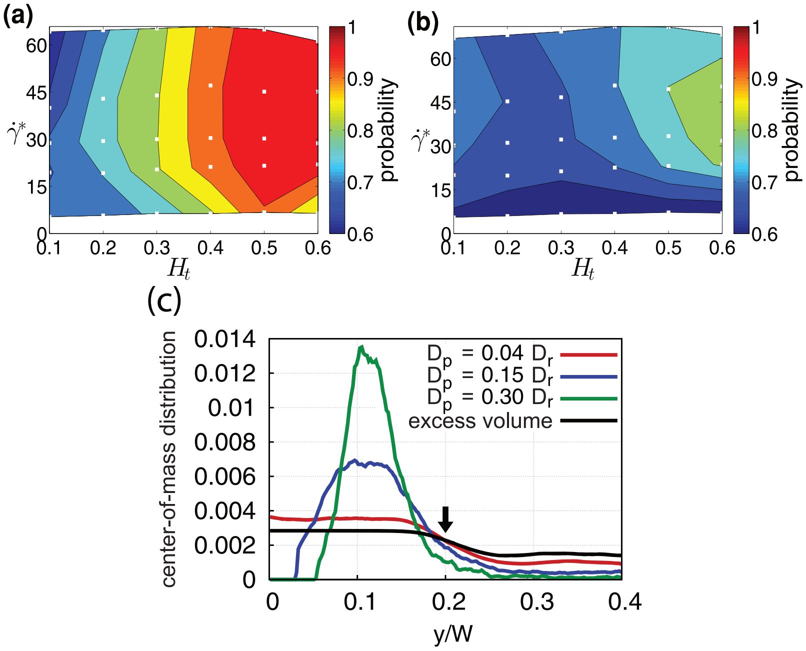

Figure 4 | **Dependence of margination on particle size.** Probability diagrams of particle margination in 2D for various H_t and $\dot{\gamma}^*$ values and for circular particles with the sizes (a) $D_p = 0.15D_r$ (0.91 μm), (b) $D_p = 0.04D_r$ (0.25 μm). The white squares (□) indicate the values of H_t and $\dot{\gamma}^*$ for which simulation were performed. The margination probability is calculated based on the RBCFL thickness. (c) Distribution of particles with different sizes across the channel for $H_t = 0.3$ and $\dot{\gamma}^* \approx 29.3$. For small particles the distribution resembles the black solid curve computed as the blood-plasma volume. The arrow denotes position of the RBCFL boundary.

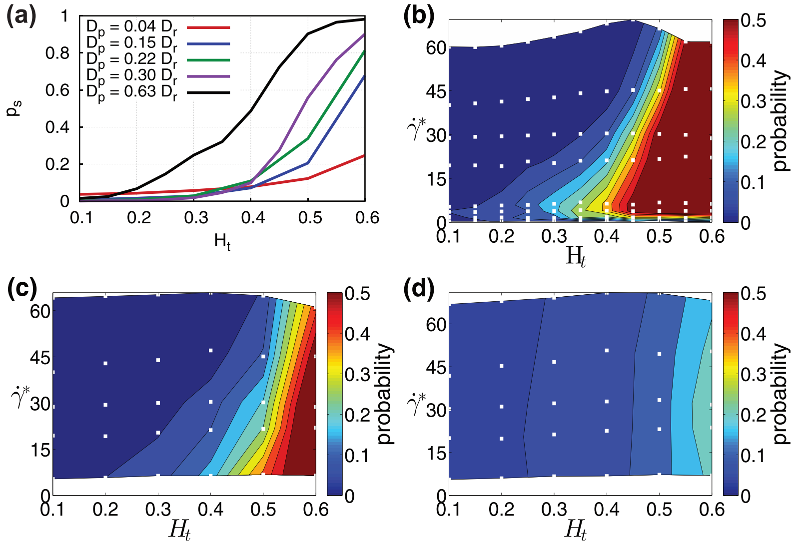

Figure 5 | Margination into a potential adhesion layer of thickness 200 nm. (a) Margination probability p_s. The curves correspond to different particle sizes, where $D_p = 0.63D_r$ (3.84 μm) is for an elliptic particle and the other curves are for circular particles. 2D simulation results for $\dot{\gamma}^* \approx 29.3$. (b–d) Margination diagrams for (b) $D_p = 0.3D_r$ (1.83 μm) (c) $D_p = 0.15D_r$ (0.91 μm), and (d) $D_p = 0.04D_r$ (0.25 μm).

the fraction of large particles within the potential adhesion layer is much higher than that for small particles. The corresponding margination diagrams are shown in Figs. 5(b–d) and support the conclusion that large particles marginate better for all considered shear rates. This indicates that micro-carriers are likely to be better for drug delivery than sub-micron particles.

Dependence of margination on vessel size. To elucidate the effect of vessel diameter, we performed a number of simulations in 2D for two additional channel widths ($W = 10$ μm and 40 μm) and two particle sizes ($D_p = 0.15D_r$ and $D_p = 0.3D_r$); corresponding simulation snapshots are displayed in the Supplementary Fig. S4. We consider margination into both the RBCFL and the potential adhesion layer.

The pronounced dependence of particle margination properties on channel width for the potential adhesion layer is illustrated by a comparison of Fig. 5(b) and Fig. 6. For particles with a size of $D_p = 0.3D_r$ (1.83 μm), particle margination into the potential adhesion layer improves considerably as the channel size decreases due to the much smaller RBCFL thickness in narrow channels. Thus, particle adhesion is expected to be more efficient in small vessels (i.e., capillaries) than in large vessels (i.e., venules and arterioles). Supplementary Fig. S5 supports this observation for particles with $D_p = 0.15D_r$ (0.91 μm). Furthermore, a reduction of margination into the potential adhesion layer with decreasing particle size is found for all channel sizes.

Particle margination based on the RBCFL thickness exhibits similar dependence on H_t and flow rate for different channel widths, see Supplementary Fig. S6. For the channel width $W = 10$ μm, margination into the RBCFL differs only slightly for different particle sizes up to $H_t \approx 0.5$. For $H_t \gtrsim 0.5$, the particle radius might be larger than the RBCFL thickness, leading to an apparent decrease in margination for the large particles. For the cases $W = 20$ and 40 μm, where the RBCFL thickness is always larger than the particle radius, we observe that large particles marginate clearly better than small particles.

Dependence of margination on particle shape. Advances in micro- and nano-particle fabrication facilitate the production of carriers of various shapes, including spherical, prolate and oblate ellipsoidal, and rod-like shapes[5]. However, advantages of different particle shapes for drug delivery are still to be explored. Thus, we investigate the effect of shape on the margination properties in blood flow. Figure 7 displays results of simulations in 2D for the margination probability (based on the RBCFL) of elliptic particles under various blood flow conditions in comparison to circular particles. The ellipse has an aspect ratio of about 7 and the longest diameter is $D_p = 0.63D_r$ (3.84 μm); the enclosed area corresponds to the area of a circle with diameter $D_p = 0.22D_r$ (1.35 μm). The plot indicates that margination of elliptic particles is slightly worse than that of circular particles. From these data we can also conclude that margination of the elliptic particles with a smaller aspect ratio than 7 is similar to that presented in Fig. 7. However, since the largest

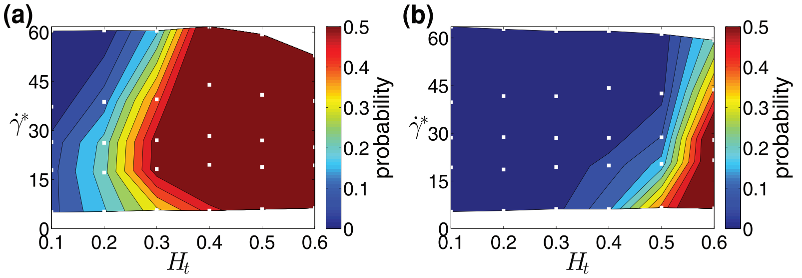

Figure 6 | Margination for different channel widths. Margination into the potential adhesion layer based on $\delta = 0.5D_p + 200$ nm, for particles with size $D_p = 0.3D_r$ (1.83 μm) and two channel widths (a) $W = 10$ μm and (b) $W = 40$ μm.

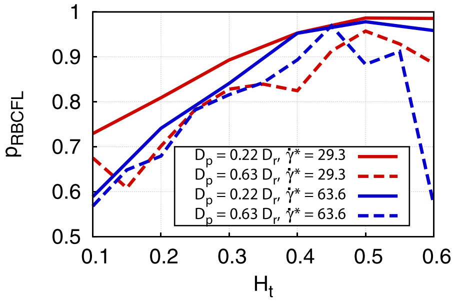

Figure 7 | Dependence of margination on particle shape. Margination probabilities of ellipse-like particles (dashed lines) for various H_t and $\dot{\gamma}^*$ values in comparison to circular particles (solid lines) of the same area. The long axis of a 2D elliptic particle is $D_p = 0.63D_r$ (3.84 μm) and the aspect ratio equals approximately 7. The margination probability is calculated based on the RBCFL thickness.

diameter of the ellipse is larger than that of a circle with the same area, its margination into the potential adhesion layer, which is defined as a probability of a particle to be within a near-wall layer of thickness $\delta = 0.5D_p + 200$ nm, appears to be considerably larger for ellipsoids than that for the corresponding sphere (see Fig. 5). We have also performed a number of 3D simulations with oblate ellipsoids having the same aspect ratio, which showed that their margination is qualitatively similar to that in 2D.

Recent theoretical[32,33] and experimental[30,31] studies suggest that ellipsoidal particles possess better adhesion properties than spheres due to a larger contact area for adhesion interactions. It is also interesting to consider drag force on an ellipsoid or sphere in shear flow near a wall. In case of an ellipsoid close and parallel to a wall, the drag force is found to be smaller than that on a sphere with the same volume, which was estimated in separate simulations of a sphere and an ellipsoid in shear flow with fixed position. Thus, adhered ellipsoidal particles experience a lower drag force due to fluid flow than the corresponding spheres with the same volume. In conclusion, the current knowledge about adhesion of ellipsoidal particles and our simulation results on margination suggest that ellipsoidal particles are very likely a better choice for drug delivery than spherical particles.

Dynamics of marginated particles. Local particle dynamics may also influence the margination and adhesion efficiency. Simulations in 3D show that the dynamics of marginated particles (i.e., within the RBCFL region) is different for spherical and ellipsoidal particles. A spherical particle is subject to a uniform rotation, while an ellipsoid displays tumbling dynamics. A quantitative analysis of the average angular velocities $\langle\omega\rangle$ of marginated particles shows that ellipsoidal particles rotate considerably slower within the RBCFL than spherical carriers, see Fig. 8. The comparison is made for a sphere and an ellipsoid of the same volume, while the long semiaxis of the ellipsoid is about twice the radius of the sphere. Within the RBCFL region it is plausible to assume a simple shear flow with the wall shear rate $\dot{\gamma}_w$, which can be computed directly from a near-wall velocity profile or estimated from the pressure gradient applied to drive the flow. In Fig. 8, we compare the average angular velocities of marginated spherical and ellipsoidal particles with the theoretical predictions by Jeffery[50] for an oblate ellipsoidal particle in shear flow, which is given by

$$\langle\omega\rangle = \frac{\dot{\gamma}_w}{r_e + 1/r_e}, \tag{2}$$

where r_e is the aspect ratio of major and minor axis. For a sphere, $r_e = 1$ which implies $\omega_s = \dot{\gamma}_w/2$, while for an ellipsoid, $r_e = 7$ which results in $\omega_e \approx 0.14\dot{\gamma}_w$, such that $\omega_e < \omega_s$. In addition, while the results for $\langle\omega\rangle$ in Fig. 8(a) for a sphere are close to the theoretical results, the computed angular velocities for an ellipsoid in Fig. 8(b) are lower than the corresponding theoretical predictions due to the confinement of the ellipsoid between the wall and flowing RBCs. A lower rotational velocity of a particle leads to a longer interaction time between the particle and a wall. Thus, adhesion of ellipsoidal particles is expected to be more efficient than for spheres with a comparable size. In conclusion, a detailed analysis of dynamics of marginated particles further supports the proposition that ellipsoidal particles are likely to be better candidates for drug delivery.

Discussion

Particle margination in blood flow depends on particle size and shape, hematocrit, vessel size, and flow rate. Margination of spherical and ellipsoidal particles increases with increasing hematocrit, while their margination properties appear to be rather similar, where a sphere marginates slightly more efficient than an ellipsoid. The presented diagrams show that larger particles have a higher margination probability in comparison to the smaller ones. Moreover, the distribution of very small particles with a diameter smaller than approximately 250 nm is well represented by the blood plasma volume of RBCs. Margination of particles into the potential adhesion layer is found to be more pronounced in small vessels, indicating that particle adhesion is likely to occur more often in capillaries than in arterioles and venules.

The simulation results are in good qualitative agreement with several experimental observations[15,17,25,30,31,48]. For example, margination of micro-particles has been observed to be more efficient than that of nano-particles in recent *in vivo* experiments[48]. However, a detailed quantitative comparison is still difficult due to two reasons. On the one hand, the majority of the simulation results is obtained for 2D systems, which provide interesting insights into the relevant mechanisms, but have limited power for quantitative predictions for 3D systems. On the other hand, experimental data on particle mar-

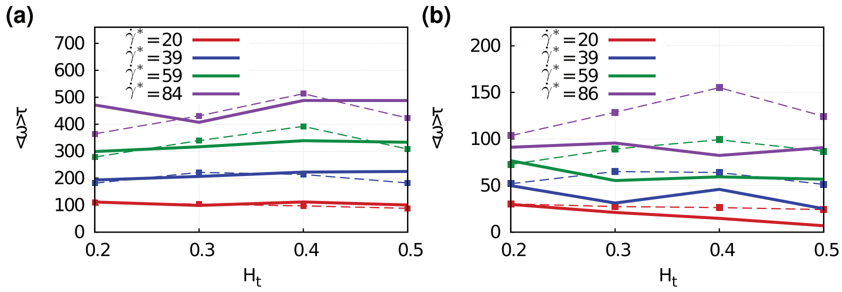

Figure 8 | Dynamics of marginated spherical and elliptical particles within the RBCFL. Comparison of average angular velocities $\langle\omega\rangle$ of (a) spherical and (b) ellipsoidal particles for various wall shear rates $\dot{\gamma}_w$ in 3D. The simulation results $\langle\omega\rangle$ (solid lines) are also compared with the theoretical prediction (dashed lines) by Jeffery[50] for a particle in simple shear flow.

gination in blood flow[15,48] are very scarce and most of the available experimental investigations (e.g., Refs. 25, 30, 31) focus on carrier adhesion. Even though margination is a necessary pre-condition for particle adhesion to vessel walls, particle margination and adhesion are not equivalent, since carrier adhesion may also depend on other factors (e.g., specific targets, the receptor/ligand density and distribution).

Clearly, the size and shape of drug carriers are important parameters not only for margination, but also for their adhesion and further transport through biological barriers (e.g., internalization). Our simulations suggest that ellipsoidal particles are expected to adhere more efficiently than spherical carriers due to a larger surface for adhesive interactions and decelerated tumbling motion within the RBCFL. Therefore, our future numerical investigations will be focused on the adhesion ability of various particles in blood flow. Further requirements for efficient drug delivery include particle transport through vessel walls, interstitial space, and cell membranes. For instance, particle internalization by endothelial cells and intracellular trafficking have been shown to be most efficient for spherical sub-micron particles, rather than for micron-size carriers with an ellipsoidal shape[10]. This observation points in the direction of smaller carrier to be most efficient for internalization. As a consequence, the concept of multi-stage drug-delivery carriers[1,7], where a larger microparticle incorporates a number of small nano-carriers, seems to be very promising. In this way, margination and carrier delivery or adhesion to a specific target within the microvasculature could be achieved using micro-particles, which would then be followed by the release of nano-particles into the tissue. In conclusion, tackling various drug-delivery challenges is a complex issue; its resolution requires an inter-disciplinary effort including *in vitro* and *in vivo* experiments and realistic numerical simulations.

Methods

Simulation method. We employ the dissipative particle dynamics (DPD) method[51,52] for 2D simulations and the smoothed DPD (SDPD) method[53] for 3D simulations, where both methods are mesoscopic particle-based simulation approaches which properly capture hydrodynamics. Both simulated systems are represented by a collection of n point particles. The particles interact locally within a selected cutoff region through three pairwise forces denoted as conservative ($\mathbf{F}^C$), dissipative ($\mathbf{F}^D$), and random ($\mathbf{F}^R$) forces. The time evolution of the velocity $\mathbf{v}_i$ and position $\mathbf{r}_i$ of particle i with the mass m_i is determined by the Newton's second law of motion $d\mathbf{r}_i = \mathbf{v}_i dt$ and $d\mathbf{v}_i = \frac{1}{m_i}\left(\mathrm{F}_i^C + \mathrm{F}_i^D + \mathrm{F}_i^R\right)dt$. More information on the DPD formulation can be found in Refs. 51, 52, while the DPD parameters used in 2D simulations are presented in Supplementary Tab. 1.

In the SDPD method, the forces are derived by a discretization of the Navier-Stokes equation similar to the smoothed particle hydrodynamics (SPH) method[54], while the implementation of thermal fluctuations is analogous to that in DPD[53]. The forces on particle i are given by the conservative force $\mathrm{F}_i^C = \sum_j \left(\frac{p_i}{\rho_i^2} + \frac{p_j}{\rho_j^2}\right)\omega_{ij}\mathbf{r}_{ij}$, the dissipative force $\mathrm{F}_i^D = -\sum_j \gamma_{ij}\left(\mathrm{v}_{ij} + \hat{\mathbf{r}}_{ij}\hat{\mathbf{r}}_{ij}\cdot\mathrm{v}_{ij}\right)$, and the random force $\mathrm{F}_i^R = \sum_j \sigma_{ij}\left(d\overline{\mathbf{W}}_{ij} + \frac{1}{3}tr\left[d\mathbf{W}_{ij}\right]\right)\cdot\hat{\mathbf{r}}_{ij}$. Thereby, $d\mathbf{W}_{ij}$ is a matrix of independent Wiener increments and $d\overline{\mathbf{W}}_{ij}$ is its traceless symmetric part. Here, p_i and p_j are particle pressures which are given by the equation of state $p = p_0(\rho/\rho_0)^\alpha - b$ with p_0, ρ_0, α, and b being model parameters, see Supplementary Tab. S2. The particle density ρ_i is calculated locally as $\rho_i = \sum_j W\left(r_{ij}\right)$, where $W(r) = \frac{105}{16\pi r_c^3}\left(1 + 3\frac{r}{r_c}\right)\left(1 - \frac{r}{r_c}\right)^3$ is the Lucy function[54] and r_c is the cutoff radius. The weight function $w(r)$ is determined by $\nabla W(r) = -\mathbf{r}w(r)$. The coefficients γ_{ij} and σ_{ij} define the strength of dissipative and random forces. The fluctuation-dissipation theorem to be satisfied requires $\sigma_{ij} = 2\sqrt{k_B T \gamma_{ij}}$. Finally, the friction coefficients are defined as $\gamma_{ij} = \frac{5\eta_0}{3}\frac{w\left(r_{ij}\right)}{\rho_i\rho_j}$.

Blood components. In 3D, a RBC membrane and suspended carriers are both modeled by a collection of discrete points, which are the vertices of a triangular network of springs on their membrane surface[55]. The network assumes fixed connectivity with the potential energy defined as

$$U_{membrane} = U_{spring} + U_{bend} + U_{area} + U_{vol}, \tag{3}$$

which includes the spring's elastic energy U_{spring}, the bending energy U_{bend}, and the area and volume conservation constraints U_{area} and U_{vol}. The spring forces mimic the elasticity of a membrane. The bending energy represents the bending resistance of a membrane, while the area and volume energies enforce area-incompressibility of a membrane and incompressibility of the inner cytosol, respectively. Detailed description of these potentials can be found in Ref. 55, while all model parameters are given in Supplementary Tab. S3.

In 2D, RBCs and micro- and nano-particles are modeled as closed bead-spring chains, which incorporate bending rigidity and an area constraint[41]. The model parameters are presented in Supplementary Tab. S4. Carriers in 2D are modeled by a collection of N_v^p particles (see Supplementary Tab. S5), which are constrained to maintain a rigid configuration.

Simulation setup. The simulation setup consists of a single channel of cylindrical shape in 3D with diameter $W = 20$ μm and length of $L = 12.3D_r$. In 2D, a slit geometry with different widths $W = 10$, 20, and 40 μm and length $L = 19.5D_r$ (independent of W) is employed. The channel is filled with fluid particles and with N suspended carriers and N_{RBC} RBCs. The number of RBCs is computed according to channel hematocrit, which corresponds to the volume fraction of RBCs in 3D and to the area fraction of RBCs in 2D. The number of suspended particles for different simulations is provided in Supplementary Tab. S5.

Boundary conditions. In the flow direction, periodic boundary conditions (BCs) were imposed, while in the other directions the suspension was confined by walls. The walls are modeled by frozen fluid particles with the same structure as the fluid, while the wall thickness is equal to r_c. Thus, the interactions of fluid particles with wall particles are the same as the interactions between fluid particles, and the interactions of suspended carriers and cells with the wall are identical to those with a suspending fluid. To prevent wall penetration, fluid particles as well as vertices of RBCs and carriers are subject to reflection at the fluid-solid interface. We employed bounce-back reflections, because they provide a better approximation for the no-slip boundary conditions in comparison to specular reflection of particles. To ensure that no-slip boundary conditions are strictly satisfied, we also add a tangential adaptive shear force[56] which acts on the fluid particles in a near-wall layer of a thickness $h_c = r_c$.

Coupling between solvent and cells/carriers. Coupling between the fluid flow and cells/carriers is achieved through viscous friction[55] between cell vertices and the surrounding fluid particles, which is implemented via the DPD interactions F^D and F^R for both 2D and 3D simulations. The strength γ of the dissipative force F^D for the interaction between a fluid particle and a membrane vertex is computed such that no-slip BCs are ensured. The derivation of γ is based on the idealized case of linear shear flow over a flat part of a membrane with area A. In a continuum hydrodynamics description, the total shear force exerted by the fluid on the area A is equal to $A\eta\dot{\gamma}$, where η is the fluid's viscosity and $\dot{\gamma}$ is the local wall shear-rate. The same fluid force has to be also transmitted onto a discrete membrane having N_A vertices within the area A. The force on a single membrane vertex exerted by the sheared fluid can be found as $F_v = \int_{V_h} ng(r)F^D dV$ where n is the fluid number density, $g(r)$ is the radial distribution function of fluid particles with respect to the membrane particles, and V_h is the half sphere volume of fluid above the membrane. Here, the total shear force on the area A is equal to $N_A F_v$. The equality of $N_A F_v = A\eta\dot{\gamma}$ results in an expression of the dissipative force coefficient in terms of the fluid density and viscosity, wall density N_A/A, and r_c. Under the assumption of linear shear flow the shear rate $\dot{\gamma}$ cancels out. This formulation results in satisfaction of the no-slip BCs for the linear shear flow over a flat membrane; however, it also serves as an excellent approximation for no-slip at the membrane surface. Note that conservative interactions between fluid and membrane particles are turned off, which implies that the radial distribution function is structureless, $g(r) = 1$. In 2D, the surface area is replaced by a line of length L with N_L particles, and the half sphere volume is replaced by the half circle area A_v.

Gathering statistics. The center-of-mass distributions of particles were calculated on the fly and were written to disk as sub-averages over short time intervals. Final averaging of the data is done during post-processing. To make sure that the final averaging of data starts from a time point which is sufficiently late for the system to be independent of the initial conditions, we have tested the sensitivity of final distributions to the choice of the starting time for averaging.

Measuring RBC-free-layer thickness. To determine the RBC-free-layer (RBCFL) thickness, we measure the outer edge of the RBC core shown in Supplementary Fig. S1, which is similar to RBCFL measurements in experiments[37,57]. The data are averaged for many RBC snapshots at different times. In 3D, the RBC core edge is measured by projecting RBC vertices onto the x-y plane, where curves of the RBC core minimum and maximum are fitted similar to that in Supplementary Fig. S1. Here, we also perform averaging over different angular orientations (to exploit the cylindrical symmetry of the channel) in addition to the temporal averaging.

1. Ferrari, M. Cancer nanotechnology: opportunities and challenges. *Nat. Rev. Cancer* **5**, 161–171 (2005).
2. Jain, R. K. & Stylianopoulos, T. Delivering nanomedicine to solid tumors. *Nat. Rev. Clin. Oncol.* **7**, 653–664 (2010).
3. Hood, E., Simone, E., Wattamwar, P., Dziubla, T. & Muzykantov, V. Nanocarriers for vascular delivery of antioxidants. *Nanomedicine* **6**, 1257–1272 (2011).

4. Duncan, R. Polymer conjugates as anticancer nanomedicines. *Nat. Rev. Cancer* **6**, 688–701 (2006).
5. Rolland, J. P. *et al.* Direct fabrication and harvesting of monodisperse, shape-specific nanobio-materials. *J. Am. Chem. Soc.* **127**, 10096–10100 (2005).
6. Davis, M. E., Chen, Z. G. & Shin, D. M. Nanoparticle therapeutics: an emerging treatment modality for cancer. *Nat. Rev. Drug Discov.* **7**, 771–782 (2008).
7. Blanco, E. *et al.* Nanomedicine in cancer therapy: innovative trends and prospects. *Cancer Sci.* **102**, 1247–1252 (2011).
8. Sanhai, W. R., Sakamoto, J. H., Canady, R. & Ferrari, M. Seven challenges for nanomedicine. *Nat. Nanotechnol.* **3**, 242–244 (2008).
9. Jain, R. K. Delivery of novel therapeutic agents in tumors: physiological barriers and strategies. *J. Natl. Cancer Inst.* **81**, 570–576 (1989).
10. Muro, S. *et al.* Control of endothelial targeting and intracellular delivery of therapeutic enzymes by modulating the size and shape of ICAM-1-targeted carriers. *Mol. Ther.* **16**, 1450–1458 (2008).
11. Huang, R. B., Mocherla, S., Heslinga, M. J., Charoenphol, P. & Eniola-Adefeso, O. Dynamic and cellular interactions of nanoparticles in vascular-targeted drug delivery (review). *Mol. Membr. Biol.* **27**, 312–327 (2010).
12. Ding, B.-S., Dziubla, T., Shuvaev, V. V., Muro, S. & Muzykantov, V. R. Advanced drug delivery systems that target the vascular endothelium. *Mol. Interv.* **6**, 98–112 (2006).
13. Bagge, U. & Karlsson, R. Maintenance of white blood cell margination at the passage through small venular junctions. *Microvasc. Res.* **20**, 92–95 (1980).
14. Goldsmith, H. L. & Spain, S. Margination of leukocytes in blood flow through small tubes. *Microvasc. Res.* **27**, 204–222 (1984).
15. Tangelder, G. J., Teirlinck, H. C., Slaaf, D. W. & Reneman, R. S. Distribution of blood platelets flowing in arterioles. *Am. J. Physiol.* **248**, H318–H323 (1985).
16. Woldhuis, B., Tangelder, G. J., Slaaf, D. W. & Reneman, R. S. Concentration profile of blood platelets differs in arterioles and venules. *Am. J. Physiol.* **262**, H1217–H1223 (1992).
17. Tilles, A. W. & Eckstein, E. C. The near-wall excess of platelet-sized particles in blood flow: its dependence on hematocrit and wall shear rate. *Microvasc. Res.* **33**, 211–223 (1987).
18. Eckstein, E. C., Tilles, A. W. & Millero III, F. J. Conditions for the occurrence of large near-wall excesses of small particles during blood flow. *Microvasc. Res.* **36**, 31–39 (1988).
19. Goldsmith, H. L., Cokelet, G. R. & Gaehtgens, P. Robin Fahraeus: evolution of his concepts in cardiovascular physiology. *Am. J. Physiol.* **257**, H1005–H1015 (1989).
20. Cantat, I. & Misbah, C. Lift force and dynamical unbinding of adhering vesicles under shear flow. *Phys. Rev. Lett.* **83**, 880–883 (1999).
21. Abkarian, M., Lartigue, C. & Viallat, A. Tank treading and unbinding of deformable vesicles in shear flow: determination of the lift force. *Phys. Rev. Lett.* **88**, 068103 (2002).
22. Kumar, A. & Graham, M. D. Mechanism of margination in confined flows of blood and other multicomponent suspensions. *Phys. Rev. Lett.* **109**, 108102 (2012).
23. Slack, J. D., Kanke, M., Simmons, G. H. & DeLuca, P. P. Acute hemodynamic effects and blood pool kinetics of polystyrene microspheres following intravenous administration. *J. Pharm. Sci.* **70**, 660–664 (1981).
24. Herant, M., Heinrich, V. & Dembo, M. Mechanics of neutrophil phagocytosis: experiments and quantitative models. *J. Cell Sci.* **119**, 1903–1913 (2006).
25. Namdee, K., Thompson, A. J., Charoenphol, P. & Eniola-Adefeso, O. Margination propensity of vascular-targeted spheres from blood flow in a microfluidic model of human microvessels. *Langmuir* **29**, 2530–2535 (2013).
26. Litzinger, D. C., Buiting, A. M. J., van Rooijen, N. & Huang, L. Effect of liposome size on the circulation time and intraorgan distribution of amphipathic poly(ethylene glycol)-containing liposomes. *Biochim. Biophys. Acta* **1190**, 99–107 (1994).
27. De Jong, W. H. *et al.* Particle size-dependent organ distribution of gold nanoparticles after intravenous administration. *Biomaterials* **29**, 1912–1919 (2008).
28. Decuzzi, P. *et al.* Size and shape effects in the biodistribution of intravascularly injected particles. *J. Control. Release* **141**, 320–327 (2010).
29. Champion, J. A. & Mitragotri, S. Role of target geometry in phagocytosis. *Proc. Natl. Acad. Sci. USA* **103**, 4930–4934 (2006).
30. Gentile, F. *et al.* The effect of shape on the margination dynamics of non-neutrally buoyant particles in two-dimensional shear flows. *J. Biomech.* **41**, 2312–2318 (2008).
31. Thompson, A. J., Mastria, E. M. & Eniola-Adefeso, O. The margination propensity of ellipsoidal micro/nanoparticles to the endothelium in human blood flow. *Biomaterials* **34**, 5863–5871 (2013).
32. Decuzzi, P. & Ferrari, M. The adhesive strength of non-spherical particles mediated by specific interactions. *Biomaterials* **27**, 5307–5314 (2006).
33. Dasgupta, S., Auth, T. & Gompper, G. Wrapping of ellipsoidal nano-particles by fluid membranes. *Soft Matter* **9**, 5473–5482 (2013).
34. Fedosov, D. A., Caswell, B., Popel, A. S. & Karniadakis, G. E. Blood flow and cell-free layer in microvessels. *Microcirculation* **17**, 615–628 (2010).
35. Fedosov, D. A., Pan, W., Caswell, B., Gompper, G. & Karniadakis, G. E. Predicting human blood viscosity in silico. *Proc. Natl. Acad. Sci. USA* **108**, 11772–11777 (2011).
36. Fedosov, D. A., Noguchi, H. & Gompper, G. Multiscale modeling of blood flow: from single cells to blood rheology. *Biomech. Model. Mechanobiol.* **13**, 239–258 (2014).
37. Kim, S., Kong, R. L., Popel, A. S., Intaglietta, M. & Johnson, P. C. Temporal and spatial variations of cell-free layer width in arterioles. *Am. J. Physiol.* **293**, H1526–H1535 (2007).
38. Crowl, L. & Fogelson, A. L. Analysis of mechanisms for platelet near-wall excess under arterial blood flow conditions. *J. Fluid Mech.* **676**, 348–375 (2011).
39. Zhao, H. & Shaqfeh, E. S. G. Shear-induced platelet margination in a microchannel. *Phys. Rev. E* **83**, 061924 (2011).
40. Reasor Jr, D. A., Mehrabadi, M., Ku, D. N. & Aidun, C. K. Determination of critical parameters in platelet margination. *Ann. Biomed. Eng.* **41**, 238–249 (2013).
41. Fedosov, D. A., Fornleitner, J. & Gompper, G. Margination of white blood cells in microcapillary flow. *Phys. Rev. Lett.* **108**, 028104 (2012).
42. Lamura, A. & Gompper, G. Dynamics and rheology of vesicle suspensions in wall-bounded shear flow. *Europhys. Lett.* **102**, 28004 (2013).
43. Popel, A. S. & Johnson, P. C. Microcirculation and hemorheology. *Annu. Rev. Fluid Mech.* **37**, 43–69 (2005).
44. Pries, A. R., Secomb, T. W. & Gaehtgens, P. Structure and hemodynamics of microvascular networks: heterogeneity and correlations. *Am. J. Physiol.* **269**, H1713–H1722 (1995).
45. Jain, R. K. Determinants of tumor blood flow: a review. *Cancer Res.* **48**, 2641–2658 (1988).
46. Yuan, F. *et al.* Vascular permeability and microcirculation of gliomas and mammary carcinomas transplanted in rat and mouse cranial windows. *Cancer Res.* **54**, 4564–4568 (1994).
47. Sevick, E. M. & Jain, R. K. Viscous resistance to blood flow in solid tumors: effect of hematocrit on intratumor blood viscosity. *Cancer Res.* **49**, 3513–3519 (1989).
48. Lee, T.-R. *et al.* On the near-wall accumulation of injectable particles in the microcirculation: smaller is not better. *Sci. Rep.* **3**, 2079 (2013).
49. Moore, N. W. & Kuhl, T. L. The role of flexible tethers in multiple ligand-receptor bond formation between curved surfaces. *Biophys. J.* **91**, 1675–1687 (2006).
50. Jeffery, G. B. The motion of ellipsoidal particles immersed in a viscous fluid. *Proc. Roy. Soc. A* **102**, 161–179 (1922).
51. Hoogerbrugge, P. J. & Koelman, J. M. V. A. Simulating microscopic hydrodynamic phenomena with dissipative particle dynamics. *Europhys. Lett.* **19**, 155–160 (1992).
52. Español, P. & Warren, P. Statistical mechanics of dissipative particle dynamics. *Europhys. Lett.* **30**, 191–196 (1995).
53. Español, P. & Revenga, M. Smoothed dissipative particle dynamics. *Phys. Rev. E* **67**, 026705 (2003).
54. Lucy, L. B. A numerical approach to the testing the fission hypothesis. *Astronom. J.* **82**, 1013–1024 (1977).
55. Fedosov, D. A., Caswell, B. & Karniadakis, G. E. A multiscale red blood cell model with accurate mechanics, rheology, and dynamics. *Biophys. J.* **98**, 2215–2225 (2010).
56. Fedosov, D. A. & Karniadakis, G. E. Triple-decker: Interfacing atomistic-mesoscopic-continuum flow regimes. *J. Comp. Phys.* **228**, 1157–1171 (2009).
57. Maeda, N., Suzuki, Y., Tanaka, J. & Tateishi, N. Erythrocyte flow and elasticity of microvessels evaluated by marginal cell-free layer and flow resistance. *Am. J. Physiol.* **271**, H2454–H2461 (1996).

Acknowledgments

This work has been supported by the DFG Research Unit FOR 1543 "SHENC - Shear Flow Regulation in Hemostasis". Dmitry A. Fedosov acknowledges funding by the Alexander von Humboldt Foundation. Kathrin Müller acknowledges support by the International Helmholtz Research School of Biophysics and Soft Matter (IHRS BioSoft). We also gratefully acknowledge a CPU time grant by the Jülich Supercomputing Center.

Author contributions

K.M. performed all the simulations and analyzed the computational results; D.A.F. and G.G. designed the research project; K.M., D.A.F. and G.G. interpreted the results and wrote the manuscript.

Additional information

Supplementary information accompanies this paper at http://www.nature.com/scientificreports

Competing financial interests: The authors declare no competing financial interests.

How to cite this article: Müller, K., Fedosov, D.A. & Gompper, G. Margination of micro- and nano-particles in blood flow and its effect on drug delivery. *Sci. Rep.* **4**, 4871; DOI:10.1038/srep04871 (2014).

P6: Deformation and dynamics of red blood cells in flow through cylindrical microchannels

D. A. Fedosov, M. Peltomäki, and G. Gompper

Soft Matter, **10**:4258-4267, 2014.

Soft Matter

PAPER

View Article Online
View Journal | View Issue

Deformation and dynamics of red blood cells in flow through cylindrical microchannels†

Cite this: *Soft Matter*, 2014, **10**, 4258

Dmitry A. Fedosov,* Matti Peltomäki and Gerhard Gompper

Received 1st February 2014
Accepted 13th March 2014

DOI: 10.1039/c4sm00248b

www.rsc.org/softmatter

The motion of red blood cells (RBCs) in microcirculation plays an important role in blood flow resistance and in the cell partitioning within a microvascular network. Different shapes and dynamics of RBCs in microvessels have been previously observed experimentally including the parachute and slipper shapes. We employ mesoscale hydrodynamic simulations to predict the phase diagram of shapes and dynamics of RBCs in cylindrical microchannels, which serve as idealized microvessels, for a wide range of channel confinements and flow rates. A rich dynamical behavior is found, with snaking and tumbling discocytes, slippers performing a swinging motion, and stationary parachutes. We discuss the effects of different RBC states on the flow resistance, and the influence of RBC properties, characterized by the Föppl–von Kármán number, on the shape diagram. The simulations are performed using the same viscosity for both external and internal fluids surrounding a RBC; however, we discuss how the viscosity contrast would affect the shape diagram.

1 Introduction

The behavior of soft mesoscopic particles (*e.g.*, polymers, vesicles, capsules, and cells) in flow has recently received enormous attention due to the wide range of applications of such suspensions and their rich physical properties.[1] To better control and/or manipulate the suspension's properties, for example in lab-on-chip applications,[2,3] a deeper understanding of the interplay among flow forces, elastic response and dynamics of soft objects is required. An important example is the motion of red blood cells (RBCs) in microcirculation, which influences many vital processes in microvasculature;[4] however, similar mechanisms and phenomena encompass a much wider class of capsule suspensions.[5,6] RBCs are extremely flexible and experience strong deformation in microcirculation due to the flow and/or geometrical constraints. RBC deformation is important for the reduction of blood flow resistance[7–11] and for ATP release and oxygen delivery.[12,13]

RBCs in microcirculation may attain various shapes including parachutes and slippers.[7,14–21] Parachutes are characterized by a rather symmetric shape resembling a semi-spherical cap and are located at a position near the tube center. Slippers correspond to asymmetric RBC shapes, and therefore their membranes are typically in motion (*e.g.*, tank-treading). Both non-centered slipper[20] and centered slipper shapes[17] have been observed experimentally, where the latter may only differ slightly from parachute shapes. The stable slipper shapes are well established at higher hematocrits due to hydrodynamic cell–cell interactions.[14,15,19] However, it is still not fully clear whether slippers are stable or transient states for single cells in flow.[7,9,17,20,21] The most convincing evidence so far comes from simulations in two dimensions (2D).[9,10,21]

Simulations of 2D vesicles in slit channels have shown the existence of stable parachutes, slippers, and a snaking dynamics of discocytes[9,10]—where snaking refers to an oscillating RBC dynamics near the tube center. A phase diagram of various shapes was predicted, depending on relative confinement and flow rate. Simulations of single RBCs in three dimensions (3D)[7,8,11,18] have been restricted so far to a limited number of studies, which only reveal (except for fluctuations and transient states) stationary parachutes and discocytes. It is important to note that these shapes (averaged over thermal fluctuations) are characterized by different symmetry classes, ranging from cylindrical symmetry (parachutes) to a single mirror plane containing the capillary axis and the RBC center (slippers). This raises several important questions: are slipper shapes also stable in 3D capillary flow? Is snaking dynamics around the center line possible in cylindrical microchannels in 3D? Do thermal fluctuations destroy the regular snaking oscillations? What is the role of the membrane shear modulus (absent in 2D) in the phase diagram?

In this paper, we present a systematic study of single RBCs flowing in microchannels. We construct diagrams of RBC shapes for different flow conditions and analyze RBC deformation. Changes in RBC properties (*e.g.*, shear elastic modulus, bending rigidity) are also considered, since they are of

---

Theoretical Soft Matter and Biophysics, Institute of Complex Systems and Institute for Advanced Simulation, Forschungszentrum Jülich, 52425 Jülich, Germany. E-mail: d.fedosov@fz-juelich.de

† Electronic supplementary information (ESI) available: Four movies of different RBC shapes in capillary flow: snaking discocytes, tumbling discocytes, swinging slippers, and parachutes. Blue particles on the RBC are firmly attached to the membrane and serve as tracers in order to visualize the membrane dynamics; these particles have no physical meaning. See DOI: 10.1039/c4sm00248b

importance in various blood diseases and disorders.[22] The presented 3D shape diagrams describe RBC deformation in microchannels, which mimic small vessels in microcirculation, and show that the parachute shape occurs mainly in small channels, while in large channels the slipper shape may occur. All simulations assume the same viscosity for both cytosol and suspending fluid; however, we discuss how the viscosity contrast would affect the shape diagram. We also compare the 3D results with the 2D shape diagrams in ref. 9 and 10 and emphasize essential differences. For instance, due to membrane shear elasticity, there exists a region of RBC tumbling in 3D, which is absent in 2D. Finally, the simulation results are compared to available experimental data.[17,20,23]

The article is organized as follows. In Section 2 we briefly describe the mesoscopic method employed for fluid flow, a RBC model, and simulation setup and parameters. In Section 3 we first present the shape diagram for cell parameters typical of a healthy RBC. Then, RBC membrane properties are varied in order to elucidate their effects on the RBC shape and dynamics in microchannel flow. We also discuss the effect of viscosity contrast between external and internal fluids on the shape diagram and the effects of different shapes on the flow resistance. We conclude briefly in Section 4.

2 Models & methods

To model tube flow, we employ the smoothed dissipative particle dynamics (SDPD) method[24] for the suspending fluid. SDPD is a particle-based mesoscopic simulation technique, where each SDPD particle represents a small volume of fluid rather than individual atoms or molecules. The RBC membrane is represented by a triangulated network model[7,8,25,26] and coupled to a fluid through friction forces.

2.1 Red blood cell model

The RBC membrane is modeled by a triangulated network of springs,[7,8,25,26] which includes elastic, bending, and viscous properties. A RBC is represented by a collection of N_v particles connected by $N_s = 3(N_v - 2)$ springs with the potential

$$U_{sp} = \sum_{j \in 1 \ldots N_s} \left[\frac{k_B T l_m \left(3x_j^2 - 2x_j^3\right)}{4\xi(1 - x_j)} + \frac{k_p}{l_j} \right], \tag{1}$$

where l_j is the length of the j-th spring, l_m is the maximum spring extension, $x_j = l_j/l_m$, ξ is the persistence length, and k_p is the spring constant. Note that this spring definition allows us to define a nonzero equilibrium spring length l_0. Then, we employ a stress-free model for the membrane[8] so that each spring has its own l_{0j} set to the spring length of an initially triangulated cell surface. In addition to the elastic contribution in eqn (1), each spring may also have dissipative and random force terms[8] in order to incorporate membrane viscosity. The bending rigidity of a membrane is modeled by the bending energy

$$U_{bend} = \sum_{j \in 1 \ldots N_s} k_b \left[1 - \cos(\theta_j - \theta_0)\right], \tag{2}$$

where k_b is the bending constant, θ_j is the instantaneous angle between two adjacent triangles having the common edge j, and θ_0 is the spontaneous angle, which is set to zero in all simulations. Finally, to maintain a constant cell area and volume which mimic area-incompressibility of the lipid bilayer and incompressibility of the inner cytosol, we introduce two potentials

$$\begin{aligned} U_{area} &= k_a \frac{(A - A_r)^2}{2A_r} + \sum_j k_d \frac{\left(A_j - A_j^0\right)^2}{2A_j^0}, \\ U_{vol} &= k_v \frac{(V - V_r)^2}{2V_r}, \end{aligned} \tag{3}$$

where k_a, k_d, and k_v are the global area, local area, and volume constraint coefficients, respectively. A and V are the instantaneous cell area and volume, while A_j is the instantaneous area of an individual face within a triangulated network. A_r, A_j^0, and V_r are the desired total RBC area, area of the j-th face (set according to the initial triangulation), and total RBC volume, respectively.

To relate the model parameters in the spring potential (1) (*e.g.*, ξ, k_p) and the bending potential (2) to the macroscopic membrane properties (*e.g.*, Young's modulus Y_r, bending rigidity κ_r), we use analytic relationships derived for a regular hexagonal network.[8,27] The ratio l_m/l_0 is set to 2.2 for all springs.[26] To relate simulation parameters to the physical properties of RBCs, we need a basic length and energy scale. Therefore, we define an effective RBC diameter $D_r = \sqrt{A_r/\pi}$ with A_r being the RBC membrane area. From A_r we can also calculate the average bond length l_0 for a given number of membrane vertices $A_r/N_t = \sqrt{3}{l_0}^2/4$ where $N_t = 2N_v - 4$ is the total number of triangular elements on a membrane. Experimental results[28] for the RBC area imply that $D_r = 6.5$ μm. Table 1 summarizes the parameters for the RBC model in units of D_r and the thermal energy k_BT, and the corresponding average values for a healthy RBC in physical units. The global area (k_a) and volume (k_v) constraint coefficients are chosen large enough to approximate closely the area-incompressibility of the lipid bilayer and incompressibility of the inner cytosol. Finally, a relationship for time scale is based on the characteristic RBC relaxation time, which is defined further below in the text.

2.2 Smoothed dissipative particle dynamics

SDPD[24] is a mesoscopic particle method, which combines two frequently used fluid-dynamics approaches: the smoothed particle hydrodynamics[29,30] and dissipative particle dynamics[31,32] methods. The SDPD system consists of N point particles of mass m_i, position $\mathbf{r}_i$ and velocity $\mathbf{v}_i$. SDPD particles interact through three pairwise forces: conservative (C), dissipative (D), and random (R), so that the force on particle i is given by

$$\begin{aligned} \mathbf{F}_i^C &= \sum_j \left(\frac{p_i}{{\rho_i}^2} + \frac{p_j}{{\rho_j}^2} \right) w_{ij} \mathbf{r}_{ij}, \\ \mathbf{F}_i^D &= -\sum_j \gamma_{ij} \left(\mathbf{v}_{ij} + (\mathbf{v}_{ij} \cdot \mathbf{e}_{ij})\mathbf{e}_{ij}\right), \\ \mathbf{F}_i^R &= \sum_j \sigma_{ij} \left(d\overline{\mathbf{W}}_{ij}^S + \frac{1}{3} tr[d\mathbf{W}_{ij}] \right) \cdot \mathbf{e}_{ij}, \end{aligned} \tag{4}$$

Table 1 RBC parameters in units of the effective RBC diameter D_r and the thermal energy k_BT, and the corresponding average values for a healthy RBC in physical units. N_v is the number of membrane vertices, A_r is the RBC membrane area, l_0 is the average bond length, V_r is the RBC volume, T is the temperature, Y_r is the membrane Young's modulus, κ_r is the membrane bending rigidity, and k_d, k_a, and k_v are the local area, global area, and volume constraint coefficients, respectively. In all simulations, we have chosen $A_r = 133.5$ and $k_BT = 0.4$, which implies that $D_r = 6.5$ and $l_0 = 0.4$

RBC parameters	Scaled units	Physical units
N_v	1000	
A_r		133.5×10^{-12} m^2
D_r	$\sqrt{A_r/\pi}$	6.5×10^{-6} m
l_0	$0.061D_r$	3.93×10^{-7} m
V_r	$0.34{D_r}^3$	93×10^{-18} m^3
T		310 K
Y_r	$1.82 \times 10^5 \dfrac{k_BT}{{D_r}^2}$	18.9×10^{-6} N m^{-1}
κ_r	$70k_BT$	3×10^{-19} J
k_d	$4.2 \times 10^4 \dfrac{k_BT}{{D_r}^2}$	4.3×10^{-6} N m^{-1}
k_a	$2.1 \times 10^6 \dfrac{k_BT}{{D_r}^2}$	2.1×10^{-4} N m^{-1}
k_v	$1.4 \times 10^7 \dfrac{k_BT}{{D_r}^3}$	220 N m^{-2}

Table 2 SDPD fluid parameters in simulation and physical units. Mass and length for the SDPD fluid are measured in units of the fluid particle mass m and the membrane bond length l_0. p_0 and b are parameters for the pressure equation, and η is the fluid's dynamic viscosity. In all simulations, we have set $m = 1$, $l_0 = 0.4$, and the thermal energy $k_BT = 0.4$

Fluid parameters	Scaled units	Physical units
p_0	$16\dfrac{k_BT}{{l_0}^3}$	1.07 Pa
b	$12.8\dfrac{k_BT}{{l_0}^3}$	0.86 Pa
η	$16 - 122\dfrac{\sqrt{mk_BT}}{{l_0}^2}$	1.2×10^{-3} Pa s
k_BT		4.282×10^{-21} J

where $\mathbf{e}_{ij} = \mathbf{r}_{ij}/|\mathbf{r}_{ij}|$ and $\mathbf{v}_{ij} = \mathbf{v}_i - \mathbf{v}_j$. p_i and p_j are particle pressures assumed to follow the equation of state $p = p_0(\rho/\rho_0)^\alpha - b$, where p_0, ρ_0, α, and b are selected parameters. The particle density is calculated locally and defined as $\rho_i = \sum_j W_L(r_{ij})$ with weight function $W_L(r) = \dfrac{105}{16\pi {r_c}^3}\left(1 + 3\dfrac{r}{r_c}\right)\left(1 - \dfrac{r}{r_c}\right)^3$ being the Lucy function, where r_c is the cutoff radius. Note that $\nabla W_L(r) = -\mathbf{r}w(r)$ so that $w(r) = \dfrac{315}{4\pi {r_c}^5}\left(1 - \dfrac{r}{r_c}\right)^2$ and $w_{ij} = w(r_{ij})$. The (distance-dependent) coefficients γ_{ij} and σ_{ij} define the strength of dissipative and random forces and are equal to $\gamma_{ij} = \dfrac{5\eta_0}{3}\dfrac{w_{ij}}{\rho_i\rho_j}$ and $\sigma_{ij} = 2\sqrt{k_BT\gamma_{ij}}$, where η_0 is the desired fluid's dynamic viscosity and k_BT is the thermal energy unit. The notation $tr[\mathrm{d}\mathbf{W}_{ij}]$ corresponds to the trace of a random matrix of independent Wiener increments $\mathrm{d}\mathbf{W}_{ij}$, and $\mathrm{d}\overline{\mathbf{W}}_{ij}^S$ is the traceless symmetric part.

The time evolution of velocities and positions of particles is determined by Newton's second law of motion

$$\mathrm{d}\mathbf{r}_i = \mathbf{v}_i\,\mathrm{d}t, \quad \mathrm{d}\mathbf{v}_i = \frac{1}{m_i}\left(\mathbf{F}_i^C + \mathbf{F}_i^D + \mathbf{F}_i^R\right)\mathrm{d}t. \tag{5}$$

The above equations of motion are integrated using the velocity-Verlet algorithm.

The SDPD fluid parameters are given in Table 2. A natural length scale in the fluid is the cut-off radius r_c; however, since we investigate the dependence of fluid properties on r_c, we use the membrane bond length l_0 instead, which is very similar in magnitude to r_c. In addition, the exponent α in the equation of state is chosen to be $\alpha = 7$, and $\rho_0 = n$, where n is the fluid's number density (in particles per ${l_0}^3$). A relatively large value of α provides a good approximation of fluid incompressibility, since even small changes in local density may lead to strong local pressure changes. Furthermore, the speed of sound, c, for the selected equation of state can be given as $c^2 = p_0\alpha/\rho_0$. The corresponding Mach numbers have been kept below 0.1 in all simulations providing a good approximation for an incompressible fluid flow.

To span a wide range of flow rates, we employed different values of fluid viscosities η in simulations with an input parameter $\eta_0 \in [15; 120]\ \sqrt{mk_BT}/{l_0}^2$ (m is the fluid's particle mass), since the fluid viscosity modifies linearly the RBC relaxation time scale defined further below. Large values of viscosity were used to model high flow rates of the physical system in order to keep the Reynolds number in simulations, based on characteristic RBC size, sufficiently low (see also an argument at the end of Section 2.3). Even though we can directly input the desired fluid viscosity η_0 in SDPD, the assumption that η_0 equals the actual fluid viscosity η is reliable only when each SDPD particle has large enough number of neighboring particles, which may require a large enough cutoff radius and/or a density of fluid particles. Therefore, it is always advisable to calculate the fluid viscosity directly (*e.g.*, in shear-flow setup) to check validity of the approximation of the simulated fluid viscosity by η_0. Note that for the fluid viscosity we have always used the precalculated values of η rather than input values of η_0.

The tube wall has been modeled by frozen particles which assume the same structure as the fluid, while the wall thickness is equal to r_c. Thus, the interactions of fluid particles with wall particles are the same as the interactions between fluid particles, and the interactions of a RBC with the wall are identical to those with a suspending fluid. The wall particles also provide a contribution to locally calculated density of fluid particles near a wall, while the local density of wall particles is set to n. To prevent wall penetration, fluid particles as well as vertices of a RBC are subject to reflection at the fluid–solid interface. We employed bounce-back reflections, because they provide a better approximation for the no-slip boundary conditions in comparison to specular reflection of particles. To ensure that no-slip boundary conditions are strictly satisfied, we also add a tangential adaptive shear force[33] which acts on the fluid particles in a near-wall layer of a thickness r_c.

Coupling between the fluid flow and RBC deformation is achieved through viscous friction between RBC nodes and surrounding fluid particles, which is implemented *via* dissipative particle dynamics interactions.[8] Each membrane vertex interacts with fluid particles within a spherical volume with a radius r_c' using dissipative and random forces similar to those in SDPD. The strength of dissipative (friction) coupling depends on the fluid viscosity and particle density as well as on the choice of r_c'. The RBC membrane also separates inner and outer fluids, which is implemented through bounce-back reflections of fluid particles on a membrane surface.[8] Finally, the local density of fluid particles near the membrane includes contributions of both inner and outer fluid particles.

2.3 Simulation setup

The simulation setup consists of a single periodic tube-like channel characterized by a diameter D and the length $L = 10D_r$, filled with a fluid and a single suspended RBC. For simplicity, the fluid viscosity inside a RBC is set to be the same as that of blood plasma. The flow is driven by a constant force f applied to each fluid particle, which is equivalent to a constant pressure gradient $\Delta P/L = fn$, where ΔP is the pressure drop. To characterize the flow we define a non-dimensional shear rate given by

$$\dot{\gamma}^* = \frac{\eta D_r^3 \bar{\dot{\gamma}}}{\kappa_r} = \tau \bar{\dot{\gamma}}, \tag{6}$$

where $\bar{\dot{\gamma}} = \bar{v}/D = Dfn/(32\eta)$ is the average shear rate (or pseudo-shear rate), $\bar{v} = Q/A$ is the average flow velocity with cross-sectional area $A = \pi D^2/4$ and volumetric flow rate $Q = \pi D^4 fn/(128\eta)$, and $\tau = \eta D_r^3/\kappa_r$ is a characteristic relaxation time of a RBC. Note that we define $\bar{\dot{\gamma}}$ based on the Poiseuille flow solution for a Newtonian fluid without a RBC, since a single RBC does not significantly affect the total flow rate. This assumption for Q also results in $\dot{\gamma}^*$ to be proportional to the pressure drop, which would be a convenient parameter to control in experiments. Furthermore, the flow behavior is determined by the cell confinement $\chi = D_r/D$ and the Föppl–von Kármán number $\Gamma = Y_r D_r^2/\kappa_r = 2662$ (average value for a healthy RBC), which characterizes relative importance of cell elasticity to bending rigidity.

To interpret the non-dimensional shear rate with respect to experimental measurements, we can compute the characteristic RBC relaxation time from eqn (6) to be $\tau = 1.1$ s. Thus, the pseudo-shear rate $\bar{\dot{\gamma}}$ used in experiments is roughly equivalent in magnitude to $\dot{\gamma}^*$ in inverse seconds. It is important to note that since we employ distinct viscosity values in different simulations, the RBC relaxation time in simulation units also changes. Therefore, the same shear rate in simulations with different viscosities corresponds to different shear rates in physical units. This approach allows us to keep the Reynolds number low in the simulations, while a large range of shear rates in physical units can be spanned.

2.4 Sensitivity of simulation results to the discretization of fluid and RBC membrane

A too coarse discretization of fluid and RBC membrane may affect simulation results. To check whether our RBC discretization is fine enough, a number of simulations have been performed using significantly different numbers of membrane vertices, $N_v = 1000$ and $N_v = 3000$. The comparison reveals that $N_v = 1000$ is sufficient to obtain accurate results for the investigated range of flow rates. Much larger flow rates may require finer RBC discretization due to strong membrane deformation.

Another potential source of error arises from the discretization of fluid flow. There are two main parameters here, which are related to each other: the particle density n and the cutoff radius r_c within the SDPD fluid. The value of r_c cannot be arbitrarily small, since the SDPD method properly functions only if each particle has a large enough number of neighboring particles. Thus, the choice of r_c is directly associated with the particle density and can be selected smaller in magnitude for higher number densities. To study the sensitivity of the results to fluid discretization, the fluid density has been varied between $n = 0.2 l_0^{-3}$ and $n = 0.8 l_0^{-3}$, while the corresponding r_c values were between $3.8 l_0$ and $2.3 l_0$. Simulation results show that values of $r_c \lesssim 3 l_0$ and $n \gtrsim 0.4 l_0^{-3}$ are small and large enough, respectively, to properly reproduce the flow around a RBC for the studied flow rates. Note that the cutoff radius does not directly reflect strong local correlations, since local interactions are scaled by the weights w_{ij}, which decay to zero at distance r_c.

Finally, coupling between the RBC and fluid flow is also performed over a smoothing length r_c'. Even though generally there are no restrictions on the choice of r_c', it has to be small enough to impose properly the coupling between RBC vertices and local fluid flow. To test the sensitivity of our simulation results to the choice of this parameter, we varied the coupling radius between $1.2 l_0$ and $2.4 l_0$. A comparison of simulation results indicated that $r_c' \lesssim 1.9 l_0$ appears to be sufficient to obtain results independent of r_c' for $\dot{\gamma}^* \lesssim 100$. All results in the paper are obtained using the discretization parameters which comply with the estimations made above.

3 Results and discussion

3.1 Shapes and dynamics of a healthy RBC

Fig. 1 shows several RBC shapes for $\chi = 0.58$ (corresponding to a channel diameter $D = 1.72 D_r$), which are typically encountered in microcirculatory blood flow; see also Movies S1–S4.† For slow flows, see Fig. 1(a), the RBC shape is similar to the biconcave discocyte shape in equilibrium. For higher flow rates, see Fig. 1(b), a slipper shape may be observed, which is characterized here by an off-center position within the tube so that the membrane displays a tank-treading motion due to local shear gradients resembling the tank-treading in shear flow.[34,35] At the highest flow rate, see Fig. 1(c), a parachute shape is obtained, where the cell flows at the channel center and the membrane is practically not moving in the lab frame.

Fig. 2 presents our main result, the shape diagram for different flow rates and confinements, where the cell parameters are similar to those of a healthy RBC. The parachute RBC shape is predominantly observed in the region of strong confinements and high enough flow rates, where large flow forces are able to strongly deform a RBC. Here, it should be

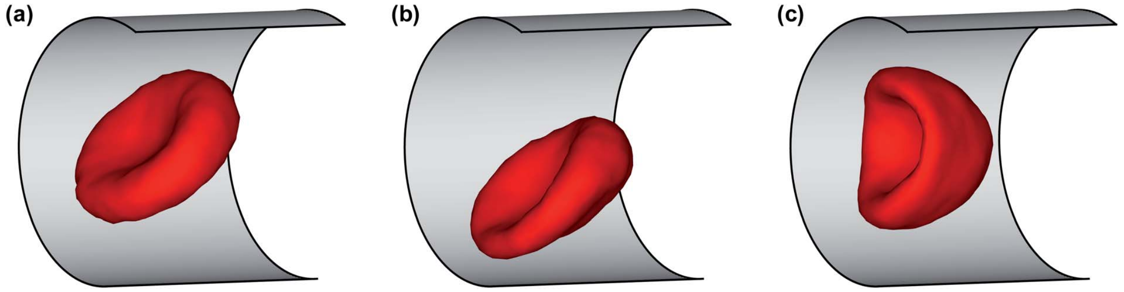

Fig. 1 Simulation snapshots of a RBC in flow (from left to right) for $\chi = 0.58$. (a) A biconcave RBC shape at $\dot{\gamma}^* = 5$; (b) an off-center slipper cell shape at $\dot{\gamma}^* = 24.8$; and (c) a parachute shape at $\dot{\gamma}^* = 59.6$. See also Movies S1–S4.†

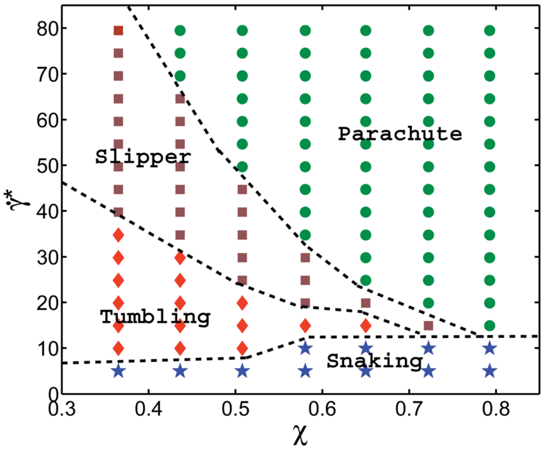

Fig. 2 A phase diagram for $\Gamma = 2662$ ($Y_r = 18.9 \times 10^{-6}$ N m^{-1}, $\kappa_r = 3 \times 10^{-19}$ J), which mimics average membrane properties of a healthy RBC. The plot shows various RBC dynamics states depending on the flow strength characterized by $\dot{\gamma}^*$ and the confinement χ. The symbols depict performed simulations, with the RBC states: parachute (green circles), slipper (brown squares), tumbling (red diamonds) and snaking (blue stars) discocytes. The phase-boundary lines are drawn schematically to guide the eye.

noticed that parachutes are also stable for weak or no confinement when the curvature of the parabolic flow in the center exceeds a critical value.[9,36] At weak confinements, we find off-center slippers with tank-treading motion for higher flow rates, and discocytes with tumbling motion for lower flow rates. Both regions arise from the transition from strongly deformed parachute to more relaxed (discocyte and slipper) shapes, similar to the transition seen in the diagram for 2D vesicles.[9,10] However, the boundary between slippers and discocytes is governed by the critical shear rate $\dot{\gamma}^*_{\mathrm{ttt}}$ of the tumbling-to-tank-treading transition of a RBC;[37,38] tumbling occurs off the tube center, when the local shear rate drops below $\dot{\gamma}^*_{\mathrm{ttt}}$. In the case of small viscosity contrast between inner and outer fluids (equal to unity here), the origin of the tumbling-to-tank-treading transition is the anisotropic shape of the spectrin network, which requires stretching deformation in the tank-treading state,[37,38] and therefore cannot be captured by simulations of 2D vesicles. In addition, near the tumbling-slipper boundary, tumbling motion of a RBC exhibits a noticeable orbital drift so that the tumbling axis is not fixed and oscillates in the vorticity direction (see Movie S2†). This effect is qualitatively similar to a rolling motion (also called kayaking) found in experiments[39] and in simulations[40] of a RBC in shear flow. Orbital oscillations of a tumbling RBC are attributed to local membrane stretching deformation due to small membrane displacements whose effect becomes reduced if a RBC transits to a rolling motion.[39]

At small shear rates $\dot{\gamma}^*$, there also exists a so-called snaking region, first observed for 2D vesicles in ref. 9 and 10, where a RBC performs a periodic oscillatory motion near the center line. In contrast to snaking in 2D, the snaking motion in 3D is fully three dimensional and exhibits an orbital drift (see Movie S1†), which is similar to that for a RBC rolling motion in shear flow occurring in a range of shear rates between RBC tumbling and tank-treading.[39,40] The origin of orbital oscillations in the snaking regime might be similar to that for a rolling RBC; however, this issue requires a more detailed investigation. Note that at very low $\dot{\gamma}^* \lesssim k_B T/\kappa_r$, the rotational diffusion of RBCs becomes important, and RBC dynamics is characterized by random cell orientation. Another striking difference between the phase diagrams in Fig. 2 and in ref. 9 and 10 is that at high confinements the "confined slipper" found in the 2D vesicle simulations is suppressed in 3D. The confined slipper in 2D found for $\chi \gtrsim 0.6$ is qualitatively similar to a slipper at low confinements, which is also called "unconfined slipper" in ref. 9 and 10, since this vesicle state exists in unbound parabolic flow. Note that the regions of confined and unconfined slippers in 2D have no common boundary. The absence of slippers at high confinements in 3D is due to the cylindrical shape of a channel, which would cause the confined slipper to conform to the wall curvature, which is energetically unfavorable.

To better understand the differences between various RBC states, we now analyze the cell orientational angle, displacement from the channel center, and asphericity. The RBC orientational angle is defined as an angle between the eigenvector of the gyration tensor corresponding to the smallest eigenvalue (RBC thickness) and the tube axis. The RBC displacement r is computed as a distance between the RBC center of mass and the tube center. The RBC asphericity characterizes the deviation of a cell from a spherical shape and is defined as $[(\lambda_1 - \lambda_2)^2 + (\lambda_2 - \lambda_3)^2 + (\lambda_3 - \lambda_1)^2]/(2R_g^4)$, where $\lambda_1 \leq \lambda_2 \leq \lambda_3$ are the eigenvalues of the gyration tensor and $R_g^2 = \lambda_1 +$

$\lambda_2 + \lambda_3$. The asphericity for a single RBC in equilibrium is equal to 0.15. Fig. 3 presents the temporal dependence of these properties for different RBC states, including snaking and tumbling discocyte, slipper, and parachute. For the snaking dynamics, the orientational angle oscillates between 40 and 90 degrees (Fig. 3(a)), the cell remains close to the channel center (Fig. 3(b)), and it shows only slight deformation compared to the equilibrium shape (Fig. 3(c)). The parachute shape is characterized by a small orientational angle (aligned with the tube axis), a cell position right in the tube center, and a small asphericity which indicates that the RBC shape attains a more spherical shape. Both tumbling discocytes and tank-treading slippers are displaced further from the channel center (Fig. 3(b)) than snaking discocytes and parachutes, and show an oscillating orientational angle. However, tumbling discocytes clearly show cell rotations, while slippers display a swinging motion characterized by small orientational oscillations around the tank-treading axis.[37] Moreover, a tumbling RBC does not experience strong deformation (Fig. 3(c)), while a slipper shows large oscillations in cell asphericity. Note that to determine the RBC shape under given conditions, we used both visual assessment of the corresponding RBC shapes in flow and the analysis of the characteristics discussed above.

3.2 Comparison with experiments

There exist several experimental studies of a RBC in microchannel flow.[17,20,23,41] In the experiments of ref. 23, the rotation of single RBCs and of their rouleaux structures in tube flow with radii ranging from 30 μm to 100 μm has been investigated. Even though the tube diameters in the experiments were larger than those used in our simulations, these experiments provide direct evidence of the existence of RBC off-center tumbling dynamics for low confinements and low flow rates with $\bar{\dot{\gamma}} \lesssim 50\ \mathrm{s}^{-1}$, in agreement with the simulation results in Fig. 2.

In the experiments of ref. 17, the imposed flow velocities were very large, ranging from 1 cm s^{-1} to 30 cm s^{-1} in a capillary with the diameter of 9 μm. This is much faster than the typical flow velocities in microcirculation, where for venules and arterioles with a similar diameter flow velocities are in the range of 0.2–7 mm s^{-1}.[4,42] The range of flow velocities we span in our simulations is about 0.2–1.0 mm s^{-1}, and is therefore comparable with that in microcirculation. The results in ref. 17 show the existence of parachute and slipper shapes, where a weak confinement favors non-centered slipper shapes, which is in qualitative agreement with the simulations in Fig. 2. Furthermore, a good agreement between experiments and simulations is found for low confinements, where parachute shapes are observed for flow rates with the velocities lower than 4–7 cm s^{-1}.[17] At flow velocities larger than approximately 7 cm s^{-1} and at low confinements, centered slippers are observed which resemble parachutes, but become slightly asymmetric.[17] Recent 2D simulations[10] have also found that at high enough flow rates centered slippers and parachutes may coexist. Currently, we are not able to reach such high flow rates in 3D simulations due to numerical limitations. In addition, this region might be of limited interest, since the corresponding flow rates are far beyond the physiologically relevant values.

Experimental data in ref. 20 were obtained for narrow capillaries with diameters ranging from 4.7 μm to 10 μm; however, the flow velocities are considerably smaller than those in ref. 17, in the range of 1–40 mm s^{-1}. For strong confinements $\chi \gtrsim 1$, centered bullet-like shapes are observed which resemble an elongated cylindrical shape with a semi-spherical cap at the front end and a semi-spherical dip at the rear end. A comparison with our simulation results for the weaker confinement of $\chi = 0.65$ shows a good agreement since centered parachute shapes are found in both experiments and simulations. The transition to the parachute shape for $\chi = 0.65$ occurred at the RBC velocity of about 0.5 mm s^{-1} in the experiments,[20] while our simulations predict the transition velocity of about 0.45 mm s^{-1}.

3.3 The effects of membrane properties on the shape diagram

In order to investigate the effects of membrane elastic parameters on the RBC phase diagram in capillary flow, we calculated

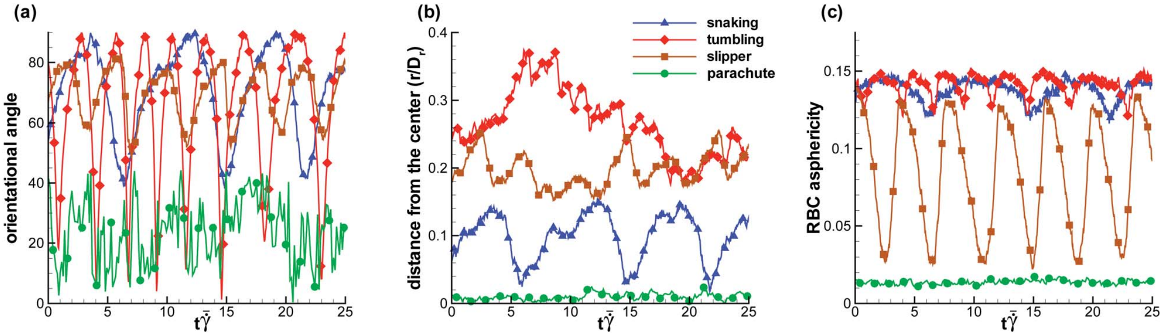

Fig. 3 Characteristics of different RBC states: blue triangle – snaking discocyte ($\dot{\gamma}^* = 9.9$, $\chi = 0.72$), red diamond – tumbling discocyte ($\dot{\gamma}^* = 14.9$, $\chi = 0.44$), brown square – slipper ($\dot{\gamma}^* = 49.7$, $\chi = 0.44$), and green circle – parachute ($\dot{\gamma}^* = 64.6$, $\chi = 0.65$). (a) Cell orientational angle between the eigenvector of the gyration tensor corresponding to the smallest eigenvalue (RBC thickness) and the tube axis. (b) Distance between the RBC center of mass and the tube center normalized by D_r. (c) RBC asphericity, which characterizes the deviation from a spherical shape. The asphericity is defined as $[(\lambda_1 - \lambda_2)^2 + (\lambda_2 - \lambda_3)^2 + (\lambda_3 - \lambda_1)^2]/(2R_g^4)$, where $\lambda_1 \le \lambda_2 \le \lambda_3$ are the eigenvalues of the gyration tensor and $R_g^2 = \lambda_1 + \lambda_2 + \lambda_3$. The asphericity for a single RBC in equilibrium is equal to 0.15. See also Movies S1–S4.†

phase diagrams for both reduced Young's modulus and increased bending rigidity. The state diagram for membrane bending rigidity increased by a factor of five, which leads to $\kappa_r = 1.5 \times 10^{-18}$ J and $\Gamma = 532$, is shown in Fig. 4. We expect a dependence of the transition lines on the membrane parameters and geometry of the channel to be of the form $\dot{\gamma}_c^* = \tilde{\Omega}(\Gamma, \chi, \kappa_r/k_BT)$, where $\tilde{\Omega}$ is a universal function for each transition. In addition, a more general form of $\dot{\gamma}_c^*$ should also include the strength of thermal fluctuations characterized by ambient temperature as an independent variable. As an example, different temperatures would affect the rotational diffusion of RBCs, which may become important at very low $\dot{\gamma}^*$ and lead to random cell orientation modifying potentially a snaking region. Also, recent experiments on vesicles[43] and a corresponding theory[44] suggest that the transition lines might be affected by thermal noise due to the sensitivity of a nonlinear dynamics to small perturbations near transition lines. A comparison of the results of Fig. 4 with those of Fig. 2 shows that for stiffer cells, the parachute and slipper/tumbling regions shift to lower values of $\dot{\gamma}^*$. This behavior is consistent with the roughly linear dependence of the shear rate $\bar{\dot{\gamma}}$ at the parachute-to-discocyte transition on RBC bending rigidity and shear modulus reported in ref. 7, which is equivalent to $\dot{\gamma}^* = c_1(\chi) + c_2(\chi)\Gamma$. Similarly, the snaking region shrinks towards lower $\dot{\gamma}^*$ values.

Fig. 5 shows the state diagram for a RBC in tube flow with the membrane Young's modulus reduced by the factor of three ($Y_r = 6.3$ μN m^{-1}) in comparison to that of a healthy RBC. This diagram should be compared with Fig. 2 and 4, which are for healthy RBCs and cells with an increased bending rigidity, respectively. In Fig. 5, the transition from snaking discocytes and swinging slippers to the parachute shape, as well as the transition from tumbling discocytes to swinging slippers occur at lower flow rates than those for a healthy RBC (Fig. 2). As a consequence, the snaking region shrinks substantially and is observed primarily at very low $\dot{\gamma}^*$. Another feature is that the tumbling region is significantly reduced in comparison to that in the diagram for healthy cells (Fig. 2). These results are consistent with the fact that the transition from discocyte to parachute shapes in Poiseuille flow depends roughly linearly on the RBC elastic properties and bending rigidity,[7] as well as that the tumbling-to-tank-treading transition of a RBC in shear flow depends nearly linearly on the RBC elastic properties such as Young's modulus.[37,38] This implies that the transition lines for a fixed ambient temperature are linear functions of the Föppl–von Kármán number Γ, as discussed above. A comparison with the results of ref. 7 for RBCs with considerably smaller bending and shear rigidities indicates that strong thermal fluctuations destroy the regular snaking oscillations.

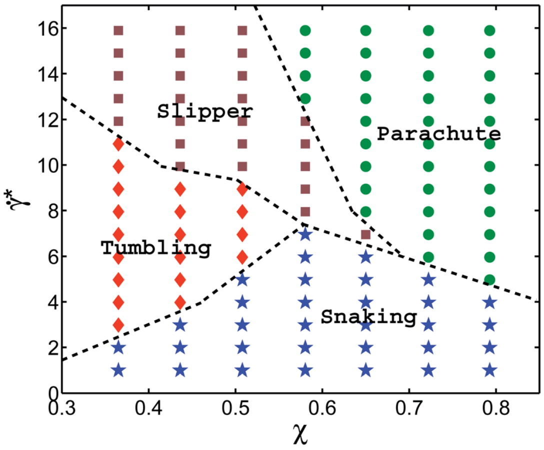

Fig. 4 A phase diagram for $\Gamma = 532$ ($Y_r = 18.9 \times 10^{-6}$ N m^{-1}, $\kappa_r = 1.5 \times 10^{-18}$ J) such that the bending rigidity of a cell membrane is five times larger than $\kappa_r = 3 \times 10^{-19}$ J of a healthy RBC. The diagram depicts RBC behavior in tube flow with respect to the dimensionless shear rate $\dot{\gamma}^*$ and confinement χ. The symbols correspond to performed simulations and RBC states are the parachute (green circles), slipper (brown squares), tumbling (red diamonds) and snaking (blue stars) discocytes. The phase-boundary lines are drawn schematically to guide the eye.

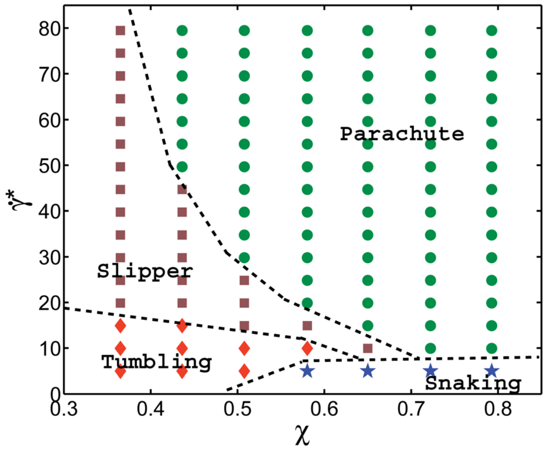

Fig. 5 A phase diagram for $\Gamma = 887$ ($Y_r = 6.3 \times 10^{-6}$ N m^{-1}, $\kappa_r = 3 \times 10^{-19}$ J) where the Young's modulus of a cell membrane is three times lower than that assumed for a healthy RBC. The plot shows different RBC dynamical states in tube flow with respect to the non-dimensional shear rate $\dot{\gamma}^*$ and the confinement χ. The symbols depict performed simulations and RBC states include the parachute (green circles), slipper (brown squares), tumbling (red diamonds) and snaking (blue stars) discocytes. The phase-boundary lines are drawn schematically to guide the eye.

Correspondence of different systems with a fixed Föppl–von Kármán number Γ is also supported by the argument that the RBC relaxation time τ is a linear function of RBC membrane elastic parameters (κ_r or equivalently Y_r for a fixed Γ). Thus, a simulation with the parameters $\{D_r, Y_r, s\kappa_r, \dot{\gamma}^*\}$ should lead to identical results as those obtained from a simulation with $\{D_r, Y_r/s, \kappa_r, \dot{\gamma}^*/s\}$, where s is a scaling constant. Even though this argument is quite general, other characteristics of a system also need to be properly considered including thermal fluctuations and Reynolds number of the flow. Finally, the assumption of linear dependence of τ on the membrane properties may become invalid for strong enough flow rates, which may lead to non-linear membrane deformation. A semi-quantitative comparison of cell shape regions can be done by looking at the state diagram of Fig. 5 for the reduced membrane Young's modulus and the state diagram of Fig. 4 for an increased membrane bending rigidity. The corresponding Föppl–von Kármán numbers are not the same, but similar in magnitude and both are considerably smaller than those for healthy RBCs. Thus, we expect that the two state diagrams for $\Gamma = 532$ (Fig. 4) and $\Gamma = 887$ (Fig. 5) should be similar, and show the same trends in comparison with the diagram for healthy cells (Fig. 2). This comparison further supports our argument about the existence of universal functions $\dot{\gamma}^*_c$ to describe the transition lines.

3.4 The effect of cytosol viscosity on the shape diagram

We have focused in our simulations on the investigation of the effect of membrane elasticity on RBC dynamics in microcapillary flow, and have therefore employed same viscosity for the suspending fluid and RBC cytosol. For a healthy RBC, the viscosity contrast λ, defined as the ratio of cytosol over blood plasma viscosity, is approximately $\lambda = 5$. Therefore, we want to discuss briefly the possible effect of the viscosity contrast on the dynamical states. Clearly, cytosol viscosity only plays a role when the internal fluid (or equivalently membrane) is in motion, *i.e.*, only when the cell tank-treads in the slipper state. Thus, we mainly need to discuss how the slipper region will be modified. Recent experiments[45] and simulations[46] indicate that the viscosity contrast indeed strongly affects the tumbling-to-tank-treading transition characterized by $\dot{\gamma}^*_{\rm ttt}$.

An increase in λ is known to shift $\dot{\gamma}^*_{\rm ttt}$ of the tumbling-to-tank-treading transition to higher shear rates.[46] Therefore, we expect that the boundary between the tumbling and slipper regions in Fig. 2 would shift to higher values of $\dot{\gamma}^*$ for a real RBC leading to the expansion of the tumbling region. A very large viscosity of either RBC membrane or cytosol, which may occur in some blood-related diseases or disorders,[22] may also lead to a complete disappearance of the slipper region, which would be replaced by the RBC tumbling state. Recent simulations of 2D vesicles with $\lambda = 1$ in ref. 9 and $\lambda = 5$ in ref. 10 have shown an expansion of the snaking region toward the slipper region, since the RBC tank-treading becomes less favorable. Note that since RBC tumbling due to membrane elastic anisotropy is not possible in 2D, the snaking region in ref. 9 and 10 has a large common boundary with the slipper region, while in 3D the snaking region has practically no boundary with the dynamical slipper region and is mainly connected to the tumbling region (Fig. 2). Thus, no significant changes in the snaking region due to the viscosity contrast is expected in 3D. In analogy with the expansion of the snaking region in 2D, an expansion of the tumbling region in 3D can be expected.

An effect of the viscosity contrast on the boundary between the slipper and parachute regions is not obvious. 2D simulations for different viscosity contrasts[9,10] indicate that the boundary is slightly altered that makes the slipper region get mildly expanded. Thus, it is plausible to expect a similarly weak effect in 3D; however, a definite statement on this issue is only possible after a systematic numerical investigation of the effect of viscosity contrast has been performed in 3D.

3.5 Snaking, tumbling, and swinging frequencies

The simulations also provide interesting information about the dependence of the snaking, tumbling (both in the discocyte state) and swinging (in the slipper state) frequencies ω on shear rate, as shown in Fig. 6 for three different confinements extracted from the state diagram of Fig. 4. In all regimes, the frequencies increase linearly with shear rate. However, the prefactors of this linear dependence are very different. The strongest dependence is found in the swinging regime, somewhat larger than that in the snaking regime, while the frequency is almost independent of $\dot{\gamma}^*$ in the tumbling regime. Increasing confinement significantly reduces the snaking, tumbling and swinging frequencies. Note that the swinging frequencies are likely to be overpredicted in Fig. 6 in comparison with those of real RBCs due to the assumption of having the same viscosity of the suspending medium and RBC cytosol.

3.6 Flow resistance

Fig. 7 presents the volumetric flow rate $Q_{\rm RBC}$ with a RBC measured in simulations and normalized by the flow rate Q without a RBC. Data are shown for different $\dot{\gamma}^*$ for the case of $\Gamma = 2662$, corresponding to the shape diagram in Fig. 2. The volumetric flow rate at low confinements remains essentially unaffected by the presence of a RBC. As the confinement is increased, the flow rate decreases and the effect of a RBC on the flow rate appears to be stronger at low $\dot{\gamma}^*$ values. Note that Fig. 7 also presents the change in flow resistance, since the apparent viscosity is inversely proportional to the volumetric flow rate. Thus, the apparent viscosity increases with increasing confinement. A reduction in the flow resistance with the increase of $\dot{\gamma}^*$ (represented by different curves in Fig. 7) is due to the transition from discocyte to parachute and slipper shapes,

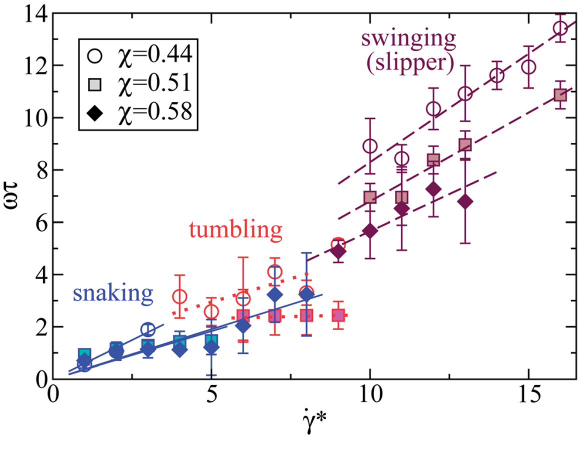

Fig. 6 Normalized snaking, tumbling, and swinging (slipper state) frequencies ω of RBCs as a function of the dimensionless shear rate $\dot{\gamma}^*$. The elastic membrane parameters are the same as in Fig. 4 ($Y_r = 18.9 \times 10^{-6}$ N m^{-1}, $\kappa_r = 1.5 \times 10^{-18}$ J), *i.e.* the bending rigidity is five times larger than that used for a healthy RBC, and $\Gamma = 532$. Three confinements are shown, as indicated. The symbols depict simulation results for various confinements. The regions of $\dot{\gamma}^*$ corresponding to different RBC states can be distinguished in the plot by colors and line types – swinging (brown, dashed line), tumbling (red, dotted line), and snaking (blue, solid line).

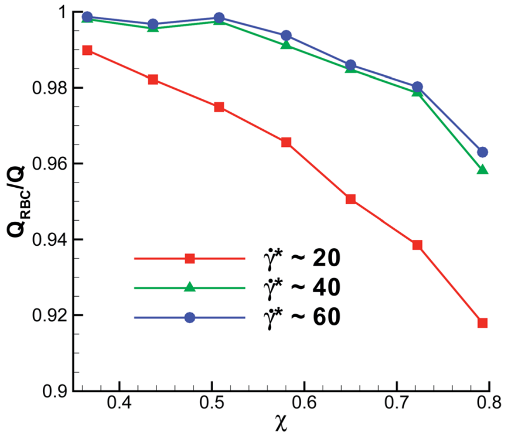

Fig. 7 The volumetric flow rate Q_{RBC} with a RBC normalized by the flow rate Q without a RBC as a function of the confinement χ for different $\dot{\gamma}^*$. The Föppl–von Kármán number $\Gamma = 2662$ is representative of healthy RBCs.

since for large enough $\dot{\gamma}^*$ no significant further changes in flow resistance occur.

Even though Fig. 7 shows the effect of confinement on Q_{RBC}, the flow resistance for different χ may be also affected by the change in hematocrit. In all simulations, the length of the channel was kept the same, while the tube diameter was varied, which means that the tube hematocrit (H_t), calculated as the ratio of the RBC volume to total tube volume, is inversely proportional to D^2. For the strongest confinement $\chi = 0.79$ ($D = 8.2$ μm) H_t is equal to 0.027, while for the lowest confinement $\chi = 0.37$ ($D = 17.8$ μm) $H_t = 0.0057$.

4 Conclusions

Even though the phase diagrams of RBC shapes show some qualitative similarities with the corresponding diagram of 2D vesicles,[9,10] there are several qualitative and quantitative differences. In 3D, slippers are essentially absent at high confinements ($\chi \gtrsim 0.7$) and low flow rates due to the cylindrical channel geometry, which requires the RBC slipper to comply with the channel wall curvature and cannot be captured by a 2D model. Therefore, parachute shapes are preferred at high χ – in agreement with the 3D results of ref. 7. At even higher confinements than those in this study, RBCs are expected to attain bullet shapes.[20] Another evident difference between RBCs in 3D and vesicles in 2D[9,10] is the existence of a RBC tumbling region, which appears in 3D due to anisotropic elastic properties of RBCs.[37,38] For vesicles in 2D, the only possibility to include tumbling is to introduce a high enough viscosity contrast between the fluids inside and outside a RBC.

The calculated state diagrams in 3D provide a better description of RBC shapes and dynamics in microvascular flow than the previous 2D results. The flow resistance is affected only weakly by the transition from discocyte to parachute and slipper shapes, most significantly at high confinements ($\chi \gtrsim 0.6$). The geometrical complexity of microvasculature induces non-trivial partitioning of RBCs, which often leads to very low cell volume fractions within various vessel structures, so that our simulation results provide an important step towards an understanding of blood flow and RBC behavior in microcirculation. Finally, similar physical mechanisms are expected for capsule suspensions.

Acknowledgements

A CPU time grant by the Jülich Supercomputing center is gratefully acknowledged. Dmitry A. Fedosov acknowledges funding by the Alexander von Humboldt Foundation. We also thank the DFG Research Unit FOR 1543 "SHENC – Shear Flow Regulation in Hemostasis" for support.

References

1 R. G. Larson, *The structure and rheology of complex fluids*, Oxford University Press, Oxford, NY, 1999.
2 J. A. Davis, D. W. Inglis, K. M. Morton, D. A. Lawrence, L. R. Huang, S. Y. Chou, J. C. Sturm and R. H. Austin, *Proc. Natl. Acad. Sci. U. S. A.*, 2006, **103**, 14779–14784.
3 H. Craighead, *Nature*, 2006, **442**, 387–393.
4 A. S. Popel and P. C. Johnson, *Annu. Rev. Fluid Mech.*, 2005, **37**, 43–69.
5 T. Omori, Y. Imai, T. Yamaguchi and T. Ishikawa, *Phys. Rev. Lett.*, 2012, **108**, 138102.
6 A. Kumar and M. D. Graham, *Phys. Rev. Lett.*, 2012, **109**, 108102.
7 H. Noguchi and G. Gompper, *Proc. Natl. Acad. Sci. U. S. A.*, 2005, **102**, 14159–14164.
8 D. A. Fedosov, B. Caswell and G. E. Karniadakis, *Biophys. J.*, 2010, **98**, 2215–2225.
9 B. Kaoui, N. Tahiri, T. Biben, H. Ez-Zahraouy, A. Benyoussef, G. Biros and C. Misbah, *Phys. Rev. E: Stat., Nonlinear, Soft Matter Phys.*, 2011, **84**, 041906.
10 N. Tahiri, T. Biben, H. Ez-Zahraouy, A. Benyoussef and C. Misbah, *Microvasc. Res.*, 2013, **85**, 40–45.
11 D. A. Fedosov, H. Noguchi and G. Gompper, *Biomech. Model. Mechanobiol.*, 2014, **13**, 239–258.
12 R. S. Sprague, M. L. Ellsworth, A. H. Stephenson, M. E. Kleinhenz and A. J. Lonigro, *Am. J. Physiol.*, 1998, **275**, H1726–H1732.
13 A. M. Forsyth, J. Wan, P. D. Owrutsky, M. Abkarian and H. A. Stone, *Proc. Natl. Acad. Sci. U. S. A.*, 2011, **108**, 10986–10991.
14 R. Skalak, *Science*, 1969, **164**, 717–719.
15 P. Gaehtgens, C. Dührssen and K. H. Albrecht, *Blood Cells*, 1980, **6**, 799–812.
16 U. Bagge, P.-I. Branemark, R. Karlsson and R. Skalak, *Blood Cells*, 1980, **6**, 231–237.
17 M. Abkarian, M. Faivre, R. Horton, K. Smistrup, C. A. Best-Popescu and H. A. Stone, *Biomed. Mater.*, 2008, **3**, 034011.
18 I. V. Pivkin and G. E. Karniadakis, *Phys. Rev. Lett.*, 2008, **101**, 118105.

19 J. L. McWhirter, H. Noguchi and G. Gompper, *Proc. Natl. Acad. Sci. U. S. A.*, 2009, **106**, 6039–6043.

20 G. Tomaiuolo, M. Simeone, V. Martinelli, B. Rotoli and S. Guido, *Soft Matter*, 2009, **5**, 3736–3740.

21 B. Kaoui, G. Biros and C. Misbah, *Phys. Rev. Lett.*, 2009, **103**, 188101.

22 M. Diez-Silva, M. Dao, J. Han, C.-T. Lim and S. Suresh, *MRS Bull.*, 2010, **35**, 382–388.

23 H. L. Goldsmith and J. Marlow, *Proc. R. Soc. London, Ser. B*, 1972, **182**, 351–384.

24 P. Espanol and M. Revenga, *Phys. Rev. E: Stat., Nonlinear, Soft Matter Phys.*, 2003, **67**, 026705.

25 D. E. Discher, D. H. Boal and S. K. Boey, *Biophys. J.*, 1998, **75**, 1584–1597.

26 D. A. Fedosov, B. Caswell and G. E. Karniadakis, *Comput. Methods Appl. Mech. Eng.*, 2010, **199**, 1937–1948.

27 H. S. Seung and D. R. Nelson, *Phys. Rev. A*, 1988, **38**, 1005–1018.

28 E. A. Evans and R. Skalak, *Mechanics and thermodynamics of biomembranes*, CRC Press, Inc., Boca Raton, Florida, 1980.

29 L. B. Lucy, *Astron. J.*, 1977, **82**, 1013–1024.

30 J. J. Monaghan, *Annu. Rev. Astron. Astrophys.*, 1992, **30**, 543–574.

31 P. J. Hoogerbrugge and J. M. V. A. Koelman, *Europhys. Lett.*, 1992, **19**, 155–160.

32 P. Espanol and P. Warren, *Europhys. Lett.*, 1995, **30**, 191–196.

33 D. A. Fedosov and G. E. Karniadakis, *J. Comput. Phys.*, 2009, **228**, 1157–1171.

34 R. Tran-Son-Tay, S. P. Sutera and P. R. Rao, *Biophys. J.*, 1984, **46**, 65–72.

35 T. M. Fischer, *Biophys. J.*, 2007, **93**, 2553–2561.

36 J. L. McWhirter, H. Noguchi and G. Gompper, *Soft Matter*, 2011, **7**, 10967–10977.

37 M. Abkarian, M. Faivre and A. Viallat, *Phys. Rev. Lett.*, 2007, **98**, 188302.

38 J. M. Skotheim and T. W. Secomb, *Phys. Rev. Lett.*, 2007, **98**, 078301.

39 J. Dupire, M. Socol and A. Viallat, *Proc. Natl. Acad. Sci. U. S. A.*, 2012, **109**, 20808–20813.

40 D. Cordasco and P. Bagchi, *Phys. Fluids*, 2013, **25**, 091902.

41 G. Tomaiuolo, V. Preziosi, M. Simeone, S. Guido, R. Ciancia, V. Martinelli, C. Rinaldi and B. Rotoli, *Ann. Ist. Super. Sanita*, 2007, **43**, 186–192.

42 A. R. Pries, T. W. Secomb and P. Gaehtgens, *Am. J. Physiol.*, 1995, **269**, H1713–H1722.

43 M. Levant and V. Steinberg, *Phys. Rev. Lett.*, 2012, **109**, 268103.

44 D. Abreu and U. Seifert, *Phys. Rev. Lett.*, 2013, **110**, 238103.

45 V. Vitkova, M.-A. Mader, B. Polack, C. Misbah and T. Podgorski, *Biophys. J.*, 2008, **95**, L33–L35.

46 A. Z. K. Yazdani and P. Bagchi, *Phys. Rev. E: Stat., Nonlinear, Soft Matter Phys.*, 2011, **84**, 026314.

P7: White blood cell margination in microcirculation

D. A. Fedosov and G. Gompper

Soft Matter, **10**:2961-2970, 2014.

Soft Matter

PAPER

View Article Online
View Journal | View Issue

White blood cell margination in microcirculation†

Dmitry A. Fedosov* and Gerhard Gompper

Cite this: *Soft Matter*, 2014, **10**, 2961

Received 12th November 2013
Accepted 22nd January 2014

DOI: 10.1039/c3sm52860j

www.rsc.org/softmatter

Proper functioning of white blood cells is not possible without their ability to adhere to vascular endothelium, which may occur only if they are close enough to vessel walls. To facilitate the adhesion, white blood cells migrate toward the vessel walls in blood flow through a process called margination. The margination of white cells depends on a number of conditions including local hematocrit, flow rate, red blood cell aggregation, and the deformability of both red and white cells. To better understand the margination process of white blood cells, we employ mesoscopic hydrodynamic simulations of a three-dimensional model of blood flow, which has been previously shown to capture quantitatively realistic blood flow properties and rheology. The margination properties of white blood cells are studied for a wide range of hematocrit values and flow conditions. Efficient white blood cell margination is found in an intermediate range of hematocrit values of $H_t \approx 0.2$–0.4 and at relatively low flow rates, characteristic of the venular part of microcirculation. In addition, aggregation interactions between red blood cells lead to enhanced white-blood-cell margination. This simulation study provides a quantitative description of the margination of white blood cells, and is also highly relevant for the margination of particles or cells of similar size such as circulating tumor cells.

1 Introduction

Leukocytes or white blood cells (WBCs) defend our body from various viral and bacterial infections and other foreign substances. They are normally located in the blood stream and in the lymphatic system, where they are able to monitor various chemical signals or stimuli. Once WBCs have detected a problem, *e.g.*, an inflammation, their cellular machinery is able to facilitate transmigration into a surrounding tissue,[1] which is necessarily preceded by their adhesion to vascular endothelium.[2,3] However, the possibility of WBC interactions with a vessel wall, and therefore adhesion, is directly associated with the probability of being close enough to a vessel wall in blood flow. A number of experimental observations[4–6] suggest that WBCs migrate toward vessel walls in blood flow, a process which is called *margination*. Thus, the WBC margination probability, which characterizes the fraction of time a WBC spends near a wall, directly affects the frequency of WBC adhesion.

A number of experimental observations[7,8] and simulations[9–12] of flowing blood have shown that red blood cells (RBCs) concentrate in the vessel center leading to a layer free of RBCs next to a wall. The migration of RBCs toward the vessel center has been attributed to a lift force,[13–15] which arises from cell-wall hydrodynamic interactions in flow due to the non-spherical discocyte shape and high deformability of RBCs. Therefore, the migration effect for various cells is different due to the differences in size, shape, and deformability of blood cells, for instance between RBCs and WBCs. Different cell-wall hydrodynamic interactions of RBCs and WBCs lead to their segregation in flow such that WBCs are likely to be present near a wall. In fact, the lift force on WBCs is expected to be much lower than that on RBCs, since WBCs have a near-spherical shape and are not very deformable. This argument supports the fact that RBCs populate the vessel center, while WBCs may get marginated to the RBC free layer. Therefore, WBC margination in blood flow is mediated by RBCs.

Existing experimental[4,6,16–18] and simulation[19–21] studies have shown that WBC margination has a non-trivial dependence on various blood flow properties including hematocrit H_t, (*i.e.* RBC volume fraction), flow rate, vessel geometry, and RBC aggregation. Early *in vivo* experiments on WBC adhesion[6] have shown a high WBC adhesion rate at low flow rates characteristic of venular blood flow and high $H_t > 0.45$. *In vitro* experiments on WBC adhesion in glass tubes[17] suggested a similar dependence of WBC adhesion on the flow rate; however, they reported no significant dependence of WBC adhesion on H_t. One of the first simulation studies in two dimensions (2D)[20] has also reported no significant effect of H_t on WBC margination. In contrast, WBC margination in microfluidic experiments[18] has been found to be pronounced within an intermediate range of $H_t \simeq 0.2$–0.3, while at both lower and higher H_t values WBC margination has been reduced. Recent simulation work in 2D[21] was able to

---

Theoretical Soft Matter and Biophysics, Institute of Complex Systems, Institute for Advanced Simulation, Forschungszentrum Jülich, 52425 Jülich, Germany. E-mail: d.fedosov@fz-juelich.de

† Electronic supplementary information (ESI) available: Two movies show simulation snapshots of blood flow with a marginated white blood cell and a non-marginated white blood cell for different hematocrits and flow rates. See DOI: 10.1039/c3sm52860j

reconcile the existing contradicting observations of WBC margination dependence on H_t, showing that a strong margination effect is achieved for an intermediate range of H_t values. At low H_t, WBC margination is weak due to a low concentration of RBCs, while at high H_t WBC margination is attenuated due to interactions of marginated WBCs with RBCs near a wall, which significantly limit the time WBCs spend near a wall. The apparent inconsistency with experiments[17] and simulations,[20] which suggests no dependence of WBC margination on H_t, has been reconciled due to the fact that the H_t values used in these studies fall almost entirely into the region of a strong WBC margination predicted in ref. 21. Furthermore, RBC aggregation has been found to result in an enhanced WBC margination and adhesion in both experiments[6,16–18] and simulations.[21]

Even though the 2D simulations[20,21] provide a qualitative picture of WBC margination, it is not clear whether WBC margination would display substantial changes in 3D. Another evident difference between 2D and 3D is that 2D simulations mimic blood flow in a slit geometry, while WBC margination in a tube geometry is of great interest, since it mimics an idealized blood vessel in microcirculation. To investigate WBC margination in idealized microvessels, we employ a particle-based mesoscopic simulation technique. WBC margination is investigated in 3D for a wide range of blood flow conditions including hematocrit, flow rate, and RBC aggregation, providing a quantitative description of WBC margination in microvessels. Our simulation results in 3D show a qualitatively similar dependence of WBC margination on H_t as in 2D, predicting a strong margination effect within an intermediate range of H_t values. Furthermore, WBC margination appears to be pronounced only for low enough flow rates characteristic of venular blood flow, consistent with existing experimental observations.[6,16,17] In addition, we estimate the forces on a marginated WBC in the normal direction to the wall, which may aid in WBC adhesion.

2 Methods and models

To model blood flow we use a particle-based mesoscopic simulation technique called the smoothed dissipative particle dynamics (SDPD) method.[22] Blood cells are represented by a network membrane model, since triangulated surfaces with curvature and stretching elasticity provide a very versatile approach to model the shapes and deformation of vesicles and cells in three dimensions.[12,23–27] Cell membranes are coupled to a background fluid (*i.e.*, blood plasma) through viscous friction. We briefly describe the employed cell model and the SDPD method.

2.1 Blood cell model

2.1.1 Membrane network model. In simulations, a cell membrane is represented by a collection of N_v particles with coordinates $\{\mathbf{x}_{i=1}\ldots N_\mathrm{v}\}$ interconnected by viscoelastic springs.[27,28] The network of springs has a fixed connectivity and is characterized by the following energy

$$U(\{\mathbf{x}_i\}) = U_\mathrm{s} + U_\mathrm{b} + U_\mathrm{a+v}, \tag{1}$$

where U_s is the elastic spring energy, U_b imposes membrane bending resistance, and $U_\mathrm{a+v}$ defines the area and volume conservation constraints. The spring's contribution U_s mimics membrane elasticity, which is, for instance, supplied by a spectrin network for a RBC membrane. In addition, each spring may contain a friction term in order to incorporate a non-zero membrane viscosity similar to that of a lipid bilayer. The term U_b implies bending resistance of a cell membrane, while the area and volume conservation constraints mimic area-incompressibility of the lipid bilayer and incompressibility of a cytosol, respectively.

The vertices on a cell membrane are connected by N_s springs with the potential energy

$$U_\mathrm{s} = \sum_{j\in 1\ldots N_\mathrm{s}} \left[\frac{k_\mathrm{B}Tl_\mathrm{m}\left(3x_j^{\,2} - 2x_j^{\,3}\right)}{4p\left(1 - x_j\right)} + \frac{k_\mathrm{p}}{l_j} \right], \tag{2}$$

where l_j is the length of the spring j, l_m is the maximum spring extension, $x_j = l_j/l_\mathrm{m}$, p is the persistence length, $k_\mathrm{B}T$ is the energy unit, and k_p is the spring constant. Note that each spring consists of the attractive wormlike chain potential and a repulsive potential such that a non-zero equilibrium spring length can be imposed. For the performance of different spring models for a RBC membrane, we refer to ref. 28.

The membrane viscosity can be modeled by a viscous force assigned to each spring. Thus, we introduce dissipative and random forces for each spring $\mathbf{F}_{ij}^\mathrm{D}$ and $\mathbf{F}_{ij}^\mathrm{R}$, respectively, similar to those in the theoretical framework of the fluid particle model.[29] This force pair satisfies the fluctuation–dissipation balance in order to maintain a consistent membrane temperature and is given by

$$\mathbf{F}_{ij}^\mathrm{D} = -\gamma^\mathrm{T}\mathbf{v}_{ij} - \gamma^\mathrm{C}(\mathbf{v}_{ij}\cdot\mathbf{e}_{ij})\mathbf{e}_{ij}, \tag{3}$$

$$\mathbf{F}_{ij}^\mathrm{R}\mathrm{d}t = \sqrt{2k_\mathrm{B}T}\left(\sqrt{2\gamma^T}\mathrm{d}\overline{\mathbf{W}_{ij}^\mathrm{S}} + \sqrt{3\gamma^\mathrm{C} - \gamma^\mathrm{T}}\ \frac{tr\left[\mathrm{d}\mathbf{W}_{ij}\right]}{3}\mathbf{1}\right)\cdot\mathbf{e}_{ij}, \tag{4}$$

where γ^T and γ^C are dissipative parameters and the superscripts T and C denote the "translational" and "central" components, $\mathbf{v}_{ij}$ is the relative velocity of spring ends, $tr[\mathrm{d}\mathbf{W}_{ij}]$ is the trace of a random matrix of independent Wiener increments $\mathrm{d}\mathbf{W}_{ij}$, and $\mathrm{d}\overline{\mathbf{W}_{ij}^\mathrm{S}} = \mathrm{d}\mathbf{W}_{ij}^\mathrm{S} - tr[\mathrm{d}\mathbf{W}_{ij}^\mathrm{S}]\mathbf{1}/3$ is the traceless symmetric part. Note that the condition $3\gamma^\mathrm{C} - \gamma^\mathrm{T} \geq 0$ has to be satisfied.

The bending energy of the RBC membrane is defined as

$$U_\mathrm{b} = \sum_{j\in 1\ldots N_\mathrm{s}} k_\mathrm{b}\left[1 - \cos\left(\theta_j - \theta_0\right)\right], \tag{5}$$

where k_b is the bending constant, θ_j is the instantaneous angle between two adjacent triangles with the common edge j, and θ_0 is the spontaneous angle. The area and volume conservation constraints are given by

$$U_\mathrm{a+v} = \sum_{j\in 1\ldots N_\mathrm{t}} \frac{k_\mathrm{d}\left(A_j - A_\mathrm{t}\right)^2}{2A_\mathrm{t}} + \frac{k_\mathrm{a}\left(A - A_0\right)^2}{2A_0} + \frac{k_\mathrm{v}\left(V - V_0\right)^2}{2V_0}, \tag{6}$$

where N_t is the number of triangles in the network, A_t is the triangle area, and k_d, k_a and k_v are the local area, global area and volume constraint coefficients, respectively. The terms A and V are the total cell area and volume, while A_0 and V_0 are the desired total area and volume, respectively. More details of the RBC model can be found in ref. 27 and 28.

2.1.2 Membrane elastic properties. A linear analysis of a regular hexagonal network[27,28] leads to relations between the model parameters and the membrane's macroscopic properties (*e.g.*, shear, area-compression, and Young's moduli). For example, the membrane shear modulus is given by

$$\mu_0 = \frac{\sqrt{3}k_\mathrm{B}T}{4pl_\mathrm{m}x_0}\left(\frac{x_0}{2(1-x_0)^3} - \frac{1}{4(1-x_0)^2} + \frac{1}{4}\right) + \frac{3\sqrt{3}k_\mathrm{p}}{4{l_0}^3}, \quad (7)$$

where l_0 is the equilibrium spring length and $x_0 = l_0/l_\mathrm{m} = 2.2$. Furthermore, the area-compression K and Young's Y moduli can be computed as $2\mu_0 + k_\mathrm{a} + k_\mathrm{d}$ and $4K\mu_0/(K+\mu_0)$, respectively. The model bending coefficient k_b can be related to the macroscopic bending rigidity κ of the Helfrich curvature–elasticity model[30] by $\kappa = \sqrt{3}k_\mathrm{b}/2$.[23,31] Finally, the membrane shear viscosity is equal to $\eta_\mathrm{m} = \sqrt{3}(\gamma^\mathrm{T} + \gamma^\mathrm{C}/4)$.

Cell macroscopic properties (μ_0, K, Y, κ, and η_m) are selected as input variables, while the mesoscopic model parameters are calculated from the above equations without any further adjustment. For instance, the spring parameters can be uniquely computed for a given μ_0 using eqn (7) and the fact that the spring force vanishes at l_0. We also assume that $x_0 = 2.2$ is a constant (see ref. 28), since it affects only non-linear cell deformation. The membrane bending rigidity and viscosity relations are rather straightforward, while the area and volume constraint coefficients are set large enough to properly approximate the incompressibility of the membrane and inner cytosol. We also employ a "stress-free" membrane model[27,28] obtained by computational annealing, which assumes that the equilibrium length ${l_0}^i$ of each spring is equal to the edge length after initial triangulation for $i = 1,\ldots,N_\mathrm{s}$. The "stress-free" model provides a membrane network free of local stress anomalies.

2.1.3 Inter-cell aggregation interactions. The cell–cell aggregation interactions between RBCs[32] are modeled phenomenologically using the Morse potential

$$U_\mathrm{M}(r) = D_\mathrm{e}[\mathrm{e}^{2\beta(r_0-r)} - 2\mathrm{e}^{\beta(r_0-r)}], \quad (8)$$

where r is the separation distance, r_0 is the zero-force distance, D_e is the well depth of the potential, and β characterizes the interaction range. The Morse potential interactions are implemented between every two vertices of separate RBCs if they are within a defined potential cutoff radius r_M. The Morse interactions consist of a short-range repulsive force when $r < r_0$ and of a long-range attractive force for $r > r_0$. However, such repulsive interactions cannot prevent two RBCs from an overlap. To guarantee no overlap among cells we also employ specular reflections of cell vertices on membranes of other cells.

The model for the above aggregation interactions describes only RBC–RBC interactions and is aimed to reproduce normal (healthy) RBC aggregation properties. RBC aggregation may change in several hematologic diseases and disorders (*e.g.*, sickle-cell anemia, Gaucher's disease),[33,34] which can be captured by proper tuning of the Morse potential strength. In some diseases (*e.g.*, sickle-cell anemia) aggregation between RBCs and WBCs may also exist,[35] where a similar modeling strategy can be employed. Finally, WBCs may adhere to vascular endothelium due to specific interactions between receptors on a WBC and ligands at a vessel wall.[1] To model such interactions, the adhesive dynamics model of ref. 36 can be employed, which is based on the stochastic bond formation/dissociation strategy. Note that in this paper only the effect of RBC–RBC aggregation interactions is included.

2.2 Smoothed dissipative particle dynamics

SDPD[22] is a particle-based mesoscale hydrodynamic simulation technique, which combines two frequently employed approaches: smoothed particle hydrodynamics[37,38] and dissipative particle dynamics.[39,40] The advantage of the SDPD approach is that the dynamic viscosity of a fluid and its equation of state can be input directly. Thus, the fluid compressibility can be well controlled. Nevertheless, the approximation for the simulated fluid viscosity is precise only if the cutoff radius and/or particle density are large enough. Therefore, it is always advisable to verify the value of the fluid viscosity independently in simulations.

The SDPD system consists of N point particles of mass m_i, position $\mathbf{r}_i$ and velocity $\mathbf{v}_i$. SDPD particles interact through three pairwise forces: conservative (C), dissipative (D), and random (R), such that the force on particle i is given by

$$\begin{aligned}\mathbf{F}_i^\mathrm{C} &= \sum_j \left(\frac{p_i}{{\rho_i}^2} + \frac{p_j}{{\rho_j}^2}\right) w_{ij}\mathbf{r}_{ij},\\ \mathbf{F}_i^\mathrm{D} &= -\sum_j \gamma_{ij}\left(\mathbf{v}_{ij} + \left(\mathbf{v}_{ij}\cdot\mathbf{e}_{ij}\right)\mathbf{e}_{ij}\right),\\ \mathbf{F}_i^\mathrm{R} &= \sum_j \sigma_{ij}\left(\mathrm{d}\overline{\mathbf{W}}_{ij}^S + \frac{1}{3}tr\left[\mathrm{d}\mathbf{W}_{ij}\right]\right)\cdot\mathbf{e}_{ij},\end{aligned} \quad (9)$$

where $\mathbf{e}_{ij} = \mathbf{r}_{ij}/|\mathbf{r}_{ij}|$ and $\mathbf{v}_{ij} = \mathbf{v}_i - \mathbf{v}_j$. p_i and p_j are particle pressures assumed to follow the equation of state $p = p_0(\rho/\rho_0)^\alpha - b$ with p_0, ρ_0, α, and b being model parameters, see Table 1. The particle density is calculated locally and defined as $\rho_i = \sum_j W(r_{ij})$ with $W(r) = \frac{105}{16\pi{r_\mathrm{c}}^3}\left(1 + 3\frac{r}{r_\mathrm{c}}\right)\left(1 - \frac{r}{r_\mathrm{c}}\right)^3$ being the Lucy function, where r_c is the cutoff radius. Note that $W(r)$ is chosen such that $\nabla W(r) = -\mathbf{r}w(r)$ with $w(r) = \frac{315}{4\pi{r_\mathrm{c}}^5}\left(1 - \frac{r}{r_\mathrm{c}}\right)^2$. The coefficients γ_{ij} and σ_{ij} define the strength of dissipative and random forces and are equal to $\gamma_{ij} = \frac{5\eta}{3}\frac{w_{ij}}{\rho_i\rho_j}$ and $\sigma_{ij} = 2\sqrt{k_\mathrm{B}T\gamma_{ij}}$, respectively. The

Table 1 SDPD fluid parameters used in simulations. n is fluid's number density and η is the dynamic viscosity. In the simulation parameters, mass is given in units of fluid particle mass m=1, length in units of r′=2r$_\mathrm{c}$/3, and energy in units of E = 2.5k$_\mathrm{B}$T, where r$_\mathrm{c}$ and k$_\mathrm{B}$T values are given in the table

p_0	ρ_0	α	b	r_c	η_0	n	$k_\mathrm{B}T$	η
100	3.0	7	80	1.5	100.0	3	0.4	107.6

notation $tr[\mathrm{d}\mathbf{W}_{ij}]$ corresponds to the trace of a random matrix of independent Wiener increments $\mathrm{d}\mathbf{W}_{ij}$, and $\mathrm{d}\bar{\mathbf{W}}_{ij}^{S}$ is the traceless symmetric part.

The time evolution of velocities and positions of particles is determined by Newton's second law of motion

$$\mathrm{d}\mathbf{r}_i = \mathbf{v}_i \mathrm{d}t, \tag{10}$$

$$\mathrm{d}\mathbf{v}_i = \frac{1}{m_i}\left(\mathbf{F}_i^{\mathrm{C}} + \mathbf{F}_i^{\mathrm{D}} + \mathbf{F}_i^{\mathrm{R}}\right)\mathrm{d}t. \tag{11}$$

The above equations of motion are integrated using the velocity–Verlet algorithm.

2.3 Simulation setup and parameters

The solvent is represented by a collection of particles with the parameters outlined in Table 1. Note that the dynamic viscosity η is slightly larger than the desired viscosity η_0, which has been computed from a Couette flow simulation. η will converge to η_0 if we increase r_c and/or n, which would also lead to a larger computational cost.

To define the cell shapes and the flow geometry, we introduce an effective RBC diameter $D_r = \sqrt{A_{0_r}/\pi}$, which is based on the RBC membrane area A_{0_r} (the subscript 'r' corresponds to the red cell). Similarly, we define an effective WBC diameter $D_w = \sqrt{A_{0_w}/\pi}$ (the subscript 'w' corresponds to the white cell). The cell shapes (biconcave for a RBC and spherical for a WBC) are imposed by a combination of the cell area A_0 and volume V_0, which can be described by a reduced volume for both cells as $V_{0_r}/(\pi D_r^3/6) = 0.642$ and $V_{0_w}/(\pi D_w^3/6) = 1.02$. Note that the imposed WBC volume is 2% larger than the volume of a corresponding sphere, which leads to weak membrane tension and reduces WBC deformability, similar to a realistic WBC.[41–43] The other cell membrane properties and parameters are given in Table 2. The blood cells are suspended in a Newtonian fluid (plasma), which is represented by a collection of SDPD particles. The cells are coupled to the fluid by friction which includes only dissipative and random forces.[27,28]

We simulate blood flow in a tube of diameter $D_t = 3.08D_r$, which is driven by a constant force applied to the solvent particles, equivalently to a constant pressure gradient. To characterize the flow, we define a dimensionless shear rate as

$$\dot{\gamma}^* = \frac{\eta D_r^{\,3}\bar{\dot{\gamma}}}{\kappa_r} = \tau\bar{\dot{\gamma}}, \tag{12}$$

where $\bar{\dot{\gamma}} = 4Q/(\pi D_t^{\,3})$ is the average shear rate (or pseudo-shear rate), Q is the volumetric flow rate, η is the solvent viscosity, and $\tau = \eta D_r^{\,3}/\kappa_r$ is a characteristic cell relaxation time. For comparison in physical units, we assume cell diameters $D_r = 6.5$ μm and $D_w = 10$ μm, which implies that $D_w \simeq 1.54D_r$, tube diameter $D_t = 20$ μm, plasma viscosity $\eta = 1.2 \times 10^{-3}$ Pa s, temperature $T = 37$ °C, membrane Young's modulus $Y_r = 18.9$ μN m^{-1}, and bending rigidity $\kappa_r = 70k_BT = 3 \times 10^{-19}$ J. Then, the characteristic RBC relaxation time is $\tau = 1.1$ s and therefore, the pseudo-shear rate $\bar{\dot{\gamma}}$ is roughly equivalent in magnitude to $\dot{\gamma}^*$ in inverse seconds.

RBC aggregation interactions, if used, were mediated by the Morse potential (eqn (8)). The Morse potential parameters were set to $D_e = 0.75k_BT$, $r_0 = 0.046D_r$, $\beta = 9.75D_r^{\,-1}$, and $r^M = 0.17D_r$. For more details see ref. 32.

3 Results and discussion

In the presentation of WBC margination results, for convenience, we schematically divide flow rates and H_t values in several groups. In the subsequent discussion, low flow rates are referred to as the rates of $\dot{\gamma}^* \lesssim 20$, intermediate flow rates are in the range of $20 \lesssim \dot{\gamma}^* \lesssim 90$, and high flow rates are for $\dot{\gamma}^* \gtrsim 90$. Physiologically, the high shear rates correspond to the rates in the arteriolar part of microcirculation, while low and intermediate shear rates are characteristic of venular blood flow.[44,45] Similarly, we define low hematocrits as $H_t \lesssim 0.2$, intermediate hematocrits as $0.2 \lesssim H_t \lesssim 0.4$, and high hematocrits as $H_t \gtrsim 0.4$. Intermediate H_t values are specifically relevant for microcirculatory blood flow, while low H_t values may still be present in some parts of microcirculation.[44] High H_t values are not likely to occur in healthy microvascular blood flow, but they are relevant within tumor microvasculature, since it is often subject to hemo-concentration due to plasma leakage.[46]

3.1 Physical basis of WBC margination

Fig. 1 shows sample snapshots from simulations for two different flow conditions. In the case of $H_t = 0.3$ and an intermediate flow rate $\dot{\gamma}^* = 32$, as displayed in Fig. 1a, a WBC is clearly marginated (*i.e.* located next to the wall), while for $H_t = 0.2$ and a high flow rate $\dot{\gamma}^* = 115$, as shown in Fig. 1b, a WBC remains in the vessel center. To characterize the WBC position within the tube, we measure its center-of-mass distribution over time, which reflects the probability of a WBC to be at a certain position r in the tube, as shown in Fig. 2. A peak near the position of $2r/D_t \approx 0.5$ (or $r \approx 5$ μm) indicates that the WBC is marginated with high probability. At low H_t, WBC margination is weak, since the volume fraction of RBCs is not high enough to effectively push the WBC close to the wall; however, at low flow rates ($\dot{\gamma}^* \approx 15$), a WBC might still get marginated, as shown in Fig. 2a. It is noteworthy that even at low H_t a WBC is expelled

Table 2 Model parameters of red (RBC) and white (WBC) blood cells

Type	N_v	$\frac{\kappa}{k_BT}$	$\frac{YD_r^2}{k_BT}$	$\frac{KD_r^2}{k_BT}$	$\frac{k_dD_r^2}{k_BT}$	$\frac{k_aD_r^2}{k_BT}$	$\frac{k_vD_r^3}{k_BT}$	$\frac{\gamma^TD_r^2}{\tau k_BT}$
RBC	500	70	1.8×10^5	2.2×10^6	4.2×10^4	2.1×10^6	1.4×10^7	66.44
WBC	1000	1300	7.8×10^6	2.6×10^7	4.2×10^5	2.1×10^7	1.4×10^8	66.44

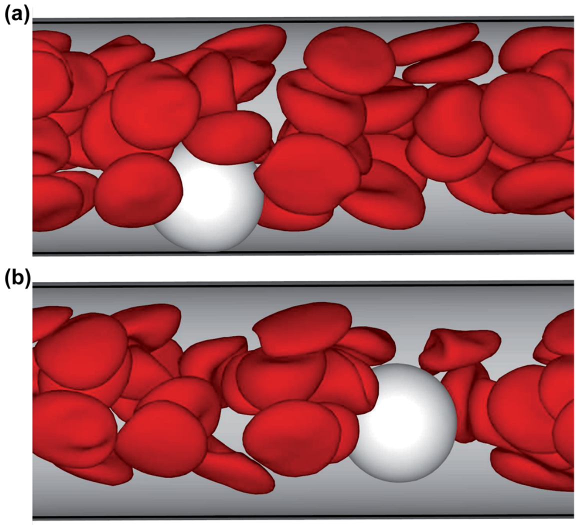

Fig. 1 Simulation snapshots of RBCs (red) and a WBC (white). The flow is from the left to the right. (a) $H_t = 0.3$ and $\dot{\gamma}^* = 32$; (b) $H_t = 0.2$ and $\dot{\gamma}^* = 115$. See also movies in the ESI.†

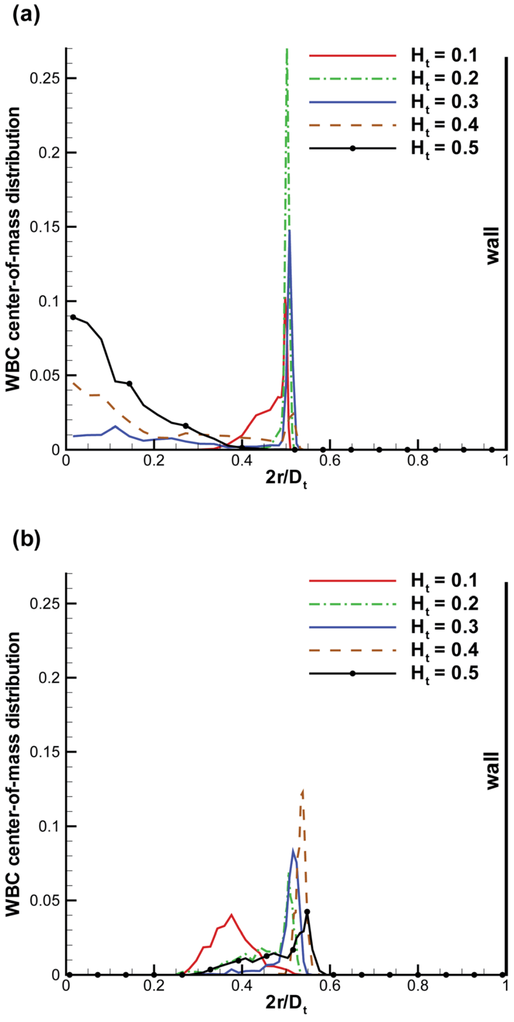

Fig. 2 WBC center-of-mass distribution with respect to the vessel position r normalized by D_t for various H_t values. (a) $\dot{\gamma}^* \approx 15$, (b) $\dot{\gamma}^* \approx 60$. The center of the vessel is at $2r/D_t = 0$, while the wall is at $2r/D_t = 1$.

from the tube center by RBCs. As hematocrit is increased, we observe stronger margination as being most efficient within the range of $H_t = 0.2$–0.4. However, at even higher $H_t = 0.5$ WBC margination seems to be attenuated, in particular, for low flow rates ($\dot{\gamma}^* \approx 15$). The mechanism for the margination attenuation phenomena at high H_t has been previously discussed in 2D simulations.[21] It arises due to interactions of a WBC with RBCs in flow. In ref. 21 it has been shown that for low enough H_t the region in front of a marginated WBC remains virtually free of RBCs, which could otherwise interfere with the WBC and lift it off the wall. However, at large enough H_t due to RBC crowding, a marginated WBC may often encounter RBCs in front, which helps to effectively displace it away from the wall, leading to a lower margination probability than for lower H_t. The effect of hematocrit becomes weaker for higher flow rates ($\dot{\gamma}^* \approx 60$), as seen in Fig. 2b(b), and a WBC is found to be marginated for essentially all investigated H_t values, but again most significantly in the range $H_t = 0.2$–0.4.

To verify this mechanism in 3D, we plot in Fig. 3 the probability of RBCs to be around a marginated WBC for different H_t values, which is proportional to the local RBC volume fraction. The RBC distribution is calculated in a co-moving coordinate system of the WBC center-of-mass and with the condition that the WBC center is less than $0.5D_w$ (5 μm) away from the wall. This condition is equivalent to the WBC nearly touching the wall. An increase of H_t from 0.4 to 0.5 results in a substantial increase of RBC crowding in the region in front of a WBC, while for $H_t \leq 0.4$ this region remains virtually void of RBCs. To demonstrate the quantitative differences in RBC crowding, one-dimensional cuts along the y-axis at an x position of 8 μm away from the WBC center are displayed in Fig. 4. At $H_t = 0.5$ a strong increase of the RBC presence in the region in front of a marginated WBC is clearly observed. This margination–attenuation mechanism at high H_t does not contradict the main hypothesis that WBC margination arises from a competition of lift forces on RBCs and WBCs and their interactions in flow, which would imply that margination should become even stronger at high H_t. We hypothesize that even at high hematocrit WBCs are constantly marginated due to the differences in lift forces and RBC–WBC interactions; however, WBCs are almost immediately sent back to the vessel center due to local interactions with RBCs near the wall. As a result, the time a WBC is marginated at high H_t can be short, which is reflected in the center-of-mass probability distribution. Finally, RBC aggregation interactions can improve WBC margination at higher H_t values, since the core of the flow consisting mainly of RBCs remains more compact due to inter-cell attractive interactions, which is consistent with findings in ref. 21. However, such an effect can only occur at low flow rates, because RBC aggregate structures are fragile and break up at high enough flow rates.

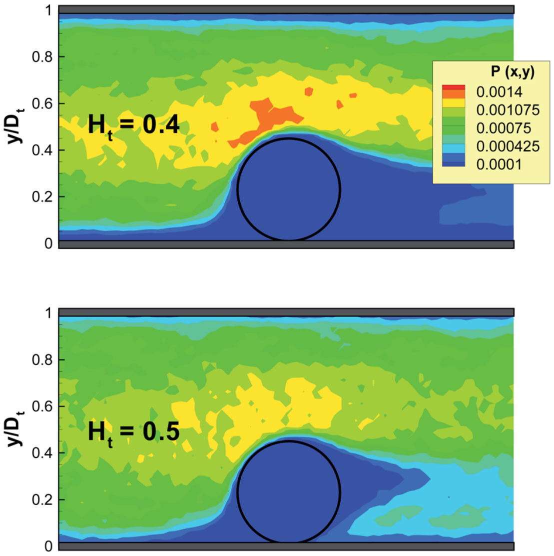

Fig. 3 Local RBC probability to be around a marginated WBC for H_t = 0.4 and H_t = 0.5 at $\dot{\gamma}^* \approx 60$. The probability is calculated in a co-moving coordinate system of the WBC center-of-mass and only for time instances, when the WBC center is within $0.5D_w$ (5 μm) from the wall. The black circle schematically shows a WBC. Only a part of the vessel is shown. No RBC aggregation is present.

3.2 WBC margination diagrams

To present our simulation data for a wide range of H_t values and flow rates, we construct WBC margination diagrams, which are based on a margination probability. The margination probability is defined as the probability of a WBC center-of-mass to be within a certain distance away from the wall, *i.e.*, for $r_w < d$, where r_w is the distance of the WBC center-of-mass from the wall and d is a selected value. In principle, the margination probability is an integral of the WBC center-of-mass probability distribution from $0.5D_t - d$ to $0.5D_t$. Fig. 5 shows two margination diagrams for d = 5 μm (*i.e.* the WBC membrane is nearly touching the vessel wall) and d = 5.5 μm (*i.e.* a distance of 0.5 μm between the WBC membrane and wall) without RBC aggregation interactions. Both diagrams show that WBC margination occurs in a certain range of H_t and $\dot{\gamma}^*$ values. In terms of hematocrit, the margination is mainly observed for $H_t \in (0.2,0.4)$, which is consistent with hematocrit values in our microcirculatory system, where H_t magnitudes are lower than the systemic hematocrit of H_t = 0.4–0.45. As we mentioned before, margination at low H_t does not occur due to a low volume fraction of RBCs, since they are responsible for WBC margination, while at high H_t the margination effect also vanishes due to WBC–RBC interactions discussed above. With respect to the flow rate, we found WBC margination to occur mainly for $\dot{\gamma}^* \lesssim 130$. This range of $\dot{\gamma}^*$ covers mainly the flow rates encountered in the venular part of microcirculation, which is consistent with experimental observations that WBC margination and adhesion primarily occurs in venules and not arterioles.[6,16,18] As an estimation, the flow rates in the venular part of microcirculation correspond to the range of $\dot{\gamma}^* \lesssim 90$, while in arteriolar part the flow rates are higher with $\dot{\gamma}^* \gtrsim 120$.[44,45]

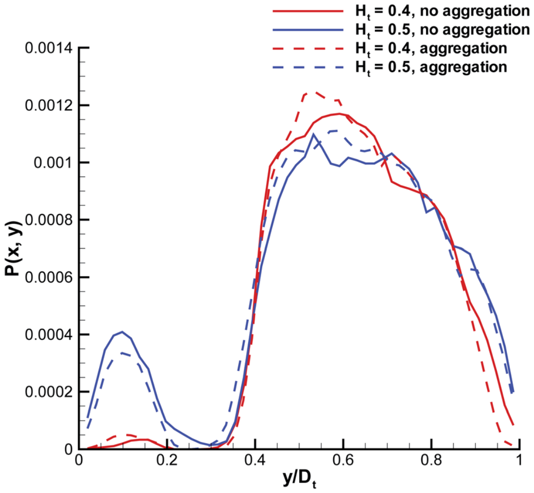

Fig. 4 Local RBC distribution cuts from the plots in Fig. 3 along the y-axis and 8 μm away from the WBC center. Both cases with and without RBC aggregation are shown.

To study the effect of RBC aggregation on WBC margination, we have also performed a set of simulations, where RBC aggregation has been explicitly included following the RBC aggregation model of ref. 32, which has been shown to reproduce the viscosity and shear-thinning behavior of whole blood very well. Fig. 6 presents the corresponding WBC margination diagrams for simulations where RBC aggregation interactions are included. The main effect of RBC aggregation is that the WBC margination region expands along the H_t axis such that RBC aggregation enhances WBC margination at high H_t values as well as at low hematocrit. As expected, a stronger effect of RBC aggregation is found at low $\dot{\gamma}^*$ leading to WBC margination even at very low flow rates. Thus, RBC aggregation presents an additional force that expels WBCs from the RBC core due to attractive interactions between RBCs. At high enough flow rates, RBC aggregation does not play a significant role,[32] and therefore there is no substantial change in the margination diagram at high $\dot{\gamma}^*$. The RBC aggregation effect on WBC margination is qualitatively similar to that observed in simulations of 2D model systems.[21] The comparison of Fig. 5 and 6 indicates that WBC margination could still be possible in the limit of $\dot{\gamma}^* \to 0$ for the case of RBC aggregation.

3.3 Deformation of a marginated WBC

A marginated WBC is subject to flow-induced deformation, since it experiences high shear stresses due to near wall fluid flow and RBCs. To quantify deformation of a marginated WBC we compute the ratios D_{xw}/D'_w and D_{rw}/D'_w (shown in Fig. 7), which describe WBC deformation along the tube axis x and along the radial direction, respectively. Note that we use the notation D_w' here, which is the WBC diameter calculated in equilibrium; it may slightly differ from D_w since the imposed WBC volume is 2% larger than the volume of a sphere with the

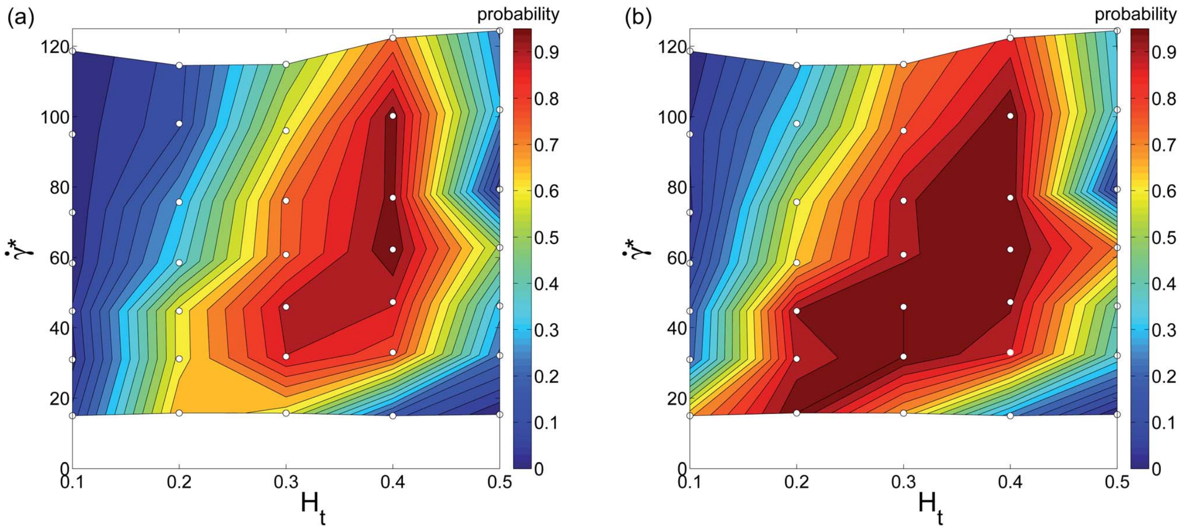

Fig. 5 WBC margination probability diagrams calculated for (a) $r_w < 5$ μm and (b) $r_w < 5.5$ μm, where r_w is the distance of the WBC center-of-mass from the wall. The small white circles in the diagrams indicate performed simulations. No aggregation interactions between RBCs are imposed here.

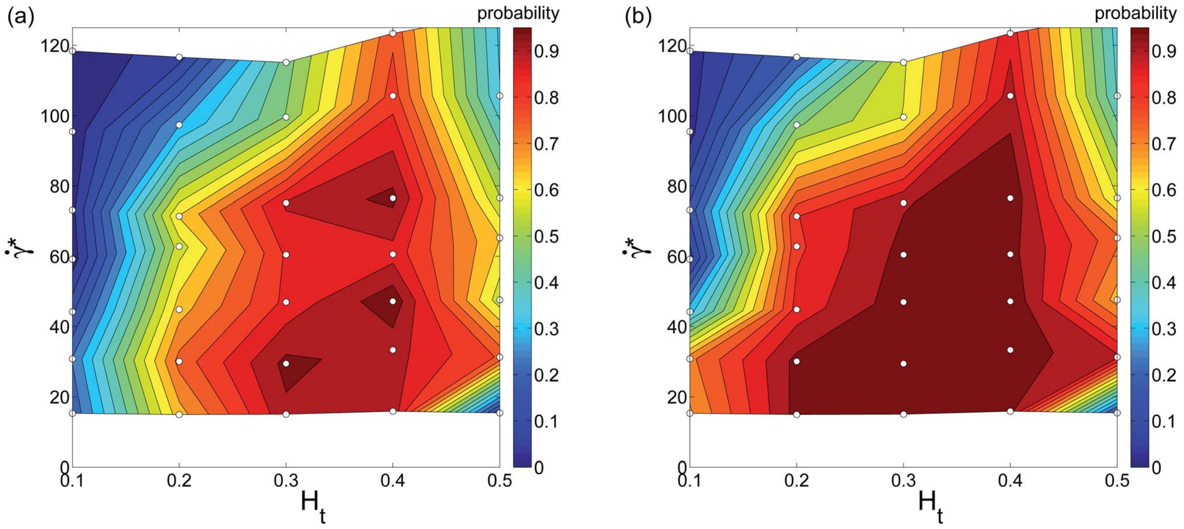

Fig. 6 WBC margination probability diagrams calculated for (a) $r_w < 5$ μm and (b) $r_w < 5.5$ μm for the case of RBC aggregation. The small white circles in the diagrams indicate performed simulations.

diameter D_w. The WBC deformation does not seem to be very significant and lies within approximately 5%. Deformation of adhered WBCs in flow has been measured both experimentally[6,47] and in simulations;[48,49] these studies indicate a WBC deformation up to about 20–30% along the flow for comparable flow rates. The deformation of a WBC in shear flow is expected to be significantly lower than that of an adhered WBC due to cell spreading on the wall in the latter case. Thus, our modeled WBC approximates a nearly non-deformable sphere in flow, which is similar to observed shapes of flowing WBCs in experiments. The mechanical properties of WBCs have been measured in a number of experiments,[41–43] which estimate cell stiffness and its cortical tension. A direct comparison of WBC mechanical properties is currently difficult, since our WBC model does not consider an inner cytoskeleton; however, the membrane tension of the modeled WBC has the right order of magnitude. The effect of WBC deformation on margination properties has been investigated for 2D model systems[21] showing that a more deformable WBC exhibits a reduction in its margination at high flow rates, since the WBC shape may significantly depart from a sphere. In 3D, a similar trend is expected.

3.4 Force on a marginated WBC

WBC deformation in the radial direction appears to be stronger than that along the flow, see Fig. 7, which points to the existence

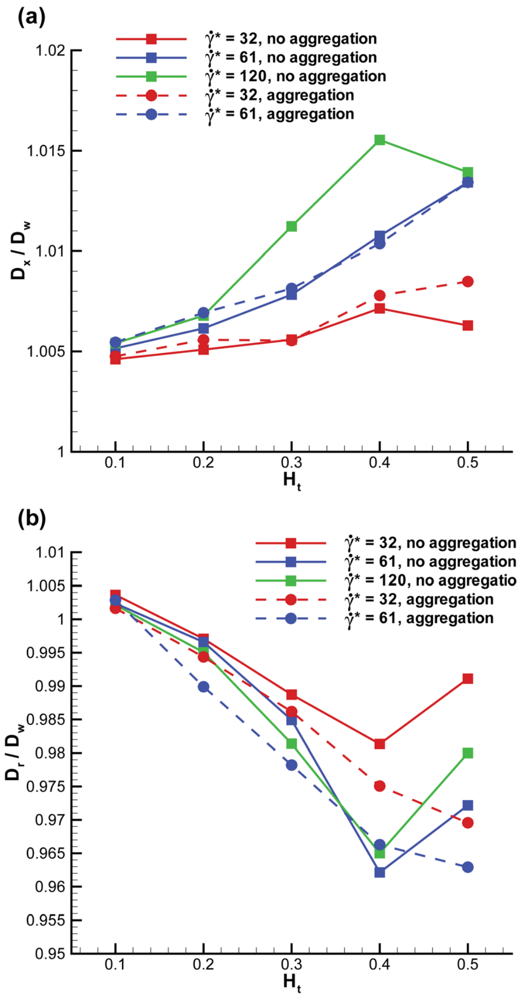

Fig. 7 Deformation of a marginated WBC (a) along the tube axis – D_{xw}/D'_w and (b) along the radial direction – D_{rw}/D'_w. D'_w denotes the WBC diameter in the absence of flow.

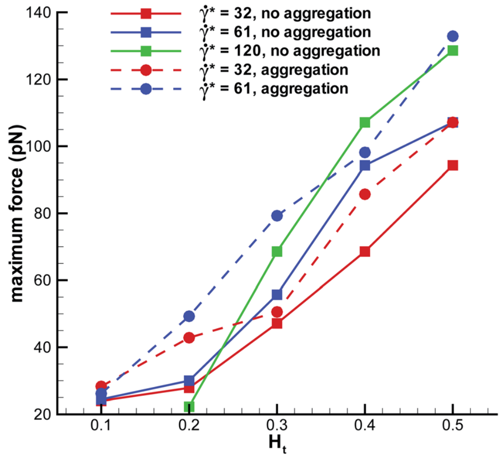

Fig. 8 Maximum force on a marginated WBC normal to the wall (radial direction). Positive force values indicate that a WBC is pushed toward the wall.

of a compressive force normal to the wall. Similar conclusion can be drawn from the fluid flow, since blood plasma and RBCs have to go past a marginated WBC. We have measured the maximum force on a marginated WBC normal to the wall, defined as a cumulative force due to interactions with the blood plasma and RBCs, which is shown in Fig. 8. The positive force values indicate that a WBC is pushed towards the wall along the radial direction. The normal force on a marginated WBC is also expected to aid efficient WBC adhesion to the wall, which is important for proper WBC functioning.[2,3] A recent simulation study[50] has attempted to estimate the maximum pressure normal to the wall on a fixed spherical-like obstacle in blood flow, which mimics an adhered WBC. The reported values for the normal pressure are up to approximately 30 Pa. If we convert our maximum force of about 130 pN to a normal pressure by dividing the force by the area $\pi D_w^2/4$ we obtain the value of about 2 Pa. This pressure is much smaller than that predicted in ref. 50, which is expected to be due to the fixed obstacle position and a much stronger WBC confinement $D_w/D_t = 0.75$ used in ref. 50 in comparison to our simulations with $D_w/D_t = 0.5$.

3.5 Effect of WBC margination on the flow resistance

We have also examined the effect of a marginated WBC on the blood flow resistance in a microvessel. To characterize the flow resistance, we define an apparent viscosity (or average blood flow viscosity), which is calculated by fitting the Poiseuille law to the measured flow rate. In order to quantify the effect of a WBC on the flow resistance, we present in Fig. 9 the relative flow resistance defined as the ratio of the computed apparent viscosity of blood with a WBC to the apparent viscosity without a WBC. At high flow rates ($\dot{\gamma}^* \approx 120$), the relative flow resistance is smaller than that for low flow rates. This is consistent with the observation in Fig. 5 that the WBC is poorly marginated at high flow rates and therefore, the resistance values mainly reflect the effect of an increased total volume fraction of cells due to the presence of a WBC. At intermediate and low flow rates, the presence of a WBC results in an increase of flow resistance by 10–30%. The relative resistance is clearly correlated with WBC margination such that WBC margination leads to a larger flow resistance. At low H_t, a WBC is not strongly marginated, and therefore the flow resistance is not significantly affected. At intermediate H_t values, where a WBC gets strongly marginated, the flow resistance reaches its maximum, while at high H_t the resistance due to a WBC slightly decreases, since WBC margination becomes less pronounced. The effect of RBC aggregation on the flow resistance due to a WBC is pronounced mainly at low flow rates, which is consistent with the RBC aggregation effect on WBC margination. Also, we expect that an increase in the flow resistance due to a marginated WBC will be smaller than 10–30% in larger vessels in comparison with the studied tube diameter of $D_t = 20$ μm.

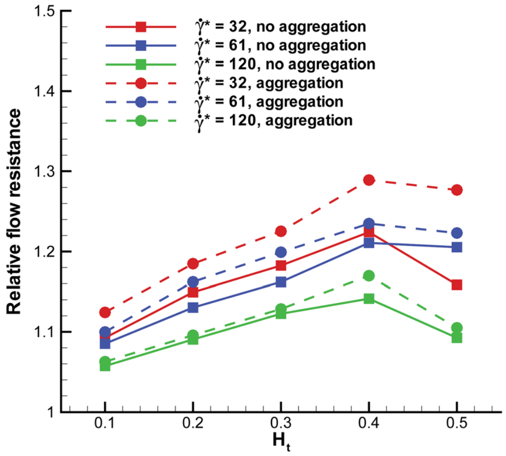

Fig. 9 Relative flow resistance for blood flow in a vessel with a WBC. It is defined as the ratio of calculated apparent viscosity with a WBC to the apparent viscosity of blood flow without a WBC.

3.6 Translational and rotational velocities of a marginated WBC

The WBC translational velocity can be used as an indicator for WBC margination, since the velocity of a marginated WBC is significantly lower than that in the vessel center, as has been pointed out in ref. 21. 3D simulation results for the translational velocity of a WBC for different flow rates and H_t values are shown in Fig. 10. A drop in WBC velocity is clearly observed when a WBC is marginated for the intermediate values of $H_t = 0.2\text{–}0.4$. Also, we notice that there is no significant dependence of the normalized translational velocity on the flow rate, so that this criterion can be universally applied for WBC margination detection. The opposite trend is found for the WBC angular velocity ω in blood flow, which is shown in Fig. 11. Here, ω increases with increasing H_t in the range $H_t = 0.2\text{–}0.4$, indicating that the rotational velocity of a marginated WBC is larger than that in the vessel center. Such an effect is expected due to larger shear rates near the wall than in the tube center. WBC rotational velocity is likely to be difficult to measure in experiments, so that this property cannot be employed easily for WBC margination detection. Finally, the rescaled angular velocity $\omega D_w/(2\bar{u})$ shows only a very weak dependence on $\dot{\gamma}^*$, which indicates that the scale factor $2\bar{u}/D_w$ captures the essential dependence of the angular velocity on the flow rate.

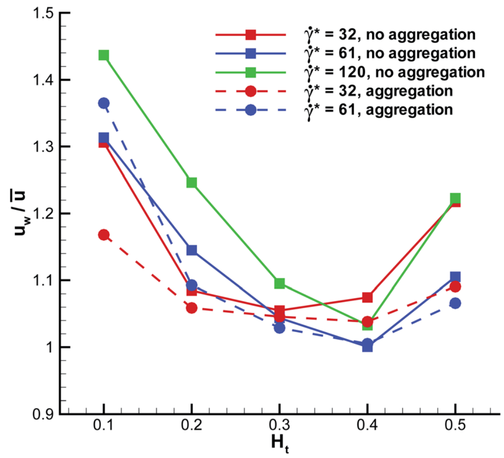

Fig. 10 Translational velocity of a WBC normalized by the average flow velocity for different flow rates and H_t values.

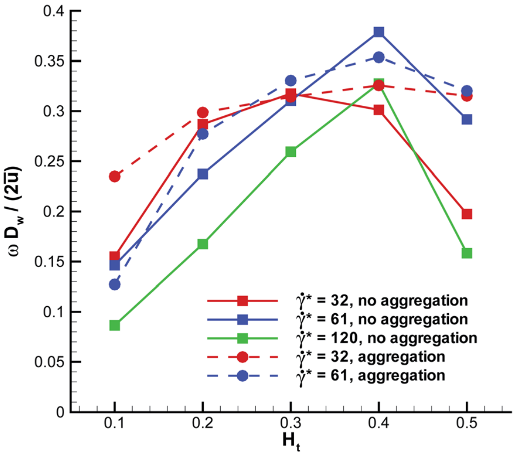

Fig. 11 Angular velocity of a WBC for different flow rates and H_t values. The angular velocity is directed perpendicular to the plane going through the tube axis and WBC center-of-mass.

4 Summary and conclusions

In blood flow, RBCs migrate toward the vessel center, while WBCs migrate or marginate to the walls. WBC margination is governed by flow-induced hydrodynamic cell-wall interactions (*i.e.*, lift forces) and interactions among blood cells. We employed 3D mesoscopic simulations of blood flow to predict WBC margination for a wide range of H_t values and flow rates. WBC margination occurs mainly within a region of intermediate hematocrits, $H_t = 0.2\text{–}0.4$, and for relatively low flow rates, $\dot{\gamma}^* \lesssim 130$. This range of flow rates is characteristic of the venular part of microcirculation. RBC aggregation slightly enhances WBC margination, especially at high H_t values. The deformation of marginated WBCs appears to be rather small, remaining within a few percent of the undisturbed shape. The force on marginated WBCs is directed in the normal direction toward the wall, can reach a value of several hundred pico-newtons, and might aid in better WBC adhesion to the wall. Marginated WBCs also contribute to an increase in flow resistance with up to approximately 30% for vessel diameters of 20 μm. The effect of WBC margination on the flow resistance is expected to subside as the tube diameter is increased to values several times larger than the WBC diameter. Finally, we also presented translational and rotational WBC velocities, which might be used for the detection of WBC margination in experiments.

The WBC margination results can be also used to predict margination of other micro-particles and cells in blood flow, if their size and mechanical properties are similar to those of WBCs. For instance, many circulating tumor cells have a similar size and are also rather stiff.[43,51] Thus, the margination of many tumor cells is also expected primarily in the venular part of microcirculation, which would imply that the tissue invasion by tumor cells present in blood largely occurs from venules. The WBC margination results can be also employed in microfluidic devices for the separation of WBCs or circulating tumor cells from whole blood. In the future, we also plan to include adhesion of WBCs explicitly in order to study their adhesive interactions with vessel walls in blood flow.

Acknowledgements

A CPU time grant by the Jülich Supercomputing center is gratefully acknowledged. Dmitry A. Fedosov also acknowledges funding by the Alexander von Humboldt Foundation. We also thank the DFG Research Unit FOR 1543 "SHENC - Shear Flow Regulation in Hemostasis" for support.

References

1 T. A. Springer, *Annu. Rev. Physiol.*, 1995, **57**, 827–872.
2 K. Ley and T. F. Tedder, *J. Immunol.*, 1995, **155**, 525–528.
3 R. Alon, D. A. Hammer and T. A. Springer, *Nature*, 1995, **374**, 539–542.
4 U. Bagge and R. Karlsson, *Microvasc. Res.*, 1980, **20**, 92–95.
5 H. L. Goldsmith and S. Spain, *Microvasc. Res.*, 1984, **27**, 204–222.
6 J. C. Firrell and H. H. Lipowsky, *Am. J. Physiol.*, 1989, **256**, H1667–H1674.
7 H. L. Goldsmith, G. R. Cokelet and P. Gaehtgens, *Am. J. Physiol.*, 1989, **257**, H1005–H1015.
8 G. R. Cokelet and H. L. Goldsmith, *Circ. Res.*, 1991, **68**, 1–17.
9 J. B. Freund and M. M. Orescanin, *J. Fluid Mech.*, 2011, **671**, 466–490.
10 S. K. Doddi and P. Bagchi, *Phys. Rev. E: Stat., Nonlinear, Soft Matter Phys.*, 2009, **79**, 046318.
11 D. A. Fedosov, B. Caswell, A. S. Popel and G. E. Karniadakis, *Microcirculation*, 2010, **17**, 615–628.
12 D. A. Fedosov, H. Noguchi and G. Gompper, *Biomech. Model. Mechanobiol.*, 2013, DOI: 10.1007/s10237-013-0497-9.
13 I. Cantat and C. Misbah, *Phys. Rev. Lett.*, 1999, **83**, 880–883.
14 M. Abkarian, C. Lartigue and A. Viallat, *Phys. Rev. Lett.*, 2002, **88**, 068103.
15 S. Messlinger, B. Schmidt, H. Noguchi and G. Gompper, *Phys. Rev. E: Stat., Nonlinear, Soft Matter Phys.*, 2009, **80**, 011901.
16 M. J. Pearson and H. H. Lipowsky, *Am. J. Physiol.*, 2000, **279**, H1460–H1471.
17 K. B. Abbitt and G. B. Nash, *Am. J. Physiol.*, 2003, **285**, H229–H240.
18 A. Jain and L. L. Munn, *PLoS One*, 2009, **4**, e7104.
19 C. Sun, C. Migliorini and L. L. Munn, *Biophys. J.*, 2003, **85**, 208–222.
20 J. B. Freund, *Phys. Fluids*, 2007, **19**, 023301.
21 D. A. Fedosov, J. Fornleitner and G. Gompper, *Phys. Rev. Lett.*, 2012, **108**, 028104.
22 P. Espanol and M. Revenga, *Phys. Rev. E: Stat., Nonlinear, Soft Matter Phys.*, 2003, **67**, 026705.
23 H. S. Seung and D. R. Nelson, *Phys. Rev. A*, 1988, **38**, 1005–1018.
24 G. Gompper and D. M. Kroll, *J. Phys.: Condens. Matter*, 1997, **9**, 8795–8834.
25 D. E. Discher, D. H. Boal and S. K. Boey, *Biophys. J.*, 1998, **75**, 1584–1597.
26 H. Noguchi and G. Gompper, *Proc. Natl. Acad. Sci. U. S. A.*, 2005, **102**, 14159–14164.
27 D. A. Fedosov, B. Caswell and G. E. Karniadakis, *Biophys. J.*, 2010, **98**, 2215–2225.
28 D. A. Fedosov, B. Caswell and G. E. Karniadakis, *Comput. Meth. Appl. Mech. Eng.*, 2010, **199**, 1937–1948.
29 P. Espanol, *Phys. Rev. E: Stat. Phys., Plasmas, Fluids, Relat. Interdiscip. Top.*, 1998, **57**, 2930–2948.
30 W. Helfrich, *Z. Naturforsch., C: J. Biosci.*, 1973, **28**, 693–703.
31 G. Gompper and D. M. Kroll, *J.Phys. I*, 1996, **6**, 1305–1320.
32 D. A. Fedosov, W. Pan, B. Caswell, G. Gompper and G. E. Karniadakis, *Proc. Natl. Acad. Sci. U. S. A.*, 2011, **108**, 11772–11777.
33 T. Adar, R. Ben-Ami, D. Elstein, A. Zimran, S. Berliner, S. Yedgar and G. Barshtein, *Br. J. Haematol.*, 2006, **134**, 432–437.
34 J. Tripette, T. Alexy, M. D. Hardy-Dessources, D. Mougenel, E. Beltan, T. Chalabi, R. Chout, M. Etienne-Julan, O. Hue, H. J. Meiselman and P. Connes, *Haematologica*, 2009, **94**, 1060–1065.
35 V. Chaar, J. Picot, O. Renaud, P. Bartolucci, R. Nzouakou, D. Bachir, F. Galacteros, Y. Colin, C. Le Van Kim and W. El Nemer, *Haematologica*, 2010, **95**, 1841–1848.
36 D. A. Hammer and S. M. Apte, *Biophys. J.*, 1992, **63**, 35–57.
37 L. B. Lucy, *Astron. J.*, 1977, **82**, 1013–1024.
38 J. J. Monaghan, *Annu. Rev. Astron. Astrophys.*, 1992, **30**, 543–574.
39 P. J. Hoogerbrugge and J. M. V. A. Koelman, *Europhys. Lett.*, 1992, **19**, 155–160.
40 P. Espanol and P. Warren, *Europhys. Lett.*, 1995, **30**, 191–196.
41 C. Dong, R. Skalak, K. L. Sung, G. W. Schmid-Schönbein and S. Chien, *J. Biomech. Eng.*, 1988, **110**, 27–36.
42 E. Evans and A. Yeung, *Biophys. J.*, 1989, **56**, 151–160.
43 M. J. Rosenbluth, W. A. Lam and D. A. Fletcher, *Biophys. J.*, 2006, **90**, 2994–3003.
44 A. S. Popel and P. C. Johnson, *Annu. Rev. Fluid Mech.*, 2005, **37**, 43–69.
45 A. R. Pries, T. W. Secomb and P. Gaehtgens, *Am. J. Physiol.*, 1995, **269**, H1713–H1722.
46 E. M. Sevick and R. K. Jain, *Cancer Res.*, 1989, **49**, 3513–3519.
47 E. R. Damiano, J. Westheider, A. Tözeren and K. Ley, *Circ. Res.*, 1996, **79**, 1122–1130.
48 S. Jadhav, C. D. Eggleton and K. Konstantopoulos, *Biophys. J.*, 2005, **88**, 96–104.
49 V. Pappu and P. Bagchi, *Comput. Biol. Med.*, 2008, **38**, 738–753.
50 A. H. G. Isfahani and J. B. Freund, *Biophys. J.*, 2012, **103**, 1604–1615.
51 K. G. Phillips, P. Kuhn and O. J. T. McCarty, *Am. J. Physiol.*, 2014, **306**, C80–C88.

P8: Computational biorheology of human blood flow in health and disease

D. A. Fedosov, M. Dao, G. E. Karniadakis, and S. Suresh

Annals of Biomedical Engineering, **42**:368-387, 2014.

Annals of Biomedical Engineering, Vol. 42, No. 2, February 2014 (*© 2013*) pp. 368–387
DOI: 10.1007/s10439-013-0922-3

Computational Biorheology of Human Blood Flow in Health and Disease

Dmitry A. Fedosov,[1] Ming Dao,[2] George Em Karniadakis,[3] and Subra Suresh[4]

[1]Institute of Complex Systems and Institute for Advanced Simulation, Forschungszentrum Jülich, 52425 Jülich, Germany; [2]Department of Materials Science and Engineering, Massachusetts Institute of Technology, Cambridge, MA 02139, USA; [3]Division of Applied Mathematics, Brown University, Providence, RI 02912, USA; and [4]Department of Materials Science and Engineering and Department of Biomedical Engineering, Carnegie Mellon University, Pittsburgh, PA 15213, USA

(Received 12 July 2013; accepted 2 October 2013; published online 12 October 2013)

Associate Editor Gang Bao oversaw the review of this article.

Abstract—Hematologic disorders arising from infectious diseases, hereditary factors and environmental influences can lead to, and can be influenced by, significant changes in the shape, mechanical and physical properties of red blood cells (RBCs), and the biorheology of blood flow. Hence, modeling of hematologic disorders should take into account the multiphase nature of blood flow, especially in arterioles and capillaries. We present here an overview of a general computational framework based on dissipative particle dynamics (DPD) which has broad applicability in cell biophysics with implications for diagnostics, therapeutics and drug efficacy assessments for a wide variety of human diseases. This computational approach, validated by independent experimental results, is capable of modeling the biorheology of whole blood and its individual components during blood flow so as to investigate cell mechanistic processes in health and disease. DPD is a Lagrangian method that can be derived from systematic coarse-graining of molecular dynamics but can scale efficiently up to arterioles and can also be used to model RBCs down to the spectrin level. We start from experimental measurements of a single RBC to extract the relevant biophysical parameters, using single-cell measurements involving such methods as optical tweezers, atomic force microscopy and micropipette aspiration, and cell-population experiments involving microfluidic devices. We then use these validated RBC models to predict the biorheological behavior of whole blood in healthy or pathological states, and compare the simulations with experimental results involving apparent viscosity and other relevant parameters. While the approach discussed here is sufficiently general to address a broad spectrum of hematologic disorders including certain types of cancer, this paper specifically deals with results obtained using this computational framework for blood flow in malaria and sickle cell anemia.

Keywords—Hematologic disorders, Dissipative particle dynamics, Coarse-graining, Malaria, Sickle cell anemia.

INTRODUCTION

Parasitic infections or genetic factors can drastically change the viscoelastic properties and the biconcave (discocyte) shape of red blood cells (RBCs).[36] For example, the parasite *Plasmodium falciparum* that invades the RBCs (Pf-RBCs) of most malaria patients markedly affects the RBC membrane properties resulting in up to a ten-fold increase of its shear modulus and a spherical shape in the later stages of the intra-cell parasite development.[36] Sickle cell anemia is another blood disorder caused by the polymerization of the hemoglobin inside the RBCs, which, in turn, leads to dramatic changes in their shape and deformability. These changes combined with the increased internal viscosity affects the flow of sickled RBCs through the post-capillary venules leading to flow occlusion.[36,77] Other hereditary diseases with similar effects are spherocytosis and elliptocytosis.[14] In the former, RBCs become spherical with reduced diameter and carry much more hemoglobin than their healthy counterparts. In the latter, RBCs are elliptical or oval in shape and exhibit reduced deformability.

These hematologic disorders, despite their differing origins as infectious diseases arising from external vectors or as hereditary abnormalities ascribed to genetic defects, also reveal some common characteristics in terms of the remodeling of cytoskeleton. Such molecular remodeling of the spectrin cytoskeleton induces a change in the structure and viscoelastic properties of individual RBCs. Therefore, studying the rheological properties of blood and its components such as the RBC can aid greatly in the understanding of many major diseases. To this end, new advanced experimental tools are very valuable in obtaining the biophysical properties of single RBCs in health and disease, which are required in formulating multiscale

---

Address correspondence to George Em Karniadakis, Division of Applied Mathematics, Brown University, Providence, RI 02912, USA. Electronic mail: gk@dam.brown.edu

methods for modeling blood flow *in vitro* and *in vivo*. Specifically, advances in experimental techniques now allow measurements down to the nanometer scale, and include micropipette aspiration,[39,159] RBC deformation by optical tweezers,[21,76,147] optical magnetic twisting cytometry,[131] three-dimensional measurement of membrane thermal fluctuations,[118,124] and observations of RBCs immersed in both shear and in pressure-driven flows.[2,66,135,148,154] Micropipette aspiration and optical tweezers techniques tend to deform the entire RBC membrane directly, while optical magnetic twisting cytometry and measurements of membrane thermal fluctuations probe the membrane response locally.

Several numerical models have been developed recently including a continuum description[46,52,69,125] and a discrete approximation on the spectrin molecular level[38,96] as well as on the mesoscopic scale.[42,44,115,122] Some of the models suffer from the assumption of a purely elastic membrane, and are able to capture only the RBC mechanical response, but cannot quantitatively represent realistic RBC rheology and dynamics. Fully continuum (fluid and solid) models often suffer from non-trivial coupling between nonlinear solid deformations and fluid flow with consequential computational expense. Semi-continuum models[46,125] of deformable particles, which use immersed boundary or front-tracking techniques, can be quite efficient. In these models, a membrane is represented by a set of points which are tracked in Lagrangian description and are coupled to an Eulerian discretization of fluid domain. However, these models employ the same external and internal fluids and do not take into account the existing viscosity contrast between them. In addition, continuum models omit some mesoscopic and microscopic scale phenomena such as membrane thermal fluctuations, which affect RBC rheology and dynamics.[114] On the microscopic scale, detailed spectrin molecular models of RBCs are limited by the demanding computational expense. Therefore, we will focus here on an accurate mesoscopic modeling of RBCs.

There exist a few mesoscopic methods[42,44,115,122] for modeling deformable particles such as RBCs. Dzwinel *et al.*[44] model RBCs as a volume of elastic material having an inner skeleton. This model does not take into account the main structural features of the RBC, namely a membrane filled with a fluid, and therefore it cannot accurately capture the dynamics of RBCs, such as the observed tumbling and tank-treading behavior in shear flow.[2,142] Three other methods[42,115,122] employ a conceptually similar approach to the method we will present here, where the RBC is represented by a network of nonlinear viscoelastic springs in combination with bending rigidity and constraints for surface-area and volume conservation. Dupin *et al.*[42] coupled the discrete RBC to a fluid described by the Lattice Boltzmann method[145] obtaining promising results. However, this model does not consider external and internal fluids separation, membrane viscosity, and thermal fluctuations. Noguchi and Gompper[115] employed Multiparticle Collision Dynamics[102] and presented encouraging results on vesicles and RBCs; however, they do not use realistic RBC properties and probe only very limited aspects of RBC dynamics. Pivkin and Karniadakis[122] used dissipative particle dynamics (DPD)[79] for a multiscale RBC model which will be the basis of the general multiscale RBC (MS-RBC) model we will present here, following the earlier versions developed in Fedosov *et al.*[56] The MS-RBC model described here is able to successfully capture RBC mechanics, rheology, and dynamics. Potential membrane hardening or softening as well as the effects of metabolic activity can also be incorporated into the model leading to predictive capabilities of the progression of diseases such as malaria. Theoretical analysis of the hexagonal network yields its mechanical properties, and eliminates the need for *ad hoc* adjustments of the model parameters. Such models can be used to represent seamlessly the RBC membrane, cytoskeleton, cytosol, the surrounding plasma and even the parasite.

This paper is organized as follows: In "Materials and Methods" section, we review the basic DPD theory and the MS-RBC models. In "Healthy Blood Flow" section, we present rheology results of healthy blood flow in capillaries and arterioles, and comparisons with available experimental observations. In "Diseased Blood Flow" section, we review recent results on modeling blood flow in malaria and in sickle cell anemia. We conclude in "Discussion" section with a brief summary and a discussion on the potential of multiscale modeling in predicting the onset and progression of other hematologic disorders.

MATERIALS AND METHODS

Fluid Flow Modeling

Fluid flow modeling is referred here to the modeling of the Newtonian solvent flow, which mimics blood plasma. In particle-based methods a fluid is represented by a collection of interacting particles, which recovers hydrodynamics on the length scales several times larger than the particle size. Examples include molecular dynamics,[6] DPD,[51,75,79] multi-particle collision dynamics,[74,102] and smoothed particle hydrodynamics (SPH).[99,110] The DPD system consists of N point particles, which interact through three pairwise forces—conservative (C), dissipative (D), and random (R)—such that the force on particle i is given by

$$\mathbf{F}_i = \sum_j \mathbf{F}_{ij} = \sum_j \left(\mathbf{F}_{ij}^C + \mathbf{F}_{ij}^D + \mathbf{F}_{ij}^R \right), \tag{1}$$

where the sum runs over all neighboring particles j within a certain cutoff radius. The conservative force mainly controls fluid compressibility, while the dissipative force governs fluid viscosity. In addition, the pair of dissipative and random forces forms a thermostat such that an equilibrium temperature can be imposed.[51]

Recently, the smoothed dissipative particle dynamics (SDPD) method[50] has been proposed, which has several advantages over the conventional DPD. The SDPD method is derived from SPH in combination with a thermostat similar to that used in DPD. In comparison to DPD, the SDPD method allows one to directly input fluid transport coefficients (e.g., viscosity) and to select an arbitrary equation of state, and therefore to have full control over fluid compressibility. Other methods for fluid flow modeling include continuum approaches such as the Navier–Stokes equation or its modifications.[161] In addition, the other two methods which are quite popular for fluid flow modeling are the lattice Boltzmann method (LBM) method[145] and Brownian dynamics.[49]

Modeling Blood Cells

Blood cells are modeled by a flexible membrane with constant area and volume. As an example, the RBC membrane is represented by a network of springs, which corresponds to a triangulation on the membrane surface.[34,38,43,56,57,96,113,122] The free energy for each cell is given by

$$V_{\text{cell}} = V_{\text{s}} + V_{\text{b}} + V_{\text{a+v}}, \tag{2}$$

where V_s is the spring's potential energy, V_b is the bending energy, and V_{a+v} corresponds to the area and volume conservation constraints. The V_s contribution supplies proper cell membrane elasticity. A "dashpot" is attached to each spring, and therefore, the spring forces are a combination of conservative elastic forces and dissipative forces, which provide membrane viscous response similar to a membrane viscosity. The bending energy mimics the bending resistance of the cell membrane, while the area and volume conservation constraints mimic area-incompressibility of the lipid bilayer and incompressibility of a cytosol, respectively. More details on the cell model can be found in Fedosov *et al.*[56,57]

Linear analysis for a regular hexagonal network allows us to relate the model parameters uniquely with the network macroscopic properties, see Fedosov *et al.*[56,57] for details. Thus, in practice, the given macroscopic cell properties serve as an input to be used to calculate the necessary mesoscopic model parameters without any manual adjustment. We also employ a "stress-free" model,[56,57] which eliminates existing artifacts of irregular triangulation. It is obtained by computational annealing such that each spring assumes its own equilibrium spring length adjusted to be the edge length after triangulation. Both internal and external fluids are simulated by a collection of free DPD particles and are separated by the cell membrane through bounce-back reflections at the membrane surface. Moreover, a dissipative force between fluid particles and membrane vertices is set properly to account for the no-slip boundary conditions at the membrane surface. More details on boundary conditions can be found in Fedosov *et al.*[56,57]

The other class of methods for cell membrane modeling corresponds to a continuum representation. Thus, cells are modeled using some type of a constitutive equation from solid mechanics. Examples here include boundary-integral formulation[125,165] and finite element discretization.[100] More details on RBC and blood flow modeling can be found in recent reviews.[62,85,97]

HEALTHY BLOOD FLOW

Blood flow in microcirculation[123] affects a number of vital processes in the human body including oxygen delivery to tissues, removal of waste products, immune response, haemostasis, *etc*. Detailed experimental measurements of blood flow *in vivo* down to a cell level are very difficult and often not feasible. This has motivated a large worldwide scientific effort to derive reliable numerical models of blood flow in order to study blood hydrodynamics in vessel networks, its rheology, and the effect on various blood-affected processes. Here, we will mainly focus on mesoscopic modeling of blood flow down to the single blood cell level; see also a recent review.[62] We also present typical average plasma and RBC properties in Table 1.

Blood Flow in Tubes

Blood flow in tubes or rectangular channels is a relatively simple problem which mimics the main characteristics of blood flow in a *in vivo* vessel. It allows the quantification of blood flow resistance for various conditions by estimating such factors as the hematocrit, flow rate, and RBC aggregation. This model also permits quantitative simulation of such processes as the migration, deformation, and dynamics

TABLE 1. Typical average plasma and RBC properties in health.

Plasma viscosity	0.0012 Pa · s
RBC cytosol	0.006 Pa · s
Temperature	37 °C
RBC membrane Young's modulus	18.9×10^{-6} N/m
RBC membrane bending rigidity	3.0×10^{-19} J
RBC membrane viscosity	2.2×10^{-8} Pa · s · m

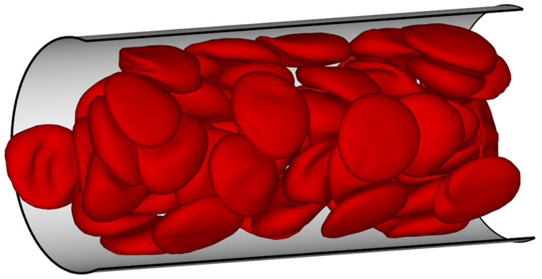

FIGURE 1. A simulation snapshot of blood flow (RBCs only) in a tube of a diameter $D = 20$ μm and at tube hematocrit $H_t = 0.45$. The thin layer between the RBC core and the tube walls is the cell-free layer.

of single cells within the flow. As an example, Fig. 1 shows a snapshot of flow of blood in a tube with diameter $D = 20$ μm.

Fahraeus Effect

Fahraeus performed *in vitro* experiments on blood flowing through glass tubes[53] and found an elevated value of discharge hematocrit (H_d), defined as the RBC volume fraction exiting a tube per unit time, in comparison with the RBC concentration within a tube called tube hematocrit (H_t). This finding, which is called the Fahraeus effect, is a consequence of the cross-stream migration of RBCs in tube flow. RBCs in blood flow migrate away from the vessel walls towards the centerline[28,72] due to hydrodynamic interactions with the walls and their deformability[4,19,40,108]; such interactions are also referred to as *lift force*. Crowding of RBCs around the tube center results in their faster motion along the tube with respect to the average blood flow velocity, thus leading to an increased H_d value measured experimentally.

The Fahraeus effect is one of the standard tests for any blood flow model, and has been modeled in simulations of blood flow in rectangular channels[43] and in tubes.[59,93] In contrast to experiments,[53,128] where H_d is the main controlled parameter and H_t has to be measured, in simulations H_t is an input and corresponds to the volume fraction of RBCs placed within the channel, while H_d is computed. In order to compute the ratio H_t/H_d in simulations a simple mass balance can be employed in flow, which yields

$$\frac{H_t}{H_d} = \frac{\bar{v}}{v_{\mathrm{RBC}}}, \tag{3}$$

where $\bar{v}$ is the average flow velocity and v_{RBC} is the average velocity of red cells. Figure 2a shows the ratio H_t/H_d for two hematocrits and various tube diameters D. The simulation results[93] are compared with the empirical fits to experimental data on blood flow in glass tubes.[128] A strong effect of RBC migration to the tube center on the discharge hematocrit is observed for tubes with diameters of up to about 200 μm. For larger tube diameters, the layer next to the wall void of RBCs, called the *cell-free layer* (CFL), becomes rather small in comparison with D, and therefore the Fahraeus effect is negligible.

Fahraeus–Lindqvist Effect

Another phenomenon directly related to RBC migration towards a vessel centerline and the formation of a CFL next to the wall is the Fahraeus–Lindqvist effect,[55] describing a decrease in blood flow resistance with decreasing tube diameter.[128] The flow resistance is affected by the CFL, which serves as an effective lubrication layer for relatively viscous flow at the core consisting primarily of RBCs. For large tube diameters the CFL thickness is small with respect to D, and therefore the bulk blood viscosity is essentially measured. As the tube diameter is reduced, the CFL thickness becomes more significant with respect to D leading to an effective decrease in flow resistance. The blood flow resistance in glass tubes is quantified by an effective viscosity, termed the *apparent blood viscosity*, using the Poiseuille law in tubes

$$\eta_{\mathrm{app}} = \frac{\pi \Delta P D^4}{128 Q L}, \tag{4}$$

where $\Delta P/L$ is the pressure drop along the tube length L and Q is the volumetric flow rate. For convenience, experimental results[128] are presented in terms of the relative apparent viscosity defined as

$$\eta_{\mathrm{rel}} = \frac{\eta_{\mathrm{app}}}{\eta_0}, \tag{5}$$

where η_0 is the blood plasma viscosity. Thus, η_{rel} characterizes the effective viscosity of blood with respect to that of plasma.

Similar to the Fahraeus effect, the Fahraeus–Lindqvist effect also serves as a standard validation test for any blood flow model. Figure 2b shows the relative apparent viscosity for different H_t values and tube diameters, where the solid curves are the fits to experimental measurements[128]; the symbols correspond

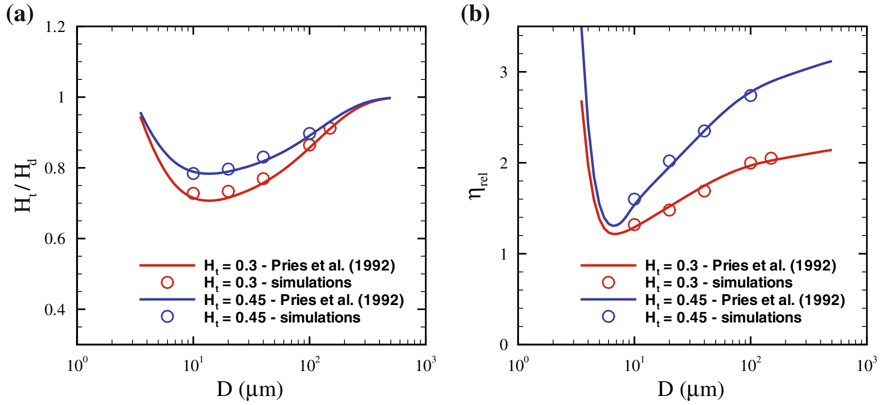

FIGURE 2. (a) Ratio of tube (H_t) to the discharge (H_d) hematocrit, and (b) Relative apparent viscosity (η_{rel}), for different H_t values and tube diameters *D*. The symbols correspond to the DPD simulations in Lei *et al.*,[93] while the curves are the fits to experimental data.[128] The figure is adopted with permission from Lei *et al.*[93]

to simulation results.[93] The minimum value of $\eta_{\rm rel}$ is found for the tube diameter of $D_{\rm m} = 7$–$8\ \mu$m. In tubes with diameters smaller than $D_{\rm m}$, RBCs have to strongly deform and squeeze through the tubes attaining bullet-like shapes,[3,140,155] which leads to a steep increase in the relative apparent viscosity. On the other hand, when $D > D_{\rm m}$, the thickness of the CFL in comparison with the tube diameter becomes smaller, leading to an effective viscosity increase.

The Fahraeus–Lindqvist effect has been quantitatively captured in 3D blood flow models in cylindrical vessels[5,59,68,93] as well as in rectangular channels.[41,43] Furthermore, this effect has also been quantitatively predicted by 2D blood flow models[9] and by the simplified blood models,[84,105,116] which do not properly capture RBC membrane deformability. This clearly indicates that the deformability and dynamics of individual cells do not significantly affect the flow resistance. Thus, it appears computationally advantageous to divide blood flowing in tubes into two regions: (i) a relatively viscous flow core consisting mainly of cells, and (ii) the CFL region devoid of RBCs. This assumption leads to the so-called two-phase model[28,71,93,138] for blood flow in tubes or vessels, where the flow is divided into core and near-wall regions having different viscosities. Although such models describe well the flow resistance in straight tubes, they might not provide realistic simulations in complex geometries (e.g., vessel networks) due to spatial variability of the CFL[88] and non-trivial partitioning of RBCs within the network.[130]

Finally, the blood flow resistance depends on flow rate and aggregation interactions between RBCs. Experimental data compiled in Pries *et al.*[128] and simulations of blood flow in small tubes[68] suggest that the dependence of flow resistance on flow rate disappears at sufficiently high flow rates exceeding the pseudo-shear rate $\dot{\gamma} = \bar{v}/D$ of approximately 50 s^{-1}. In fact, fits to experimental data presented in Fig. 2 are based solely on experimental studies, where the pseudo-shear rates are higher than 50 s^{-1}.[128] As the flow rate is decreased such that $\dot{\gamma} < 50\,\mathrm{s}^{-1}$, the blood flow resistance increases for RBC suspensions[68,134] without aggregation interactions between cells. RBC aggregation in whole blood occurs in equilibrium or at sufficiently low shear rates. Viscometric measurements of whole blood viscosity[25,106,141] have shown a steep viscosity increase for shear rates below 10 s^{-1} due to RBC aggregation in comparison with analogous non-aggregating RBC suspension. Thus, the flow resistance of blood in tubes is not affected by RBC aggregation for sufficiently high flow rates, and this has been confirmed experimentally[28,134] and in simulations.[93] At sufficiently low flow rates, experimental studies[28,54,111,134] report a decrease in the relative apparent viscosity due to RBC aggregation, but this has not been yet explored in simulations.

Cell-Free Layer

The CFL is a layer of blood plasma near the wall that is devoid of RBCs due to their migration to the vessel center. The viscosity in the CFL region is equal to that of blood plasma, while the viscosity in the tube-core region populated with RBCs is several times larger. Hence, the formation of CFL leads to a better efficiency for the RBC core to flow resulting in the aforementioned Fahraeus and Fahraeus–Lindqvist effects. The thickness of CFL δ may serve as an alternative indicator for blood flow resistance. In *in vitro*[17,134] and *in vivo*[88,101,163] experiments, the outer edge of the RBC core has been tracked to calculate its average position and deduce the CFL thickness. A similar approach has also been employed in

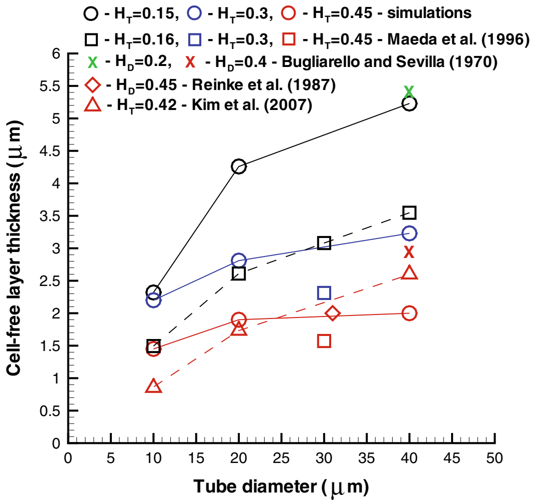

FIGURE 3. Cell-free layer thickness for different hematocrits and tube diameters. The figure is adopted with permission from Pan *et al.*[117]

simulations[43,59,93,116] and a comparison of CFL thicknesses measured experimentally and in simulations is shown in Fig. 3. The simulations predict an increase in δ with tube diameter. However, the ratio of δ/D in fact decreases,[41,93] which is consistent with the Fahraeus and Fahraeus–Lindqvist effects. The simulated CFLs show only partial agreement with the corresponding experimental data in Fig. 3. The agreement is good when compared with *in vitro* experiments on blood flow in glass tubes,[17,134] while for the *in vivo* experimental data[88,101] noticeable discrepancies exist especially at low H_t values. The variability in CFL thicknesses also exists across various CFL experimental measurements,[88,101,163] so the agreement of the simulation results with *in vivo* data is expected to be qualitative. Several factors may contribute to the variability of *in vivo* measurements of CFL and the discrepancies with simulations including the glycocalyx layer at vessel walls, variations in vessel diameter and length, close proximity of the site of CFL measurements to vessel bifurcations, vessel elasticity, and spatial resolution of the recorded data.[47,59,88,127]

An alternative means to compute the thickness of CFL in simulations is to analyze the local hematocrit distribution (see Fig. 4a), which drops quickly as we exit the RBC core region and enter the CFL moving along the tube radial direction.[9,41,68] The simulation of non-aggregating RBC suspension in tube flow[68] showed that δ increases as the pseudo-shear rate is increased from 0 to approximately 50 s^{-1}. This result indicates that the flow resistance is decreasing in agreement with the experimental measurements in Reinke *et al.*[134] For flow rates above 50 s^{-1}, the CFL thickness remains nearly constant,[68] which supports the argument that the flow resistance becomes independent of the flow rate as discussed in "Fahraeus–Lindqvist Effect" section. In contrast to a constant δ for high flow rates, *in vivo* experiments[88] and 3D simulations[59] have shown a mild decrease in the CFL thickness with increasing flow rate. Finally, the effect of RBC aggregation, which is important only at low shear rates, leads to an increase in the CFL thickness as the flow rate is reduced due to the possibility to form a more compact RBC core of the flow.[89,134] Consequently, RBC aggregation results in a lower flow resistance as the flow rate is decreased. Note that RBC aggregability reverses the trend of the flow resistance for low flow rates in comparison with a non-aggregating suspension; the RBC aggregation effect has not been yet investigated by simulations.

RBC Distribution and Deformation in Flow

Migration of RBCs in blood flow leads to a variation in local RBC density and hematocrit. Departures from normal blood flow characteristics are potential indicators of disease pathology. For tube flow, the local hematocrit $H(r)$ is defined as the volume fraction of RBCs within an annular region with the radius r and thickness Δr. Figure 4a presents the local hematocrit distributions for various H_t values and tube diameters. For small tube diameters, $H(r)$ in the tube center is significantly larger than H_t in agreement with the simulation results in Freund and Orescanin[68] Thus, RBCs are mainly located at the tube center, however their dynamics and structure depend on H_t.[93] At low H_t, RBCs attain a parachute shape and move in a train-like arrangement, which has been also reported in McWhirter *et al.*[104] In contrast, at high H_t, RBCs arrange into the so-called zig-zag mode found experimentally in Gaehtgens *et al.*[70] and in simulations.[104] As the tube diameter is increased, the local hematocrit converges towards the H_t value. However, for low H_t a peak in $H(r)$ may still exist around the tube center due to close packing of RBCs within the centerline region where local shear rates are small. For tube diameters $D \gtrsim 200\ \mu m$ a nearly homogeneous distribution of RBCs is expected, and therefore a continuum approximation for blood flow in large tube is appropriate.[93]

Quantitative analysis of local RBC deformation in tube flow can be conveniently performed using the RBC gyration tensor.[103] Eigenvalues of the gyration tensor characterize cell shape along the directions defined by the tensor eigenvectors. The distributions of the largest eigenvalue λ_{max} for the RBC across the tube are shown in Fig. 4b indicating that RBCs are slightly compressed in the tube center and get stretched more

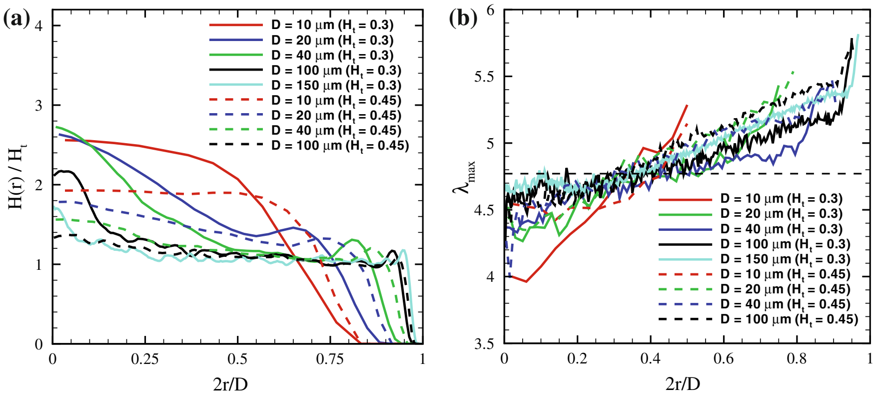

FIGURE 4. (a) Local hematocrit values in blood flow across the tube for different H_t values and tube diameters. (b) Local RBC deformation in tube flow characterized by the largest eigenvalue ($\lambda_{\max}$) of the RBC gyration tensor for different tube diameters and H_t values. The horizontal dashed line denotes the equilibrium value of $\lambda_{\max}$ equal to approximately 4.77. The figure is adopted with permission from Lei *et al.*[93]

and more by the flow as we approach the CFL region. The $\lambda_{\max}$ distributions can be qualitatively divided into the three regions: i) a centerline region, where $\lambda_{\max}$ is nearly constant; ii) the region between the tube center and CFL, where $\lambda_{\max}$ slowly increases; iii) a region next to the CFL, where $\lambda_{\max}$ steeply increases. Similar conclusions for RBC deformation in tube flow have also been reported in Alizadehrad *et al.*[5] Finally, for sufficiently large D the function of $\lambda_{\max}(r)$ converges to a common curve, and therefore the dependence on tube diameter disappears.

Blood Rheology

A major aim of computational cell biorheology is to predict the macroscopic flow properties of a suspension (e.g., shear viscosity, yield stress) from the mesoscopic properties of the constituent particles (e.g., size, deformability, inter-particle interactions). Bulk blood properties under shear have been measured in a number of laboratories[25,106,121,137,141,150] predicting a non-Newtonian shear thinning behavior. Here, we draw attention to two different sets of viscometric measurements. The first set corresponds to whole blood, where no significant changes are introduced to freshly drawn blood except for a necessary initial stabilization with an anti-coagulant. Such procedure for sample preparation leaves the aggregation properties among RBCs virtually unaffected, and therefore cell aggregates, known as *rouleaux*, can be observed.[23,24,106,107] The second set of viscometric measurements corresponds to the so-called non-aggregating RBC suspensions, where RBCs are washed and re-suspended into a neutral solvent. RBC aggregation interactions strongly depend on the nature and concentration of available proteins or polymers[24,107] and can be triggered by adding them to non-aggregating RBC suspensions.[107,126,144] Whole blood is also known to exhibit a yield stress[27,29,106] defined as a threshold stress that must be exceeded for flow to begin.

Reversible Rouleaux Formation

Aggregation interactions among RBCs lead to the formation of rouleaux structures in equilibrium or in relatively weak flows. A rouleaux resemble stacks of coins as illustrated in Fig. 5 showing a simulation snapshot in equilibrium. There exist two different hypotheses for the RBC aggregation in polymer or protein solutions: (i) the bridging model, which suggests that cross-linking between cells may be achieved by polymer adsorption or adhesion on a cell surface,[16,22] and (ii) the depletion model, which suggests that RBC aggregation arises from depletion interactions.[13,112] In equilibrium, rouleaux formation consisting of a few RBCs is first observed, followed by further coalescence into branched rouleaux networks.[106,136,137] In flow, the large rouleaux break up into smaller ones. However, at sufficiently high shear rates, rouleaux structures no longer exist.[168] The aggregation process is reversible once the shear rate is decreased.

RBC aggregation has been simulated in 2D,[11,158,164] where aggregation and disaggregation of several cells in shear flow has been studied. The effect of RBC aggregation on blood rheology has also been investigated in 3D simulations.[98] However, the marked viscosity increase at low shear rates has not been captured due to the very small size of a simulated system with only six RBCs. Finally, recent 3D simulations[63] led to

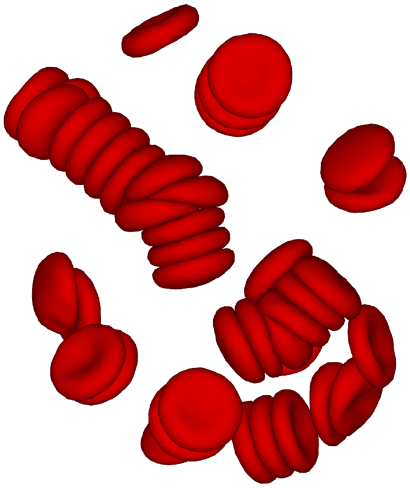

FIGURE 5. A simulation snapshot showing sample RBC-rouleaux structures in equilibrium.

quantitative predictions for the strength of RBC aggregation and its effect on blood viscosity.

Blood Viscosity and Yield Stress

As noted earlier, the viscosity of whole blood is strikingly different from that of non-aggregating RBC suspension due to aggregation interactions between RBCs. Figure 6 presents the relative viscosity of blood, defined as the ratio of RBC suspension viscosity to the solvent viscosity, vs. shear rate at $H_t = 0.45$. The blood viscosity was calculated in shear flow[63] using the MS-RBC model.[56] The model results compare very well with the experimental viscometric measurements.[25,106,141] The correct predictions of viscosity by the model facilitates calculation of the strength of aggregation forces between two RBCs, which appears to be in the range of 3.0 pN to 7 pN. Note that these forces are much smaller than those used in single RBC stretching tests with optical tweezers.[147]

Whole blood is considered a fluid with a yield stress (a threshold stress for flow to begin),[27,29,106,121] which is usually calculated by extrapolation of available viscometric data to the zero shear rate. For blood the Casson's equation[20] is often used

$$\tau_{xy}^{1/2} = \tau_y^{1/2} + \eta^{1/2}\dot{\gamma}^{1/2}, \tag{6}$$

where τ_{xy} is the shear stress, τ_y is a yield stress and η is the suspension viscosity at large $\dot{\gamma}$. The Casson's relation has been used to compute yield stress for pigment-oil suspensions,[20] Chinese ovary hamster cell suspensions,[81] and blood.[107] Figure 7 shows the simulation results from Fedosov *et al.* [63] where computed shear stresses are extrapolated to the zero shear rate using a polynomial fit in Casson coordinates. The extrapolated τ_y values are virtually zero for non-aggregating RBC suspensions, while the presence of RBC aggregation leads to a non-zero yield stress. The simulation results support the hypothesis that whole blood has a non-zero yield stress due to aggregation interactions between RBCs.[27,29,106] Moreover, the simulated values of τ_y lie within the range of 0.0015 Pa and 0.005 Pa for yield stress measured experimentally.[106]

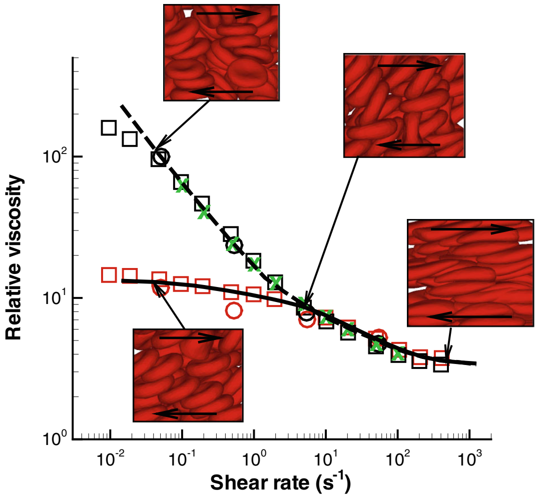

FIGURE 6. Non-Newtonian relative viscosity of blood (the cell suspension viscosity divided by the solvent viscosity) as a function of shear rate at H_t = 0.45. The simulation curves are: dashed—whole blood model; solid—non-aggregating RBC suspension. The experimental data are as follows: Whole blood: green crosses—Merril *et al.*,[106] black circles—Chien *et al.*,[25] black squares—Skalak *et al.*[141] Non-aggregating RBC suspension: red circles—Chien *et al.*,[25] red squares—Skalak *et al.*.[141] The insets show simulation snapshots at different shear rates. The figure is reproduced with permission from Fedosov *et al.*[62]

Another aspect which has been discussed in Fedosov *et al.*,[63] is a link between RBC suspension macroscopic properties and its microscopic characteristics such as cell structure, deformation, and dynamics. The analysis of the suspension's structure has confirmed that a steep rise in viscosity for the aggregating RBC suspension at low shear rates is due to the existence of small aggregates consisting of 2–4 RBCs. As the shear rate is increased, the suspension's structure completely disappears, and therefore the viscosity at high shear rates becomes independent of RBC aggregation. Furthermore, the shear-thinning property of a non-aggregating RBC suspension is strongly associated with the transition of RBCs from tumbling to the tank-treading dynamics[2,142] and the alignment of tank-treading RBCs with the shear flow. Simulations of a single elastic oblate-shape capsule in shear flow,[10] which mimic a dilute solution, have also shown a shear thinning behavior which mainly occurs

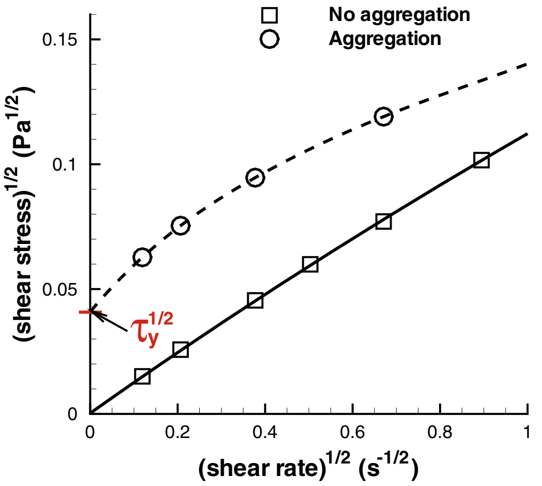

FIGURE 7. Casson plots for the extrapolated yield stress (using a polynomial fit) for simulated MS-RBC suspensions with and without aggregations at H_t = 0.45. The figure is reproduced with permission from Fedosov *et al.*[62]

within the capsule tank-treading regime. Another simulation study of dense near-spherical capsules[26] have also shown a slight shear-thinning behavior due to the deformation of capsules in shear flow. In addition, normal stress differences have been computed for the capsule suspensions.

Numerical studies of the rheology of dense suspensions of deformable particles and cells are still rather limited. Such simulations can be used to investigate a wide class of complex fluids (e.g., cell, vesicle, and capsule suspensions) and to tune their properties to modulate cell behavior. In addition, such 3D high-fidelity simulations will allow one to study in detail the connection between macroscopic and microscopic properties of such suspensions.

Margination of White Blood Cells and Platelets

Margination of different solutes (e.g., white blood cells, platelets, drug carriers) in blood flow is the migration process of the solutes towards vessel walls. The margination process is essential for many blood solutes in order to perform their function, as they come into contact with vessel walls when necessary. For example, white blood cells (WBC) have to marginate towards the walls[12,65,73] in order to be able to efficiently adhere to vascular endothelium and eventually transmigrate into the surrounding tissues.[143] The margination mechanism is mediated by RBCs, which migrate towards the vessel center[28,72] due to the hydrodynamic lift force,[4,19,40,108] and effectively push out various solutes from the central region into the CFL. More precisely, the margination mechanism is a consequence of the competition between lift forces on RBCs and blood solutes, and their interactions in flow. Recently, a margination theory for binary suspensions[90,91] has been proposed through two mechanisms: (i) wall-induced particle migration due to lift force, and (ii) particle displacement due to pair collisions of different solutes or their interactions in flow; the latter mechanism is also often referred to as shear-induced diffusion.

White Blood Cell Margination

WBC margination has been studied in a number of experiments[1,12,65,73,83,119] and simulations.[61,67,146] Several blood and flow properties contribute to WBC margination including H_t, flow rate, RBC aggregation, and vessel geometry. *In vivo* experiments on mesenteric venules of rat[65] showed an increase of WBC adhesion rate (and consequently margination) for high $H_t \gtrsim 0.45$ as the flow rate was decreased. A recent microfluidics study[83] concluded that the most efficient WBC margination occurs within intermediate $H_t \simeq 0.2$–0.3, while at lower or higher H_t values WBC margination is attenuated. In contrast, *in vitro* experiments in glass tubes[1] and 2D simulations[67] have reported no significant sensitivity of WBC margination on blood hematocrit. The effect of flow rate on WBC margination is consistent across various studies,[61,65,67,83,119] which show strong WBC margination at low flow rates, characteristic for venular blood flow. Furthermore, RBC aggregation leads to an enhancement of WBC margination,[1,61,65,83,119] while the effect of complex geometries (e.g., vessel contraction, expansion, and bifurcation) on WBC margination has a very limited interpretation so far. The 2D simulation study[146] and microfluidic experiments[83] mimicking a vessel expansion suggest that the WBC margination is enhanced in post-capillary venular expansions. Finally, a combined *in vitro* and *in vivo* study of blood flow around bifurcations[156] have shown preferential adhesion of WBCs near bifurcations.

Recent 2D simulations[61] provided a systematic study of WBC margination for various conditions including flow rate, H_t, WBC deformability, and RBC aggregation, and attempted to reconcile existing contradicting observations. Using blood flow simulations, WBC center-of-mass distributions were computed for various flow rates and H_t values with an example shown in Fig. 8. Clearly, the strongest WBC margination is found within a range of intermediate $H_t = 0.25$–0.35, while at lower and higher H_t values WBC margination is attenuated. The weak WBC margination at low H_t has been expected due to low concentration of RBCs. Surprisingly, however, no significant WBC margination at high H_t was observed. The mechanism of WBC margination attenuation at high H_t appeared to be also related to the presence of RBCs in flow. Thus, at low enough H_t the region in front of a marginated WBC in blood flow remains virtually void of RBCs as they pass above the slowly moving WBC. As we increase H_t to a certain value, RBCs may often enter that region due to high cell crowding, and effectively lift off the WBC away from the walls.[61] This lift-off mechanism is different from the lift force due to cell-wall hydrodynamic interactions and is governed by the particulate nature of blood.

Having calculated WBC distributions, one can define a WBC margination probability by integrating the probability distributions, for instance, up to a distance of $1.1R_{WBC}$ away from the walls, where R_{WBC} is the WBC radius. Figure 9 presents a WBC margination diagram for a wide range of flow rates and hematocrits. It shows that efficient WBC margination occurs only within intermediate ranges of flow rates and H_t values. These results are consistent with experimental observations, which report WBC adhesion mainly in venular (not arteriolar) part of microcirculation, since the characteristic values of $\dot{\gamma}^*$ in venules of a comparable diameter are in the range $\dot{\gamma}^* = 1-25$, while in arterioles $\dot{\gamma}^* \gtrsim 30$.[61,123,129] The simulation results also agree with *in vitro* experiments on WBC margination,[83] which identified optimal WBC margination in the range $H_t = 0.2$–0.3. The discrepancies with previous simulations[67] and experiments,[1] which found WBC margination and adhesion to be independent of H_t, can also be rationalized by noting that the studied flow rates and H_t values in Abbitt and Nash[1] and Freund[67] fell almost entirely into the region of strong WBC margination.

The effect of WBC deformability has also been explored in Fedosov *et al.*,[61] where the region of strong WBC margination shrinks substantially as a WBC becomes more deformable. This is due to an increase of the lift force on a deformed WBC, since it may significantly depart from a spherical shape, which leads to a reduction in its margination. RBC aggregation has also been shown to enhance WBC margination.[61] In particular, no significant differences in WBC margination between aggregating and non-aggregating RBC suspensions have been found for high flow rates similar to the effect of RBC aggregation on blood viscosity discussed in "Blood Rheology" section. However, WBC margination becomes more pronounced at high H_t values due to RBC aggregation. Here, RBC aggregation interactions lead to a less dispersed flow core, and therefore the shedding of RBCs into the region in front of a marginated RBC is much reduced. Future studies of WBC margination will likely focus on 3D realistic models, and WBC margination and adhesion in complex microvascular networks.

Similar margination mechanisms are of importance in a number of diseases. For instance, margination of circulating tumor cells, which affects their adhesion to vascular endothelium, is expected to resemble that of WBCs due to the similarities in cell shapes and sizes. The WBC margination results are also relevant in spherocytosis disorder and in malaria, where spherically-shaped cells are expected to be mainly present near vessel walls resulting in an increased blood flow resistance and an enhanced cell adhesion when possible. Furthermore, the margination effect directly applies to segregation of various cells and particles in flow due to the differences in their deformability and shape. Recent numerical and theoretical investigations[90,91] have shown that less deformable cells or capsules are preferably segregated toward channel

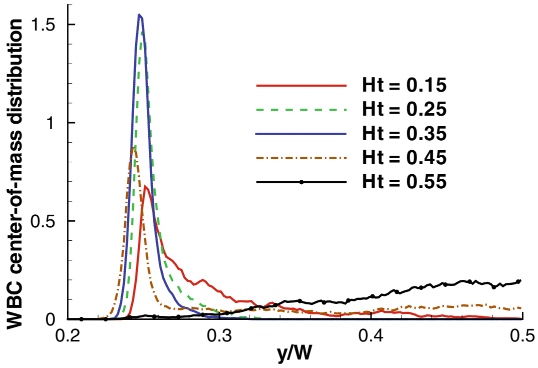

FIGURE 8. WBC center-of-mass distribution for various H_t values. The position y is normalized by the width of a channel W such that $y = 0$ corresponds to the wall position and $y/W = 0.25$ to the WBC radius. The figure is reproduced with permission from Fedosov *et al.*[61]

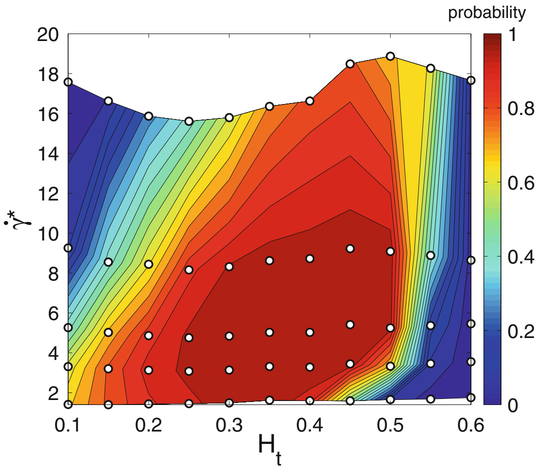

FIGURE 9. Probability diagram of WBC margination for various flow rates characterized by a non-dimensional shear rate $\dot{\gamma}^*$ and H_t values. The WBC is assumed to be rigid. The "○" symbols correspond to the simulations performed. The figure is reproduced with permission from Fedosov *et al.*[61]

walls. Such an effect is expected to play a role in malaria and sickle-cell anemia, where margination of stiff cells (e.g., Pf-RBCs) contributes to their adhesive potential. On the other hand, margination and segregation properties of different cells in blood flow can be exploited in diagnostics and treatment which might require rare cell detection and separation.[15,78,80] Finally, solutes smaller than WBCs (e.g., platelets, large globular proteins such as von Willebrand factor) are also subject to margination in blood flow, which is relevant for margination (and therefore adhesion) of micro- and nano-carriers used for drug delivery. Next, the margination effect for platelets is discussed.

Margination of Platelets

Preferential migration of platelets towards the vessel walls in blood flow is critical for haemostasis and thrombosis, since marginated platelets can better respond to injuries at the vessel wall. Margination of platelets as well as of WBCs is strongly affected by local hematocrit, flow rate, vessel geometry, and RBC aggregation properties. These characteristics might be significantly altered in different diseases in comparison with a healthy state leading to irreversible changes in cell margination properties which might affect their proper function. An increased concentration of platelets near the walls has been confirmed in *in vitro*[45,151,157] and *in vivo*[149,162] experiments. Experiments in glass channels with a suspension of RBCs and latex beads mimicking platelets[45,151] for different H_t values have shown strong bead margination at high $H_t \gtrsim 0.3$ values. The experiments for various flow rates[45,151] demonstrated a non-trivial bead margination dependence. At low shear rates platelet margination was weak and it increased with increasing flow rates, while the margination decreased again at very high shear rates; this behavior is qualitatively similar to that of WBCs. *In vivo* experiments[162] have found that platelet margination is different in arterioles and venules confirming the effect of shear rate on margination. In view of these observations, it is plausible to expect that the mechanism of platelet margination is similar to that for WBCs described above, however its detailed understanding is still an open question.

There exist a number of numerical studies of platelet margination and its mechanisms.[7,32,33,133,152,153,166,167] The 2D simulations of blood flow using ellipsoid-like RBCs and circular platelets[7] have shown an increased platelet margination with increasing H_t as well as with an increase of shear rate in agreement with the experimental observations. The other set of 2D simulations[32,33] has led to similar conclusions for the effects of H_t and shear rates on platelet margination. The local drift and diffusion of platelets have also been measured[32,33] in an attempt to describe the platelet margination process using the continuum drift-diffusion equation. The drift-diffusion equation results in a good qualitative description of platelet margination, where the drift can be hypothesized to arise from wall-platelet hydrodynamic interactions (i.e., lift force), while the shear-induced diffusivity of platelets is due to their collisions (or interactions) with RBCs in blood flow. Recent 3D simulations on platelet margination[166,167] have found the margination process to be diffusional, which fits well into the drift-diffusion mechanism. Another 3D simulation study[133] have confirmed the effect of H_t on platelet margination, and, in addition, reported that spherical platelets marginate better than those having an ellipsoidal shape. Although the drift-diffusion mechanism for platelet margination seems to provide plausible explanation, it is still not clear whether it will lead to a universal description of the margination process. For instance, a recent theoretical model[152] for platelet adhesion in blood flow suggests a rebounding collision mechanism for platelets due to their interactions with the flow core consisting primarily of RBCs.

DISEASED BLOOD FLOW

Rheology in Malaria

Red blood cells parasitized by the malaria-inducing *Plasmodium falciparum* (Pf) parasites, referred to here as Pf-RBCs, are subject to changes in their mechanical and rheological properties as well as in their morphology[30,139,147] during intra-erythrocytic parasite development, which includes three intra-erythrocytic stages that span the 48-h asexual cycle: from ring → trophozoite → schizont stages. Gradual progression through these stages leads to considerable stiffening of Pf-RBCs as found in optical tweezers stretching experiments[35,109,147] and in diffraction phase microscopy by monitoring the membrane fluctuations.[37,118] Pf development also results in vacuoles formed inside of RBCs possibly changing the cell volume. Thus, Pf-RBCs at the final stage (schizont) often show a "near spherical" shape, while in the preceding stages maintain their biconcavity. These changes greatly affect the rheological properties and the dynamics of Pf-RBCs, and may lead to obstruction of small capillaries[139] impairing the ability of RBCs to circulate.

In this section, we present results of the application of the computational framework we discussed for healthy RBCs to Pf-RBCs. In particular, we first consider single RBCs for validation purposes and subsequently we present simulations for whole infected blood as suspension of a mixture of healthy and Pf-RBCs in order to investigate its rheological behavior.

In Bow *et al.*[15] a new microfluidic device with periodic obstacles to red blood cell flow was employed to perform experiments for the late ring-stage *P. falciparum*-infected RBCs that are infected with a gene encoding green fluorescent protein (GFP). This device consisted of triangular obstacles (in converging and diverging form). For both the converging and diverging geometries infected RBCs exhibit lower average velocities than healthy RBCs (see Fig. 10a). In the DPD simulations, the infected cells are modeled with increased shear modulus and membrane viscosity values obtained from optical tweezers experiments. The parasite was modeled as a rigid sphere of two microns in diameter[48] placed inside the cell. Time lapse images from the simulations showing passage of an infected RBC through the periodic obstacles with converging and diverging opening geometries are shown in Fig. 10b.

The DPD model is able to capture the effect of changes of RBC properties arising from parasitization on the movement of healthy RBCs and Pf-RBCs quite accurately. A quantitative comparison of the simulation results with experimental data for the average velocity of uninfected RBCs and Pf-RBCs as a function of applied pressure gradient is shown in Fig. 11.

In order for the DPD simulation to provide insights into the design of microfluidic devices that are potentially capable of diagnosing disease states, it is essential to develop computational capabilities for the biorheology of whole blood (containing multiple components) where only a small volume fraction of the total cell population contains diseased cells. Next we present simulation results of blood flow in malaria as a suspension of healthy and Pf-RBCs at the trophozoite stage and hematocrit $H_{\rm t} = 0.45$. Several realistic (low parasitemia levels) and hypothetical parasitemial levels (percentage of Pf-RBCs with respect to the total number of cells in a unit volume) from 5 to 100% are considered in vessels with diameters 10 and 20 μm. The inset of Fig. 12a shows a snapshot of RBCs flowing in a tube of diameter 20 μm at a parasitemia level of 25%.

The main result in Fig. 12a is given by the plot of the relative apparent viscosity in malaria obtained at different parasitemia levels. The effect of parasitemia level appears to be more prominent for small diameters and high $H_{\rm t}$ values. Thus, at $H_{\rm t} = 0.45$ blood flow resistance in malaria may increase up to 50% in vessels of diameters around 10 μm and up to 43% for vessel diameters around 20 μm. These increases do not include any contributions from the interaction of Pf-RBCs with the glycocalyx[123,160]; such important interactions are complex as they may include cytoadhesion.

In Fig. 12b we also present the bulk viscosity of infected blood (schizont stage) simulated in a Couette type device at shear rate $\dot{\gamma} = 230\,s^{-1}$. The DPD simulations compare favorably with the experimental data obtained with a corresponding rheometer in Raventos-Suarez *et al.*[132] These validated predictions were obtained without an explicit adhesion model between Pf-RBCs. It seems that such cell-cell interactions are not important at this high shear rate value.

With regards to the *cytoadherence* of Pf-RBCs, microfluidic experiments have been conducted in Antia *et al.*[8] to investigate the enhanced cytoadherence of Pf-RBCs in flow chambers. These experiments revealed that the adhesive dynamics of Pf-RBCs can be very different than the well-established adhesive dynamics of leukocytes. For example, the adhesive dynamics of Pf-RBCs on purified ICAM-1 is characterized by stable and persistent flipping (rolling) behavior for a wide range of wall shear stresses (WSS)[8] but also by intermittent pause and sudden flipping due to the parasite mass inertia. This interesting adhesive dynamics was simulated in Fedosov *et al.*[60] where a systematic study was conducted to estimate the magnitude of the

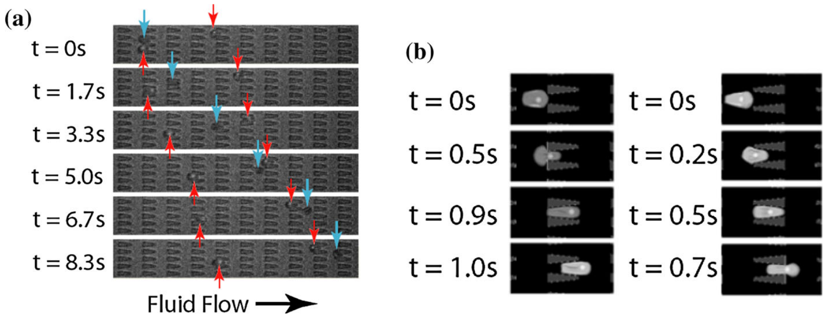

FIGURE 10. (a) Experimental images of ring-stage *P. falciparum*-infected (red arrows) and uninfected (blue arrows) RBCs in the channels at a pressure gradient of 0.24 Pa/μm. The small fluorescent dot inside the infected cell is the GFP-transfected parasite. At 8.3 *s*, it is clear that the uninfected cell moved about twice as far as each infected cell. (b) DPD simulation images of *P. falciparum*-infected RBCs traveling in channels of converging (left) and diverging (right) opening geometry at 0.48 Pa/μm. The figure is reproduced with permission from Bow *et al.*[15]

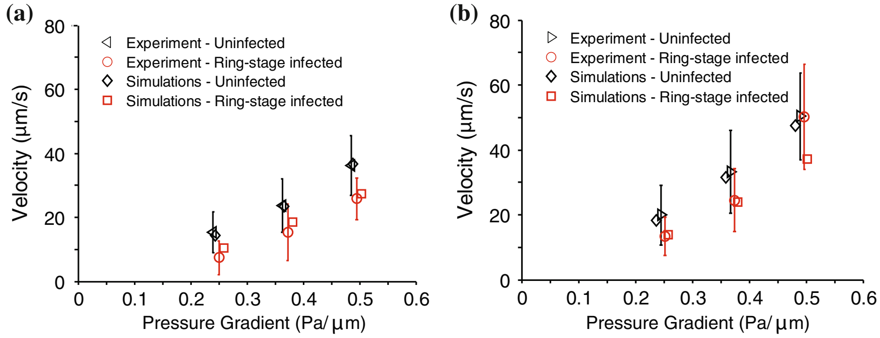

FIGURE 11. Average velocity of uninfected and ring-stage malaria infected RBCs as a function of pressure gradient and comparison of simulation and experimental results. Results are for diverging (a) and converging (b) geometries. The figure is reproduced with permission from Bow *et al.*[15]

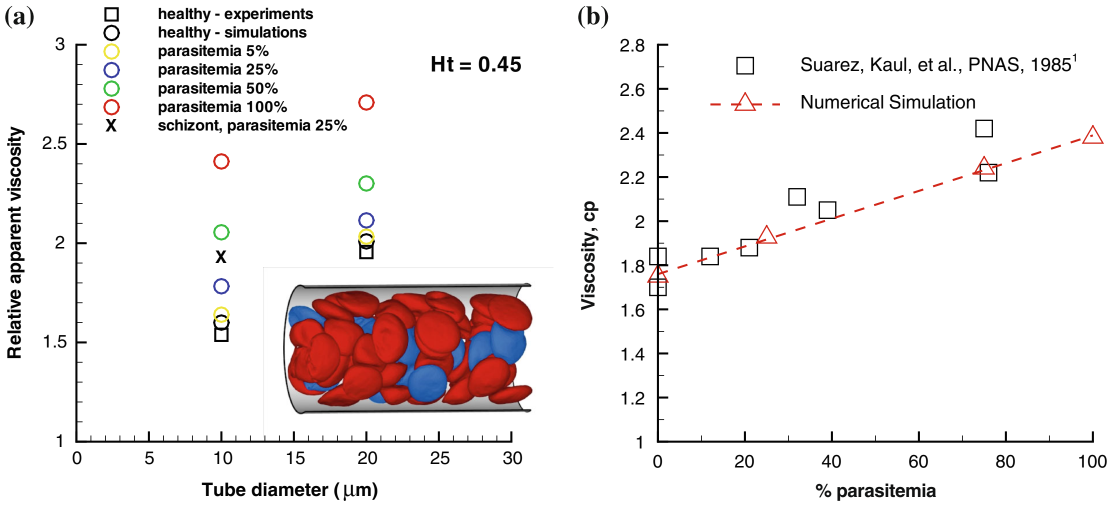

FIGURE 12. Flow resistance in malaria: (a) Healthy (red) and Pf-RBCs (blue) in Poiseuille flow in a tube of diameter $D = 20$ μm. $H_t = 0.45$, parasitemia level 25%. Plotted is the relative apparent viscosity of blood in malaria for various parasitemia levels and tube diameters. Symbol "*x*" corresponds to the schizont stage with a near-spherical shape. Experimental data from the empirical fit by Pries *et al.*[128] The figure is reproduced with permission from Fedosov *et al.*[60] (b) Bulk viscosity vs. parasitemia level for 30% hematocrit using a Couette device setup at shear rate 230 s^{-1}. The square symbols are measurements from Raventos-Suarez *et al.*[132] and the triangles are simulations of Huan Lei (Brown University).

adhesion force. It was found to be in agreement with the adhesion force measured in related experiments by Cravalho *et al.*[31] using an atomic force microscope (AFM). A Pf-RBC may exhibit firm adhesion at a WSS lower than a certain threshold and can completely detach from the wall at higher WSS. At low WSS, adhesion forces are strong enough to counteract the stress exerted on the cell by the flow resulting in its firm sticking to the wall. On the contrary, at high WSS existing bonds do not provide sufficiently strong adhesive interactions which yields RBC detachment from the wall. RBC visualizations showed that its detachment at high WSS occurs during the relatively fast motion of RBC flipping, since the contact area at that step corresponds to its minimum.[58] However, in experiments[8] Pf-RBCs which moved on a surface coated with the purified ICAM-1 showed persistent and stable rolling over long observation times and for a wide range of WSS values. This suggests that there must be a mechanism which stabilizes rolling of infected RBCs at high WSS. This fact is not surprising since, for example, leukocyte adhesion can be actively regulated depending on flow conditions and biochemical constituents present.[64,143]

Rheology in Sickle Cell Anemia

The abnormal rheological properties of sickle cell RBCs (SS-RBCs) are correlated with the changes in their shapes and with the stiffened cell membrane. This was measured by micropipette experiments in Itoh *et al.*[82] at different deoxygenated stages. The shear modulus of the full deoxygenated sickle cell falls within a wide range of values depending on the intracellular sickle hemoglobin HbS polymerization and it is more than 100 times the value of healthy cells. In the simulation studies in Lei and Karniadakis,[94] the shear modulus of the full deoxygenated sickle cell was set at very high value, e.g., 2000 times the value of the healthy cells to ensure a fully rigid SS-RBC. The bending rigidity of sickle cells under different deoxygenations was also set to be 200 times the value of the healthy RBC as no detailed values are available in the literature. In Lei and Karniadakis[94] sickle blood was modeled by a suspension of SS-RBCs in a solvent, which is represented by a collection of coarse-grained particles with DPD interactions. Different sickle cell morphologies were obtained based on a simulated annealing procedure and medical image analysis of clinical data.[94]

To investigate the relationship between the effect of the rate of deoxygenation and the rheology of sickle blood, Kaul *et al.*[87] examined the shear viscosity of sickle blood subjected to both fast and gradual deoxygenation procedures. Sickle blood subjected to gradual deoxygenation procedure showed monotonic elevation of shear viscosity and the formation of the sickle shape of blood cells over a period of 30 minutes until the full deoxygenated state was achieved. On the contrary, sickle blood subjected to the fast deoxygenation procedure exhibits two distinct phases. The shear viscosity of the sickle blood showed fast elevation within the first 7 minutes of deoxygenation accompanied with the cell morphology transition to granular shape. However, the shear viscosity decreased gradually during further deoxygenation. A large portion of cells appears extremely elongated with the intracellular HbS fibers aligned in one direction. To study the morphology effect on the rheological behavior of the sickle blood, in Lei and Karniadakis[94] simulation results were presented for shear flow of the sickle blood with the three distinct types of sickle cell reported in the experiment (Hct = 40%). Figure 13 plots the shear viscosity of the deoxygenated sickle blood; the shear modulus of the cell membrane is the same for all the three types. The sickle blood shows elevated and shear-independent viscosity values for all three types. Moreover, the sickle blood with granular and sickle morphology shows larger viscosity compared with the elongated shape, which explains the progressive decrease of the viscosity value with further deoxygenation, since a large portion of granular cells transforms into the elongated shape during the procedure. This result is probably due to the different effective volume for each type of the sickle blood in the shear flow system,[87] which affects the momentum transport ability between the cells.

The hemodynamics of sickle blood was studied in an isolated vasculature in Kaul *et al.*[86] While the oxygenated sickle blood exhibits hemodynamics similar to healthy blood, the deoxygenated sickle blood shows distinctive dynamic properties for different RBC types. In the simulation, sickle blood in a tube flow system with Hct = 30% was considered similar to the experiment although precise morphology details are difficult to extract from the experiments. The deoxygenated sickle blood flow was represented by a suspension of RBCs with sickle and granular shapes. Blood plasma and cytosol are explicitly represented by DPD, and they are separated by the cell membrane through the bounce-back reflection on membrane surface. The viscosity of the cytosol is set to $4\eta_0$ and $50\eta_0$ for the healthy and deoxygenated blood flow, where η_0 is the viscosity of the blood plasma. Figure 14 plots the increase of the flow resistance with different oxygen tension for the sickle and granular shapes. While both types of blood flow show further increase in flow resistance at deoxygenated state, the granular type of blood flow shows a more pronounced elevation compared with the sickle shape. One possible explanation proposed by the Kaul *et al.*[86] is the different distribution of SS-RBCs in the capillary. The inset plot of Fig. 14 shows the snapshots of the

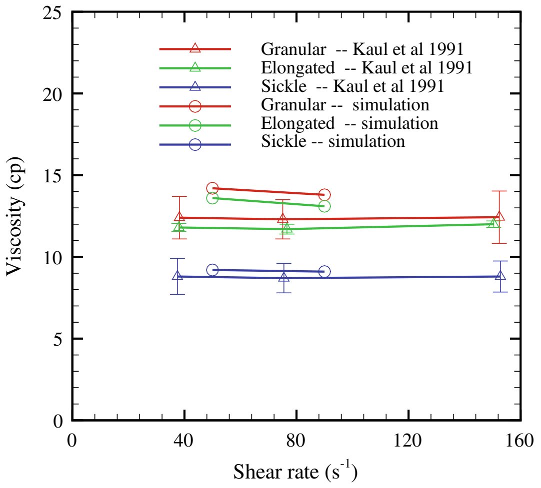

FIGURE 13. Shear viscosity of the sickle blood flow with different cell morphologies reported in Kaul *et al.*,[87] Hct = 40%; the simulation data are from Lei and Karniadakis.[94]

sickle and granular cells in the tube flow. The cells of sickle shape tend to flow along the axis of the tube as observed in experimental studies in LaCelle[92]; specific distributions of SS-RBC orientation were presented in Lei and Karniadakis.[94]

In this section we presented DPD simulations of sickle blood flow and compared them with existing experimental results primarily on flow resistance. New microfluidic experiments, like the ones presented in the previous section on malaria, will be very useful in further validation of the DPD models, especially as a function of deoxygenation rate. Such experiments on a microfluidic cytometer are currently under way by the MIT co-author of this paper. In addition, quantifying—both experimentally and through DPD simulations—the SS-RBC membrane fluctuations will characterize better the precise state of the SS-RBCs. In a recent study in Byun *et al.*,[18] it was found that the membrane fluctuations are significantly reduced for SS-RBCs taken from a sickle cell disease patient at ambient oxygen concentration. Careful analysis identified that high cytoplasmic viscosity is primarily responsible for the decreased membrane fluctuations, while irreversibly sickled cells were found to have higher membrane stiffness than that from other types of RBCs in sickle cell disease. Similarly, new microfluidic experiments are needed, in addition to the published results,[77] to elucidate the mechanism of cytoadhesion and occlusion in sickle cell blood flow, and to validate the recent findings of Lei and Karniadakis[95] on the precise mechanisms of vaso-occlusion in post-capillaries.

DISCUSSION

We have presented a new computational framework for simulating hematologic disorders based on DPD, derived from the molecular dynamics method. This is a Lagrangian mesoscopic approach that can model seamlessly blood cells, proteins, plasma, and arterial walls, and can predict accurately blood flow in health and disease. To make this approach patient-specific we rely on single-RBC experiments, e.g., using optical tweezers, atomic force microscopy, *etc*., and novel microfluidic devices in order to obtain data from which we can extract the macroscopic parameters of the model, which, in turn, can be related to the microscopic parameters required in DPD modeling. Moreover, these single-RBC data sets can serve as a validation testbed over a wide range of operating conditions. The utility of the DPD models is then to predict *whole blood* behavior in health or disease without any further ''tuning'' of the models' parameters. We demonstrated that this is indeed the case for healthy and malaria-infected as well as sickle whole blood. We can also employ the DPD models for sensitivity studies, hence interacting more meaningfully with the experiments, and suggest specific measurements or parameter variations or even probe certain biophysical interactions, e.g., the interaction of the lipid bilayer with the cytoskeleton in a RBC,[120] not accessible with experimental techniques alone.

The two diseases we studied have some common biophysical characteristics, however, their biorheology is distinctly different. Hence, combining computational-experimental studies, as we have been pursuing in our research groups, can help greatly in quantifying fundamental biophysical mechanisms and possibly identifying unique biomarkers for these diseases. Our computational framework is general and employs patient-specific model input, hence it can be also used for other hematologic diseases, such as diabetes, HIV, and even in cancer metastasis. In the flow resistance results we presented in the current paper, we modeled

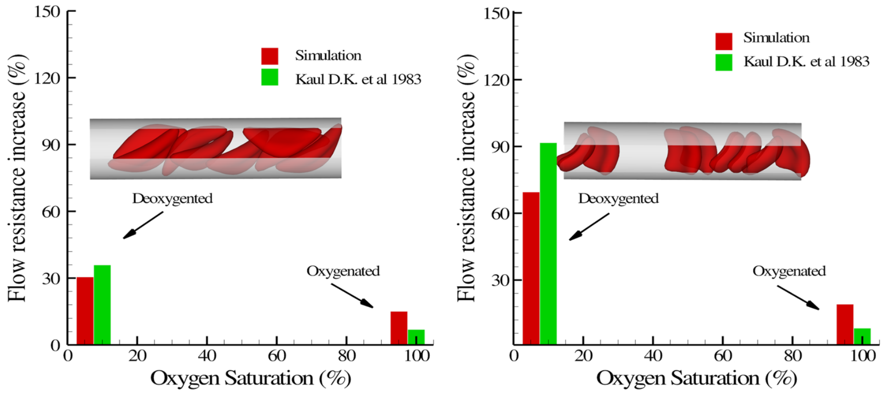

FIGURE 14. Increase of the flow resistance induced by the sickle blood flow for both sickle (left) and granular (right) shapes. The inset plot shows a snapshot of the sickle cells in the tube flow. The figure is reproduced with permission from Lei and Karniadakis.[94]

whole blood as suspension of RBCs in plasma, hence ignoring the effect of white cells (about 0.7%) and platelets (less than 0.5%), also the effect of other proteins in the plasma, or the interaction with the endothelial surfaces of the blood vessel walls. From the numerical modeling standpoint, there is no particular difficulty in also modeling these other cells as we have done for margination studies in the subsection "Margination of White Blood Cells and Platelets", or modeling the endothelium, which may contribute significantly in specific biomedical studies, e.g., in thrombosis, immune response. From the biorheological view point, however, as we demonstrated for both malaria and sickle cell anemia, the presence of the other cells is not important unlike the endothelium that can modify significantly the blood flow resistance.

ACKNOWLEDGMENTS

This work was supported by NIH and the new Collaboratory on Mathematics for Mesoscopic Modeling of Materials (CM4), sponsored by DOE. Simulations were performed at the DOE supercomputing centers *via* an INCITE DOE award, and at the Jülich supercomputing center. Dmitry A. Fedosov acknowledges funding by the Alexander von Humboldt Foundation. MD and SS acknowledge partial support from the Singapore-MIT Alliance for Research and Technology (SMART) Center.

REFERENCES

[1] Abbitt, K. B., and G. B. Nash. Rheological properties of the blood influencing selectin-mediated adhesion of flowing leukocytes. *Am. J. Physiol.* 285:H229–H240, 2003.

[2] Abkarian, M., M. Faivre, and A. Viallat. Swinging of red blood cells under shear flow. *Phys. Rev. Lett.* 98:188302, 2007.

[3] Abkarian, M., M. Faivre, R. Horton, K. Smistrup, C. A. Best-Popescu, and H. A. Stone. Cellular-scale hydrodynamics. *Biomed. Mater.* 3:034011, 2008.

[4] Abkarian, M., C. Lartigue, and A. Viallat. Tank treading and unbinding of deformable vesicles in shear flow: determination of the lift force. *Phys. Rev. Lett.* 88:068103, 2002.

[5] Alizadehrad, D., Y. Imai, K. Nakaaki, T. Ishikawa, and T. Yamaguchi. Quantification of red blood cell deformation at high-hematocrit blood flow in microvessels. *J. Biomech.* 45:2684–2689, 2012.

[6] Allen, M. P., and D. J. Tildesley. Computer Simulation of Liquids. New York: Clarendon Press, 1987.

[7] AlMomani, T., H. S. Udaykumar, J. S. Marshall, and K. B. Chandran. Micro-scale dynamic simulation of erythrocyte–platelet interaction in blood flow. *Ann. Biomed. Eng.* 36:905–920, 2008.

[8] Antia, M., T. Herricks, and P. K. Rathod. Microfluidic modeling of cell–cell interactions in malaria pathogenesis. *PLoS Pathog*. 3:939–945, 2007.

[9] Bagchi, P. Mesoscale simulation of blood flow in small vessels. *Biophys. J.* 92:1858–1877, 2007.

[10] Bagchi, P., and R. M. Kalluri. Dynamic rheology of a dilute suspension of elastic capsules: effect of capsule tank-treading, swinging and tumbling. *J. Fluid Mech.* 669:498–526, 2011.

[11] Bagchi, P., A. S. Popel, and P. C. Johnson. Computational fluid dynamic simulation of aggregation of deformable cells in a shear flow. *J. Biomech. Eng*. 127:1070–1080, 2005.

[12] Bagge, U., and R. Karlsson. Maintenance of white blood cell margination at the passage through small venular junctions. *Microvasc. Res.* 20:92–95, 1980.

[13] Bäumler, H., E. Donath, A. Krabi, W. Knippel, H. Budde, and A. Kiesewetter. Electrophoresis of human red blood cells and platelets: evidence for depletion of dextran. *Biorheology* 33:333–351, 1996.

[14] Beck, W. S. (ed.). Hematology, 5th ed. Cambridge: MIT Press, 1991.

[15] Bow, H., I. V. Pivkin, M. Diez-Silva, S. J. Goldfless, M. Dao, J. C. Niles, S. Suresh, and J. Han. A microfabricated deformability-based flow cytometer with application to malaria. *Lab Chip* 11:1065–1073, 2011.

[16] Brooks, D. E. The effect of neutral polymers on the electrokinetic potential of cells and other charged particles. *J. Colloid Interface Sci.* 43:700–713, 1973.

[17] Bugliarello, G., and J. Sevilla. Velocity distribution and other characteristics of steady and pulsatile blood flow in fine glass tubes. *Biorheology* 7:85–107, 1970.

[18] Byun, H. S., T. Hillman, J. Higgins, M. Diez-Silva, Z. Peng, M. Dao, R. Dasari, S. Suresh, and Y.-K. Park. Optical measurements of biomechanical properties of individual erythrocytes from a sickle patient. *Acta Biomater.* 8:4130–4138, 2012.

[19] Cantat, I., and C. Misbah. Lift force and dynamical unbinding of adhering vesicles under shear flow. *Phys. Rev. Lett.* 83:880–883, 1999.

[20] Casson, N. Rheology of Disperse Systems. New York: Pergamon Press, 1992.

[21] Chaudhuri, O., S. Parekh, W. Lam, and D. Fletcher. Combined atomic force microscopy and side-view optical imaging for mechanical studies of cells. *Nat. Methods* 6:383–387, 2009.

[22] Chien, S., and K.-M. Jan. Ultrastructural basis of the mechanism of rouleaux formation. *Microvasc. Res.* 5:155–166, 1973.

[23] Chien, S., S. Usami, R. J. Dellenback, M. I. Gregersen, L. B. Nanninga, and N. M. Guest. Blood viscosity: influence of erythrocyte aggregation. *Science* 157:829–831, 1967.

[24] Chien, S., S. Usami, R. J. Kellenback, and M. I. Gregersen. Shear-dependent interaction of plasma proteins with erythrocytes in blood rheology. *Am. J. Physiol.* 219:143–153, 1970.

[25] Chien, S., S. Usami, H. M. Taylor, J. L. Lundberg, and M. I. Gregersen. Effects of hematocrit and plasma proteins on human blood rheology at low shear rates. *J. Appl. Physiol.* 21:81–87, 1996.

[26] Clausen, J. R., D. A. Reasor, Jr., and C. K. Aidun. The rheology and microstructure of concentrated non-colloidal suspensions of deformable capsules. *J. Fluid Mech.* 685:202–234, 2011.

[27] Cokelet, G., E. W. Merrill, E. R. Gilliland, H. Shin, A. Britten, and J. R. E. Wells. The rheology of human blood-

measurement near and at zero shear rate. *Trans. Soc. Rheol.* 7:303–317, 1963.

[28]Cokelet, G. R., and H. L. Goldsmith. Decreased hydrodynamic resistance in the two-phase flow of blood through small vertical tubes at low flow rates. *Circ. Res.* 68:1–17, 1991.

[29]Copley, A. L., C. R. Huang, and R. G. King. Rheogoniometric studies of whole human blood at shear rates from 1,000-0.0009 sec^{-1}. Part I. Experimental findings. *Biorheology* 10:17–22, 1973.

[30]Cranston, H. A., C. W. Boylan, G. L. Carroll, S. P. Sutera, J. R. Williamson, I. Y. Gluzman, and D. J. Krogstad. Plasmodium falciparum maturation abolishes physiologic red cell deformability. *Science* 223:400–403, 1984.

[31]Cravalho, P., M. Diez-Silva, H. Chen, M. Dao, and S. Suresh. Cytoadherence of erythrocytes invaded by *Plasmodium falciparum*: quantitative contact-probing of a human malaria receptor. *Acta Biomater.* 9:6349–6359, 2013.

[32]Crowl, L., and A. L. Fogelson. Computational model of whole blood exhibiting lateral platelet motion induced by red blood cells. *Int. J. Numer. Methods Biomed. Eng.* 26:471–487, 2010.

[33]Crowl, L., and A. L. Fogelson. Analysis of mechanisms for platelet near-wall excess under arterial blood flow conditions. *J. Fluid Mech.* 676:348–375, 2011.

[34]Dao, M., J. Li, and S. Suresh. Molecularly based analysis of deformation of spectrin network and human erythrocyte. *Mater. Sci. Eng. C* 26:1232–1244, 2006.

[35]Dao, M., C. T. Lim, and S. Suresh. Mechanics of the human red blood cell deformed by optical tweezers. *J. Mech. Phys. Solids* 51:2259–2280, 2003.

[36]Diez-Silva, M., M. Dao, J. Han, C.-T. Lim, and S. Suresh. Shape and biomechanical characteristics of human red blood cells in health and disease. *MRS Bull.* 35:382–388, 2010.

[37]Diez-Silva, M., Y.-K. Park, S. Huang, H. Bow, O. Mercereau-Puijalon, G. Deplaine, C. Lavazec, S. Perrot, S. Bonnefoy, M. S. Feld, J. Han, M. Dao, and S. Suresh. Pf155/RESA protein influences the dynamic microcirculatory behavior of ring-stage *Plasmodium falciparum* infected red blood cells. *Sci. Rep.* 2:614, 2012.

[38]Discher, D. E., D. H. Boal, and S. K. Boey. Simulations of the erythrocyte cytoskeleton at large deformation. II. Micropipette aspiration. *Biophys. J.* 75:1584–1597, 1998.

[39]Discher, D. E., N. Mohandas, and E. A. Evans. Molecular maps of red cell deformation: hidden elasticity and in situ connectivity. *Science* 266:1032–1035, 1994.

[40]Doddi, S. K., and P. Bagchi. Lateral migration of a capsule in a plane Poiseuille flow in a channel. *Int. J. Multiphase Flow* 34:966–986, 2008.

[41]Doddi, S. K., and P. Bagchi. Three-dimensional computational modeling of multiple deformable cells flowing in microvessels. *Phys. Rev. E* 79:046318, 2009.

[42]Dupin, M. M., I. Halliday, C. M. Care, L. Alboul, and L. L. Munn. Modeling the flow of dense suspensions of deformable particles in three dimensions. *Phys. Rev. E* 75:066707, 2007.

[43]Dupin, M. M., I. Halliday, C. M. Care, and L. L. Munn. Lattice boltzmann modeling of blood cell dynamics. *Int. J. Comput. Fluid Dyn.* 22:481–492, 2008.

[44]Dzwinel, W., K. Boryczko, and D. A. Yuen. A discrete-particle model of blood dynamics in capillary vessels. *J. Colloid Interface Sci.* 258:163–173, 2003.

[45]Eckstein, E. C., A. W., and F. J. Millero III. Conditions for the occurrence of large near-wall excesses of small particles during blood flow. *Microvasc. Res.* 36:31–39, 1988.

[46]Eggleton, C. D., and A. S. Popel. Large deformation of red blood cell ghosts in a simple shear flow. *Phys. Fluids* 10:1834, 1998.

[47]Enden, G., and A. S. Popel. A numerical study of plasma skimming in small vascular bifurcations. *J. Biomech. Eng.* 116:79–88, 1994.

[48]Enderle, T., T. Ha, D. F. Ogletree, D. S. Chemla, C. Magowan, S. Weiss. Membrane specific mapping and colocalization of malarial and host skeletal proteins in the *Plasmodium falciparum* infected erythrocyte by dual-color near-field scanning optical microscopy. *Proc. Natl Acad. Sci. U.S.A.* 94:520–525, 1997.

[49]Ermak, D. L., and J. A. McCammon. Brownian dynamics with hydrodynamic interactions. *J. Chem. Phys.* 69:1352–1360, 1978.

[50]Espanol, P., and M. Revenga. Smoothed dissipative particle dynamics. *Phys. Rev. E* 67:026705, 2003.

[51]Espanol, P., and P. Warren. Statistical mechanics of dissipative particle dynamics. *Europhys. Lett.* 30:191–196, 1995.

[52]Evans, E. A., and R. Skalak. Mechanics and Thermodynamics of Biomembranes. Boca Raton, FL: CRC Press, 1980.

[53]Fahraeus, R. The suspension stability of blood. *Physiol. Rev* 9:241–274, 1929.

[54]Fahraeus, R. The influence of the rouleau formation of the erythrocytes on the rheology of the blood. *Acta Med. Scand.* 161:151–165, 1958.

[55]Fahraeus, R., and T. Lindqvist. Viscosity of blood in narrow capillary tubes. *Am. J. Phys.* 96:562–568, 1931.

[56]Fedosov, D. A., B. Caswell, and G. E. Karniadakis. A multiscale red blood cell model with accurate mechanics, rheology, and dynamics. *Biophys. J.* 98:2215–2225, 2010.

[57]Fedosov, D. A., B. Caswell, and G. E. Karniadakis. Systematic coarse-graining of spectrin-level red blood cell models. *Comput. Methods Appl. Mech. Eng.* 199:1937–1948, 2010.

[58]Fedosov, D. A., B. Caswell, and G. E. Karniadakis. Wall shear stress-based model for adhesive dynamics of red blood cells in malaria. *Biophys. J.* 100:2084–2093, 2011.

[59]Fedosov, D. A., B. Caswell, A. S. Popel, and G. E. Karniadakis. Blood flow and cell-free layer in microvessels. *Microcirculation* 17:615–628, 2010.

[60]Fedosov, D. A., B. Caswell, S. Suresh, and G. E. Karniadakis. Quantifying the biophysical characteristics of Plasmodium falciparum-parasitized red blood cells in microcirculation. *Proc. Natl Acad. Sci. U.S.A.* 108:35–39, 2011.

[61]Fedosov, D. A., J. Fornleitner, and G. Gompper. Margination of white blood cells in microcapillary flow. *Phys. Rev. Lett.* 108:028104, 2012.

[62]Fedosov, D. A., H. Noguchi, and G. Gompper. Multiscale modeling of blood flow: from single cells to blood rheology. *Biomech. Model. Mechanobiol.*, 2013. DOI:10.1007/s10237-013-0497-9.

[63]Fedosov, D. A., W. Pan, B. Caswell, G. Gompper, and G. E. Karniadakis. Predicting human blood viscosity in silico. *Proc. Natl Acad. Sci. U.S.A.* 108:11772–11777, 2011.

[64]Finger, E. B., K. D. Puri, R. Alon, M. B. Lawrence, U. H. von Andrian, and T. A. Springer. Adhesion through

L-selectin requires a threshold hydrodynamic shear. *Nature (London)* 379:266–269, 1996.

[65] Firrell, J. C., and H. H. Lipowsky. Leukocyte margination and deformation in mesenteric venules of rat. *Am. J. Physiol*. 256:H1667–H1674, 1989.

[66] Fischer, T. M. Shape memory of human red blood cells. *Biophys. J*. 86:3304–3313, 2004.

[67] Freund, J. B. Leukocyte margination in a model microvessel. *Phys. Fluids* 19:023301, 2007.

[68] Freund, J. B., and M. M. Orescanin. Cellular flow in a small blood vessel. *J. Fluid Mech*. 671:466–490, 2011.

[69] Fung, Y. C. Biomechanics: Mechanical Properties of Living Tissues, 2nd ed. New York: Springer, 1993.

[70] Gaehtgens, P., C. Dührssen, and K. H. Albrecht. Motion, deformation, and interaction of blood cells and plasma during flow through narrow capillary tubes. *Blood Cells* 6:799–817, 1980.

[71] Gidaspow, D., and J. Huang. Kinetic theory based model for blood flow and its viscosity. *Ann. Biomed. Eng*. 38:1534–1545, 2009.

[72] Goldsmith, H. L., G. R. Cokelet, and P. Gaehtgens. Robin Fahraeus: evolution of his concepts in cardiovascular physiology. *Am. J. Physiol*. 257:H1005–H1015, 1989.

[73] Goldsmith, H. L., and S. Spain. Margination of leukocytes in blood flow through small tubes. *Microvasc. Res*. 27:204–222, 1984.

[74] Gompper, G., T. Ihle, D. M. Kroll, and R. G. Winkler. Multi-particle collision dynamics: a particle-based mesoscale simulation approach to the hydrodynamics of complex fluids. *Adv. Polym. Sci*. 221:1–87, 2009.

[75] Groot, R. D., and P. B. Warren. Dissipative particle dynamics: bridging the gap between atomistic and mesoscopic simulation. *J. Chem. Phys*. 107:4423–4435, 1997.

[76] Henon, S., G. Lenormand, A. Richert, and F. Gallet. A new determination of the shear modulus of the human erythrocyte membrane using optical tweezers. *Biophys. J*. 76:1145–1151, 1999.

[77] Higgins, J. M., D. T. Eddington, S. N. Bhatia, and L. Mahadevan. Sickle cell vasoocclusion and rescue in a microfluidic device. *Proc. Natl Acad. Sci. U.S.A*. 104:20496–20500, 2007.

[78] Holm, S. H., J. P. Beech, M. P. Barrett, and J. O. Tegenfeldt. Separation of parasites from human blood using deterministic lateral displacement. *Lab Chip* 11:1326–1332, 2011.

[79] Hoogerbrugge, P. J., and J. M. V. A. Koelman. Simulating microscopic hydrodynamic phenomena with dissipative particle dynamics. *Europhys. Lett*. 19:155–160, 1992.

[80] Hou, H. W., A. A. S. Bhagat, A. G. L. Chong, P. Mao, K. S. W. Tan, J. Han, C. T. Lim. Deformability based cell margination—a simple microfluidic design for malaria-infected erythrocyte separation. *Lab Chip* 10:2605–2613, 2010.

[81] Iordan A, Duperray A, Verdier C (2008) Fractal approach to the rheology of concentrated suspensions. *Phys. Rev. E* 77:011911.

[82] Itoh, T., S. Chien, and S. Usami. Effects of hemoglobin concentration on deformability of individual sickle cells after deoxygenation. *Blood* 85:2245–2253, 1995.

[83] Jain, A., and L. L. Munn. Determinants of leukocyte margination in rectangular microchannels. *PLoS ONE* 4:e7104, 2009.

[84] Janoschek, F., F. Toschii, and J. Harting. Simplified particulate model for coarse-grained hemodynamics simulations. *Phys. Rev. E* 82:056710, 2010.

[85] Ju, M., S. S. Ye, B. Namgung, S. Cho, H. T. Low, H. L. Leo, and S. Kim. A review of numerical methods for red blood cell flow simulation. *Computer Methods Biomech. Biomed. Eng*., 2013. DOI:10.1080/10255842.2013.783574.

[86] Kaul, D. K., M. E. Fabry, P. Windisch, S. Baez, and R. L. Nagel. Erythrocytes in sickle-cell-anemia are heterogeneous in their rheological and hemodynamic characteristics. *J. Clin. Invest*. 72:22–31, 1983.

[87] Kaul, D. K., and H. Xue. Rate of deoxygenation and rheologic behavior of blood in sickle cell anemia. *Blood* 77:1353–1361, 1991.

[88] Kim, S., L. R. Long, A. S. Popel, M. Intaglietta, and P. C. Johnson. Temporal and spatial variations of cell-free layer width in arterioles. *Am. J. Physiol*. 293:H1526–H1535, 2007.

[89] Kim, S., P. K. Ong, O. Yalcin, M. Intaglietta, and P. C. Johnson. The cell-free layer in microvascular blood flow. *Biorheology* 46:181–189, 2009.

[90] Kumar, A., and M. D. Graham. Margination and segregation in confined flows of blood and other multicomponent suspensions. *Soft Matter* 8:10536–10548, 2012.

[91] Kumar, A., and M. D. Graham. Mechanism of margination in confined flows of blood and other multicomponent suspensions. *Phys. Rev. Lett*. 109:108102, 2012.

[92] LaCelle, P. L. Oxygen delivery to muscle cells during capillary vascular occlusion by sickle erythrocytes. *Blood Cells* 3:263–272, 1977.

[93] Lei, H., D. A. Fedosov, B. Caswell, and G. E. Karniadakis. Blood flow in small tubes: quantifying the transition to the non-continuum regime. *J. Fluid Mech*. 722:214–239, 2013.

[94] Lei, H., and G. E. Karniadakis. Quantifying the rheological and hemodynamic characteristics of sickle cell anemia. *Biophys. J*. 102:185–194, 2012.

[95] Lei, H., and G. E. Karniadakis. Probing vaso-occlusion phenomena in sickle cell anemia via mesoscopic simulations. *Proc. Natl Acad. Sci. U.S.A*. 110:11326–11330, 2013.

[96] Li J, Dao M, Lim CT, Suresh S (2005) Spectrin-level modeling of the cytoskeleton and optical tweezers stretching of the erythrocyte. *Biophys. J*. 88:3707–3719.

[97] Li, X., P. M. Vlahovska, and G. E. Karniadakis. Continuum- and particle-based modeling of shapes and dynamics of red blood cells in health and disease. *Soft Matter* 9:28–37, 2013.

[98] Liu, Y., and W. K. Liu. Rheology of red blood cell aggregation by computer simulation. *J. Comput. Phys*. 220:139–154, 2006.

[99] Lucy, L. B. A numerical approach to testing the fission hypothesis. *Astronom. J*. 82:1013–1024, 1977.

[100] MacMeccan, R. M., J. R. Clausen, G. P. Neitzel, and C. K. Aidun. Simulating deformable particle suspensions using a coupled lattice-Boltzmann and finite-element method. *J. Fluid Mech*. 618:13–39, 2009.

[101] Maeda, N., Y. Suzuki, J. Tanaka, and N. Tateishi. Erythrocyte flow and elasticity of microvessels evaluated by marginal cell-free layer and flow resistance. *Am. J. Physiol*. 271:H2454–H2461, 1996.

[102] Malevanets, A., and R. Kapral. Mesoscopic model for solvent dynamics. *J. Chem. Phys*. 110:8605–8613, 1999.

[103] Mattice, W. L., and U. W. Suter. Conformational Theory of Large Molecules: The Rotational Isomeric State Model in Macromolecular Systems. New York: Wiley Interscience, 1994.

[104] McWhirter, J. L., H. Noguchi, and G. Gompper. Flow-induced clustering and alignment of vesicles and red blood

cells in microcapillaries. *Proc. Natl Acad. Sci. U.S.A.* 106:6039–6043, 2009.

[105] Melchionna, S. A model for red blood cells in simulations of large-scale blood flows. *Macromol. Theory Simul.* 20:548–561, 2011.

[106] Merrill, E. W., E. R. Gilliland, G. Cokelet, H. Shin, A. Britten, J. R. E. Wells. Rheology of human blood near and at zero flow. *Biophys. J.* 3:199–213, 1963.

[107] Merrill, E. W., E. R. Gilliland, T. S. Lee, and E. W. Salzman. Blood rheology: effect of fibrinogen deduced by addition. *Circ. Res.* 18:437–446, 1966.

[108] Messlinger, S., B. Schmidt, H. Noguchi, and G. Gompper. Dynamical regimes and hydrodynamic lift of viscous vesicles under shear. *Phys. Rev. E* 80:011901, 2009.

[109] Mills, J. P., M. Diez-Silva, D. J. Quinn, M. Dao, M. J. Lang, K. S. W. Tan, C. T. Lim, G. Milon, P. H. David, O. Mercereau-Puijalon, S. Bonnefoy, and S. Suresh. Effect of plasmodial RESA protein on deformability of human red blood cells harboring *Plasmodium falciparum*. *Proc. Natl Acad. Sci. U.S.A.* 104:9213–9217, 2007.

[110] Monaghan, J. J. Smoothed particle hydrodynamics. *Rep. Prog. Phys.* 68:1703–1759, 2005.

[111] Murata, T. Effects of sedimentation of small red blood cell aggregates on blood flow in narrow horizontal tubes. *Biorheology* 33:267–283, 1996.

[112] Neu, B., and H. J. Meiselman. Depletion-mediated red blood cell aggregation in polymer solutions. *Biophys. J.* 83:2482–2490, 2002.

[113] Noguchi, H., and G. Gompper. Fluid vesicles with viscous membranes in shear flow. *Phys. Rev. Lett.* 93:258102, 2004.

[114] Noguchi, H., and G. Gompper. Dynamics of fluid vesicles in shear flow: effect of the membrane viscosity and thermal fluctuations. *Phys. Rev. E* 72:011901, 2005.

[115] Noguchi, H., and G. Gompper. Shape transitions of fluid vesicles and red blood cells in capillary flows. *Proc. Natl Acad. Sci. U.S.A.* 102:14159–14164, 2005.

[116] Pan, W., B. Caswell, and G. E. Karniadakis. A low-dimensional model for the red blood cell. *Soft Matter* 6:4366–4376, 2010.

[117] Pan, W., D. A. Fedosov, B. Caswell, and G. E. Karniadakis. Predicting dynamics and rheology of blood flow: a comparative study of multiscale and low-dimensional models of red blood cells. *Microvasc. Res.* 82:163–170, 2011.

[118] Park, Y. K., M. Diez-Silva, G. Popescu, G. Lykotrafitis, W. Choi, M. S. Feld, and S. Suresh. Refractive index maps and membrane dynamics of human red blood cells parasitized by *Plasmodium falciparum*. *Proc. Natl Acad. Sci. U.S.A.* 105:13730–13735, 2008.

[119] Pearson, M. J., and H. H. Lipowsky. Influence of erythrocyte aggregation on leukocyte margination in postcapillary venules of rat mesentery. *Am. J. Physiol.* 279:H1460–H1471, 2000.

[120] Peng, Z., X. Li, I. Pivkin, M. Dao, G. E. Karniadakis, and S. Suresh. Lipid-bilayer and cytoskeletal interactions in a red blood cell. *Proc. Natl Acad. Sci. U.S.A.* 110:13356–13361, 2013.

[121] Picart, C., J. M. Piau, and H. Galliard. Human blood shear yield stress and its hematocrit dependence. *J. Rheol.* 42:1–12, 1998.

[122] Pivkin, I. V., and G. E. Karniadakis. Accurate coarse-grained modeling of red blood cells. *Phys. Rev. Lett.* 101:118105, 2008.

[123] Popel, A. S., and P. C. Johnson. Microcirculation and hemorheology. *Annu. Rev. Fluid Mech.* 37:43–69, 2005.

[124] Popescu, G., Y.-K. Park, R. R. Dasari, K. Badizadegan, and M. S. Feld. Coherence properties of red blood cell membrane motions. *Phys. Rev. E* 76:031902, 2007.

[125] Pozrikidis, C. Numerical simulation of cell motion in tube flow. *Ann. Biomed. Eng.* 33:165–178, 2005.

[126] Pribush, A., D. Zilberman-Kravits, and N. Meyerstein. The mechanism of the dextran-induced red blood cell aggregation. *Eur. Biophys. J.* 36:85–94, 2007.

[127] Pries, A. R., K. Ley, M. Claassen, and P. Gaehtgens. Red cell distribution at microvascular bifurcations. *Microvasc. Res.* 38:81–101, 1989.

[128] Pries, A. R., D. Neuhaus, and P. Gaehtgens. Blood viscosity in tube flow: dependence on diameter and hematocrit. *Am. J. Physiol.* 263:H1770–H1778, 1992.

[129] Pries, A. R., T. W. Secomb, and P. Gaehtgens. Structure and hemodynamics of microvascular networks: heterogeneity and correlations. *Am. J. Physiol.* 269:H1713–H1722, 1995.

[130] Pries, A. R., T. W. Secomb, and P. Gaehtgens. Biophysical aspects of blood flow in the microvasculature. *Cardiovasc. Res.* 32:654–667, 1996.

[131] Puig-de Morales-Marinkovic, M., K. T. Turner, J. P. Butler, J. J. Fredberg, and S. Suresh. Viscoelasticity of the human red blood cell. *Am. J. Physiol.* 293:C597–C605, 2007.

[132] Raventos-Suarez, C., D. Kaul, and R. Nagel. Membrane knobs are required for the microcirculatory obstruction induced by *Plasmodium falciparum*-infected erythrocytes. *Proc. Natl Acad. Sci. U.S.A.* 82:3829–3833, 1985.

[133] Reasor, Jr., D. A., M. Mehrabadi, D. N. Ku, and C. K. Aidun. Determination of critical parameters in platelet margination. *Ann. Biomed. Eng.* 41:238–249, 2013.

[134] Reinke, W., P. Gaehtgens, and P. C. Johnson. Blood viscosity in small tubes: effect of shear rate, aggregation, and sedimentation. *Am. J. Physiol.* 253:H540–H547, 1987.

[135] Rosenbluth, M., W. Lam, and D. Fletcher. Analyzing cell mechanics in hematologic diseases with microfluidic biophysical flow cytometry. *Lab Chip* 8:1062–1070, 2008.

[136] Samsel, R. W., and A. S. Perelson. Kinetics of rouleau formation: I. A mass action approach with geometric features. *Biophys. J.* 37:493–514, 1982.

[137] Schmid-Schönbein, H., and R. E. Wells. Rheological properties of human erythrocytes and their influence upon the ''anomalous'' viscosity of blood. *Ergeb. Physiol. Biol. Chem. Exper. Pharmakol.* 63:146–219, 1971.

[138] Sharan, M., and A. S. Popel. A two-phase model for flow of blood in narrow tubes with increased effective viscosity near the wall. *Biorheology* 38:415–428, 2001.

[139] Shelby, J. P., J. White, K. Ganesan, P. K. Rathod, and D. T. Chiu. A microfluidic model for single-cell capillary obstruction by *Plasmodium falciparum*-infected erythrocytes. *Proc. Natl Acad. Sci. U.S.A.* 100:14618–14622, 2003.

[140] Skalak, R., and P. I. Branemark. Deformation of red blood cells in capillaries. *Science* 164:717–719, 1969.

[141] Skalak, R., S. R. Keller, and T. W. Secomb. Mechanics of blood flow. *J. Biomech. Eng.* 103:102–115, 1981.

[142] Skotheim, J. M., and T. W. Secomb. Red blood cells and other nonspherical capsules in shear flow: oscillatory dynamics and the tank-treading-to-tumbling transition. *Phys. Rev. Lett.* 98:078301, 2007.

[143] Springer, T. A. Traffic signals on endothelium for lymphocyte recirculation and leukocyte emigration. *Annu. Rev. Physiol.* 57:827–872, 1995.

[144] Steffen, P., C. Verdier, and C. Wagner. Quantification of depletion-induced adhesion of red blood cells. *Phys. Rev. Lett.* 110:018102, 2013.

[145]Succi, S. The Lattice Boltzmann Equation for Fluid Dynamics and Beyond. Oxford: Oxford University Press, 2001.

[146]Sun, C., C. Migliorini, and L. L. Munn. Red blood cells initiate leukocyte rolling in postcapillary expansions: a lattice Boltzmann analysis. *Biophys. J.* 85:208–222, 2003.

[147]Suresh, S., J. Spatz, J. P. Mills, A. Micoulet, M. Dao, C. T. Lim, M. Beil, and T. Seufferlein. Connections between single-cell biomechanics and human disease states: gastrointestinal cancer and malaria. *Acta Biomater.* 1:15–30, 2005.

[148]Suzuki, Y., N. Tateishi, M. Soutani, and N. Maeda. Deformation of erythrocytes in microvessels and glass capillaries: effect of erythrocyte deformability. *Microcirculation* 3:49–57, 1996.

[149]Tangelder, G. J., H. C. Teirlinck, D. W. Slaaf, and R. S. Reneman. Distribution of blood platelets flowing in arterioles. *Am. J. Physiol.* 248:H318–H323, 1985.

[150]Thurston, G. B. Viscoelastic properties of blood and blood analogs. In Advances in Hemodynamics and Hemorheology, Vol. 1, edited by T. V. How. Greenwich, CT: JAI Press, 1996, pp. 1–30.

[151]Tilles, A. W., and E. C. Eckstein. The near-wall excess of platelet-sized particles in blood flow: its dependence on hematocrit and wall shear rate. *Microvasc. Res.* 33:211–223, 1987.

[152]Tokarev, A. A., A. A. Butylin, and F. I. Ataullakhanov. Platelet adhesion from shear blood flow is controlled by near-wall rebounding collisions with erythrocytes. *Biophys. J.* 100:799–808, 2011.

[153]Tokarev, A. A., A. A. Butylin, E. A. Ermakova, E. E. Shnol, G. P. Panasenko, and F. I. Ataullakhanov. Finite platelet size could be responsible for platelet margination effect. *Biophys. J.* 101:1835–1843, 2011.

[154]Tomaiuolo, G., V. Preziosi, M. Simeone, S. Guido, R. Ciancia, V. Martinelli, C. Rinaldi, B. Rotoli. A methodology to study the deformability of red blood cells flowing in microcapillaries in vitro. *Ann Ist Super Sanita* 43:186–192, 2007.

[155]Tomaiuolo, G., M. Simeone, V. Martinelli, B. Rotoli, and S. Guido. Red blood cell deformation in microconfined flow. *Soft Matter* 5:3736–3740, 2009.

[156]Tousia, N., B. Wang, K. Pant, M. F. Kiani, and B. Prabhakarpandian. Preferential adhesion of leukocytes near bifurcations is endothelium independent. *Microvasc. Res.* 80:384–388, 2010.

[157]Uijttewaal, W. S., E. J. Nijhof, P. J. Bronkhorst, E. Den Hartog, and R. M. Heethaar. Near-wall excess of platelets induced by lateral migration of erythrocytes in flowing blood. *Am. J. Physiol.* 264:H1239–H1244, 1993.

[158]Wang,T., T.-W. Pan, Z. W. Xing, and R. Glowinski. Numerical simulation of rheology of red blood cell rouleaux in microchannels. *Phys. Rev. E* 79:041916, 2009.

[159]Waugh, R., and E. A. Evans. Thermoelasticity of red blood cell membrane. *Biophys. J.* 26:115–131, 1979.

[160]Weinbaum, S., J. M. Tarbell, and E. R. Damiano. The structure and function of the endothelial glycocalyx layer. *Annu. Rev. Biomed. Eng.* 9:121–167, 2007.

[161]Wendt, J. F. (ed.). Computational Fluid Dynamics, 3rd ed. Berlin: Springer, 2009.

[162]Woldhuis, B., G. J. Tangelder, D. W. Slaaf, and R. S. Reneman. Concentration profile of blood platelets differs in arterioles and venules. *Am. J. Physiol.* 262:H1217–H1223, 1992.

[163]Yamaguchi, S., T. Yamakawa, and H. Niimi. Cell-free plasma layer in cerebral microvessels. *Biorheology* 29:251–260, 1992.

[164]Zhang, J., P. C. Johnson, and A. S. Popel. Red blood cell aggregation and dissociation in shear ows simulated by lattice Boltzmann method. *J. Biomech.* 41:47–55, 2008.

[165]Zhao, H., A. H. G. Isfahani, L. N. Olson, and J. B. Freund. Molecular dynamics simulations of tethered membranes with periodic boundary conditions. *J. Comput. Phys.* 229:3726–3744, 2010.

[166]Zhao, H., and E. S. G. Shaqfeh. Shear-induced platelet margination in a microchannel. *Phys. Rev. E* 83:061924, 2011.

[167]Zhao, H., E. S. G. Shaqfeh, and V. Narsimhan. Shear-induced particle migration and margination in a cellular suspension. *Phys. Fluids* 24:011902, 2012.

[168]Zhao, Q., L. G. Durand, L. Allard, and G. Cloutier. Effects of a sudden flow reduction on red blood cell rouleau formation and orientation using RF backscattered power. *Ultrasound Med. Biol.* 24:503–511, 1998.

P9: Multiscale modeling of blood flow: from single cells to blood rheology

D. A. Fedosov, H. Noguchi, and G. Gompper

Biomechanics and Modeling in Mechanobiology, **13**:239-258, 2014.

Biomech Model Mechanobiol (2014) 13:239–258
DOI 10.1007/s10237-013-0497-9

ORIGINAL PAPER

Multiscale modeling of blood flow: from single cells to blood rheology

**Dmitry A. Fedosov · Hiroshi Noguchi ·
Gerhard Gompper**

Received: 14 July 2012 / Accepted: 27 April 2013 / Published online: 14 May 2013

Abstract Mesoscale simulations of blood flow, where the red blood cells are described as deformable closed shells with a membrane characterized by bending rigidity and stretching elasticity, have made much progress in recent years to predict the flow behavior of blood cells and other components in various flows. To numerically investigate blood flow and blood-related processes in complex geometries, a highly efficient simulation technique for the plasma and solutes is essential. In this review, we focus on the behavior of single and several cells in shear and microcapillary flows, the shear-thinning behavior of blood and its relation to the blood cell structure and interactions, margination of white blood cells and platelets, and modeling hematologic diseases and disorders. Comparisons of the simulation predictions with existing experimental results are made whenever possible, and generally very satisfactory agreement is obtained.

Keywords Red blood cell · Dissipative particle dynamics · Multiparticle collision dynamics · Blood rheology · Shear-thinning · Capillary flow · Microvessels · Discocyte, parachute, and slipper shapes

Abbreviations

MD	Molecular dynamics
DPD	Dissipative particle dynamics
MPC	Multiparticle collision dynamics
SPH	Smoothed particle hydrodynamics
BD	Brownian dynamics
LBM	Lattice Boltzmann method
CFD	Computational fluid dynamics
IBM	Immersed boundary method
FTM	Front tracking method
RBC	Red blood cell
WBC	White blood cell
GUV	Giant unilamellar vesicle
KS	Keller–Skalak theory
RDF	Radial distribution function
CFL	Cell-free layer
Pf	Plasmodium falciparum
ATP	Adenosine triphosphate
2D	Two dimensions
3D	Three dimensions

1 Introduction

Blood performs a large variety of essential functions in our body, ranging from the transport of oxygen to immune response and wound healing. Therefore, blood diseases have severe consequences for our health. Prominent examples are plaque formation in arteries which may lead to heart attacks, diabetes as a cause of reduced microcirculation and tissue damage, excessive blood clotting leading to stroke, reduced blood clotting which causes excessive bleeding, etc. Therefore, blood and blood flow have attracted the interest of natural and medical scientists for centuries. With modern tools of chemical analysis, diagnostics, and simulation, the field has made considerable progress in recent years.

The second important motivation for a detailed understanding of the dynamical behavior of blood and its com-

---

D. A. Fedosov ( ) · G. Gompper
Theoretical Soft Matter and Biophysics, Institute of Complex Systems and Institute for Advanced Simulation, Forschungszentrum Jülich, 52425 Jülich, Germany
e-mail: d.fedosov@fz-juelich.de

H. Noguchi
Institute for Solid State Physics, University of Tokyo,
Chiba 277-8581, Japan

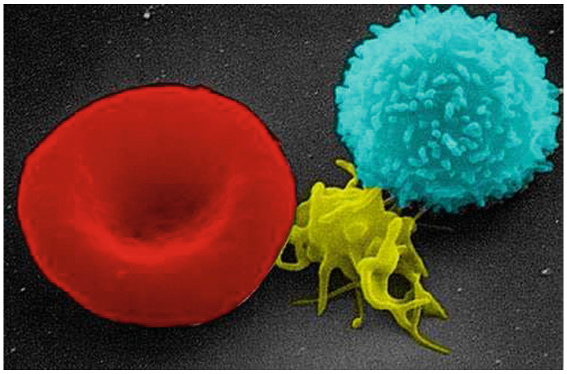

Fig. 1 A scanning electron micrograph of blood cells. From *left* to *right* red blood cell (*red*), activated platelet (*yellow*), and white blood cell (*cyan*). *Source* The National Cancer Institute at Frederick (NCI-Frederick)

ponents is the advent of modern microfluidic devices and techniques. Not only such knowledge is essential for the design of new devices with unprecedented functions, but also such devices allow the control and manipulation of blood on the level of single cells, which are illustrated in Fig. 1. Here, advanced simulation techniques can provide insight into the flow behavior on the cellular level, as well as into the emergence of macroscopic flow properties from the structure, deformability, dynamics, and interactions of single cells.

From a simulation point of view, already the dynamics of model fluids consisting of a solvent and various solutes such as different molecules, colloidal particles, and cells is a difficult problem. There exist a large gap in the length- and time-scales between the atomistic scale of the solvent and the mesoscopic scale of the suspended particles, which typically ranges from tens of nanometers to tens of micrometers. Furthermore, many physical mechanisms are also important including the deformability of the particles, the hydrodynamic interactions between them and with walls, and thermal fluctuations.

In order to surmount the numerical problems, several mesoscale hydrodynamics simulation techniques have been developed in the last decade. The Lattice Boltzmann method (LBM) (Succi 2001), dissipative particle dynamics (DPD) (Hoogerbrugge and Koelman 1992; Espanol and Warren 1995), and multi-particle collision dynamics (MPC) (Malevanets and Kapral 1999; Kapral 2008; Gompper et al. 2009) have shown a rapid advancement in recent years, and are now well-established techniques for the numerical investigation of the dynamics of complex fluids.

We focus in this review on the application of mesoscale hydrodynamics approaches to studies of blood flow. Since red blood cells are much more abundant by volume than other cells and solutes, they determine the flow behavior and rheology of blood. Nevertheless, it is also essential to understand the behavior of other cells such as white blood cells and platelets under flow conditions, because their physiological role as part of the immune system and of wound healing is strongly affected by flow.

Mesoscale hydrodynamics have been employed in two (2D) and three dimensions (3D) to model giant unilamellar vesicles (GUVs) and red blood cells (RBCs) in flow. From a mechanical point of view, RBCs are distinguished from vesicles by their nonzero shear elasticity. This distinction can only be made in 3D, since shear elasticity does not exist for membranes (i.e., lines) in 2D. It is interesting to study both GUV in 3D and model cells in 2D, because a comparison of the results helps to elucidate the importance of specific material properties of the cells for their flow behavior. Due to the large size, GUVs and RBCs have to be modeled on a mesoscopic level, for instance by triangulated surfaces in 3D (Gompper and Kroll 1997, 2004; Noguchi and Gompper 2005b; Fedosov et al. 2010a) and by polyhedral lines in 2D (Finken et al. 2008; Messlinger et al. 2009). For fluid vesicles, a phase-field approach has also been employed (Du et al. 2004; Biben et al. 2005), where a scalar "concentration" field is used to define the interior and exterior of the vesicle, and thereby the membrane in-between.

In 2D, individual vesicles and cells have been investigated in shear flow to study the effect of flow on the spectrum of undulation modes (Finken et al. 2008), which changes with the flow strength inducing membrane tension. Tank-treading and tumbling behavior of 2D vesicles and cells in shear flow (Messlinger et al. 2009; Beaucourt et al. 2004; Kaoui et al. 2012) has been extensively investigated with the main finding that the transition between these two modes can be induced by a viscosity contrast between external and internal fluids as well as by vesicle confinement. Using the 2D studies on shear and Poiseuille flow, the lift force on a vesicle near a wall (Messlinger et al. 2009) has also been measured, which governs the migration of vesicles and cells away from the walls (Kaoui et al. 2008, 2009, 2011). Simulations of 2D systems with many cells in flow through small vessels and the rheology of cell suspensions (Sun and Munn 2005; Bagchi 2007; Freund 2007; Fedosov et al. 2012) predict cell migration, distributions, and interactions in flow. In 3D, single GUVs under flow have been studied to investigate their tank-treading, tumbling, and swinging (also called vacillating-breathing or trembling) dynamics, in simple shear flow (Noguchi and Gompper 2005b; Biben et al. 2005; Noguchi and Gompper 2004; Misbah 2006; Noguchi and Gompper 2007; Zhao et al. 2010; Zhao and Shaqfeh 2011a) as well as in capillary flow in both homogeneous (Noguchi and Gompper 2005a) and structured microchannels (Noguchi et al. 2010). In these simulations, detailed information has been obtained on the transitions between different flow behavior modes of vesicles as well as on vesicle deformation.

Here, our main aim is to provide an overview of recent work on the deformation, dynamics, and rheology of RBC suspensions in 3D. Flow of single RBCs (or of periodic arrays of RBCs) in capillaries has first been investigated with the assumption of axisymmetric shapes by the boundary integral method (Pozrikidis 2005). Using efficient mesoscale hydrodynamics simulation techniques, the assumptions of symmetric shapes are no longer required. For a single RBC in capillary flow, simulations have predicted a symmetry breaking with a perpendicular orientation of the RBC axis to the flow direction for small flow rates and a transition from discocyte to parachute shapes for larger flow rates (Fedosov et al. 2010a; Noguchi and Gompper 2005a; Reasor et al. 2012). Simulations of several RBCs in a narrow microchannel showed cell clustering at low hematocrits (the volume fraction of RBCs) (McWhirter et al. 2009, 2011), while at higher hematocrits, RBCs displayed several different arrangements including a zigzag structure of slipper-shaped cells (McWhirter et al. 2009). Numerical investigations of flow behavior of many RBCs in wider channels (Reasor et al. 2012; Dupin et al. 2007; Doddi and Bagchi 2009; Fedosov et al. 2010b; Freund and Orescanin 2011; Krüger et al. 2011) demonstrate the existence of a cell-free layer near the walls and crowding of RBCs in the channel center due to their migration away from the walls. Finally, simulations of blood rheology in simple shear flow have shown that the large increase in the apparent viscosity at low shear rates is due to a small attraction (RBC aggregation) between cells and the resulting rouleaux formation (Fedosov et al. 2011b).

In order to perform simulations with a much larger number of RBCs, which may be required to study larger parts of the circulatory system, simplified RBC models have been developed. The existing models range from hard oblate ellipsoids (Janoschek et al. 2010) and deformable ellipsoids with a rotational degree of freedom for the membrane (Melchionna 2011) to a ring-like arrangement of a few connected spheres (Pan et al. 2010). In the latter case, the simplified model has been shown to capture the rheological behavior of the fully deformable RBC model very well (Fedosov et al. 2011b; Pan et al. 2011).

The rapid progress in the development of numerical methods to study blood flow already allows to go beyond simple RBC suspensions and to investigate more complex systems. Simulations of malaria-infected cells show a flipping motion of adhered cells at the wall (Fedosov et al. 2011c,d). Simulations of RBCs affected by sickle cell anemia show abnormal cell shapes and an increased hydrodynamic resistance in tube flow (Lei and Karniadakis 2012a,b). Simulations of mixtures of RBCs and platelets under flow in 3D microvessels demonstrate the migration of platelets to the vessel wall (Zhao and Shaqfeh 2011b). A similar behavior is predicted for white blood cells (WBCs) in blood flow (Freund 2007; Fedosov et al. 2012) in 2D. In both cases, the lift force (Messlinger et al. 2009; Cantat and Misbah 1999; Sukumaran and Seifert 2001; Abkarian et al. 2002) on highly non-spherical RBCs directed away from the vessel wall is responsible for expelling the other cells from the vessel center. However, it is important to note that platelets are much smaller than RBCs, while WBCs are somewhat larger (see Fig. 1); also, platelets are at least an order of magnitude more numerous than WBCs. Thus, the detailed mechanisms of margination as well as the margination dependence on hematocrit, flow rate, and RBC aggregation are expected to be different.

This review is organized as follows. In Sect. 2, we briefly introduce the most frequently used models for RBCs and blood flow. In Sect. 3, single RBC mechanics and dynamics are investigated. Section 4 presents results on blood rheology and its relation to the suspension structure and single cell deformation and dynamics. In Sect. 5, we will show results on blood flow simulations in tubes or microvessels, while in Sect. 6, we will briefly review margination of white blood cells and platelets in blood flow. Section 7 provides several examples of modeling hematologic diseases and disorders. Finally, we conclude in Sect. 8 with a brief discussion.

2 Methods and models

A variety of methods to model cells and vesicles in flow has been recently applied and developed. These methods are generally mesoscopic, because microscopic modeling of cells is not feasible computationally; here, microscopic modeling refers to a representation on the scale of single atoms and molecules. Furthermore, a flow of cells and vesicles often cannot be described on a macroscopic level, since the properties and dynamics of single cells play an important role in the flow, but enter into macroscopic methods only approximately via constitutive equations.

To make an overview of different methods, it is convenient to divide methodological challenges into the three groups: (1) modeling fluid flow, (2) modeling deformable cells, and (3) coupling between the fluid flow and cell deformation. Below we briefly review different methods which can be employed for each modeling task.

2.1 Modeling Newtonian solvent

Modeling fluid flow of a Newtonian solvent is probably the most developed methodological area out of the three groups identified above. Continuum fluid flow modeling is often performed using the Navier–Stokes equation or its modifications, which has resulted into the development of the computational fluid dynamics (CFD) field (Wendt

2009). Generally, fluid flow is described by a set of partial differential equations and satisfies the conservation laws and continuum assumption. The equations can be solved numerically using various discretization techniques (e.g., finite difference, finite element), initial and boundary conditions. The advantages of continuum modeling include speed and robustness of methods and rather well-established numerical techniques and codes. However, in these methods, it may be non-trivial to include some features present at the micro- and mesoscale, for instance thermal fluctuations.

Another class of efficient numerical techniques to model fluid flow comprises particle-based methods, which will be the main focus of this review article. Examples are molecular dynamics (MD) (Allen and Tildesley 1987), dissipative particle dynamics (DPD) (Hoogerbrugge and Koelman 1992; Espanol and Warren 1995), multi-particle collision dynamics (MPC) (Malevanets and Kapral 1999; Kapral 2008; Gompper et al. 2009), and smoothed particle hydrodynamics (SPH) (Lucy 1977; Monaghan 2005). Generally, MD is considered to be a microscopic method and the others to be mesoscopic; however, they all recover macroscopic hydrodynamic behavior at large enough length scales. In these methods, a fluid is modeled by a collection of particles which interact with each other through specified forces or collisions. Theoretical foundations of these methods are well established, and it has been shown that they are able to recover proper hydrodynamic behavior. In comparison with the continuum techniques, particle-based simulations are generally more expensive computationally; however, desired micro- and mesoscopic features can be included here rather straightforwardly. Therefore, particle-based methods are very popular in modeling complex fluids at the micro- and mesoscale.

There also exist several other numerical methods, which do not strictly belong to the continuum or particle-based method groups, but they can be used to efficiently model fluid flow. These include the Lattice Boltzmann method (LBM) (Succi 2001) and Brownian dynamics (Ermak and McCammon 1978), which are often considered to be mesoscopic. In LBM, the Boltzmann equation is solved on a pre-defined lattice leading to proper fluid hydrodynamics. In BD, hydrodynamic interactions between suspended objects are described by the Oseen or Rotne–Prager tensors, which describe hydrodynamic interactions without explicit fluid modeling. In comparison with conventional CFD methods, LBM has several advantages such as modeling complex boundaries and mesoscopic features, since the method has local interactions similar to particle-based techniques. The locality of interactions also allows for an efficient parallelization of the algorithm. The BD algorithm is very fast for a small number of suspended entities; however, the cost increases substantially as the number of solutes becomes large.

2.2 Red blood cell model

Human red blood cells (RBCs) are biconcave with a diameter of about 8 μm and a thickness of about 2 μm. A RBC is comprised of a membrane filled with a viscous cytosol (hemoglobin solution), which is usually assumed to be a Newtonian fluid with a viscosity several times larger than that of blood plasma under physiological conditions. The RBC membrane consists of a lipid bilayer re-enforced by two-dimensional spectrin–protein cytoskeleton attached to the back side of the bilayer. The lipid bilayer is fluidic and area-preserving (Fung 1993), while the spectrin network supplies RBC elastic resistance, which is required to sustain large deformations when passing through relatively narrow capillaries with the diameter down to 3 μm.

Motivated by the RBC biological structure, a realistic RBC membrane model has to take into account elastic and viscous properties of a RBC membrane, its bending resistance, and the viscosity contrast between the blood plasma and cytosol. There exist essentially two types of RBC models, a continuum approach and a network model. In a continuum model, RBC membrane properties are described by a set of constitutive equations. For instance, RBC membrane elasticity can be defined by Hookean or neo-Hookean law (Doddi and Bagchi 2009; Liu and Liu 2006), while RBC bending rigidity is often modeled by the Helfrich's curvature elasticity model (Helfrich 1973). Such constitutive laws are implemented through various discretizations including finite-element (Liu and Liu 2006) and boundary integral (Freund and Orescanin 2011; Pozrikidis 1989) methods. Further information about continuum cell modeling can be found, e.g., Pozrikidis (2005), MacMeccan et al. (2009), Doddi and Bagchi (2009).

The network model of a RBC is built by a set of points which form a two-dimensional triangulated network on a RBC surface (Fedosov et al. 2010a; Noguchi and Gompper 2005a; Dupin et al. 2007; Discher et al. 1998; Li et al. 2005; Pivkin and Karniadakis 2008; Fedosov et al. 2010c), see Fig. 2. The vertices of a network are connected by springs, and the potential energy of the system is defined as

$$U(\{\mathbf{x}_i\}) = U_\mathrm{s} + U_\mathrm{b} + U_\mathrm{a} + U_\mathrm{v}, \tag{1}$$

where U_s is the spring's potential energy, U_b is the bending energy, and U_a and U_v correspond to the area and volume conservation constraints, respectively. The U_s part of the total RBC energy mimics membrane elasticity similar to that of a spectrin network. It is also possible to attach a dashpot to each spring in order to capture viscous response of the network similar to RBC membrane viscosity. The curvature energy term supplies bending resistance of the lipid bilayer, while the area and volume conservation constraints mimic the area incompressibility of the lipid bilayer and incompressibility of a cytosol, respectively. The RBC biconcave shape is

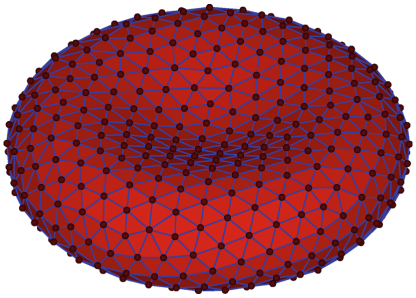

Fig. 2 Mesoscopic representation of a RBC membrane by a triangular network of bonds

also characterized by the reduced volume $V^* = V_0/(\frac{4}{3}\pi R_0^3)$, where V_0 is the RBC volume and $R_0 = \sqrt{A_0/(4\pi)} = 3.25$ µm, with A_0 being the area of a RBC. The reduced volume of a healthy RBC is about $V^* = 0.6$; at this reduced volume, the discocyte shape minimizes the curvature energy of a fluid lipid vesicle (Deuling and Helfrich 1976).

We consider two types of network models. The first model is a generic model of two composite membranes with bending and stretching energies (Noguchi and Gompper 2005a). It consists of a dynamically triangulated network, which describes the fluidic lipid bilayer, connected at the vertices to another elastic network of fixed connectivity. In this model, the dynamic network supplies viscous response of a RBC membrane, while the fixed mesh of springs provides cell elastic properties. The second model is designed more specifically for RBCs. It is build as a single network of fixed connectivity, which simultaneously includes membrane elasticity and viscous dissipation (Fedosov et al. 2010a,c).

In continuum models, the membrane macroscopic properties (e.g., shear and bending moduli, membrane viscosity) are a direct input. The network model parameters (e.g., spring constant, bending constant) can be related to the network macroscopic properties through a linear analysis of the deformation of regular hexagonal or random triangular networks (Gompper and Kroll 2004; Fedosov et al. 2010a,c; Seung and Nelson 1988; Gompper and Kroll 1996; Dao et al. 2006; Schmidt and Fraternali 2012). Thus, in practice, the given macroscopic RBC properties may serve as an input for calculating the necessary mesoscopic model parameters without any ad hoc adjustment.

Numerical studies of the RBC equilibrium shape (Li et al. 2005; Fedosov et al. 2010c) have found that the use of a uniform equilibrium length for all springs leads to non-vanishing intra-membrane stresses depending on triangulation quality and the reference shape chosen for initial triangulation. Such stresses may lead to an irregular or even non-biconcave RBC shape in equilibrium. To eliminate the artifacts of irregular triangulations, a stress-free membrane model (Fedosov et al. 2010a,c) has been proposed. The model is obtained by computational annealing, such that each spring assumes its own equilibrium spring length adjusted to be the edge length after triangulation.

In this review, various biological structures including blood cells and vessels are described on a mesoscopic level. On the one hand, these are distinguished from the microscale, reaching up to several nanometers such that atomistic and molecular details are present. On the other hand, macroscopic description of blood flow is only possible in vessels with the diameters larger than approximately 100 microns. Mesoscale simulation techniques are therefore optimally suited to study blood flow in microcirculation.

2.3 Coupling between the fluid flow and cell deformation

There exist several strategies on how RBC deformation can be coupled to fluid flow. Full continuum representation (fluid flow and cells) is very complex, since cell motion and deformation require frequent mesh adaptation for the fluid flow. Therefore, other algorithms have been developed, which model fluid flow in an Eulerian framework (fixed mesh), while cells move in a Lagrangian fashion and are coupled to fluid flow through the immersed boundary method (IBM) (Bagchi 2007; Liu and Liu 2006) or front tracking method (FTM) (Doddi and Bagchi 2009). The IBM assumes that cell vertices move with the local fluid velocity, while in return, they exert a force on the fluid flow, which is similar to the FTM. The IBM coupling strategy might be quite stiff limiting the time step in simulations, since a solid structure is advected with the fluid motion. Another method is to introduce viscous coupling of cell vertices to the fluid flow, which applies frictional forces on both the fluid and cells in order to match their local velocities (Ahlrichs and Dünweg 1999). This coupling technique is usually less prohibitive in terms of numerical stability and time step; however, it may lead to a partial slip at fluid–cell interface. The separation of external/internal fluids (for instance, needed when their viscosities are different) requires tracking of the fluid mesh nodes inside and outside a cell, respectively.

In particle-based methods, the internal and external fluids are modeled by a number of free particles. External/internal fluid separation (non-mixing) is achieved through bounce-back reflections of fluid particles at a moving membrane surface. In addition, the no-slip boundary conditions at the membrane surface are enforced through viscous force coupling in DPD (Fedosov et al. 2010a) or collisions in MPC (Noguchi and Gompper 2005a) between fluid particles and membrane vertices, which is similar to the viscous coupling mentioned above.

Another consideration, which has to be taken into account, is the resolution used for modeling fluid flow and membrane, respectively. For the fluid component, it is important to employ a sufficiently fine grid in case of a continuum solver or a sufficiently large particle density in case of particle meth-

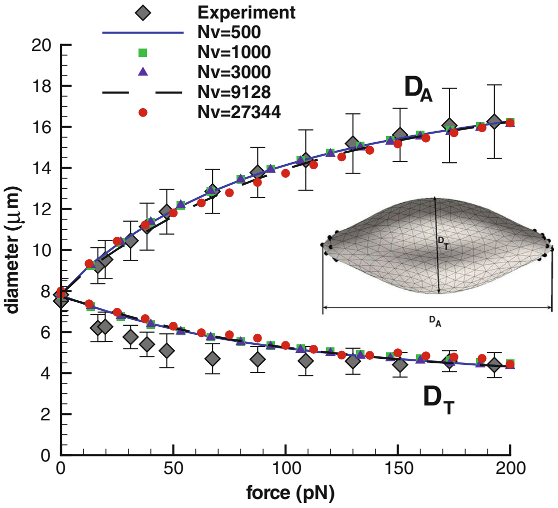

Fig. 3 Stretching response of the modeled RBC for different coarse-graining levels compared with the optical tweezers experiments (Suresh et al. 2005). Simulation data are shown for different numbers N_v of membrane vertices in the RBC representation, as indicated in the legend. The *inset* schematically shows a stretched RBC with *black dots* denoting vertices where the force is applied

ods in order to properly resolve fluid flow around and inside deformable cells. Similarly, the cell membrane network has to be fine enough to adequately resolve membrane deformations in fluid flow. In general, these considerations are problem dependent and ideally have to be tested for grid/particle density refinement. As a rule of thumb, we generally assume similar length-scale resolution for both cell membrane and suspending fluid.

3 Single cell properties and dynamics

3.1 RBC mechanics

RBC elasticity has been probed by micropipette aspiration (Waugh and Evans 1979; Discher et al. 1994; Mohandas and Evans 1994), atomic force microscopy (Scheffer et al. 2001), and in optical tweezers experiments (Henon et al. 1999; Suresh et al. 2005). In particular, a RBC was stretched by a force applied by laser tweezers to two silica microbeads attached at the opposite sides of the RBC (Suresh et al. 2005). To mimic this experiment in simulations (Fedosov et al. 2010a; Dupin et al. 2007; Pivkin and Karniadakis 2008; Fedosov et al. 2010c; Dao et al. 2006; Noguchi 2009a; Vaziri and Gopinath 2008), a total stretching force f is applied to N_- and N_+ vertices ($N_- = N_+ = \varepsilon N_\mathrm{v}$) along opposite directions, as indicated in Fig. 3. Here, N_v is the number of vertices in the membrane representation, which can vary from $N_\mathrm{v} = 27344$ (spectrin-level) to the highly coarse-grained network of $N_\mathrm{v} = 500$, while $\varepsilon = 0.02$ corresponding to the contact diameter of the attached silica bead with diameter 2 μm used in experiments (Suresh et al. 2005). Figure 3 compares the simulated axial and transverse diameters of a stretched RBC with the experimental data (Suresh et al. 2005). Good agreement between simulations and experiments is found for the shear modulus of 6.3 μN/m independently of N_v. This value also falls within the range of 4–9 μN/m obtained in RBC micropipette aspiration experiments (Waugh and Evans 1979; Discher et al. 1994).

3.2 RBC dynamics in shear flow

Single RBCs in shear flow show tumbling at low shear rates and tank-treading at high shear rates as observed in a number of experiments (Tran-Son-Tay et al. 1984; Fischer 2004, 2007; Abkarian et al. 2007). A RBC marked by several attached microbeads, subjected to tank-treading motion for several hours, was found to relax back to its original state after the shear flow has been stopped (Fischer 2004). Thus, the tumbling-to-tank-treading transition is attributed to the existence of a RBC minimum energy state, such that the RBC has to exceed a certain energy barrier in order to transit to the tank-treading motion. In addition, a tank-treading RBC also swings around the preferred inclination angle of tank-treading with a certain frequency and amplitude (Fedosov et al. 2010a; Abkarian et al. 2007; Skotheim and Secomb 2007; Noguchi 2009b; Yazdani et al. 2011).

Figure 4 shows tumbling and tank-treading frequencies of a simulated RBC in shear flow in comparison with experiments (Tran-Son-Tay et al. 1984; Fischer 2007). Here, η_o and η_i denote the external and internal fluid viscosities, while η_m is the RBC membrane viscosity. Comparison of simulations and experiments reveals that a purely elastic RBC with or without internal fluid is not able to correctly predict cell tank-treading frequencies, because such a membrane model lacks viscous dissipation. Addition of the membrane viscosity decreases the tank-treading frequencies leading to a good agreement with experiments for the membrane viscosity $\eta_m = 22 \times 10^{-3}$ Pa s. In all cases, a finite region of intermittent dynamics is observed around the tumbling-to-tank-treading transition, where a RBC experiences strong deformations and shows partially both tumbling and tank-treading dynamics. Also, the intermittent region is found to become wider for a nonzero internal fluid and membrane viscosity and shifts to higher shear rates. The degree of RBC deformations in the intermittent region depends on the Föppl-von Kármán number $\gamma = 4\mu R_0^2/\kappa$, where μ is shear elastic modulus and κ is the bending rigidity. As an example, an increase in the RBC bending rigidity by a factor of five implies that the aforementioned shape deformations are considerably reduced, while the factor of ten in κ value leads to virtually no shape deformations in the intermittent region.

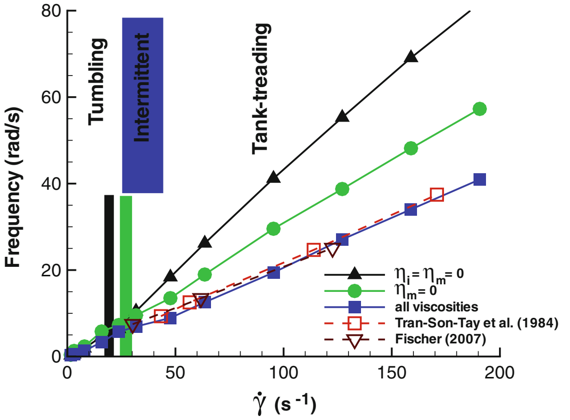

Fig. 4 Tumbling and tank-treading frequency of a RBC in shear flow for different cases: (1) $\eta_o = 5 \times 10^{-3}$ Pa s, $\eta_i = \eta_m = 0$ (*triangles*); (2) $\eta_o = \eta_i = 5 \times 10^{-3}$ Pa s, $\eta_m = 0$ (*circles*); (3) $\eta_o = \eta_i = 5 \times 10^{-3}$ Pa s, $\eta_m = 22 \times 10^{-3}$ Pa s (*squares*), where η_o, η_i, and η_m are the external, internal fluid, and membrane viscosities, respectively. The region of intermittent dynamics is marked by corresponding *colored boxes* around the tumbling-to-tank-treading transition

Finally, the swinging frequency of a RBC is equal to twice the tank-treading frequency, because the spectrin network has to perform two ‘flipping’ motions to make a full rotation.

The dynamics of fluid vesicles in shear flow is quantitatively predicted by the Keller–Skalak (KS) theory (Keller and Skalak 1982). Recently, the KS theory was extended to capsules with fixed ellipsoidal shapes in order to account for a free-energy barrier, which affects the transition between three modes: tumbling, intermediate (intermittent), and tank-treading (Skotheim and Secomb 2007). When cell shape deformation is also taken into account, two types of swinging oscillation modes coexist: one induced by the shape deformation similar to fluid vesicles and the other induced by the tank-treading energy barrier (Noguchi 2010a). For typical quasi-spherical synthetic microcapsules, where no local energy minimum exists for shape deformation, these two modes are always synchronized and no intermediate modes appear. For RBCs and other capsules accompanied by a local energy minimum, coupling of these two modes generates a more complicated phase behavior. In oscillatory shear flow, RBCs (Noguchi 2010b) and fluid vesicles (Noguchi 2010c) exhibit various types of oscillatory dynamics such as the coexistence of two or more limit-cycle oscillations at high shear frequencies.

3.3 RBC dynamics in capillary flow

RBC dynamics in Poiseuille flow in tubes with a diameter comparable with the RBC diameter was the subject of investigation in several experiments (Suzuki et al. 1996; Abkarian et al. 2008; Tomaiuolo et al. 2009). The main feature of this flow is the transition from the biconcave RBC shape at rest to a parachute-like shape or bullet shape depending on the flow rate and confinement. A RBC may attain the parachute shape when it is deformed by the flow at the tube center. Slipper shapes, which are characterized by a non-axisymmetric shape, are also observed for high flow rates. However, it is not yet entirely clear, whether these states are transient (e.g., determined by the conditions at inflow into the capillary) or stationary. The transition to the parachute shape of a RBC in Poiseuille flow has been simulated in a tube with a radius in the range $R_{\text{cap}} = 4$–$6\,\mu$m (Fedosov et al. 2010a; Noguchi and Gompper 2005a; McWhirter et al. 2011; Pivkin and Karniadakis 2008); a typical conformation of the parachute shape at flow rates just above the transition velocity is shown in Fig. 5. Poiseuille flow can be characterized by the mean flow velocity defined as $\bar{v} = \int v(r) dA/A$, where A is the area of the tube cross-section, and $v(r)$ is the axial flow velocity.

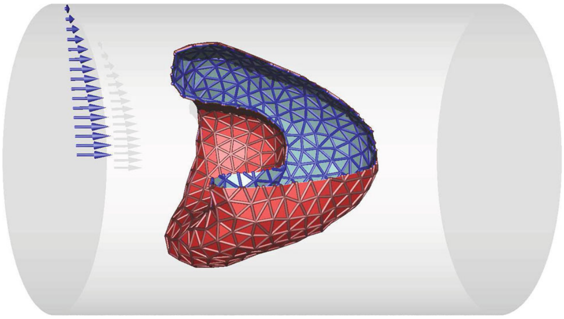

Fig. 5 Simulation snapshot of the parachute shape of a RBC in a microchannel of radius $R_{\text{cap}} = 4.6\,\mu$m, which forms when a threshold flow rate is exceeded

At small flow velocities, isolated fluid vesicles and modeled RBCs assume a discoidal shape at a reduced volume $V^* = 0.59$ with a non-axial symmetry, where the symmetry axis of the discocyte is oriented perpendicular to the capillary axis. In addition, the perfect rotationally symmetric shape of the discocyte is somewhat distorted, such that the rim is pulled backwards near the walls, and pushed forward in the center. As the flow velocity increases, a RBC exhibits a shape transition from discocyte to parachute shape, while a fluid vesicle of the same reduced volume and bending rigidity transforms into a prolate shape, see the inset of Fig. 6(a) (Noguchi and Gompper 2005a). Since the transformation to a prolate shape implies a much larger in-plane deformation of the membrane than to a parachute, the shear elasticity of RBCs suppresses a prolate shape.

An interesting aspect is the dependence of the transition velocities on the bending rigidity κ and shear elastic modulus μ of model RBCs. In both cases, the dependence of the transition velocity on the elastic parameters is linear shown in Fig. 6. This behavior can be traced back to the balance of

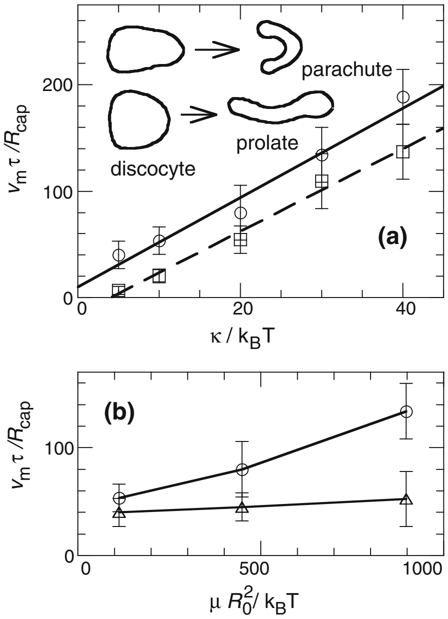

Fig. 6 Dependence of the shape-transition velocity on (**a**) the bending rigidity κ and (**b**) the shear modulus μ in the dilute suspension at $R_{\mathrm{cap}}/R_0 = 1.4$. (**a**) Transitions of model RBCs (with $\mu R_0^2/k_{\mathrm{B}}T = 110$) from discocyte to parachute (*circles*), as well as transitions of fluid vesicles from discocyte to prolate (*squares*) are shown. *Solid and broken lines* are linear fits to the data. The sliced snapshots for $\kappa/k_{\mathrm{B}}T = 20$ show model RBCs at $v_{\mathrm{m}}\tau/R_{\mathrm{cap}} = 52$ and 107 (*top row*), and fluid vesicles at $v_{\mathrm{m}}\tau/R_{\mathrm{cap}} = 41$ and 69 (*bottom row*). (**b**) Transition velocities of elastic vesicles for $\kappa/k_{\mathrm{B}}T = 10$, at the discocyte-to-parachute transition (*top curve*) and at the parachute-to-discocyte transition (*bottom curve*). The time unit $\tau = \eta_0 R_{\mathrm{cap}}^3/k_{\mathrm{B}}T$ is the longest relaxation time of a quasi-spherical fluid vesicle with a reference bending rigidity $k_{\mathrm{B}}T$. Reused with permission from Noguchi and Gompper (2005a)

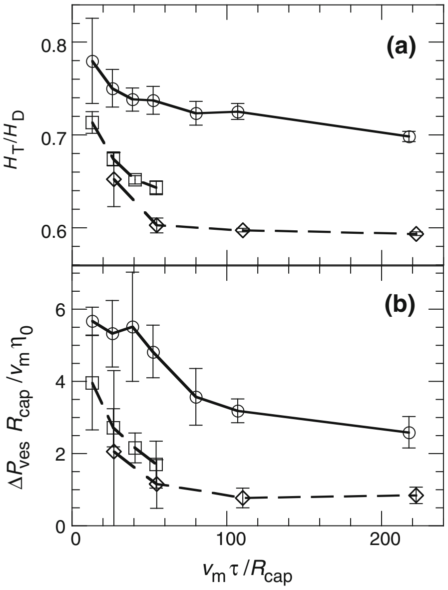

Fig. 7 Flow velocity v_{m} dependence of (**a**) hematocrit ratio $H_{\mathrm{T}}/H_{\mathrm{D}} = v_{\mathrm{m}}/v_{\mathrm{ves}}$ and (**b**) flow resistance $\Delta P_{\mathrm{ves}}/v_{\mathrm{m}}$ per vesicle, in the dilute suspension for $\kappa/k_{\mathrm{B}}T = 20$, $\mu R_0^2/k_{\mathrm{B}}T = 110$, and $R_{\mathrm{cap}}/R_0 = 1.4$. The *solid and broken lines* correspond to model RBCs and fluid vesicles, respectively. Reused with permission from Noguchi and Gompper (2005a)

elastic and flow forces at the transition, and the linear dependence of these forces on the elastic moduli and the average flow velocity, respectively. For large Föppl- von Kármán numbers γ, a shape hysteresis appears, which implies different transition velocities with increasing or decreasing flow rates, as indicated in Fig. 6(b). With decreasing flow velocity, fluid vesicles transform from prolate to discocyte shape via an intermediate banana shape. The transition velocity at other combinations of elastic parameters can be estimated from the linear dependence on κ and μ; in particular, the discocyte–parachute transition of RBCs is predicted to occur at 0.2 mm/s for $R_{\mathrm{cap}} = 4.6$ µm under physiological conditions. This is consistent with experimental results (Suzuki et al. 1996) and is in the range of velocities of microcirculation in the human body.

Transition to the slipper shape in Poiseuille flow has been numerically investigated for vesicles in 2D (Kaoui et al. 2009, 2011), where it has been found that the slipper shape for vesicles occurs at strong enough confinements as well as at low confinements. This shape transition also leads to a slight decrease in the flow resistance similar to the parachute transition. New simulations of RBCs in 3D cylindrical capillaries are needed to investigate the possible region of flow properties and confinements, where stable slipper shapes exist.

The ratio $H_{\mathrm{T}}/H_{\mathrm{D}}$ of tube hematocrit (H_{T}) of RBCs in a microcapillary and discharge hematocrit (H_{D}) decreases with increasing flow velocity. This effect was first observed in 1929 and is called the Fahraeus effect (Fahraeus 1929). Simulation results for the hematocrit ratio $H_{\mathrm{T}}/H_{\mathrm{D}}$ and the pressure drop ΔP_{ves} per vesicle/cell for both fluid vesicles and model RBCs are shown in Fig. 7. The hematocrit ratio is given by the ratio of vesicle velocity v_{ves} and mean flow velocity v_{m} as

$$H_{\mathrm{T}}/H_{\mathrm{D}} = v_{\mathrm{m}}/v_{\mathrm{ves}}. \tag{2}$$

The pressure drop ΔP_{ves} per vesicle is calculated by

$$\Delta P_{\mathrm{ves}} = 8\eta_0(v_0 - v_{\mathrm{m}})L_{\mathrm{ves}}/R_{\mathrm{cap}}^2, \tag{3}$$

where v_0 is the mean velocity of fluid flow without vesicle presence for the same pressure gradient, and L_{ves} is the capillary length per vesicle/cell. Since vesicles/cells are more deformed and feel a stronger lift force away from the walls at higher flow velocity, they occupy a narrower region in the center of the capillary, and thereby flow faster than the surrounding fluid/plasma (which implies the Fahraeus effect)

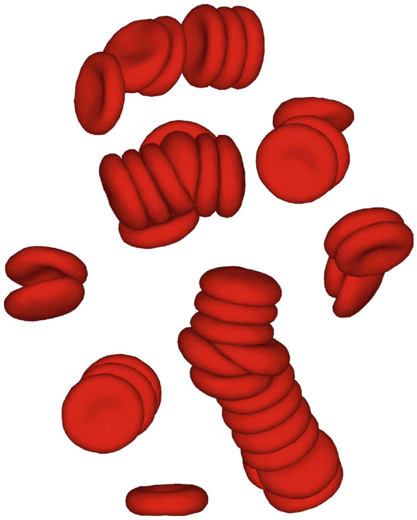

Fig. 8 Rouleaux structures formed in equilibrium at $H_t = 0.1$. The aggregation forces between RBCs are modeled using the Morse potential (Fedosov et al. 2011b)

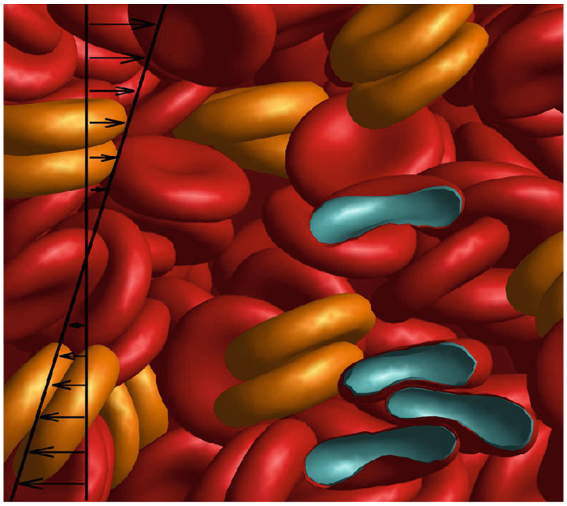

Fig. 9 Simulation of blood under shear flow. RBCs are shown in *red* and in *orange*, where *orange color* depicts the rouleaux structures formed due to aggregation interactions between RBCs. The image also displays several cut RBCs with the inside drawn in *cyan* to illustrate RBC shape and deformability

and disturb the original Poiseuille flow less (which implies a reduction in the pressure drop).

4 Blood rheology and structure

Rheological properties of blood are governed by RBCs due to their high volume fraction. RBCs in whole blood are able to form aggregate structures called “rouleaux,” which resemble stacks of coins (Merrill et al. 1963, 1966; Chien et al. 1970). The RBC aggregation is associated with the plasma proteins (Merrill et al. 1966; Chien et al. 1970) such that an increase in fibrinogen concentration leads to a significant increase in blood viscosity (Merrill et al. 1966). Moreover, whole blood appears to exhibit a yield stress (a threshold stress for flow to begin) (Merrill et al. 1963; Cokelet et al. 1963; Copley et al. 1973). In simulations, blood is modeled as a suspension of RBCs, which is characterized by a bulk hematocrit H_t.

Rouleaux structures in blood are formed at rest or at sufficiently small shear rates. As the shear rate is increased, the rouleaux structures break up into smaller ones, while at high shear rates, the RBCs are fully dispersed (Zhao et al. 1998). The aggregation process is reversible, and rouleaux can reform if the shear rate is decreased or flow is stopped. The formation–destruction behavior of rouleaux is well reproducible in simulations (Fedosov et al. 2011b), and Fig. 8 shows simulated rouleaux structures in equilibrium.

4.1 Blood viscosity and RBC aggregation forces

The viscosity of whole blood and of non-aggregating RBC suspension has been measured at physiological temperature 37 °C for different H_t values in several rheological experiments (Merrill et al. 1963; Chien et al. 1966; Skalak et al. 1981). The blood viscosity in simulations (Fedosov et al. 2011b) has been obtained from a RBC suspension in simple shear flow, as shown in Fig. 9. The blood viscosity was computed over a wide range of shear rates $\dot{\gamma}$ from $0.01\,\mathrm{s}^{-1}$ to approximately $1{,}200.0\,\mathrm{s}^{-1}$ and is presented in Fig. 10, in comparison with experimental measurements (Merrill et al. 1963; Chien et al. 1966; Skalak et al. 1981) at $H_t = 0.45$. The plot shows the relative viscosity—the RBC suspension viscosity normalized by the viscosity of the suspending media—for aggregating and non-aggregating RBC suspensions. The model predictions are in excellent agreement with the experimental data, and the model clearly captures the effect of aggregation on the viscosity at low shear rates. Other attempts in modeling (Bagchi et al. 2005; Wang et al. 2009) of two-cell and of multiple-cell aggregates (Liu and Liu 2006) focused mainly on their flow behavior. For instance, Liu and Liu (2006) studied the dependence of viscosity on RBC aggregation in simulations of up to ten aggregated RBCs in shear flow; however, the viscosity predictions did not reproduce the steep increase in viscosity at low shear rates.

The strength of RBC aggregation in simulations was calibrated based on the viscosity value for a single shear rate, since exact RBC aggregation forces are not known (Fedosov et al. 2011b). The correct model predictions for whole blood with RBC aggregation shown in Fig. 10 allow an estimate of the maximum force required to break up two aggregated RBCs. The breakup force in the normal direction was found to be in the range 3.0–7 pN, where the lower

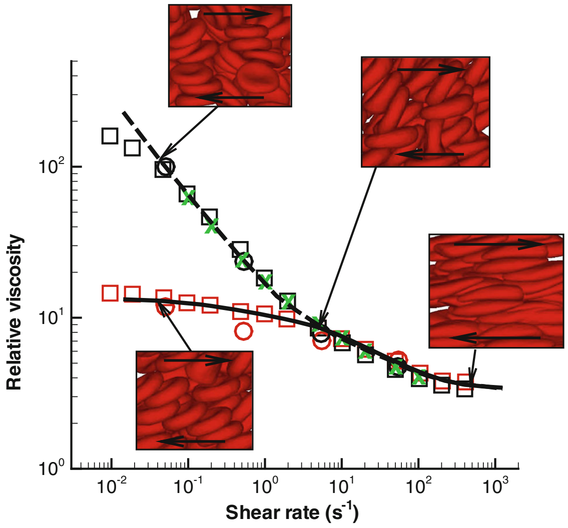

Fig. 10 Non-Newtonian relative viscosity (the cell suspension viscosity normalized by plasma viscosity) of whole blood as a function of shear rate at $H_t = 0.45$ and 37 °C: simulation results Fedosov et al. (2011b) are shown as *black full and dashed lines*; experimental data are for: **whole blood** *green crosses*—Merrill et al. (1963); *black circles*—Chien et al. (1966), *black squares*—Skalak et al. (1981). **Non-aggregating RBC suspension**: *red circles*—Chien et al. (1966); *red squares*—Skalak et al. (1981)

value corresponds to a peeling breakup. Tangential or sliding breakup needs a force of about 1.5–3 pN. These forces are quite small, which is consistent with the fact that rouleaux structures break up at relatively low shear stresses (or equivalently shear rates). A fluid shear stress required for RBC disaggregation has been measured in shear flow experiments (Chien et al. 1977) and lies between 0.01 and 0.1 Pa. The analogous simulations (Fedosov et al. 2011b) resulted in the estimation of the RBC disaggregation stress to be about 0.02 Pa.

4.2 Blood yield stress

Whole blood is believed to require a nonzero threshold shear stress for flow to begin, which is called a yield stress (Merrill et al. 1963; Cokelet et al. 1963; Copley et al. 1973). The existence of yield stress is difficult to confirm both experimentally and theoretically; this is usually done by an extrapolation of viscosity data to zero shear rate, as it has been done, for example, for blood by Merrill et al. (1966). Following the same extrapolation method (Merrill et al. 1966), a polynomial is fitted to the simulated data for $H_t = 0.45$ (Fedosov et al. 2011b) (see Fig. 11) in coordinates $(\dot{\gamma}^{1/2}, \tau_{xy}^{1/2})$, where $\dot{\gamma}$ is the shear rate and τ_{xy} the shear stress (Casson plot). The fitted curves show that the extrapolated yield stress τ_y is nonzero for the aggregating RBC suspension, while it vanishes for a suspension without cell aggregation.

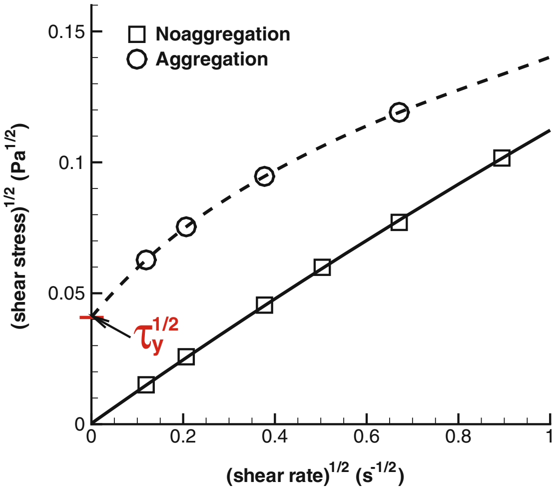

Fig. 11 RBC aggregation and yield stress. A Casson plot with a polynomial fit showing the extrapolated intercept τ_y for simulated suspensions with (*dashed lines*) and without (*solid lines*) aggregation at $H_t = 0.45$

The yield stress for whole blood has been associated with the existence of rouleaux structures (Merrill et al. 1963; Cokelet et al. 1963; Copley et al. 1973); simulations (Fedosov et al. 2011b) confirm this proposition. In practice, a direct measurement of yield stress is not feasible and yield stresses derived from viscometric data may not be consistent with those derived from non-rheological measurements (Picart et al. 1998). For human blood, the yield stress was found experimentally to lie between 0.0015 and 0.005 Pa at $H_t = 0.45$ (Merrill et al. 1963), while the simulations (Fedosov et al. 2011b) predict τ_y to be about 0.0017 Pa.

4.3 Blood structure and single-cell dynamics

The non-Newtonian viscosity and yield stress in blood arise from RBC deformability, dynamics, and inter-cell interactions. Simulations allow the examination of the structure and dynamics of the RBC suspension on the single cell level, while such information may be difficult or not feasible to obtain experimentally. The local microstructure of blood can be characterized by the radial distribution function (RDF) of RBC centers shown in Fig. 12(a) (Fedosov et al. 2011b). Except for the “correlation hole” at small distances $r \lesssim 2\,\mu\text{m}$ due to excluded volume interactions, no significant structures are found for the no-aggregation case over a wide range of shear rates. Only at small shear rates, a noticeable peak in the red solid curve is observed at $r = 8\,\mu\text{m}$, which corresponds to the long RBC diameter and indicates that neighboring RBCs have a preference for alignment with the flow. The other solid curves demonstrate that any microstructure fully disappears at higher shear rates, and therefore the shear-

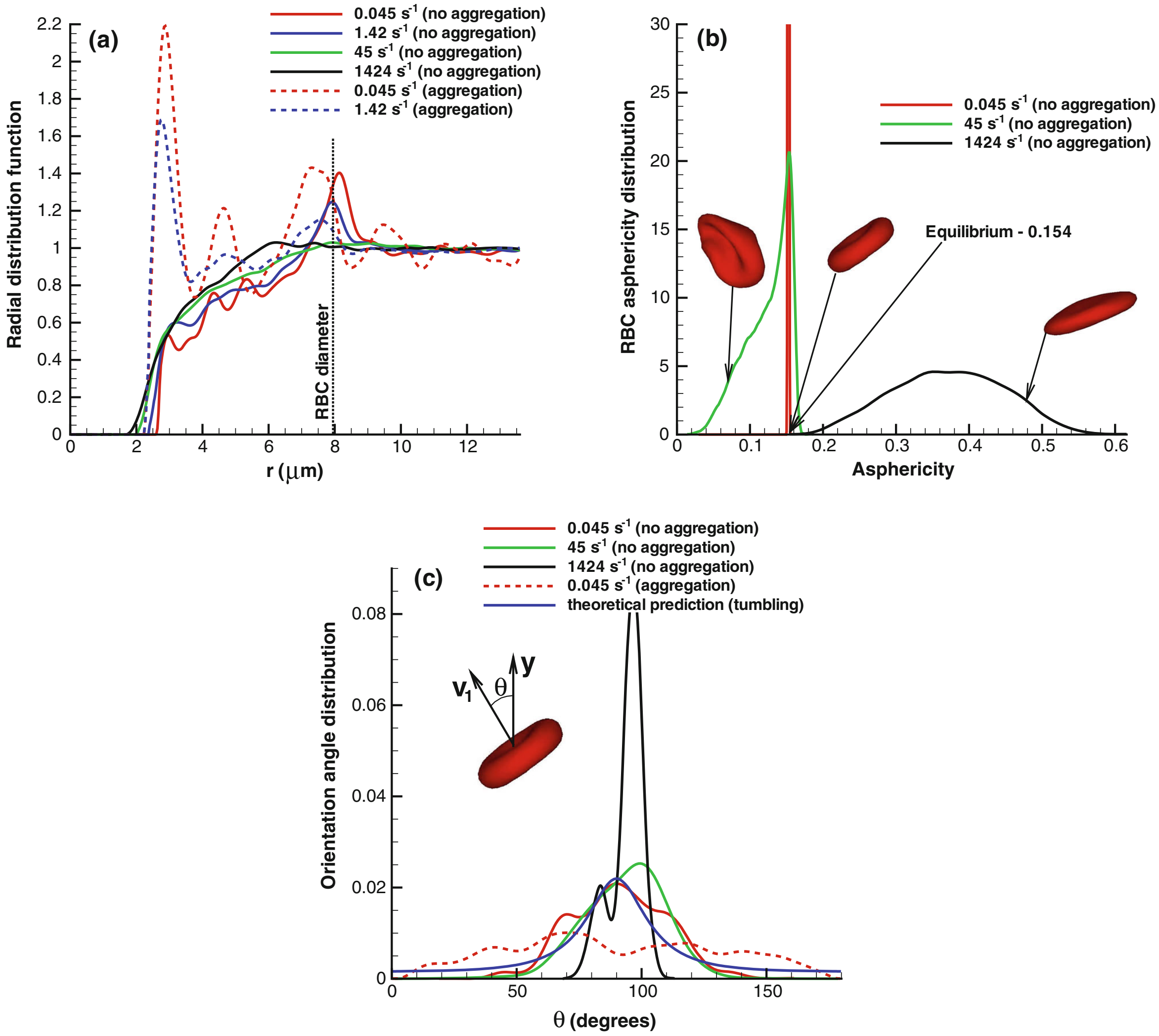

Fig. 12 Structural and dynamical properties of RBC suspension at $H_t = 0.45$ with sample snapshots of RBC conformations. (**a**) RBC suspension's structure characterized by the radial distribution function. (**b**) RBC asphericity distributions to describe cell deformations through the deviation from a spherical shape. The asphericity is defined as $[(\lambda_1 - \lambda_2)^2 + (\lambda_2 - \lambda_3)^2 + (\lambda_3 - \lambda_1)^2]/(2R_g^4)$, where $\lambda_1 \leq \lambda_2 \leq \lambda_3$ are the eigenvalues of the gyration tensor and $R_g^2 = \lambda_1 + \lambda_2 + \lambda_3$. The asphericity for a RBC in equilibrium is equal to 0.154. (**c**) Orientational angle distributions for various shear rates. The RBC orientational angle is defined by the angle between the eigenvector V_1 of the gyration tensor and the flow gradient direction (y). The theoretical prediction curve corresponds to the orientational angle distribution of a single tumbling RBC in shear flow calculated using the theory by Abkarian et al. (2007). Plots are reused with permission from Fedosov et al. (2011b)

thinning behavior of a non-aggregating RBC suspension is not related to microstructural changes. In contrast, the aggregating RBC suspension displays the presence of small RBC structures (2–4 RBCs) at low shear rates as indicated in the case of $\dot{\gamma} = 0.045\,\mathrm{s}^{-1}$ by the large peak at $r \simeq 3\,\mu\mathrm{m}$ in Fig. 12(a). An increase in the shear rate results in the gradual dispersion of rouleaux, while at high shear rates, observation indicates that any difference in microstructure has disappeared between the aggregating and non-aggregating RBC suspension. Thus, it is clear that it is the aggregation interactions between RBCs which lead to the steep increase in blood viscosity at low shear rates and to yield stress, since larger rouleaux structures have to be broken apart before blood is able to flow.

In Sect. 3.2, we discussed the dynamics of a single RBC in shear flow, which can be described by the tumbling motion at low shear rates and tank-treading motion at high shear rates. Similar RBC behavior is expected within a sheared cell suspension. Figure 12(b, c) illustrate average RBC deformation and dynamics in a suspension at different shear rates

(Fedosov et al. 2011b). At low shear rates, RBCs tumble, which is indicated by the nearly constant RBC asphericity of about 0.154 (equilibrium value for a discocyte shape) and by the broad orientation angle (θ) distribution in Fig. 12(c). Due to large cell crowding, RBC tumbling is slightly hindered in non-aggregating suspensions compared to the theoretical prediction of tumbling of a single RBC. RBC aggregation leads to a nearly uniform orientation angle distribution at low shear rates. At high shear rates, $\dot{\gamma} \gtrsim 200\,\mathrm{s}^{-1}$, RBCs transit to tank-treading motion characterized by a narrow θ distribution in Fig. 12(c). RBCs also strongly elongate, as indicated by the shift of the asphericity distribution to higher values in Fig. 12(b).

In the intermediate range of shear rates, between 5 and $200\,\mathrm{s}^{-1}$, RBCs experience strong deformations shown by a smaller RBC asphericity than that in equilibrium (Fig. 12(b)), which indicates that RBCs attain on average a more spherical shape and go through transient folded conformations. Note that RBC aggregation does not affect blood viscosity in this range of shear rates, and therefore a more spherical RBC shape leads to shear thinning through a reduction in shear stresses due to lower tumbling constraints in comparison with the biconcave RBC shape. Moreover, the tumbling-to-tank-treading transition further decreases the shear stresses resulting in shear thinning.

5 Blood flow and RBC clustering

5.1 Fahraeus–Lindqvist effect

The Fahraeus–Lindqvist effect (Fahraeus and Lindqvist 1931) describes a decrease in the apparent blood viscosity with decreasing tube diameter found in experiments of blood flow in glass tubes (Pries et al. 1992). The apparent viscosity is calculated as follows

$$\eta_{\mathrm{app}} = \frac{\pi \Delta P D^4}{128 Q L} = \frac{\Delta P D^2}{32 \bar{v} L}, \tag{4}$$

where $D = 2R_{\mathrm{cap}}$ is the tube diameter, Q is the flow rate, and $\Delta P/L$ is the pressure drop in a tube of length L. For higher hematocrit H_{T}, the apparent viscosity increases, since higher cell crowding leads to a larger flow resistance. For convenience, we define the relative apparent viscosity as

$$\eta_{\mathrm{rel}} = \frac{\eta_{\mathrm{app}}}{\eta_o}, \tag{5}$$

where η_o is the plasma viscosity. Figure 13 presents simulation results (Fedosov et al. 2010b) in comparison with the empirical fit to experiments (Pries et al. 1992) for tube diameters from 10 to 40 µm and H_{T} values in the range 0.15 to 0.45. Excellent agreement between simulations and experiments further supports the validity of the blood flow model and numerically verifies the Fahraeus–Lindqvist effect. Similar results for the Fahraeus–Lindqvist effect were also obtained in other simulation approaches, see Bagchi (2007), Doddi and Bagchi (2009), Freund and Orescanin (2011).

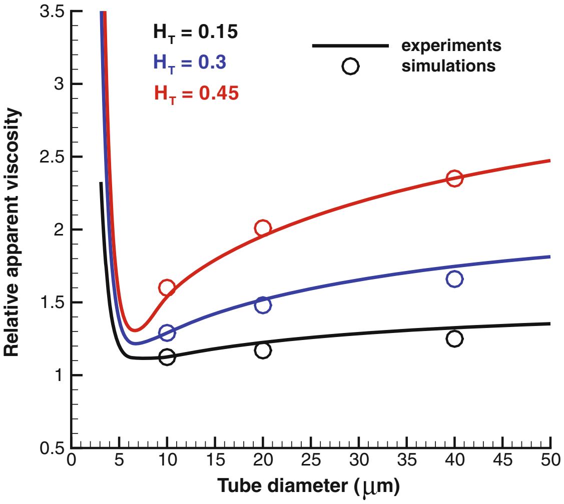

Fig. 13 Simulated relative apparent viscosity of blood (Fedosov et al. 2010b) in comparison with experimental data (Pries et al. 1992) for different H_{T} values and tube diameters

5.2 Cell-free layer

The cell-free layer (CFL) is a near-wall layer of blood plasma void of RBCs. In tube flow, RBCs migrate toward the tube center due to hydrodynamic interactions (lift force) with the wall, which results in a near-wall layer free of cells. The viscosity in the CFL region is nearly equal to the plasma viscosity, and thus much smaller than in the tube center populated with RBCs. The CFL serves as an effective lubrication layer for the viscous RBC core to flow. The thickness of the CFL is associated with the Fahraeus–Lindqvist effect such that in small tubes, the CFL thickness is comparable with the tube diameter resulting in a smaller relative apparent viscosity, while in larger tubes, the CFL thickness is negligible with respect to the tube diameter.

To calculate the CFL thickness δ in simulations, the outer edge of the RBC core is determined as shown in Fig. 14, which is similar to the experimental CFL measurements (Maeda et al. 1996; Kim et al. 2007). In this approach, the cell edge is obtained by projecting the RBC vertices of a simulation snapshot onto the x–y plane, and the curves of RBC core were fitted at the bottom and the top using the projected vertices with the smallest and largest y coordinates. The average distance from the wall to the cell edge is then taken to be the CFL thickness. Figure 15 presents CFLs for different tube diameters and H_{T} values in compari-

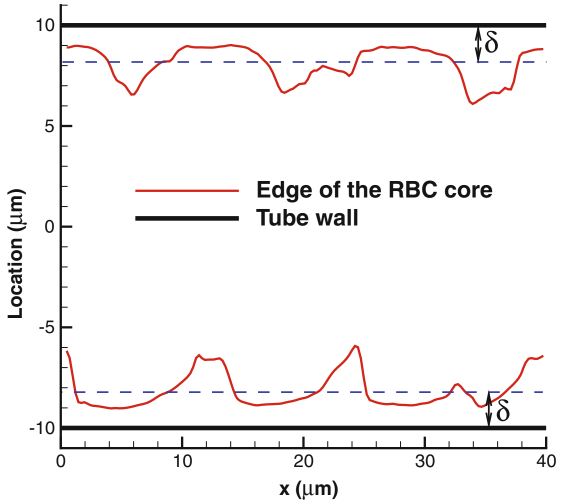

Fig. 14 An example of a CFL edge for $H_T = 0.45$ and $D = 20$ μm. Reused with permission from Fedosov et al. (2010b)

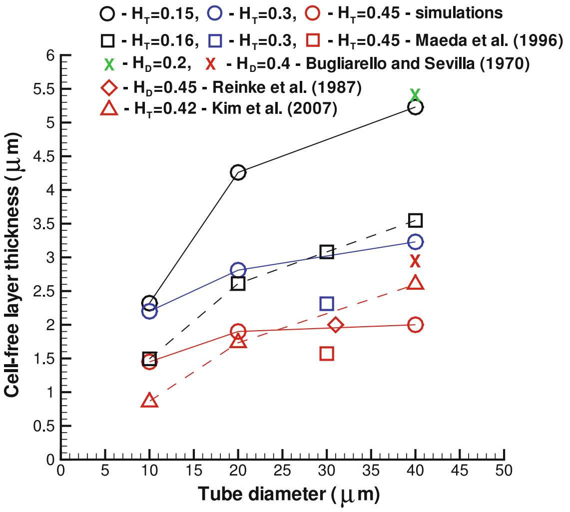

Fig. 15 CFLs obtained in blood flow simulations in comparison with experimental data (Maeda et al. 1996; Kim et al. 2007; Reinke et al. 1987; Bugliarello and Sevilla 1970) for various H_T values and tube diameters

son with in vitro experiments (Reinke et al. 1987; Bugliarello and Sevilla 1970) and in vivo experiments (Maeda et al. 1996; Kim et al. 2007). The CFL thicknesses δ are consistent with the Fahraeus–Lindqvist effect. CFLs are wider for lower H_T and larger tube diameters indicating migration of RBCs to the tube center.

The comparison of CFLs in simulations and experiments in Fig. 15 shows only partial agreement. An experimental in vitro study (Bugliarello and Sevilla 1970) of blood flow in glass tubes for controlled discharge hematocrits H_D (corresponding to tube hematocrits $H_T = 0.14$ and $H_T = 0.31$ with the empirical fit by Pries et al. (1992)) yields CFLs in good agreement with simulation results. Later experiments (Reinke et al. 1987) at higher hematocrit $H_D = 0.45$ in glass tubes provide CFL data which also agree well with simulation results. Note that simulations mimic blood flow in rigid and long tubes, and therefore in vitro data are best for comparison. CFLs from in vivo experiments (Maeda et al. 1996; Kim et al. 2007) display satisfactory agreement with the simulations for high H_T values, while for low H_T the comparison is rather poor. Note that available in vivo measurements of CFLs show a considerable scatter. The CFL in cat cerebral microvessels was found to be approximately 4 μm, independent of vessel diameter (Yamaguchi et al. 1992). Measurements of CFLs within a rabbit mesentery provide thicknesses in the range of 1.0–1.8 μm for vessel diameters 10–40 μm at $H_T = 0.45$ (Maeda et al. 1996). Finally, CFLs in the range of 0.5–3 μm, increasing with the tube diameter at $H_T = 0.42$, were reported in an experimental study, where a rat cremaster muscle was perfused (Kim et al. 2007). The scatter of in vivo CFL measurements and their discrepancies with simulations may be due to several reasons, such as the existence of the glycocalyx layer, variations in vessel width, use of a short vessel, close proximity of the site of CFL measurements to vessel bifurcations, vessel elasticity, and spatial resolution of the measurements (Fedosov et al. 2010b; Kim et al. 2007).

5.3 Clustering and alignment of RBCs in microcapillaries

In microcapillaries with diameters of 10 μm or less, the particulate nature of blood plays a particularly important role, because the cell and the capillary size are nearly the same. Therefore, in this regime, small variations of the capillary radius can lead to drastic changes in the arrangements of the cells and their flow behavior.

In dense suspensions of RBCs in narrow capillaries with radii $R_{\text{cap}}/R_0 = 1.23$ and 1.4, which correspond to diameters of 8.4 and 9.6 μm, respectively, three distinct phases are obtained in simulations (McWhirter et al. 2009, 2012), which are shown in Fig. 16: (a) Disordered biconcave-disk-shaped RBCs at low density and low velocity, (b) Parachute-shaped RBCs aligned in a single file at low density and high velocity, (c) Slipper-shaped RBCs arranged as two parallel interdigitated rows at high density. At the low density $R_0/L_{\text{ves}} \lesssim 0.7$, the RBCs show the transition from discocyte to parachute similar to the isolated RBCs in Sect. 3.3. At low velocities, however, the symmetry axes of the RBCs deviate from the perpendicular orientation to the capillary axis observed for single cells (see Sect. 3.3), due to the hydrodynamic interaction between the RBCs; instead, the RBC positions and the directions of their symmetry axes are rather randomly distributed. In contrast, the parachute-shaped RBCs at high flow velocities are aligned in a single file. This implies that the

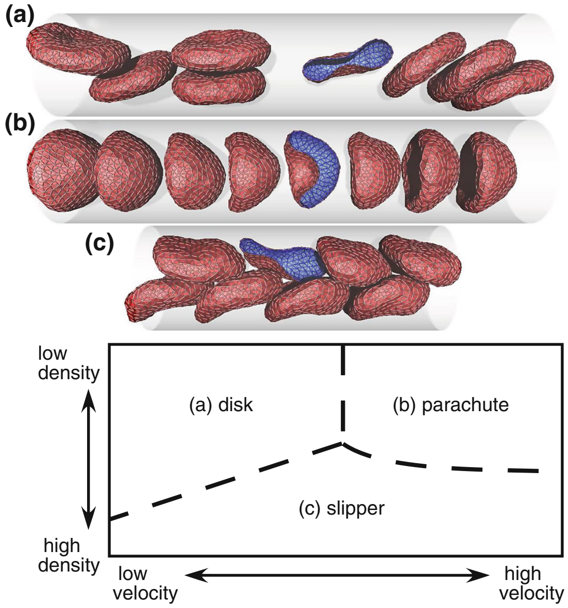

Fig. 16 Phase diagram of RBCs in dense suspension at $\kappa/k_BT = 20$, $\mu R_0^2/k_BT = 110$, and $R_{cap}/R_0 = 1.4$. (**a**) Disordered-discocyte phase. (**b**) Aligned-parachute phase. (**c**) Zigzag-slipper phase

RBCs move with nearly identical velocity. At high densities $R_0/L_{ves} \gtrsim 0.7$, the aligned-parachute phase becomes unstable and is replaced by the zigzag-slipper phase. The lift force from capillary wall and hydrodynamic interactions between neighboring RBCs stabilize the zigzag arrangement. When a parachute-shaped RBC comes close to the capillary wall due to thermal fluctuations, the next RBC moves toward the opposite side. Subsequently, the zigzag alignment propagates backwards.

For a wider capillary with $R_{cap}/R_0 = 1.58$, corresponding to a capillary diameter of 10.8 μm, the alignment is less pronounced and the boundaries between phases with different structural arrangements are blurred (McWhirter et al. 2012). Near a phase boundary, two structural arrangements often coexist. At high hematocrit, the interlocking rows of the zigzag alignment are intermittently replaced by an asymmetric distribution of RBCs in two rows, as shown in Fig. 17. Thus, a sufficiently small radius of the capillary is required to form clear aligned phase. The aligned-parachute and zigzag-slipper phase of RBCs have been observed experimentally in glass capillaries (Gaehtgens et al. 1980) and in microvessels (Skalak 1969).

The hydrodynamic interactions between RBCs can induce clustering of the parachute-shaped RBCs even at hematocrits $H_T < 0.1$. Long-lived clusters are observed in simulations—*without* attractive interactions between RBCs—when the flow velocity is large enough to induce parachute shapes of single RBCs, shown in Fig. 18 (McWhirter et al. 2009, 2011).

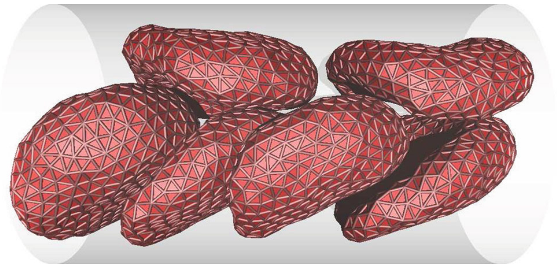

Fig. 17 The asymmetric slipper phase of RBCs with $\kappa/k_BT = 20$ and $\mu R_0^2/k_BT = 110$, in microcapillaries of radius $R_{cap}/R_0 = 1.58$ at hematocrit $H_T = 0.37$

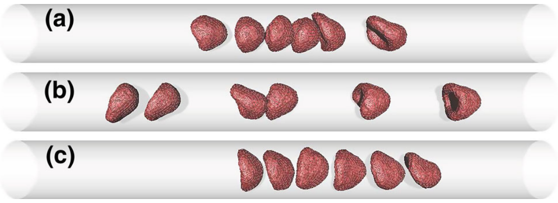

Fig. 18 Sequential snapshots of six RBCs in dilute suspension at $\kappa/k_BT = 20$, $\mu R_0^2/k_BT = 110$, and $R_{cap}/R_0 = 1.58$. Clusters of RBCs are formed

Cluster stability increases with increasing flow velocity. At velocity close to the threshold of the discocyte–parachute transition, the front RBC often detaches from the cluster, and therefore the size of the clusters is strongly fluctuating. It is interesting to notice that RBCs in a cluster are not touching each other, but remain at a finite, rather well-defined distance.

Two physical mechanisms are responsible for the formation and stability of such clusters. First, in the clusters, the shear stress on a RBC is partially shielded by other RBCs, so that the RBCs are less deformed than isolated single RBCs. Thus, a single RBC can move a little faster with the flow, catch up with a cluster in front, and thereby contribute to cluster growth. Second, the fluid flow in the microcapillary induces a fluid vortex (called "bolus") between neighboring RBCs (Wang and Skalak 1969; Goldsmith and Skalak 1975), which keeps the cells at a distance comparable to the RBC size. The formation of a bolus can be understood most easily by considering a co-moving reference frame with the RBCs in the cluster. In the stationary state, the parachute-shaped RBCs move like solid objects, while the flow near the wall moves "backwards" with high velocity; this induces a vortex-like flow between the RBCs—the bolus.

6 White blood cell and platelet margination

White blood cells (WBCs) participate in the organism defense against various infections. To perform their function, WBCs are able to adhere to the vascular endothelium

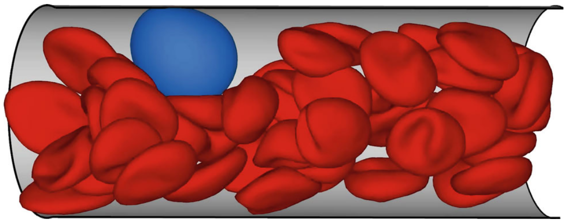

Fig. 19 A simulation snapshot of WBC margination in tube flow with diameter $D = 20\ \mu$m at $H_T = 0.45$. The marginated WBC is plotted in *blue*. The flow is from *left* to *right*

(Alon et al. 1995) and transmigrate into the surrounding tissue (Springer 1995). WBC adhesion is only possible if they are in close proximity (a few tens of nanometers) to a vessel wall. Migration of WBCs to the vessel walls is called margination (Bagge and Karlsson 1980; Goldsmith and Spain 1984; Firrell and Lipowsky 1989), and this process is facilitated by flowing RBCs in blood. As we discussed in Sect. 5, RBCs migrate to the vessel center due to cell-wall hydrodynamic interactions (lift force) (Messlinger et al. 2009; Cantat and Misbah 1999; Sukumaran and Seifert 2001; Abkarian et al. 2002). The lift force on RBCs is larger than that on WBCs because of the non-spherical biconcave shape and deformability of RBCs. These interactions are believed to lead to the margination of WBCs in microvessels shown in Fig. 19 such that WBCs remain mostly near a wall (Goldsmith and Spain 1984; Firrell and Lipowsky 1989) in blood flow, and therefore they have high chances for adhesion whenever necessary.

It is plausible to expect that WBC margination is affected by various blood flow properties including hematocrit H_T, local flow rate and geometry, and RBC aggregation (Freund 2007; Fedosov et al. 2012; Bagge and Karlsson 1980; Firrell and Lipowsky 1989; Pearson and Lipowsky 2000; Abbitt and Nash 2003; Jain and Munn 2009). For instance, an increase in WBC adhesion (and therefore also margination) was observed with decreasing flow rate at relatively high $H_T > 0.45$ in in vivo experiments in mesenteric venules of rat (Firrell and Lipowsky 1989). However, recent in vitro experiments in microfluidic channels (Jain and Munn 2009) have identified an intermediate range of $H_T \simeq 0.2$–0.3, where the strongest WBC margination occurs. In contrast, the experiments on WBC adhesion in glass capillaries (Abbitt and Nash 2003) showed no dependence of WBC adhesion and margination on H_T. It has been also found consistently that WBC margination and adhesion is enhanced at low flow rates and due to RBC aggregation interactions (Firrell and Lipowsky 1989; Pearson and Lipowsky 2000; Abbitt and Nash 2003; Jain and Munn 2009).

Adhesive dynamics of WBCs on a surface have been studied in simulations (King and Hammer 2001; Khismatullin and Truskey 2005; Jadhav et al. 2005; Korn and Schwarz 2008) under a flow without RBCs, and therefore the WBC margination effect was not considered. 2D simulations (Sun et al. 2003) with rigid discoidal RBCs and a circular WBC qualitatively showed that flowing RBCs participate in WBC margination. In the other 2D numerical study with deformable, and therefore more realistic, cells (Freund 2007), it was quantitatively shown that WBC margination is enhanced with decreasing flow rate, in agreement with the available experiments. However, these simulations claimed virtually no dependence of WBC margination on H_T. In addition, WBC margination has been found to be relatively insensitive to RBC deformability, which suggests that the RBC discoidal shape mainly determines the lift force on a RBC (Freund 2007). Recent 2D simulation study (Fedosov et al. 2012) considered WBC margination for wide ranges of flow rates and H_T values as well as for RBC aggregation. Attenuation of WBC margination with increasing flow rate has been found to be consistent with previous numerical and experimental studies (Freund 2007; Firrell and Lipowsky 1989; Pearson and Lipowsky 2000; Jain and Munn 2009); however, a pronounced effect of H_T on WBC margination has been identified such that it first increases with increasing hematocrit, but then decreases again at higher hematocrits (Fedosov et al. 2012). These results are in good agreement with the experiments on WBC margination in rectangular microchannels (Jain and Munn 2009), where WBC margination was optimal in the range $H_T = 0.2$–0.3. The results of Fedosov et al. (2012) have also provided an explanation for the seeming independence of WBC margination and adhesion on H_T found in previous simulations (Freund 2007) and experiments (Abbitt and Nash 2003), such that considered flow rates and H_t values used by Abbitt and Nash (2003), Freund (2007) were almost entirely within the region of strong WBC margination. Moreover, WBC deformability has a strong effect on margination since a deformed WBC may significantly depart from the spherical shape, and RBC aggregation enhances WBC margination at high H_T values (Fedosov et al. 2012).

Platelets take part in the hemostasis, a process which stops bleeding from an injured vessel. This process also requires platelets to be marginated to the vessel walls such that their concentration is high enough in the near-wall layer (Tangelder et al. 1985). The platelet margination process is similar to that for WBCs, where RBCs expel the other cells from the vessel center to the wall. However, in comparison with WBCs, platelets are much smaller and relatively rigid; also they possess an ellipsoid-like shape. Therefore, the physical mechanisms of margination as well as the margination dependence on various blood flow properties may be different for platelets and WBCs. Recent 2D simulations (Crowl and Fogelson 2010, 2011) found that a near-wall platelet excess develops more quickly at high flow rates, while platelet concentration next to the wall is dependent on H_T. Another theoretical investigation (Tokarev et al. 2011) suggests that finite size of platelets may be responsible for the platelet margination effect due to excluded volume interactions between platelets and RBCs and to the shear dispersion of platelets in flow. 3D simulations of platelet margination in microvessels (Zhao and Shaqfeh 2011b) demonstrated their migration toward the vessel walls, which was explained by the platelet expulsion effect and their enhanced lateral diffusivity in blood flow.

7 Modeling hematologic diseases and disorders

Hematologic diseases and disorders such as hypertension, atherosclerosis, malaria, sickle cell anemia may strongly alter normal blood circulation. One of the most common problems in hematologic diseases and disorders is a change in shape, structure, and viscoelastic properties of individual RBCs. For example, RBCs infected by the Plasmodium falciparum (Pf) parasite in malaria are subject to a tenfold increase in their membrane shear modulus and a spherical shape at the later stages of the intra-cell parasite development (Shelby et al. 2003; Diez-Silva et al. 2010). In addition, infected RBCs in malaria become adhesive and may bind to endothelium and other healthy or parasitized cells (Brown et al. 1999) leading blood flow obstructions in small vessels (Shelby et al. 2003). Another example is sickle cell anemia, which is a blood disorder where polymerized hemoglobin causes irreversible changes to RBC shape and deformability. These changes may result in blood flow occlusion in the microcirculation (Diez-Silva et al. 2010; Higgins et al. 2007). Other hematologic diseases with similar effects are spherocytosis and elliptocytosis (Beck 1991).

The mechanics of Pf-RBCs in malaria was simulated by Fedosov et al. (2011c), Fedosov et al. (2011a), Hosseini and Feng (2012); the results are in agreement with optical tweezers experiments (Suresh et al. 2005) for different stages of intra-RBC parasite development. To characterize the increase in blood flow resistance in malaria, a Poiseuille flow of a suspension of healthy and Pf-RBCs at the trophozoite stage (the second stage of intra-cell parasite development with five times larger membrane shear modulus than that of healthy RBCs) was simulated by Fedosov et al. (2011c). Margination of a Pf-RBC and hemodynamic resistance in microvessels have been also investigated by Imai et al. (2010, 2011). Figure 20 shows the relative apparent viscosity of malaria-infected blood for different parasitemia levels (percentage of Pf-RBCs with respect to the total number of cells in a unit volume) and tube diameters. The effect of parasitemia level on measured flow resistance appears to be more significant for small diameters and high H_T values. For instance, at $H_T = 0.45$, blood flow resistance in malaria may increase up to 50 % in vessels with diameters around 10 μm, while for vessel diameters close to 20 μm, the resistance may go up by not more than about 43 %. These simulations do not include the effects of cytoadhesion, which may strongly affect blood flow resistance especially in small vessels. Adhesive dynamics of Pf-RBCs at a coated surface has been investigated by Fedosov et al. (2011c,d), where a flipping behavior of Pf-RBC was found, similar to the experimental observations (Antia et al. 2007). In other studies (Quinn et al. 2011; Bow et al. 2011), the flow properties and deformation of Pf-RBCs within microfluidic devices were investigated.

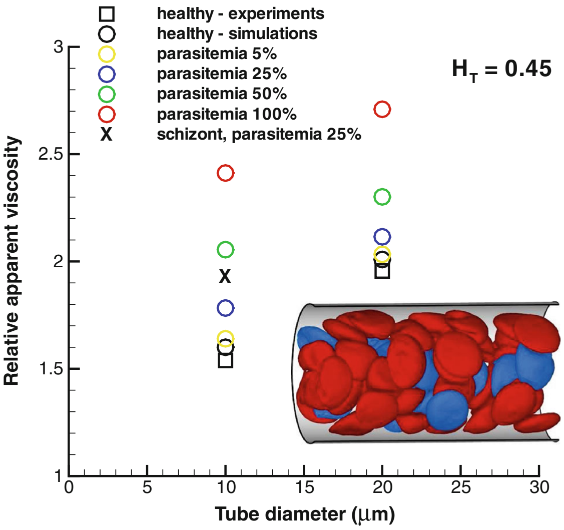

Fig. 20 Relative apparent viscosity of blood in malaria for various parasitemia levels (percentage of Pf-RBCs with respect to the total number of cells in a unit volume) and tube diameters. The *multiplication symbol* denotes the schizont stage (the latest stage of intra-cell parasite development) with a nearly spherical shape. Experimental data are from the empirical fit by Pries et al. (1992) for healthy blood. The *inset* shows blood flow in malaria with healthy (*red*) and Pf-RBCs (*blue*) in a tube of diameter 20 μm, $H_T = 0.45$, and parasitemia level 25 %. Reused with permission from Fedosov et al. (2011c)

Recent simulations of RBCs and blood in sickle cell anemia (Lei and Karniadakis 2012a,b) took into account complex changes of RBC shapes. RBC morphology, and the viscosity of sickled blood in shear and tube flows have been investigated. It has been found that blood flow occlusion occurs in sickle cell disorder under the condition of intercell and cell-wall adhesive interactions. These results serve as the first steps in realistic modeling of the processes in sickle cell anemia.

8 Conclusions and outlook

The models and results presented in this review demonstrate that state-of-the-art RBC and blood modeling accurately captures RBC mechanics, rheology, and dynamics. This computational framework for the modeling of blood flow on the cellular level is very general and can be employed to investigate other cell, vesicle, and capsule suspensions with potential usage in biology, medicine, and engineering. The suspension properties may be tuned to yield a desired behavior by changing the solvent viscosity, material properties of suspended cells, and inter-cell interactions.

This opens up the possibility for several new directions in the future. First, the accurate predictions of the non-Newtonian behavior of cell suspensions from simulations allow further explorations of blood rheology and other cell suspensions. For instance, abnormal rheological behavior of blood can be associated with many diseases such as deep venous thrombosis, atherosclerosis, AIDS, myeloma, and diabetes mellitus, which may appear at various sites of the cardiovascular system (Dintenfass 1980; Lowe 1998; Robertson et al. 2008; Franceschini et al. 2010). Such rheological measurements had virtually no theoretical guidelines for their interpretation. Experiments on single cells (Bao and Suresh 2003) are able to provide a base for modeling of various cells, which would also include abnormal and diseased cells. Then, simulations of their suspensions in combination with the inter-cell interactions would allow for quantitative comparisons with experimental rheological measurements and a guidance of clinical measurements for a better diagnosis (Franceschini et al. 2010). Second, blood mediates many different functions in the body including the transport of oxygen, many proteins, and cells, which play essential role in various body processes. These processes do not occur independently of each other, but they might be intimately connected, as shown recently for the link between RBC dynamics, shear viscosity, and ATP release (Forsyth et al. 2011). Cell-level blood flow simulations can play an important role in understanding the intricate interplay between the relevant blood components. Third, microfluidic devices have been developed for the sorting of different blood components, in particular for the separation of pathogens and diseased cells from healthy cells (Abkarian et al. 2006; Davis et al. 2006; Inglis et al. 2008; Hou et al. 2010; Holm et al. 2011). The development and optimization of new devices will strongly benefit from modeling and simulations of realistic flow in microfluidic channels.

The predictive capability of accurate modeling of cell and capsule suspensions can readily be extended to a variety of engineering and material science applications. Such simulations may aid in the development of new soft materials and may drive the tuning process and optimization of their properties. Accurate modeling of such suspensions opens up great opportunities, since simulations are usually more robust and significantly cheaper than equivalent large sets of experimental tests. Moreover, rapid development of the computational capacity of modern supercomputers allows to perform very large and sophisticated simulations, which can closely mimic, extend, or even replace various experimental systems.

Acknowledgments We would like to acknowledge support by the German Science Foundation (DFG) through the research unit FOR 1543, “Shear flow regulation of hemostasis—bridging the gap between nanomechanics and clinical presentation (SHENC)”. We thank the Jülich Supercomputing Centre (JSC) at the Forschungszentrum Jülich for providing computer resources. D.A.F. acknowledges funding by the Alexander von Humboldt Foundation.

References

Abbitt KB, Nash GB (2003) Rheological properties of the blood influencing selectin-mediated adhesion of flowing leukocytes. Am J Physiol 285:H229–H240

Abkarian M, Lartigue C, Viallat A (2002) Tank treading and unbinding of deformable vesicles in shear flow: determination of the lift force. Phys Rev Lett 88:068103

Abkarian M, Faivre M, Stone HA (2006) High-speed microfluidic differential manometer for cellular-scale hydrodynamics. Proc Natl Acad Sci USA 103:538–542

Abkarian M, Faivre M, Viallat A (2007) Swinging of red blood cells under shear flow. Phys Rev Lett 98:188302

Abkarian M, Faivre M, Horton R, Smistrup K, Best-Popescu CA, Stone HA (2008) Cellular-scale hydrodynamics. Biomed Mater 3:034011

Ahlrichs P, Dünweg B (1999) Simulation of a single polymer chain in solution by combining lattice Boltzmann and molecular dynamics. J Chem Phys 111:8225–8239

Allen MP, Tildesley DJ (1987) Computer simulation of liquids. Clarendon Press, New York

Alon R, Hammer DA, Springer TA (1995) Lifetime of the P-selectin-carbohydrate bond and its response to tensile force in hydrodynamic flow. Nature (London) 374:539–542

Antia M, Herricks T, Rathod PK (2007) Microfluidic modeling of cell-cell interactions in malaria pathogenesis. PLoS Pathogens 3(7):939–945

Bagchi P, Popel AS, Johnson PC (2005) Computational fluid dynamic simulation of aggregation of deformable cells in a shear flow. J Biomech Eng 127(7):1070–1080

Bagchi P (2007) Mesoscale simulation of blood flow in small vessels. Biophys J 92:1858–1877

Bagge U, Karlsson R (1980) Maintenance of white blood cell margination at the passage through small venular junctions. Microvasc Res 20:92–95

Bao G, Suresh S (2003) Cell and molecular mechanics of biological materials. Nature Mater 2:715–725

Beaucourt J, Rioual F, Séon T, Biben T, Misbah C (2004) Steady to unsteady dynamics of a vesicle in a flow. Phys Rev E 69:011906

Beck WS (ed) (1991) Hematology, 5th edn. MIT Press, Cambridge

Biben T, Kassner K, Misbah C (2005) Phase-field approach to three-dimensional vesicle dynamics. Phys Rev E 72:041921

Bow H, Pivkin IV, Diez-Silva M, Goldfless SJ, Dao M, Niles JC, Suresh S, Han J (2011) A microfabricated deformability-based flow cytometer with application to malaria. Lab Chip 11:1065–1073

Brown H, Hien TT, Day N, Mai NTH, Chuong LV, Chau TTH, Loc PP, Phu NH, Bethe D, Farrar J, Gatter K, White N, Turner G (1999) Evidence of blood-brain barrier dysfunction in human cerebral malaria. Neuropathol Appl Neurobiol 25(4):331–340

Bugliarello G, Sevilla J (1970) Velocity distribution and other characteristics of steady and pulsatile blood flow in fine glass tubes. Biorheology 7:85–107

Cantat I, Misbah C (1999) Lift force and dynamical unbinding of adhering vesicles under shear flow. Phys Rev Lett 83:880–883

Chien S, Usami S, Taylor HM, Lundberg JL, Gregersen MI (1966) Effects of hematocrit and plasma proteins on human blood rheology at low shear rates. J Appl Physiol 21(1):81–87

Chien S, Usami S, Kellenback RJ, Gregersen MI (1970) Shear-dependent interaction of plasma proteins with erythrocytes in blood rheology. Am J Physiol 219(1):143–153

Chien S, Sung LA, Kim S, Burke AM, Usami S (1977) Determination of aggregation force in rouleaux by fluid mechanical technique. Microvasc Res 13:327–333

Cokelet G, Merrill EW, Gilliland ER, Shin H, Britten A, Wells JRE (1963) The rheology of human blood-measurement near and at zero shear rate. Trans Soc Rheol 7:303–317

Copley AL, Huang CR, King RG (1973) Rheogoniometric studies of whole human blood at shear rates from 1,000–0.0009 sec^{-1}. Part I. Experimental findings. Biorheology 10:17–22

Crowl L, Fogelson AL (2010) Computational model of whole blood exhibiting lateral platelet motion induced by red blood cells. Int J Numer Methods Biomed Eng 26:471–487

Crowl L, Fogelson AL (2011) Analysis of mechanisms for platelet near-wall excess under arterial blood flow conditions. J Fluid Mech 676:348–375

Dao M, Li J, Suresh S (2006) Molecularly based analysis of deformation of spectrin network and human erythrocyte. Mater Sci Eng C 26:1232–1244

Davis JA, Inglis DW, Morton KM, Lawrence DA, Huang LR, Chou SY, Sturm JC, Austin RH (2006) Deterministic hydrodynamics: taking blood apart. Proc Natl Acad Sci USA 103:14779

Deuling HJ, Helfrich W (1976) Red blood cell shapes as explained on the basis of curvature elasticity. Biophys J 16:861–868

Diez-Silva M, Dao M, Han J, Lim CT, Suresh S (2010) Shape and biomechanical characteristics of human red blood cells in health and disease. MRS Bull 35:382–388

Dintenfass L (1980) Molecular rheology of human blood; its role in health and disease (today and tomorrow). In: Astarita G, Marrucci G, Nicilais L (eds) Proceedings of 8th international congress on rheology (Naples), vol 3, pp 467–480.

Discher DE, Mohandas N, Evans EA (1994) Molecular maps of red cell deformation: hidden elasticity and in situ connectivity. Science 266:1032–1035

Discher DE, Boal DH, Boey SK (1998) Simulations of the erythrocyte cytoskeleton at large deformation. II. Micropipette aspiration. Biophys J 75(3):1584–1597

Doddi SK, Bagchi P (2009) Three-dimensional computational modeling of multiple deformable cells flowing in microvessels. Phys Rev E 79:046318

Du Q, Liu C, Wang X (2004) A phase field approach in the numerical study of the elastic bending energy for vesicle membranes. J Comput Phys 198:450–468

Dupin MM, Halliday I, Care CM, Alboul L, Munn LL (2007) Modeling the flow of dense suspensions of deformable particles in three dimensions. Phys Rev E 75(6):066707

Ermak DL, McCammon JA (1978) Brownian dynamics with hydrodynamic interactions. J Chem Phys 69:1352–1360

Espanol P, Warren P (1995) Statistical mechanics of dissipative particle dynamics. Europhys Lett 30(4):191–196

Fahraeus R (1929) The suspension stability of blood. Physiol Rev 9:241–274

Fahraeus R, Lindqvist T (1931) Viscosity of blood in narrow capillary tubes. Am J Phys 96:562–568

Fedosov DA, Caswell B, Karniadakis GE (2010a) A multiscale red blood cell model with accurate mechanics, rheology, and dynamics. Biophys J 98(10):2215–2225

Fedosov DA, Caswell B, Popel AS, Karniadakis GE (2010b) Blood flow and cell-free layer in microvessels. Microcirculation 17:615–628

Fedosov DA, Caswell B, Karniadakis GE (2010c) Systematic coarse-graining of spectrin-level red blood cell models. Comput Methods Appl Mech Eng 199:1937–1948

Fedosov DA, Lei H, Caswell B, Suresh S, Karniadakis GE (2011a) Multiscale modeling of red blood cell mechanics and blood flow in malaria. PLoS Comput Biol 7:e1002270

Fedosov DA, Pan W, Caswell B, Gompper G, Karniadakis GE (2011b) Predicting human blood viscosity in silico. Proc Natl Acad Sci USA 108:11772–11777

Fedosov DA, Caswell B, Suresh S, Karniadakis GE (2011c) Quantifying the biophysical characteristics of plasmodium-falciparum-parasitized red blood cells in microcirculation. Proc Natl Acad Sci USA 108:35–39

Fedosov DA, Caswell B, Karniadakis GE (2011d) Wall shear stress-based model for adhesive dynamics of red blood cells in malaria. Biophys J 100(9):2084–2093

Fedosov DA, Fornleitner J, Gompper G (2012) Margination of white blood cells in microcapillary flow. Phys Rev Lett 108:028104

Finken R, Lamura A, Seifert U, Gompper G (2008) Two-dimensional fluctuating vesicles in linear shear flow. Eur Phys J E 25:309–321

Firrell JC, Lipowsky HH (1989) Leukocyte margination and deformation in mesenteric venules of rat. Am J Physiol 256:H1667–H1674

Fischer TM (2004) Shape memory of human red blood cells. Biophys J 86(5):3304–3313

Fischer TM (2007) Tank-tread frequency of the red cell membrane: dependence on the viscosity of the suspending medium. Biophys J 93(7):2553–2561

Forsyth AM, Wan J, Owrutsky PD, Abkarian M, Stone HA (2011) Multiscale approach to link red blood cell dynamics, shear viscosity, and ATP release. Proc Natl Acad Sci USA 108:10986–10991

Franceschini E, Yu FT, Destrempes F, Cloutier G (2010) Ultrasound characterization of red blood cell aggregation with intervening attenuating tissue-mimicking phantoms. J Acoust Soc Am 127:1104–1115

Freund JB (2007) Leukocyte margination in a model microvessel. Phys Fluids 19:023301

Freund JB, Orescanin MM (2011) Cellular flow in a small blood vessel. J Fluid Mech 671:466–490

Fung YC (1993) Biomechanics: mechanical properties of living tissues, 2nd edn. Springer, New York

Gaehtgens P, Dührssen C, Albrecht KH (1980) Motion, deformation, and interaction of blood cells and plasma during flow through narrow capillary tubes. Blood Cells 6:799–812

Goldsmith HL, Skalak R (1975) Hemodynamics. Annu Rev Fluid Mech 7:213–247

Goldsmith HL, Spain S (1984) Margination of leukocytes in blood flow through small tubes. Microvasc Res 27:204–222

Gompper G, Kroll DM (1996) Random surface discretizations and the renormalization of the bending rigidity. J Phys I France 6:1305–1320

Gompper G, Kroll DM (1997) Network models of fluid, hexatic and polymerized membranes. J Phys Condens Matter 9: 8795–8834

Gompper G, Kroll DM (2004) Triangulated-surface models of fluctuating membranes. In: Nelson DR, Piran T, Weinberg S (eds) Statistical mechanics of membranes and surfaces, 2nd edn. World Scientific, Singapore, pp 359–426

Gompper G, Ihle T, Kroll DM, Winkler RG (2009) Multi-particle collision dynamics: a particle-based mesoscale simulation approach to the hydrodynamics of complex fluids. Adv Polym Sci 221:1–87

Helfrich W (1973) Elastic properties of lipid bilayers: theory and possible experiments. Z. Naturforschung C 28:693–703

Henon S, Lenormand G, Richert A, Gallet F (1999) A new determination of the shear modulus of the human erythrocyte membrane using optical tweezers. Biophys J 76:1145–1151

Higgins JM, Eddington DT, Bhatia SN, Mahadevan L (2007) Sickle cell vasoocclusion and rescue in a microfluidic device. Proc Natl Acad Sci USA 104(51):20496–20500

Holm SH, Beech JP, Barrett MP, Tegenfeldt JO (2011) Separation of parasites from human blood using deterministic lateral displacement. Lab Chip 11:1326–1332

Hoogerbrugge PJ, Koelman JMVA (1992) Simulating microscopic hydrodynamic phenomena with dissipative particle dynamics. Europhys Lett 19(3):155–160

Hosseini SM, Feng JJ (2012) How malaria parasites reduce the deformability of infected RBC. Biophys J 103:1–10

Hou HW, Bhagat AAS, Chong AGL, Mao P, Tan KSW, Han J, Lim CT (2010) Deformability based cell margination–a simple microfluidic design for malaria-infected erythrocyte separation. Lab Chip 10:2605–2613

Imai Y, Kondo H, Ishikawa T, Lim CT, Yamaguchi T (2010) Modeling of hemodynamics arising from malaria infection. J Biomech 43:1386–1393

Imai Y, Nakaaki K, Kondo H, Ishikawa T, Lim CT, Yamaguchi T (2011) Margination of red blood cells infected by Plasmodium falciparum in a microvessel. J Biomech 44:1553–1558

Inglis DW, Davis JA, Zieziulewicz TJ, Lawrence DA, Austin RH, Sturm JC (2008) Determining blood cell size using microfluidic hydrodynamics. J Immunol Methods 329:151–156

Jadhav S, Eggleton CD, Konstantopoulos K (2005) A 3-D computational model predicts that cell deformation affects selectin-mediated leukocyte rolling. Biophys J 88:96–104

Jain A, Munn LL (2009) Determinants of leukocyte margination in rectangular microchannels. PLoS ONE 4:e7104

Janoschek F, Toschii F, Harting J (2010) Simplified particulate model for coarse-grained hemodynamics simulations. Phys Rev E 82:056710

Kaoui B, Ristow GH, Cantat I, Misbah C, Zimmermann W (2008) Lateral migration of a two-dimensional vesicle in unbounded Poiseuille flow. Phys Rev E 77:021903

Kaoui B, Biros G, Misbah C (2009) Why do red blood cells have asymmetric shapes even in a symmetric flow? Phys Rev Lett 103: 188101

Kaoui B, Biros G, Misbah C (2011) Complexity of vesicle microcirculation. Phys Rev E 84:041906

Kaoui B, Krüger T, Harting J (2012) How does confinement affect the dynamics of viscous vesicles and red blood cells? Soft Matter 8:9246–9252

Kapral R (2008) Multiparticle collision dynamics: simulation of complex systems on mesoscales. Adv Chem Phys 140:89–146

Keller SR, Skalak R (1982) Motion of a tank-treading ellipsoidal particle in a shear flow. J Fluid Mech 120:27–47

Khismatullin DB, Truskey GA (2005) Three-dimensional numerical simulation of receptor-mediated leukocyte adhesion to surfaces: effects of cell deformability and viscoelasticity. Phys. Fluids 17:031505

Kim S, Long LR, Popel AS, Intaglietta M, Johnson PC (2007) Temporal and spatial variations of cell-free layer width in arterioles. Am J Physiol 293:H1526–H1535

King MR, Hammer DA (2001) Multiparticle adhesive dynamics: Hydrodynamic recruitment of rolling leukocytes. Proc Natl Acad Sci USA 98:14919–14924

Korn CB, Schwarz US (2008) Dynamic states of cells adhering in shear flow: from slipping to rolling. Phys Rev E 77(4):041904

Krüger T, Varnik F, Raabe D (2011) Particle stress in suspensions of soft objects. Philos Trans R Soc A 369:2414–2421

Lei H, Karniadakis GE (2012a) Predicting the morphology of sickle red blood cells using coarse-grained models of intracellular aligned hemoglobin polymers. Soft Matter 8:4507–4516

Lei H, Karniadakis GE (2012b) Quantifying the rheological and hemodynamic characteristics of sickle cell anemia. Biophys J 102: 185–194

Li J, Dao M, Lim CT, Suresh S (2005) Spectrin-level modeling of the cytoskeleton and optical tweezers stretching of the erythrocyte. Biophys J 88:3707–3719

Liu Y, Liu WK (2006) Rheology of red blood cell aggregation by computer simulation. J Comput Phys 220:139–154

Lowe GDO (1998) Clinical blood rheology, vol I. CRC Press, Boca Raton, FL, II

Lucy LB (1977) A numerical approach to testing the fission hypothesis. Astron J 82:1013–1024

MacMeccan RM, Clausen JR, Neitzel GP, Aidun CK (2009) Simulating deformable particle suspensions using a coupled lattice-Boltzmann and finite-element method. J Fluid Mech 618:13–39

Maeda N, Suzuki Y, Tanaka J, Tateishi N (1996) Erythrocyte flow and elasticity of microvessels evaluated by marginal cell-free layer and flow resistance. Am J Physiol 271(6):H2454–H2461

Malevanets A, Kapral R (1999) Mesoscopic model for solvent dynamics. J Chem Phys 110(17):8605–8613

McWhirter JL, Noguchi H, Gompper G (2009) Flow-induced clustering and alignment of vesicles and red blood cells in microcapillaries. Proc Natl Acad Sci USA 106(15):6039–6043

McWhirter JL, Noguchi H, Gompper G (2011) Deformation and clustering of red blood cells in microcapillary flows. Soft Matter 7:10967–10977

McWhirter JL, Noguchi H, Gompper G (2012) Ordering and arrangement of deformed red blood cells in flow through microcapillaries. New J Phys 14:085026

Melchionna S (2011) A model for red blood cells in simulations of large-scale blood flows. Macromol Theory Simul 20: 548–561

Merrill EW, Gilliland ER, Cokelet G, Shin H, Britten A, Wells JRE (1963) Rheology of human blood near and at zero flow. Biophys J 3:199–213

Merrill EW, Gilliland ER, Lee TS, Salzman EW (1966) Blood rheology: effect of fibrinogen deduced by addition. Circ Res 18:437–446

Messlinger S, Schmidt B, Noguchi H, Gompper G (2009) Dynamical regimes and hydrodynamic lift of viscous vesicles under shear. Phys Rev E 80:011901

Misbah C (2006) Vacillating breathing and tumbling of vesicles under shear flow. Phys Rev Lett 96:028104

Mohandas N, Evans E (1994) Mechanical properties of the red cell membrane in relation to molecular structure and genetic defects. Annu Rev Biophys Biomol Struct 23:787–818

Monaghan JJ (2005) Smoothed particle hydrodynamics. Rep Progress Phys 68:1703–1759

Noguchi H, Gompper G (2004) Fluid vesicles with viscous membranes in shear flow. Phys Rev Lett 93:258102

Noguchi H, Gompper G (2005a) Shape transitions of fluid vesicles and red blood cells in capillary flows. Proc Natl Acad Sci USA 102(40):14159–14164

Noguchi H, Gompper G (2005b) Dynamics of fluid vesicles in shear flow: effect of the membrane viscosity and thermal fluctuations. Phys Rev E 72(1):011901

Noguchi H, Gompper G (2007) Swinging and tumbling of fluid vesicles in shear flow. Phys Rev Lett 98:128103

Noguchi H (2009a) Membrane simulation models from nanometer to micrometer scale. J Phys Soc Jpn 78:041007

Noguchi H (2009b) Swinging and synchronized rotations of red blood cells in simple shear flow. Phys Rev E 80:021902

Noguchi H, Gompper G, Schmid L, Wixforth A, Franke T (2010) Dynamics of fluid vesicles in flow through structured microchannels. Europhys Lett 89:28002

Noguchi H (2010a) Dynamic modes of microcapsules in steady shear flow: effects of bending and shear elasticities. Phys Rev E 81:056319

Noguchi H (2010b) Dynamics of fluid vesicles in oscillatory shear flow. Phys Rev E 81:0619201

Noguchi H (2010c) Dynamics of fluid vesicles in oscillatory shear flow. J Phys Soc Jpn 79:024801

Pan W, Caswell B, Karniadakis GE (2010) A low-dimensional model for the red blood cell. Soft Matter 6:4366–4376

Pan W, Fedosov DA, Caswell B, Karniadakis GE (2011) Predicting dynamics and rheology of blood flow: a comparative study of multiscale and low-dimensional models of red blood cells. Microvasc Res 82:163–170

Pearson MJ, Lipowsky HH (2000) Influence of erythrocyte aggregation on leukocyte margination in postcapillary venules of rat mesentery. Am J Physiol 279:H1460–H1471

Picart C, Piau JM, Galliard H (1998) Human blood shear yield stress and its hematocrit dependence. J Rheol 42:1–12

Pivkin IV, Karniadakis GE (2008) Accurate coarse-grained modeling of red blood cells. Phys Rev Lett 101(11):118105

Pozrikidis C (1989) A study of linearized oscillatory flow past particles by the boundary integral method. J Fluid Mech 202:17–41

Pozrikidis C (2005) Axisymmetric motion of a file of red blood cells through capillaries. Phys Fluids 17:031503

Pries AR, Neuhaus D, Gaehtgens P (1992) Blood viscosity in tube flow: dependence on diameter and hematocrit. Am J Physiol 263(6):H1770–H1778

Quinn DJ, Pivkin I, Wong SY, Chiam KH, Dao M, Karniadkais GE, Suresh S (2011) Combined simulation and experimental study of large deformation of red blood cells in microfluidic systems. Ann Biomed Eng 39(3):1041–1050

Reasor DA Jr, Clausen JR, Aidun CK (2012) Coupling the lattice-Boltzmann and spectrin-link methods for the direct numerical simulation of cellular blood flow. Int J Numer Methods Fluids 68:767–781

Reinke W, Gaehtgens P, Johnson PC (1987) Blood viscosity in small tubes: effect of shear rate, aggregation, and sedimentation. Am J Physiol 253:H540–H547

Robertson AM, Sequeira A, Kameneva MV (2008) Hemodynamical flows. Modeling, analysis and simulation. In: Oberwolfach seminars, vol 37. Birkhauser Verlag, Basel, pp 63–120.

Scheffer L, Bitler A, Ben-Jacob E, Korenstein F (2001) Atomic force pulling: probing the local elasticity of the cell membrane. Eur Biophys J 30:83–90

Schmidt B, Fraternali F (2012) Universal formulae for the limiting elastic energy of membrane networks. J Mech Phys Solids 60:172–180

Seung HS, Nelson DR (1988) Defects in flexible membranes with crystalline order. Phys Rev A 38:1005–1018

Shelby JP, White J, Ganesan K, Rathod PK, Chiu DT (2003) A microfluidic model for single-cell capillary obstruction by Plasmodium falciparum-infected erythrocytes. Proc Natl Acad Sci USA 100:14618–14622

Skalak R (1969) Deformation of red blood cells in capillaries. Science 164:717–719

Skalak R, Keller SR, Secomb TW (1981) Mechanics of blood flow. J Biomech Eng 103:102–115

Skotheim JM, Secomb TW (2007) Red blood cells and other nonspherical capsules in shear flow: oscillatory dynamics and the tank-treading-to-tumbling transition. Phys Rev Lett 98:078301

Springer TA (1995) Traffic signals on endothelium for lymphocyte recirculation and leukocyte emigration. Annu Rev Physiol 57:827–872

Succi S (2001) The Lattice Boltzmann equation for fluid dynamics and beyond. Oxford University Press, Oxford

Sukumaran S, Seifert U (2001) Influence of shear flow on vesicles near a wall: a numerical study. Phys Rev E 64:011916

Sun C, Migliorini C, Munn LL (2003) Red blood cells initiate leukocyte rolling in postcapillary expansions: a lattice Boltzmann analysis. Biophys J 85:208–222

Sun C, Munn LL (2005) Particulate nature of blood determines macroscopic rheology: a 2D lattice-Boltzmann analysis. Biophys J 88:1635–1645

Suresh S, Spatz J, Mills JP, Micoulet A, Dao M, Lim CT, Beil M, Seufferlein T (2005) Connections between single-cell biomechanics and human disease states: gastrointestinal cancer and malaria. Acta Biomaterialia 1:15–30

Suzuki Y, Tateishi N, Soutani M, Maeda N (1996) Deformation of erythrocytes in microvessels and glass capillaries: effect of erythrocyte deformability. Microcirciculation 3(1):49–57

Tangelder GJ, Teirlinck HC, Slaaf DW, Reneman RS (1985) Distribution of blood platelets flowing in arterioles. Am J Physiol 248:H318–H323

Tokarev AA, Butylin AA, Ermakova EA, Shnol EE, Panasenko GP, Ataullakhanov FI (2011) Finite platelet size could be responsible for platelet margination effect. Biophys J 101:1835–1843

Tomaiuolo G, Simeone M, Martinelli V, Rotoli B, Guido S (2009) Red blood cell deformation in microconfined flow. Soft Matter 5:3736–3740

Tran-Son-Tay R, Sutera SP, Rao PR (1984) Determination of RBC membrane viscosity from rheoscopic observations of tank-treading motion. Biophys J 46(1):65–72

Vaziri A, Gopinath A (2008) Cell and biomolecular mechanics in silico. Nat Mater 7:15–23

Wang H, Skalak R (1969) Viscous flow in a cylindrical tube containing a line of spherical particles. J Fluid Mech 38:75–96

Wang T, Pan TW, Xing ZW, Glowinski R (2009) Numerical simulation of rheology of red blood cell rouleaux in microchannels. Phys Rev E 79(4):041916

Waugh R, Evans EA (1979) Thermoelasticity of red blood cell membrane. Biophys J 26(1):115–131

Wendt JF (ed) (2009) Computational fluid dynamics, 3rd edn. Springer, Berlin

Yamaguchi S, Yamakawa T, Niimi H (1992) Cell-free plasma layer in cerebral microvessels. Biorheology 29:251–260

Yazdani AZK, Kalluri RM, Bagchi P (2011) Tank-treading and tumbling frequencies of capsules and red blood cells. Phys Rev E 83:046305

Zhao Q, Durand LG, Allard L, Cloutier G (1998) Effects of a sudden flow reduction on red blood cell rouleau formation and orientation using RF backscattered power. Ultrasound Med. Biol. 24:503–511

Zhao H, Isfahani AHG, Olson LN, Freund JB (2010) A spectral boundary integral method for flowing blood cells. J Comput Phys 229:3726–3744

Zhao H, Shaqfeh ESG (2011a) The dynamics of a vesicle in simple shear flow. J Fluid Mech 674:578–604

Zhao H, Shaqfeh ESG (2011b) Shear-induced platelet margination in a microchannel. Phys Rev E 83:061924

P10: Conformational and dynamical properties of ultra-soft colloids in semi-dilute solutions under shear flow

S. P. Singh, D. A. Fedosov, A. Chatterji, R. G. Winkler, and G. Gompper

Journal of Physics: Condensed Matter, **24**:464103, 2012.

IOP Publishing Journal of Physics: Condensed Matter
J. Phys.: Condens. Matter **24** (2012) 464103 (11pp) doi:10.1088/0953-8984/24/46/464103

Conformational and dynamical properties of ultra-soft colloids in semi-dilute solutions under shear flow

Sunil P Singh[1], **Dmitry A Fedosov**[1], **Apratim Chatterji**[1,2], **Roland G Winkler**[1] **and Gerhard Gompper**[1]

[1] Theoretical Soft Matter and Biophysics, Institute of Complex Systems and Institute for Advanced Simulation, Forschungszentrum Jülich, 52425 Jülich, Germany
[2] Indian Institute of Science Education and Research (IISER), Pune 411021, India

E-mail: s.p.singh@fz-juelich.de, d.fedosov@fz-juelich.de, apratim@iiserpune.ac.in, r.winkler@fz-juelich.de and g.gompper@fz-juelich.de

Received 23 April 2012, in final form 10 June 2012
Published 31 October 2012
Online at stacks.iop.org/JPhysCM/24/464103

Abstract
We investigate structural and dynamical properties of ultra-soft colloids in dilute and semi-dilute solutions by hybrid mesoscale simulations under linear shear flow. In particular, the influence of functionality on these properties is addressed. Our study combines molecular dynamics simulations for the solute with the multiparticle collision dynamics approach for the coarse-grained solvent. The star polymers exhibit large conformational and orientational changes in shear flow, which we characterize by the radius of gyration tensor and the alignment angle. These quantities show a universal dependence on a concentration- and functionality-dependent Weissenberg number with slight deviations at high shear rates. Moreover, the star polymers display a rotational dynamics with a shear-rate- and concentration-dependent rotation frequency. We attribute the concentration dependence to the screening of hydrodynamic interactions in semi-dilute star-polymer solutions.

S Online supplementary data available from stacks.iop.org/JPhysCM/24/464103/mmedia

(Some figures may appear in colour only in the online journal)

1. Introduction

Macromolecular systems are enormously versatile in their structural and dynamical properties. This has led to their widespread use as structural and functional materials, as well as fluids with tailored properties. The origin of the versatility is that polymer length, polymer architecture, polymer internal composition (in form of multi-block copolymers) and polymer interactions can be easily tuned, with a strong impact on material properties. The large number of variables and the emergent properties in semi-dilute and dense suspensions imply that a detailed theoretical understanding is required to achieve a knowledge-based design of new materials and their flow properties.

In this article, we focus on a special class of macromolecular architectures, which consist of several linear polymers of equal length, tied together at one of their ends to a common center [1]. These star polymers are technologically important in several applications, such as viscosity modifiers in the oil industry [1], or as novel drug-delivery agents [2–4]. Star polymers have very soft interactions, which increase only logarithmically with decreasing distance between their centers [5–8]. Therefore, star polymers are also known as ultra-soft colloids.

The structural, dynamical, and rheological properties of star-polymer solutions strongly depend on the arm number—the functionality f—the lengths of the arms, and the concentration c [9–13]. Experimentally, star polymers have been investigated over a wide range of functionalities, in particular for low and intermediate functionalities $4 \leq f \leq 128$ in [14–16] and for very large functionality $f = 390$ in [17]. For concentrations below and moderately above the overlap concentration c^*, star-polymer solutions are in the fluid phase, while for high concentrations the solution (or melt) becomes glassy [13, 17], in particular for large functionalities. These studies mainly focus on the rheological properties. In the fluid regime, the zero-shear viscosity of star-polymer solutions interpolates between that of linear polymers and hard spheres at fixed volume fraction—defined by the hydrodynamic radius of an individual macromolecule [15]; here, the viscosity is found to strongly depend on the functionality, but only very weakly on the arm length.

Simulations of star-polymer solutions by mesoscale hydrodynamics methods with a molecularly resolved polymer model have mainly focused on the structural and dynamical behavior of individual stars in dilute solution [18, 19], on the dynamic friction between two dragged stars [20], and on rheological behavior of semi-dilute solutions of low-functionality star polymers (with $f = 10$) [21]. In a complementary theoretical description of soft colloids [22–24]—such as block-copolymer micelles, hairy colloids, and star polymers, each colloid is represented by just one point particle with effective, coarse-grained interactions. This approach with an equilibrium interaction potential has been employed in [22] to study the nonequilibrium properties of dense solutions of such ultra-soft colloids by mesoscale hydrodynamics simulations. Naturally, such an approach does not capture the flow-induced deformation of the star polymers, and is therefore suitable in the limit of nearly spherical colloids only. As will be illustrated in the article, such deformations are quite pronounced even in concentrated systems and determine the rheological properties of the solution. Furthermore, the use of an equilibrium interaction potential does not include the effect of transient entanglements between the polymer arms [23] or the time-irreversible deformation of the corona [20]. Such transient effects can be mimicked by a memory contribution to the (still spherically symmetric) interaction potential [23]; such an approach has been successfully employed, for example, to predict the dynamics of star-polymer solutions with start-up or step-down shear stress [24].

We focus in this paper on the role of concentration and functionality—with $10 \le f \le 50$—on the structural and dynamical properties of star polymers in semi-dilute suspensions. We address the deformation and orientation of individual star polymers and unravel their universal behavior in terms of shear rate and functionality. Moreover, we study the scaling properties of the structure factor of individual arms under shear flow. Similar studies have been performed for linear polymers (a star of functionality $f = 2$) [25]. As shown in [18, 19], star polymers with $f \gtrsim 5$ exhibit a tank-treading-like motion, where individual arms undergo collapse and stretching cycles. This leads to a rotation of the whole star, with a frequency which depends upon the shear rate. Here, the questions arise how the star-polymer concentration affects the rotational dynamics, and whether the frequency dependence is similar to the tank-treading motion of vesicles.

The article is organized as follows. In section 2, we introduce the star-polymer model and the mesoscopic hydrodynamics simulation technique, and discuss the choice of model parameters. In section 3, we present our results for the conformational properties, the flow alignment, and the structure factor of star polymers in semi-dilute solution under shear flow. Results for the flow-induced rotational dynamics of stars are presented in section 4. Finally, the results are summarized in section 5.

2. Method and model

2.1. Multiparticle collision dynamics

Multiparticle collision dynamics (MPC) is a particle-based hydrodynamic simulation technique [26–28]. In the MPC algorithm, the solvent is modeled by N_s point particles with positions $\boldsymbol{r}_i$ and velocities $\boldsymbol{v}_i$ ($i = 1, \ldots, N_s$). The dynamics proceeds in discrete time increments h, denoted as collision time, by alternating streaming and collision steps [27, 28]. In the streaming step, the solvent particles of mass m move ballistically with their respective velocities and their positions are updated as

$$\boldsymbol{r}_i(t+h) = \boldsymbol{r}_i(t) + h\boldsymbol{v}_i(t). \tag{1}$$

In the collision step, the simulation box is partitioned in cubic cells of linear dimension a and the solvent particles are sorted into these cells. Their relative velocities, with respect to the center-of-mass velocity of the cell, are rotated around a randomly oriented axis by an angle α, so that

$$\boldsymbol{v}_i(t+h) = \boldsymbol{v}_i(t) + (\mathbf{R}(\alpha) - \mathbf{I})(\boldsymbol{v}_i(t) - \boldsymbol{v}_{\mathrm{cm}}(t)), \tag{2}$$

where $\mathbf{R}$ is the rotation matrix, $\mathbf{I}$ is the unit matrix, and $\boldsymbol{v}_{\mathrm{cm}} = \sum_{j=1}^{N_c} \boldsymbol{v}_j / N_c$ is the center-of-mass velocity of the cell with N_c particles. In this stochastic process mass, momentum, and energy are conserved, which ensures that hydrodynamic behavior emerges on larger length scales.

The transport properties of the solvent depend on the collision time h, the rotation angle α, and the average number of particles $\langle N_c \rangle$ per cell. Tuning these variables allows us to attain solvents with a high Schmidt number, where momentum transport dominates over mass transport. Here, the Schmidt number is defined as $Sc = \nu/D$, where $\nu = \eta/(m\langle N_c \rangle)$ is the kinematic viscosity and D is the diffusion coefficient of a MPC particle. We use the parameters $h/\sqrt{ma^2/(k_B T)} = 0.1$, $\alpha = 130°$, and $\langle N_c \rangle = 10$, which yields the solvent viscosity $\eta_s = 8.7\sqrt{mk_B T/a^4}$ and the Schmidt number $Sc \approx 17$.

2.2. Star-polymer model

A star polymer consists of f linear polymers with one of their ends linked to a common center. A polymer has N_m monomers of mass M, which are connected by harmonic springs with the potential

$$V_b = \frac{k_s}{2}(R_{i,i+1} - l)^2, \tag{3}$$

where l is the equilibrium bond length, $\boldsymbol{R}_{i,i+1} = \boldsymbol{R}_{i+1} - \boldsymbol{R}_i$ is the bond vector, and $R_{i,i+1} = |\boldsymbol{R}_{i,i+1}|$. The spring constant k_s

is chosen such that even under strong shear flow the change in the equilibrium bond length remains less than a few per cent. Excluded-volume interactions between monomers are taken into account through the repulsive truncated and shifted Lennard-Jones (LJ) potential

$$V_{\mathrm{LJ}}(r) = 4\epsilon\left[\left(\frac{\sigma}{r}\right)^{12} - \left(\frac{\sigma}{r}\right)^{6} + \frac{1}{4}\right]\Theta(2^{1/6}\sigma - r), \qquad (4)$$

where $\Theta(r)$ is the Heaviside step function ($\Theta(r) = 0$ for $r < 0$ and $\Theta(r) = 1$ for $r \geq 0$).

The equilibrium bond length of each center-arm connection l_{c} and LJ diameter of the central monomer σ_{c} are taken to be twice as large as those for a normal monomer, while the mass of the center monomer is the same as for any other monomer. Moreover, we set $\epsilon = k_{\mathrm{B}}T$ and $a = l$. We use the spring constant $k_{\mathrm{s}}/(k_{\mathrm{B}}T/l^2) = 10^3$, the diameter of a monomer $\sigma/l = 0.8$ and its mass $M = 10m$. We consider polymer arms with $N_{\mathrm{m}} = 30$ monomers. The velocity Verlet algorithm is used to integrate Newton's equations of motion of the star polymers with the time step $h_{\mathrm{m}} = 5 \times 10^{-3}\sqrt{ml^2/(k_{\mathrm{B}}T)}$.

The solute–solvent coupling occurs in the collision step, where the velocities of the polymer monomers are rotated according to equation (2) [28–30], but with the center-of-mass velocity of the cell

$$v_{\mathrm{cm}}(t) = \frac{\sum_{i=1}^{N_{\mathrm{c}}} m v_i(t) + \sum_{j=1}^{N_{\mathrm{c}}^{m}} M v_j(t)}{m N_{\mathrm{c}} + M N_{\mathrm{c}}^{m}}. \qquad (5)$$

Here, N_{c}^{m} is number of the monomers in the considered cell. Thereby, momentum is redistributed between solvent and monomers in the same cell.

We apply three-dimensional periodic boundary conditions for the MPC fluid and the star polymers, and Lees–Edwards boundary conditions to impose shear flow [31, 32]. The latter is a boundary-driven algorithm, where the *primary* simulation box is fixed in space along with all its periodic replicas along the flow direction. Replicated neighboring boxes in the positive (negative) gradient direction move with constant velocity $v_{\mathrm{B}} = L\dot{\gamma}$ along (opposite to) the flow direction, where $\dot{\gamma}$ is the shear rate. When a particle enters a moving box along the gradient direction, it acquires the extra velocity v_{B}. This yields a linear fluid velocity profile $v_x = \dot{\gamma}y$ in the flow direction (x-axis) as a function of the particle positions along the gradient direction (y-axis). A local cell-based Maxwellian thermostat (MBS) is applied by which velocities are scaled to maintain the desired temperature of the system [33].

3. Structural properties of star polymers in shear flow

We place the star polymers in a cubic simulation box with linear dimension $L = 100l$ and periodic boundary conditions. Their number N_{sp} depends on concentration and is given in table 1 together with other parameters. We will present results for the arm length $N_{\mathrm{m}} = 30$ and the functionalities $f = 10, 20, 30$, and 50. The polymer concentration is measured relative to the overlap concentration,

$$c^* = [\tfrac{4}{3}\pi R_{\mathrm{h}}^3]^{-1}, \qquad (6)$$

where R_{h} is the hydrodynamic radius, which is obtained from the diffusion coefficient of a star in dilute solution extrapolated to infinite system size [34]. The strength of the shear flow is characterized by the concentration-dependent Weissenberg number $Wi_{\mathrm{c}} = \beta\dot{\gamma}\tau_z$, where $\tau_z = \eta_{\mathrm{s}}N_{\mathrm{m}}^2 l^3/k_{\mathrm{B}}T$ is the Zimm relaxation time of a polymer arm and $\beta = \beta(c/c^*)$ is a concentration-dependent scale factor. We introduce the factor β to account for the concentration dependence of the characteristic relaxation time of a star polymer, i.e., $\beta\tau_z$ is—up to a constant—equal to the concentration-dependent relaxation time. We consider the relative deformation δG_{xx} (equation (8)) and determine the concentration dependence of β by calculating the ratio between the shear-rate-dependent actual δG_{xx} data at a given concentration and the comparable data for the lowest concentration given in table 1. The obtained β-function is then also applied to other quantities. The same idea has been applied in [21, 35] to study concentration-dependent rheological properties of linear and star-polymer solutions for stars with $f = 10$. Several independent simulation runs are performed for fixed solution conditions in order to obtain reliable averages of the properties of interest.

Table 1. Simulation parameters for N_{sp} star polymers of functionality f. R_{g0} and R_{h} are the equilibrium radius of gyration and hydrodynamic radius in dilute solution, respectively, and c indicates the range of considered concentrations, with c^* denoting the overlap concentration.

f	N_{sp}	R_{g0}/l	R_{h}/l	c/c^*
10	100–750	7.1	7.1	0.15–1.13
20	50–375	7.9	9.1	0.16–2.37
30	34–250	8.5	10.7	0.17–2.57
50	20–150	9.2	13.2	0.19–2.92

3.1. Conformational properties

Typical conformations of star polymers in semi-dilute solution under shear flow are shown in figure 1 for $f = 10$ and $f = 50$. Comparison of the two functionalities demonstrates that large-functionality stars are less deformed and less aligned with the flow direction than low-functionality star polymers.

The conformational properties of the star polymers can be characterized quantitatively by the radius of gyration tensor, which is defined as

$$G_{\gamma\gamma'} = \frac{1}{N}\sum_{i=1}^{N} \Delta r_{i,\gamma}\Delta r_{i,\gamma'}, \qquad (7)$$

where Δr_i is the position of the ith monomer relative to the star center of mass, $\gamma, \gamma' \in \{x, y, z\}$, and $N = fN_{\mathrm{m}} + 1$ is the total number of monomers in a star. At equilibrium, all diagonal components of $G_{\gamma\gamma'}$ are equal, i.e., $\langle G_{\gamma\gamma}\rangle = \langle G_{\gamma\gamma}^{0}\rangle$, where the superscript indicates the equilibrium value at a particular concentration. In the dilute regime $\langle G_{\gamma\gamma}\rangle = \langle G_{\gamma\gamma}^{00}\rangle = R_{\mathrm{g0}}^2/3$, where the radius of gyration R_{g0}^2 follows the scaling relation $R_{\mathrm{g0}}^2 \sim l^2 N_{\mathrm{m}}^{2\nu} f^{1-\nu}$ in terms of arm length and functionality [5, 9, 36, 37], with the exponent $\nu \approx 0.63$ for

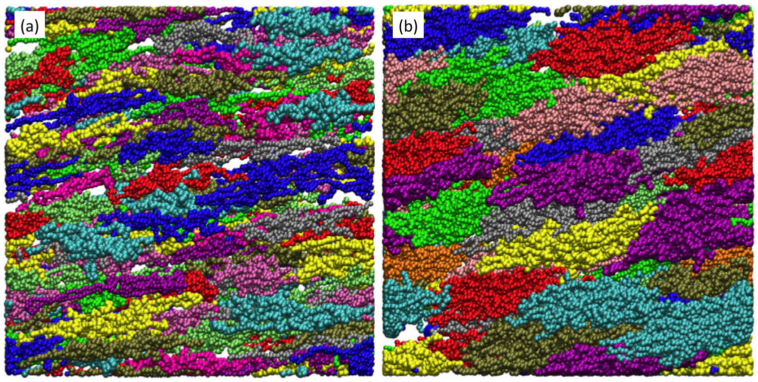

Figure 1. Simulation snapshots of star-polymer solutions with (a) functionality $f = 10$ and concentration $c/c^* = 1.13$ as well as (b) $f = 50$ and $c/c^* = 1.46$ for the same Weissenberg number $Wi_c \approx 10^2$. Only star polymers with their centers in a slice of thickness of $3R_{g0}$ parallel to the flow-gradient plane are shown. Multiple colors are used to distinguish the various star polymers more easily. A movie is provided as supplemental material (available at stacks.iop.org/JPhysCM/24/464103/mmedia).

our system. Our scaling exponent is slightly larger than that for polymers in dilute solution due to the relatively short arm length. Longer arms would lead to the same exponent as for linear chains ($\nu \approx 3/5$) [38].

In linear shear flow, polymers become deformed, which is measured by the relative deformation

$$\delta G_{xx}(c/c^*) = \frac{\langle G_{xx}(c/c^*)\rangle - \langle G^0_{xx}(c/c^*)\rangle}{\langle G^0_{xx}(c/c^*)\rangle} \qquad (8)$$

in terms of the gyration tensor. Simulation results of δG_{xx} for star polymers of various functionalities in dilute solution are displayed in the inset of figure 2(a). It is clear that δG_{xx} decreases with increasing functionality at a given shear rate, or Wi_c, due to a difference in the shear resistance, which increases for larger functionalities.

The star-polymer relaxation time depends on its arm number. The relative dependence of the relaxation time on the functionality can be estimated by shifting the δG_{xx} curves to the highest-functionality curve in the inset of figure 2(a). Figure 2(a) itself shows the scaled curves as a function of $\phi_f Wi_c$, where ϕ_f is a f-dependent scale factor. Clearly, the scaled data follow a common curve within the accuracy of the simulations, which indicates universal behavior of this structural property.

Values of the relative deformation ratio for various concentrations, above and below the overlap concentration, are displayed in figure 2(b). Evidently, a universal curve is obtained as a function of $\phi_f Wi_c = \phi_f \beta \mathrm{Wi}$ over a wide range of Weissenberg numbers. At low $\phi_f Wi_c < 1$, a quadratic dependence of the relative deformation on the Weissenberg number is found for all concentrations and functionalities [18, 21, 35, 39]. At high shear rates, the deformation of the polymers saturates and δG_{xx} assumes a maximum value, which depends on the length of polymer arms as well as on the functionality. This finite-polymer-length effect breaks the universality as reflected in the figure. Note that the equilibrium value of the radius of gyration increases with increasing functionality, which partially accounts for the decrease of δG_{xx} at high Weissenberg numbers.

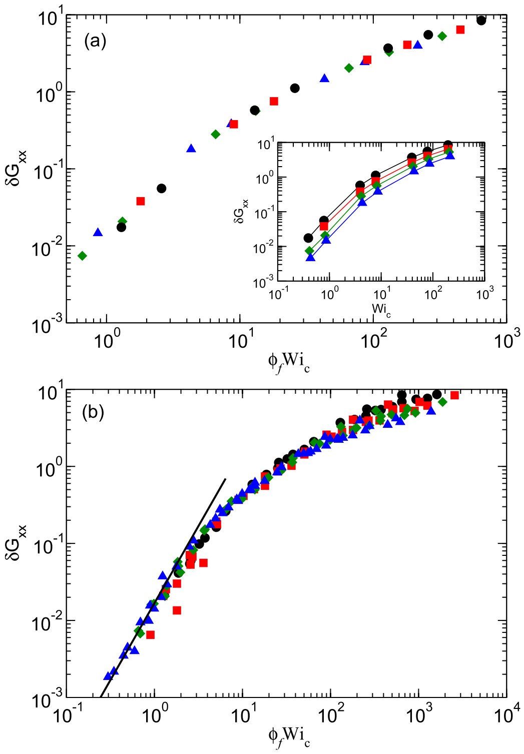

Figure 2. Relative deformation δG_{xx} of star polymers along the flow direction as a function of the functionality-dependent Weissenberg number $\phi_f Wi_c$. (a) Dilute solution data at the lowest concentrations given in table 1 for $f = 10$ (bullets), $f = 20$ (squares), $f = 30$ (diamonds), and $f = 50$ (triangles). The inset presents the relative deformations as a function of Wi_c only. (b) Simulation data for all concentrations and functionalities.

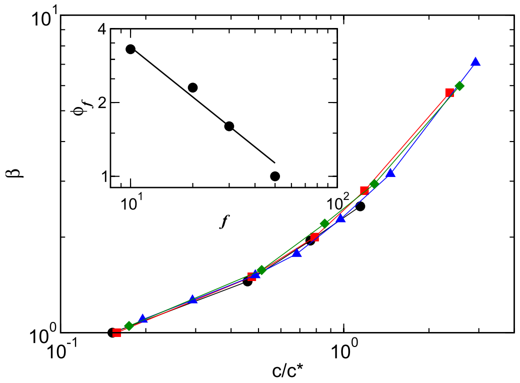

Figure 3. Concentration-dependent scale factor β for the relaxation time $\tau(c) = \beta(c/c^*)\tau_z$ obtained from the scaling of the radius of gyration tensor and the alignment along the shear direction. The inset shows the functionality dependence of the scale factor ϕ_f. The line indicates the power-law dependence $\phi_f \sim f^{-2/3}$.

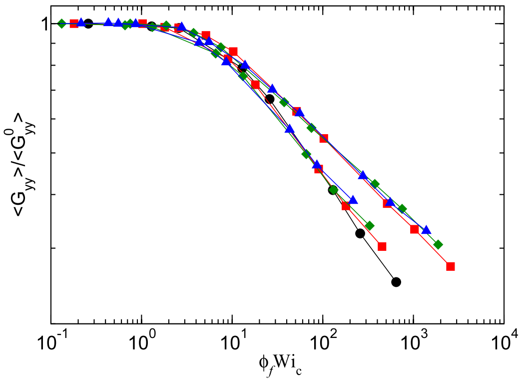

Figure 4. Normalized radius of gyration tensor along the gradient direction $\langle G_{yy}\rangle/\langle G^0_{yy}\rangle$ as a function of $\phi_f Wi_c$ for dilute systems of the lowest concentrations (bottom set of curves) and the highest concentrations (upper set of curves) given in table 1. The symbols are the same as in figure 2.

Figure 3 displays the concentration dependence of the scale factor $\beta(c/c*)$. We find a universal curve for the various considered functionalities [21]. As emphasized, β measures the concentration dependence of the star-polymer characteristic relaxation time. Evidently, this time increases significantly with concentration. The inset of figure 3 shows the functionality dependence of ϕ_f, which decreases with increasing f in a power-law manner, with an exponent of $-2/3$. This is surprising, because it implies that the relaxation time of a star polymer determining the Weissenberg number decreases with increasing functionality. This is in contradiction with the relaxation time of an individual polymer arm, which is predicted [10] to follow the dependence $f^{(2-3\nu)/2}$, with $(2 - 3\nu)/2 \simeq 0.1$ for $\nu = 0.6$, i.e., this relaxation time increases with increasing functionality.

The radii of gyration tensor components along the gradient direction are displayed in figure 4 for dilute systems and star-polymer concentrations well above c^* as a function of $\phi_f Wi_c$. The star-polymer size $\langle G_{yy}\rangle$ decreases with increasing shear rate. Thereby, a weak dependence on functionality is revealed—beyond the effect captured by ϕ_f. At large Weissenberg numbers, higher-functionality star polymers exhibit a somewhat smaller deformation. More importantly, low- and high-concentration systems show a qualitatively different dependence on shear rate, expressed by the different slope of the corresponding data sets. Dilute systems exhibit a stronger shrinkage than concentrated systems at the same value of $\phi_f Wi_c$. This might be explained by the fact that the equilibrium radius of gyration of star polymers in concentrated systems is smaller than that of dilute systems. The associated denser packing of monomers of individual stars is maintained even at high shear rates and leads to smaller deformations compared to the dilute case. Along the vorticity direction, the conformations of the star polymers are less affected by the flow, as already shown in [18] for dilute systems.

In equilibrium, a star polymer is a spherically symmetric object on average. As evident from the above results, this symmetry is broken under shear flow. We characterize the shear-induced asphericity of a star polymer by the ratio of the largest and smallest eigenvalues of the average gyration tensor $\langle G_1\rangle$ and $\langle G_3\rangle$. Here, the average gyration tensor is obtained by averaging the gyration tensor first and then by diagonalizing it to calculate the eigenvalues $\langle G_1\rangle$, $\langle G_3\rangle$. For a spherically symmetric object, $\langle G_1\rangle/\langle G_3\rangle - 1$ is zero and increases as the object becomes asymmetrically deformed, and diverges for a thin rod. Similarly, for star polymers the asphericity is small at low shear rates, while it increases with increasing shear rates, as displayed in figure 5(a). For low and moderate $\phi_f Wi_c$, a universal curve for all functionalities and concentrations is obtained, indicating that the f and c/c^* dependence is absorbed in $\phi_f Wi_c$. At large $\phi_f Wi_c \gg 1$, the asphericity curves split for the various concentrations and functionalities. At high concentrations, the asphericity is smaller. Higher concentrations lead to a slower decrease of $\langle G_{yy}\rangle$ (see figure 4) and to a larger $\langle G_3\rangle$.

In addition, we present in figure 5(b) the instantaneous asphericity $\bar{G}_1/\bar{G}_3 - 1$, where the $\bar{G}_i$ are the averages of the eigenvalues of the diagonalized instantaneous radius of gyration tensor. At high shear rates the instantaneous asphericity is equal to the average one, while at low shear rates plateau values are obtained, which depend on functionality and arm length. These shear-independent values characterize the deviation of a star polymer from a perfectly spherical object in equilibrium. Thus, stars of low functionality are more aspherical in comparison to those with high f. This property reflects a change in the star structure as functionality increases, namely the inner compact region of a star swells, while the outer soft region is reduced, leading to smaller variations in the star's instantaneous shape.

The inset of figure 5(b) shows the instantaneous asphericity for the highest considered concentrations. Here, we also find a universal behavior of stars with different

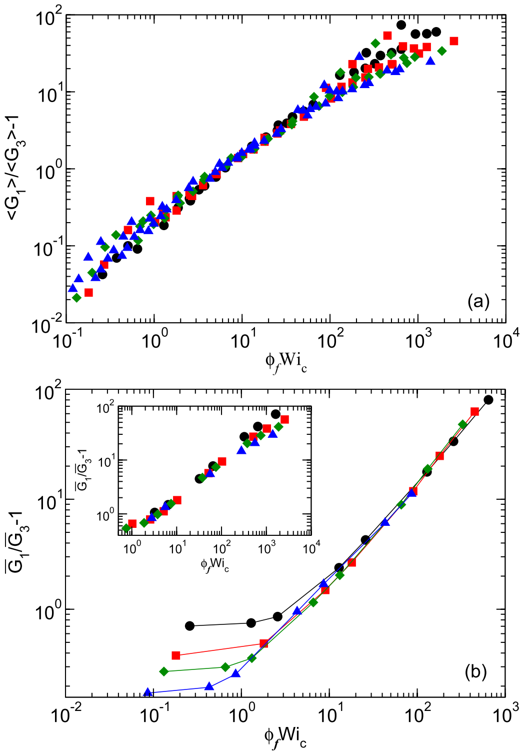

Figure 5. (a) Ratios of the largest-to-smallest eigenvalues of the average gyration tensor as a function of the concentration- and functionality-dependent Weissenberg number $\phi_f Wi_c$. The data are for the functionalities $f = 10$ (bullets), 20 (squares), 30 (diamonds), and 50 (triangles) and all concentrations. (b) Ratios of the averaged largest and smallest eigenvalues of the gyration tensor for dilute systems (see table 1). The inset shows data for the highest considered concentrations at the various functionalities (see table 1).

functionalities over a wide range of Weissenberg numbers. Only at large $\phi_f Wi_c$ do curves for the various values of f split. This could be related to the fact that the packing of monomers increases with increasing functionality. The difference between the various curves seems to decrease with increasing concentration and we expect an asymptotic curve for sufficiently high concentrations.

As a measure of the asphericity of star polymers in equilibrium and in dilute solution, we use the quantity [28, 40]

$$A = \left\langle \frac{(\bar{G}_1 - \bar{G}_2)^2 + (\bar{G}_1 - \bar{G}_3)^2 + (\bar{G}_2 - \bar{G}_3)^2}{(\bar{G}_1 + \bar{G}_2 + \bar{G}_3)^2} \right\rangle. \tag{9}$$

Results for the various functionalities are presented in figure 6. As expected [41–43], the asphericity decreases with increasing functionality and shows a strong dependence on f. We find a stronger decrease with f than the theoretically predicted power law f^{-1} [41, 42]; at large functionalities, our data decay approximately as $A \sim f^{-3/2}$. However, our data are in good agreement with the Monte Carlo simulations of [43] for small functionalities. Note that these simulations predict a very weak dependence of A on polymer length only for the considered low-functionality stars polymers. The discrepancy between our simulation data and theory could be related to the relative short length $N = 30$ of the polymer arms and the high monomer packing at large functionalities. The length-independent regime might be accessible for longer polymers only.

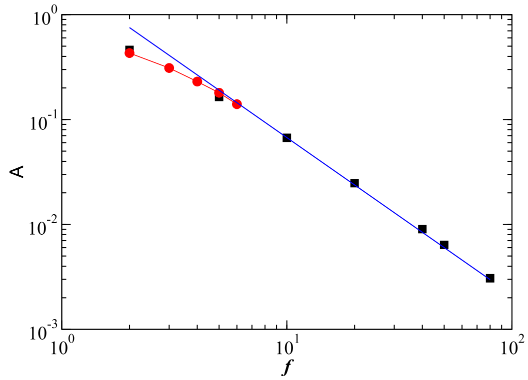

Figure 6. Asphericity A of star polymers in equilibrium and in dilute solution calculated according to equation (9) (squares). The bullets represent Monte Carlo simulation results of [43]. The straight line indicates the power law $A \sim f^{-3/2}$.

3.2. Flow alignment

Aside from being deformed, star polymers under shear are also aligned with the flow field. The extent of alignment can be characterized by the angle χ_G between the eigenvector corresponding to the largest eigenvalue of the average radius of gyration tensor and the flow direction. It is obtained as

$$\tan(2\chi_G) = \frac{2\langle G_{xy}\rangle}{\langle G_{xx}\rangle - \langle G_{yy}\rangle}. \tag{10}$$

In figure 7, alignment angles are plotted as a function of $\phi_f Wi_c$ for various concentrations and functionalities. In the linear response regime $\langle G_{xy}\rangle \sim \phi_f Wi_c$ and $\langle G_{xx}\rangle - \langle G_{yy}\rangle \sim (\phi_f Wi_c)^2$, which implies that at low Weissenberg numbers $\tan(2\chi_G) \sim Wi_c^{-1}$ [44, 45]. This power-law dependence is approached for $\phi_f Wi_c < 5$. At higher $\phi_f Wi_c$, star polymers assume an approximately ellipsoidal shape, and the angle χ_G decreases with increasing shear rate. Again, we obtain a universal curve for different concentrations and functionalities over a certain $\phi_f Wi_c$ range, where $\phi_f \beta(c/c^*)$ absorbs any functionality and concentration dependences. The alignment angle at high shear rates follows the scaling law $\tan(2\chi_G) \sim (\phi_f Wi_c)^{-\delta}$ with the exponent $\delta \approx 0.43$. As for other properties discussed in section 3.1, the alignment angle data split at high shear rates due to the finite size of the polymers. For $\phi_f Wi_c > 50$, star polymers with a smaller number of arms are slightly more aligned with the flow direction than those with a larger number of arms. We would like to emphasize that for $\tan(2\chi_G)$ only the shear rate can be scaled to obtain a universal curve,

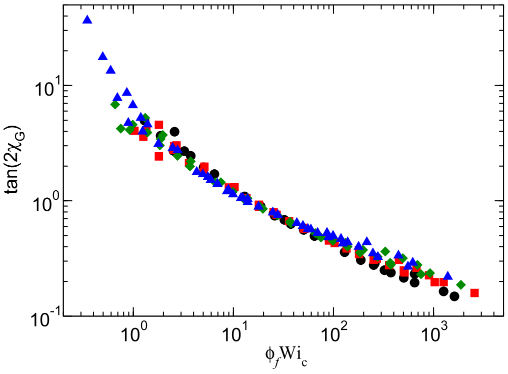

Figure 7. Alignment angle of star polymers $\tan(2\chi_G)$ as a function of $\phi_f Wi_c$ for various concentrations and functionalities $f = 10$ (bullets), $f = 20$ (squares), $f = 30$ (diamonds), and $f = 50$ (triangles).

since $\tan(2\chi_G)$ is dimensionless. The obtained universality for $\phi_f Wi_c \lesssim 50$ confirms that $\phi_f Wi_c$ is a suitable combination of the functionality and concentration dependence of the relaxation time.

3.3. Static structure factor

Structural changes of a star polymer under flow at different length scales are reflected in its static structure factor

$$S(\boldsymbol{q}) = \frac{1}{N}\sum_{i=1}^{N}\sum_{j=1}^{N}\langle \mathrm{e}^{-\mathrm{i}\boldsymbol{q}(\boldsymbol{r}_i-\boldsymbol{r}_j)}\rangle. \tag{11}$$

Figure 8(a) displays equilibrium structure factors along the flow direction for various functionalities in dilute solution. At small wavevectors $q_x l \ll 1$, $S(q_x)$ is approximately constant. It then decays very rapidly for $q_x R_{g0} > 1$ according to the power law q^{-4} for large functionalities, corresponding to the behavior of a spherical particle. In the range $4l/R_{g0} < q_x l < \pi$, the internal structure of the ultra-soft polymer is reflected. For low functionality, we find the approximate power-law decay $S(q_x) \sim q^{-1/\nu}$ with $\nu \approx 0.63$. At higher functionalities, additional features appear and no clear power-law regime is visible. The decrease of $S(q)$ with increasing functionality at $q_x l \approx 1$ indicates a stretching of the polymers due to increased packing at larger functionalities. At $q_x l \approx 2\pi$, a peak appears by scattering from nearest neighbor monomers.

Figure 8(b) presents the structure factors S_a of the individual arms within a star. The curves for the various functionalities show small differences at $q_x R_{g0} \approx 1$ caused by the increase of the radius of gyration with increasing functionality. In the range $6l/R_{g0} < q_x l < \pi$, we find a universal, self-similar behavior with a power-law regime corresponding to the scaling behavior of an individual polymer of similar length.

The deformation of a star polymer under shear flow is also reflected in the structure factor. Since a star is anisotropic, we determine the structure factors along the flow, gradient, and vorticity direction separately. An example of structure factors along the flow direction for various shear rates is provided in figure 9. The increase of the radius of gyration $\langle G_{xx}\rangle$ leads to a shift of the curves to smaller q_x values. More importantly, the power-law exponent ν in $S(q_x) \sim q_x^{-1/\nu}$ depends on shear rate. The inset of figure 9 shows the exponents ν for various functionalities as a function of the Weissenberg number. ν increases with increasing Weissenberg number and seems to saturate at large Wi_c, which indicates a stretching of the individual polymers. Since some of the polymers are stretched and others are in a coiled state, we expect the exponent to be always smaller than unity. Evidently, there is only a very weak dependence on functionality. As shown in figure 4, the polymers shrink along the gradient direction. Here, we find a very minor change of the power-law exponent ν toward smaller values. A similar behavior is observed along the vorticity direction.

A comparable change in the scaling behavior of the structure factor of linear polymers under shear flow has been found in [25] by molecular dynamics simulations. In contrast to our star polymers, however, a significantly modified scaling behavior is obtained for linear polymers along the minor axis. The exponent ν along this axis decreases significantly below the equilibrium value.

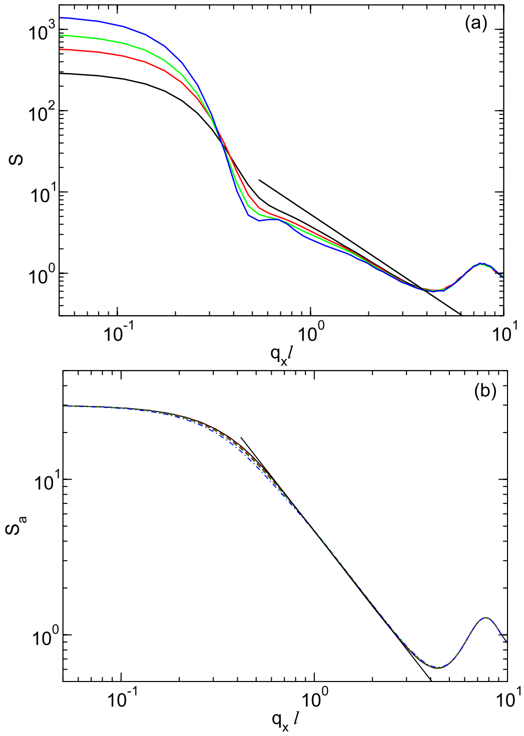

Figure 8. (a) Equilibrium structure factors $S(q_x)$ of star polymers and of (b) individual arms $S_a(q_x)$ for the functionalities $f = 10$ (black), 20 (red), 30 (green), and 50 (blue). The straight lines indicate the power law $q^{-1/\nu}$ with $\nu = 0.63$.

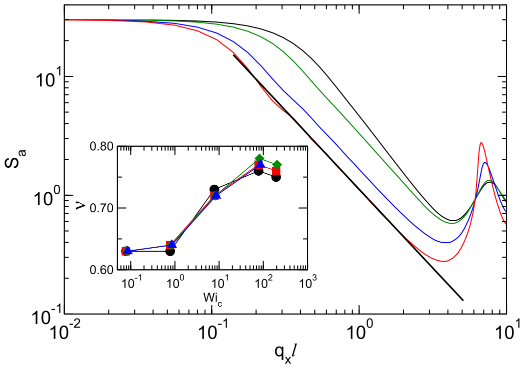

Figure 9. Structure factors of polymer arms under shear flow for q-values along the flow direction for the Weissenberg numbers $Wi_c = 0$ (black), $Wi_c = 7.8$ (green), $Wi_c = 78$ (blue), and $Wi_c = 196$ (red). The functionality is $f = 10$. The solid black line corresponds to power law $S_a \sim q_x^{-1/\nu}$ with $\nu = 0.8$. The inset shows the shear-rate dependence of the exponent ν for the various functionalities.

4. Rotational dynamics of star polymers in shear flow

4.1. Angular rotation frequency and tank-treading

Under linear shear flow the vorticity is non-zero, which implies a rotational motion of a star with a non-zero rotational frequency. The dynamics of a star polymer is quite different from that of a linear polymer. A linear polymer exhibits tumbling motion [39, 45–48], whereas star polymers show a tank-treading-like rotation for functionalities $f \gtrsim 5$ [18, 19], where individual arms are subject to a cyclic stretching and collapse motion. The rotational dynamics can be characterized by the rotational frequency $\boldsymbol{\omega}$ of the star, which is obtained from the angular momentum [19, 49, 50]

$$\boldsymbol{L} = \sum_{i=1}^{N} M \Delta \boldsymbol{r}_i \times \Delta \dot{\boldsymbol{r}}_i \tag{12}$$

and the inertia tensor $\boldsymbol{\Theta}$, with its components

$$\Theta_{\gamma\gamma'} = \sum_{i=1}^{N} M(\Delta \boldsymbol{r}_i^2 \delta_{\gamma\gamma'} - \Delta r_{i,\gamma} \Delta r_{i,\gamma'}), \tag{13}$$

via the relation $\boldsymbol{L} = \Theta \boldsymbol{\omega}$. For a rigid body, this yields the average frequency

$$\omega_z = \left\langle \sum_{\gamma} \Theta^{-1}_{\gamma z} L_{\gamma} \right\rangle \tag{14}$$

for a rotation around the vorticity axis. Since a star polymer is not a rigid body, we neglect terms containing fluctuations in ω_i of the individual monomers around the mean value $\boldsymbol{\omega}$. If we neglect the off-diagonal elements of the inertia tensor (13) and replace Θ_{zz} by its average, we find

$$\langle L_z \rangle \approx \langle \Theta_{zz} \rangle \omega_z^L = M(\langle G_{xx} \rangle + \langle G_{yy} \rangle)\omega_z^L. \tag{15}$$

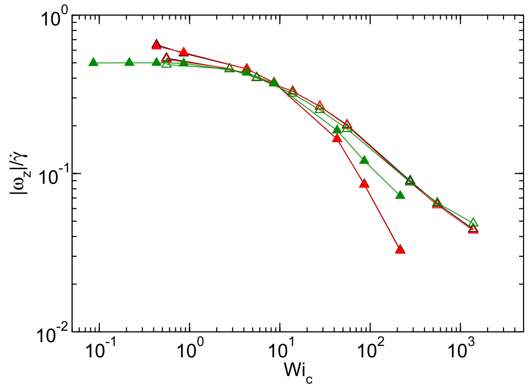

Figure 10. Shear-rate dependence of angular frequencies $|\omega_z|$ of star polymers with $f = 50$ and the concentrations $c/c^* = 0.19$ (full triangles) and $c/c^* = 2.92$ (open triangles). Results are compared for the definitions (14) (black), (17) (red), and (18) (green).

Another approximation for the angular momentum is obtained when the local velocity of a particle is replaced by the flow field, i.e., $\Delta \dot{\boldsymbol{r}}_i \approx \boldsymbol{v}(\boldsymbol{r}_i)$. With $\boldsymbol{v}(\boldsymbol{r}_i) = (\dot{\gamma} \Delta y_i, 0, 0)^{\mathrm{T}}$ follows

$$\langle L_z^G \rangle = -\dot{\gamma} \langle G_{yy} \rangle, \tag{16}$$

where the superscript indicates an approximation in terms of the radius of gyration tensor component G_{yy}. Hence, we obtain the frequencies

$$\omega_z^L = \frac{\langle L_z \rangle}{M(\langle G_{xx} \rangle + \langle G_{yy} \rangle)}, \tag{17}$$

$$\omega_z^G = -\dot{\gamma} \frac{\langle G_{yy} \rangle}{M(\langle G_{xx} \rangle + \langle G_{yy} \rangle)}. \tag{18}$$

Figure 10 shows an example of rotational frequencies obtained by the various definitions at low and high star-polymer concentrations. The data obtained by equations (14) and (17) are hardly distinguishable, whereas equation (18) yields somewhat larger frequencies $|\omega_z^G|$ at large shear rates. Remarkably, the differences between the various definitions are smaller at larger concentrations.

Figure 11(a) presents reduced rotational frequencies $|\omega_z|/\dot{\gamma}$ calculated according to equation (14) for systems in dilute solution and various functionalities. For weak flow strengths $\phi_f Wi_c \ll 1$, the expected dependence $|\omega_z| = \dot{\gamma}/2$ is recovered. At higher shear rates, the reduced frequency decreases with increasing Weissenberg number according to the power law $|\omega_z|/\dot{\gamma} \sim (\phi_f Wi_c)^{-1}$, which implies that the angular frequency is independent of $\dot{\gamma}$. The figure also demonstrates that the reduced frequency essentially follows a universal curve. Figure 11(b) shows $|\omega_z|/\dot{\gamma}$ for various concentrations and the functionality $f = 50$. Interestingly, a strong concentration dependence is obtained, with reduced slopes for frequency curves at higher concentrations. Starting from the power law Wi_c^{-1} at low concentrations, the rotational frequency curves approach a $Wi_c^{-2/3}$ dependence for high concentrations. Such a dependence has also been

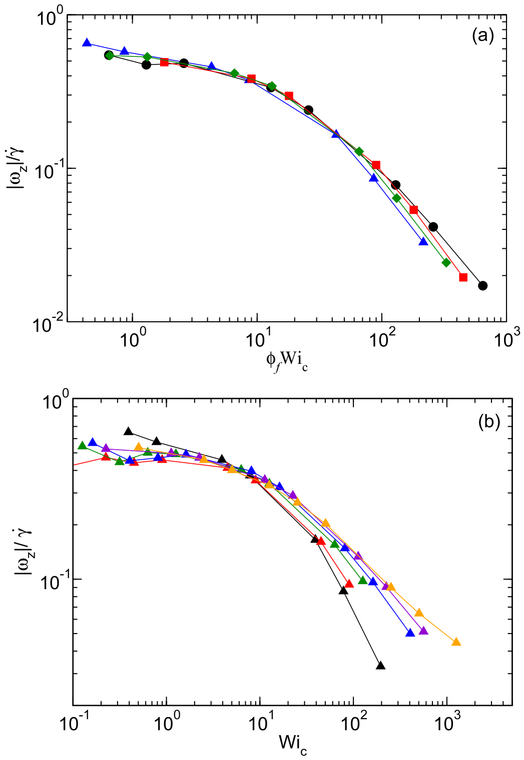

Figure 11. Reduced rotational frequency $|\omega_z|/\dot{\gamma}$ of star polymers according to equation (14). (a) Dilute solutions of the functionalities $f = 10$ (bullets), 20 (squares), 30 (diamonds), and 50 (triangles). (b) Concentration dependence for star polymers with $f = 50$ for $c/c^* = 0.19$ (black), 0.49 (red), 0.68 (green), 0.98 (blue), 1.46 (purple), and 2.92 (orange).

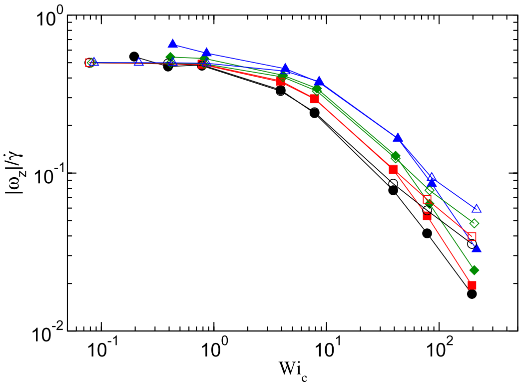

Figure 12. Comparison of the reduced angular frequency $|\omega_z|/\dot{\gamma}$ calculated according to equation (14) (full symbols) of star polymers at low concentration with the predictions by the Keller–Skalak model (open symbols) for a tank-treading ellipsoid in shear flow. The ratio of inner-to-outer viscosity is assumed to be $\lambda = 4$ for all cases.

found in [19] in flow simulations of individual stars without hydrodynamic interactions. Hence, we attribute the concentration dependence to the screening of hydrodynamic interactions at concentrations $c/c^* > 1$. A similar screening of hydrodynamic interactions was found for semi-dilute solutions of linear polymers in [35, 48]. The comparison in figure 10 shows that the dynamical quantity ω_z can be equally well obtained by any of the proposed definitions at high concentrations. Since equation (18) uses stationary state properties only, this might be expected to be applicable when correlations in the fluid are negligible, which is the case at high concentrations where hydrodynamic interactions are screened. At low concentrations, we expect dynamical quantities to be governed by hydrodynamic interactions beyond a simple rescaling of relaxation times, although the effect may be small as for linear polymers in shear flow [48].

4.2. Comparison of star polymer and vesicle rotational dynamics

The tank-treading dynamics of star polymers in shear flow has a striking resemblance to the tank-treading behavior of lipid vesicles [51]. To describe the tank-treading motion of a vesicle in shear flow, Keller and Skalak [51] proposed a model (KS model) for a viscous tank-treading ellipsoid. The details of the model are presented in the appendix. The KS model predicts the time dependence of the angle ϕ between a material point on the ellipsoid and the x-axis to describe tank-treading, and of the inclination angle θ between the main ellipsoidal axis and the x-axis. To compare the predictions of the KS model for tank-treading with our results on star polymers, we identify the ellipsoidal axes a_i ($i = 1$–3) to be the main axes of the star radius of gyration tensor, i.e., $a_i = \sqrt{\langle G_i \rangle}$. The only unknown parameter is the inner-to-outer fluid viscosity ratio λ in the KS model, which slows down the rotational tank-treading frequency as it increases for a fixed shear rate. It is plausible to expect λ to be greater than unity, because polymer arms in a star contribute to the star inner viscosity. We vary λ in the range $\lambda = 1$–6 in order to fit the relative rotational frequency of star polymers at low concentration and the functionality $f = 10$, and achieve the best fit for $\lambda = 4$. The ratio λ expresses the viscosity difference of the fluids inside and outside of a vesicle. For a star polymer, the inside viscosity is the effective viscosity of a polymer solution, with a strong contribution from intramolecular interactions. Similarly, the ratio η_G/η of the viscosity coefficient η_G of a polymer globule in bad solvent and the solvent viscosity η has been determined in [52] by Brownian dynamics simulations. η_G is also determined by intramolecular interactions, but arises here from volume-exclusion and effective attractive interactions between the monomers. Thus, a direct comparison of the viscosity ratios of these two systems is not possible. Nevertheless, it is interesting to note that the simulations of polymer globules yield $\eta_G/\eta = 2.6$, a value of the same order as our λ value.

Figure 12 shows the comparison of the reduced angular frequency of star polymers according to equation (14) at low concentration with the KS model using $\lambda = 4$. The KS model predictions agree very well with the simulation data at small and intermediate shear rates. However, at high shear rates a deviation is clearly observed. It is not fully clear whether the star-polymer dynamics at high shear rates becomes dissimilar to that of vesicles or the KS approximation breaks down. The KS theory assumes surface-incompressibility of the flow on the ellipsoid, which is not the case for star polymers. Also, our previous work [21]—where we measured monomer density distribution around the star center for $f = 10$—shows that the star-polymer shape at high shear rates resembles a rhombus rather than an ellipsoid. This shape information is not taken into account in the KS model. In addition, at high shear rates the monomer density within a star is inhomogeneous and the assumption of a constant λ ratio may be too crude. Nevertheless, the KS model confirms the similarity of the star and vesicle dynamics for small and intermediate shear rates.

5. Conclusions

We have studied the conformational and dynamical properties of star polymers under shear flow for various functionalities and concentrations. With increasing functionality, star polymers become more spherical and less deformable. Therefore, high-functionality stars are less elongated and less aligned with the flow direction at a given shear rate. The main result of our simulations is that the dependence of many static and dynamic properties of semi-dilute star-polymer solutions on concentration and functionality can be absorbed into an effective Weissenberg number, which can be factorized into a Weissenberg number $Wi = \dot{\gamma}\tau$ of a single polymer arm, a concentration-dependent factor $\beta(c/c^*)$, and a functionality-dependent factor ϕ_f.

Interestingly, the factor ϕ_f is found to be a decreasing function of f. In contrast, the equilibrium relaxation time τ_f of an individual star polymer in solution has been predicted [9]—based on the Daoud–Cotton approach—to display a power-law dependence $f^{(2-3\nu)/2}$, with $(2-3\nu)/2 = 0.1$ for $\nu = 0.6$; this would imply an effective Weissenberg number which slowly increases with f. There is an obvious contradiction between these two results. A possible explanation for the discrepancy is that our simulation results are derived for moderate arm lengths and functionalities, while the scaling arguments apply to very long arms and large functionalities. It would certainly be interesting to investigate star-polymer relaxation times in equilibrium in more detail to clarify this issue.

The second intriguing result is that a comparison of the star-polymer rotation dynamics with the dynamics of fluid vesicles shows a very similar tank-treading behavior for small and intermediate shear rates. This comparison can be used to extract an effective internal viscosity of a star, which is about a factor four larger than the solvent viscosity. It will be interesting to see whether it is possible to predict the viscosity of a dilute star-polymer solution based on this effective internal viscosity.

Acknowledgments

We thank J K G Dhont, D Richter, M Ripoll, J Stellbrink (Jülich), and D Vlassopoulos (FORTH Crete) for stimulating discussions. Financial support by the Deutsche Forschungsgemeinschaft (DFG) through the Collaborative Research Center 'Physics of Colloidal Dispersions in External Fields' (SFB TR6), and by the EU through the Collaborative Research Project 'NanoDirect' (NMP4-SL-2008-213948) is gratefully acknowledged. DAF acknowledges funding by the Humboldt Foundation through a postdoctoral fellowship.

Appendix. Keller–Skalak theory

The Keller–Skalak (KS) theory [51] describes tank-treading motion of a vesicle membrane in shear flow. The membrane is assumed to move along a fixed ellipsoidal path. The tank-treading motion is defined by the equations

$$\begin{aligned} \frac{\partial\phi}{\partial t} &= -\frac{\dot{\gamma}\cos(2\theta)}{z_1(z_2(\lambda-1)+2)}, \\ \frac{\partial\theta}{\partial t} &= -\frac{\dot{\gamma}}{2} - z_0\frac{\partial\phi}{\partial t} + \frac{\dot{\gamma}}{2}z_0 z_1\cos(2\theta), \end{aligned} \tag{19}$$

where ϕ is the angle between a material point on the ellipsoid and the x-axis to describe tank-treading, θ is the inclination angle between the main ellipsoidal axis and the x-axis to define orientation of the ellipsoid, t is time, and λ is the inner-to-outer fluid viscosity ratio. The parameters z_i ($i =$ 0–2) are determined by the geometrical characteristics of the ellipsoid and are given by

$$\begin{aligned} z_0 &= \frac{2a_1a_2}{a_1^2+a_2^2}, & z_1 &= \frac{a_1^2-a_2^2}{2a_1a_2}, \\ z_2 &= g\left(\alpha_1^2+\alpha_2^2\right), & \alpha_i &= \frac{a_i}{(a_1a_2a_3)^{1/3}}, \\ g &= \int_0^\infty (\alpha_1^2+s)^{-3/2}(\alpha_2^2+s)^{-3/2}(\alpha_3^2+s)^{-1/2}\,\mathrm{d}s, \end{aligned} \tag{20}$$

where the a_i ($i =$ 1–3) are the semiaxes of the ellipsoid. This model predicts tank-treading motion of a viscous ellipsoid (vesicle) with the inclination angle

$$\cos(2\theta) = \frac{z_1}{z_0}\left(z_1^2 + \frac{2}{z_2(\lambda-1)+2}\right)^{-1} \tag{21}$$

and the angular frequency

$$\omega/\dot{\gamma} = \frac{\cos(2\theta)}{z_1(z_2(\lambda-1)+2)}. \tag{22}$$

The dependence of $\omega/\dot{\gamma}$ on shear rate, which is displayed in figure 12, arises from the implicit dependence of the z_i on $\dot{\gamma}$. Note that at low λ values the ellipsoid shows tank-treading, while at high λ the ellipsoid may exhibit tumbling dynamics.

References

[1] Grest G S, Fetters L J, Huang J S and Richter D 1996 *Adv. Chem. Phys.* **94** 67

[2] Peppas N A, Keys K B, Torres-Lugo M and Lowman A M 1999 *J. Control Release* **62** 81

[3] Qiu L Y and Bae Y H 2006 *Pharm. Res.* **23** 1

[4] Wiltshire J T and Qiao G G 2007 *Aust. J. Chem.* **60** 699

[5] Daoud M and Cotton J P 1982 *J. Phys. (Paris)* **43** 531

[6] Likos C N, Löwen H, Watzlawek M, Abbas B, Jucknischke O, Allgaier J and Richter D 1998 *Phys. Rev. Lett.* **80** 4450

[7] Jusufi A, Watzlawek M and Löwen H 1999 *Macromolecules* **32** 4470

[8] Likos C N 2001 *Phys. Rep.* **348** 267

[9] Grest G S, Kremer K and Witten T A 1987 *Macromolecules* **20** 1376

[10] Grest G S, Kremer K, Milner S T and Witten T A 1989 *Macromolecules* **22** 1453

[11] Fetters L J, Kiss A D, Pearson D S, Quack G F and Vitus F J 1993 *Macromolecules* **26** 647

[12] Stellbrink J, Lonetti B, Rother G, Willner L and Richter D 2008 *J. Phys.: Condens. Matter* **20** 404206

[13] Vlassopoulos D and Fytas G 2010 *Adv. Polym. Sci.* **236** 1

[14] Pakula T, Vlassopoulos D, Fytas G and Roovers J 1998 *Macromolecules* **31** 8931

[15] Vlassopoulos D, Fytas G, Pakula T and Roovers J 2001 *J. Phys. Condens. Matter* **13** R855

[16] Helgeson M E, Wagner N J and Vlassopoulos D 2007 *J. Rheol.* **51** 297

[17] Erwin B M, Cloitre M, Gauthierd M and Vlassopoulos D 2010 *Soft Matter* **6** 2825

[18] Ripoll M, Winkler R G and Gompper G 2006 *Phys. Rev. Lett.* **96** 188302

[19] Ripoll M, Winkler R G and Gompper G 2007 *Eur. Phys. J.* E **23** 349

[20] Singh S P, Winkler R G and Gompper G 2011 *Phys. Rev. Lett.* **107** 158301

[21] Fedosov D A, Singh S P, Chatterji A, Winkler R G and Gompper G 2012 *Soft Matter* **8** 4109

[22] Nikoubashman A, Kahl G and Likos C N 2012 *Soft Matter* **8** 4121

[23] Briels W J 2009 *Soft Matter* **5** 4401

[24] Padding J T, van Ruymbeke E, Vlassopoulos D and Briels W J 2010 *Rheol. Acta* **49** 473

[25] Pierleoni C and Ryckaert J-P 1995 *Macromolecules* **28** 5097

[26] Malevanets A and Kapral R 1999 *J. Chem. Phys.* **110** 8605

[27] Kapral R 2008 *Adv. Chem. Phys.* **140** 89

[28] Gompper G, Ihle T, Kroll D M and Winkler R G 2009 *Adv. Polym. Sci.* **221** 1

[29] Malevanets A and Yeomans J M 2000 *Europhys. Lett.* **52** 231

[30] Ripoll M, Mussawisade K, Winkler R G and Gompper G 2004 *Europhys. Lett.* **68** 106

[31] Lees A W and Edwards S F 1972 *J. Phys. C: Solid State Phys.* **5** 1921

[32] Allen M P and Tildesley D J 1987 *Computer Simulation of Liquids* (Oxford: Clarendon)

[33] Huang C-C, Chatterji A, Sutmann G, Gompper G and Winkler R G 2010 *J. Comput. Phys.* **229** 168

[34] Westpahl E, Singh S P, Huang C-C, Gompper G and Winkler R G preprint

[35] Huang C-C, Winkler R G, Sutmann G and Gompper G 2010 *Macromolecules* **43** 10107

[36] Birshtein T M and Zhulina E B 1984 *Polymer* **25** 1453

[37] Birshtein T M, Zhulina E B and Borisov O V 1986 *Polymer* **27** 1078

[38] Doi M and Edwards S F 1986 *The Theory of Polymer Dynamics* (Oxford: Clarendon)

[39] Schroeder C M, Teixeira R E, Shaqfeh E S G and Chu S 2005 *Phys. Rev. Lett.* **95** 018301

[40] Rudnick J and Gaspari G 1986 *J. Phys. A: Math. Gen.* **19** L191

[41] Wei G and Eichinger B E 1990 *J. Chem. Phys.* **93** 1430

[42] Jagodzinski O 1994 *J. Phys. A: Math. Gen.* **27** 1471

[43] Bishop M, Clarke J H R, Rey A and Freire J J 1991 *J. Chem. Phys.* **94** 4009

[44] Aust C, Kröger M and Hess S 1999 *Macromolecules* **32** 5660

[45] Winkler R G 2010 *J. Chem. Phys.* **133** 164905

[46] Schroeder C M, Teixeira R E, Shaqfeh E S G and Chu S 2005 *Macromolecules* **38** 1967

[47] Winkler R G 2006 *Phys. Rev. Lett.* **97** 128301

[48] Huang C-C, Sutmann G, Gompper G and Winkler R G 2011 *Europhys. Lett.* **93** 54004

[49] Aust C, Hess S and Kröger M 2002 *Macromolecules* **35** 8621

[50] Winkler R G, Mussawisade K, Ripoll M and Gompper G 2004 *J. Phys.: Condens. Matter* **16** S3941

[51] Keller S R and Skalak R 1982 *J. Fluid Mech.* **120** 27

[52] Alexander-Katz A, Wada H and Netz R R 2009 *Phys. Rev. Lett.* **103** 028102

P11: Semi-dilute solutions of ultra-soft colloids under shear flow

D. A. Fedosov, S. P. Singh, A. Chatterji, R. G. Winkler, and G. Gompper

Soft matter, **8**:4109-4120, 2012.

View Article Online / Journal Homepage / Table of Contents for this issue
Dynamic Article Links

Soft Matter

Cite this: *Soft Matter*, 2012, **8**, 4109

www.rsc.org/softmatter

PAPER

Semidilute solutions of ultra-soft colloids under shear flow†

Dmitry A. Fedosov,[a] Sunil P. Singh,[a] Apratim Chatterji,[ab] Roland G. Winkler[a] and Gerhard Gompper*[a]

Received 20th October 2011, Accepted 5th January 2012
DOI: 10.1039/c2sm07009j

We study semidilute star-polymer solutions under shear flow by hybrid mesoscale simulations. Hydrodynamic interactions are modeled by two particle-based simulation techniques, multiparticle collision dynamics (MPC) and dissipative particle dynamics (DPD). Star polymers are considered as a paradigmatic model for ultra-soft colloids with variable softness. The influence of concentration and shear rate on their structural and rheological properties is investigated. Under flow, a star polymer elongates and displays a well-defined alignment angle with respect to the flow direction. Moreover, the structural and rheological properties exhibit a universal behavior as a function of a concentration-dependent Weissenberg number for various concentrations at a given arm length. The rheological properties are characterized by the shear viscosity and the normal-stress coefficients. In dilute solution, the zero-shear viscosity follows the Einstein relation with an effective radius given by the hydrodynamic radius of a star polymer. At high shear rates, the solutions exhibit shear-thinning behavior, where the viscosity decreases faster with increasing shear rate at higher concentrations. We demonstrate that the results obtained from MPC and DPD agree in all scaling properties, with minor quantitative deviations in the numerical values.

1 Introduction

The flow properties of solutions of macromolecules and colloids are of enormous importance for the behavior of many complex fluids, ranging from motor oils and drilling fluids to blood and the cytosol of living cells.[1] In many colloidal dispersions, the suspended particles are solid, but a much larger class of complex fluids contains deformable particles such as flexible synthetic polymers, semiflexible biopolymers, droplets, vesicles, capsules, and cells.

Linear and star polymers are particularly interesting model systems, because their size and architecture can be tailored in many different ways.[2] Studies of such systems are essential to obtain a detailed understanding of the rheological properties of complex fluids containing soft particles, which is required to design and control the flow behavior of fluids in technological or medical applications.

Star polymers consist of f identical linear polymer chains, which are linked at one of their ends to a common center. Each polymer arm contains N_m segments. By changing the arm length $L = N_m l$, where l is the bond length, and the functionality f, star-polymer properties can be varied between linear polymers (for $f = 2$) to nearly hard-sphere colloids (large functionality, short arms) and ultra-soft colloids (intermediate functionality, long arms).[2–5]

The equilibrium properties of star polymers have been studied in considerable detail.[3,5–8] The architecture of star polymers implies that the monomer density is high in the core region and decreases toward the corona. A consequence of this architecture and of the inhomogeneous density distribution is that the interaction is ultra-soft for sufficiently long chains, with a logarithmic dependence on the distance between two stars.[3–5] The ultra-soft interaction gives rise to an unusual phase diagram, for example with body-centered cubic (bcc) phases, which are not stable in systems of hard spheres,[9–12] reentrant melting,[5,13] and fcc-to-bcc transitions.[5,10,14]

Much less is known about the dynamical and rheological behavior of star-polymer solutions. Experiments show that self-diffusion decreases with increasing polymer concentration c according to a power law.[2,15] The diffusion coefficient of a star polymer in solution is larger than the diffusion coefficient of a hard-sphere colloid at equivalent volume fractions (defined by the hydrodynamic radius R_h in the case of star polymers). This is a direct consequence of the deformability and ultra-soft interactions of star polymers, which allow them to squeeze through gaps between other particles more easily. The same mechanism is responsible for the slower increase of the zero-shear viscosity with concentration for soft compared to hard particles.[2,15] In particular, it is observed that the viscosity of star-polymer solutions is finite even above the overlap concentration.[15,16] In

---

[a] *Theoretical Soft Matter and Biophysics, Institute of Complex Systems and Institute for Advanced Simulation, Forschungszentrum Jülich, 52425, Jülich, Germany. E-mail: g.gompper@fz-juelich.de*
[b] *Indian Institute of Science Education and Research (IISER), Pune, 411021, India*

† Electronic Supplementary Information (ESI) available: Two movies show simulation animations of semidilute star-polymer solutions for different shear rates. See DOI: 10.1039/c2sm07009j/

a related system of single DNA-grafted colloids, a strong dependence of the effective hydrodynamic radius on the conformation of the grafted polymer chains has been found.[17]

Theory and simulations have focused on the shape, orientation, and rotation of individual stars in shear flow,[18,19] on the dynamical frictional interactions between two stars[20] (both by an explicit bead-spring model of polymer chains), and on the rheology of concentrated solutions[21,22] (by a coarse-grained description with transient forces[23] between star centers).

The aim of the present study is to bridge the gap between the configurational and dynamical properties of individual star polymers, their hydrodynamic and steric interactions and the macroscopic flow behavior of semidilute solutions. So far, such systems have not been studied by simulations. Our investigations will help to establish a relation between the molecular architecture and microscopic deformation of individual soft colloids, and the macroscopic rheological behavior. Computer simulations of *linear* polymers in semidilute solutions show large deformations and a strong alignment of polymers along the flow direction in simple shear flow.[24,25] More importantly, in the stationary state, the *conformational* and *rheological properties* for various concentrations are universal functions of the Weissenberg number $Wi_c = \dot{\gamma}\tau(c)$, where $\dot{\gamma}$ is the shear rate and $\tau(c)$ the concentration-dependent polymer end-to-end vector relaxation time at equilibrium. Hence, with decreasing concentration, hydrodynamic interactions affect the conformational and rheological properties only by decreasing relaxation time $\tau(c)$. Experiments on DNA in shear flow[26] and simulations of polymer brushes[27] lead to a similar conclusion. We investigate here whether ultra-soft colloids in solution display a similar universal behavior in shear flow.

We use a standard bead–spring model to construct a polymer star. In order to account for hydrodynamic interactions, we employ two particle-based mesoscale simulation techniques, multiparticle collision dynamics (MPC)[28–30] and dissipative particle dynamics (DPD),[31,32] which are introduced in Sec. 2. This serves two purposes. On the one hand, we want to elucidate to what extend the two methods provide quantitatively equivalent results, and thereby test the suitability of these methods for predicting the non-equilibrium behavior of complex fluids; on the other hand, we want to establish method-independently the flow properties of ultra-soft colloids.

We will present and discuss in Sec. 3 several structural properties of star polymers in solutions under shear flow—such as the radius-of-gyration tensor and the alignment angle—as well as the corresponding bulk rheological properties of these solutions—such as shear-dependent viscosity and normal-stress coefficients. Finally, the results obtained by the two simulation techniques are compared with each other and with available experimental data in Sec. 4.

2 Methods and models

To model star-polymer solutions we employ two different mesoscopic simulation techniques: (i) multiparticle collision dynamics (MPC), also called stochastic rotation dynamics (SRD),[29,30] and (ii) dissipative particle dynamics (DPD).[31,32] Both methods implement proper hydrodynamic interactions and have been used in simulations of various soft matter and biological systems.[30,33]

2.1 Star-polymer model

We consider N_{sp} star polymers, where each star consists of f flexible linear polymer arms with one of their ends attached to a common center, which is illustrated in Fig. 1. Consecutive monomers of a polymer chain (arm) are connected by harmonic springs with the potentials

$$V_b = \frac{k_s}{2}(R_{i,i+1} - l)^2, \qquad (1)$$

where $\boldsymbol{R}_{i,\,i+1} = \boldsymbol{R}_{i+1} - \boldsymbol{R}_i$ is the bond vector, $R_{i,\,i+1} = |\boldsymbol{R}_{i,\,i+1}|$, and l is the equilibrium bond length. The spring constant k_s is chosen such that even under strong shear stress the change in the equilibrium bond length remains less than a few percent. Excluded volume interactions between star monomers are implemented through the repulsive (truncated and shifted) Lennard-Jones (LJ) potential[34]

$$V_{LJ}(r) = 4\varepsilon\left[\left(\frac{\sigma}{r}\right)^{12} - \left(\frac{\sigma}{r}\right)^{6} + \frac{1}{4}\right]\Theta(2^{1/6} - r), \qquad (2)$$

where $\Theta(r)$ is the Heaviside step function ($\Theta(r) = 0$ for $r < 0$ and $\Theta(r) = 1$ for $r \geq 0$). Since many polymer arms are attached to the center particle, the equilibrium bond length l_c of each center-arm connection and the LJ diameter σ_c of the central bead are taken to be twice as large as those for a normal monomer. We employ l as the unit of length, $\varepsilon = k_BT$ as the unit of energy, and m_s, the solvent particle mass, as the unit of mass. The unit of time is defined as $\tau = \sqrt{m_s l^2/(k_BT)}$. The parameters for star polymers for both MPC and DPD are listed in Table 1. The velocity Verlet algorithm is used to integrate Newtons' equations of motion of the star polymers with time step $h_m = 5 \times 10^{-3}\tau$ in MPC and $h_m = 8 \times 10^{-3}\tau$ in DPD.

2.2 Multiparticle collision dynamics

In the MPC algorithm, the solvent is modeled by N_s point particles with positions $\boldsymbol{r}_i$ and velocities $\boldsymbol{v}_i$ ($i = 1, \ldots, N_s$). The dynamics of these particles proceeds in discrete time increments

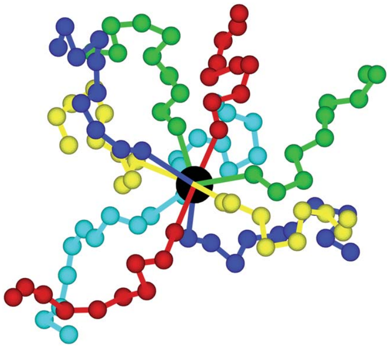

Fig. 1 A star polymer represented by a bead–spring model with $f = 10$ linear-polymer arms, connected to a common central (black sphere). The length of each arm is $N_m = 10$. The arms are colored for better visual differentiation.

Table 1 Star-polymer parameters in MPC and DPD simulations, where subscripts '*m*' and '*c*' denote arm monomers and central bead, respectively

	$k_s l^2/k_B T$	l_c/l	σ_m/l	σ_c/l	M_m/m_s	M_c/m_s
MPC	1000	2.0	0.8	1.6	10	10
DPD	125	2.0	0.8	1.6	2	10

h, denoted as collision time, by alternating streaming and collision steps.[29,30] In the streaming step, the solvent particles of mass m_s move ballistically with their respective velocities, and their positions are updated as

$$\boldsymbol{r}_i(t + h) = \boldsymbol{r}_i(t) + h\boldsymbol{v}_i(t). \tag{3}$$

After each streaming step, solvent particles are sorted into the cells of a simple cubic lattice with lattice constant a. Their relative velocities, with respect to the center-of-mass velocity of the cell, are rotated around a randomly oriented axis by an angle α, so that

$$\boldsymbol{v}_i(t + h) = \boldsymbol{v}_i(t) + (\mathbf{R}(\alpha) - \mathbf{I})(\boldsymbol{v}_i(t) - \boldsymbol{v}_{cm}(t)), \tag{4}$$

where $\mathbf{R}$ is the rotation matrix, $\mathbf{I}$ is the unit matrix, and $\boldsymbol{v}_{cm} = \frac{1}{N_c}\sum_{j=1}^{N_c}\boldsymbol{v}_j$ is the center-of-mass velocity of the cell with N_c particles. The collision step is a stochastic process, where mass, energy, and momentum are conserved, which ensures that hydrodynamic behavior emerges on larger length scales.

The star polymers are coupled to the solvent during the collision step, where their monomers are included in the collisions together with the solvent particles.[35,36] Thereby, momentum is redistributed between solvent and monomers in the same cell.

Transport properties of the solvent depend on the collision time h, the rotation angle α, and the average number density per cell. Tuning these variables allows us to attain solvents with a high Schmidt number, where momentum transport dominates over mass transport. Some of the simulation parameters for MPC system are summarized in Table 2. These parameters correspond to the solvent viscosity $\eta_s = 8.7\sqrt{m_s\varepsilon/l^4}$ and the Schmidt number $Sc \approx 17$.

Lees–Edwards boundary conditions are applied for the solvent particles and the monomers in order to impose shear flow.[37] This yields a linear fluid velocity profile $v_x = \dot{\gamma}y$ in the flow direction (x-axis) as a function of their position along the gradient direction (y-axis), where $\dot{\gamma}$ is the shear rate. A local cell-wise Maxwellian thermostat is applied to maintain the desired temperature of the fluid.[38]

2.3 Dissipative particle dynamics

Similar to MPC, a DPD system consists of a collection of N_s point particles. DPD particles interact through simple pairwise-additive forces corresponding to a conservative force F_{ij}^C, a dissipative force F_{ij}^D, and a random force F_{ij}^R. The total force exerted on a particle i by particle j consists of the three terms given by

$$\begin{aligned} \boldsymbol{F}_{ij}^C &= b\left(1 - \frac{r_{ij}}{r_C}\right)\hat{\boldsymbol{r}}_{ij}, \\ \boldsymbol{F}_{ij}^D &= -\gamma\omega^D\left(r_{ij}\right)\left(\boldsymbol{v}_{ij}\cdot\hat{\boldsymbol{r}}_{ij}\right)\hat{\boldsymbol{r}}_{ij}, \\ \boldsymbol{F}_{ij}^R &= \sigma_{ran}\omega^R\left(r_{ij}\right)\frac{\xi_{ij}}{\sqrt{h}}\hat{\boldsymbol{r}}_{ij}, \end{aligned} \tag{5}$$

where $\boldsymbol{r}_{ij} = \boldsymbol{r}_i - \boldsymbol{r}_j$, $\hat{\boldsymbol{r}}_{ij} = \boldsymbol{r}_{ij}/r_{ij}$, and $\boldsymbol{v}_{ij} = \boldsymbol{v}_i - \boldsymbol{v}_j$. The coefficients b, γ, and σ_{ran} determine the strength of conservative, dissipative, and random forces, respectively. ω^D and ω^R are weight functions and ξ_{ij} is a symmetric normally-distributed random variable with zero mean and unit variance. All forces act within a sphere of cutoff radius r_c. The random and dissipative forces must satisfy the fluctuation-dissipation theorem[32] in order for the DPD system to maintain the equilibrium temperature T, which is enforced through the two conditions $\omega^D(r_{ij}) = [\omega^R(r_{ij})]^2$ and $\sigma_{ran}^2 = 2\gamma k_B T$. The usual choice for the weight function is $\omega^R(r_{ij}) = (1 - r_{ij}/r_c)^p$, where $p = 1$ for the original DPD method. However, other choices (*e.g.*, $p = 0.25$) for these envelopes have been used[39,40] in order to increase the viscosity of the DPD fluid and bring the Schmidt number in DPD to values representative of real liquids. The time evolution of velocities and positions of particles is determined by Newton's second law of motion, which is integrated using the velocity–Verlet algorithm.

The simulation parameters for the DPD system are listed in Table 3. With these parameters, we obtain a Schmidt number $Sc = 1011$. The time step is set to $h = h_m = 8 \times 10^{-3}\tau$. Star polymers are constructed similarly to that described in Sec. 2.1 and are coupled to the fluid through DPD forces with $b_{ps}l/\varepsilon = 0$, $\gamma_{ps}\tau/m_s = 7.5$, and $p_{ps} = 0.25$, where the subscript ps denotes polymer–solvent interactions. Lees–Edwards boundary conditions are employed to model steady shear flow, as described above in Sec. 2.2.

3 Results and discussion

A list of parameters of star-polymer solutions for both mesoscale hydrodynamic simulation techniques is given in Table 4; it provides information about the size of simulation box $L_x \times L_y \times L_z$, the range of number of star polymers N_{sp}, and the ranges of simulated shear rates $\dot{\gamma}$ and concentrations c. All results are obtained for functionality $f = 10$, with arm lengths in the range $N_m = 10$–30. Specifically, MPC simulations are performed for $N_m = 10$ and 30, DPD simulations for $N_m = 10$ and 20. The simulations for $N_m = 10$ are performed with both MPC and DPD in order to compare the results and to show that the predictions for the properties of star-polymer solutions are independent of the

Table 2 MPC fluid parameters in the simulations. $\langle N_c \rangle$ is the average number of solvent particles per cell

a/l	α	$<N_c>$	h/τ	$\eta_s/\sqrt{m_s k_B T/l^4}$
1.0	130°	10.0	0.1	8.7

Table 3 DPD fluid parameters in simulations. The subscript *ss* denotes the corresponding parameters for solvent–solvent interactions. *n* is the solvent number density

$b_{ss}l/\varepsilon$	$\gamma_{ss}\tau/m_s$	p_{ss}	r_c/l	nl^3	$\eta_s/\sqrt{m_s k_B T/l^4}$
20.0	5.0	0.15	3.0	0.375	8.21

Table 4 List of simulation parameters. L_x, L_y, and L_z denote the dimensions of the simulation box and $\dot{\gamma}$ is the shear rate. R_{g0} and R_h are the equilibrium radius of gyration and hydrodynamic radius in dilute solution, respectively, and τ_z is the Zimm relaxation time

Method	N_m	N_{sp}	$L_x/l \times L_y/l \times L_z/l$	R_{g0}/l	R_h/l	τ_z/τ	c/c^*	$\dot{\gamma}\tau$
MPC	10	20–200	30 × 30 × 30	3.54	3.74	870	0.17–1.65	10^{-5}–5×10^{-2}
MPC	30	100–750	100 × 100 × 100	7.14	7.10	7830	0.15–1.13	10^{-5}–2.5×10^{-2}
DPD	10	23–299	50 × 34 × 36.2	4.06	4.10	821	0.1–1.3	5×10^{-5}–1.6×10^{-2}
DPD	20	30–390	76 × 52 × 51.8	5.80	5.46	3285	0.1–1.3	5×10^{-5}–1.6×10^{-2}

employed method. In the other set of simulations with $N_m = 20$ in DPD and $N_m = 30$ in MPC, we intend to obtain the solution properties for a wider range of arm lengths N_m. We measure concentration relative to the overlap concentration

$$c^* = \left[\frac{4}{3}\pi R_h^3\right]^{-1} \tag{6}$$

where R_h is the hydrodynamic radius.

The applied shear flow is characterized by the dimensionless Weissenberg number $Wi = \dot{\gamma}\tau_z$, where $\tau_z = \eta_s N_m^2 l^3 / k_B T$ is the Zimm relaxation time of a polymer arm in dilute solution. At low shear rates or small $Wi \ll 1$, star polymers are close to their equilibrium structure. However, at large $Wi \gg 1$, they are strongly deformed and aligned with the flow as shown by the snapshots in Fig. 2. The relaxation time of a star polymer increases with concentration, which suggests to use the concentration-dependent Weissenberg number $Wi_c = \beta\,(c/c^*)\,Wi$ to take this change into account. As has been shown recently for semidilute solutions of *linear polymers*, the concentration dependence of structural and rheological properties are captured very well in this way and universal curves are obtained.[24,25]

The lengths of typical simulation runs were at least several tens of times the equilibrium polymer relaxation time τ, and up to several hundred times τ for low shear rates.

3.1 Radius-of-gyration tensor

Two characteristic conformations of star polymers in solution at intermediate and high shear rates are shown in Fig. 2. To quantitatively characterize the effect of shear flow on the structural properties of star polymers we calculate the radius of gyration tensor of a star polymer according to

$$G_{\alpha\beta} = \frac{1}{N}\left\langle \sum_{i=1}^{N} \Delta r_i^\alpha \Delta r_j^\beta \right\rangle, \tag{7}$$

where $N = fN_m + 1$ is the total number of monomers in a star, Δr_i is the position of the i^{th} monomer relative to the star center of mass, and $\alpha, \beta \in \{x, y, z\}$. In equilibrium, all diagonal components of $G_{\alpha\beta}$ are equal, *i.e.*, $G_{\alpha\alpha} = G_{\alpha\alpha}^{00} = R_{g0}^2/3$, where R_{g0} is the radius of gyration. In the dilute regime, the radius of gyration follows the scaling relation $R_{g0}^2 \sim l_0^2 N_m^{2\nu} f^{1-\nu}$ in terms of arm length and functionality,[3,6–8] with the exponent $\nu \approx 0.63$ for our system.

Under shear flow, polymers along the flow direction become elongated; their relative deformation in this direction is calculated as

$$\delta G_{xx}(c/c^*) = \frac{G_{xx}(c/c^*) - G_{xx}^0(c/c^*)}{G_{xx}^0(c/c^*)}, \tag{8}$$

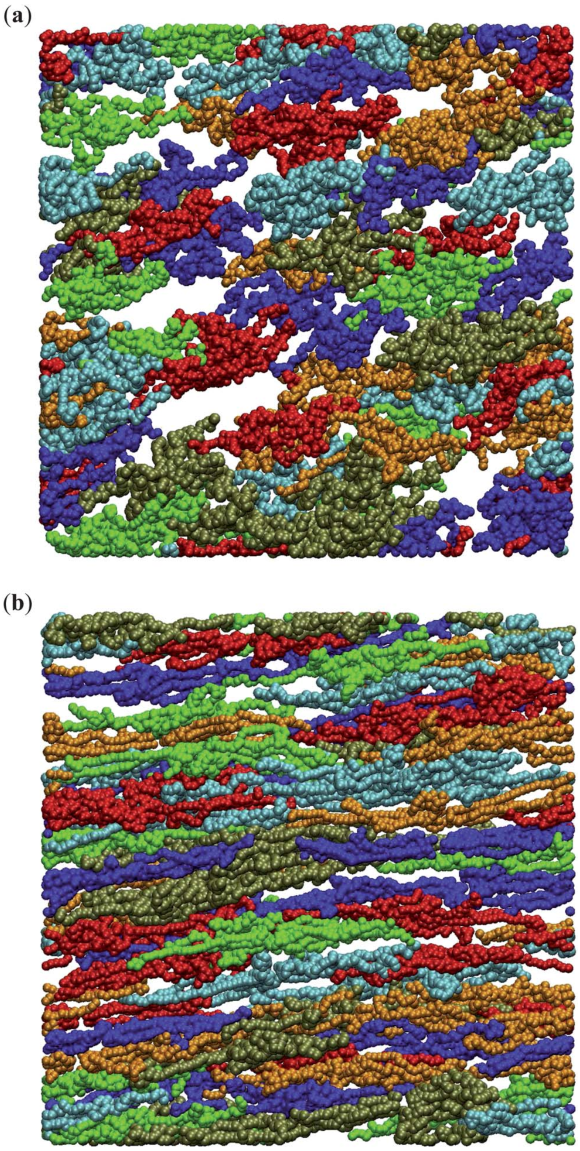

Fig. 2 Simulation snapshots of star-polymer solutions with functionality $f = 10$, arm length $N_m = 30$, and concentration $c/c^* = 0.75$ (where c^* is the overlap concentration, see Sec. 3). (a) Intermediate shear rate with concentration-dependent Weissenberg number $Wi_c = 15$, and (b) high shear rate with $Wi_c = 153$ (for definition of Wi_c see Sec. 3). Only star polymers with their centers in a slice of thickness of twice the radius of gyration R_{g0} parallel to the flow-gradient plane are shown. The multiple colors serve to make different star polymers easily distinguishable. Corresponding movies are shown in the ESI.†

where G^0_{xx} is the radius of gyration at equilibrium for a given concentration. A comparison of simulation data of δG_{xx} for various concentrations and arm lengths at the same Weissenberg number Wi shows that stars at higher concentrations exhibit a stronger stretching than those at lower c/c^*. This is due to differences in the relaxation times, which increase with increasing concentration.[24] We can estimate the concentration dependence of the relaxation time by scaling the Weissenberg number by a factor $\beta\ (c/c^*)$, in order to shift δG_{xx} for high concentrations to the lowest concentration curve. A universal curve is then obtained for the relative deformation δG_{xx} as function of $Wi_c = \beta\ (c/c^*)\ Wi$ for the various polymer lengths and both simulation methods, as shown in Fig. 3. At large shear rates, the extension of star polymers saturates at a maximum value, which depends on the length of the polymer arms. At low $Wi_c < 1$, a quadratic dependence of the relative deformation (solid black line) as a function of shear rate is observed, which has also been seen in previous MPC simulations of single star polymers[18] and of semidilute solutions of linear polymers,[24] as well as in experiments.[41]

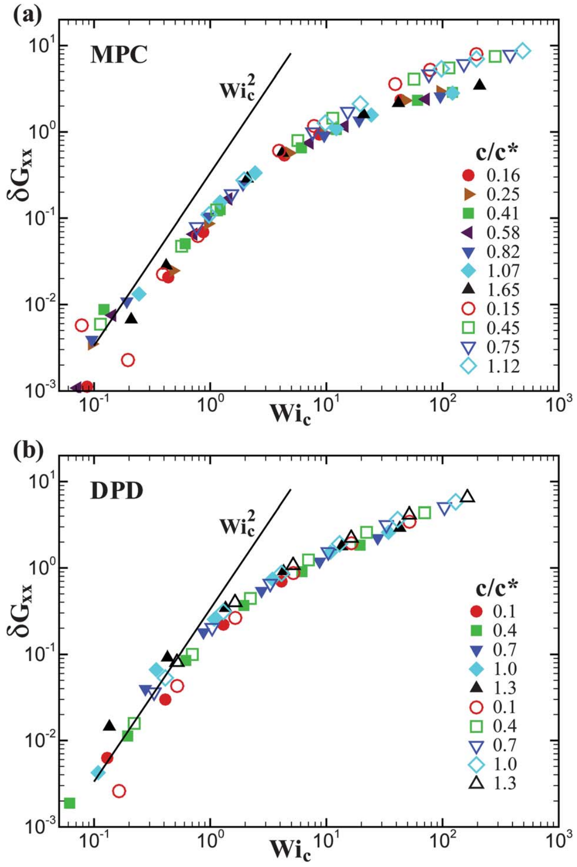

Fig. 3 Relative deformation δG_{xx} of star polymers along the flow direction as function of the concentration-dependent Weissenberg number Wi_c. (a) MPC simulation results, with arm lengths $N_m = 10$ (filled symbols) and $N_m = 30$ (open symbols), and various concentrations c/c^*, as indicated. (b) DPD simulation results for various star-polymer concentrations, as indicated, and $N_m = 10$ (filled symbols) and $N_m = 20$ (open symbols). The black solid lines indicate a quadratic dependence of the relative deformation on Wi_c at low shear rates; these lines are identical in (a) and (b).

The scale factors $\beta\ (c/c^*)$ are displayed in Fig. 4 as a function of concentration. The values of $\beta\ (c/c^*)$ from the MPC simulations for $N_m = 10$ and 30 and DPD simulations for $N_m = 10$ and 20 are nearly independent of arm length. In Fig. 3, the scaling of δG_{xx} with Wi_c and the functional dependence are in very good agreement for both methods; there is a small difference in the absolute values, which will be discussed in more detail in Sec. 4. Since the scale factor is proportional to the ratio of star relaxation times for different concentrations, the characteristic relaxation time on the star concentration appears to be nearly independent of the arm length.

Along the shear-gradient and vorticity directions, star polymers shrink at high Wi_c. Fig. 5 displays the scaled curves for the gyration tensor G_{yy}/G^{00}_{yy} as a function of Wi_c, where G^{00}_{yy} corresponds to the y component of the radius of gyration in equilibrium and in the dilute limit. The differences in the plateau values of G_{yy}/G^{00}_{yy} at low Wi_c are associated with the change in star-polymer size at various concentrations indicating that the stars become more compact due to their crowding. Compression in the vorticity direction is quite small in comparison with the gradient direction, consistent with previous results for single star polymers.[18]

3.2 Star-polymer alignment

Flow-induced alignment of star polymers can be characterized by the angle χ_G, which is the angle between the eigenvector of the gyration tensor with the largest eigenvalue and the flow direction. It can be computed from the components of the gyration tensor as

$$\tan(2\chi_G) = \frac{2G_{xy}}{G_{xx} - G_{yy}}. \qquad (9)$$

Fig. 6 shows the alignment angle of star polymers as function of Wi_c for various concentrations and both simulation methods.

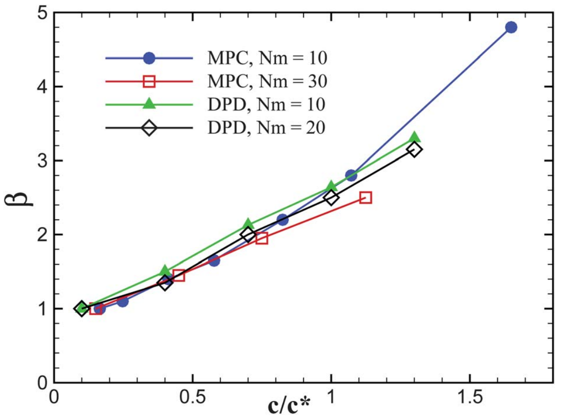

Fig. 4 Concentration-dependent scale factor for the relaxation time ($\tau\ (c) = \beta\ (c)\tau_z$) obtained from the scaling of the radius-of-gyration tensor along the shear direction. MPC and DPD results are shown for various arm lengths N_m, as indicated.

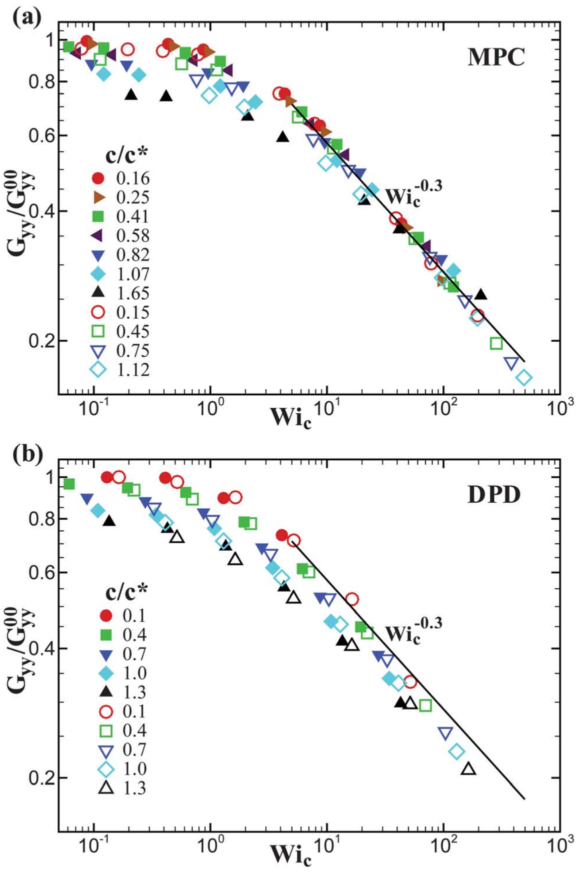

Fig. 5 Star-polymer deformation along the gradient direction, G_{yy}/G_{yy}^{00}, as function of Wi_c. (a) MPC simulation results, with arm lengths $N_m = 10$ (filled symbols) and $N_m = 30$ (open symbols), and various concentrations c/c^*, as indicated. (b) DPD simulation results for various star-polymer concentrations, as indicated, and $N_m = 10$ (filled symbols) and $N_m = 20$ (open symbols).

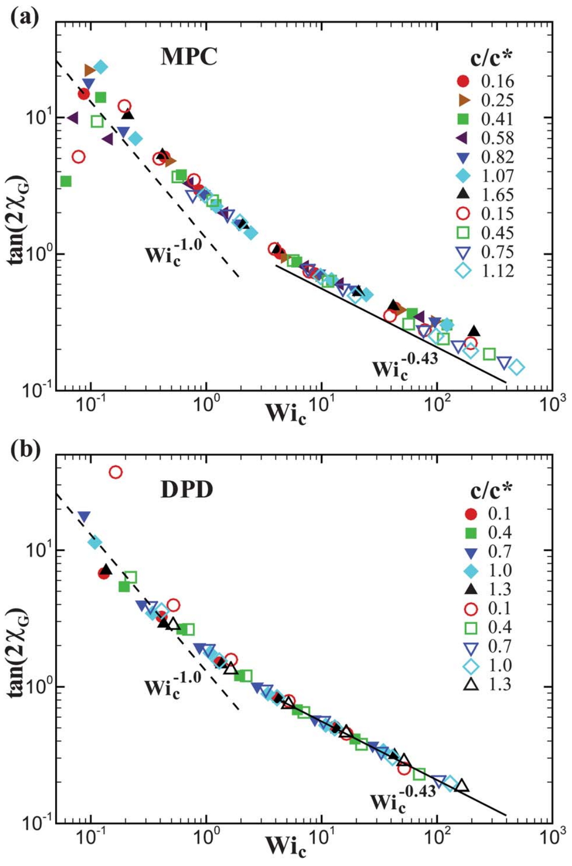

Fig. 6 Orientation of star polymers $\tan(2\chi_G)$ as function of Wi_c. (a) MPC simulation results, with arm lengths $N_m = 10$ (filled symbols) and $N_m = 30$ (open symbols), and various concentrations c/c^*, as indicated. (b) DPD simulation results for various star-polymer concentrations, as indicated, and $N_m = 10$ (filled symbols) and $N_m = 20$ (open symbols). The dashed black lines indicate a scaling behavior $\tan(2\chi_G) \sim Wi_c^{-1}$ and the solid black lines correspond to $\tan(2\chi_G) \sim Wi_c^{-0.43}$. Note that lines in (a) and (b) are identical.

At low shear rates the alignment angle χ_G is close to the equilibrium value $\pi/4$. For $0 < Wi_c < 1$, the data in Fig. 6(a) obey the expected scaling behavior[42,43] $\tan(2\chi_G) \sim Wi_c^{-1}$, which follows from the fact that $G_{xy} \sim Wi_c$ and $G_{xx} - G_{yy} \sim Wi_c^2$ in that regime. At high Wi_c, star polymers deform into an ellipsoidal shape, and the angle χ_G decreases due to alignment of the star along the flow direction. Again, a universal curve is obtained for different star-polymer concentrations and both MPC and DPD methods as a function of Wi_c. At high Wi_c, the alignment angle follows the scaling law

$$\tan(2\chi_G) \sim (Wi_c)^{-\delta} \tag{10}$$

with the exponent of $\delta \approx 0.43$. The master curve obtained for different arm lengths is almost independent of N_m for $Wi_c < 20$. At higher Wi_c, effects of finite arm length may play a role, as in systems of linear polymers.[24] Stars with longer arms appear to be more aligned with the flow direction than those with shorter arms at $Wi_c > 20$. This is due to the fact that the crossover from the behavior $\tan(2\chi_G) \sim Wi_c^{-1}$ to the asymptotic behavior $\tan(2\chi_G) \sim Wi_c^{-1/3}$, predicted by theory for linear polymers,[43] appears at smaller Wi_c for longer polymers.

The shear-induced structural deformation and alignment of star polymers can be visualized in terms of their monomer density distribution in the flow-gradient plane. In Fig. 7, such distributions of individual stars are presented for $Wi_c = 0.78$, 7.8, and 78. At very low shear rates, the stars are close to their equilibrium shape and the density distribution is spherically symmetric. An increase of the shear rate leads to the alignment of star polymers along the flow direction. For $Wi_c \gg 1$, star arms are highly stretched along the flow and compressed in the gradient direction. Particularly at high shear rates, the density distribution is not of elliptical but rather of rhombic shape, with nearly flat parts along the flow direction.

3.3 Rheology

To characterize the rheological properties of the star-polymer solutions, we determine various components of the stress tensor,

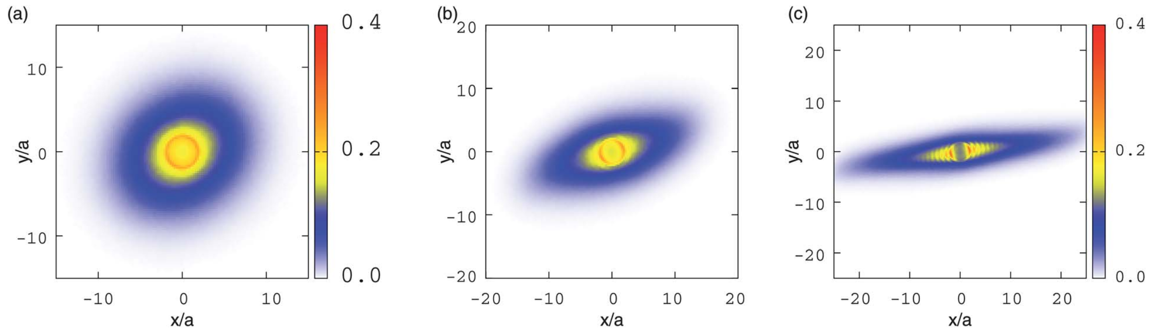

Fig. 7 Monomer density distributions of individual star polymers in the flow-gradient plane for various Weissenberg numbers, (a) $Wi_c = 0.78$, (b) $Wi_c = 7.8$, and (c) $Wi_c = 78.0$. The arm length is $N_m = 30$ and the polymer concentration is $c/c^* = 0.15$. The density distributions are indistinguishable between the two simulation approaches. The strip-like density modulations in (c) reflect the monomer-density modulations of the strongly stretched and aligned polymers.

in particular σ_{xy}, σ_{xx}, σ_{yy}, and σ_{zz}, using the Irving–Kirkwood formula for the virial.[44,45] We consider only the star-polymer contributions to the virial, which includes their bond and excluded-volume contributions. The shear viscosity as a function of shear rate follows from $\eta(\dot{\gamma}) = \sigma_{xy}(\dot{\gamma})/\dot{\gamma}$. In addition, we compute the corresponding first and second normal-stress coefficients Ψ_1 and Ψ_2 defined as

$$\Psi_1(\dot{\gamma}) = \frac{\sigma_{xx}(\dot{\gamma}) - \sigma_{yy}(\dot{\gamma})}{\dot{\gamma}^2}, \qquad \Psi_2(\dot{\gamma}) = \frac{\sigma_{yy}(\dot{\gamma}) - \sigma_{zz}(\dot{\gamma})}{\dot{\gamma}^2}. \tag{11}$$

For many polymeric fluids, the viscosity function and normal-stress coefficients display zero-shear rate plateaus at low shear rates, which is often referred to as low-shear-rate Newtonian regime.

Fig. 8 shows shear stresses σ_{xy} normalized by σ^0_{xy} for different arm lengths and concentrations as a function of Wi_c. σ^0_{xy} follows from the relation $\sigma_{xy} = \sigma^0_{xy}\, Wi_c$ in the limit of small shear rates; its dependence on concentration is presented in Fig. 9.

Evidently, the shear stress is a linear function of shear rate for $Wi_c < 1$ independent of concentration. At larger Weissenberg numbers, a crossover can be observed to a weaker dependence on Wi_c. In that regime, we observe a non-universal concentration dependence; $\sigma_{xy}/\sigma^0_{xy}$ is larger at smaller concentrations, but the data seem to converge toward a common limiting behavior with increasing concentration. Both, MPC and DPD simulations exhibit the same behavior.

The dimensionless stress scale factors $\sigma^0_{xy}R_h^3/(k_BT)$ in Fig. 9 are virtually independent of the star-polymer arm length. This demonstrates that the characteristic relaxation time of a star polymer exhibits a similar length dependence as R_h^3. A slight deviation is found between the stress scale factors for MPC and DPD simulations. We attribute this deviation to differences in the way a star polymer is coupled to the solvent in the two approaches.

The viscosities of the star-polymer solutions are displayed in Fig. 10 for various arm lengths and concentrations. The curves are scaled by the corresponding zero-shear viscosity η_0 in order to verify and find a scaling behavior. The values of η_0 for the systems with $N_m = 10$ can directly be extracted from simulations. However, for the systems of longer chains, the zero-shear plateau appears only at extremely low shear rates, which is difficult to

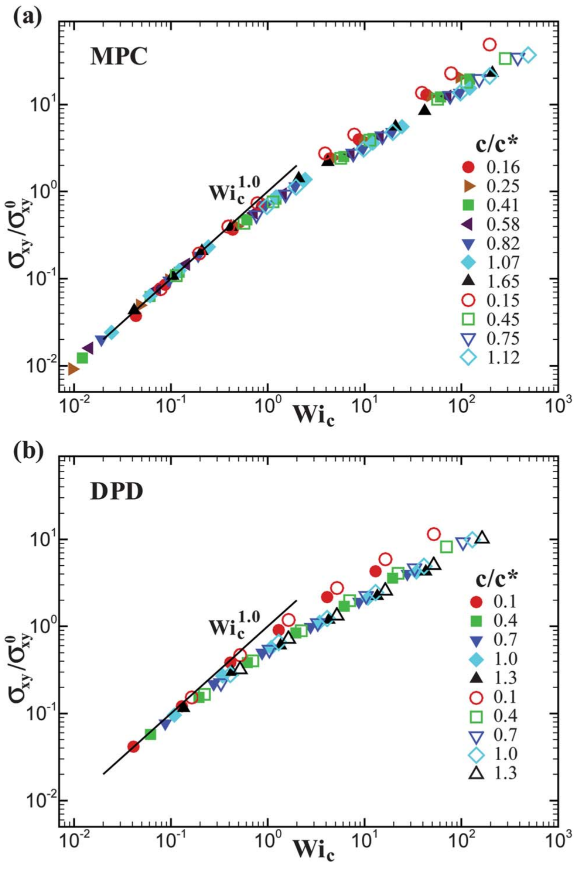

Fig. 8 Normalized shear stress $\sigma_{xy}/\sigma^0_{xy}$ of star-polymer solutions with respect to Wi_c, where $\sigma_{xy} = \sigma^0_{xy}Wi_c$ as $\dot{\gamma} \to 0$, see Fig. 9. (a) MPC simulation results, with arm lengths $N_m = 10$ (filled symbols) and $N_m = 30$ (open symbols), and various concentrations c/c^*, as indicated. (b) DPD simulation results for various star-polymer concentrations, as indicated, and $N_m = 10$ (filled symbols) and $N_m = 20$ (open symbols). Only polymer contributions to the virial are included.

View Article Online

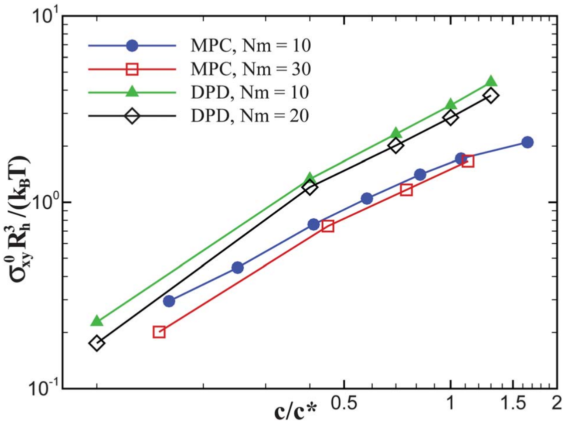

Fig. 9 Scaling factors σ^0_{xy} (normalized by k_BT/R_h^3) for the shear stress of star-polymer solutions at different concentrations. σ^0_{xy} values are computed as σ_{xy}/Wi_c at low shear rates ($\dot{\gamma} \rightarrow 0$).

access in simulations, since thermal fluctuations overwhelm average flow properties and reliable statistics are difficult to obtain. An additional simulation complexity for star systems with long arms is related to the characteristic relaxation time of such stars, which becomes very long in comparison to that of the stars with relatively short arms and leads to demanding simulation times. Therefore, the various viscosity curves for $N_m = 20$ and 30 in Fig. 10 were scaled to match the lowest available concentration results at low shear rates, which may not necessarily be within the zero-shear plateau, but are likely within the transition region to the power-law regime.

At $Wi_c > 1$, the viscosities exhibit a power-law decay with increasing shear rate (Fig. 10). An interesting feature is that the power-law exponent appears to dependent on the star-polymer concentration, a dependence already visible for the shear stress in Fig. 8. At low concentrations, the exponent is equal to approximately −0.3, while at high star concentrations $c/c^* \simeq 1.3$ it is about −0.4. Such a dependence has not been predicted by any theory and appears to be independent of arm length, but is consistently obtained with both simulation techniques. The concentration dependence results in a poor scaling of the viscosity curves, suggesting that a common master curve for the shear viscosity behavior may not exist. This is in contrast to simulations results for linear polymers, where the viscosities hardly exhibit a concentration dependence when data are plotted as a function of Wi_c.[24] It is not evident what causes the differences in the behavior of linear and star polymers, keeping in mind that the stress tensor is in essence determined by the virial term of the polymer-bond contributions. We would like to point out, however that the star-polymer dynamics under flow is distinctly different from that of a linear polymer—a linear polymer undergoes tumbling motion,[25] whereas star polymers show a tank-treading-like rotation[18] for functionalities $f > 5$.

Fig. 11 presents the zero-shear viscosity values for various arm lengths with respect to star concentration extracted from the scaling of the polymer contribution η_p to the viscosity. For the star solutions with $N_m = 10$, in DPD simulations we have also used an alternative method, called reverse Poiseuille flow (RPF), in order to estimate the zero-shear viscosity.[46] The RPF is generated from two Poiseuille flows driven by uniform body forces in opposite directions along two halves of a periodic computational domain. The zero-shear viscosities computed with RPF are in excellent agreement with those values obtained by proper scaling of the viscosity curves as done in Fig. 10.

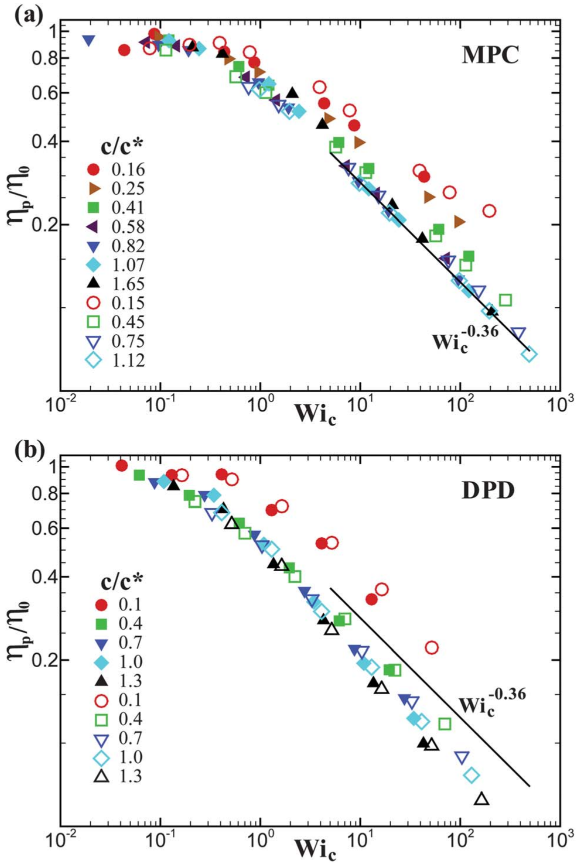

Fig. 10 Shear-rate-dependent viscosity of simulated star-polymer solutions for various arm lengths and concentrations as a function of Wi_c. (a) MPC simulation results, with arm lengths $N_m = 10$ (filled symbols) and $N_m = 30$ (open symbols), and various concentrations c/c^*, as indicated. (b) DPD simulation results for various star-polymer concentrations, as indicated, and $N_m = 10$ (filled symbols) and $N_m = 20$ (open symbols). Only polymer contributions to the viscosity are shown. The viscosity curves are scaled with the corresponding values of the zero-shear viscosity η_0 for different concentrations. The solid lines indicate the power-law dependence $\eta_p \sim Wi_c^{-0.36}$; they are identical in (a) and (b).

Evidently, the star-polymer concentrations exceed the linear regime, where $\eta_0/\eta_s = 2.5\phi$ applies as predicted by Einstein[47] for colloids of volume fraction ϕ—in our case $\phi = c/c^*$. The MPC data follow the dependence $\eta_0/\eta_s = 2.5\phi + 6.2\phi^2$ proposed for Brownian solutions.[48] The DPD simulations yield somewhat larger viscosity ratios η_0/η_s, but the dependence on c/c^* is very similar. In addition, the dependence $(1 - \phi/\phi_m)^{-2.5\phi_m}$ is plotted, which is valid for a colloidal solution.[49]

It is clear that there is only a weak dependence of the zero-shear viscosity on the arm length N_m. This is again an indication that certain properties of star-polymer solutions may be absorbed in the star hydrodynamic radius R_h, which determines the

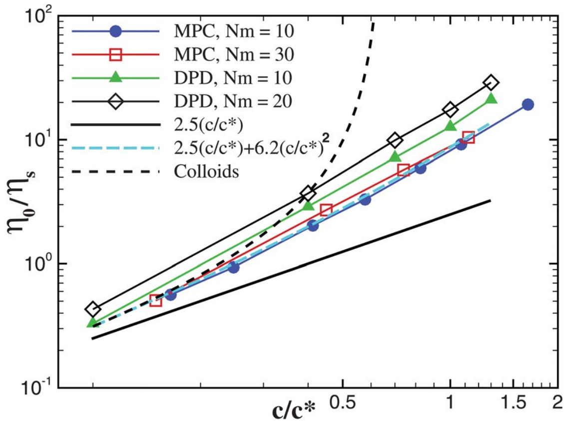

Fig. 11 Zero-shear viscosity normalized by η_s as a function of star-polymer concentration c/c^*, for various N_m as indicated. Several theoretical predictions for a colloidal solution are also plotted. The solid black line corresponds the linear regime $\eta_0/\eta_s = 2.5\phi$ predicted by Einstein[47] for colloids, where $\phi = c/c^*$. The cyan dashed curve displays the dependence of $\eta_0/\eta_s = 2.5\phi + 6.2\phi^2$ for Brownian solutions.[48] The black dashed curve indicates the dependence of $(1-\phi/\phi_m)^{-2.5\phi_m}$, which is valid for a solution of colloids.[49]

solution concentration. In contrast to these results are experimental measurements of η_0 for star solutions with different functionalities,[15] which show a strong dependence of η_0 on f such that the star solution viscosity approaches the viscosity curve for a colloidal solution at high f. This is likely a consequence of the increasing monomer concentration around the star center, which is altered substantially for varying f. Thus, star functionality would be directly associated with star softness, while N_m effectively changes the size of a star polymer.

We have introduced three scale factors, β, σ_{xy}^0, and η_0, which are not independent. They are rather related and the ratio $\eta_0/(\sigma_{xy}^0\beta)$ is approximately constant.

Fig. 12 shows the normalized first normal-stress coefficient Ψ_1. The curves of Ψ_1 for various concentrations are scaled by factors ψ_1^0, which are displayed in Fig. 14. As expected, we find a plateau at low $Wi_c < 1$. At high Wi_c, the shear-dependent Ψ_1 exhibit a power-law behavior with an exponent of approximately -1, independent of the arm length and the employed simulation method. Note that the power-law exponent becomes slightly larger for high c/c^* values in comparison with the solutions at low star concentrations; however, the differences in the exponents seem to be less pronounced than those for the viscosity curves in Fig. 10. We expect that in the asymptotic limit of large c/c^* the exponent approaches $-4/3$, as predicted by theory and observed for polymers.[24,43,50–54]

The corresponding normalized second normal-stress coefficients Ψ_2 are presented in Fig. 13 as a function of Wi_c. The values of Ψ_2 are noticeably noisier than the values of Ψ_1 and it is not fully clear if the zero-shear plateau can be reliably estimated from the simulation data. The power-law region at high Wi_c corresponds to the exponent of about -1.4 for all simulated N_m, close to the theoretically expected value for ψ_1. Finally, the simulated normal-stress coefficients agree very well for both, the MPC and DPD method.

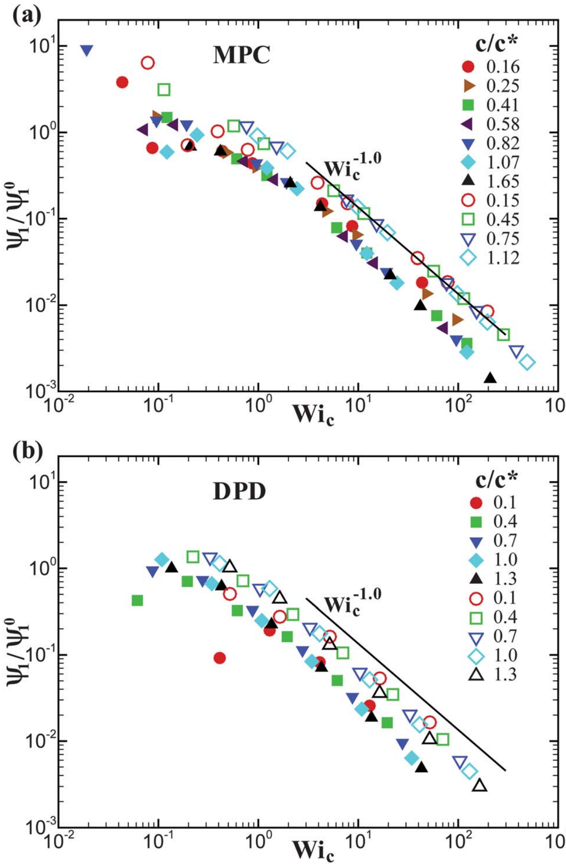

Fig. 12 First normal-stress coefficient Ψ_1, normalized by a concentration-dependent factor ψ_1^0 (see Fig. 14), as a function of Wi_c. (a) MPC simulation results, with arm lengths $N_m = 10$ (filled symbols) and $N_m = 30$ (open symbols), and various concentrations c/c^*, as indicated. (b) DPD simulation results for various star-polymer concentrations, as indicated, and $N_m = 10$ (filled symbols) and $N_m = 20$ (open symbols). The solid lines indicate a power-law dependence $\psi_1 \sim Wi_c^{-1}$; they are identical in (a) and (b).

The scale factors ψ_1^0 and ψ_2^0 normalized by $\eta_s^2 R_h^3/(k_B T)$ are shown in Fig. 14. These factors were obtained by scaling the normal-stress coefficients for various concentrations to the lowest available concentration for a given N_m. Under the assumption of a universal scaling of Ψ_1 and Ψ_2 for various concentrations, the factors ψ_1^0 and ψ_2^0 are proportional to the corresponding zero-shear-rate plateau values of the normal-stress coefficients. The factors ψ_1^0 and ψ_2^0 are rather similar for a given arm length, for both, the MPC and DPD calculations. Moreover, the MPC and DPD values agree very well for $N_m = 10$. The decrease of the values with increasing chain length is due to scaling by the hydrodynamic radius $R_h^3 \sim N_m^2$. The factors ψ_1^0, ψ_2^0 themselves exhibit a weak arm-length dependence only. The magnitude of the scale factors for both, the first and second normal-stress coefficients seem to be nearly identical, which points to a similar dependence of the zero-shear-rate plateau values on concentration for both Ψ_1 and Ψ_2.

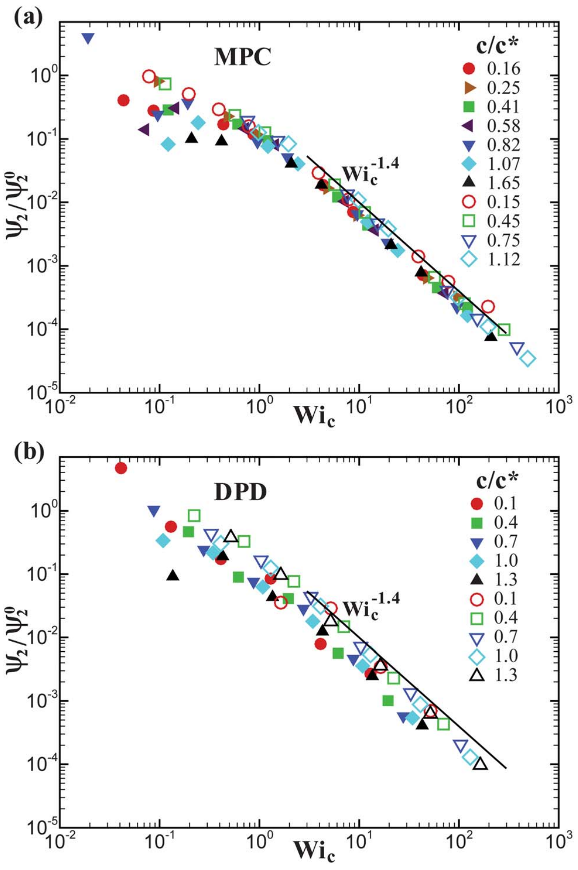

Fig. 13 Second normal-stress coefficient Ψ_2, normalized by a concentration-dependent factor ψ_2^0 (see Fig. 14), as a function of Wi_c. (a) MPC simulation results, with arm lengths $N_m = 10$ (filled symbols) and $N_m = 30$ (open symbols), and various concentrations c/c^*, as indicated. (b) DPD simulation results for various star-polymer concentrations, as indicated, and $N_m = 10$ (filled symbols) and $N_m = 20$ (open symbols).

4 Summary and conclusions

We have investigated the flow behavior of dilute and semidilute solutions of star polymers in shear flow by two mesoscale hydrodynamics simulation techniques. The simulations show that many structural, dynamical, and rheological properties of star-polymer solutions can be described very well in terms of a concentration- and arm-length-dependent Weissenberg number $Wi_c = \dot{\gamma}\tau(c)$. This implies that the main effect of steric and hydrodynamic interactions on the star dynamics in dilute and semidilute solutions can be absorbed in the concentration- and arm-length-dependent relaxation time $\tau(c)$. Furthermore, we find that the behavior in the regime of small or large Weissenberg numbers is often well described by power laws, similar to those of semidilute solutions of linear polymers.[24]

An important aspect of our study is a detailed comparison of the predictions obtained by two frequently used particle-based hydrodynamics simulation techniques, MPC and DPD. As mentioned several times in Sec. 3, the agreement of the results for relaxation time, data collapse with concentration-dependent Weissenberg number, and power-law behavior is excellent. This is not self-evident, but requires that the parameters are chosen in the appropriate regime; here, it is particularly important to guarantee a sufficiently high Schmidt number (the ratio between momentum and mass transport). The good agreement between the two approaches strongly indicates that our results allow quantitative predictions and comparison with experimental results.

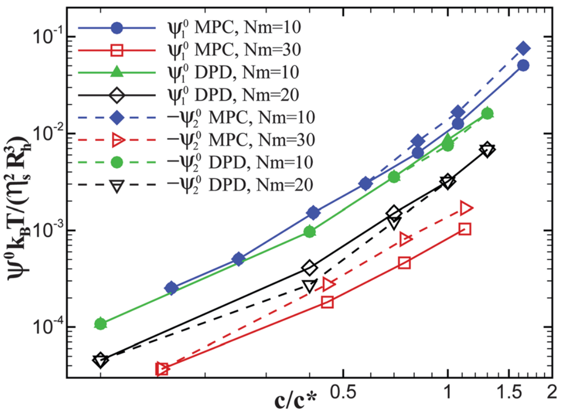

Fig. 14 Scaling factors ψ_1^0 and $-\psi_2^0$ (normalized by $\eta_s^2 R_h^3/(k_B T)$) for the normal-stress coefficients of star-polymer solutions for various concentrations. These factors are obtained by scaling the normal-stress coefficient curves for various concentrations (Fig. 12 and 13) to a reference curve, which corresponds to the lowest available concentration for a fixed N_m.

A careful look at corresponding figures for MPC and DPD reveals that there are small differences in the absolute values of several quantities. This can be seen most easily by comparing the simulation data to the lines indicating the power laws, because these lines are identical in corresponding figures. We attribute these differences mainly to small discrepancies in the star relaxation times of the two simulation approaches. We used the Zimm time to define a Weissenberg number, which appropriately captures the arm-length dependence, but is not necessarily identical to the relaxation time governing the dynamical properties of a star. Our simulation results suggest that the ratio of the Zimm time τ_z and the characteristic relaxation time of a star polymer is somewhat larger in MPC than in DPD simulations.

Scaling of conformational and dynamical properties of dilute and semidilute solutions with a concentration-dependent Weissenberg number Wi_c was obtained previously for *linear* polymers.[24] This raises the question about the similarities and differences in the flow behavior of linear and star-polymer solutions. Not unexpectedly, the qualitative behavior is similar in the two systems. It is also clear that the absolute values of deformation and orientation, viscosity and normal-stress coefficients are different. In general, star polymers seem to be less stretched and less aligned with the flow direction than linear polymers at a comparable Wi_c, and have a higher zero-shear viscosity—because stars resist stretching more than linear polymers due to the repulsive entropic and enthalpic interactions between their arms. Interestingly, similar power-law regimes are obtained for the various quantities for both, linear polymers and star polymers of functionality $f = 10$. This suggests that the star properties are determined to a considerable extent by the polymer arms. To what extent the asymptotic behavior predicted for linear polymers is reached by the star-polymer systems remains to be investigated.

Finally, we can compare our simulation results with experimental studies of rheological properties.[15] The zero-shear viscosity increases more rapidly with concentration (with $\eta_0/\eta_s = 2.5\phi + 6.2\phi^2$) than for linear polymers[24] (where $\eta_0/\eta_s = 2.5\phi + 6.25k_H\phi^2$ with the Huggins coefficient[55,56] $k_H \simeq 0.3$), but less strongly than for hard-sphere colloids. Furthermore, the zero-shear viscosity as a function of c/c^* depends only very weakly on the arm length. A comparison of the experimental data for $f = 34$, $f = 62$, and $f = 124$ with the simulation results for $f = 10$ and $f = 2$ (linear polymers) is shown in Fig. 15. This shows a very consistent trend of an increase of the zero-shear viscosity with increasing functionality at constant concentration c/c^*, and demonstrates the crossover of star-polymer properties from ultra-soft to hard-sphere colloids with increasing functionality. A more detailed comparison requires simulations for larger functionalities and arm lengths.

The viscosity of star-polymer solutions of very high functionality $f \simeq 390$ has also been measured experimentally at concentrations in the fluid and glassy phases.[16] In the semidilute regime, the shear stress shows a linear increase at low shear rates, followed by a less pronounced growth with effective exponent of approximately 0.5; this effective exponent decreases with increasing concentration.[16] Both observations are consistent with our simulation results. The exponent of the power law of the shear stress for intermediate Weissenberg number is important, because a value larger than unity signals shear banding. Such a behavior has indeed been predicted for concentrated solutions.[22] On the basis of our simulations, no shear banding is predicted for $f = 10$ stars in the investigated concentration range. We expect that considerably larger functionalities are necessary to observe shear banding.

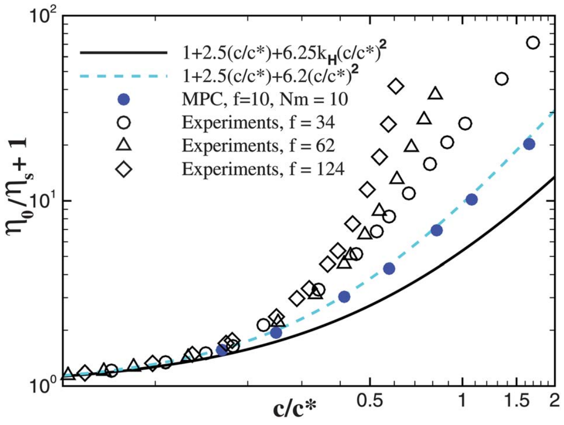

Fig. 15 Experimental and simulation results for the zero-shear viscosity of solutions of star polymers of different architecture. Experimental results (open symbols) for functionalities $f \geq 34$ are extracted from Fig. 6 of ref. 15. They are compared with the results for star polymers with $f = 10$ (closed symbols, dashed line) and for linear polymers (24) (solid line).

Acknowledgements

We thank J. K. G. Dhont, J. Stellbrink, D. Richter, M. Ripoll (Jülich), and D. Vlassopoulos (FORTH Crete) for stimulating discussions. Financial support by the Deutsche Forschungsgemeinschaft (DFG) through the Collaborative Research Center "Physics of Colloidal Dispersions in External Fields" (SFB TR6), and by the EU through the Collaborative Research Project "NanoDirect" (NMP4-SL-2008-213948) is gratefully acknowledged. D.A.F. acknowledges funding by the Humboldt Foundation through a postdoctoral fellowship.

References

1 R. G. Larson, *The Structure and Rheology of Complex Fluids*, Oxford University Press, New York, 1999.
2 D. Vlassopoulos and G. Fytas, *Adv. Polym. Sci.*, 2010, **236**, 1–54.
3 M. Daoud and J. P. Cotton, *J. Phys.*, 1982, **43**, 531.
4 C. N. Likos, H. Löwen, M. Watzlawek, B. Abbas, O. Jucknischke, J. Allgaier and D. Richter, *Phys. Rev. Lett.*, 1998, **80**, 4450–4453.
5 C. N. Likos, *Phys. Rep.*, 2001, **348**, 267–439.
6 T. M. Birshtein and E. B. Zhulina, *Polymer*, 1984, **25**, 1453.
7 T. M. Birshtein, E. B. Zhulina and O. V. Borisov, *Polymer*, 1986, **27**, 1078.
8 G. S. Grest, K. Kremer and T. A. Witten, *Macromolecules*, 1987, **20**, 1376.
9 M. Watzlawek, C. N. Likos and H. Löwen, *Phys. Rev. Lett.*, 1999, **82**, 5289–5292.
10 M. Laurati, J. Stellbrink, R. Lund, L. Willner, D. Richter and E. Zaccarelli, *Phys. Rev. Lett.*, 2005, **94**, 195504.
11 P. Ziherl and R. D. Kamien, *J. Phys. Chem. B*, 2001, **105**, 10147–10158.
12 G. M. Grason, B. A. DiDonna and R. D. Kamien, *Phys. Rev. Lett.*, 2003, **91**, 058304.
13 G. A. McConnell and A. P. Gast, *Macromolecules*, 1997, **30**, 435.
14 K. Ishizu, *Prog. Polym. Sci.*, 1998, **23**, 1383.
15 D. Vlassopoulos, G. Fytas, T. Pakula and J. Roovers, *J. Phys.: Condens. Matter*, 2001, **13**, R855–R876.
16 B. M. Erwin, M. Cloitre, M. Gauthierd and D. Vlassopoulos, *Soft Matter*, 2010, **6**, 2825–2833.
17 O. Ueberschär, C. Wagner, T. Stanger, C. Gutsche and F. Kremer, *Polymer*, 2011, **52**, 1829.
18 M. Ripoll, R. G. Winkler and G. Gompper, *Phys. Rev. Lett.*, 2006, **96**, 188302.
19 M. Ripoll, R. G. Winkler and G. Gompper, *Eur. Phys. J. E*, 2007, **23**, 349–354.
20 S. P. Singh, R. G. Winkler and G. Gompper, *Phys. Rev. Lett.*, 2011, **107**, 158301.
21 J. T. Padding, E. van Ruymbeke, D. Vlassopoulos and W. J. Briels, *Rheol. Acta*, 2010, **49**, 473–484.
22 W. J. Briels, D. Vlassopoulos, K. Kang and J. K. G. Dhont, *J. Chem. Phys.*, 2011, **134**, 124901.
23 W. J. Briels, *Soft Matter*, 2009, **5**, 4401–4411.
24 C.-C. Huang, R. G. Winkler, G. Sutmann and G. Gompper, *Macromolecules*, 2010, **43**, 10107–10116.
25 C.-C. Huang, G. Sutmann, G. Gompper and R. G. Winkler, *Europhys. Lett.*, 2011, **93**, 54004.
26 J. Hur, E. S. G. Shaqfeh, H. P. Babcock, D. E. Smith and S. Chu, *J. Rheol.*, 2001, **45**, 421.
27 A. Galuschko, L. Spirin, T. Kreer, A. Johner, C. Pastorino, J. Wittmer and J. Baschnagel, *Langmuir*, 2010, **26**, 6418.
28 A. Malevanets and R. Kapral, *J. Chem. Phys.*, 1999, **110**, 8605–8613.
29 R. Kapral, *Adv. Chem. Phys.*, 2008, **140**, 89.
30 G. Gompper, T. Ihle, D. M. Kroll and R. G. Winkler, *Adv. Polym. Sci.*, 2009, **221**, 1–87.
31 P. J. Hoogerbrugge and J. M. V. A. Koelman, *Europhys. Lett.*, 1992, **19**, 155–160.
32 P. Espanol and P. Warren, *Europhys. Lett.*, 1995, **30**, 191–196.
33 I. V. Pivkin, B. Caswell and G. E. Karniadakis, *Reviews in Computational Chemistry*, John Wiley & Sons, Inc., Hoboken, NJ, USA, 2010, vol. 27, pp. 85–110.

34 M. P. Allen and D. J. Tildesley, *Computer Simulation of Liquids*, Clarendon Press, Oxford, 1987.
35 A. Malevanets and J. M. Yeomans, *Europhys. Lett.*, 2000, **52**, 231.
36 M. Ripoll, K. Mussawisade, R. G. Winkler and G. Gompper, *Europhys. Lett.*, 2004, **68**, 106.
37 A. W. Lees and S. F. Edwards, *J. Phys. C: Solid State Phys.*, 1972, **5**, 1921–1928.
38 C.-C. Huang, A. Chatterji, G. Sutmann, G. Gompper and R. G. Winkler, *J. Comput. Phys.*, 2010, **229**, 168.
39 X. Fan, N. Phan-Thien, S. Chen, X. Wu and T. Y. Ng, *Phys. Fluids*, 2006, **18**, 063102.
40 D. A. Fedosov, I. V. Pivkin and G. E. Karniadakis, *J. Comput. Phys.*, 2008, **227**, 2540–2559.
41 C. M. Schroeder, R. E. Teixeira, E. S. G. Shaqfeh and S. Chu, *Phys. Rev. Lett.*, 2005, **95**, 018301.
42 C. Aust, M. Kröger and S. Hess, *Macromolecules*, 1999, **32**, 5660.
43 R. G. Winkler, *J. Chem. Phys.*, 2010, **133**, 164905.
44 J. H. Irving and J. G. Kirkwood, *J. Chem. Phys.*, 1950, **18**, 817–829.
45 R. G. Winkler and C.-C. Huang, *J. Chem. Phys.*, 2009, **130**, 074907.
46 D. A. Fedosov, G. E. Karniadakis and B. Caswell, *J. Chem. Phys.*, 2010, **132**, 144103.
47 A. Einstein, *Investigations on the theory of the Brownian movement*, Dover, New York, 1956.
48 G. K. Batchelor, *J. Fluid Mech.*, 1977, **83**, 97–117.
49 I. M. Krieger and T. J. Dougherty, *J. Rheol.*, 1959, **3**, 137–152.
50 A. V. Lyulin, D. B. Adolf and G. R. Davies, *J. Chem. Phys.*, 1999, **111**, 758.
51 D. Petera and M. Muthukumar, *J. Chem. Phys.*, 1999, **111**, 7614.
52 R. M. Jendrejack, J. J. de Pablo and M. D. Graham, *J. Chem. Phys.*, 2002, **116**, 7752.
53 C.-C. Hsieh and R. G. Larson, *J. Rheol.*, 2004, **48**, 995.
54 C. M. Schroeder, R. E. Teixeira, E. S. G. Shaqfeh and S. Chu, *Macromolecules*, 2005, **38**, 1967.
55 R. Pamies, J. G. Hernández Cifre, M. C. López Martínez and J. García de la Torre, *Colloid Polym. Sci.*, 2008, **286**, 1223.
56 Y. Takahashi, Y. Isono, I. Noda and M. Nagasawa, *Macromolecules*, 1985, **18**, 1002.

P12: Margination of white blood cells in microcapillary flow

D. A. Fedosov, J. Fornleitner, and G. Gompper

Physical Review Letters, **108**:028104, 2012.

PRL **108,** 028104 (2012) PHYSICAL REVIEW LETTERS week ending 13 JANUARY 2012

Margination of White Blood Cells in Microcapillary Flow

Dmitry A. Fedosov, Julia Fornleitner, and Gerhard Gompper
Theoretical and Soft Matter Biophysics, Institute of Complex Systems and Institute for Advanced Simulation,
Forschungszentrum Jülich, 52425 Jülich, Germany

(Received 21 September 2011; published 11 January 2012)

Margination of white blood cells (WBCs) towards vessel walls is an essential precondition for their efficient adhesion to the vascular endothelium. We perform numerical simulations with a two-dimensional blood flow model to investigate the dependence of WBC margination on hydrodynamic interactions of blood cells with the vessel walls, as well as on their collective behavior and deformability. We find WBC margination to be optimal in intermediate ranges of red blood cell (RBC) volume fractions and flow rates, while, beyond these ranges, it is substantially attenuated. RBC aggregation enhances WBC margination, while WBC deformability reduces it. These results are combined in state diagrams, which identify WBC margination for a wide range of flow and cell suspension conditions.

DOI: 10.1103/PhysRevLett.108.028104 PACS numbers: 87.19.U−, 83.50.Ha, 83.80.Lz, 87.16.D−

Introduction.—Leukocytes or white blood cells (WBCs) are part of our immune system, performing various organism defense functions. In order to reach the sites of action (e.g., inflammation), WBCs have to migrate to the vessel walls through a process called margination [1–3], adhere efficiently to vascular endothelium (mediated by adhesion proteins [4,5]), and further transmigrate into the surrounding tissues [6]. The efficiency of WBC adhesion in blood flow is correlated with the contact frequency of WBCs with the vessel walls, and thus with margination.

The mechanism for WBC margination in microvessels is related to the presence of red blood cells (RBCs) in blood. RBCs in microvessels migrate to the vessel center [7,8]. This process is governed by cell-wall hydrodynamic interactions [9] (often called lift force), which drive the cells away from the wall, and by cell-cell interactions, which tend to disperse RBCs [10]. WBC margination is believed to be a consequence of the competition between lift forces on RBCs and WBCs, where the lift force on a RBC is larger than that on a WBC due to the nonspherical discocyte shape and high deformability of RBCs. These interactions result in WBC margination (i.e., segregation), such that their concentration becomes higher near a vessel wall [2,3].

Several blood and flow properties may contribute to WBC margination, which include hematocrit H_t (i.e., RBC volume fraction), flow rate, vessel geometry, and RBC aggregability [1,3,11–14]. *In vivo* experiments on WBC margination in the mesenteric venules of rats [3] showed a substantial increase of the WBC adhesion rate (and consequently margination), with the decreasing flow rate at relatively high $H_t > 0.45$. A different dependence of WBC margination on H_t was reported in recent *in vitro* experiments on blood flow in microfluidic channels [14], where the strongest margination effect was found at intermediate $H_t \simeq 0.2$–0.3, while, at lower or higher H_t values, WBC margination was attenuated. In contradiction to these experiments, recent results on WBC adhesion in glass capillaries [12] show no dependence of WBC adhesion, and therefore margination, on hematocrit. The effect of flow rate on WBC margination and adhesion seems to be consistent across the various studies [3,11,14] which showed a significant enhancement at low flow rates comparable with those in venular blood flow. In addition, RBC aggregation has been found to result in an increased WBC margination and adhesion [3,11,12,14] at the vessel walls.

Simulations of a two-dimensional blood model in Ref. [13] showed increasing margination with decreasing flow rate, in agreement with experiments, but only a weak dependence on hematocrit. WBC margination is found to be insensitive to RBC deformability, which suggests that the RBC biconcave shape is the main governing parameter for the lift force on a RBC [13].

In order to integrate these various, sometimes apparently contradicting, observations into a coherent picture, a more extensive study of the dependence of WBC margination on hematocrit, flow rate, WBC deformability, and RBC aggregation is clearly necessary. We focus here on a two-dimensional (2D) model of blood flow; see Fig. 1 and

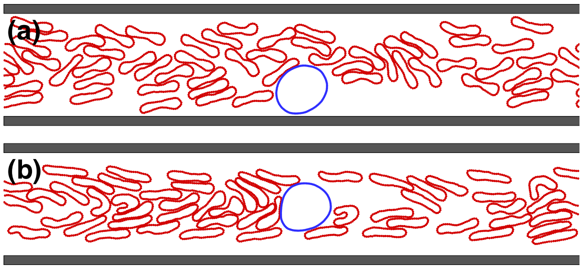

FIG. 1 (color online). Simulation snapshots of the flow (from left to right) at $H_t = 0.35$ and dimensionless shear rate (a) $\dot{\gamma}^* = 1.59$ and (b) $\dot{\gamma}^* = 19.68$. The large quasispherical particle is the WBC [15].

Ref. [15]. In particular, we show that there is a pronounced effect of hematocrit on WBC margination and provide new insights into the physical mechanism. We find a reentrant behavior, where margination first increases with increasing hematocrit but then decreases again at higher hematocrits. Furthermore, changes in WBC deformability strongly affect margination, since a deformed WBC may significantly depart from the spherical shape.

Models and methods.—We employ the dissipative particle dynamics method [16], a particle-based mesoscopic simulation technique, to model blood cells suspended in a fluid. A dissipative particle dynamics system consists of N point particles, which interact through pairwise soft forces and move according to Newton's second law of motion. Both two-dimensional cell types are modeled by a collection of N_v particles (50 for RBCs and 100 for WBCs) [15] connected by $N_s = N_v$ springs with the potential [17]

$$V_{sp} = \sum_{j\in 1\ldots N_s}\left[\frac{k_BTl_m(3x_j^2 - 2x_j^3)}{4p(1-x_j)} + \frac{k_p}{l_j}\right], \tag{1}$$

where l_j is the length of the spring j, l_m is the maximum spring extension, $x_j = l_j/l_m$, p is the persistence length, k_BT is the energy unit, and k_p is the spring constant. A balance between the two force terms in Eq. (1) determines a nonzero equilibrium spring length l_0. The cell model also incorporates a bending energy

$$V_{\text{bend}} = \sum_{j\in 1\ldots N_v} k_b[1 - \cos(\theta_j)], \tag{2}$$

where k_b is the bending constant and θ_j is the instantaneous angle between two adjacent springs having the common vertex j. In addition, a constraint to maintain a constant cell area is imposed on each cell by the potential $V_{\text{area}} = k_a(A - A_0)^2/2$, where k_a is the area constraint coefficient, A is the instantaneous cell area, and A_0 is the specified (target) area. The combination of A_0 and the cell perimeter N_sl_0 determines the shape of a cell. The RBC diameter is chosen to be $D_r \equiv 2\sqrt{A_0/\pi} = 0.417D_w$, where D_w is the WBC diameter in equilibrium. The RBC equilibrium spring length is $l_0 = 0.0384D_w$ and $l_m/l_0 = 2.2$. The RBC shape is biconcave, while WBCs have a circular shape in equilibrium. In all simulations, $k_b = 50k_BT$ for RBCs and $k_b = 500k_BT$ for WBCs. The blood cells (72 RBCs and one WBC at $H_t = 0.45$) are suspended in plasma, which is modeled by a collection of solvent particles.

We consider Poiseuille flow in the channel of width $W = 2D_w$, which is driven by a constant force applied to the solvent particles equivalently to a constant pressure gradient. To characterize the flow, we define a dimensionless shear rate as

$$\dot{\gamma}^* = \frac{\eta D_r^3 \bar{\dot{\gamma}}}{\kappa_r} = \tau\bar{\dot{\gamma}}, \tag{3}$$

where $\bar{\dot{\gamma}} = Q/W^2$ is the average shear rate, Q is the flow rate, η is the solvent viscosity, $\kappa_r = k_bl_0$ is the RBC bending rigidity, and $\tau = \eta D_r^3/\kappa_r$ is a characteristic relaxation time. The other important nondimensional number, which characterizes the ratio of cell elasticity to bending rigidity, is $\alpha = YD^2/\kappa$, where $Y = (-\partial^2 V_{sp}/\partial l^2)|_{l_0}$ is the stretching modulus. $\alpha_r = 1340$ for RBCs, which was roughly estimated to mimic a RBC stretching experiment [18], while α_w is assumed to be about 10 times larger. In addition, to make a WBC less deformable, $A_{0,w}$ is set to be 2% larger than the area of a circle with diameter D_w, which implies that the springs of WBCs are initially under a small strain. For comparison in physical units in three dimensions (3D), we assume that $D_w = 10\ \mu\text{m}$, $D_r = 4.17\ \mu\text{m}$, $W = 20\ \mu\text{m}$, $\eta = 10^{-3}\ \text{Pa}\cdot\text{s}$, $T = 37\,^\circ\text{C}$, $\kappa_r = 50k_BT$, and $Y = 18.9\ \mu\text{N/m}$.

Results and discussion.—Figure 2 presents the WBC center-of-mass distributions for various H_t values. The flow rate is approximately constant for different H_t with $\dot{\gamma}^* \approx 3.34$. The corresponding WBC distributions are averaged over the two halves of the channel and indicate WBC margination towards the wall ($y = 0$) with a peak around $y/W = 0.25$. The strongest margination effect is observed for a range of $H_t = 0.25$–0.35 (see also Fig. 1 and Ref. [15]), while WBC margination is attenuated at both lower and higher H_t values. As expected at low H_t, WBC margination is weak due to a low concentration of RBCs. However, at high H_t values, the simulated results seem to contradict the main hypothesis for WBC margination: a higher RBC concentration is expected to lead to more RBC crowding in the channel center, and therefore to stronger WBC migration towards the wall. Also, we notice that the peak position is slightly closer to the wall for higher H_t values; this shift is due to WBC deformability, such that the force on a WBC from flowing RBCs is stronger at a higher H_t, resulting in a more compressed WBC shape.

To identify the physical mechanism responsible for this observation, we examined the RBC distribution around a

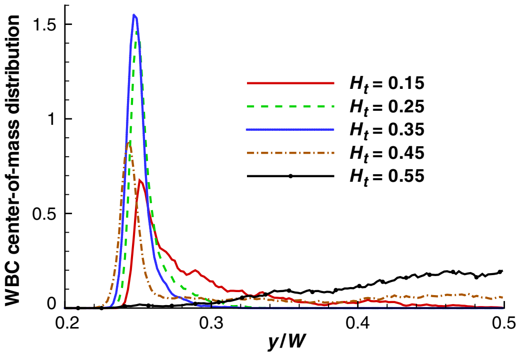

FIG. 2 (color online). WBC center-of-mass distribution for various H_t values at $\dot{\gamma}^* = 3.34$.

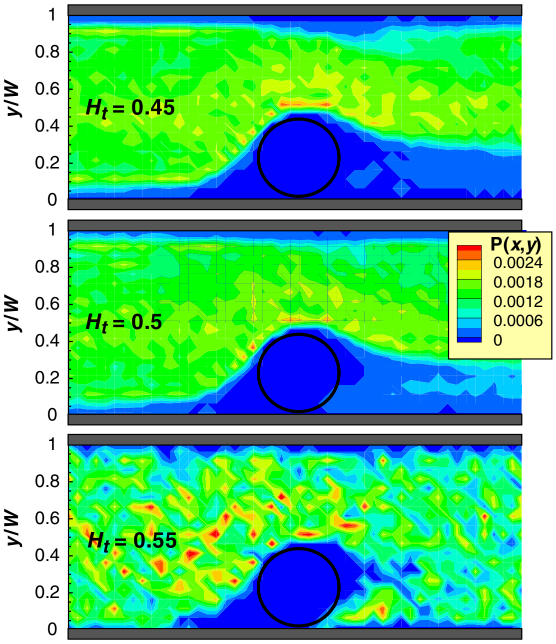

FIG. 3 (color online). RBC center-of-mass distributions around a marginated hard WBC for various H_t values at $\dot{\gamma}^* = 3.34$. The circle schematically shows the WBC location. The flow direction is from left to right.

marginated WBC. Figure 3 shows RBC center-of-mass distributions for various H_t and $\dot{\gamma}^* = 3.34$, computed in a comoving coordinate system of the WBC center of mass and with the condition that the WBC center is less than $0.55D_w$ away from one of the walls. This condition is equivalent to the WBC nearly touching the wall. At $H_t = 0.45$, the region downstream of the WBC near the wall is virtually void of RBCs and it remains free of RBCs during most of the simulated time of about 845τ. As hematocrit is increased to $H_t = 0.55$, RBCs are found to often enter the region downstream of the WBC due to high RBC crowding. RBCs in that region move slower than the WBC next to the wall, so that a RBC may enter the gap between the WBC and the wall and force the WBC to move away from the wall. This *"lift-off"* mechanism for the WBC is different from the lift force [19] due to cell-wall hydrodynamic interactions and is governed by the particulate nature of blood. The RBC distributions in Fig. 3 show that such lift-off events occur frequently at $H_t = 0.55$ and lead to the attenuation of WBC margination illustrated in Fig. 2 and Ref. [15].

Next, the effects of flow rate and WBC deformability on WBC margination are explored. In addition to the previously described setup referred to as "hard" WBCs, we consider both solid (nondeformable) WBCs and "soft" WBCs. The stretching modulus of a soft WBC is 3.2 lower than that of a hard WBC, and the specified area A_0 is set exactly to $\pi D_w^2/4$. The investigated average shear rates are $\dot{\gamma}^* \in \{1.57, 3.34, 5.41, 9.34, 18.68\}$. Such a thorough study of WBC margination allows us to construct WBC margination diagrams with respect to flow rate and hematocrit, as shown in Fig. 4. The probability of WBC margination is defined as the probability of the WBC center of mass being not further than $0.55D_w$ away from the channel walls. From these plots, we can see that the strongest WBC margination occurs within a certain range of H_t values and flow rates. For example, in the case of solid WBCs, WBC margination occurs with high probability for the ranges of $H_t = 0.2$–0.5 and $\dot{\gamma}^* = 1$–10. As the WBC becomes softer, the region of high probability for WBC margination shrinks considerably. Specifically, there is a pronounced dependence of WBC margination on flow rate, since a WBC may substantially deform at high flow rates and thus experience a strong lift force from the wall.

Our simulation results are also consistent with experimental observations that WBC adhesion occurs mainly in venules (not in arterioles) in the organism. The characteristic values of $\dot{\gamma}^*$ in venules of a comparable diameter are approximately in the range of $\dot{\gamma}^* = 1$–25, while, in arterioles, $\dot{\gamma}^* \gtrsim 30$ [20,21]. This estimation is based on the physiological parameters stated above; for example, $\dot{\gamma}^* = 10$ corresponds to the pseudoshear rate of 30 s^{-1} and the

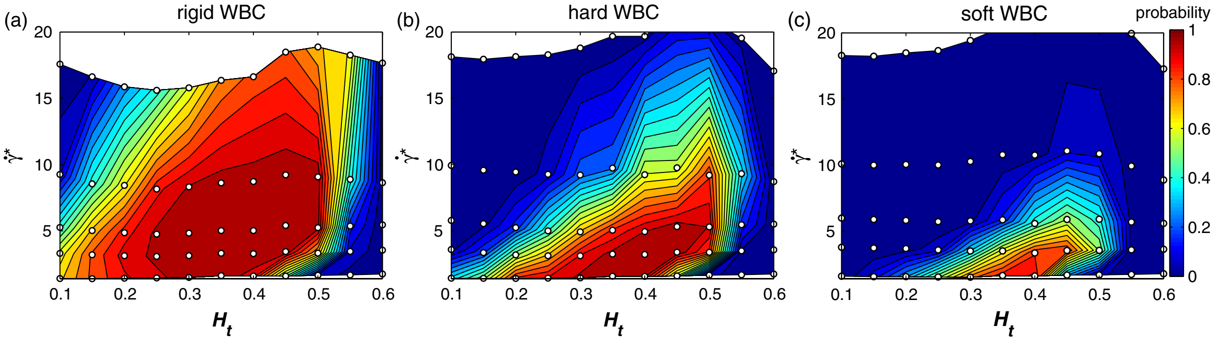

FIG. 4 (color online). Probability diagrams of WBC margination with respect to $\dot{\gamma}^*$ and H_t for various WBC deformabilities: (a) rigid WBC, (b) hard WBC, and (c) soft WBC. Symbols (○) indicate the values of H_t and $\dot{\gamma}^*$ for which simulations were performed.

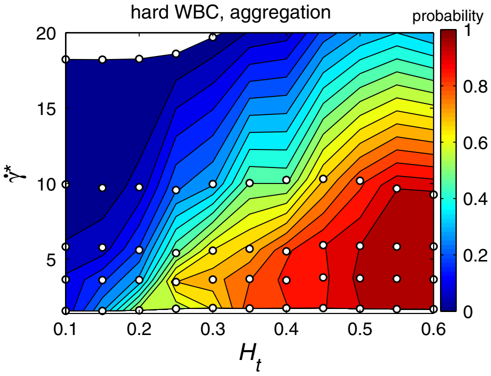

FIG. 5 (color online). Effect of RBC aggregation on WBC margination for the case of hard WBCs. Symbols (○) correspond to the performed simulations.

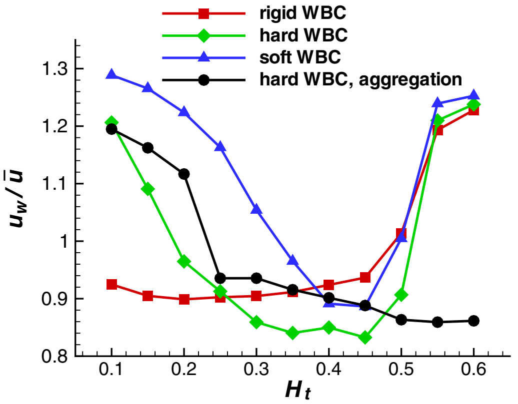

FIG. 6 (color online). WBC average velocity u_w for various H_t values normalized by the average flow velocity $\bar{u} = Q/W$. The curves for different cases correspond to $\dot{\gamma}^* \approx 3.34$.

average flow velocity of 0.6 mm/s. Thus, efficient WBC margination and consequent adhesion are mainly expected in the venular part of a microvascular network. Our results for the cases of soft and hard WBCs [Figs. 4(b) and 4(c)] show a more narrow range of $\dot{\gamma}^*$, where a WBC is marginated in comparison with the range of $\dot{\gamma}^* = 1$–25. Thus, we conclude that our rigid WBCs in 2D [Fig. 4(a)] provide the most realistic description of WBC margination phenomena in 3D. Of course, predictions of 2D simulations for 3D flows can only be semiquantitative and it is likely that the $\dot{\gamma}^*$ range for WBC margination is slightly shifted or expanded in 3D. However, our results are in good agreement with the experiments on leukocyte margination in rectangular microchannels [14], where the optimal hematocrit for WBC margination was identified to be in the range $H_t = 0.2$–0.3. They are also able to explain discrepancies with previous simulations [13] and experiments [12], which found WBC margination and adhesion to be independent of H_t, because studied flow rates and H_t values in Refs. [12,13] almost entirely fell into the region of strong WBC margination.

RBC aggregation is believed to enhance WBC margination in blood flow. In our model, aggregation interactions between RBCs are described by a Morse potential, with a strength adjusted to a force in the range of 3–7 pN, as estimated in recent 3D simulations on blood rheology [22]. Figure 5 shows the effect of RBC aggregation on WBC margination for the case of hard WBCs. In comparison with Fig. 4(b), the strong WBC margination region extends now to higher flow rates and H_t values. This is likely a consequence of a tighter RBC packing due to the aggregation forces, which result in a less-dispersed RBC core. The computed RBC distributions around the WBC for various H_t have confirmed that the region downstream of the WBC remains virtually free of RBCs even for high $H_t > 0.45$ values due to RBC aggregation, which substantially reduces the displacing effect of RBCs at high H_t, as illustrated in Fig. 3. Finally, no significant effect of RBC aggregation on WBC margination is found at high $\dot{\gamma}^*$ because RBC aggregates are completely dispersed at high shear rates [22,23].

WBC margination is closely related to WBC flow velocities. Results for the average WBC velocity normalized by the average flow velocity $\bar{u} = Q/W$ as a function of H_t are presented in Fig. 6 at $\dot{\gamma}^* \approx 3.34$. When margination occurs and the WBC moves near the wall, its velocity is significantly reduced in comparison with a WBC flowing near the center of the channel. In our simulations, the ratio $W/D_w = 2$ is relatively small, and therefore the velocity difference shown in Fig. 6 is only approximately 30%–40%. For larger channel widths, this difference is expected to increase quadratically with W/D_w. The reduced velocity of marginated WBCs compared to the average blood flow results in a many-fold increase of the WBC concentration in microcirculation (determined by the ratio of the average RBC and WBC velocities). This reduced velocity for marginated WBCs could also play an important role in an efficient adhesion [24,25] because it reduces the required adhesion forces accordingly.

In conclusion, WBC margination strongly depends on flow hydrodynamics (e.g., lift force), as well as on particulate properties of blood, including hematocrit, elasticity characteristics of blood cells, and their interactions. These 2D simulation results will be used to guide realistic 3D simulations in the future, which are able to quantitatively explore the WBC margination phenomena.

D. A. F. acknowledges funding by the Humboldt Foundation.

[1] U. Bagge and R. Karlsson, Microvasc. Res. **20**, 92 (1980).
[2] H. L. Goldsmith and S. Spain, Microvasc. Res. **27**, 204 (1984).
[3] J. C. Firrell and H. H. Lipowsky, Am. J. Physiol. **256**, H1667 (1989).

[4] K. Ley and T. F. Tedder, J. Immunol. **155**, 525 (1995).

[5] R. Alon, D. A. Hammer, and T. A. Springer, Nature (London) **374**, 539 (1995).

[6] T. A. Springer, Annu. Rev. Physiol. **57**, 827 (1995).

[7] H. L. Goldsmith, G. R. Cokelet, and P. Gaehtgens, Am. J. Physiol. **257**, H1005 (1989).

[8] G. R. Cokelet and H. L. Goldsmith, Circ. Res. **68**, 1 (1991).

[9] M. Abkarian, C. Lartigue, and A. Viallat, Phys. Rev. Lett. **88**, 068103 (2002).

[10] H. L. Goldsmith, Federation Proceedings **30**, 1578 (1971).

[11] M. J. Pearson and H. H. Lipowsky, Am. J. Physiol. **279**, H1460 (2000).

[12] K. B. Abbitt and G. B. Nash, Am. J. Physiol. **285**, H229 (2003).

[13] J. B. Freund, Phys. Fluids **19**, 023301 (2007).

[14] A. Jain and L. L. Munn, PLoS ONE **4**, e7104 (2009).

[15] See Supplemental Material at http://link.aps.org/supplemental/10.1103/PhysRevLett.108.028104 for simulation animations of WBC margination.

[16] P. J. Hoogerbrugge and J. M. V. A. Koelman, Europhys. Lett. **19**, 155 (1992).

[17] D. A. Fedosov, B. Caswell, and G. E. Karniadakis, Biophys. J. **98**, 2215 (2010).

[18] S. Suresh, J. Spatz, J. P. Mills, A. Micoulet, M. Dao, C. T. Lim, M. Beil, and T. Seufferlein, Acta Biomaterialia **1**, 15 (2005).

[19] S. Messlinger, B. Schmidt, H. Noguchi, and G. Gompper, Phys. Rev. E **80**, 011901 (2009).

[20] A. S. Popel and P. C. Johnson, Annu. Rev. Fluid Mech. **37**, 43 (2005).

[21] A. R. Pries, T. W. Secomb, and P. Gaehtgens, Am. J. Physiol. **269**, H1713 (1995).

[22] D. A. Fedosov, B. Pan, W. Caswell, G. Gompper, and G. E. Karniadakis, Proc. Natl. Acad. Sci. U.S.A. **108**, 11 772 (2011).

[23] Q. Zhao, L. G. Durand, L. Allard, and G. Cloutier, Ultrasound Med. Biol. **24**, 503 (1998).

[24] M. R. King and D. A. Hammer, Proc. Natl. Acad. Sci. U.S.A. **98**, 14 919 (2001).

[25] C. Korn and U. S. Schwarz, Phys. Rev. Lett. **97**, 138103 (2006).

P13: Predicting human blood viscosity in silico

D. A. Fedosov, W. Pan, B. Caswell, G. Gompper, and G. E. Karniadakis

Proceedings of the National Academy of Sciences USA, **108**:11772-11777, 2011.

Predicting human blood viscosity in silico

Dmitry A. Fedosov[a,b], Wenxiao Pan[b,c], Bruce Caswell[b], Gerhard Gompper[a], and George E. Karniadakis[b,1]

[a]Institute of Complex Systems and Institute for Advanced Simulation, Forschungszentrum Jülich, 52425 Jülich, Germany; [b]Division of Applied Mathematics, Brown University, Providence, RI 02912; and [c]Pacific Northwest National Laboratory, Richland, WA 99352

Edited by Charles S. Peskin, New York University, and approved June 13, 2011 (received for review January 24, 2011)

The viscosity of blood has long been used as an indicator in the understanding and treatment of disease, and the advent of modern viscometers allows its measurement with ever-improving clinical convenience. However, these advances have not been matched by theoretical developments that can yield a quantitative understanding of blood's microrheology and its possible connection to relevant biomolecules (e.g., fibrinogen). Using coarse-grained molecular dynamics and two different red blood cell models, we accurately predict the dependence of blood viscosity on shear rate and hematocrit. We explicitly represent cell–cell interactions and identify the types and sizes of reversible rouleaux structures that yield a tremendous increase of blood viscosity at low shear rates. We also present the first quantitative estimates of the magnitude of adhesive forces between red cells. In addition, our simulations support the hypothesis, previously deduced from experiments, of yield stress as an indicator of cell aggregation. This non-Newtonian behavior is analyzed and related to the suspension's microstructure, deformation, and dynamics of single red blood cells. The most complex cell dynamics occurs in the intermediate shear rate regime, where individual cells experience severe deformation and transient folded conformations. The generality of these cell models together with single-cell measurements points to the future prediction of blood-viscosity anomalies and the corresponding microstructures associated with various diseases (e.g., malaria, AIDS, and diabetes mellitus). The models can easily be adapted to tune the properties of a much wider class of complex fluids including capsule and vesicle suspensions.

blood rheology | blood modeling | shear thinning | aggregation force | dissipative particle dynamics

Rheological and material properties of cell, capsule, and vesicle suspensions have many applications in medicine, biology, engineering, and materials science. One of the main examples of such suspensions is blood, which consists of RBCs, predominant by volume, and a small fraction of other cells and proteins suspended in the plasma. Understanding blood flow and its relation to cellular properties and interactions may lead to advances in biomedical applications (e.g., drug delivery, blood substitutes). Moreover, a change in blood rheological and flow properties is often associated with hematological diseases or disorders (e.g., sickle-cell anemia, malaria), and therefore the viscosity of blood has long been used as an indicator in the understanding and treatment of disease.

Modern rheometry techniques and instruments yield reliable measurements of macroscopic properties of cell suspensions with ever-improving convenience—for example, the bulk properties of blood measured in various laboratories (1–6). Virtually all blood-viscosity measurements are necessarily in vitro, and before newly drawn blood is introduced into a viscometer it must at least be stabilized with an anticoagulant, which is then called "whole blood." Under flow conditions at small deformation rates, the RBCs in whole blood have been observed to aggregate into structures called "rouleaux," which resemble stacks of coins (1, 7–9). The aggregation process appears to be strongly correlated to the presence of the plasma proteins (7, 9). Experiments with washed RBCs resuspended in pure saline, to which fibrinogen was added progressively (7), showed a tremendous viscosity increase at low deformation rates with respect to fibrinogen concentration. In addition, such suspensions exhibit a yield stress (1, 10, 11)—i.e., a threshold stress for flow to begin.

However, these advances have not been accompanied by theoretical developments that can yield quantitative predictions of rheological and flow properties of blood. Recent theoretical and numerical studies focused mostly on the behavior of a single RBC in various flows (12–16). Several studies have been performed to simulate a suspension of multiple cells (16–19) in tube flow. So far, the connection between the rheology of a cell suspension and its microscopic properties on a single-cell level, such as structure or arrangement, cell viscoelastic properties, and local dynamics, is not well understood. In addition, cell suspensions are often further complicated by intrinsic cell interactions (e.g., RBC aggregation; refs. 1, 7–9). In this paper, we will establish such a link between bulk properties and microstructure, and will focus on the *quantitative* prediction of rheological properties and dynamics of blood flow by employing multiscale modeling of interacting red blood cells.

Results and Discussion

We consider suspensions of RBCs to mimic the experimental set up of washed RBCs suspended in pure saline, to which fibrinogen was added progressively (7), and we will refer to them as erythrocyte suspensions (ES). We simulate them with dissipative particle dynamics (DPD), a coarse-grained version of molecular dynamics suited to the seamless modeling of liquids and soft matter (14, 20, 21). Two different cell models are employed. The first, a multiscale RBC model (MS-RBC) (15) represents the RBC membrane with a few hundred DPD particles connected by viscoelastic springs into a triangular network in combination with out-of-plane elastic bending resistance, similar to the mesoscopic model in Refs. 12, 18, and 22. The characteristic biconcave RBC shape is achieved by imposition of constraints for constant membrane area and constant cell volume. Fitting of the model parameters is performed through a number of static and dynamic experiments on single real RBCs (15) and no further adjustment is made for the RBCs in suspension. Because simulations with MS-RBC are computationally expensive, we also employ a low-dimensional model (LD-RBC) of an RBC (23) for efficiency in parametric studies. LD-RBC is constructed as a closed torus-like ring of only 10 large hard colloidal particles, see *Methods* for more details. LD-RBC allows exploration of simulated blood flows over a wide range of hematocrits at computational costs considerably below those for their multiscale counterparts. In addition to the LD-RBC and MS-RBC models, we developed an aggregation model to reproduce the reversible rouleaux formation and destruction, which is essential to capture blood flow behavior, especially at low shear rates. Next, we present results for the ES viscosity with

---

Author contributions: D.A.F., W.P., B.C., G.G., and G.E.K. designed research; D.A.F. and W.P. performed research; D.A.F carried out multiscale RBC simulations; W.P. carried out low-dimensional RBC simulations; D.A.F. and W.P. analyzed data; D.A.F., W.P., B.C., G.G., and G.E.K. wrote the paper.

The authors declare no conflict of interest.

This article is a PNAS Direct Submission.

[1] To whom correspondence should be addressed. E-mail: george_karniadakis@brown.edu.

This article contains supporting information online at www.pnas.org/lookup/suppl/doi:10.1073/pnas.1101210108/-/DCSupplemental.

and without aggregation, rouleaux formation and magnitude of aggregation forces, yield stress, and the micro-to-macro link in ES.

In Silico Versus in Vitro Blood Viscosity. The experimental bulk viscosities of well-prepared nonaggregating ES and of whole blood were measured for various hematocrit values (H) at physiological temperature 37 °C in refs. 1–3. The blood viscosity in our work was derived from simulations of plane Couette flow using the Lees–Edwards periodic boundary conditions for both the MS-RBC and the LD-RBC suspensions. The shear rate and the cell density in our simulations were verified to be spatially uniform on average over time, and the viscosities were computed, with and without aggregation, as functions of the shear rate over the range 0.005–1,000.0 s^{-1} (this corresponds to the range of dimensionless shear rate or capillary number $\eta\dot{\gamma}D/Y$ between 2.5×10^{-6} and 0.5, where η is the solvent viscosity, D is the RBC diameter, and Y is the membrane Young's modulus). Fig. 1*A* shows the relative viscosity (RBC suspension viscosity normalized by the viscosity of the suspending media) against shear rate at hematocrit $H = 45\%$. The MS-RBC model predictions are in excellent agreement with the blood viscosities measured in three different laboratories (1–3). The ES model, consisting only of RBCs in suspension, clearly captures the effect of aggregation on the viscosity at low shear rates and suggests that cells and molecules other than RBCs have little effect on the viscosity, at least under healthy conditions. The LD-RBC model underestimates somewhat the experimental data, but is generally in good agreement over the whole range of shear rates, and again demonstrates the effect of aggregation. The agreement is remarkable in view of the simplicity and economy of that model. Errors in simulated viscosities shown in Fig. 1*A* are approximately 30% for the shear rate $\dot{\gamma} = 0.014\ \mathrm{s}^{-1}$ and decrease rapidly with the increase of $\dot{\gamma}$, becoming about 1–3% at high shear rates.

The dependence of whole blood and ES viscosity on hematocrit is demonstrated in Fig. 1*B*. The curves are measured viscosities as a function of H at constant shear rate by Chien et al. (2), and the points are calculated with the LD-RBC model. The plot clearly shows how the latter captures the (hematocrit) H dependence on viscosity, and that the model again demonstrates aggregation to be crucial for a quantitative account of the difference between the viscosity of whole blood and that of washed ES. Recent attempts in modeling (24, 25) of two-cell and multiple-cell aggregates (17) simulated only their flow behavior. Specifically, in ref. 17, the link of viscosity to RBC aggregation was investigated, but the viscosity predictions failed to capture the steep rise of that function at low shear rates.

Reversible Rouleaux Formation. The formation of rouleaux in blood occurs in equilibrium and at sufficiently small shear rates, whereas large shear rates result in immediate dispersion of fragile RBC structures. Experimentally, aggregation is observed (1, 4, 26) to be a two-step process: the formation of a few RBCs into short linear stacks, followed by their coalescence into long linear and branched rouleaux. As the shear rate increases, the large rouleaux break up into smaller ones, and at higher values, the suspension ultimately becomes one of monodispersed RBCs (27). This process then reverses as the shear rate is decreased.

This typical formation–destruction behavior of rouleaux is consistent with the results of our simulations using both the LD-RBC and the MS-RBC models as shown in Fig. 2 (see *SI Text*). At low shear rates (left frames), the initially dispersed RBCs aggregate into large rouleaux of up to about 20 RBCs; as the shear rate is increased to moderate values (middle frames), these structures are reduced in size until at high rates (right frames) they are dispersed almost completely into individual RBCs. Reversibility is demonstrated by reduction of the shear rate to the formation value, at which point individual RBCs begin to reaggregate.

Yield Stress and Aggregation. Whole blood is believed to exhibit a yield stress (i.e., a threshold stress for flow to begin) (1, 10, 11), but this has been difficult to confirm experimentally or theoretically. The most reproducible yield stresses for whole blood are those extrapolated to zero shear rate from viscometric data on the basis of Casson's equation given by (28)

$$\tau_{xy}^{1/2} = \tau_y^{1/2} + \eta^{1/2}\dot{\gamma}^{1/2}, \qquad [1]$$

where τ_y is a yield stress and η is the suspension viscosity at large $\dot{\gamma}$. Note that when the yield stress τ_y vanishes, Eq. **1** reduces to the Newtonian liquid. The assumptions of Casson's relation appear to hold at least at low shear rates, which was successfully demonstrated for pigment-oil suspensions (28), Chinese ovary hamster

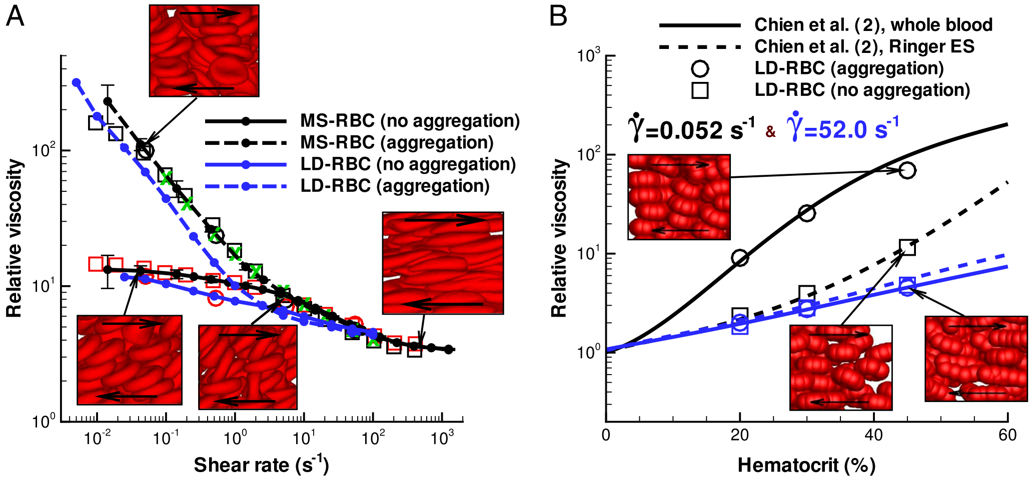

Fig. 1. Validation of simulation results for whole blood and Ringer ES. (*A*) Plot of non-Newtonian relative viscosity (the cell suspension viscosity normalized by the solvent viscosity) as a function of shear rate at $H = 45\%$ and 37 °C. Simulated curves of this work, as indicated and experimental points as follows: Whole blood: green crosses, Merril et al. (1); black circles, Chien et al. (2; black squares, Skalak et al. (3). Ringer ES: red circles, Chien et al. (2); red squares, Skalak et al. (3). Error bars on the MS-RBC viscosity curves reflect one standard deviation and each point on the simulated curves corresponds to a single simulation. (*B*) Plot of relative viscosity as a function of hematocrit (H) at shear rates 0.052 (black) and 5.20 (blue) s^{-1}: simulated (LD-RBC points), and Chien et al. (2) experimental fits for whole blood (solid lines), and Ringer ES (dashed lines).

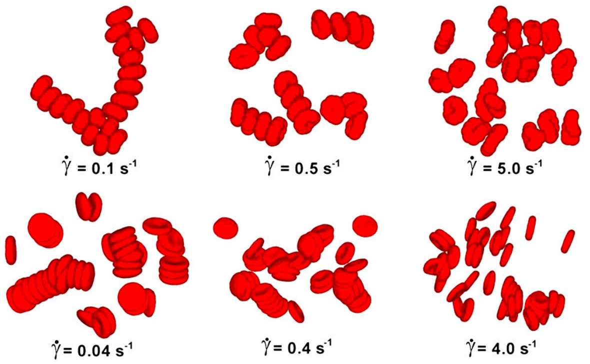

Fig. 2. Visualization of aggregation. Simulated reversible rouleaux are formed by LD-RBC model (*Upper*) and MS-RBC model (*Lower*) with $H = 10\%$. The left column corresponds to low shear rates, center column to moderate share rates, and right column to high shear rates as indicated on the plots; see *SI Text*.

cell suspensions (29), and blood (7). Following the extrapolation method in ref. 7, we fit a polynomial in Casson coordinates ($\dot{\gamma}^{1/2}$, $\tau_{xy}^{1/2}$) to the simulated data for a $H = 45\%$ suspension shown in Fig. 3*A*. The fitting clearly indicates the extrapolated τ_y to be nonzero for the aggregating RBC suspension and zero without cell aggregation.

The yield stress for blood has previously been attributed to the presence of rouleaux in experiments reported in refs. 1, 10 and 11. In practice, the measurement of yield stress is complicated by the nature of suspension and type of instrument used (30). As an example, at the lowest shear rates sedimentation and viscometer wall effects are complicating factors, and yield stresses derived from viscometric data are not consistent with those derived from nonrheological measurements (6). Merrill et al. (1) found τ_y of healthy human blood to lie between 0.0015 and 0.005 Pa at $H = 45\%$, and to vary as $H^{1/3}$, similar to the dependence Thurston (31) described for the elastic modulus of blood. Copley et al. (11) measured blood properties at very low shear rates down to 0.001 s^{-1}, and still found evidence for a yield stress. Fig. 3*B* shows that the simulated τ_y obtained by the extrapolation in Casson coordinates are in good agreement with viscometric data, consistent with the agreement between the computed and the measured viscosities.

Micro-to-Macro Link. The non-Newtonian nature of blood (e.g., shear thinning, yield stress) emerges from the interactions between cells and from their properties and dynamics. Therefore, we examined the structure and dynamics of the modeled suspensions on the level of single cells. We found null pair correlations of RBC *centers of mass* for each direction (x,y,z), which indicates that the cell suspensions do not self-assemble or order themselves in any direction at $H = 45\%$. This finding contradicts with suspensions of spherical colloids, which have been shown (32) to self-assemble near the close-packing concentration. To examine the cell suspension's local microstructure, we calculate the radial distribution function (RDF) of RBC centers shown in Fig. 4*A*. An equivalent isotropic structure factor can be found in *SI Text*. For the no-aggregation case, we find that no significant structures formed over the entire range of shear rates. At the lowest shear rate (red solid line), several small peaks in RDF indicate the presence of infrequent intermediate structures because RBCs may have enough time to relax locally at very low shear rates. A larger peak of the red solid curve at $r = 8$ µm, which is equal to the cell diameter, indicates that neighboring RBCs are often aligned with each other in the flow. As seen from the other solid curves (blue, green, and black), the correlations completely disappear at higher shear rates, and therefore the shear thinning behavior of a nonaggregating suspension is clearly not due to a change in microstructure. In contrast, several large peaks in the RDF function for the aggregating case at the lowest shear rate $\dot{\gamma} = 0.045$ s^{-1} (red dashed line) indicate the formation of rouleaux of two to four RBCs. An increase of the shear rate leads to the dispersion of rouleaux shown by the blue dashed curve in Fig. 4*A*, where predominant RBC aggregates are formed by only two RBCs. At shear rates above approximately 5–10 s^{-1}, no difference in microstructure is detected between aggregating and nonaggregating cell suspensions. As a conclusion, the steep increase in viscosity of the aggregating blood at low shear rates is mainly due to the cell aggregation into rouleaux. In addition, rouleaux formation also provides a plausible explanation for the existence of yield stress, because with decrease of shear rate, larger rouleaux structures are formed resulting in an eventual "solidification" of the suspension.

The dynamics of a single RBC in shear flow is characterized by the tumbling motion at low shear rates and membrane tank-treading at high shear rates (13–15). The tumbling-to-tank-treading transition occurs within a certain range of intermediate shear rates, where an RBC may experience high bending deformations

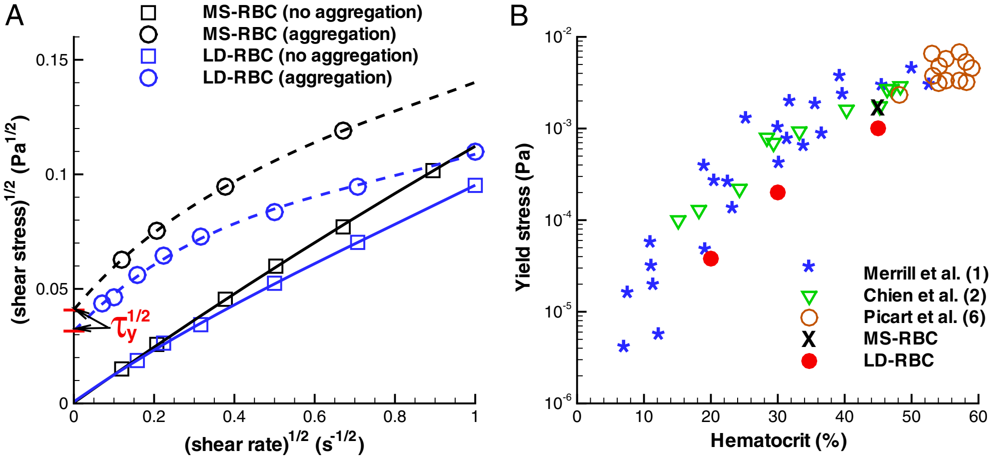

Fig. 3. Correlation of aggregation with yield stress. (*A*) Casson plots with a polynomial fit showing the extrapolated intercept τ_y for simulated MS-RBC and LD-RBC suspensions with (dashed lines) and without (solid lines) aggregation at $H = 45\%$. (*B*) Yield stress as a function of hematocrit H for simulated suspensions with aggregation compared with experimental values derived from viscosity measurements: blue stars, Merril et al. (1); green triangles, Chien et al. (2); open circles, Picart et al. (6).

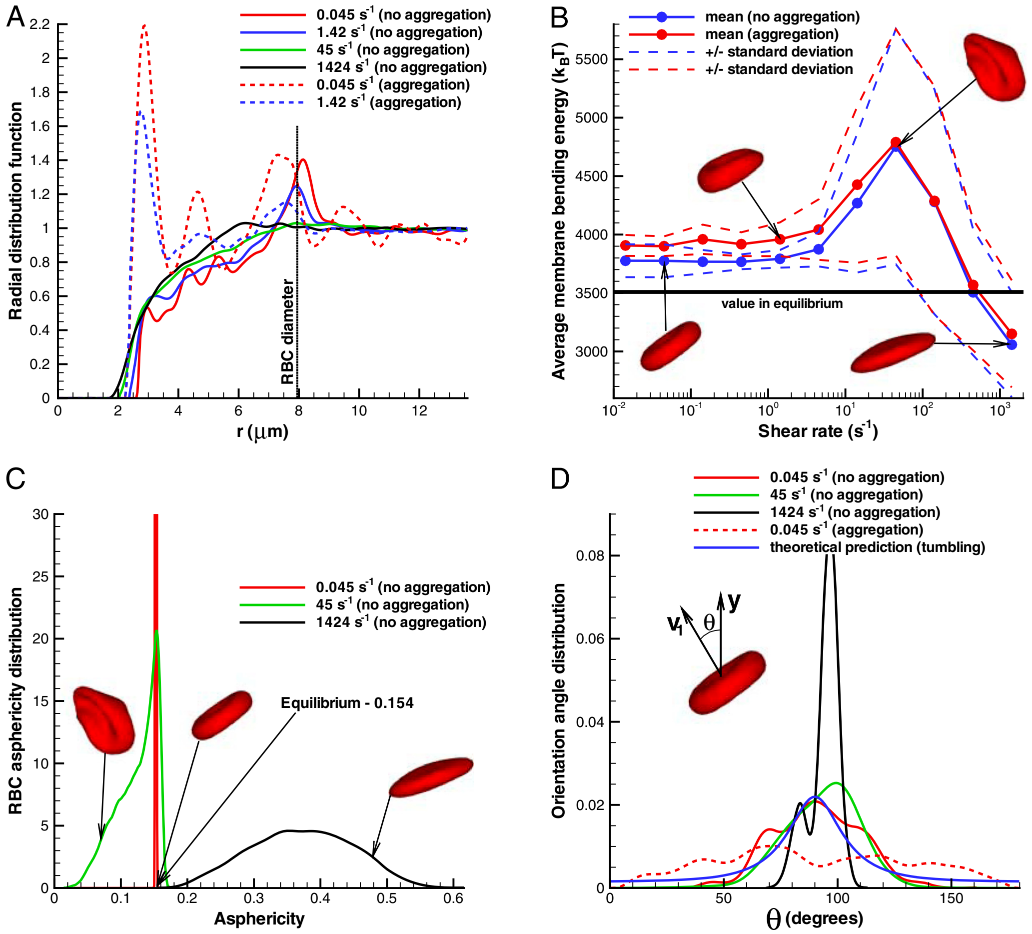

Fig. 4. Structural and dynamical properties of RBC suspensions with $H = 45\%$ for the MS-RBC model. Snapshots show sample RBC conformations from simulations. (*A*) Radial distribution function showing cell suspension's structure. (*B*) Average membrane bending energy with respect to shear rate showing correlation between single-cell deformation and dynamics. Dashed lines are the corresponding mean values ±1 SD. (*C*) RBC asphericity distributions characterizing the deviation from a spherical shape as a function of shear rate. The asphericity is defined as $[(\lambda_1-\lambda_2)^2+(\lambda_2-\lambda_3)^2+(\lambda_3-\lambda_1)^2]/(2R_g^4)$, where $\lambda_1 \le \lambda_2 \le \lambda_3$ are the eigenvalues of the gyration tensor and $R_g^2 = \lambda_1+\lambda_2+\lambda_3$. The asphericity for a single RBC in equilibrium is equal to 0.154. (*D*) Orientational angle distributions for various shear rates that illustrate single-cell dynamics. The cell orientational angle is given by the angle between the eigenvector V_1 of the gyration tensor and the flow-gradient direction (y). Theoretical prediction showing the orientational angle distribution of a single tumbling RBC in shear flow is calculated from the theory in ref. 13.

(15). The deformation, orientation, and dynamics of cells within the suspension is illustrated in Fig. 4 *B–D*. These plots show that cells in the suspension mostly tumble and retain their biconcave shape at low shear rates below 5 s^{-1}, which is confirmed by essentially no change in RBC bending energy and in its standard deviation (Fig. 4*B*), by the extremely narrow asphericity distribution around the equilibrium value of 0.154 (Fig. 4*C*), and by the wide orientational angle (θ) distribution in Fig. 4*D*. Cell tumbling at low shear rates is slightly hindered in nonaggregating suspensions in comparison to tumbling of a single RBC in shear flow due to cell crowding, which results in sliding of cells over each other; this is shown by a higher peak in the orientational angle distribution (green curve) in Fig. 4*D* with respect to the theoretical prediction (blue curve). In contrast, RBC tumbling in aggregating suspensions appears to be nearly uniform because RBCs tumble within multiple-cell rouleaux structures. At high shear rates, larger than about 200 s^{-1}, individual RBCs are subject to tank-treading motion illustrated by a narrow θ distribution (black line) in Fig. 4*D*. At yet higher shear rates, RBCs become strongly elongated as indicated by the RBC asphericity distribution in Fig. 4*C*.

The most interesting and complex cell dynamics, however, occurs in the broad intermediate regime of shear rates between 5 and 200 s^{-1}, where RBC aggregation interactions can be neglected. This range also corresponds to the main region of shear thinning for the nonaggregating cell suspension. In this range of shear rates, RBCs within the suspension experience severe deformations documented by a pronounced increase in the membrane bending energy and in its variation shown in Fig. 4*B*. The asphericity distribution for $\dot{\gamma} = 45$ s^{-1} in Fig. 4*C* shows that RBCs attain on average a more spherical shape, indicating transient folded conformations. These deformations may result in a reduction of shear stresses due to collisional constraints of cell tumbling, and therefore in shear thinning. In addition, the transition of some cells to the tank-treading motion further reduces the shear stresses contributing to the viscosity thinning.

Tunable Properties of Cell Suspensions. The computational framework presented herein is general and can be employed to investigate other cell, vesicle, and capsule suspensions with potential usage in biology, medicine, and engineering. The suspension properties may be tuned to yield a desired behavior by changing

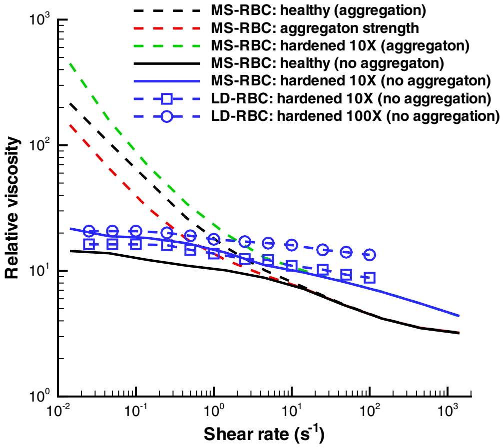

Fig. 5. Tunable properties of cell suspensions. MS-RBC and LD-RBC models with $H = 45\%$. Black lines are viscosities of healthy blood with and without aggregation by MS-RBC. Red line illustrates a decrease in cell aggregation strength reduced twice. Blue and green lines represent the viscosities of hardened RBC suspensions with 10× (MS-RBC and LD-RBC) and 100× (LD-RBC) higher Young's modulus than that in health. Each point on the simulated curves corresponds to a single simulation.

the solvent viscosity, material properties of suspended cells, and intercell aggregation interactions. Fig. 5 shows several examples of the tunable properties of cell suspensions. Results for cells with 10 and 100 times higher Young's modulus than healthy RBCs (blue and green curves) show a considerable increase of viscosity. Hardened RBCs are known (33, 34) to increase their suspension viscosities, and they are highly relevant in many hematologic disorders and diseases, e.g., malaria, sickle-cell anemia, spherocytosis. In addition, aggregating suspensions of stiffer cells show a steeper rise in viscosity at low shear rates resulting in a substantially higher yield stress. Fig. 5 also illustrates the expected decrease, relative to whole blood, in the suspension viscosity at low shear rates (red curve) due to a twofold reduction in the aggregation strength (D_e, see *Methods*). The significant change in viscosity observed above implies a strong dependence of flow properties on cell deformability and adhesive cell interactions.

Magnitude of Aggregation Forces. The predictions of Fig. 1 show that a suspension of modeled RBCs captures the viscosity of healthy whole blood with cell aggregation. The plausibility of the aggregation strength was checked by calculation of the maximum force needed to break up two aggregated RBCs (see *SI Text*). The breakup pulling force in the normal direction is about 3.0–7 pN, where the lower value corresponds to a peeling breakup. Tangential or sliding breakup requires a force in the range of 1.5–3 pN. These forces are much smaller than those imposed on single RBCs in stretching tests with optical tweezers (35), and they are consistent with observations of rouleaux, which do not show any large cell deformations. In addition, measurements of a disaggregation force in shear flow by Chien et al. (36) indicate that the shear stress required to break up a rouleaux structure lies approximately between 0.01 and 0.1 Pa, whereas the analogous simulations with the MS-RBC model yield about 0.02 Pa (see *SI Text*).

Conclusions. The accurate prediction of the non-Newtonian behavior from simulations of cell suspensions suggests a new paradigm for rheology of cell suspensions and blood in particular. As an example, an abnormal increase in RBC aggregation is a pathological state associated with many diseases, such as deep venous thrombosis, atherosclerosis, AIDS, myeloma, and diabetes mellitus, which may afflict many different sites of the human arterial tree (37–40). However, such correlations have had few theoretical guidelines for their interpretation. The modeling of cells whose parameters are determined from experiments on single cells (41) can be extended to abnormal and diseased cells, and in combination with the aggregation model, their suspensions can be simulated to allow quantitative comparison with rheological measurements and to guide in vivo ultrasonic measurements to yield a more precise diagnosis of the aforementioned diseases (40). The predictive capability of accurate modeling of cell and capsule suspensions can be readily extended to a variety of engineering and material science applications. Such simulations may aid in the development of new soft materials and may drive the tuning process and optimization of their properties.

Methods

Simulation Method. The DPD method (20, 21) is a particle-based mesoscopic simulation technique. A DPD system is represented by N point particles, which interact through pairwise soft potentials and move according to the Newton's second law of motion; see also *SI Text*.

RBC Models. An MS-RBC (15) is constructed by a collection of discrete points (500 in this work), which are the vertices of a triangular network of springs with a "dashpot" on the membrane surface. The network assumes fixed connectivity and supplies the elastic and the viscous response of an RBC membrane. To mimic membrane bending rigidity, a bending resistance is implemented between all neighboring triangular plaquettes. In addition, area and volume constraints are enforced to model incompressibility of an RBC membrane and the cytosol, respectively. The LD-RBC model (23) is constructed as a closed torus-like ring of 10 overlapping colloidal particles connected by springs. Each colloidal particle is represented by a single DPD particle with a repulsive core. A bending resistance between two neighboring springs is also incorporated. More details on the RBC models can be found in the *SI Text*.

Aggregation Models. For a blood suspension, the attractive cell–cell interactions are crucial for simulation of aggregation into rouleaux. These forces are approximated using the Morse potential $U(r) = D_e[e^{2\beta(r_0-r)} - 2e^{\beta(r_0-r)}]$, where r is the separation distance, r_0 is the zero force distance, D_e is the well depth of the potential, and β characterizes the interaction range. For the MS-RBC model, the Morse potential interactions are implemented between every pair of vertices of separate RBCs if they lie within a defined potential cutoff radius. For the LD-RBC model, the aggregation force acts between centers of mass of different RBCs if the cells are properly aligned. Thus, the Morse potential is applied only if the angle between the normals of two cells does not exceed a critical angle. The aggregation forces for blood were calibrated for a single shear rate and no further adjustments were made in the subsequent computation of suspension viscosity. More details on the aggregation models can be found in the *SI Text*.

ACKNOWLEDGMENTS. This work was supported by National Institutes of Health Grant R01HL094270 and simulations were performed on the Cray XT5 at the National Science Foundation–National Institute for Computational Science and at the Jülich Supercomputing Center in Germany.

1. Merrill EW, et al. (1963) Rheology of human blood near and at zero flow. *Biophys J* 3:199–213.
2. Chien S, Usami S, Taylor HM, Lundberg JL, Gregersen MI (1966) Effects of hematocrit and plasma proteins on human blood rheology at low shear rates. *J Appl Physiol* 21:81–87.
3. Skalak R, Keller SR, Secomb TW (1981) Mechanics of blood flow. *J Biomech Eng* 103:102–115.
4. Schmid-Schönbein H, Wells RE (1971) Rheological properties of human erythrocytes and their influence upon the "anomalous" viscosity of blood. *Ergeb Physiol Biol Chem Exp Pharmakol* 63:146–219.
5. Thurston GB (1996) *Advances in Hemodynamics and Hemorheology*, ed TV How (JAI Press, Greenwich, CT), pp 1–30.
6. Picart C, Piau JM, Galliard H (1998) Human blood shear yield stress and its hematocrit dependence. *J Rheol* 42:1–12.

7. Merrill EW, Gilliland ER, Lee TS, Salzman EW (1966) Blood rheology: Effect of fibrinogen deduced by addition. *Circ Res* 18:437–446.
8. Chien S, et al. (1967) Blood viscosity: Influence of erythrocyte aggregation. *Science* 157:829–831.
9. Chien S, Usami S, Kellenback RJ, Gregersen MI (1970) Shear-dependent interaction of plasma proteins with erythrocytes in blood rheology. *Am J Physiol* 219:143–153.
10. Cokelet G, et al. (1963) The rheology of human blood—measurement near and at zero shear rate. *Trans Soc Rheol* 7:303–317.
11. Copley AL, Huang CR, King RG (1973) Rheogoniometric studies of whole human blood at shear rates from 1000 to 0.0009 sec^{-1}. I. Experimental findings. *Biorheology* 10:17–22.
12. Noguchi H, Gompper G (2005) Shape transitions of fluid vesicles and red blood cells in capillary flows. *Proc Natl Acad Sci USA* 102:14159–14164.
13. Abkarian M, Faivre M, Viallat A (2007) Swinging of red blood cells under shear flow. *Phys Rev Lett* 98:188302.
14. Pivkin IV, Karniadakis GE (2008) Accurate coarse-grained modeling of red blood cells. *Phys Rev Lett* 101:118105.
15. Fedosov DA, Caswell B, Karniadakis GE (2010) A multiscale red blood cell model with accurate mechanics, rheology, and dynamics. *Biophys J* 98:2215–2225.
16. Pozrikidis C (2010) *Computational Hydrodynamics of Capsules and Biological Cells*, ed C Pozrikidis (CRC, Boca Raton, FL).
17. Liu Y, Liu WK (2006) Rheology of red blood cell aggregation by computer simulation. *J Comput Phys* 220:139–154.
18. McWhirter JL, Noguchi H, Gompper G (2009) Flow-induced clustering and alignment of vesicles and red blood cells in microcapillaries. *Proc Natl Acad Sci USA* 106:6039–6043.
19. Fedosov DA, Caswell B, Suresh S, Karniadakis GE (2010) Quantifying the biophysical characteristics of *Plasmodium-falciparum*-parasitized red blood cells in microcirculation. *Proc Natl Acad Sci USA* 108:35–39.
20. Hoogerbrugge PJ, Koelman JMVA (1992) Simulating microscopic hydrodynamic phenomena with dissipative particle dynamics. *Europhys Lett* 19:155–160.
21. Espanol P, Warren P (1995) Statistical mechanics of dissipative particle dynamics. *Europhys Lett* 30:191–196.
22. Noguchi H, Gompper G (2004) Fluid vesicles with viscous membranes in shear flow. *Phys Rev Lett* 93:258102.
23. Pan W, Caswell B, Karniadakis GE (2010) A low-dimensional model for the red blood cell. *Soft Matter* 6:4366–4376.
24. Bagchi P, Popel AS, Johnson PC (2005) Computational fluid dynamic simulation of aggregation of deformable cells in a shear flow. *J Biomech Eng* 127:1070–1080.
25. Wang T, Pan TW, Xing ZW, Glowinski R (2009) Numerical simulation of rheology of red blood cell rouleaux in microchannels. *Phys Rev E Stat Nonlin Soft Matter Phys* 79:041916.
26. Samsel RW, Perelson AS (1982) Kinetics of rouleau formation: I. A mass action approach with geometric features. *Biophys J* 37:493–514.
27. Zhao Q, Durand LG, Allard L, Cloutier G (1998) Effects of a sudden flow reduction on red blood cell rouleau formation and orientation using RF backscattered power. *Ultrasound Med Biol* 24:503–511.
28. Casson N (1992) *Rheology of Disperse Systems*, ed CC Mill (Pergamon, New York), pp 84–104.
29. Iordan A, Duperray A, Verdier C (2008) Fractal approach to the rheology of concentrated suspensions. *Phys Rev E Stat Nonlin Soft Matter Phys* 77:011911.
30. Meiselman HJ (1980) *Erythrocyte Mechanics and Blood Flow*, eds GR Cokelet, HJ Meiselman, and DE Brooks (Liss, New York), pp 75–117.
31. Thurston GB (1972) Viscoelasticity of human blood. *Biophys J* 12:1205–1217.
32. Pan W, Caswell B, Karniadakis GE (2010) Rheology, microstructure and migration in Brownian colloidal suspensions. *Langmuir* 26:133–142.
33. Chien S, Usami S, Dellenback RJ, Gregersen MI (1967) Blood viscosity: Influence of erythrocyte deformation. *Science* 157:827–829.
34. Brooks DE, Goodwin JW, Seaman GV (1970) Interactions among erythrocytes under shear. *J Appl Physiol* 28:172–177.
35. Suresh S, et al. (2005) Connections between single-cell biomechanics and human disease states: Gastrointestinal cancer and malaria. *Acta Biomater* 1:15–30.
36. Chien S, Sung LA, Kim S, Burke AM, Usami S (1977) Determination of aggregation force in rouleaux by fluid mechanical technique. *Microvasc Res* 13:327–333.
37. Dintenfass L (1980) Molecular rheology of human blood: Its role in health and disease (today and tomorrow). *Proc 8th Int Cong Rheol (Naples)*, eds G Astarita, G Marrucci, and L Nicilais 3 (Springer, New York), pp 467–480.
38. Lowe GDO (1998) *Clinical Blood Rheology*, (CRC, Boca Raton, FL), 1–2.
39. Robertson AM, Sequeira A, Kameneva MV (2008) Hemodynamical flows. *Modeling, Analysis and Simulation)*, 37 (Birkhauser, Basel), pp 63–120.
40. Franceschini E, et al. (2010) Ultrasound characterization of red blood cell aggregation with intervening attenuating tissue-mimicking phantoms. *J Acoust Soc Am* 127:1104–1115.
41. Bao G, Suresh S (2003) Cell and molecular mechanics of biological materials. *Nat Mater* 2:715–725.